NASA Technical Memorandum 80339

Reports of Planetary Geology Program, 1978–1979

JUNE 1979

NASA

NASA Technical Memorandum 80339

Reports of Planetary Geology Program, 1978–1979

Compiled by Joseph Boyce and Patricia S. Collins
NASA Office of Space Science
Washington, D.C.

NASA
National Aeronautics
and Space Administration

Scientific and Technical
Information Branch

1979

FOREWORD

This is a compilation of abstracts of reports from Principal Investigators of NASA's Office of Space Science, Planetary Division, Planetary Geology Program.

The purpose is to provide a document which succinctly summarizes work conducted in this program. Each report reflects significant accomplishments within the area of the author's funded grant or contract.

No attempt has been made to introduce editorial or stylistic uniformity; on the contrary, the style of each report is that of the Principal Investigator and may best portray his research. Bibliography information will be included in a separately published document.

Full reports of selected abstracts were presented to the annual meeting of Planetary Geology Principal Investigators at Brown University June 6-8, 1979. This year marks the tenth anniversary of the annual meeting of Planetary Geology Principal Investigators.

Stephen E. Dwornik
Discipline Scientist
Planetary Geology Program

Joseph M. Boyce
Staff Scientist
Planetary Geology Program

CONTENTS

CHAPTER 1-ASTEROID, COMETS AND SATELLITES

CHAPTER 2-STRUCTURE TECTONICS AND STRATIGRAPHY

CHAPTER 2-STRUCTURE TECTONICS AND STRATIGRAPHY (Continued)

CHAPTER 2-STRUCTURE TECTONICS AND STRATIGRAPHY (Continued)

CHAPTER 3-CRATERING AS A PROCESS, LANDFORM AND DATING METHODS

CHAPTER 3-CRATERING AS A PROCESS, LANDFORM AND DATING METHODS (Continued)

CHAPTER 3-CRATERING AS A PROCESS, LANDFORM AND DATING METHODS (Continued)

CHAPTER 4-VOLATILES AND REGOLITH

CHAPTER 4-VOLATILES AND REGOLITH (Continued)

CHAPTER 5-VOLCANIC PROCESSES

CHAPTER 5-VOLCANIC PROCESSES (Continued)

CHAPTER 6-EOLIAN PROCESSES

CHAPTER 6-EOLIAN PROCESS (Continued)

CHAPTER 7-FLUVIAL PROCESSES

CHAPTER 7-FLUVIAL PROCESSES (Continued)

CHAPTER 8-RADAR STUDIES OF PLANETARY SURFACES

CHAPTER 9-GALILEAN SATELLITES

CHAPTER 10-INSTRUMENT DEVELOPMENT AND TECHNIQUES

CHAPTER 10-INSTRUMENT DEVELOPMENT AND TECHNIQUES (Continued)

CHAPTER 11-PLANETARY CARTOGRAPHY, GEODESY AND GEOLOGIC MAPPING

CHAPTER 11-PLANETARY CARTOGRAPHY, GEODESY AND GEOLOGIC MAPPING (Continued)

CHAPTER 12-WORKSHOPS AND SPECIAL PROGRAMS

CHAPTER 12-WORKSHOPS AND SPECIAL PROGRAMS (Continued)

Chapter 1

ASTEROIDS, COMETS AND SATELLITES

“PAGE MISSING FROM AVAILABLE VERSION”

Earth-crossing Asteroids: Orbital classes, Population, and Fluctuation of Population in Late Geologic Time

E. M. Shoemaker, J. G. Williams, E. F. Helin, and R. F. Wolfe, California Institute of Technology, Pasadena, California 91125

The term Earth-crossing asteroid is here taken to mean a minor planet on an orbit which, as a consequence of secular perturbations, can intersect the orbit of the Earth. Known classes of Earth-crossing asteroids include Aten asteroids ($a < 1.0$ AU, $Q \geq 0.983$ AU), Apollo asteroids ($a \geq 1.0$ AU, $q \leq 1.017$ AU), and Amor asteroids ($a > 1.0$ AU, $1.017 \text{ AU} < q \leq 1.3$ AU). All three known Atens, all but one or two of the 23 known Apollos, and half of the 20 known Amors are Earth crossers. The total population of Earth-crossing asteroids to V(1,0) = 18 is estimated at ~ 1.3×10^3, of which ~ 8% are Atens, ~ ½ are Apollos, and ~ 40% are Amors.

A wide variety of physical types is represented among the Earth crossers, including four objects with UBV colors in the C field, several S-type objects, and several objects of distinctive colors that fall outside the C and S fields. The Earth crossers probably are of diverse origin; some probably have been derived from a residual population of old Mars crossers, some from widely separated regions of the main asteroid belt, and some from short-period comets. The principal sources appear to be extinct comet nuclei and collision fragments from regions in the main asteroid belt bordering the $\dot{\nu}_5$ and $\dot{\nu}_6$ secular resonances and the 3:1 and 5:2 commensurabilities with Jupiter.

A revised theory for the probability of collision of Earth-crossing asteroids with the Earth has been developed which takes appropriate account of the secular variation of the orbital elements of the asteroids and of the Earth. The present collision rate of Earth-crossing asteroids with the Earth is estimated at ~ 3½ objects to absolute magnitude 18 per million years (table 1).

Table 1
Collision rate with Earth of known classes of Earth-crossing asteroids

	Population to V(1,0)=18	Mean Collision Probability	Collision Rate to V(1,0)=18
		10^{-9}yr^{-1}	10^{-6}yr^{-1}
Atens	~ 100	9.1	~ 0.9
Apollos	700 ± 300	2.7	1.9 ± 0.8
Earth-crossing Amors	~ 500	~ 1	~ 0.5
Total	~1300		~ 3½

An important set of observations of asteroids in 1978 was the discovery of new Earth-crossing asteroids of low albedo. If UBV colors in the C color domain are taken as evidence for probable low albedo, then 1978 SB, the largest Earth crosser now known, probably is a low albedo object, and the bulk of the volume of known Earth crossers is contained in low albedo objects. This suggests that at least half and probably the majority of Earth crossers, to any given size limit, are dark objects. As shown in Table 2, this leads to a significant increase in the estimated present rate of crater production on the Earth.

Table 2
Estimates of Present Cratering Rate on Earth

	Calculated production of craters $\geq$ 10 km diameter	Last 1/2 b.y. record on North America
	$10^{-14} km^{-2} yr^{-1}$	$10^{-14} km^{-2} yr^{-1}$
All objects bright ($p_V = 0.14$)	~ 1.6	2.2 ± 1.1
Half bright, half dark	~ 2.4	
All objects dark ($p_V = 0.037$)	~ 3.6	
Equivalent cratering rate on Earth from last 3.3 b.y. record on Moon		1.1 ± 0.5

Assuming that half of the Earth-crossing asteroids are similar in albedo to S-type asteroids (mean $p_V = 0.14$) and half are similar in albedo to C-type asteroids (mean $p_V = 0.037$), the estimated present production of craters $\geq$ 10 km diameter on Earth is $\sim 2.4 \times 10^{-14} km^{-2} yr^{-1}$. This estimate takes into account probable differences in density between S and C objects, void space in the asteroids due to brecciation, corrections to the estimated volumes of the asteroids required for irregular shapes of their surfaces, and collapse of craters $\geq$ 10 km diameter found on the Earth. The resulting estimated cratering rate is practically indistinguishable from the estimated average production of impact craters in the last half billion years on North America (table 2).

The cratering rate estimated from asteroid data and that estimated from the Phanerozoic geologic record in North America have comparable uncertainties. Both estimates are likely to be minimum values, as they depend on completeness of survey of regions sampled. Both estimates are twice as high as the equivalent average cratering rate on Earth derived from the density of craters on 3.3 billion year old surfaces on the Moon. Corrections are made in deriving the terrestrial cratering rate from the lunar record for differences in the capture cross-sections of the Earth and Moon, for differences in crater scaling in the gravity fields of the two bodies, and for collapse of craters $\geq$ 10 km diameter on the Earth. The estimate of long term average cratering rate derived from the lunar record is a maximum, owing to the fact that craters older than 3.3 b.y. may sometimes be erroneously counted as formed on 3.3 b.y. lava surfaces.

It now appears that the difference between the 3.3 b.y. average cratering rate obtained from the Moon and the 0.5 b.y. average cratering rate obtained from the Earth probably should be regarded as real. A factor of 2 increase in cratering rate in the last half billion years implies a corresponding increase in the population of Earth-crossing asteroids. If the Earth-crossing asteroids are derived primarily from extinct comets, the increase in Earth-crossing asteroids may be related to an increase in the flux of long period comets crossing the orbit of Jupiter. Fluctuation in the comet flux reflects changes in the number or mass of stars passing near the Sun that perturb the Oort cometary cloud. We tentatively conclude that the average flux of stars in the solar neighborhood has been higher during the last half billion years than during the preceeding 3 billion years.

Asteroid Collisions and Evolution. Clark R. Chapman, Donald R. Davis, Richard J. Greenberg, Planetary Science Institute, 2030 East Speedway, Tucson, Arizona, 85719, and John Wacker, Department of Planetary Science, University of Arizona, Tucson, Arizona 85721.

Collisions have been the dominant process affecting asteroids since their formation early in solar system history. Understanding asteroid fragmentation processes and collisional evolution is necessary to investigate the early history of asteroids and to understand the processes that shaped the present asteroid size-frequency distribution, rotational states and orbital distribution. Dohnanyi (1) found that a population with a power law mass frequency distribution having a slope 11/6 (cumulative) is an equilibrium population, independent of the initial slope. The theoretical equilibrium slope agreed well with the observed value of 1.839 that Dohnanyi found using PLS data. Hence, he concluded that the distribution for most asteroids had collisionally relaxed to an equilibrium distribution. Subsequent new data on asteroid diameters indicated that the asteroid population could not be adequately represented by a power law distribution. In an earlier work, Chapman and Davis (2) argued on the basis of preliminary computer models that the present asteroid belt was possibly the remnant of a much larger population and, based on a genetic model for the "C" and "S" types of asteroids developed by Chapman (3,4), the initial C population was estimated to be about 300 times its present value.

Based on improved collisional models, Chapman et al. (5) argued that many large, gravitationally bound, asteroids may be thoroughly fractured gravitationally bound "rubble piles." We have continued to investigate asteroid collisional evolution over the 4.5 Gy age of the solar system using two computer models; one treats the simultaneous mass and orbital distribution of a single population, including erosive cratering collisions as well as catastrophic disruptive collisions, while the second program models the simultaneous mass evolution of two interacting populations having different physical properties and mean collision speeds, but considering only catastrophic collisions. A description of the collisional physics and computational algorithms in these programs is given in Davis et al. (6)

The collisional evolution of different combinations of initial populations and physical parameters was traced to find those which evolve to the present belt. Three different shapes for the initial asteroid population were considered: (a) power law, (b) segmented power law of the type found by Greenberg et al. (7), having a few large (∿1000 km diameter) bodies but most of the mass in much smaller bodies, and (c) "Gaussian" about a mean size. Numerical values of important parameters used in our models are given in Table 1. Values of impact strength, adopted from Greenberg et al. (7), are experimentally determined values appropriate for solid rock and basalts for S asteroids, while for C asteroids, the value chosen is representative of weakly bonded material such as consolidated dirt clumps investigated by Hartmann (8). The value for f_{KE} is typical of values computed by O'Keefe and Ahrens (9) for anorthosite and iron projectiles impacting anorthosite targets at speeds of 5-45 km/sec. Collisional fragments are assumed to have a velocity distribution which we model as $f = (v/v_c)^{-k}$, where f is the fraction of ejecta mass moving with speed >v, v_c is a parameter varying with the total ejecta kinetic energy. The slope of the ejecta velocity distribution, v_b, is derived from Gault et al. (10), while cratering mass excavation coefficients are those adopted by Greenberg et al. for weak (C) and rocky (S) material. Most populations distributed as (a) or (b) evolve to the present belt; only those having a much larger number of bodies bigger than ∿400 km diameter fail to match the present belt. Figure 1 shows the evolution of 3 initial populations. However, populations distributed as (c) about a mean diameter ∿100 km fail to match the present belt for reasonable collisional parameters.

Both small and large initial belt masses evolve to the present belt using plausible collisional parameters, provided they are distributed as in (b) above, but only modestly larger belts are possible with power law distributions. (a) collisional models to date do not give a unique answer to the question of what was the asteroid population at the time mean collision velocities were increased to their present value of ∿5 km/sec. As asteroid collisions alter rotations, the asteroid rotation theory developed by Harris (11) was applied to determine if additional constraints could be placed on the initial asteroid population or collisional parameters. This theory calculates rotation rates as the equilibrium values between infrequent large collisions tending to spin up asteroids and numerous small collisions which dampen rotation. For populations with a power law distribution, the predicted rotation rate for large gravitationally bound asteroids agrees with the observed mean rotation rate, only if most (50-100%) of the collisional kinetic energy is converted into kinetic energy of ejecta. This is a much larger fraction than the ∿10% we adopt for collisional evolution (Table 1), hence, unless large scale collisions are much more efficient in converting collisional energy into ejecta kinetic energy than we currently believe, asteroids larger than ∿100 km diameter have not yet been spun up to their theoretical equilibrium value. If earlier populations were significantly larger than the present one, equilibrium rotations would be reached on timescales shorter than the age of the solar system, consequently, earlier populations could not have been much bigger than what we see today; a result which agrees with collisional evolution modeling. Present rotational theory is not capable of treating non-power law population distributions such as those of (b) above.

TABLE 1: COLLISIONAL EVOLUTION PROGRAM PARAMETERS

	C ASTEROIDS	S ASTEROIDS
Density (g/cc)	2.5	3.5
Impact Strength (erg/cm^3)	6×10^4	3×10^7
Mean Collision Speed (km/sec)	5	5
Fraction of Collisional KE Partitioned into Ejecta KE (f_{KE})	0.1	0.1
Slope of Ejecta Velocity Distribution	-2.25	-2.25
Mass Excavation for Cratering Impacts (gm/erg)	10^{-8}	10^{-9}

The effect of a population of Jupiter-scattered planetesimals (JSP) on the asteroid belt was investigated. Such populations are effective at collisionally destroying asteroids (provided the JSP population mass and distribution is comparable to that of the target asteroid belt), since the JSP collision speed is ≳ 3 km/sec. In most cases, the collision speed is comparable to or greater than that in the present belt. A massive early asteroid belt could have been collisionally ground down by JSP; however, collisions with JSP are not a viable mechanism to explain the high mean collision speed in the present belt. For plausible JSP distributions, asteroids will be collisionally destroyed before their orbits can be appreciably changed by cratering impacts. Velocities might be augmented among the fragments of a catastrophic collision and several generations of fragmentation could result in significant orbital changes for the debris; however, the typical size of a multi-generation fragment would be smaller than most asteroids. Pallas, moving on a highly inclined eccentric orbit, is the best argument against such a scenario. There is, however, another mechanism by which JSP would have stirred up asteroid orbits enough to account for the present high collision speed, namely by gravitational scattering. If the largest JSP were at least as massive as Mars, direct scattering by such bodies as they swept through the asteroid belt could have perturbed asteroid orbits to their present distribution by the time the JSP were ejected from the solar system or accreted by Jupiter. We suggest that such a mechanism is the most plausible way by which JSP could account for the moderate eccentricities and inclinations of asteroid orbits.

References: (1) J. S. Dohnanyi, in Physical Studies of Minor Planets (T. Gehrels, ed.), NASA SP-267, 263-295 (1971); (2) C. R. Chapman and D. R. Davis, Science 190, 553-556; (3) C. R. Chapman, Geophys. Res. Lett. 1, 341 (1974); (4) C. R. Chapman, Geochim. Cosmochim. Acta 40, 701 (1976); (5) C. R. Chapman, D. R. Davis, R. Greenberg, in NASA TM-79729, 25-27 (1978); (6) D. R. Davis, C. R. Chapman, R. Greenberg, S. J. Weidenschilling, A. R. Harris, in press (1979); (7) R. Greenberg, J. F. Wacker, W. K. Hartmann, and C. R. Chapman, Icarus 35, 1-26 (1978); (8) W. K. Hartmann, Icarus 33, 50-61 (1978); (9) J. D. O'Keefe and T. J. Ahrens, PLSC 8, 3357-3374 (1977); (10) D. E. Gault, E. M. Shoemaker, H. J. Moore, NASA TN D-1767 (1963); (11) A. W. Harris, in press (1979).

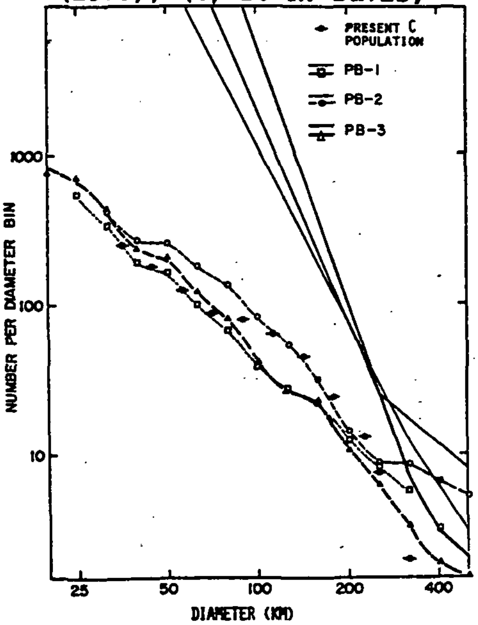

Figure 1: Evolutionary outcomes for initial distributions of the type found by Greenberg et al. (7) at the end of their simulation of intermediate-state planet growth by accretion. These distributions have a few large bodies (500-1000 km diameter), but most of the mass of the population is in smaller bodies. Population PB-1 has an initial mass 0.01 $M_\oplus$, PB-2 contains 0.05 $M_\oplus$; while PB-3 has an initial mass of nearly 1 $M_\oplus$.

Downslope Movement of Material on Deimos.

P. Thomas and J. Veverka, Laboratory for Planetary Studies, Cornell University, Ithaca, N.Y. 14853 and T. Duxbury, Jet Propulsion Laboratory, 4800 Oak Grove Drive, Pasadena, California 91103.

Deimos has numerous bright markings, most of which are tapered streamers trending downhill from major ridge crests and crater rims (Figure 1). The surface of the satellite can be divided into the smooth areas that are bounded by the major ridges. Streamers down the flanks of two "hills" near the south pole are nearly 4 km in length. Sources of the bright material are rims of impact craters, some ejecta blocks, and perhaps ridge crests themselves. Downhill movement of the bright material within the streamers is interrupted by small relief features such as crater rims and blocks. These features include some degraded craters 20 m across which probably have rims less than 1 m high. Thus the streamers are quite thin, and may well be much less than 1 m in depth.

There are deposits of sediment inside craters that, unlike the bright streamers, are demonstrably thick. Several craters that have substantial fill are close to, or on, ridge crests. Craters that have sediment fill also have raised rims that clearly interrupt the movement of the bright material; thus they could not have been filled by the surface creep. The fill in the craters probably arrived ballistically, as ejecta from other craters on Deimos. The preservation of small blocks and the visibility of small crater rims show that the sediment is thinnest on ridges and most concentrated in depressions. The sediment is ponded asymmetrically in many craters; in some it has filled the crater to the level of the downslope rim. It must be concluded that the widespread ejecta are also subject to the downslope movement indicated by the bright streamers.

The occurrence of effective downslope movement on an object with a surface gravity of about 0.25 cm s^{-2} suggests that asteroid regoliths may be subject to considerable redistribution. The apparent lack of downslope movement on Phobos may be related to more inefficient retention of ejecta than on Deimos, or it may be the result of Phobos being composed of slightly different material. Under any circumstances, the results suggest that asteroids should have a great variety of regolith stratigraphies and significant albedo features.

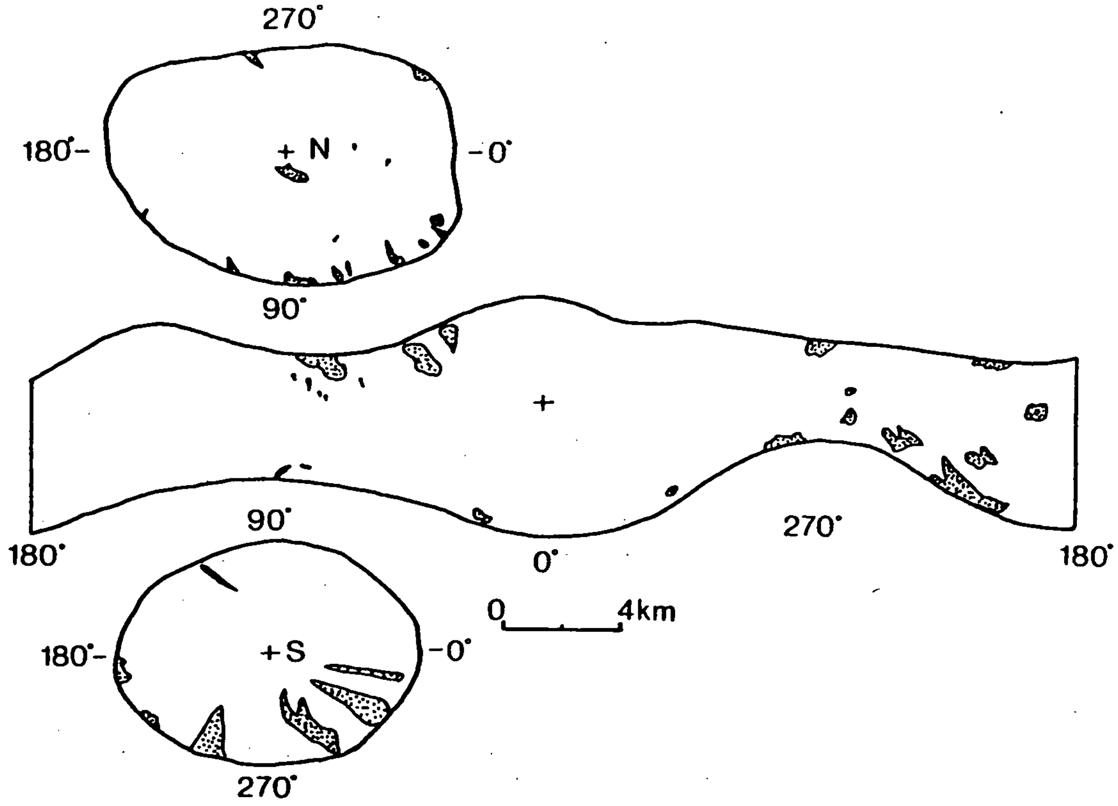

FIGURE 1. Bright albedo features on Deimos. The satellite has been divided into three sections: A smooth, dome-shaped region at high northern latitudes; a smooth low latitude surface; and a saddle-shaped area at high southern latitudes. "Hill" crests occur near the 0° and 180° longitudes; the south pole is in a saddle between the hills. The scale is only approximate. The sub-Mars point is at (0°W, 0°N). Stippled areas represent bright albedo features. The margins of the sections correspond to the major ridge crests on Deimos.

Limb Darkening of Carbonaceous Materials Near Opposition. Or — Why Some Asteroids May Seem Darker Than Carbonaceous Meteorites.

L. French and J. Veverka, Laboratory for Planetary Studies, Cornell University, Ithaca, New York 14853.

As part of our program to study the spectrophotometric properties of carbonaceous chondrites we have discovered that even these very dark materials show some limb darkining near zero phase angle. Measurements at $\lambda = 0.52$ μm yield limb darkening parameters of $k = 0.56$ to 0.57 (Fig. 1). The values are essentially the same for the Orgueil (C1), Murchison (C2) and Allende (C3) chondrites.

At opposition the phase angle $\alpha = 0°$ and the limb darkening across a model planet can be represented by

$$I(\mu) \sim \mu^{2k-1}$$

where I is the intensity of the scattered light, μ is the cosine of the emission angle and k is the limb darkening parameter (Veverka et al, 1978). If there is no limb darkening $k = 0.5$; surfaces which are limb darkened have $k > 0.5$ at opposition.

Our measurements were made at $\alpha = 4°$, but the values of k derived can be shown to be very close to the values expected at exactly $\alpha = 0°$.

The near opposition value of k is essentially independent of wavelength for these materials (Table 1), but does depend somewhat on the degree of surface roughness. Increasing the degree of surface roughness decreases k from 0.57 to 0.54 for Murchison, for example.

Since $k \neq 0.5$, our results indicate that the geometric albedos (p) of asteroids made of these materials will not be equal to the normal reflectances (r_n) of the meteorites measured in the laboratory. For spherical bodies the geometric albedos will be 5-10% lower than r_n, since $p = r_n/(k+0.5)$ for a sphere. For non-spherical asteroids the difference will be larger — probably explaining <u>in part</u> why the observed geometric albedos of some C-asteroids are lower than the values of r_n measured for carbonaceous chondrites in the laboratory.

We note that there are indications in the Viking orbiter data that Phobos and Deimos — bodies for which a carbonaceous composition has been suggested — show a slight amount of limb darkening near $\alpha = 0°$ (K. Klaussen, private communication).

References

Veverka, J., Goguen, J., Yang, S. and Elliot, J. L. (1978). Near-opposition limb darkening of solids of planetary interest. Icarus, 33, 368-379.

λ(μm)	.40	.50	.75	.90	
B_o	.048	.061	.065	.065	±0.001
k	.55	.56	.54	.56	±0.01

TABLE 1: Murchison (45-75 μm particles)

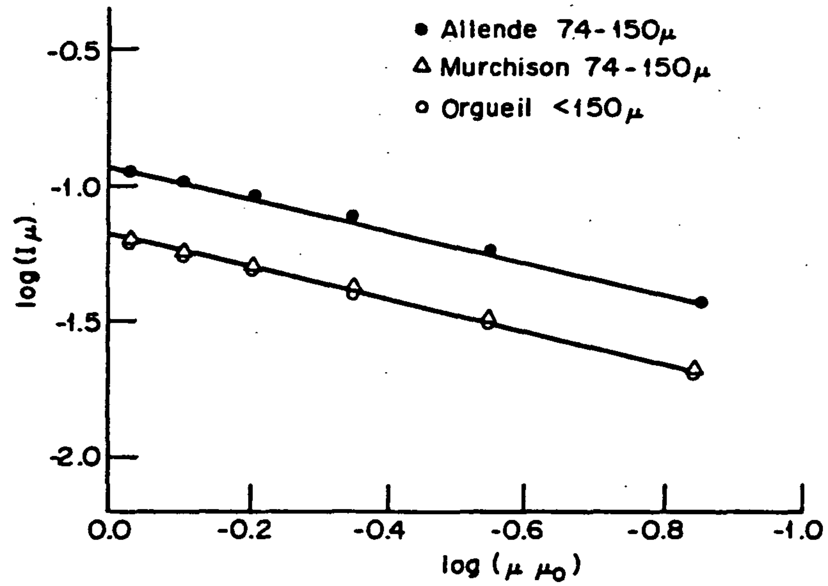

Figure 1: Limb darkening of carbonaceous chondrites at a phase angle of 4°. The slope of the straight lines fitted to the data points gives the limb darkening parameter k. If k > 0.50 the sample shows limb darkening. The measurements yield k = 0.56, 0.56, 0.57, for Allende (C3), Murchison (C2), and Orgueil (C1), respectively. The range of particle sizes in the samples is indicated in the figure; the measurements were made at λ = 0.52 μm with the Cornell Goniometer. The normal reflectances of these samples are 0.061 for Orgueil, 0.063 for Murchison and .114 for Allende.

The Oort Cloud as a Source of Apollo/Amor Asteroids.

John A. Wood, Center for Astrophysics, 60 Garden Street, Cambridge, Massachusetts 02138.

Most (∿80%) of the meteorites that fall to Earth are stones classified as Ordinary Chondrites. It seems clear that these most abundant meteorites are fragments of Apollo/Amor asteroids: there is spectral correspondence between ordinary chondrites and several Apollo/Amor asteroids, and the cosmic-ray exposure ages of ordinary chondrites (∿10^7 yr) are consistent with the mean lifetime against planetary capture of objects in Apollo/Amor orbits. However, because of their relatively short orbital lifetimes, new Apollo/Amor asteroids have to be supplied to the inner solar system at a rate of ∿$15/10^6$ yr to maintain the present population in a steady state. The source of Apollo/Amor asteroids has been a long-standing puzzle. It is not at all clear that they can be obtained from the asteroid belt. For one thing, no belt asteroid has been found to have a spectral signature close to that of ordinary chondrites (or the several corresponding Apollo/Amor asteroids). For another, no dynamic mechanism is known to a high degree of probability that would transfer objects from belt orbits to Apollo/Amor orbits at the required high rate of ∿$15/10^6$ yr.

The orbits of Apollo/Amor asteroids are similar to those of short-period comets; the rate at which new comets must be entering short-period orbits is more than adequate to serve as a source for Apollo/Amor asteroids. For this reason, it has been proposed that the Apollo/Amors and ordinary chondrites derive ultimately from the involatile component of cometary nuclei rather than from belt asteroids. A major difficulty with this scheme, however, lies in the physical nature of the ordinary chondrites. Their anhydrous, reduced minerals and the petrographic evidence in them of protracted (∿10^8 yr) cooling from very high temperatures (∿1000°C) are hard to reconcile with evolution in a small frozen mass of ices of water and other volatile materials.

The immediate source of comets is the "Oort Cloud," a host of small icy objects that move in huge orbits (a ∿50,000 AU) far from the sun. There is much uncertainty about the orgin of the Oort cloud, but a popular view is that its members accreted as icy planetesimals in the outer solar system when the planets were being formed. A fraction of these planetesimals, instead of being captured by the Jovian planets, were ejected from the solar system by gravitational interactions with Jupiter. A fraction of those ejected did not escape the solar system altogether, but entered extremely eccentric, long-period orbits. These were vulnerable to eventual planetary capture or total ejection, but a fraction of them in turn were perturbed while near aphelion by other stars in the galaxy, into new orbits with perihelia outside the planetary system (the Oort cloud). There they can persist for very long times, being vulnerable only to additional stellar perturbations. The latter can have the effect (among other possibilities) of reversing the evolutionary step just named; that is, Oort cloud objects can be perturbed back into the inner solar system in near-parabolic, long-period orbits. This is held to be the source of "new" comets. A new comet with an orbit that happens to lie near the plane of the ecliptic, have direct motion, and reach perihelion near Jupiter can be further perturbed by passages near that planet with the result that its orbit evolves into that of a short-period comet. Short-period comets are understood to have this origin.

It has been shown that, if the terrestrial planets formed by the accretion of smaller rocky planetesimals (a widely held point of view), the capture of these planetesimals would not have been 100% efficient, but a fraction of them also would have been perturbed into orbits that allowed Jupiter to sling them from the solar system. A fraction of these rocky planetesimals too must have joined the Oort cloud, in a manner exactly analogous to that described for the icy planetesimals; and a fraction of these, in turn, is eligible for return to the inner solar system in orbits identical to those of (at first) "new" comets and then (for some) short-period comets. The purpose of the present paper is to propose this as the source of the Apollo/Amor asteroids and ordinary chondrites. Such a source would have the dynamical advantages of short-period comet orbits, but would not have the disadvantage of requiring an association of high-temperature chondritic material with icy comet nuclei. If this model is correct, the ordinary chondrites are more nearly representative of the primitive raw materials from which Earth and the other terrestrial planets formed than are the carbonaceous chondrites and other meteorite types, which presumably derive from the asteroid belt.

In the absence of a clear understanding of the process by which the planets formed, and because of our ignorance of many other quantities that would be needed to accurately model the ejection of planetesimals from the outer and inner solar system, it is not possible to apply a definitive quantitative test to this concept. However, the ratio of required resupply rates of Apollo/Amor asteroids to short-period comets ($\approx 1/10^4$) makes it appear that only a very small rocky component of the Oort cloud is called for, and the ejection efficiency from the inner solar system can have been substantially smaller than that from the region of the Jovian planet.

CRATER POPULATIONS ON THE SATELLITES OF MARS

Peter Thomas and Joseph Veverka, Laboratory for Planetary Studies, Cornell University, Ithaca, New York, 14853, and Clark R. Chapman, Planetary Science Institute, 2030 East Speedway, Tucson, Arizona, 85719

The crater populations on the surfaces of Phobos and Deimos should provide a valuable record of the history of impacts at Mars' distance from the Sun. In particular, one expects that this cratering history will be less confused than that of Mars by atmospheric, hydrologic and other endogenic erosional and obliterative processes. Furthermore, the comparison of crater populations between Phobos and Deimos can shed light on the origin of the satellites, on the nature of impact processes on small bodies, and on the possible role of escaping ejecta captured in Mars orbit.

Crater counts for Phobos and Deimos were obtained in the early 1970's from Mariner 9 images. Early reports noted the relatively high crater densities on these bodies, but definitive characterization of the crater populations was not possible, especially for Deimos. We now have obtained a wealth of data on crater populations on these bodies, including small units, from the Viking Orbiter images. All of Phobos has been imaged to 100 meter resolution and half of Deimos to 150 meter resolution. Representative small areas have been imaged at better than 10 m on Phobos and better than 3 m on Deimos. Counts have been made of the total number of craters visible in certain selected photographs (including craters of all degradational states, excepting only those craters readily identified as being associated with grooves). The counts are grouped in bins of width $D\sqrt{2}$ where D is crater diameter and have been plotted in several standard methods of presentation.

We qualitatively describe the principle features of the composite size-frequency curves for Phobos and for Deimos with respect to a <u>reference line</u> representing equal density (slope = -2 on the standard cumulative log-log plot), derived by an extrapolation to smaller diameters of Hartmann's (1973) curve for the lunar uplands. The distribution for Phobos is about a factor of 1.5 below the reference density (at 1 km), with a slight tendency (slope = -1.9) for lesser densities in the 50 to 200 m diameter range. The distribution for Deimos has a similar overall trend (slope = -1.9), but the trend is less uniform and the overall crater density is less than that on Phobos, about a factor of 2 1/2 below the reference density at 1 km. There is a suggestion, which requires future verification, that on Deimos, there are reduced crater densities at diameters around 200 m and larger than 1 1/2 km than there are at intermediate diameters or at diameters of a few tens of meters.

There are real differences in crater density on different parts of Phobos, with a spread of as much as a factor of 3. The densities within Stickney and within grooves are intermediate while the region antipodal to Stickney is, if anything, older than Stickney. Less information is available on regional differences in crater densities on Deimos, but there is qualitative evidence for more craters on ridges and fewer craters in gravitationally low areas.

A question of major importance is whether the crater populations are in equilibrium or production. Several important observations concerning Phobos are: (1) Crater densities tend toward the -2 slope consistent with equilibrium. (2) The density level is below that of some supposed equilibrium populations (e.g. the extrapolation of Hartmann's uplands curve), but higher than others (e.g.) small craters in the lunar maria. (3) All degradation states of craters are represented, a requirement of equilibrium conditions although the proportion of fresh craters in the small size ranges is larger than would be consistent with perfect equilibrium. (4) The significant differences in density from region to region might argue against equilibrium, although such regional differences are observed as well among small lunar maria craters believed to be in equilibrium. (5) The steep slope predicted by Neukum and Wise (1976) for primaries at small diameters is not recorded on Phobos, implying either that Neukum and Wise are wrong about the shape of the production function or that the population is in equilibrium.

If the crater ejecta-blanketing were the dominant obliterative process on Phobos, it should be dominated by the larger crater events (e.g. those that formed Stickney and Hall) and hence should be episodic in character. One might thus consider the craters to be in a kind of quasi-equilibrium with an inherently episodic process of crater saturation. On the other hand the craters might represent a relatively unmodified production function of modest slope, as suggested by the large fraction of fresh craters and the relatively low density level.

If the crater population is in production, it need not necessarily date from the earliest epochs of solar system history. Indeed, the densities may be controlled by the fragmentation lifetime of Phobos itself. It can be shown that the present crater densities are about the maximum possible prior to the catastrophic disruption of Phobos itself (which would be caused by a cratering event not much more energetic than the one that formed Stickney), assuming the slope of the production function is similar to that of the observed crater population.

The crater population on Deimos is less readily interpreted. There are some interesting, and possibly contradictory, features of the crater curve near the level of statistical significance. The more degraded appearance of craters on Deimos and lower density level compared with that on Phobos suggests more active obliterative processes. Yet, the absence of craters, especially large ones, cannot be readily ascribed to ejecta blanketing since there is no evidence for large craters on Deimos analogous to Stickney on Phobos. Possibly a source for depositional material exists on the unobserved side of Deimos. Otherwise, the history of Deimos has proceeded in a manner strikingly different from Phobos. Several speculative scenarios will be proposed including the possibility that Deimos in some sense "formed" relatively recently.

Using the best available information on crater production rates, we have calculated that the surfaces of Phobos and Deimos are quite old, perhaps 3 and 2 billion years respectively. Uncertainties in these estimates are great so that ages younger than 1 b.y. and ages approaching the age of the solar system are also quite possible.

References:

Hartmann, W. K. (1972). Paleocratering of the Moon. Review of post-Apollo data, Astrophys. Spa. Sci., 17, 48

Neukum, G., and Wise, D. U. (1976). Mars: A standard crater curve and possible new time scale, Science 194, 1381.

Grooves on Phobos: Evidence for Possible Secondary Cratering Origin. James W. Head and Mark J. Cintala, Dept. of Geological Sciences, Brown University, Providence, RI 02912.

The abundant groove structures detected on Phobos by Viking Orbiter images may be a class of features which represent an important process on small bodies such as asteroids. Theories to account for the grooves include 1) impact fracturing,[1,2] 2) tidal distortion,[3] and 3) drag forces generated during hypothetical capture of the satellite.[4] Recent work on the detailed morphology and distribution of these features[2,5] provides important data on possible modes of origin. These studies conclude that the grooves formed coincident with the impact of the 10 km diameter crater Stickney as fractures opening along zones of preexisting weakness and associated drainage of regolith into and/or ejection from, the fractures. It is hypothesized that expulsion of regolith was aided by impact energy causing the expansion of vapor phases.[2,5] However, it has recently been shown that the decay and distribution of stresses in a typical impact is such that vapor phases would probably not be generated in areas other than the immediate vicinity of the crater.[6] Secondly, the energy levels required to produce such a fracture system and to open it sufficiently to drain the regolith into the fissures would likely have resulted in vertical ground motions of high enough amplitude to eject much regolith material from Phobos. Assuming a density of 2.2 g/cm^3 and taking 10^{26} ergs for the Stickney event,[2] Phobos would have been subjected to an energy density of $\sim 8\times10^6$ ergs/g. Experimental data[8] show that the surface effects would have been considerable. This phenomenon does not appear to have occurred. The grooves seem clearly associated with the crater Stickney but many of their characteristics are not compatible with secondary crater chains as seen on other bodies such as the Moon. The purpose of this study is to examine the grooves in the context of the characteristics of the cratering processes on small bodies to evaluate the evidence for a secondary cratering origin of the grooves.

Cratering process on small bodies - The small radii of curvature and weak gravity fields of most small bodies will cause the impact cratering process to be significantly different from that on larger planets. During the initial (compression) stage of a relatively large impact event on a small target body, the shock wave will intersect the curving surface at oblique angles; depending on the relative intensities of reflected tensile and shear waves, this portion of the target will acquire a component of velocity subradial to the shock source and, if the original compressional wave is sufficiently intense, will be ejected at relatively low angles. As the impact-initiated compressional wave reflects from the free surfaces, seismic effects will manifest themselves as high acceleration (relative to the small surface gravity) ground motions and possible antipodal spallation. A large fraction of material ejected during the rarefaction phase, including the most highly shocked component, could escape from the target body; the exact amount will depend on the physical characteristics of the target material and the strength of the gravity field. The lowest velocity fraction of ejecta -- that subjected to the lowest shock levels -- will be retained. The low gravities and large curvatures will cause the non-escaping ejecta to be widespread over the surface; any rim topography associated with the resulting crater should thus be largely structural in nature.

Observations of groove characteristics - The grooves are linear depressions made up of coalesced pits 100-200 m in width and 10-20 m deep; they are widest and deepest nearest Stickney and are absent at the approximate Stickney antipode. The surface traces of grooves follow the intersection of several sets of parallel planes with the surface of Phobos. The time of formation is restricted and close to that of the crater Stickney, within which grooves are found.[2,5]

Assessment of a possible secondary crater origin of the grooves - (a) Similarities to planetary secondary craters: Grooves are made up of chains of craters, which often have raised rims. The largest craters within the grooves are near Stickney. The smallest occur at the antipodal ends of the grooves, where strings of isolated craters are occasionally observed as the grooves become narrower and rapidly disappear. The region antipodal to Stickney is devoid of these features. (b) Differences from planetary secondary craters: Grooves are observed within the rim crest of Stickney. Craters comprising the grooves are nearly circular in plan, rather than oval, and rarely exhibit the herringbone pattern typical of low angle lunar or mercurian secondary impact craters. Grooves are of uniform width over great distances and show relatively sharp edges and correspondingly uniform pit diameters; the pits rarely overlap each other.

Discussion - Three major differences between the cratering process on small bodies and larger bodies may explain many of the seemingly anomalous aspects of the Phobos grooves.

1) Stress-wave reflections from the free surface - The reflection of stress waves from the surface of Phobos probably would have mobilized any regolith on the satellite; the low-gravity environment would allow this to occur at relatively low stress levels. In particular, antipodal "regolith spallation"[9] would be expected; should this material have reached escape velocity ($\sim$10 m/s), it would have (1.) provided an environment not conducive to low velocity secondary cratering processes and (2.) exposed once-blanketed craters formed in the more competent substrate beneath the regolith -- thus giving the region an apparent age older than that of the Stickney event. No grooves are observed in the antipodal region, and this area of Phobos appears to be older than Stickney on the basis of crater counts.[2] In this model, weaker stress waves resulting from attenuation and oblique incidence at the surface would spall regolith from around the satellite, but at less than escape velocity. Upon low velocity reaccretion, the regolith would present a target highly conducive to the formation of low velocity secondary craters.[10] It is noted that large-scale fracturing of Phobos and subsequent regolith drainage should be mutually exclusive events in most circumstances: stress levels high enough to open new (or even pre-existing) fractures as large as those required to explain the grooves would have ejected any regolith at high velocities, while the lack of such ejection would imply very low stresses.

2) Compressional nature of secondary craters - Impacts at very low velocity into fragmental material are dominated by compression of the sub-

strate rather than by excavation and ejection. Boulder tracks observed on the Moon are an end member of this phenomenon. In this case a dislodged boulder rolls or bounces down a slope, leaving a linear groove characterized by coalesced craters with raised rims.[11] Observation of such a boulder track on Apollo 17[12] showed that the crater chain was dominated by compression and local movement of material rather than by excavation and ballistic ejection. Although the mode of formation of the Phobos grooves is not likely to be due to tracks formed by a single boulder (groove continuity across variable slopes; no deviations with changing topography, etc.), the characteristics of the patterns nonetheless illustrate how low velocity ballistic impacts might appear -- including the lack of ejecta/herringbone patterns and rays (at high sun), and the presence of raised rims due to "plastic" deformation of substrate.

3) *Rotation of small body during an impact event* - Another potentially important factor in causing differences between crater deposits on small bodies and those on larger bodies is the rotation of the body during the course of the impact event. Two sources of rotation include that caused by the impact itself and the normal rotation of the body. For example, at just under escape velocity it would take ejecta from Stickney ∿0.5 hours to reach the end of the presently mapped grooves (assuming a spherically symmetric gravity field). During such a time interval, the present orbital characteristics of Phobos are such that the body would rotate approximately 25 degrees in a counterclockwise direction, as seen from the north pole of Phobos. If such a rotation occurred during the Stickney event, it would cause the body to rotate under the expanding ejecta plume and produce the following effects: 1) offset of the ejecta "excluded zone" in a direction opposite to and in an amount equivalent to the rotation; 2) emplacement of ejecta and formation of chains inside Stickney as the crater rotates under part of the ejecta plume; 3) formation of grooves at angles to each other and angles other than radial to Stickney as the nonspherical body rotates under the plume. Many of the characteristics of the grooves are compatible with a rotation of Phobos at its present rate under the expanding Stickney ejecta plume. Although this may well be coincidental, it illustrates the fact that such an effect could be important in explaining seemingly anomalous ejecta patterns on asteroids and small bodies.

In conclusion, several major characteristics of the cratering process on small bodies provide potential explanations for many of the observed features of the grooves on Phobos that seem anomalous when compared to secondary ejecta patterns on larger bodies. These factors, coupled with some difficulties in explaining the grooves by fracturing and devolatilization and/or drainage, suggest that the Phobos grooves may have formed as secondary crater chains from the Stickney cratering event.

References: [1]**Veverka J. and Duxbury T.C.** (1977) J. Geophys. Res. 82, 4213-4223. [2]Thomas P.C. (1978) Ph.D. Thesis, Cornell Univ. [3]Soter S. and Harris A. (1977) Nature 268, 421-422. [4]Pollack J.B. and Burns J.A. (1977) Bull. Amer. Astron. Soc. 9, 518-519. [5]Thomas P. et al. (1978) Submitted to J. Geophys. Res. [6]Cintala M.J. (1979) 2nd Internat. Coll. on Mars, p. 16. [7]Cintala et al. (1978) PLPSC 9, 3803-3830. [8]Gault D.E. and Wedekind J.A. (1969) J. Geophys. Res. 74, 6780-6794. [9]Cintala M.J. et al. (1979) Submitted to Asteroids (T. Gehrels, ed.). [10]Clark L.V. and McCarty J.L. (1963) NASA TN D-1519. [11]Moore H.J. (1970) U.S.G.S. Interagency Report: Astrogeol. 22. [12]Mitchell J.K. et al. (1973) Apollo 17 Prelim. Sci. Report, p. 8-1 - 8-22.

Chapter 2

STRUCTURE, TECTONICS AND STRATIGRAPHY

Geologic Problems in the Northern Plains of Mars*, D. H. Scott, U.S. Geological Survey, Flagstaff, AZ.

Plains materials lying mostly below the 0 km elevation datum occupy the greater part of the northern hemisphere of Mars. On Mariner 9 images they appeared flat to gently rolling, were relatively smooth with few topographic irregularities, and were generally interpreted to consist of lava flows with varying amounts of eolian cover. The plains are separated from the more rugged highlands to the south by a scarp that is discontinuous and irregular in both its local and regional aspects. On the basis of rather broad morphologic variations shown by the Mariner pictures, the plains were subdivided into several different units (Greeley and Guest, 1978; Underwood and Trask, 1978; and Scott and Carr, 1978). Viking orbiter images have revealed a wide variety of surface textures, albedo contrasts and other morphologic characteristics within, as well as between, the individual plains units. Thus, the Viking data allow for the recognition of new rock units in many places and the further subdivision of others. Mapping problems arise, however, as the visibility of morphologic variations is enhanced by the high resolution and quality of the Viking frames. A geologic unit once considered to be relatively smooth and homogeneous on Mariner images, for example, may exhibit a hackly surface in places or ridges and troughs forming simple to complex patterns. Boundaries between these subunits are seldom sharp and in many areas appear to be gradational. Also, it is difficult to distinguish whether these textural changes reflect primary surface forms or are secondary forms produced by erosion or other processes. Such distinctions are fundamental in geologic mapping, particularly in the recognition and definition of rock-stratigraphic units (Cohee and Geologic Names Committee, 1970). Although overlap, embayment, and transection relations between subunits of the northern plains commonly are not well expressed on the Viking pictures, crater counts indicate that age differences do exist. This is supported by a certain order or similarity of association between the plains units from place to place suggesting that they may be in some degree homotaxial and therefore represent rock-stratigraphic units. A somewhat similar problem occurs in some mare regions of the Moon where crater distribution studies (Boyce, 1978) indicate a wide disparity in ages across a seemingly uniform surface and where no visible evidence of material boundaries exists on high resolution photographs.

Probably the most difficult plains unit to define and interpret is the very extensive mottled terrain that nearly encircles the planet in a zone between about 50° and 70° north latitude. Mariner 9 images were degraded in this region by atmospheric haze and high sun angles that produced strong albedo contrasts. For this reason, lithologic variations that ordinarily might be expected over such a large area were not visible and the entire region was mapped as a single material unit. Strips within and across the boundaries of this mottled zone were targeted for Viking orbiter pictures. Many of these images have now been examined. The mottled appearance is produced chiefly by impact crater ejecta blankets that are relatively bright compared to intercrater areas. The ejecta blankets are of various sizes and ages, but even the older ones, as indicated by their more eroded edges, remain lighter colored than the background

---

*Abstract published 1979, Tenth Lunar and Planetary Science Conference.

surface. Intercrater areas have numerous conical hills that resemble on a smaller scale the knobby remnants of plateau materials scattered along the base of the highland scarp. The crests of the hills, like the rim crests of craters within the mottled plains, are darker than their flanks and this also contributes to albedo contrasts in the unit. Some of the hills have summit craters and may be of volcanic origin. Most of the hills appear subdued and many of the craters have filled or partly filled floors. Narrow grabens and lineaments transect the unit and curved channel-like features occur in places. All of the landforms appear to be older and to have more relief than bordering plains materials. Although the mottled plains are removed 500 km and more from the highlands to the south, they may be a part of this ancient surface. Possibly they represent lower more deeply eroded remnants of the highlands that have survived an episode of crustal separation and volcanism, with flood basalts filling the intervening region and forming the smoother plains between the segregated parts.

The problem of subdividing the mottled plains into more units has not yet been accomplished. Where Viking pictures are clear, the surface of the mottled plains appears to be uniform and consists, as described, of small hills interspersed with low relief craters and their contrasting ejecta blankets. In many areas, however, the pictures have a muddy appearance and textural details of the surface are not clear enough to show any distinctive variations should they exist. A computer enhancement of selected frames is being attempted to help resolve this problem.

References

1) Greeley, R. and Guest, J. E., 1978, U. S. Geological Survey, Miscellaneous Geologic Investigation Map I-1038.
2) Underwood, J. R., Jr. and Trask, N. J., 1978, U. S. Geological Survey, Miscellaneous Geologic Investigation Map I-1048.
3) Scott, D. H. and Carr, M. H., 1978, U. S. Geological Survey, Miscellaneous Geologic Investigation Map I-1083.
4) Cohee, G. V. and Geologic Names Committee, 1970, Stratigraphic Nomenclature in Reports of the U. S. Geological Survey.
5) Boyce, J. M., 1978, U. S. Geological Survey Open-file Report 78-879.

Mars: Viking Appraisal of Mariner Geologic Mapping*, David H. Scott, U.S. Geological Survey, Flagstaff, AZ.

The systematic geologic mapping of Mars using Mariner-9 images was completed in 1978 and produced 30 geologic quadrangle maps of the entire planet and a smaller scale geologic map representing a compilation in part of the larger scale map series. The quality of many of the Mariner-9 photos was degraded by atmospheric haze and high-sun angles producing strong albedo contrasts, particularly in the high northern and southern latitude belts. Geologic maps of these regions reflect these deficiencies but at present are the only ones available that cover the entire planet.

Geologic mapping using Viking images has allowed comparisons to be made with the previous work. Most of the initial studies are in the northern hemisphere and involve rock units of the subpolar region, lowland plains, and the border land between plains and the highland plateau. On a broad scale, the Mariner mapping delineated geologic boundaries between and within these physiographic provinces reasonably well. Important rock units and subdivision of units, however, were not recognized because of the quality and resolution of the Mariner pictures. This discussion describes these rocks and their relations to the time stratigraphy of Mars.

The most extensive geologic units appearing on the Mariner pictures in the northern hemisphere are mottled plains, cratered plains, and smooth plains. They occupy vast areas of the lowlands and extend to the boreal region (Scott and Carr, 1978). These rocks, as their names imply, are characterized respectively by, contrasting light and dark patches, common superimposed craters and broad featureless expanses. The cratered and smooth plains were interpreted as lava plains covered by a veneer of eolian deposits of varying thickness; where the eolian mantle was relatively thin, craters in the underlying lava flows were more visible, thus giving the appearance of older age to these regions. The mottled plains are easily recognized on Mariner images but difficult to interpret both as to lithology and probable origin. They were variously considered to represent sediments with pore spaces filled by permafrost (Elston, 1978), ancient terrain exhumed by wind erosion (Underwood and Trask, 1978), or having a surface texture produced by frost heaving or other frost phenomena (Greeley and Guest, 1978).

Viking pictures clearly show that the previously mapped cratered plains and smooth plains units occupying the Vastitas Borealis region of Mars have many differences in texture, topographic expression, color, and other physical characteristics that require their further subdivision. Some 10 different types of plains materials presently comprise the two originally mapped rock units. The mottled plains, however, are not yet capable of similar differentiation. Viking photos in these regions show numerous bright haloed craters and relatively small hills and knobs which provide a hummocky texture to the terrain but their relationship to the dark patches are not clear nor are stratigraphic relations at their boundary with both the smooth and cratered plains materials.

---

*Abstract published Second International Colloquium on Mars, 1979.

References

1) Elston, W. E., 1978, Geologic map of the Cebrenia quadrangle of Mars: U.S. Geological Survey, Miscellaneous Geologic Investigation Map, in press.
2) Greeley, R. and Guest, J. E., 1978, Geologic map of the Casius quadrangle of Mars: U.S. Geological Survey, Miscellaneous Geologic Investigation Map I-1038.
3) Scott, D. H. and Carr, M. H., 1978, Geologic map of Mars: U.S. Geological Survey, Miscellaneous Geologic Investigation Map I-1083.
4) Underwood, J. R., Jr. and Trask, N. J., 1978, Geologic map of the Mare Acidalum quadrangle of Mars: U.S. Geological Survey, Miscellaneous Geologic Investigation Map I-1048.

WHITE ROCK - AN ILLUSION?

Nancy Evans, Jet Propulsion Laboratory, California Institute of Technology, Pasadena, California 91103.

The images exployed in this study were those obtained during the Mariner 9 and Viking Missions which included the White Rock feature in whole or in part. Some Viking coverage gathered during the dust storm period was excluded for lack of sufficient information. Table 1 gives the parameters of the data set.

TABLE 1. WHITE ROCK STUDY - DATA SET

Picno	Sequence or Target	Filter	Range	Scale
DAS6786778	8.2°S 334.7°W	MBL	1733	51 m/p
DAS8189794	8.2°S 334.9°W	MBL	1783	52 m/p
DAS261824	8.2°S 334.6°W	MBL	1996	68 m/p
REV84A30-62	So. Hemisphere Mapping	R/V	3000	75 m/p
REV618A01-16	Med. Range Mapping	R	9500	231 m/p
REV623A61-78	Syst. Low Res. Stereo	R	24000	600 m/p
REV623A81-98	Syst. Low Res. Stereo	R	28000	700 m/p
REV749A01-30	White Rock	MBL	731	18 m/p
REV826A21-44	White Rock	R	1150	29 m/p
REV826A51-44	White Rock	B	975	24 m/p

The highest resolution sequences to contain the entire feature were obtained during the two color-stereo sequences on revolution 826 by the Viking Orbiter 1 cameras. A mosaic of the images of White Rock taken through the red filter appears as Figure 1. Those taken in the second sequence, imaged minutes later through the blue filter, are mosaicked in Figure 2. The scales of these mosaics are 28.9 meters/pixel and 24.4 meters/pixel respectively.

The images taken of the White Rock feature by the Mariner 9 "B" camera were imaged at ranges between 1700 and 2000 km, resulting in scales from 68 to 51 meters/pixel.[1] DAS8189794 is included as Figure 3. All figures have been cropped to display a similar area of coverage.

Visual comparison of the images taken six years apart reveals no apparent change in the White Rock or its immediate surroundings. The most striking phenomenon is that the feature appears so similar at different resolutions. The Viking images, containing information at half the scale of those obtained by the Mariner 9 camera, are very little more revealing of the surface characteristics. In fact, nearly as much information about the White Rock surface is contained in 84A61-62 taken from 3000 km. Further enhancement of the higher resolution Viking images was indicated and is in progress.

---

[1] The focal length of the Mariner 9 "B" optical system was 500 mm and the sensor array was 700 by 832 pixels. JPL Technical Memorandum 33-585, 1974.

Examination of the unprojected data through a stereoscope using 826A34, 35, 36, 66, 68 and DAS8189794 indicates the height of the feature to be some tens of meters. Further study by this technique awaits computer rectification. However, the following is apparent in the unrectified images:

- The highest point is located centrally at the base of the reentrants and decreases in all directions though not at the same rate or to the same extent
- The tips of the promontories drop abruptly to the crater floor rather than tapering into the floor
- The dissected area, opposite the reentrants, expresses the least relief
- The reentrants appear to cut through the feature to the crater floor.

The two color imagery indicates a higher reflectance through the red filter than through the blue filter.

A correlation with the IRTM data obtained during the same revolution (826A) was more revealing. The feature is not highly reflective. Thermal data indicate a reflectivity of 11 percent for the dark material on the crater floor and 18 to 20 percent for the surface of the feature. [T. Z. Martin - personal communication.] The Viking IRTM experiment has provided bolometric reflectivities for Mars indicating the mean albedo in the equatorial region to be 0.214 ±0.06 [2] or 21 percent. The input histograms of images 826A36 and 66 support the IRTM measurements. The histograms, as well as pertinent processing information for these images, are provided in Figure 4. Radiometric profiles for these images should be completed prior to presentation.

Conclusions

White Rock is an illusion - as in the engravings by M. C. Escher, the eye is fooled into seeing things as they are not. The scene, a lighter object surrounded by a darker background, coupled with an automated data processing procedure which discards the highest and lowest data numbers and stretches the remaining data to enhance the contrast has created the illusion of a stark white shape in a blackened field. Many "White Rocks" may exist on Mars, less suitably delineated and therefore more difficult to see. The temptation to practice "eyeball science" has proven misleading with respect to White Rock.

This abstract presents the results of one phase of research conducted at the Jet Propulsion Laboratory, California Institute of Technology, under NASA Contract NAS7-100 sponsored by the Viking and Planetary Geology Program, Office of Space Science, National Aeronautics and Space Administration.

[2] Kieffer, H. H. et al., Thermal and Albedo Mapping of Mars During the Viking Primary Mission, J. Geophys. Res., Vol 82, No. 28, 1977.

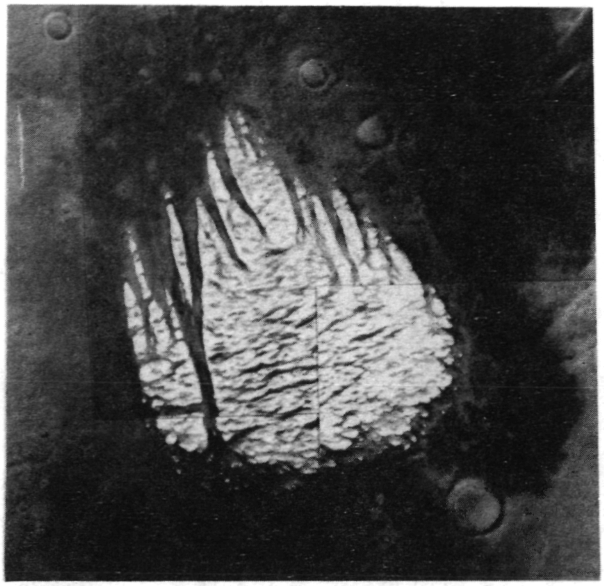

Figure 1. White Rock as it appeared through a red filter, a mosaic including portions of 826A34-36.

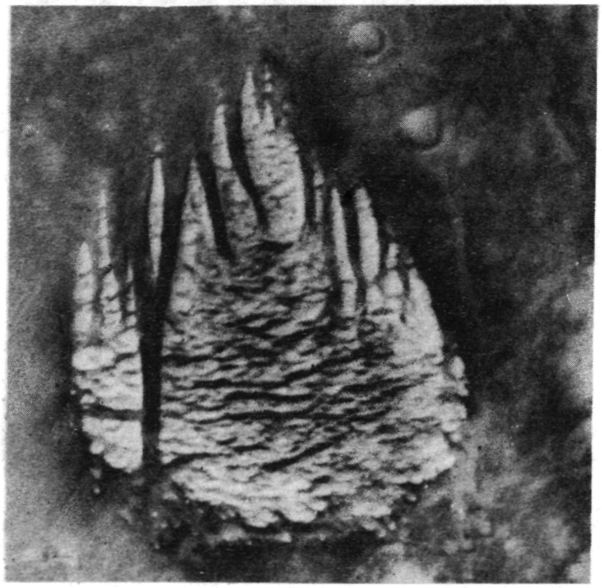

Figure 3. White Rock as viewed by the Mariner 9, "B" camera. The image was produced by IPL

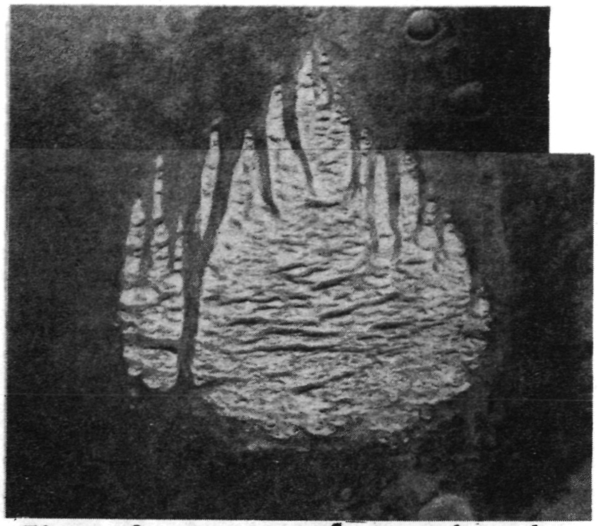

Figure 2. The same feature imaged minutes later through a blue filter, a mosaic including portions of 826A66, 68.

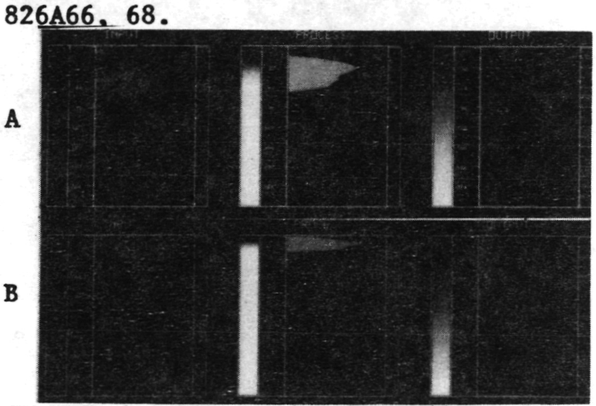

Figure 4. These histograms A, 826A36 and B, 826A66, indicate a very low input DN for both images, following the Viking processing formula the lower 5% and upper 2.2% of the DN are eliminated and the data stretched to the new parameters with the following results:

A. Low DN of 24 set to 05
B. Low DN of 06 set to 05

A. High DN of 61 set to 250
B. High DN of 20 set to 250

Ridges and scarps in the equatorial belt of Mars*

B. K. Lucchitta and J. L. Klockenbrink, U. S. Geological Survey, Flagstaff, Arizona 86001.

A survey of ridges and lobate scarps that have affinities with mare ridges on the Moon was conducted for the martian quadrangles MC-8 through MC-23 comprising the ± 30 latitude region. The survey was restricted to the areas covered by Viking orthophotomosaic subquadrangles of scale 1:1,250,000 and 1:2,000,000. No Mariner coverage was included in order to assure uniformity of image resolution.

The survey showed that ridges and lobate scarps on Mars consist of several distinctive types with characteristic morphologies. These types, however, may grade into each other regionally and are transitional morphologically, which suggests a common denominator for their origin.

The type that most resembles mare ridges on the Moon consists of ridges that are long, broad swells with superposed irregular, crenulated, narrow crests. The type is well represented in the Chryse basin, in Lunae Planum, and in the plains south of Coprates Chasma. A second type consists of ridges that are subdued, irregular and short swells, and of similar scarps. Both are bifurcating or anastomosing and locally have thin crenulated crests. They occur mostly in highland areas that appear smoothed, and they reflect subjacent topography such as buried crater rims and ejecta blankets. A third type consists mostly of well-defined lobate scarps with a rolling top and a sharp break in slope at the base. Crenulated crests on top or below the scarp occur locally. This type occurs in places at the boundary between cratered highland terrain and adjacent low-lying plains.

Erosion of ridges on Mars may shed light on their internal structure. Where ridges intersect erosional scarps tributary valleys have developed, indicating that the ridges occupy zones of weakness susceptible to erosion. Locally, however, prongs or spurs may be developed indicating resistance to erosion. Fault zones, associated with less resistant breccia in some places, or with more resistant indurated breccia or dikes in others may explain the differential erosion. Some ridges transgress erosional scarps, and appear to have developed after the erosion that formed the scarps. Erosion across ridges in the Chryse basin has exposed a series of ledges on the channel floor. The ledges could be beveled edges of upturned lava layers and support an origin by buckling.

Ridges on Mars of the anastomosing type appear to be preferentially associated with Noachian hilly and cratered materials and cratered plateau materials of Scott and Carr (1). Well defined ridges that are similar to those on the Moon occur preferentially on the Hesperian ridged plains, some Amazonian crater plains (1), and inside young volcanic calderas. Ridges generally are not found on smooth plains units that have distinctive flow lobes, such as the plains surrounding the Tharsis volcanoes, and on the flanks of volcanic shields. They also do not appear to occur on rough topography, such as the aureole deposits (2) or the fractured plains (3). They do not occur on fresh thick ejecta blankets, but locally transgress thin ejecta blankets. They usually do not occur on sedimentary layers such as are found in the southern part of Amazonis Planitia, and on the floors of the chasmas, the chaotic terrain, and some channels. Ridges seem to be developed mostly in areas flooded by lavas, and with the exception of flow-lobe lavas, are best developed in the areas where the flooding appears to have been deep.

Ridges occur on units of all ages ranging from those resulting from early highland flooding to those on the floors of young calderas. Their formation seems to post-date the emplacement of the units as they locally transgress units of different ages, or transgress erosional scarps.

Structural observations of the ridges on Mars revealed a dominance of northerly trends in the investigated regions. This trend is particularly obvious in the long, continuous ridges that most resemble those on the Moon. Orthogonal grid patterns occur locally, especially in highland areas where buried craters may have angular shapes. Many graben trends are at angles to those of ridges, such as south of the chasmas where graben trends are westerly and ridge trends northerly. In places, however, graben trends are parallel to those of ridges or ridges merge with grabens.

The origin of ridges on Mars is probably diverse, as that suggested for ridges on the Moon (4). In support of a structural origin for ridges on Mars it can be cited that many ridges and scarps occur along offsets in the regional surface level, and that some are continuous with grabens, which imply association with faults. Grid patterns or dominance of certain trends suggest structural influence. Preferential erosion along ridges implies structural zones of weakness, and erosion into ledges may reflect upturned beds. Expression of subjacent topography implies draping, which may have been accentuated by settling and compaction. If ridges are structures, the long continuous ones may be anticlines resulting from regional stresses; the anastomosing ones in highlands may reflect draping over subjacent topography. A volcanic origin for ridges is suggested by their association with apparent lava plains and their development inside calderas. Prongs or spurs on erosional scarps could be caused by resistant dike rock. Ridges are not likely to be eruptive fissures, as known fissures in the Tharsis area (5) and on earth (6) are remarkably linear cracks locally punctuated by craters, or, on earth, cratered constructional features. However, some ridges could be elongate domal uplifts over laccolithic intrusive bodies along faults.

Mare ridges on the Moon are similar to ridges on Mars, and both have some resemblance to anticlinal ridges on the Columbia River Plateau near Yakima in south-central Washington. These ridges were discussed as analogs for lunar mare ridges by Greeley and Spudis (7), who considered mostly planimetric details and size relations. Additionally, the Yakima ridges resemble planetary ridges, as a) they are developed in thick competent units of flood basalts; b) the deformation of the top-most layers took place near the surface, that is, without thick layers of overburden (9); c) they are arranged en echelon across a major structural trend (10); d) they have varying symmetry along their trends, with steep limbs or faults occurring on alternate sides of the folds; e) they are anticlines that have the form of box folds with flat tops and steeply dipping limbs, which is similar to the cross-sectional shape of lunar mare ridges; f) they are paralleled by tight subsidiary anticlines and synclines, some of which occur on the downthrown side of the faults; crenulations on planetary ridges behave similarly; and g) they are interpreted to be over basement faults expressed at the surface as either faults or monoclinal warps similar to the interpretation given to mare ridges that developed along faults on the Moon (11).

Even though the Yakima ridges have much larger structural relief than ridges on the Moon and Mars, and their origin may be linked to plate tectonics

(12), the morphologic resemblance suggests that the mechanics of deformation may have been similar. The reason for this could be that both developed in thick competent stacks of flood basalts near the surface. Therefore, all ridges on planetary basalts may have analogous shapes regardless whether their origin is updoming over a linear intrusive, surface buckling under compressional stresses or stresses from gravitational gliding, anticlinal draping over subsurface compressive upthrusts, or passive settling over subsurface topography due to compaction.

References:

(1) Scott, D. H. and Carr, M. H., 1977, U. S. Geological Survey Misc. Inv. Map I-1083.
(2) Morris, E.C. and Dwornik, S. E., 1978, U. S. Geological Survey Misc. Inv. Map I-1049.
(3) Masursky, Harold, Dial, A. L., Jr. and Strobell, M. E., 1978, U. S. Geological Survey Misc. Inv. Map I-896.
(4) Schultz, P. H., 1976, Moon Morphology, Univ. of Texas Press, 626 p.
(5) Schaber, G. G., Horstman, K. C. and Dial, A. L., 1978, The distribution and eruptive history of lava-flow materials - Tharsis region of Mars (abs): In Lunar and Planetary Science IX, p. 1002-1003
(6) Thorarinsson, S., 1970, Bull. Volcanologique, v. 70, p. 910-929.
(7) Greeley, Ronald and Spudis, P. D., 1978, Ridges in western Columbia Plateau Washington - Analogs to mare-type ridges? In Lunar and Planetary Science IX, p. 411-412, Lunar and Planetary Institute, Houston, Texas.
(8) Smith, G. O., 1903, Journal Geology, v. 11, p. 166-177.
(9) Waters, A. C., 1955, Geol. Society America Bulletin, v. 66, p. 663-684.
(10) Bentley, R. D., 1977, Stratigraphy of the Yakima ridges in the western Columbia Plateau. In Geol. Excursions in the Pacific Northwest, Geological Society of America 1977 Ann. Mtg., Seattle, p. 339-389.
(11) Lucchitta, B. K., 1977, Proc. Lunar Science Conference, 8th, p. 2691-2703.
(12) Swanson, D. A., 1967, Geological Society America Bulletin, v. 78, p. 1077-1110.

*Presented at 10th Lunar and Planetary Science Conference, March 1979, and published in Lunar and Planetary Science X, part 2, p. 750-752.

Debris Flows on Olympus Mons, B. K. Lucchitta, U. S. Geological Survey, Flagstaff, AZ 86001.

A blanket of debris, about 400 km long, rests against the west-side scarp at the base of the Olympus Mons volcanic shield (Blasius, 1976). The debris has flow lobes that attain dimensions of as much as 180 km long and 90 km wide. The scarp from which the debris flowed measures 1 to 2 km in height (U.S. Geological Survey, 1976) and the surface on which the flows rest slopes gently westward toward the aureole materials surrounding Olympus Mons (Morris and Dwornik, 1978).

The scarp is locally obliterated at the head of the debris flows; in two places 70 and 100 km segments of the scarp are recessed 40 to 60 km, and the debris flows originate at the juncture of the reentrants with the surface of the volcanic shield. No scar is visible; instead the breakaway is marked by a wavy line of cracks and irregular depressions. In other places, the scarp at the head of the debris flows is steep and covered with talus and is locally disrupted by slump blocks composed of entire mountain spurs. In one place an aligned break in slope extends for about 60 km along the scarp face and probably marks an incipient slump.

The debris flows merge to form a continuous blanket near the scarp. Near their toes separate lobes can be recognized that locally overlap each other. Generally the debris flows have coarse, mountainous materials at their heads that have a longitudinal pattern where the scarp is destroyed, and an irregular pattern where the scarp is preserved. The mountainous material gives way to finer hummocky and knobby material in the direction of flow. Both the mountainous and hummocky materials are dotted with irregular depressions. On several of the debris aprons the knobby material is strung out into lobate belts surrounding smoother cores. The margins of the debris aprons are paralleled by numerous continuous curvilinear ridges that are about 1 km wide and may extend uninterruptedly for more than 50 km.

Superposition relations within the aprons suggest several pulses of emplacement; locally the curvilinear ridges transgress lobes of knobby material, elsewhere a lobe of knobby material cuts the curvilinear ridges. A fringe of angularly pitted material surrounds the margin of one lobe and cuts off the ridges within it, suggesting that this apron was recessed by erosion.

The debris aprons locally bury the mountains of the aureole material. Where the aprons are thin, the curvilinear ridges are superposed without deflection on these mountains. This superposition onto mountains of considerable relief suggest a gentle lowering of the ridge material from above and implies a process involving substantial loss of material from the debris aprons. Locally deposits that resemble eolian blankets (Scott et al., 1979) bury the mountains of the aureole, and the debris aprons in places rest on top of this material. Therefore, the lowering of the debris aprons and their undeflected ridges onto the aureole material could also be attributed to loss of substance from this intervening deposit. Ice is the most likely material that is easily lost to the atmosphere from either the debris aprons or the eolian sediments.

The age of the debris flows is difficult to assess. Only one crater of 3 km diameter was found superposed on the deposits and six to eight smaller craters may exist, but their identification is tentative because of the rough and pitted surface texture of the debris aprons. The dearth of craters suggests a young age. The debris flows are superposed on and therefore are younger than the mountains of the aureole and its partial eolian blanket. They are also superposed on young lava flows below the scarp. Lava flows that cascaded over the scarp next to one of the debris flows appear to bury the side of its scar and could be younger than the debris, but the relation is not clearly seen and therefore uncertain.

The debris flows on Olympus Mons are similar in many respects to those on the other Tharsis volcanoes, which suggests a similar origin. They are morphologically distinct from those in the Valles Marineris, which have been interpreted as landslides (Sharp, 1973; Lucchitta, 1978). The slide aprons in the martian chasmas are characterized by longitudinal grooves, the flow aprons on Olympus Mons by continuous semi-concentric curvilinear ridges. On earth, debris flows that display the latter morphology are emplaced slowly by creep, and generally involve ice as a lubricating agent. Examples are the Malaspina Glacier in southeastern Alaska and rock glaciers of alpine environments. That ice was involved in the emplacement of the debris flows on Olympus Mons is therefore suggested by the terrestrial analogs and by the superposition of undeflected ridges onto the mountains of the aureole. The mechanism of motion was probably similar to that of rock glaciers, as has been suggested for the erosion of scarps elsewhere on Mars (Squyres, 1978). The lubricating ice may have come from interbeds in the volcanic shield, as suggested by the local disintegration of the scarp by flow. Ice may also have been banked against the scarp (Hodges and Moore, 1978) and incorporated into collapsing volcanic debris, may have drifted into slump deposits by eolian action or settled from the atmosphere.

References

1) Blasius, K. R., 1976, Topical studies of the geology of the Tharsis region of Mars: Ph.D. thesis, California Institute of Technology, 85 p.
2) Hodges, C. A. and Moore, H. J., 1978, Tablemountains of Mars, in Lunar and Planetary Science IX, p. 532-535.
3) Lucchitta, B. K., 1978, A large landslide on Mars: Geological Survey of America Bulletin, v. 89, no. 11, p. 1601-1609.
4) Morris, E. C. and Dwornik, S. E., 1978, Geologic map of the Amazonis Quadrangle of Mars: U. S. Geological Survey Miscellaneous Geologic Investigation Map I-1049, scale 1:5 million.
5) Scott, D. H., Horstman, K. C., Schaber, G. G., and Dial, A. L., Lava flows of the Tharsis Montes, in Reports of Planetary Geology Program, 1978-1979, in press.
6) Sharp, R. P., 1973, Mars: troughed terrain: Journal of Geophysical Research, v. 78, p. 4063-4073.
7) Squyres, S. W., 1978, Martian fretted terrain: flow of erosional debris: Icarus 34, p. 600-613.
8) U. S. Geological Survey, 1976, Topographic map of Mars: U. S. Geological Survey Miscellaneous Geologic Investigation Map I-961, scale 1:25 million.

Survey of Cold-Climate Features on Mars*, B. K. Lucchitta, U. S. Geological Survey, Flagstaff, AZ 86001.

Introduction: On earth, glacial and periglacial features are common in areas of cold climate. On Mars, the temperature of the present day surface is appropriate for permafrost (1), and the presence of water is suspected from data relating to the outgassing of the planet (2), from remote sensing measurements over the polar caps and the martian surface (3,4), and from recognition of morphological features such as channels (5). These observations and the possibility that ice could be in equilibrium with the atmosphere north and southward from the 40° latitude line (6) suggest that glacial and periglacial features should exist on the planet. Morphological studies of the planet since the return of Mariner pictures have shown that such features occur (7,8) and since the return of Viking pictures many more have been detected. Carr and Schaber (9) summarized the new discoveries, and the present report builds on their discussion and adds some new observations. Excluded here are investigations into the composition and structure of the polar caps.

Mass wasting features: On earth, rapid and slow mass wasting is a powerful erosive agent in cold-climate regions. On Mars, as on earth, rockfalls build vast talus aprons wherever steep slopes occur, particularly on the walls of the Valles Marineris system of graben. There, talus aprons measure several thousand meters in height and have slope angles near 30 degrees. The martian aprons resemble terrestrial ones in having rocky ramparts near the top and coalescing fans below.

Avalanche deposits are also common in the Valles Marineris. They contain vast amounts of debris and resemble landslides in Alaska. Both the martian and Alaskan slides have longitudinally grooved debris aprons, a morphology that is restricted to landslides on earth that moved over glacier ice. The similar morphology suggests that ice possibly underlay the martian chasma floors or that it was dispersed in the moving debris. (10).

Slow mass movement features on Mars have attracted attention since the early return of Viking pictures. Spectacular examples are found in piedmont aprons around massifs near the Hellas and Argyre basins and around erosional remnants of the fretted terrain at the northern highland boundary. Longitudinally striped valley fill between mesas of the fretted terrain has been interpreted as debris moving slowly by frost creep or gelifluction (9), or as rock glaciers lubricated by interstitial ice (11).

Of similar origin may be the so-called "landslides" on the martian volcanoes (12). Below the Olympus Mons scarp, several large debris aprons resemble terrestrial rock glaciers or piedmont glaciers, such as the Malaspina glacier of Alaska as seen on Landsat images. The aprons locally bury mountains of the aureole material surrounding Olympus Mons. The aprons are bounded by regular and continuous curvilinear ridges that look like moraines. In places, where the aprons are thin, the bounding ridges are superposed without deflection on mountains of the aureole material. This superposition onto mountains of considerable relief suggests a gentle lowering of the ridge material from above, and it implies a process involving a substantial loss of material from the debris aprons. This material was probably ice. It is here proposed that the so-called landslides on Olympus Mons were glaciers or rock glaciers, issuing from near the scarp that surrounds the mountain.

Vast hummocky blankets bounded by continuous, subparallel curvilinear ridges are also found on the flanks of several other volcanoes, and they have been interpreted as landslides (9). The ridges on Arsia Mons resemble moraines and transgress a crater without deflection, similar to the ridges on Olympus Mons. Flow lobes that resemble those seen on rock glaciers on earth occur within the blanket farther up on the side of the volcano. The flow morphology and the moraines suggest that these blankets also consisted of ice mixed with debris. They may be the remnants of a former ice cap on the flanks of the volcanoes; perhaps a mixture of erupted ash and frozen volatiles caused the buildup of these caps.

Other subparallel curvilinear ridges in Utopia Planitia of the northern plains separate hilly terrain with polygonal patterned ground to the northeast from smooth terrain to the southwest. The ridges could be end moraines marking the southernmost reaches of a former extent of the north polar cap.

Patterned ground: A large part of the northern plains is underlain by a surface marked by polygonal patterns. Locally the polygons consist of well-defined cracks that have level floors; elsewhere the pattern is ill-defined with low swales bounding hills with roundish outlines. The polygons, which may reach 20 km in diameter, are invariably much larger than those of known patterned ground on earth (13). The possibility that the martian polygonal ground is related to permafrost contraction cracks has been suggested by Carr and Schaber (9). In support of the periglacial hypothesis is that (1) the polygons occur prominantly and pervasively in the northern plains near the polar cap; (2) polygons near the ice cap have upturned edges similar to actively developing polygons of the ice-wedge type on earth (14). Morris and Underwood (15) disagree with the periglacial hypothesis and favor contraction cooling of lavas for the origin. Both hypotheses suffer from the lack of an explanation for the large size of the polygons. A third alternative that does not suffer from size limitations is that the polygons are of tensional tectonic origin (16).

Curvilinear patterned ground consisting mostly of depressions may also be the result of a cracking process. Whether contraction of ice or dessication of clays may be involved is discussed by Rossbacher (7).

Thermokarst features: The presence of thermokarst on Mars has been suspected since the discovery of the chaotic terrain which consists of irregular depressions that may have formed by collapse (18). Also attributed to thermokarst was the fretted terrain whose morphology was compared by Gatto and Anderson (19) with that of thermokarst basins in Alaska. Irregular depressions and scalloped scarps near the Viking 1 landing site have been interpreted as alases (9). The chain craters that parallel the graben of the Valles Marineris occur along faults and look like collapse pits. They, too, may be thermokarst features that developed along the faults due to higher heat flow and preferential melting of ground ice. The melting of ground ice may also be responsible for the bottleneck shape and convex valley floors of incipient tributaries to the Valles Marineris troughs; the tributaries have the shape of thermokarst niches developed in the ice-rich banks of the Lena River in Russia (20). Deposits on the floors of some long tributaries to the troughs resemble valley glaciers or rock glaciers that transport debris from the valley floors into the troughs.

Volcanism and ice: The interaction of volcanism and ice on Mars has been explored by Hodges and Moore (21) who discovered mesa-like structures on the martian surface that resemble tablemountains in Iceland. These are volcanoes that grew largely underneath a cap of ice (22). Lobate features on Mars in the vicinity of Deuteronilus Mensae resemble lava flows but are sunken beneath the surrounding ground. They may have formed where the lava melted ice contained in the underlying ground causing collapse of the surface. Small circular depressions on these lobes may be pseudocraters that resulted from steam venting through the flows. Some curvilinear depressions on these flows may be coalesced pseudocraters.

Conclusion: Evidence that water and ice played an important role in the development of the martian surface is accumulating rapidly as the detailed study of Viking pictures progresses. Many more features of glacial and periglacial origin will undoubtedly be found in the future and contribute to an understanding of the evolution of the martian planet.

References

(1) Sinton, W. M. and Strong, J., 1960, Astrophysical Journal, v. 131, no. 2, p. 459-469; (2) Owen, T., Biemann, K., Rushneck, D. R., Biller, J. E., Howarth, D. W., and LaFleu, A. L., 1976, Science, v. 194, p. 1293-1295; (3) Kieffer, H. H., Chase, S. C., Martin, T. Z., Miner, E. D., and Palluconi, F. D., 1976, Science, v. 194, p. 1341-1344; (4) Farmer, C. B., Davies, D. W., and LaPorte, D. D., 1976, Science, v. 194, p. 1339-1341; (5) Milton, D. J., 1973, Journal Geophysical Research, v. 78, p. 4037-4047; (6) Fanale, F. R., 1976, Icarus, v. 28, p. 179-202; (7) Belcher, D., Veverka, J., and Sagan, C., 1971, Icarus, v. 15, p. 241-252; (8) Anderson, D. M., Gatto, L. W., and Ugolini, F., 1973, in Permafrost: the North American Contribution to the Second International Conference, National Academy of Sciences, Washington, D.C., p. 449-508; (9) Carr, M. H., and Schaber, G. G., 1977, Journal Geophysical Research, v. 28, no. 28, p. 4039-4054; (10) Lucchitta, B. K., 1978, Geological Society of America Bulletin, v. 89, no. 11, p. 1601-1609; (11) Squyres, S. W., 1978, Icarus, v. 34, p. 600-613; (12) Blasius, K. R., 1976, Ph.D. Thesis, California Institute of Technology, 85 p.; (13) Washburn, A. L., 1973, Periglacial processes and environments: St. Martin's New York, 320p. (14) Pewe, T. L., 1975, U. S. Geological Survey Professional Paper 835, 145 p.; (15) Morris, E. C., and Underwood, J. R., 1978, NASA Tech. Memo. 79729, p. 97-99; (16) Pechman, James, 1977, EOS American Geophysical Union Transactions, v. 58, no. 12, p. 1182; (17) Rossbacher, L. A. 1978, Second Coloquium on Planetary Water and Polar Processes, Hanover, NH, 16-18 Oct. 1978, in press; (18) Sharp, R. P., 1973, Journal Geophysical Research, v. 78, p. 4073-4083; (19) Gatto, L. W., and Anderson, D.M., 1975, Science, v. 188, no. 4185, p. 255-257; (20) Jahn Alfred, 1975, Polish Scientific Publishers, Warszawa, 223 p.; (21) Hodges, C. A. and Moore, H. J., 1978, in Lunar and Planetary Science IX, p. 523-525; (22) Van Bemmelen, R. W. and Rutten, M. G., 1958, Tablemountains of northern Iceland.

*Presented at and in press in Second Colloquium on Planetary Water and Polar Processes, Hanover, New Hampshire, 16-18 October 1978.

Tectonics of Venus: George E. McGill, Dept. of Geology and Geography, University of Massachusetts, Amherst, MA 01003

From the presence of very large and presumably ancient craters (1), Schaber and Boyce (2) argue that Venus is tectonically less active than Earth because its crust is dryer and thus more viscous. The abundances of ^{40}Ar in the atmospheres of terrestrial planets provide a crude measure of relative tectonic activity (here meant to include all processes such as volcanism and mountain building, and associated erosion, that bring fresh rock to the surface and liberate trapped ^{40}Ar). There are two Pioneer Venus measurements of ^{40}Ar mixing ratios in the lower atmosphere of Venus, one suggesting an abundance (in g/g of planet) about equal to that in Earth's atmosphere (3), the other suggesting an abundance about an order of magnitude less (4). The lower value is consistent with the ideas of Schaber and Boyce, but the higher value is not. It is important to consider the tectonic consequences if we assume that Earth and Venus atmospheres contain equal abundances of ^{40}Ar.

Relative abundances of ^{40}Ar are ambiguous without knowledge of the relative abundances of K. K, U, and Th are geochemically coherent elements with extremely low partitioning coefficients (5, 6) so that their concentration into the earliest-formed fraction of partially fused mantle rock is very efficient. The measured K, U, and Th abundances in Venus surface rocks are very similar to those in common differentiated igneous rocks on Earth (7). From these facts it can be argued that the planetary abundance of K on Venus is similar to that on Earth, and that the characteristic % of partial fusion on the two planets also is similar:

1. Assume much less K on Venus than on Earth. The low partitioning coefficient requires fusion of a smaller fraction of the mantle on Venus to produce melt with % K the same as on Earth. Less melt implies less volcanism and a lower level of tectonic activity. But if less K in the planet is to produce equal ^{40}Ar in the atmosphere, there must be more volcanism and tectonic activity, not less.

2. Assume much more K on Venus than on Earth. Now a larger fraction of the mantle on Venus must melt to dilute K down to the Earth %. More K means more U and Th, and thus greater heat generation. Both imply more volcanism and tectonic activity than on Earth. But the combination of more K and more volcanic and tectonic activity requires that atmospheric ^{40}Ar be much more abundant on Venus than on Earth, a result inconsistent with all Venus ^{40}Ar determinations.

Thus if the ^{40}Ar abundances in the atmospheres are about equal we are left with the probability that K is about as abundant on Venus as on Earth, and that both bodies are characterized by about equal levels of tectonic activity. How can this be reconciled with the presence of large and presumably primordial craters and with the possibility of a dry mantle on Venus?

1. On Earth there are continental regions that, though severely metamorphosed, have resisted recycling into the mantle for as much as 3.8 by (8), and there is no reason to believe that the oldest surviving crustal rocks have been found. The ancient surfaces of these continental plates have long since disappeared because of erosion and deposition, and thus we see no ancient craters. Without liquid water, erosion and burial on Venus should be

much slower, so it is possible for buoyant continental plates to retain vestiges of their ancient surfaces.

2. It is not at all obvious that Venus is totally dry. Much less than 1% H_2O is needed to reduce both the T of the solidus for partial fusion and the effective viscosity of solid mantle. Tectonic activity on Earth seems critically related to the depth of the lithosphere/asthenosphere boundary, a boundary that may be controlled by partial fusion in the presence of a trace of volatiles (9), or by concentration of shear stress in a narrow zone because of strong P, T, and stress dependence of the effective viscosity of solid mantle (10). The tectonic consequences of 4 models of volatile content and temperature of the upper mantle of Venus are explored on Figs. 1 and 2.

a. Venus upper mantle dry but hotter than Earth (thermal gradient in equilibrium with the high surface T). Curve A, Fig. 1, a conservative gradient for this model (parallel to Earth shield geotherm), intersects the dry solidus for mantle rocks at a depth of ∿150 km. Curve A, Fig. 2, indicates a change in effective viscosity with depth very similar to that for a wet-mantle Earth. Thus, a dry but hot Venus will have a lithosphere with a thickness similar to the Earth lithosphere.

b. Venus upper mantle dry but at about the same T as Earth. No partial fusion is possible because the geotherms do not cross the dry solidus (Fig. 1). Also, effective viscosities are very high (curve B, Fig. 2). For this model, the Venus lithosphere would be hundreds of km thick (if an asthenosphere existed at all).

c. Venus upper mantle both wet and hot. Even a conservative thermal gradient (curve A, Fig. 1) crosses the wet solidus (∿0.2% H_2O) at a depth of about 50 km. In addition, effective viscosities of the solid become very low at depths even less than 50 km (curve C, Fig. 2).

d. Obviously, if Venus is wet and has upper mantle temperatures similar to Earth, then the lithosphere should be about as thick as on Earth.

Only one of these models (b) predicts a very thick Venusian lithosphere. Because it seems unlikely that the high surface T of Venus is of recent origin, the upper mantle and crust of Venus probably are hotter than on Earth. Thus the Venus lithosphere is most likely the same thickness or, if a trace of H_2O is present, even somewhat thinner than the Earth lithosphere. If it is thinner, Venus tectonics may exhibit patterns similar to those resulting from Precambrian tectonic activity on Earth.

(1) R.M. Goldstein, et al., J. Geophys. Res., 81, 4807, 1976. (2) G.G. Schaber & J.M. Boyce, Lunar Sci. VIII, 835, 1977. (3) J.H. Hoffman, et al., Science, 203, 800, 1979. (4) V.I. Oyama, et al., Science, 203, 802, 1979. (5) J.A. Philpotts & C.C. Schnetzler, Geoch. Cosmoch. Acta, 34, 307, 1970. (6) M. Tatsumoto, Earth Planet. Sci. Lett., 38, 63, 1978. (7) D.M. Hunten, et al., Space Sci. Rev., 20, 265, 1977. (8) S.R. Hart & S.S. Goldich, Geotimes, 20, 22, 1975. (9) B.O. Mysen & A.L. Boettcher, J. Petrol., 16, 520, 1975. (10) C. Froidevaux & G. Schubert, J. Geophys. Res., 80, 2553, 1975. (11) I. Kushiro, et al., J. Geophys. Res., 73, 6023, 1968. (12) A.E. Ringwood, Am. Geophys. Union, Geophys. Mon. 13, 1, 1969. (13) D.H. Eggler, Geology, 4, 69, 1976. (14) D.H. Green, Earth Planet. Sci. Lett., 19, 37, 1973. (15) D.H. Eggler & J.H. Holloway, Ore. Dept. Geol. Min. Ind., Bull 96, 16, 1977.

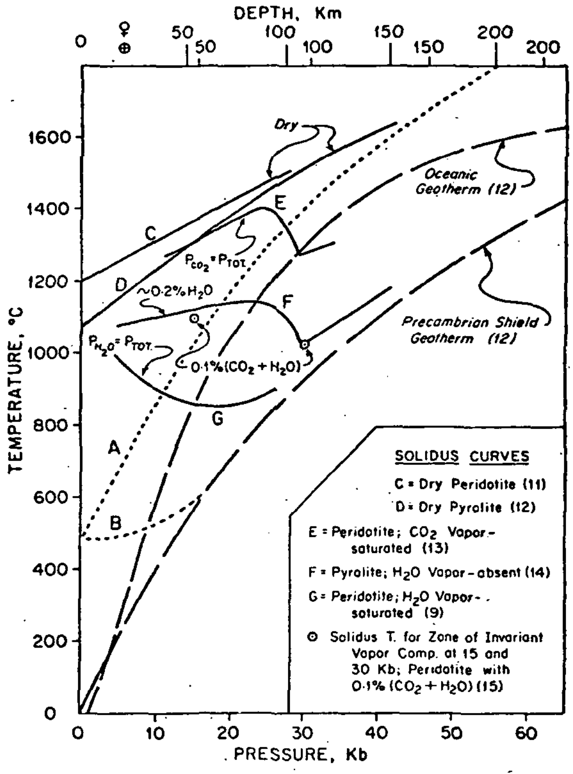

Fig. 1: Solidus curves for dry and wet mantle materials compared with oceanic and shield Earth geotherms. Two model Venus thermal gradients are shown, both starting at a surface T of 475°C: A) parallel to the shield geotherm but 475° hotter, and B) shallow near the surface but following the Earth shield geotherm at greater depths. Gradient B implies that the high surface T of Venus probably is not primordial.

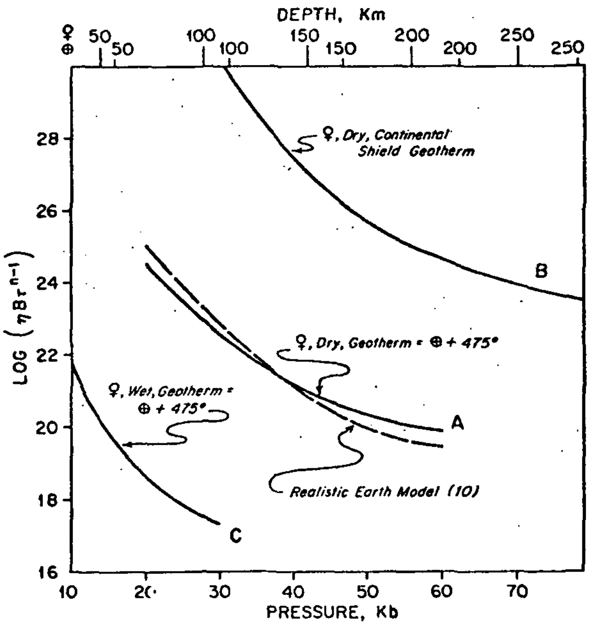

Fig. 2: Normalized effective viscosities as functions of depth for various models of T and volatile content of the upper mantle of Venus. Values are calculated from:

$$\eta = \frac{T\exp\{(E^*+PV^*)/RT\}}{2B\tau^{n-1}}$$

η = effective viscosity in poises
T = temperature in °K
E*= activation energy for steady-state creep
V*= activation volume for steady-state creep
P = confining pressure
R = gas constant
τ = shear stress
B = material-dependent constant
n = mechanism-dependent constant

T and P are derived from Fig. 1; V* is 20 cm^3/mol, corresponding to the most realistic model for Earth (10); E* is 95 kcal/mol in the presence of H_2O, 135 kcal/mol for totally dry conditions. Effective viscosity depends somewhat on petrology (B) and strongly on shear stress (τ^{n-1}). Because B and τ are not known, the curves show $\eta(B\tau^{n-1})$ vs. depth rather than η vs. depth. Thus the figure permits comparison of creep response to similar stresses assuming similar rocks.

Terrestrial and Martian Rock Labyrinths, George A. Brook, Department of Geography, University of Georgia, Athens, GA 30602

Rock labyrinths are produced when intersecting networks of faults and joints are selectively eroded. Deep terrestrial labyrinths are known in sandstone (e.g. southeastern Utah), basalt (channelled scablands of Washington State), and dolerite (Wright Dry Valley, Antarctica) but are most common and reach their greatest dimensions in limestone and dolomite (karst) terrains. Karst labyrinths have been identified in northwest Canada, the southwest Celebes, Sarawak, New Guinea, Australia, Brazil, and Cuba (Brook & Ford 1978). They have developed in climates ranging from humid tropical to subarctic, indicating that they are not climate- or latitude-dependent; they are structurally controlled landscapes.

During early stages of labyrinth karst development water draining underground via vertical fissures creates strings of vertical-walled solution dolines, circular to elliptical in plan view. By enlargement and coalescence along the fractures strings of dolines are converted to intersecting networks of karst streets. As streets deepen and widen, the intervening rock ridges are dissected and ultimately destroyed. Replacing them are large closed depressions of angular planform called karst platea. As platea expand rock towers are left which rise from uneven karst margin plains. Depths range from a few centimeters to a few hundred meters; streets may be several kilometers long. The evolutionary development of terrestrial labyrinths in non-karst rocks appears to parallel that in karst areas (Selby & Wilson 1971).

Pitted, etched, fretted, grooved, fractured plain, chaotic, and troughed terrains on Mars (Sharp et al. 1971 a,b; Sharp 1973 a, b, c; Sharp & Malin 1975; Woronow 1972; McCauley et al. 1972; Masursky 1973) resemble terrestrial rock labyrinths. Pitted and etched landscapes are common in the blanket "sedimentary" material of the Martian polar regions. Pits are topographically closed depressions 0.5 km to several tens of kilometers across and up to 400 m deep. As pits enlarge they become integrated forming etched terrains (Sharp 1973c). Pitted terrain appears to correspond to the doline-street stage of labyrinth karst development and etched terrain to the platea-tower stage.

The morphologic characteristics of fretted and chaotic terrains have been discussed by Sharp (1973b) who suggests that they are genetically related. Fretted terrain develops by scarp recession which isolates buttes, mesas, and towers; and superficially resembles terrestrial inselberg relief. However, closed depressions behind the retreating scarp indicate that fretted terrain is a late platea-tower stage in rock labyrinth development.

Grooved and fractured plain landscapes on Mars consist of parallel linear depressions similar to karst streets. Terrestrial karst topography of similar morphology is called zanjon karst (Monroe 1964).

The area of Mars that most resembles deep terrestrial rock labyrinths is the troughed terrain (Sharp 1973a) of Labyrinthus Noctis at the western end of Valles Marineris. Although developed on a much grander scale than anything on Earth the resemblance between it and the labyrinth karst of the Nahanni region of northern Canada is striking (Fig. 1). On upland surfaces near troughs there are frequently linear chains of pits, circular or elliptical in outline, 1-15 km wide and 0.5 km deep. Sharp (1973a) and Blasius et al. (1977) have noted that as the pits grow they become integrated along the fracture, eventually forming a small trough. The early stages of trough development on Mars are identical to the early stages of street development on Earth.

There is no consensus of opinion on the origin of labyrinths on Mars or on their origin in non-karst rocks on Earth. The Washington scablands were formed by catastrophic flooding and it has been suggested that the Wright Dry Valley labyrinth and some labyrinths on Mars were produced in a similar way (Smith 1965; Baker 1978). The processes involved in the development of labyrinth karst are better understood. Weathering is by solution; dissolved material is removed in waters that drain underground.

Volcanic bedrock is not highly soluble under terrestrial conditions. Extensive areas of volcanic rock on Mars may be susceptible along fractures to some other form of weathering which breaks the rock down into small particles. Weathering processes of possible importance include salt weathering (Malin 1974), hydrolytic disintegration (Huguenin 1974), abrasion (Baker & Milton 1974; Cutts et al. 1978) and impacting (Sharp 1973a). In karst regions weathered rock (in solution) is carried away in groundwaters; on Mars weathered debris of clay- or silt-size may be removed by wind. Deflation is an attractive hypothesis because it can produce closed depressions, and because global dust storms prove its importance on Mars.

References

Baker, V. R. (1978). The Spokane flood controversy and the Martian outflow channels. Science, 202: 1249-1256.

Baker, V. R. and Milton, D. J. (1974). Erosion by catastrophic floods on Mars and Earth. Icarus, 23: 27-41.

Blasius, K. R., Cutts, J. A., Guest, J. E., and Masursky, H. (1977). Geology of the Valles Marineris: First analysis of imaging from the Viking I Orbiter primary mission. J. Geophys. Res., 82: 4067-4091.

Brook, G. A. and Ford, D. C. (1978). The origin of labyrinth and tower karst and the climatic conditions necessary for their development. Nature, 275: 493-496.

Cutts, J. A., Blasius, K. R. and Roberts, W. J. (1978). Chaotic terrain and channels associated with Chryse Planitia, Mars: An alternative erosional model. NASA Tech. Memo 79729: 277-279.

Huguenin, R. L. (1974). The formation of goethite and hydrated clay minerals on Mars. J. Geophys. Res., 79: 3895-3905.

Malin, M. C. (1974). Salt weathering on Mars. J. Geophys. Res., 79: 3888-3894.

Masursky, H. (1973). An overview of geological results from Mariner 9. J. Geophys. Res., 78: 4009-4030.

McCauley, J. F., Carr, M. H., Cutts, J. A., Hartmann, W. K., Masursky, H., Milton, D. J., Sharp, R. P. and Wilhelms, D. E. (1972). Preliminary Mariner 9 report on the geology of Mars. Icarus, 17: 289-327.

Monroe, W. H. (1964). The zanjón, a solution feature of karst topography in Puerto Rico. U.S. Geol. Surv. Prof. Pap. 501-B: B126-B129.

Selby, M. J. and Wilson, A. T. (1971). The origin of the labyrinth, Wright Valley, Antarctica. Geol. Soc. Amer. Bull., 82: 471-476.

Sharp, R. P. (1973a). Mars: Troughed terrains. J. Geophys. Res., 78: 4063-4072.

Sharp, R. P. (1973b). Mars: Fretted and chaotic terrains. J. Geophys. Res., 78: 4073-4083.

Sharp, R. P. (1973c). Mars: South polar pits and etched terrain. J. Geophys. Res., 78: 4222-4230.

Sharp, R. P. and Malin, M. C. (1975). Channels on Mars. Geol. Soc. Amer. Bull. 86: 593-609.

Sharp, R. P., Murray, B. C., Leighton, R. B., Soderblom, L. A. and Cutts, J. A. (1971a). The surface of Mars 4. South polar cap. J. Geophys. Res., 76: 357-368.

Sharp, R. P., Soderblom, L. A., Murray, B. C. and Cutts, J. A. (1971b). The surface of Mars 2. Uncratered terrains. J. Geophys. Res., 76: 331-342.

Smith, H. T. U. (1965). Anomalous erosional topography in Victoria Land, Antarctica. Science, 148: 941-942.

Woronow, A. (1972). Origin of the Martian chaotic terrains. Science, 178: 649-650.

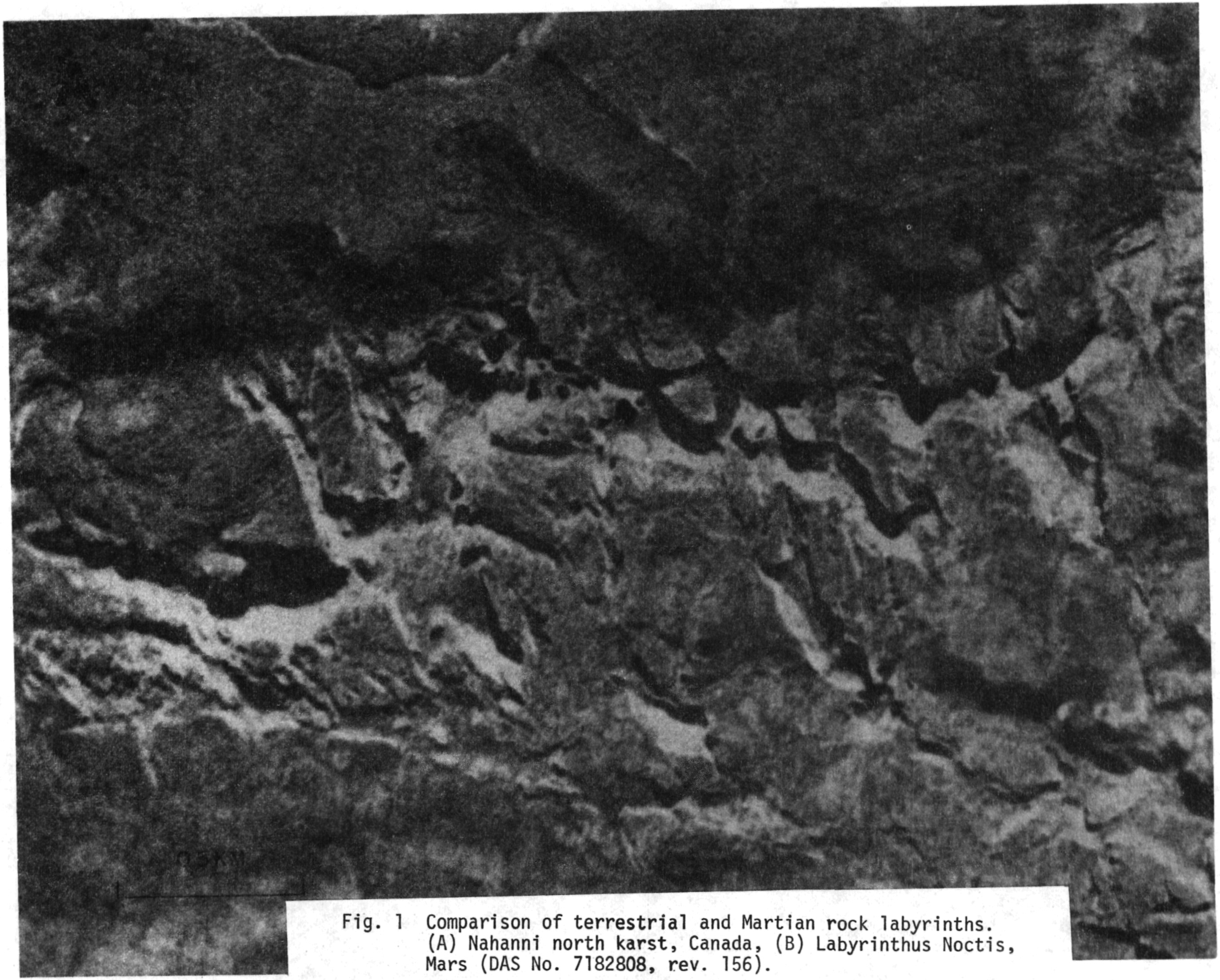

Fig. 1 Comparison of terrestrial and Martian rock labyrinths. (A) Nahanni north karst, Canada, (B) Labyrinthus Noctis, Mars (DAS No. 7182808, rev. 156).

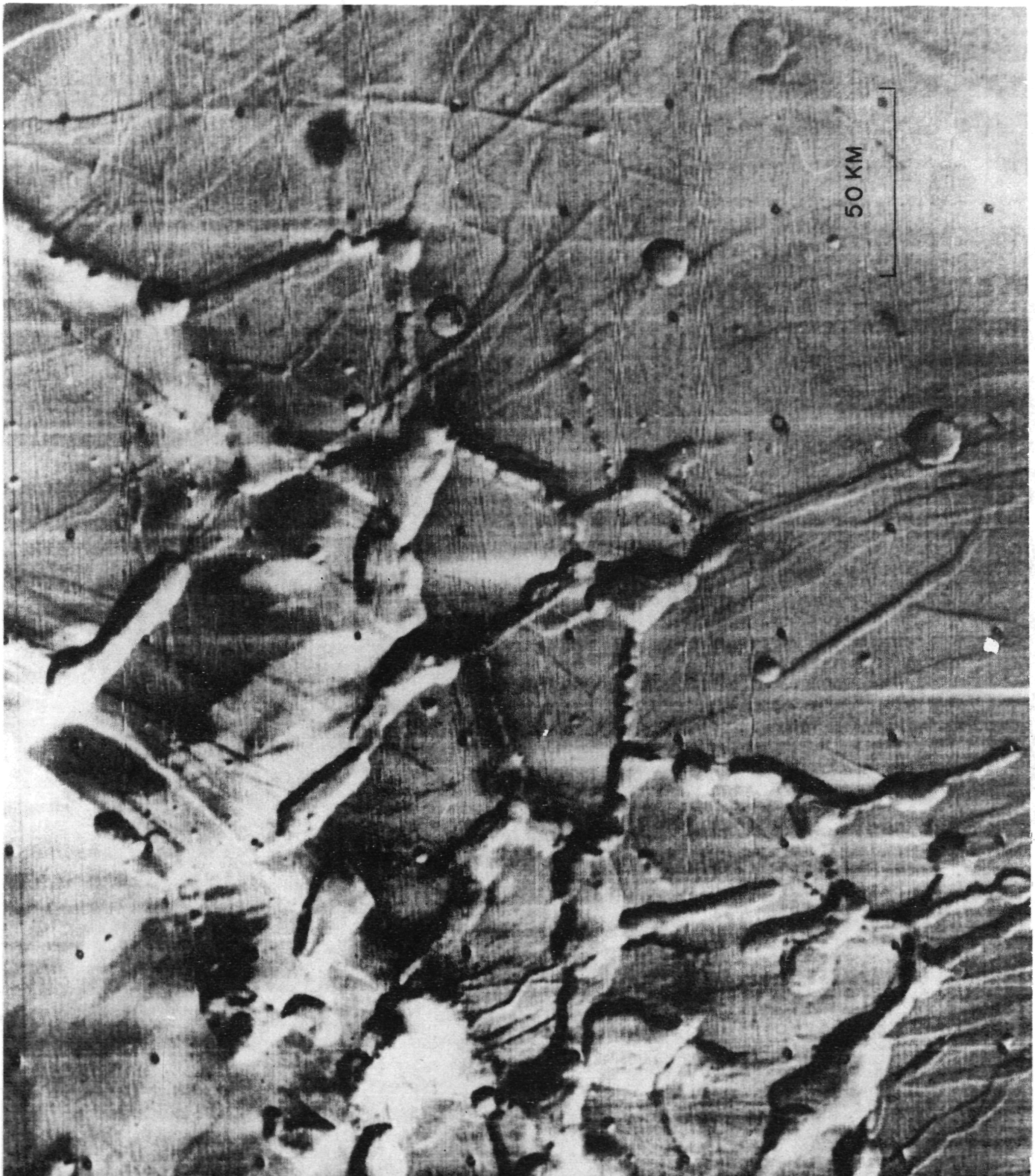
50 KM

Tectonism of the Tharsis Region, J. B. Plescia, Jet Propulsion Laboratory, California Institute of Technology, Pasadena, CA 91103/Dept. of Geological Sciences, Univ. So. Calif., Los Angeles, CA 90007 and R.S. Saunders, Jet Propulsion Laboratory, California Institute of Technology, Pasadena, CA 91103

In understanding the geologic and tectonic history of Mars, one of the most important regions is Tharsis, the site of most of the major volcanic edifices as well as a region of intense faulting. The two most common structural features of the region are graben and irregular ridges resembling those on the lunar maria. The graben, as well as most of the other faults and lineaments, are interpreted to be the expression of tensional forces. The ridges have been interpreted to be compressional in origin as were similar features on the Moon (1). Additional features observed are unpaired normal faults, lineaments, a possible thrust fault, and chains of coalescing pits that form linear depressions. Series of graben occur in groups and singly throughout Tharsis, with the groups being more common.

The Sirenum-Memnonia Fossae region exhibits a pattern of en echelon graben. The en echelon graben are typically only a few km long, while the zones extend for hundreds of km. A final type of feature is seen in the Tantalus Fossae and Memnonia-Sirenum Fossae region. Series of pits coalesce down strike into a feature that resembles a graben. This type of feature is particularly common on volcanic shields, and appears to represent some of the most recent activity.

A series of long scarps, up to 1800 km in length, represent the recent activity of the Claritas-Thaumasia Fossae region. The strike of these scarps is approximately SE, but changes locally along strike and as branches splay out, or join the main fracture. The two sets outline a large graben-like structure approximately 75-100 km wide. This feature may be analogous to a proto- Valles Marineris, which either is just beginning to form, or which was aborted in its early stages of development.

The only interpreted compressional features that have been recognized are the irregular ridges which occur on the plains type material. Surfaces in the Solis-Sinai-Lunae Planum regions, as well as western Amazonis and individual large basins of Sirenum region have these linear ridges. The ridges seem to be generally concentric to the central Tharsis region. Plains similar to Lunae Planum in both age and structural style occur in other regions of Mars. This might suggest that the Lunae Planum plains and the ridges which occur on them are not directly related to Tharsis activity.

The Tharsis region on a global scale is the center of a series of radiating fractures and circumferential ridges (Carr (2)). The fracture systems, as well as local volcanic morphology have a preferred NE/SW crustal weakness. We have prepared a pair of stereo plots of the major faults of the region. It is our contention that fractures can be separated into two individual centers of differing age. Figures 1 and 2 are stereo plots of the faults related to each of the two centers. One center, the older of the two, is located in northern Syria Planum, just south of Noctis Labryrinthus at 100°W, 8°S. The second, and younger center is located approximately at the position of Pavonis Mons at 110°W, 4°S.

The fracture pattern centered on Syria includes the fractures associated with the following areas: Ceranumius Fossae, the NNE/SSW fractures SE of Uranius Patera, the fractures north of Noctis Labyrithus, and several isolated windows throughout Tharsis.

The fracture pattern, centered on Pavonis, is more limited in extent, and is principally exposed as the fractures of Tempe-Mareotis Fossae and the Memnonia-Sirenum Fossae regions. Additionally, fractures are exposed in the Solis Planum region and superimposed on older fractured terrain of the Claritas-Thaumasia Fossae region and other areas.

From geologic and crater counting data the following generalized tectonic history is proposed. An early fracture system centered in southern Thaumasia - perhaps related to an uplift (Frey (3)). This system is poorly represented, save in a few windows in the Solis Planum region and perhaps structural control for the Valles Marineris.

The center of activity apparently then moved northward to the center in northern Syria. This stage of fracturing apparently began just after the emplacement of Lunae Planum and equivalent units, as these age units are in places cut by Syria faults. This episode of faulting is also contemporaneous with the early construct building mechanism in northeast Tharsis. Faulted surfaces of this age are believed to underlie much of the Tharsis region, and are now covered by later plains units. Only those topographically high regions are now exposed as windows in the plains units.

The faulting associated with this center appears to have been constrained in a generally north/south direction. Surfaces that predate this episode of faulting, the plains south of Eos and western Coprates Canyons, are not extensively cut by faults, and only a few structures of the Memnonia-Sirenum region to the west can be correlated with this system.

Following this episode of faulting the plains units of Syria-Sinai-Solis Planum were formed. Additional units in the Memnonia Sirenum region were also formed at this time. It is unknown if the plains forming volcanism was contemporaneous with the faulting or if it ceased during this time, and resumed post faulting.

A new center of faulting was then established in the region of Pavonis Mons, which at this time did not exist. The fractures of this system may be related to an episode of uplift preceeding the Tharsis volcanic plains and volcanoes (Hartmann (4)). The fracture patterns are also consistent with a failure model of Phillips et al. (5). This system includes the fractures of Mareotis-Tempe Fossae and the fractures of Memnonia-Sirenum Fossae. The fracturing principally is restricted to a NE/SW direction, and did not affect the regions to the SE or NW. This general strike of these fractures follows the present alinement of the Tharsis Montes volcanoes.

The Tharsis plains were then emplaced over this faulted surface. The Tharsis volcanic plains flood several structural features developed during the previous faulting episode. Following the emplacement of the distal Tharsis cover, the shields began to develop. The development of the Tharsis Montes volcanics appears to have been northeastward. Arsia Mons is the oldest, then Pavonis Mons, and finally Ascraeus Mons. Olympus Mons is the youngest of the Tharsis volcanic constructs.

Apparently post dating the fracturing of the Tharsis region, and the emplacement of the plains units of Syria Planum, tectonic activity resumed at the Syria center. This renewed activity seems to have been a second doming event which generated the graben system of the Noctis Labyrinthus region, and the present topographic high in the area.

Following the development of the volcanoes, and apparently in response to lithosphere loading by the volcanoes, the fracture system center on the Pavonis site was reactivated. These fractures cut the Tharsis cover, and in some cases extended to near the shields. The fractures of this system are small graben, undifferentiated lineaments, and a series of pits that coalesce to form graben-like structures. This system is poorly developed and represents only a few of the Tharsis fractures.

REFERENCES: 1. Howard, K. and Muehlberger, W., 1973, Apollo 17 Preliminary Sci. Report; 2. Carr, M., 1973, JGR, 78, 4047-4062; 3. Frey, H., 1977, Goddard Space Flight Center Report X-922-77-241; 4. Hartmann, W., 1973, Icarus 19, 550-575; 5. Phillips, R., Saunders, R.S. and Banerdt, B., 1979, JGR (in press); 6. Wise, D., 1976, Geol. Romana 15, 430-433.

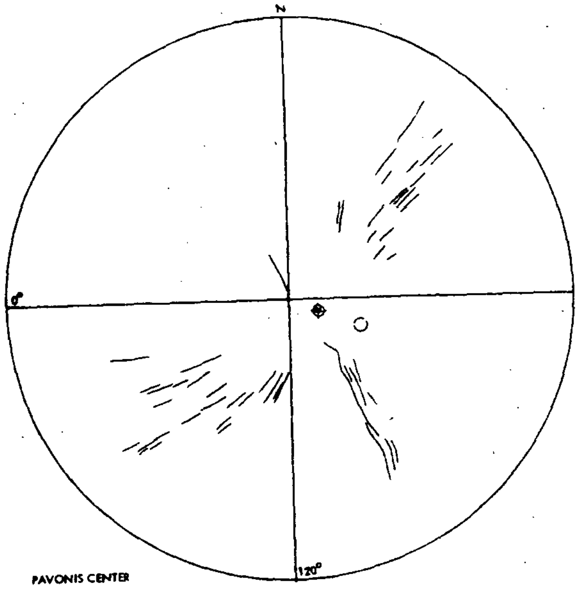

Figure 2. Faults associated with the center in the Pavonis Mons region, centered at 110°W, 4°S. Filled circle indicates Pavonis center, open circle, Syria center.

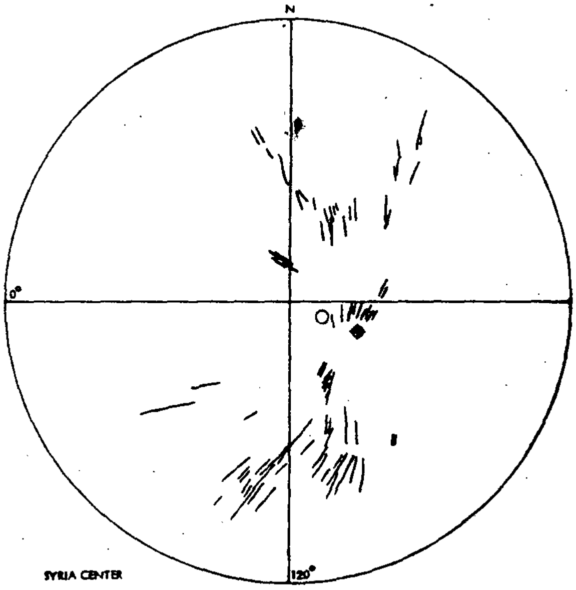

Figure 1. Faults associated with the center in the Syria Planum region at 100°W, 8°S. Filled circle indicates center of fractures, open circle - Pavonis center.

THE DISTRIBUTION OF LOBATE DEBRIS APRONS ON MARS

S. Squyres, Department of Geological Sciences
and Laboratory for Planetary Studies, Cornell
University, Ithaca, New York, 14853

Planet-wide mapping of lobate debris aprons and other similar flows at the bases of escarpments on Mars shows a strong concentration in two latitudinal bands roughly 25° wide and centered at 40°N and 45°S (see Fig.). These should also be latitudes that receive high seasonal H_2O frost deposition relative to the rest of the planet. The distribution therefore supports the hypothesis (Squyres, 1978) that these flows form when erosional debris is transported downslope and becomes mixed with ice deposited seasonally from the atmosphere, creating a mass that slowly deforms and flows due to creep of the interstitial ice.

The distribution <u>within</u> the two latitudinal bands is not uniform, but is concentrated in distinct regions. Because the flow process is limited by the supply of mass-wasted debris as well as that of ice, the distribution may be a useful indicator of the relative amounts of mass-wasting that have occurred in different regions within the bands. In the northern band, flows are found virtually everywhere old highland surfaces are exposed. The only large escarpments in this band that are consistently free of flows are those clearly associated with volcanic landforms. In the southern hemisphere, however, flows are only found in highlands adjacent to the two major impact basins, Hellas and Argyre. Large regions of the southern hemisphere highlands lie within the latitude range that should receive high H_2O deposition, possess abundant large escarpments, and yet exhibit no lobate debris aprons. Because the highlands in the northern band are generally no older than those in the south, this distribution probably reflects real differences in mass-wasting rates. The relatively rapid mass-wasting near Hellas and Argyre may be due to material weakening associated with the basin-forming impacts. The reason for the general contrast in mass-wasting rates between the two latitudinal bands (rapid in the north, show in the south) is unclear, but may be closely related to the marked north-south geologic asymmetry of the planet.

Reference: Squyres, S. W. (1978). Martian fretted terrain: flow of erosional debris. Icarus, 34, 600-613.

Figure Caption: Map showing the global distribution of flows. Squares indicate lobate debris aprons; circles indicate small craters possessing concentric fill. Large symbols denote regions of unusually high concentration of flows.

This work was supported by NASA Grant NSG 7156.

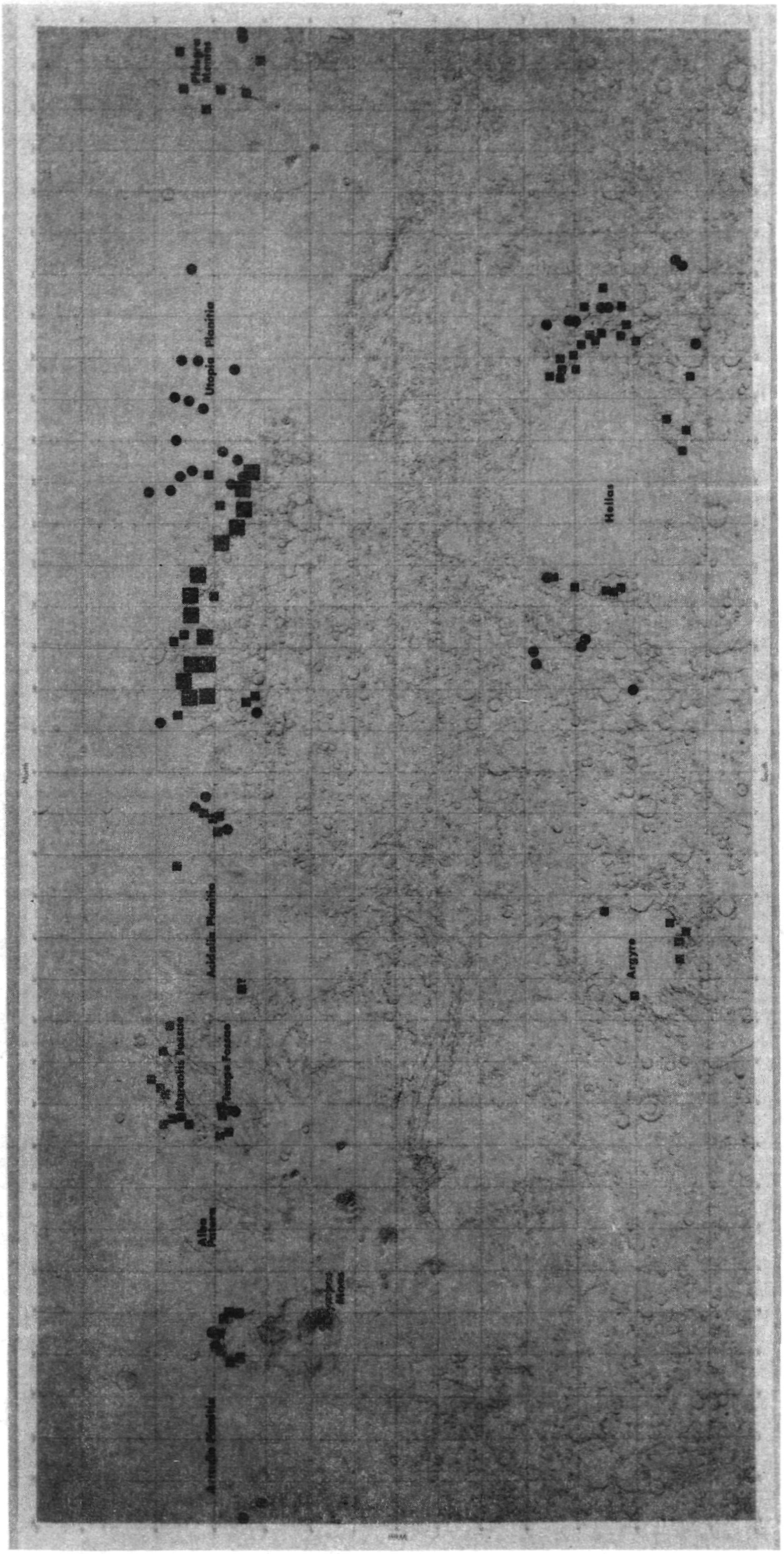

Squyres' figure

Color Changes At The Viking Landing Sites Over The Course Of A Mars Year,

E. Guinness, R. Arvidson, L. Gehret and L. Bolef, Dept. of Earth and Planetary Sciences, Washington University, St. Louis, Mo., 63130

The Viking Lander imaging observations provide a unique data set, allowing observations of the martian surface in sufficient detail so as to be able to decipher subtle changes and to infer how they are controlled by the physicial properties of the sites. The information derived from lander images can help to constrain hypotheses dealing with global scale changes seen on Mars, namely those changes induced by wind erosion, transport and deposition of sediment. We have tracked the distribution of soil color over time from Lander data by examining images formed by dividing the brightness of the surface in red light by the brightness in blue. The effective wavelength for the Lander camera red channel is 0.669 microns and 0.500 microns for the blue channel. The results and implications of our preliminary examination of color changes at the Viking landing sites over the course of the past Mars year can be summarized as follows.

(1) There have been significant color changes at both Viking landing sites (fig. 1). Both surfaces exhibited an increase in the red to blue ratio (R/B) of the soil, a loss of contrast between soil units, and an overall brightening of the scene. These changes were first detected during the northern spring season after major dust storm activity had ceased. The color changes are consistent with a blanketing of the sites by a thin layer of bright dust, probably only microns in thickness. Such a conclusion is consistent with the mild aeolian regime inferred for Mars by Arvidson _et_. _al_., (1979).

(2) A systematic variation in the R/B of the soil can be seen in the VL2 post-dust storm data (fig. 1d). The R/B of the dust increases as the phase angle increases (fig. 2). One possible explanation of the R/B dependence on phase angle is that the surface has brightened enough to introduce a wavelength dependence in the photometric function due to multiple scattering (Veverka _et_. _al_., 1978). Alternately the variation of the R/B with phase angle could be due to the combination of a backscattering surface and color differences between the sunlight and skylight components of the illumination function. In any case, the variation of color with lighting and viewing geometry must be accounted for when trying to compare martian reflectance spectra with laboratory spectra.

(3) Changes in contrast of a drift at VL1 (fig. 1a) were related to aeolian stripping and deposition of material. The stripping occurred before the onset of the first global dust storm observed by Viking, indicating that threshold velocities needed to entrain soil are reached or exceeded at times other than those corresponding to global storms. An accumulation of soil on the drift occurred after most of the dust had settled out of the atmosphere from the second global storm. Such observations are consistent with evidence of aeolian activity not associated with the global dust storms as observed by orbital spacecraft and by earth-based astronomers (Sagan et. al., 1973; Baum, 1974).

(4) Residual patches of the condensate deposit detected at VL2 (Jones _et_. _al_., 1979) when corrected for the color of the sunlight and skylight clearly are not gray, but have a reddish tint. The condensate would be gray if the material were free from dust (Kieffer, 1970; Johnson and McCord, 1970).

The reddish tint of the condensate thus implies that it is mixed with or coated by a red dust. From preliminary analysis of earlier data it appears that the condensate always had a R/B > 1, which supports the hypothesis proposed by Jones et. al., (1979) that the dust acted as nuclei for condensation of CO_2, H_2O, and clathrates.

(5) Finally, the changes that have occurred to the landing sites over the course of the past Mars year may help explain how bright and dark regions are generated by aeolian processes. The bright red dust that blanketed the two sites is probably equivalent to material that covers bright regions, since McCord et. al., (1977) show that bright areas and dust clouds are among the brightest and reddest features on Mars. Our data indicate that brightening of a region is a blanketing process, needing only microns worth of material to mask the spectral properties of underlying deposits. The general brightening and reddening of the landing sites made the surface merge with the color of the drift at VL2 shown in Figures 1c and 1d and the drift at VL1 shown in Figures 1a and 1b. A number of other discrete red drifts can be seen extending toward the horizon at both landing sites, giving a "checkerboard" appearance to the sites, if seen from overhead. Areas covered with red material may be regions where winds can not erode the surface as readily as surrounding areas, because a cluster of boulders or other topographic obstacles disturbs the flow field and protects the drifts from wind erosion. Thus, the generation of dark regions on Mars may be a much more complex process than the generation of bright areas. Namely, the extent of stripping of a surface is spatially heterogeneous and probably controlled by the distribution of roughness elements of sufficient size so as to disturb the atmospheric flow field.

References

Arvidson, R., E. Guinness and S. Lee, 1979. Differential Aeolian Redistribution Rates on Mars. Nature, in press.

Baum, W., 1974. Earth-based Observations of Martian Albedo Changes. Icarus, Vol. 22, 363-370.

Johnson, T. and T. McCord, 1970. Galilean Satellites: The Spectral Reflectivity 0.30-1.10 Micron. Icarus, Vol. 13, 37-42.

Jones K., R. Arvidson, E. Guinness, S. Bragg, S. Wall, C. Carlston and D. Pidek, 1979. Viking Lander Observations of Sediment Transport and H_2O-condensates. Science, in press.

Kieffer, H., 1970. Spectral Reflectance of CO_2 - H_2O Frosts. J. Geophysical Research, Vol. 75, 501-509.

McCord, T., R. Clark and R. Huguenin, 1977. Mars: Near Infrared Spectral Reflectance and Compositional Implications. J. Geophysical Research, Vol. 83, 5433-5441.

Sagan, C., et. al., 1973. Variable Features on Mars, 2, Mariner 9 Global Results. J. Geophysical Research, Vol. 78, 4163-4196.

Veverka, J., J. Gouguen, S. Yong and J. Elliot, 1978. Near-opposition Limb Darkening of Solids of Planetary Interest. Icarus, Vol. 33, 368-379.

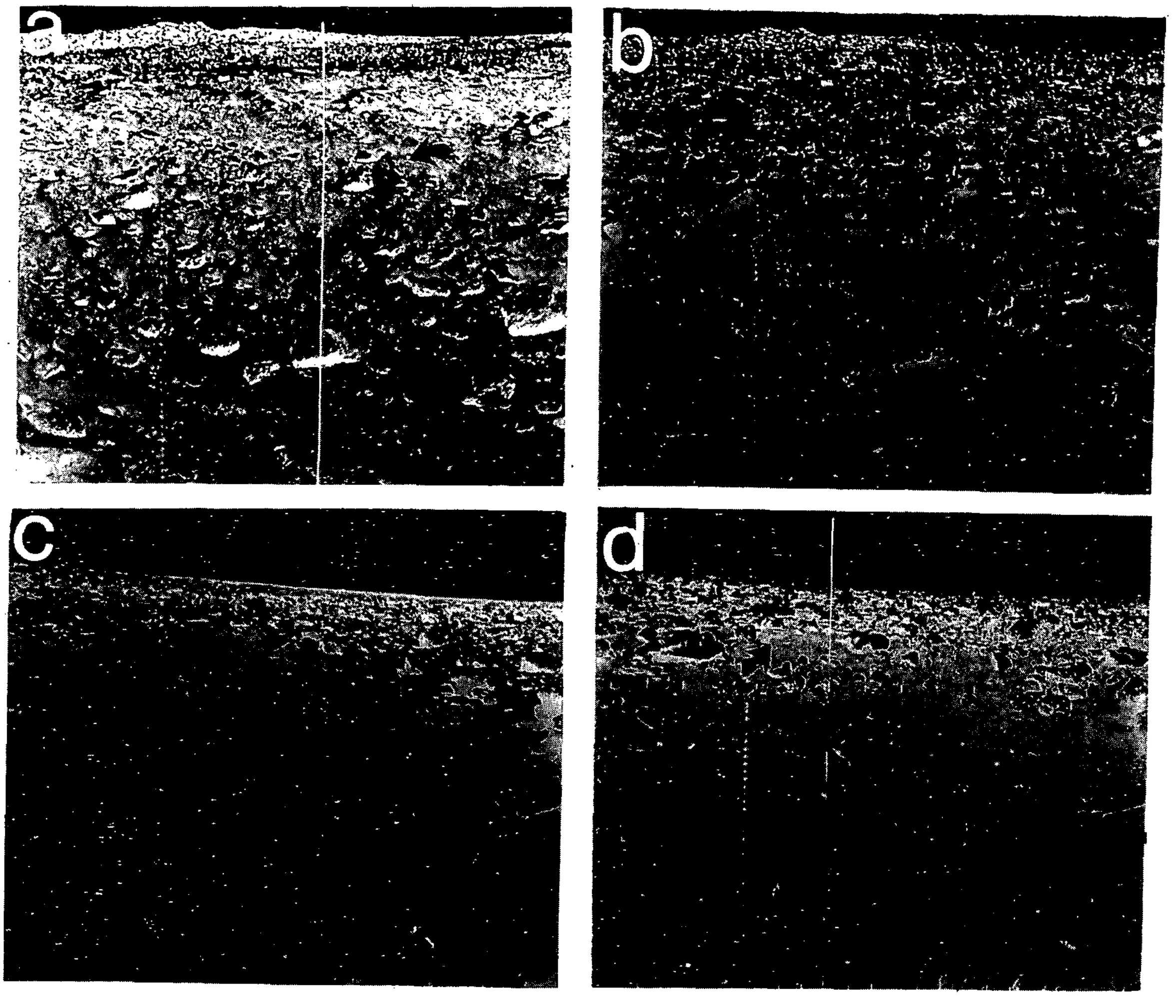

Figure 1: The frames are R/B image pairs for VL1 (a,b) and VL2 (c,d) taken before and after the global dust storms, with similar lighting conditions. The images are displayed such that high R/B values are light (i.e. shadows around rocks) and low R/B values are dark. The VL1 pair were constrast enhanced by the same amount. The VL2 Primary Mission R/B image (c) was contrast enhanced more than the VL1 R/B images (a,b) so that the VL2 R/B image has the same brightness range in the figure as VL1 R/B image. The VL2 post-dust storm R/B image (d) was contrast enhanced even more than the pre-dust storm one (c) in order to illustrate the R/B dependence on phase angle (fig. 2). The arrows in a & b point to soil patches that merged in color in the post-dust storm data. The arrows in c & d point to a drift at VL2 that has the same color as the new dust layer at VL2. (A) VL1 frame 12A168/028 (solar azimuth = 82°, elevation = 82°) (B) 12H196/615 (AZ. = 79°, EL. = 82°) (C) VL2 frame 22A190/023 (AZ. = 188°, EL. = 61°) (D) 22G105/525 (AZ. = 208°, EL. = 59°).

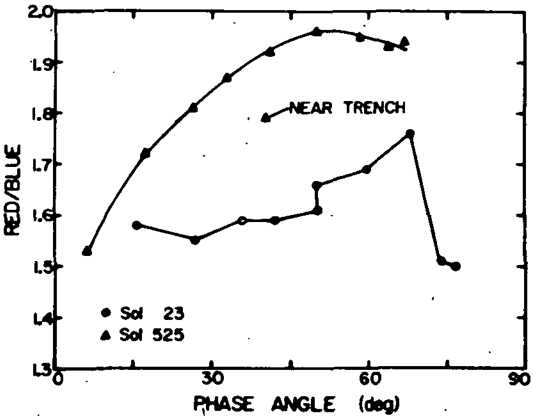

Figure 2: The R/B of selected soil patches are plotted versus phase angle for the VL2 sol 525 image (triangles) and the sol 23 image (circles). The R/B dependence on phase angle could occur because either the surface has brightened enough to introduce a wavelength dependence in the surface photometric function due to multiple-scattering (Veverka et. al., 1978) or the surface preferentially backscatters a less red sunlight component of the illumination function at small phase angles. The effect is less pronounced in the sol 23 image probably because the surface consisted of a mixture of soil units with differing photometric properties.

SOIL STRATIGRAPHY AND ROCK COATINGS OBSERVED IN COLOR ENHANCED VIKING LANDER IMAGES, E.L. Strickland III, McDonnell Center for the Space Sciences, Washington Univ., St. Louis, Mo. 63130.

Subtle color variations of martian surface materials were enhanced in eight Viking Lander color images processed at the U.S.G.S. Flagstaff Image Processing Facility. Before enhancement, the image data was computer stenciled to blacken any portions of the image containing saturated data. "Equalized color" images were constructed with the color balance adjusted so that the median color of the martian surface is protrayed as neutral gray. "Color information" ratio images were constructed for each color: Blue/(Green + Red), Green/(B + R), and Red/(B + G). These were composited to form images portraying relative colors without any brightness information. The ratio images were contrast stretched and combined with brightness information from the red image to yield "enhanced color" images. These portray relative color variations of materials in a generally reddish scene. Color artifacts due to the lander cameras are minor and do not hamper image analysis. Two tests demonstrate that colors in the enhanced images represent real features of the martian scene. Overlapping images taken with separate cameras reveal the same relative colors. Two images of the same scene taken at different times of day show that colors of sunlit materials do not depend strongly on illumination direction.

Because the color information in each band was enhanced separately, with green being enhanced the most, and red the least, hue shifts occur for most colors. Relative color relationships are uneffected by the enhancement process, and colors in the enhanced images can be interpreted in a natural manner. Colors referred to in this report will represent relative colors as seen in the color enhanced images.

1.) Soils. Five soil surface colors have been recognized at the Viking 1 site. Three soil stratigraphic units have been tentatively identified. The uppermost unit is a bright "red" soil that forms a thin discontinuous layer covering other soils. This unit is at most a few centimeters thick near the lander, and may be only microns thick. Underlying the bright "red" soil, both in rocky areas and dust drifts, is a dark "blue" soil. It is present in the walls of the "sandy flats" trench, and is exposed near the lander where retrorocket exhaust apparently stripped away the bright "red" soil. It also is exposed in irregular patches adjacent to many rocks beyond the range of visible landing disturbance. The third soil unit is exposed in one patch under retrorocket 2, where "blue" soil appears to have been eroded by exhaust. This patch of bright "orange-red" soil, previously identified (1) as duricrust, is uniquely colored. The extent and depth of this soil is not apparent in available images.

The fourth soil color, not assigned a stratigraphic unit, is "blue-green". This color appears at the "rocky flats" patch of duricrust, and on several patches on the smooth dust drifts. This color could be attributed to a hypothetical thin layer of "blue-green" soil between the "blue" and "red" soils, but other evidence for such a soil unit is lacking. The fifth soil color at the Viking 1 site is the dark soil that forms a cap on the "Big Joe" boulder, and surrounds other boulders northeast of the lander. This fifth soil unit is definitely "redder" than the bright "red" soil. The "dark red" soil's stratigraphic position cannot be deduced from the enhanced images.

Relative soil colors at the Viking 2 site are similar to those seen on the other side of the planet. Duricrust-textured surfaces are "redder" than the scene median. A darker "blue" soil appears to have been exposed when.

reddish duricrust under retrorocket 2 was eroded, and deposited both on duricrust near the rocket and on duricrust colored soil coating footpad 3. This "blue" soil is also exposed in two trenches where duricrust was sampled. A thin layer of intermediate brightness "green-blue" soil is present as smooth patches that fill shallow dips and hollows in the duricrust. This soil also appears to form the small drifts of soil in the linear trough several meters from the lander. Just beyond the trough, and in many patches further towards the horizon, are smooth surfaced drifts of bright "red" soil identical in color to the duricrust. These patches nowhere appear to be covered by the "green-blue" soil, and may thus be the uppermost of these four soil stratigraphic units.

The similar relative soil colors seen at the two landing sites are matched by similarities in inferred stratigraphy. "Red" non-duricrust soils are the uppermost, underlain by "green-blue" or a possible "blue-green" (VL-1) soil. Lowermost are the duricrusts and "blue" soils. The "dark red" soil at VL-1 has no counterpart at VL-2.

2.) Rocks. At Viking 1, most probable bedrock and many loose rocks near the lander have very light surfaces, with a green/(blue + red) ratio greater than any other surface material. They appear bright "green" in the enhanced images. Edges and corners often appear darker, very "blue", and do not show the "green" excess brightness. Color patterns on rock surfaces do not correlate with surface textures. No soils are visible that have a color similar to these rocks. The visual impression is that of a thin (millimeters to microns thick) surface coating formed on the rock. This material is interpreted to be a weathering product formed in situ on the rock surfaces.

East of Lander 1, a well defined field of "very blue" rocks is present. These rocks appear to have only minor surface areas of "green" color. "Big Joe" and other boulders north-east of VL-1 may belong to this field. A working hypotheses to be further investigated is that "green" coatings develop slowly, and the "very blue" boulder field may be relatively recent ejecta from a nearby impact crater. Apparent soil coatings on rocks are uncommon at this site.

At the Viking 2 site, only one color population of rocks appears to be present. "Green" colored surfaces are moderately abundant on rocks of all textures. Many rocks appear to have a thin ($<$ millimeters) coating of "red" soil that is identical in color to the "red" drifts and duricrust. The brightest rock surfaces are "yellow" areas that appear at the boundaries of "red" and "green" rock surfaces, and on projections where the "red" coating appears to be thinner. A speculation is that the "yellow" material may form on "green" surfaces that are covered by the "red" soil.

Relative rock colors seen at both sites are nearly identical, though proportions of each vary between sites. Only a few rocks at VL-1 appear to have soil coatings. The fraction of rock surfaces that have the "green" color at VL-2 is intermediate between those of the two rock populations at VL-1. "Yellow" surfaces are also quite rare at VL-1. It should be noted here that the "very blue" rock surfaces appear nearly gray in natural color images.

3.) Conclusions and implications. Significant color variations occur for soil and rock surfaces on Mars, and these can be used to infer soil stratigraphies and the presence of rock coatings at both sites. The great similarities in relative soil colors at both sites imply that planetwide, and not locally important processes are involved. While global mixing of soils probably is a major process, complete homogenization has not occured. The similar interpreted soil stratigraphy seen at the two sites suggests that globally distributed soil stratigraphic units may be present on Mars. The stratigraphic sequence of different colored soils may represent changes in the global supply of soils being eroded and redistributed planetwide. It may be possible to search for and tentatively identify global sources for soils of the colors seen at the Viking sites using enhanced color imagery from the Viking Orbiters, and earth-based spectral maps.

The relative colors of rock surfaces seen at both sites are extraordinarily similar. The observations are consistant with the presence of igneous rocks that develop "green" weathering coatings, and that may have thin coatings of adhering soil. If the rocks were "ferricrete" (1) or perhaps impact lithified soil, their colors would probably indicate their relationship to the soils. Other than a tendency for the inferred weathering and soil coatings to appear thinner on edges and protuberances, and for small amounts of soil collected in pits on rocks, textural control of rock colors is absent. If the color variations of rock surfaces do not reflect mineralogic variation within the underlying rock, it can be concluded they are the result of globally active environmental processes.

This work was carried out as a graduate summer internship at the U.S.G.S. Flagstaff Field Center, under the guidance of Dr. Elliot Morris and Dr. Larry Soderblom.

Reference: Mutch, T.A., et al., (1976). Science <u>194</u>, 1277-1283.

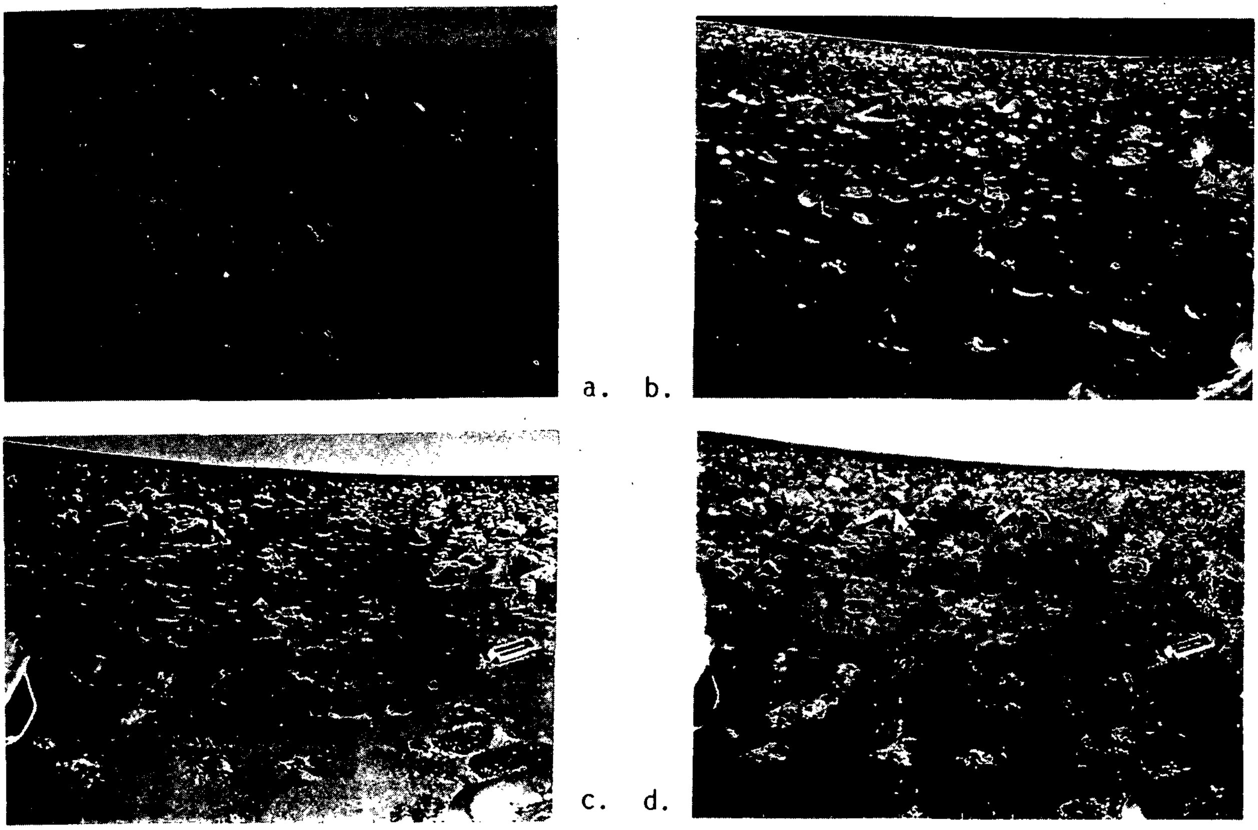

a. b.

c. d.

Figure. Frame 22A190/023 (a) Stenciled red image. (b) Red/(B+G) ratio. (c) Blue/(G+R) ratio. (d) Green/(B+R) ratio.

THICKNESS OF THE MARTIAN LITHOSPHERE FROM TECTONIC FEATURES: EVIDENCE FOR LITHOSPHERIC THINNING BENEATH VOLCANIC PROVINCES

Sean C. Solomon[1], James W. Head[2], and Robert P. Comer[1]

[1]Dept. of Earth and Planetary Sciences, Massachusetts Institute of Technology, Cambridge, MA 02139; [2]Dept. of Geological Sciences, Brown University, Providence, RI 02912.

The lithosphere on Mars is thought to be substantially thicker than on the Earth, and thus capable of statically supporting larger shear stresses, on the grounds of the roughness of the planetary gravity field [1], the heights of the youngest shield volcanoes [2,3], the lack of appreciable seismicity [4], and global thermal history models [5]. It has been suggested that evidence for a thickening of the Martian lithosphere with time is given by an apparent increase in the heights of Martian volcanic constructs with time [6] and a decrease in the intensity of circumferential fracturing around major shields [7]. Superisostatic loading on a planetary surface leads to lithospheric flexure and, for sufficiently large loads, to bending stresses capable of fracturing the lithosphere. The radial distance of fractures from a given load is a sensitive indicator of the thickness of the elastic lithosphere [8], i.e. the upper third to half of the thermal lithosphere capable of supporting large shear stresses for geologically long times. In this paper, we use plate flexure theory and observed lithospheric failure features associated with several Martian features to evaluate the thickness of the elastic lithosphere as a function of time and space. Such calculations have previously been reported for Olympus Mons [9] and Pavonis Mons [10].

The features included in this study, in approximate order of decreasing age, are the Isidis basin, Alba Patera, Elysium Mons, Arsia Mons, Pavonis Mons, Ascraeus Mons and Olympus Mons. All are known, on the basis of Viking orbiter gravity data [11], to be associated with large free-air gravity highs and thus to exert a substantial vertical load on the Martian lithosphere. Except for Olympus Mons, all these features have associated graben and normal faults with generally concentric orientations, though, often these faults are also elements of larger-scale regional trends [12].

The bending stress in the Martian lithosphere is modeled using flexure theory for thin shells [12], and the loads are assumed to be circularly symmetric. The load for the Isidis basin fill is taken from the total excess mass [11], and from a model for the radial distribution of the load, concentrated at the center, to a radius of outermost fill of 600 km. The loads for Olympus Mons, Arsia Mons, and Alba Patera are taken from the total excess mass [11] and the assumption of a conical shape for the shields. The loads for Elysium, Pavonis and Ascraeus Mons are based on the assumption that these shields have the same ratio of excess mass to volume ($2.45\ g/cm^3$) as Arsia Mons [11,14,15].

A fit of the radial distances of peak extensional stresses to the observed range in distances of extensional failure features gives the values for thickness T of the elastic lithosphere shown in Table 1: $T = 125 \pm 25$ for the Isidis basin, $T = 50 \pm 14$ km for Elysium Mons, and $T = 25$ to 50 km beneath the three

Tharsis shields. The absence of failure features surrounding Olympus Mons permits only a lower bound to be placed on lithospheric thickness there; if extensional stresses are less than the 2+ kbar effective elastic stresses indicated for the failed regions around the other shields, then T > 150 km [9]. The thickness for the Isidis basin region might be less if there are extensional features, now buried by volcanic plains, inward of the innermost graben still preserved. The thickness for the region of the three Tharsis shields may be somewhat greater if there are graben outward of those visible buried by younger flows, but T must even so be less than 75 km to account for the innermost observed graben. For comparison, Phillips et al. [10] obtained T = 50 to 90 km from the position of the graben concentric to Pavonis Mons.

From Table 1, it is clear that there is not a progressive increase with time in T for Mars. The largest values for lithospheric thickness are for the oldest and youngest loads in the table.

We suggest that a more important control on T than age of the load is proximity to a major volcanic province. If the major volcanic regions (e.g., Elysium, Tharsis) during their period of peak activity are characterized by widespread heating of the upper mantle, such heating may be sufficiently pervasive and of such a magnitude as to substantially thin the effective thickness of the overlying elastic lithosphere. Thus roughly comparable values for T (25 to 50 km), as determined by the local lithospheric response to loading, are obtained for the Alba Patera region, for Elysium and for Tharsis. The Isidis basin, located far from any contemporaneous volcanic center, and Olympus Mons, situated well off the main Tharsis uplift as well as more youthful than the Tharsis shields, show in their tectonics the signature of much thicker (100-200 km) elastic lithospheres. A thinning of the lithosphere beneath Tharsis has also been proposed on the basis of isostatic compensation of long-wavelength topography [14,16].

The results of this study and the hypothesis that major volcanic provinces on Mars have thermally thinned lithospheres provide a quantitative basis for assessing the complete tectonic history of Mars.

References: [1] Lorell, J. et al., Science, 175, 317, 1972. [2] Carr, M.H., JGR, 78, 4049, 1973. [3] Vogt, P.R., Earth Planet. Sci. Lett., 23, 337, 1974. [4] Anderson, D.L. et al., JGR, 82, 4524, 1977. [5] Toksöz, M.N. and A.T. Hsui, Icarus, 34, 537, 1978. [6] Carr, M.H., Sci. Am., 234, 32, 1975. [7] Plescia, J.B. et al., Lunar and Planetary Science X, 989, 1979. [8] Solomon, S.C. and J.W. Head, J. Geophys. Res., in press, 1979 [9] Thurber, C.H. and M.N. Toksöz, GRL, 5, 997, 1978. [10] Phillips, R.J. et al., JGR, in press, 1979. [11] Sjogren, W.L., Science, 203, 1006, 1979. [12] Scott, D.H. and M.H. Carr, Geologic Map of Mars, U.S.G.S. Map I-1083, 1978. [13] Brotchie, J.F., Mod. Geol., 3, 15, 1971. [14] Blasius, K.R. and J.A. Cutts, PLSC 7th, 3561, 1976. [15] Malin, M.C., Geol. Soc. Amer. Bull., 88, 908, 1977. [16] Sleep, N.H. and R.J. Phillips, GRL, submitted, 1979.

Table 1. Estimates of the thickness of the elastic lithosphere on Mars.

Feature	Diameter, km	Load at center, 10^9 dyne/cm^2	Lithospheric thickness T, km
Isidis	1200	0.25 [11]	125±25
Alba Patera	600	0.45	25-50
Elysium Mons	200	1.2	50±20
Arsia Mons	420	1.7	25-50
Pavonis Mons	320	1.6	25-50
Ascraeus Mons	400	1.8	25-50
Olympus Mons	600	3.2	>150 [9]

Yield Strengths of Diverse Flows on the Flanks of Elysium, Ascraeus, and Arsia Montes, Mars, H. J. Moore, U.S. Geological Survey, Menlo Park, CA 94025.

There is a wide variety of flow phenomena on Mars that includes lava flows, debris flows, and possibly rock glaciers or mud flows. The evidence for lava flows and debris flows is convincing, but the evidence for distinguishing possible rock glaciers or mud flows from lava flows appear to be somewhat equivocal at this time. Quantitative estimates of the stresses required for flow suggest that yield conditions for most lava flows are substantially different from the other types of flows, but yield strengths for rock glaciers, silicic lava flows, and possibly mud flows are nearly the same.

Yield strengths of lava flows on the flanks of Elysium and Ascraeus Montes were calculated from their widths, heights, levee widths, and estimated topographic gradients using equations for Bingham plastics (Bingham, 1922; Hulme, 1974; and Moore et al., 1978). The average yield strengths (2000 ± 1600 N/m^2) of Elysium and Tharsis flows are the same as those of flows on comparable topographic gradients, thus it appears probable that chemical compositions of the flows in the Elysium and Tharsis regions are roughly the same. Flows of Ascraeus Mons on steep topographic gradients ($\simeq 0.05$) also have yield strengths (10,200 ± 7800 N/m^2) comparable to Tharsis flows on similar gradients.

Yield strengths (17,000 ± 11,000 N/m^2) of the SP flow (57% SiO_2) near Flagstaff, Arizona are higher than those of terrestrial flows with 50% silica but lower than terrestrial flows with 63% silica on comparable gradients ($\simeq 0.02$). Comparisons of yield strengths of martian lava flows with those of terrestrial lava flows suggest that the martian flows typically have silica contents between 50 and 57% (Moore et al., 1978). Some martian flows have yield strengths and topographic gradients as low as the Imbrium flows of the Moon; these lunar flows may have silica contents near 40% (Moore et al., 1978).

The lava flows considered above appear to be substantially different from martian debris flows (Squyres, 1978) and terrestrial rock glaciers (Wahrhaftig and Cox, 1969). Morphologically, the debris flows resemble terrestrial piedmont glaciers and valley glaciers whereas the lava flows extend great distances as long, narrow units unconfined by steep valley walls and usually are associated with volcanic edifices. Yield strengths of martian debris flows that rest on gentle topographic gradients are on the order of 10^5 N/m^2 (Squyres, 1978) whereas the yield strengths of the lava flows on equally gentle gradients are about two orders of magnitude lower than 10^5 N/m^2. Rock glaciers, like the martian lava flows, form long, narrow topographic units. The well-defined levees commonly observed as part of the lava flows are not present in rock glaciers. Yield strengths of rock glaciers are on the order of 10^5 N/m^2 (Wahrhaftig and Cox, 1969) but martian lava flows rarely have yield strengths of this magnitude and those with measured yield strengths this large have well-defined levees.

Flows of uncertain origin are present at elevations near 16 km on the northwest flank of Arsia Mons where thick (a few hundred meters) lobate forms extend downslope on a topographic gradient near 0.15. Yield strengths for these lobate forms are of the order of 10^5 N/m^2 which is comparable to those of terrestrial rock glaciers (Wahrhaftig and Cox, 1969), silicic lava flows on comparable topographic gradients (Moore et al., 1978), and possibly mud flows. The lobate flows, interpreted as rock glaciers, would be consistent with the former presence of glacial ice on the flank of Arsia Mons (Williams, 1978). A geologic model that might account for most of the puzzling features on the WNW flank of Arsia as described by Carr et al. (1977) is as follows: (1) a glacial cap of water ice once existed on the northwest flank of Arsia Mons (and perhaps elsewhere), (2) volcanic debris was admixed with the glacier causing it to become increasingly "dirty" with time, (3) flow of the glacier carried rock material downslope, (4) climatic conditions changed causing the glacier to retreat, leaving terminal moraines, (5) continued sublimation of the ice and ablation resulted in the deposition of hummocky deposits of debris (ground moraine) near the base and on the flanks of Arsia, and (6) the last vestiges of flow are represented by the lobate forms, or rock glaciers, at elevations near 16 km. Thus, the lobate forms, interpreted as rock glaciers, are consistent with the postulated former presence of glacial water-ice on the flank of Arsia Mons (Williams, 1978) as well as other edifices (Hodges and Moore, 1978).

If the lobate forms are lava flows, the yield strengths would imply that they are silicic flows, perhaps analogous to the trachytes of Hawaii (Cross, 1904) and that magmatic differentiation has occurred. The question of mud flows will be deferred to a later date.

References:

Bingham, E. C. (1922) Fluidity and Plasticity, McGraw-Hill, N.Y., 440 p.

Carr, M. H., Greeley, R., Blasius, K. R., Guest, J. E., and Murray, J. B. (1977) Some martian volcanic features as viewed from Viking Orbiters, Jour. Geophys. Res., v. 82, p. 3985-4015.

Cross, W. (1904) An occurrence of trachyte on the island of Hawaii, Jour. Geol., v. 12, p. 510-523.

Hodges, C. A. and Moore, H. J. (1978) The subglacial birth of Olympus Mons, Geol. Soc. Amer. Abstracts with Programs, v. 10, p. 422.

Hulme, G. (1974) The interpretation of lava flow morphology, Geophys. J. Roy. Astron. Soc., v. 39, p. 361-383.

Moore, H. J., Arthur, D. W. G., and Schaber, G. G. (1978) Yield strengths of flows on the Earth, Mars, and Moon, Proc. Lunar Planet. Sci. Conf. 9th, p. 3351-3378.

Squyres, S. W. (1978) Martian fretted terrain: flow of erosional debris, Icarus, v. 34, p. 600-613.

Wahrhaftig, C. and Cox, A. (1969) Rock glaciers in the Alaskan Range, Geol. Soc. Amer., v. 79, p. 383-436.

Williams, R. S. (1978) Geomorphic processes in Iceland and on Mars: a comparative appraisal from orbital images, Geol. Soc. Amer., Abs. with Programs, v. 10, p. 517.

Preliminary Thickness Study of Plains-Forming Materials in the Caloris Basin Region of Mercury. R. A. De Hon, Department of Geosciences, Northeast Louisiana University, Monroe, LA 71209.

The distributional pattern of the smooth plains and ridged plains of the Caloris basin region of Mercury resembles that of the lunar maria. Many buried and partially-buried craters are evident within the plains and can be used to estimate the thickness of plains-forming materials. Thickness studies of this type provide data concerning the distribution and volume of materials. They also provide insight into the subsurface configuration prior to the deposition of the plains-forming materials.

An overall impression of thickness variations of plains-forming materials may be gained by observing size range and density of partially buried craters. A high density of partially-buried craters is common in regions of thin materials. As thickness increases, small craters are totally buried, and the number of exposed craters decreases. Thick materials typically underlie plains of low crater density, and the remaining exposed craters are large. As thickness approaches approximately 2 km, all craters are buried and obscured. Once crater rim height to diameter relationships are established (1), numerical estimates of absolute thickness are possible. Ideally, the thickness is equal to the original rim height (as estimated from crater diameter) minus the exposed rim height. If a sufficient areal distribution of thickness estimates is obtained, an isopach map can be constructed.

A preliminary isopach of the plains-forming materials in the region of the Caloris basin (Fig. 1) was constructed using techniques similar to those used to construct the preliminary isopach map of Oceanus Procellarum (2). As a regional reconnaissance, the isopach map was constructed by averaging thickness estimates for 5° squares. The average thickness was plotted on a 5° x 5° grid over the region of plains. Contact between plains and more heavily cratered terrain was similarily defined by 5° point spacing. The resulting grid of data was then contoured. In general, some crater selection was required to obtain reasonable and consistent results. The smallest exposed craters were selected for inclusion in the data base in preference to large craters, except where small craters were obviously situated on the rims of large craters. The point density coeffiecent for data spacing is 1.62 (random to uniform), but resolution is low (approximately 10°).

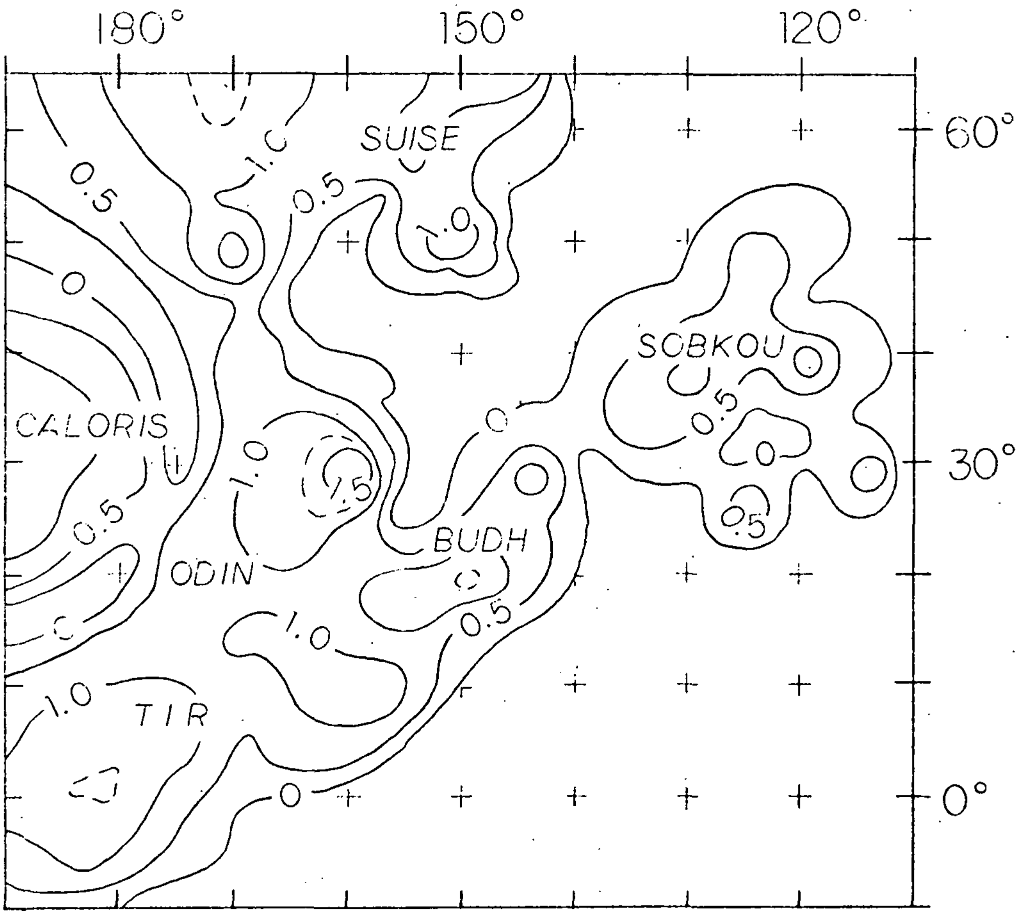

Fig. 1. Isopach map of the plainsforming materials associated with the Caloris basin. Isopach interval is 0.5km. 1.25 km isopach (dashed line) used to accentuate thick lenses.

The isopach map (Fig. 1) portrays the generalized distribution of plains-forming materials in the region surrounding the Caloris basin. No effort was made to separate various plains units. The size of the grid mandates that thickness variations less than $10^o \times 10^o$ are not readily resolved and that features may be displaced by several degrees. Photographic resolution limits accurate estimates in the thinnest regions, and lack of exposed craters limits accurate estimates in the thickest lenses. Nevertheless, significant trends in thickness distributions are apparent on the map (Fig. 1).

Plains-forming materials are concentrated in an annulus concentric to the rim of the Caloris basin and inundate low-lying regions peripheral to the outer annulus. Major thickening lenses are located in roughly circular depressions (basins) or regions of coalescing circular basins (3). Maximum measured thickness is approximately 1700-1800 m, but it may be greater in the center of large circular basins. The average thickness is about 600m.

The distribution of plains-forming materials is similar to that of the lunar mare basalts around the Imbrium basin. Mercurian materials are emplaced in depressed regions; contact with older terrain exhibits typical embayment patterns; lunar-like mare ridges are common; and partially-buried craters have characteristically flooded appearance rather than mantled appearances. These characteristics are more readily identified with material emplaced as a fluid (lava) rather than an impact breccia. Lavas were emplaced in regional and local low-lying areas after formation of the Caloris basin. Peripheral rings of low-lying terrain are common around lunar basins (4,5) and they apparently exist on Mercury. Distribution is similar to that seen around Mare Imbrium where mare basalts flood an annular depression (comprised of Mare Figoris, Sinus Roris, Mare Insularum, Sinus Aestruum, and Mare Vaporum) and spread outward to other low-lying terrain (Oceanus Procellarum).

References

(1) Cintala M. J. and Head J. W. (1979) Lunar and Planet. Sci. X, LPI, Houston, 204-206.
(2) De Hon R. A. (1978) Lunar and Planet. Sci. IX, LPI, Houston, 229-231.
(3) Wright M. B. and De Hon R. A. (1979) This volume.
(4) Head J. W. (1975) Conf. on Origins of Mare Basalt, LSI, Houston, 61-65.
(5) De Hon R. A. and Waskom J. D. (1976) Proc. Lunar Sci. Conf. 7th, 2729-2746.

Stratigraphy of the North Polar Region of Mars: Implications for the Source of the Circumpolar Dune Fields,

Michael E. Botts, Dept. of Earth and Planetary Sciences, Washington University, Saint Louis, MO., 63130

I propose that the rock stratigraphic sequence of the North Polar Region (here defined as > 70° N. lat.) be divided into four units: (a) bulbous ground, (b) mantled ground, (c) dune material, and (d) layered deposits (fig. 1). The nature of the layered deposits has been discussed by others (1,2) and will not be further described here.

Bulbous and Mantled Grounds

Bulbous ground is the most heavily cratered terrain in the North Polar Region and is characterized by frequent debris flow craters and a mottled, bulbous appearance. The mottled, bulbous appearance is a result of bright material surrounding dark, highly irregular polygons, which are 3-8 km wide [reference Viking Orbiter mosaic 211-5746 (538B01-538B16)]. Bulbous ground is interpreted as volcanic plains based on its low albedo, a possible exposed dike, and the bulbous appearance which greatly resembles the surface of terrestrial lava plains.

Mantled ground displays a higher albedo, within the same Viking Orbiter frame, than either bulbous ground or dune material, and has a crater population characterized by a deficiency of small craters (< 2 km) relative to bulbous ground and by shallow craters commonly lacking ejecta (appearance of burial). Covering bulbous ground in varying thicknesses, it ranges from lightly mantled ground where some bulbous ground characteristics, such as abundant craters and a mottled appearance, are retained [reference frames 531B21-531B36], to moderately and heavily mantled ground, where bulbous characteristics are no longer present [reference frames 211-5573 (frames 71B61-71B62, 71B41-71B45) and 211-5562 respectively]. Due to its generally massive appearance, mantled ground is believed to have resulted from deposition of wind-blown dust onto bulbous ground. The layered deposits probably represent a facies of mantled ground in which dust is deposited onto the ice cap rather than directly onto the ground (1). The presence of mesa-like landforms in moderately mantled areas indicates that the mantled ground has experienced a period of deflation.

Figure 2 shows cumulative size-frequency distribution plots of 0.1 to 20 km craters on bulbous and mantled grounds. The plot for bulbous ground exhibits a production slope of -3.4 for craters 0.8 to 2 km and a slope of -0.6 for craters 2 to 20 km. The power law slope of -0.6 is consistent with the -0.69 slope presented by Oberbeck (3) for craters less than 50 km on heavily cratered terrain. Whether such a slope is a "natural kink" in the production function (3,4) or represents an obliteration episode (5,6,7) is still controversial. Cumulative crater-size spectra for mantled ground resemble bulbous ground with smaller craters removed. This is consistent with my interpretation of mantled ground burying bulbous ground.

Although my interpretation of a dust mantle overlying a more heavily cratered surface agrees in theory with the stratigraphy proposed by Squyres (1), there are serious discrepancies in the mapping of the units. His single exposure of "cratered plains" is my type locale for heavily mantled ground, and is actually 1 to 2 orders of magnitude less cratered than most of his overlying "debris mantle".

Dune Material

Dune material overlies both bulbous and mantled grounds and is characterized by its very low albedo relative to all other North Polar units, and commonly by linear and arcuate patterns interpreted as dunes (2). However, thin sheets of dune material are inferred from Mariner 9 imagery showing the dark circumpolar collar of dune material extending into generally duneless areas of bulbous and lightly mantled grounds.

Dune material is distributed asymmetrically around the North Polar Cap. Dune fields in the 90-270 W longitude region are extensive and generally uninterrupted while dune material in the region of 270-0-90 W longitude is distributed as scant fields with numerous outliers, or as thin sheets. In the North Polar Region of Mars dune formation is generally confined to moderate and heavily mantled regions while dune material on bulbous and lightly mantled ground exist predominantly as sheet "sands". It appears that mantling provides the proper substratum for dune formation. An excellent example of the relationship of bulbous ground, mantled ground, and dune material can be seen in Viking Orbiter mosaic 211-5744 (525B01-525B16).

Wind directions within the North Polar Region have been inferred by myself and others (8,9) on the basis of dune orientations. Although there is evidence for wind reversals with seasons (this paper, 8), the winds predominantly responsible for transport of dune material are westerlies with locally occurring northerly and southerly components.

Although the presence or absence of dunes in many areas is probably a function of the smoothness of the substratum (thus, the degree of mantling), the presence and gradual "thinning-out" of extensive dune fields downwind of extensive exposures of bulbous ground implies that bulbous ground may be the source of the North Polar dune material.

Scenario of Circumpolar Deposition

I propose that a plausible scenario for the formation of deposits in the North Polar Region of Mars is as follows: (a) extensive lava flooding followed by crater production and retention to produce bulbous ground, (b) deposition of atmospheric dust onto bulbous ground to produce mantled ground in some regions and into the ice cap to form layered deposits, (c) deflation within mantled ground to leave "mesas" and deflation of dune material from bulbous ground with accumulation into dunes on moderately and heavily mantled ground.

References:

(1) Squyres, S., Icarus, in press; (2) Cutts, J. et al (1976), Science 194, 4271; (3) Oberbeck, V. (1977), NASA TM X-3511; (4) Oberbeck, V. et al (1975), NASA TM X-62,501; (5) Chapman, C. (1974), Icarus 22, 272; (6) Opik, E. (1966), Science 153, 255; (7) Jones, K. (1974), JGR 79, 3917; (8) Tsoar, H. et al (1979), 10th LPSC Abstracts; (9) Leach, J. (1979), 2nd International Colloq. on Mars (abstracts).

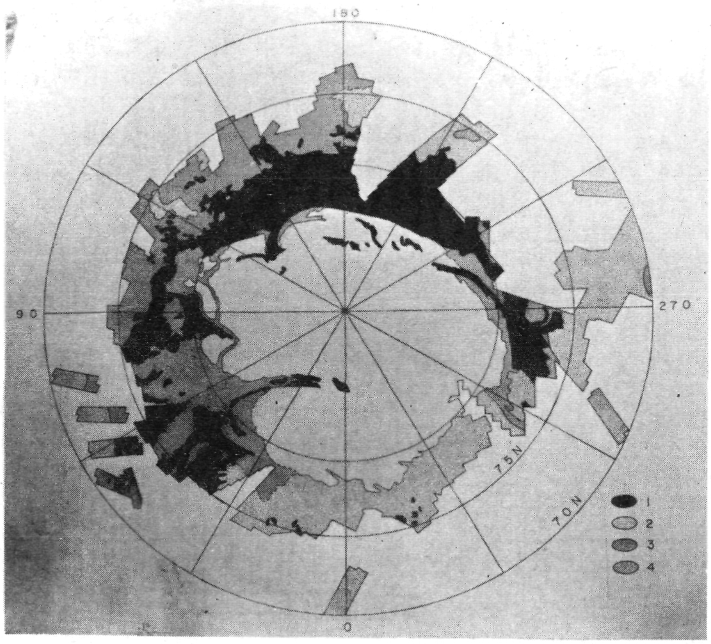

Figure 1-
Stratigraphic Map of North Polar Region of Mars.
1. Dune Material
2. Layered Deposits
3. Moderate to heavily mantled ground
4. Bulbous ground and lightly mantled bulbous ground

Figure 2-
Cumulative crater size-frequency distribution plots for (a) bulbous ground and (b) moderately and heavily cratered grounds. Counts are for type locales as listed in the text.

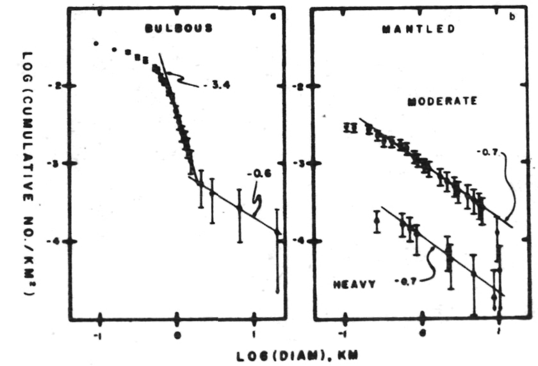

Martian Soil Units and Rock Surfaces: Spectral Estimate Ratios,

Edwin L. Strickland III, Department of Earth and Planetary Sciences, Washington University, St. Louis, Mo., 63130

Color enhanced Viking Lander images revealed several distinctively colored soil units and rock surface materials at each site (1). These images, however, can display information from only three of the cameras' six narrowband channels at once. Ratios of spectral radiance estimates are being used to further characterize these surface units, and as a check on the utility of color (B,G,R) data for discriminating units.

Estimates of the spectral radiance of the light entering the Lander's cameras are obtained using a modification of the technique described by Huck et. al. (2). Although the camera responds to light from 0.35 to 1.10 micrometers, at wavelengths $\leq$ 0.45 and $\geq$ 1.00 micrometers the solution becomes increasingly unconstrained and should be considered invalid. Only six spectral channels are used to generate these spectral estimates. Thus, only the gross features of the real spectral radiance entering the camera can be reproduced. In addition, because of gaps between the responses of some adjacent diodes, the estimates are subject to spectral aliasing. Despite these limitations, spectral estimates from Lander camera data can be used to quantitatively characterize first order spectral differences of surface materials.

Spectral radiance estimates are calculated for 14 to 21 pixels covering each soil patch or rock surface selected from the enhanced color images (1). These spectra are averaged to provide one estimate for each feature. Spectral reflectance estimates can be constructed by dividing this radiance estimate by the radiance estimate of a dust free, sunlit gray patch on one of the Lander's test charts (2). Estimates constructed for soil units closely resemble those published by Huck et. al. (2). The current mode of investigation, however, is directed towards determining relative differences between various soil and rock surface materials by constructing spectral estimate ratios.

After estimate ratios were constructed for 12 selected features in frames 12A168/028 (color) and 12A170/028 (infrared), these estimates were averaged. The twelve features are listed in Table 1 and displayed in Figure 1. Each of the twelve spectra was divided by the spectral average to obtain twelve spectral estimate ratios. These ratios portray differences in the spectral radiance in each wavelength region relative to the average of the selected features. These spectral estimates are shown in Figure 2. These spectra have not been normalized at some arbitrary wavelength. Except for spectrum BB-1B, on the side of a boulder which was obliquely illuminated, differences in the average level of each spectrum are primarily due to intrinsic differences in the spectral reflectance of each material.

Features seen in the spectral ratios correlate extremely well with the relative color of each unit displayed by the color enhanced images (1). The spectral ratios of the dark "blue boulder": BB-1B, and the dark "blue" patch on a cobble near the lander: BRX-2, are very similar in shape. Two "blue" soils were examined: BS-3, located by a boulder some 10 m. from the lander, and BS-8, the dark soil disturbed by the arm latch pin dropped by the lander. Despite differences in mechanical state and phase angle (BS-3: undisturbed, $g = {}^{\sim}70^{\circ}$; BS-8: disturbed, $g = \sim 30^{\circ}$.) The shapes of the two spectral ratios is strikingly similar. A third dark soil, the "blue-green"soil at the rocky flats patch of "duricrust", resembles the "blue"soils. The rise at the blue end of the spectrum is much less sharp for this soil. Significantly, the blue rise in the curves for the "blue" rocks starts at a longer wavelength than that for the "blue" soils.

The spectral ratios of two "red" soils: RS-2 and RS-5, are very similar in shape and are totally distinct from the ratios of the "blue" and "blue-green" soils, particularly for the visable half of the spectrum. The two units of "orange-red" soil: ORS-1 and ORS-2 are located in the patch of duricrust exposed by retrorocket exhaust. These two soils and totally distinct spectrally from the surface of the rocky flats patch of duricrust.

"Green" bedrock: GBR-2, a small "green" rock: GRX-3, and the extremely bright "yellow" rock: YRX all produce spectral ratios that are concave downwards in the vicinity of the green channel (0.55 micrometers). These bright, relatively "green" surfaces were interpreted (1) as weathering coatings on rocks. The spectra of GRX-3 and YRX resemble each other, with a decline between red and IR-3, and a flat region in the IR. The "green" bedrock's spectrum is distinctly different in the IR, rising instead of declining. Neither "blue"rocks' spectra, nor any soils' spectra resembles those of these "green" rocks. This is new support for the hypothesis that these surfaces are chemically and/or physically distinct materials. It appears unlikely that any of the soils observed at the landing sites could have been produced directly from the "green" rock surface coatings (1) by mechanical erosion alone, and an additional weathering reaction would be necessary.

References:

1. Strickland, E.L., 1979. Soil Stratigraphy and Rock Coatings Observed in Color Enhanced Viking Lander Images., LPSC-X Abstracts.

2. Huck, et. al., 1977. Spectrophotometric and Color Estimates of The Viking Landing Sites., J. Geophys. Res. 82. 28, 4401-4411.

3. Huck, R.O., et. al., 1975. Radiometric Performance of The Viking Mars Lander Cameras. NASA TMX-72692.

TABLE 1

POINT	UNIT	ROW	SAMPLE	APPARENT ALBEDO	ENHANCED COLOR
1	BB-1B	45	94	Very Low	Blue
2	BRX-2	335	345	Very Low	Blue
3	BS-3	175	483	Low	Blue
4	BS-8	490	237	Very Low	Blue
5	BGS-4	245	425	Average	Green-Blue
6	GBR-2	95	120	High	Gray-Green
7	GRX-3	315	315	High	Green
8	YRX	412	185	Very High	Yellow
9	RS-2	23	420	High	Red
10	RS-5	270	665	Average	Red
11	ORS-1	475	125	High	Orange-Red
12	ORS-2	495	110	Very High	Orange-Red

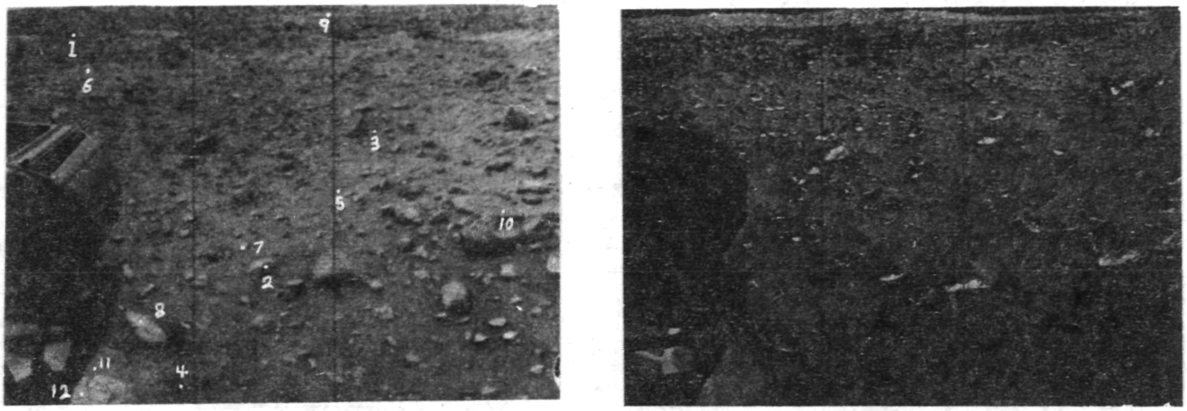

a. Stenciled red image.

b. Red/(B+G) Ratio.

c. Blue/(G+R) Ratio.

d. Green/(B+R) Ratio.

Figure 1. Frame 12A168/028 Stenciled red image and "color information" ratio images containing points for which spectra were obtained. Locations of points for which spectra were obtained are indicated in (a).

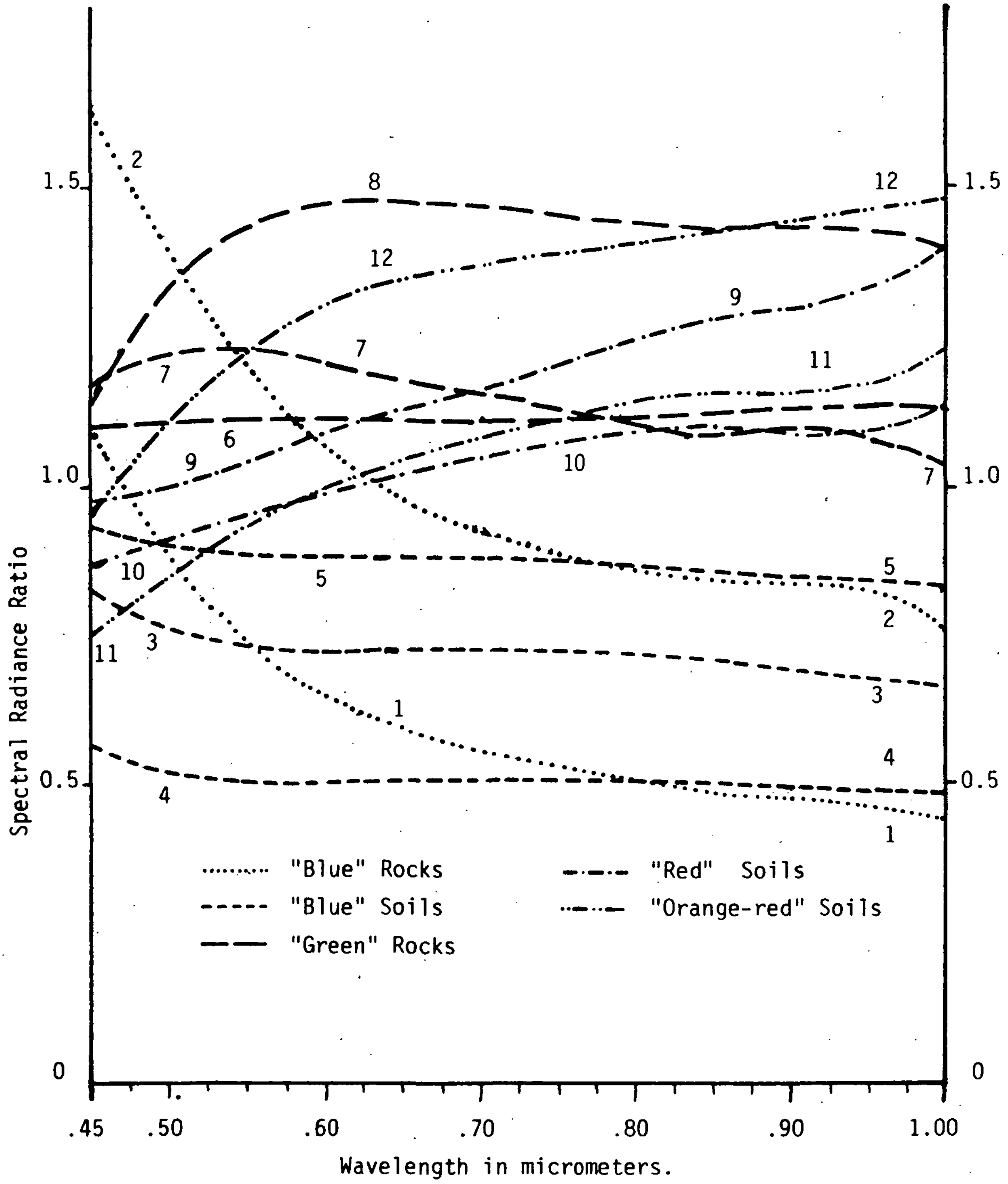

Figure 2. Spectral Radiance Estimate Ratios. Numbers correspond to points on red image and listed in table.

A Martian Global Plains System Represented by Lunae Planum Surface Units,

Therese Gregory, Jet Propulsion Laboratory, California Institute of Technology, Pasadena, CA 91103/California State University, Northridge, Northridge, CA 91330, R.S. Saunders, Jet Propulsion Laboratory, California Institute of Technology, Pasadena, CA 91103, and J.B. Plescia, Jet Propulsion Laboratory/California Institute of Technology, Pasadena, CA 91103/Univ. S. Calif., Los Angeles, CA 90007

A total area of 3.6×10^6 km^2 was analyzed to determine if surface units of Lunae Planum material found in widely scattered regions on Mars could represent a global episode of plains formation. Surface features common to all such plains are wrinkle ridges. These ridges are similar to those found in the Lunar Maria. All the areas covered in this study have wrinkle ridges on their surfaces. It is inferred that the ridges resulted from compression possibly due to local or regional stress systems, (Howard and Muehlberger, 1973) although other mechanisms are possible. In many instances the ridge patterns appear to reflect underlying topography such as crater rims.

Lunae Planum is estimated to be one of the oldest major plains units on Mars at 3.9 billion years old (Neukum and Wise, 1976). The scattered regions on the Martian surface that we have examined thus far appears to have crater populations with similar density as those of Lunar Planum. 20 km appears to be the upper limit of crater diameters with most of the craters falling within less than 10 km size range.

Distinct wrinkle ridges are characteristic features of the Lunae Planum Plains. These ridges are generally parallel to one another striking north-south. There is significant variance in their heights and widths. The spacings between adjacent ridges range between 47 km and 15 km. Ridge lengths vary from a few tens of kilometers to hundreds of kilometers crossing the entire Lunae Planum region. The pattern of the wrinkle ridges on the thick Lunae Planum surface may imply a uniform compressional stress applied over the entire area. The implied stress patterns in Lunae Planum are consistent with a crustal load centered on the Tharsis region (Phillips, Saunders and Banerdt, in preparation).

Other regions on Mars, notably Hellas Planitia (94A and 504B), Syrtis major Planitia (496A), Acidalia Planitia (524A), Noachic Region (539B), Hesperia Planum (553A), Utopia Planitia (573A), Chryse Planitia (20A), Sinai Planum (44A and 46A), and Amazonis Planitia, also have wrinkle ridges on their surfaces. Crater count curves have been made of these areas and are illustrated in Figure 1. Crater diameters from these areas fall close to the Lunae Planum size range. Crater densities per 10^6 km^2 also resembles Lunae Planum crater populations. The intercept for 1 and 2 km are listed in Table 1.

It has been suggested that these regions of similar crater density exhibiting wrinkle ridges, make up a global plains system that first developed after the uplands degradation (Soderblom et al. 1974).

Wrinkle ridges in Lunae Planum are parallel and trend north-south. Northeast trending ridges in Chyrse Planitia, Utopia Planitia, Hesperia Planum, northwest trending ridges in Syria Planum, Sinai Planum and Syrtis, and north-south trending ridges in Acidalia Planitia are also parallel. In the Noachis region ridges are of two forms. They either are concentric to a basin or represent a distinct rectangular pattern. The area covered in Hellas Planitia exhibits rectangular ridges. In the mottled rough terrain material east of Hellas ridges generally trend northwest and form a rectangular pattern. It appears that parallel ridges are more abundant in the plains of the northern hemisphere whereas rectangular and concentric ridges dominate the southern hemisphere plains. Parallel ridges are generally younger than pre-Lunae Planum surface and rectangular ridges in the southern hemisphere plains are older, however most span a narrow range of time.

References:

Howard, K.A. and W.R. Muehlberger, Lunar Thrust Faults in the Taurus-Littrow Region, Apollo 17, Prel. Sci. Rept, NASA SP-330, 1973.

Neukum, G. and D.U. Wise, Mars: A Standard Crater Curve and Possible New Time Scales, Science 194, 1976.

Soderblom, L.A., C.D. Condit, R.A. West, B.M. Herman, and T.J. Kreidler, Martian Planetwide Crater Distributions: Implications for Geologic History and Surfaces Processes, Icarus 22, 1974.

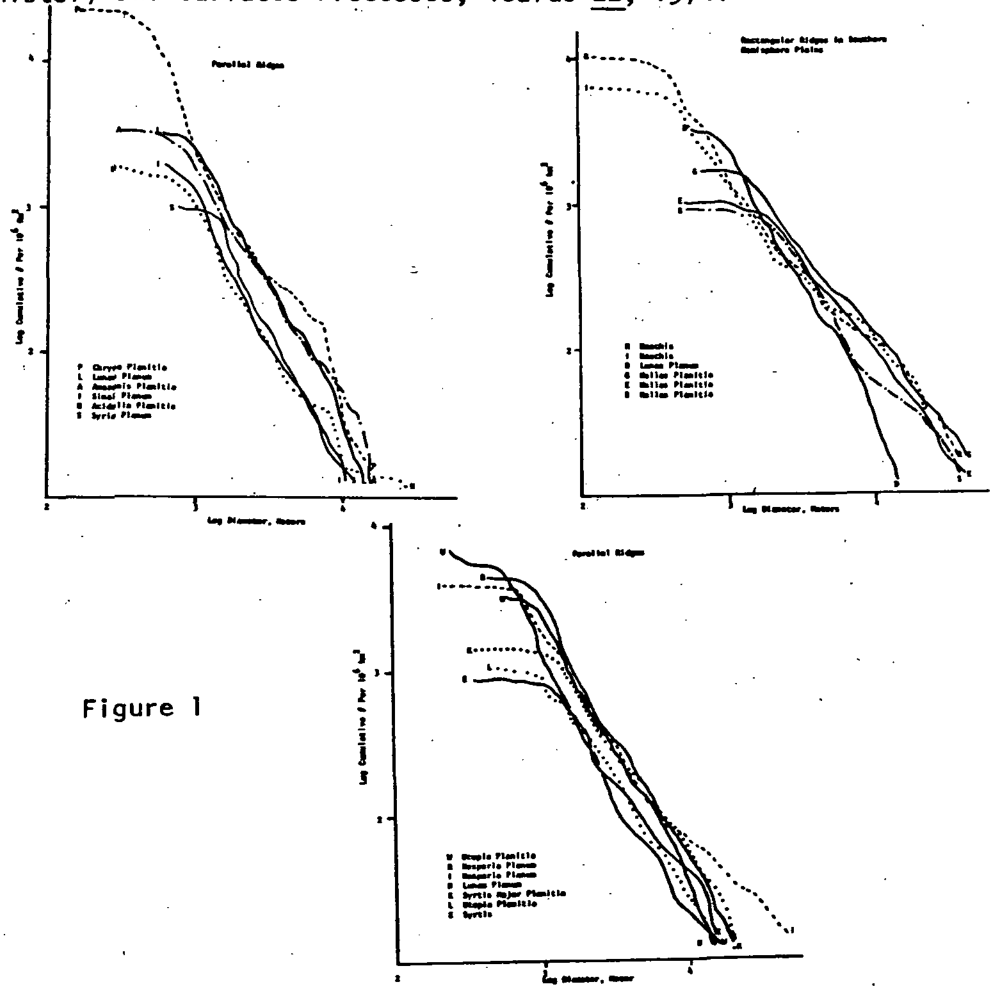

Figure 1

TABLE 1

Location	Picno	Geology	1 km Intercept	2 km Intercept	Center Point		Quadrangle	Ridge Pattern
					Lat.	Long.		
Lunae Planum	519A-520A	Lunae Planum Smooth plain material	2500	690	65°	17°	MC-10 Lunae Palus	Parallel
Chryse Planitia	20A16-54	Smooth plains	2100	660	22°	50°	MC-10 Lunae Palus	Parallel
Sinai Planum	44A11-28 46A11-28	Plains	1300	280	-10°	95°	MC-17 Phoenicus Lacus MC-18 Coprates	Parallel
Hellas Planitia	94A72	Ridged plains material and densely cratered plains material	1720	760	-57°	300°	Noachis MC-27 Hellas MC-28	Rectangular
Syrtis	496A67-73	Ridged plains	1780	590	10°	285°	Syrtis major MC-13	Parallel
Hellas Planitia	504B28-36	Densely cratered plains material & mottled rough terrain material with NW trending ridges	2100	1020	-63°	260°	Hellas MC-28 Eridania MC-29	Rectangu-
Acidalia Planitia	524A01-15	Plains and dissected plateau material	950	240	35°	30°	Mare Acidalium MC-4	Parallel
Noachis	539B47-56	Mottled plains material, plains, & mottled rough terrain material with NW trending ridges	1400	500	-60°	220°	Eridania MC-29	Concentric & Rectangular
Noachis	539B81-96	" " " "	1500	560	-60°	210°	Eridania MC-29	" " "
Amazonis	545A23-29	Smooth plains material	1800	560	20°	170°	Amazonis MC-8	
Hesperia Planum	553A06-14	Ridged plains material	3400	780	-25°	255°	Mare Tyrrhenum MC-22	Parallel
Hesperia Planum	553A47-52	Ridged plains material	1900	620	-33°	248°	Mare Tyrrhenum MC-22	Parallel
Utopia Planum	573A01-7	Lowland plains material	880	350	40°	267°	Casius MC-6	Parallel
Utopia Planum	573A08-10	Lowland plains material	1300	380	40°	267°	Casius MC-6	Parallel

Noctis Labyrinthus Geomorphology: Structural and Geothermal Origins.

Philippe MASSON, Laboratoire de Géologie Dynamique Interne,
Université Paris-Sud, F-91405 Orsay Cedex, France.(+)

Noctis Labyrinthus area is one of the dramatic geomorphic features observed within the western equatorial part of Mars. It continues the western part of the Valles Marineris system toward the Claritas Fossae fractured system extending southward. These three systems lie on the Eastern and Southern flanks of the Syria Planum-Tharsis Montes uplifted zone. This dome culminates at 11 kilometres in Noctis Labyrinthus center. Syria Planum area is surrounded by Noctis Labyrinthus (to the North) and Claritas Fossae (to the West) systems.

Noctis Labyrinthus shows an intensively fractured network of relatively fresh graben looking like features. In 1977 (1) three main directions of tectonic trends were identified: N.NE/S.SW, E.NE/W.SW and W.NW/E.SE. These trends are expressed in the old terrains (unit pf1 of the geologic map of the Phoenicis Lacus Quadrangle of Mars) (2). According to our interpretation of Mariner 9 frames, these trends are part of an old structural pattern related to a domical structure.

A detailed structural and geomorphic study of this area based on Viking Orbiter 1 and 2 images, shows that this old structural pattern seems to control the graben's network. The walls of these grabens are freshly eroded and they show a large display of landslide features. Their floors are overlaid by slumped materials (collapsed boulders, landslide debris, mudflow looking like deposits) mapped as slope and bedrock materials (sb unit of the inferred geologic map) (2).

The materials observed on the floors and walls of these grabens do not seem to be due to any exogeneous erosional agent (i.q. fluvial or aeolian activity). These slumps could be due to a slow creep of surface materials related to freeze-thaw of ground ice, as it has been described previously in the other parts of the planet (3). This process would have enlarged and widened these valleys or canyons along the old tectonic trends previously described (1).

During an early stage of uplifting, tensional fractures appeared in the Noctis Labyrinthus region creating the old fractured pattern. The major phase of uplifting movement in Syria Planum - Tharsis Montes area generated the major tectonic trends which controlled Valles Marineris and Claritas Fossae formation, and rejuvenated the old structural pattern in Noctis Labyrinthus. An encrease of the heat flow occurred in the Syria Planum - Noctis Labyrinthus dome area. This geothermal activity is probably related to the volcanic activity of the Tharsis Montes.

This phenomena could have molten the ground ice along the structural trends observed in the Noctis Labyrinthus area where the updoming deformation seems to be the most intensively expressed. Due to this freeze-thaw of ground ice wall materials collapsed and grabbens widened by creeping and slumping processes.

According to this interpretation Noctis Labyrinthus appears to be the consequence of both tectonic and geothermal activities which have the same origin, e.g. Syria Planum general updoming movement.

References:

(1) Ph. Masson, 1977 - Structure Pattern Analysis of the Noctis Labyrinthus - Valles Marineris Regions of Mars, Icarus 30, n°2, 49-62.

(2) Harold Masursky, A. L. Dial, Jr. and M. H. Strobell, 1978 - Geologic Map of the Phoenicis Lacus Quadrangle of Mars, USGS Miscellaneous Investigations Series Map I-896.

(3) M. H. Carr, G. G. Schaber, 1977 - Martian Permafrost Features, J. G. R. vol. 82, n°28, 4039-4054.

(+) ATP INAG "Planétologie 1977", Research Contract n° 3702.

A POST VIKING VIEW OF MARTIAN GEOLOGIC EVOLUTION, Raymond E. Arvidson, McDonnell Center for the Space Sciences, Dept. of Earth and Planetary Sci., Washington University, St. Louis, Mo., 63130

1. Mars has been the subject of intensive spacecraft exploration for the past decade. The scientific intent of the exploration has been to unravel the character and evolution of the atmosphere, surface, and interior of Mars, in addition to searching for signs of present or past biota. With the closure of the Viking mission, it is time to inventory the data pertinent to our understanding the geologic evolution of the planet, especially since the next couple decades of missions are now in conception stages.

2. We find that the distribution of crater abundances on the planet point to two episodes of internal activity, beginning with creation of an initial cratered terrain shortly after accretion. A second pulse of activity occurred, as evidenced by the extensive resurfacing recorded by the volcanic plains, both within and without of cratered terrain. The timing of this pulse sensitively depends on the assumed cratering rate used to date the percent of the surface covered by terrain of a given age. Most probably, the first pulse occurred within the first half billion years of Mars history, while the second pulse peaked about 2 to 3 billion years ago and lasted over most of geologic time. As such, it may not be fair to term the volcanic resurfacing a "pulse". Such a scenario is consistent with thermal evolution models. At present, Mars has a thick, cool lithosphere, which allows little if any volcanism.

3. Geologic features which directly or indirectly support the presence of ground ice on Mars include the residual north polar water ice cap and associated deposits; channels, both of the dendritic variety, which occur in oldest terrains, and the large, break-out variety; rampart craters, which can be interpreted as ejecta emplacement via wet debris flows; debris aprons; polygonal ground in higher latitudes; and the direct measurement of ~1% absorbed water in soil samples as shown from remote observations and Viking Lander experiments. It is difficult to estimate the column abundance of H_2O and CO_2 needed to generate these features, although it would appear that the estimated abundance of ~ 10 to 50 meters of H_2O based on noble gas arguements is on the low side.

4. The Viking Lander estimates of the major element chemistry of the soils is compatable with a mixture of iron-rich weathering products. Such a mixture in turn is compatable with derivation from an iron rich igneous rock. Constraints placed on the density of the mantle via moment of inertia and bulk density indicate, in fact, an FeO rich mantle. Depending on the sulfur and volatile content, very iron rich partial melts, equivalent to olivine picrites, should be erupted. Such melts may have very low viscosities which seems to fit the Viking Orbiter observations of very long lava flows (up to 1000 KM). Earth-based and Viking colorimetric observations demonstrate that dark areas have significant geographic variations in mineralogy, suggesting that they are partially stripped of the bright dust mantle that apparently makes up most bright areas.

5. Data acquired during the Viking mission have provided an opportunity to examine the effects of aeolian processes on Mars integrated over billions of years, tens of thousands of years, and over the course of a single year. The effect on aeolian activity can be sampled over geologic timescales by examining

the extent of modification of features large enough to be seen by the Viking Orbiters. The degree of preservation of the impact craters and wrinkle ridges at the Viking Lander 1 (VL1) site implies that rock breakdown and removal has been limited to meters in depth. Using the crater abundances within a 100 km radius of the landing site we obtain an age for the surface of about 3.5 billion years, within a factor of 2 or 3. Despite the age uncertainty, the computed rock breakdown and removal rate of meters per billions of years is surprisingly small, $\sim 10^{-3}$ microns per year. In contrast, there has been several hundred meters of wind erosion within a few hundred kilometers of the Viking Lander 2 (VL2) site, based on the relief between pedestal craters and the surrounding fine-grained aeolian deposits. The pedestal crater abundances indicate that the partially stripped deposits are about the same age as the VL1 site. The erosion rate for the aeolian deposits, averaged over such a lifetime, would be a few tenths of a micron per year, which is two orders of magnitude greater than the computed rate of rock removal at VL1. Such a large difference in erosion rates between rock and soil is in fact mandatory if the pedestral craters have resisted stripping due to a bouldery surface. Windblown drifts seen at both landing sites may provide information on the intensity of aeolian processes averaged over tens of thousands of years. The drifts have morphologies indicative of accumulation duringa prevailing north to south wind regime - the situation prevalent during the annual global dust storms occurring near perihelion. Due to precessional effects the subsolar latitude at perhelion (SLP) migrates ± 25° in latitude about the equator with a 50,000 year period. Because of the enhanced stripping associated with regions close to the SLP, it seems probable that the drifts at VL1, with their strictly north to south trend, must have accumulated since the SLP was last over the landing site latitude (24° N. lat.), which would have been about 15,000 years ago. If this line of reasoning is accepted, then an average accumulation rate of about 10 centimeters (mean drift thickness) per 15,000 years, or several microns/year, can be computed. A redistribution rate of microns per year is also consistent with the observations made by the Lander cameras over the past year. A thin layer (microns thick) of dust was deposited at VL2 site during the second of the two global dust storms observed during the mission. Conditions at VL1 have been similarly quiet, with the removal of a thin, bright dust layer, again probalby only microns in thickness, being the dominant activity. In summary, results for the Viking landing sites indicate that little rock breakdown and removal by wind has occurred over approximately the past 3 billion years. On the other hand, relatively rapid redistribution of friable or loose, fine-grained materials has occurred. Many of the landforms seem in higher resolution Viking Orbiter frames covering other parts of Mars are consistent with such interpretations. Many volcanic flow fronts, well preserved crater populations, and other features indicative of little to no significant modification can be discerned. In other regions, the surface has been stripped, yardangs have formed, and in general the topography appears to have largely been configured by aeolian activity. Such regions must be composed of friable deposits, such as volcanic ash or older aeolian materials. Finally, the similarity of redistribution rates for aeolian deposits averaged over three vastly different time-scales implies that roughly the present aeolian environment has been operative for a significant fraction of geologic time.

CORRELATION OF REMOTE SENSING DATA AND CRATER DENSITY AGES OF FLOW UNITS IN THE FAR EASTERN LUNAR MARIA

J.M. Boyce (NASA Headquarters, SL-4,
Washington, D.C. 20546; and USGS,
Flagstaff, AZ 86001)

The distribution of major geologic units of uniform relative age exposed in the far eastern maria (i.e., Mare Marginis, Mare Smythii, and Mare Crisium) and Mare Humorum were previously mapped by Boyce and Johnson (1978). Correlation of crater densities and radiometric ages of Apollo landing sites provide estimates of the absolute age for the units. Results indicate that the far eastern maria were emplaced over a period of approximately 1.25 b.y., from about 3.75 b.y.,to 2.5 b.y., before present. Extensive young mare units (2.5 ± 0.5 b.y.) occur in all three large far eastern Maria. Major old units (3.65 ± 0.05 b.y.) occur in central Mare Crisium and eastern Mare Marginis. Correlation of the age data and remote sensing data suggest: (1) both young and old units have relatively high Mg/Al ratios and low values of Fe and Ti. A similar relationship was previously noted for other maria suggesting that this is the general relationship throughout the lunar maria (Bielefeld et al, 1976; Soderblom et al, 1977; Andre et al, 1979); (2) older units generally have higher remnant magnetism than younger units - a relationship also previously noted for other lunar maria and attributed to a steady decline of a primodial lunar magnetic field (Soderblom et al, 1977); and (3) all age units in the eastern maria have relatively low natural radioactivity or abundances of Th, K, and U compared to the western maria (particularly in the Mare Imbrium area). The presence of young lava flows in both the eastern and western maria suggests that the relative abundance of these radioactive elements have played only a minor role controlling the duration and location of mare volcanism.

Andre, C.G., Wolfe, R.W., and Adler, L., 1979, Are Early Magnesium-Rich Basalts Widespread on the Moon? (abs) in Lunar and Planetary Science X, The Lunar and Planetary Institute, Houston, Texas, V. 1, p.

Bielefeld, M.J., Andre, C.G., Eliason, E.M., Clark, P.E., Adler, I., and Trombka, J.I., 1976, Surface Chemistry of Selected Lunar Regions: Proceedings Lunar Science Conference Seventh, Geochemica et Cosmochimica Acta, Supp. 7, V. 3, p. 2661-1200.

Boyce, J.M., and Johnson, D.A., 1978, Age of Flow Units Eastern Maria and Implications for Basin-Filling History: Proceedings Lunar and Planetary Science Conference Ninth, Geochimica et Cosmochimica Acta, Supp. 10, V. 3, p. 3275-3284.

Soderblom, L.A., Arnold, J.R., Boyce, J.M., and Lin, R.P., 1977, Regional Variations in the Lunar Maria: Age, Radioactivity, Remnant Magnetism: Proceedings Lunar Science Conference Eighth, Geochimica et Cosmochimica Acta, Supp. 8, V. 1, p. 1191-1200.

Small- and Large-Scale Patterned Ground at Viking Lander 2 Site: Possible Analogues in SE Libya and Trans-Pecos Texas, James R. Underwood, Jr., Department of Geology, Kansas State University, Manhattan, Kansas 66506

The Viking Lander 2 site was described by Mutch and others (1977, p. 4452-4467) as ". . . a flat plain of fine-grained sediment overlain by dispersed, evenly distributed boulders . . . . Polygonal sediment-filled cracks may have been formed by ice wedging . . . Alternatively, they may be desiccation polygons." The sediment-filled cracks are referred to elsewhere in the same report as troughs, the best studied of which lies 8 m north of the space craft and is 1 m wide, 10 cm deep, and trends approximately east-west in a gentle arc over an observed distance of some 10 m. The northern wall of the trough is described as higher than the south wall; the trough is reported to be bordered along both margins by low, rounded to sharp ridges, up to 10 cm high to the north and rising up only 5 cm or so to the south. The trough contains fine-grained sediment, drifted in places, together with a few scattered rocks, some of which are partly buried. Compared to the rest of the site, rocks in the troughs are markedly sparse. In view near the lander, there are other troughs with different trends, together with several trough junctions. The junctions suggest that the troughs form a polygonal pattern, although because of oblique and obstructed views, this is partly conjecture.

Camera event 21A024 shows the trough just north of the lander. This picture is reminiscent of photographs of patterned ground northeast of Kufra Oasis in southeast Libya (Underwood, 1974). The region is one in which buttes and mesas of the Nubian Sandstone (Lower Cretaceous) rise 100 m or so above the nearly level desert surface which is underlain by quartz, silt, sand, and gravel weathered from the Nubian. Over several areas of tens of square kilometers, polygons consist of angular, tabular gravel (pebbles and cobbles of Nubian Sandstone and silcrete) that floats in medium-to-coarse sand; the borders, distinctive because of their lack of pebbles and cobbles, are 10-15 cm wide zones of granules and medium-to-coarse sand. The polygons are sorted, have sides which range up to 10 m long, and mostly orthogonal intersections. Their pattern, based on the classification of Neal (1965) and Neal and others (1968), is "oriented orthogonal" in some areas and intermediate between regular and irregular "random orthogonal" in others.

The Libyan patterned ground is interpreted to reflect downward movement into fractures in bedrock of the overlying sediment blanket. The first step is the development of a desert pavement or armor (a serir). The underlying bedrock may have a rectangular system of joints into which material from the overlying sediment can move. If the movement initially is abrupt, immediately following development of joints or perhaps triggered by the release of energy during an earthquake, a depression or trough would develop at the surface. Fine-grained, windblown material then would fill the trough and produce oriented orthogonal patterned ground characterized by coarse-grained material in polygons that are bounded by finer-grained materials.

The random orthogonal pattern could most likely be produced by the development of desiccation fissures in clay-rich sediments underlying the blanket of debris. Downward movement of material into these fissures would likewise produce surface depressions which would subsequently be filled by wind-blown, fine-grained material. The random orthogonal pattern produced, however, would be distinctly different from that of the joint-controlled polygons.

The suggestion thus is put forward that at the Viking Lander 2 site, one possible origin of the troughs is that they formed by movement of material with a desert pavement surface downward into fissures (joints or fractures produced by desiccation or by cooling) in the underlying bedrock. Fine-grained material then blew into the troughs, partly or totally filling them.

Viking orbiter images of the Lander 2 region show depressions outlining polygons 10 to 20 km across. Morris and Underwood (1978) pointed out that on earth the polygonal patterns closest to the size of these on Mars are those dessiccation fissures described by Pratt (1958) in the alluvial fill of Salt Basin near Van Horn, Texas and by Underwood (1963) and Underwood and De Ford (1969, 1975) elsewhere in Trans-Pecos Texas. The largest of the polygons in these systems ranges up to a kilometer in maximum diameter. As suggested by Neal (1965) for similar polygons elsewhere, the polygons probably developed during prolonged periods of drought or during extended periods of heavy pumping of ground water, either or both of which lowered significantly the water table in the fine-grained basin fill in which the fissures developed. The fractures develop at depth, then are propagated upward and reach the surface initially merely as a hairline fracture in the slightly gypsiferous or calcareous crust of the surface of the basin fill. The fissures become strikingly apparent at the surface only following heavy rainfall when water begins to channel down through the unconsolidated material and widens the fissures dramatically. It has been suggested that where these fissures are enlarged by occasional episodes of rapid, downward flowing water, the fissures may represent a major fracture system lasting perhaps hundreds of years, or until the water level in the basin fill rises appreciably (Underwood and De Ford, 1975).

References:

Morris, E. C. and J. R. Underwood, Jr., 1978, Polygonal fractures of the Martian plains: NASA Tech. Memo. 79729, p. 97-99.

Mutch, T. A.,R. E. Arvidson, A. R. Binder, E. A. Guiness, and E. C. Morris, 1977, The geology of the Viking 2 Lander site: Jour. Geophys. Res., v. 82, no. 28, p. 4452-4467.

Neal, J. T., 1965, Giant desiccation polygons of Great Basin playas: Air Force Cambridge Research Lab. Environmental Research Paper 123, 30 p.

Neal, J. T., A. M. Langer, and P. F. Kerr, 1968, Giant desiccation polygons of Great Basin playas: Geol. Soc. America Bull., v. 79, no. 1, p. 69-90

Pratt, W. E., 1958, Large-scale polygonal jointing: Am. Assoc. Petroleum Geologists Bull., v. 42, no. 9, p. 2249-2251.

Underwood, J. R., Jr., 1963, Geology of Eagle Mountains and vicinity, Hudspeth County, Texas: Univ. Texas Bur. Econ. Geol. Quad. Map no. 26, with 32 p. text.

__________, 1974, Contrasting types of patterned ground in southeast Libya: Geol. Soc. America Abstracts with Programs for 1974, v. 5, no. 2, p. 125-126.

Underwood, J. R., Jr. and R. K. De Ford, 1969, Large-scale desiccation fissures in alluvium, Trans-Pecos Texas and northern Chihuahua: Geol. Soc. America Abstracts with Programs for 1969, Part 2 (South Central Section), p. 31.

__________, 1975, Large-scale desiccation fissures in alluvium, Eagle Mountain area in C. M. Callick (Ed.), Geology of the Eagle Mountains and vicinity, Trans-Pecos Texas: Soc. Econ. Paleont. and Mineralogists, Permian Basin Section, Field Trip Guidebook 75-15, p. 135-139.

Review of Libyan Desert Glass, SW Egypt, and Report on 1978 Expedition,

James R. Underwood, Jr., Department of Geology, Kansas State University, Manhattan, Kansas 66506

Libyan Desert glass, a unique natural, high-silica glass was discovered in the southwest desert of Egypt on December 29, 1932 by P. A. Clayton of the Egyptian Desert Survey (Clayton and Spencer, 1934). The glass occurs as scattered pieces on the sandy floor of the 2-5 km wide corridors or streets between north-northwest trending linear dunes (seifs), which rise 100 m or so above the intervening essentially flat desert surface of the corridors. The sparse outcrops of the Nubian Sandstone (Lower Cretaceous) indicate that the strata in the glass area, which is about 130 km north-south and 50 km east-west (Spencer, 1939), essentially are flat lying.

Although Libyan Desert glass is considered by many to be a variety of tektite, the glass does not show ablation features. Almost certainly it has not passed through the Earth's atmosphere, although it may have been transported locally by streams. Paleolithic man of the Aterian culture used it to a limited degree and he, and perhaps Arabs as well, have transported small amounts of it up to 225 km away (Spencer, 1939). None has been reported among pharonic materials nor have any glass artifacts been discovered that represent the Acheulean cultural stage.

Clayton returned to the glass site briefly in 1933, and in December 1934 he and L. J. Spencer of the British Museum and O. H. Little of the Egyptian Survey spent nine days collecting glass and studying the environment of its occurrence (Spencer, 1939; Giegengack and Issawi, 1975). The region also was visited in the 1930's by such explorers as R. A. Bagnold, W. B. Shaw, and K. S. Sandford. Except for traverses through the general area during World War II by teams of the Long Range Desert Group of the British Eighth Army, the next expeditions to the glass site were those of Barnes and Underwood (1976, p. 117-122) in 1971 and Underwood and Said in 1978 (Underwood, 1979). In the period late 1976 - early 1979, however, Continental Mid-Delta Petroleum Company had a geophysical contractor, GEOSOURCE, running seismic lines in the region, and numerous members of the GEOSOURCE crews, as well as Continental geologists, collected an unrecorded number of specimens of Libyan Desert glass.

In 1971 Barnes and Underwood collected 26 pieces from the western margin of the glass site; in 1978 Underwood and Said collected from the central part of the site more than 350 pieces, which range in maximum dimension from 1.5 cm to 21 cm and weigh up to 1.75 kg (Underwood, 1979). The most common shape of the pieces of glass in this collection is tabular; some are elongate but show no preferred orientation. Color ranges from colorless to milky white to pale yellow green to dark green to black. Many pieces are etched and pitted; others are smooth and have a waxy or resinous luster. Scattered outcrops of quartz sandstone in the glass area were examined to see if any had fused, glassy surfaces. None was seen.

Although Libyan Desert glass has been analyzed and studied for almost 50 years, its origin is still uncertain. The intriguing possibility exists that it represents the product of an encounter with the Earth of an extra-terrestrial body, an encounter that produced an intense but short-lived thermal event.

Although Libyan Desert glass is much more homogenous than most glass (impactite) produced by meteorite impact, the melting of the quartzose Nubian Sandstone at point of impact of a meteorite and subsequent rapid cooling of the melt remains one possible origin of the glass. The plausibility of this origin is enhanced by the occurrence of two impact structures 150 km westward in Libya: The "B. P. structure", 2.8 km in diameter and the "Oasis structure", 11.5 km in diameter (French and others, 1972; French and others, 1974; Underwood, 1975, 1976, 1979; Underwood and others 1975; Underwood and Fisk, 1978). Pieces of Libyan Desert glass, or other impactite, have not been identified at either structure or in the region separating the glass site and the structures. It seems unlikely that the ejecta of such relatively small structures would carry 150 km or result in such a localized occurrence of impactite. The glass, however, may well have been transported to, and concentrated in, its present location by streams in an earlier, wetter time. In fact, if the glass cannot be related to impact structures, then the glass producing thermal event may have been related to an exploding or grazing comet.

Based on the work of numerous investigators the general properties of Libyan Desert glass are as follows:

1. Chemical composition of Libyan Desert glass and Nubian Sandstone.
   Silica content of Libyan Desert glass (Table 1) is in excess of 97 percent, whereas silica content of conventional tektites ranges from about 70-80 percent (Barnes and Barnes, 1973). Based on major element composition, the Nubian Sandstone is a suitable parent material for Libyan Desert glass.
2. Color
   Ranges from colorless to black; most common are light yellowish green and light straw yellow. Specimens with abundant bubbles are milky white.
3. Hardness
   Approximately 6 on Mohs Scale.
4. Specific gravity
   For 15 specimens collected in 1971, ranges from 2.120 to 2.215 (Barnes and Underwood, 1976).
5. Index of Refraction
   For 15 specimens collected in 1971, ranges from 1.4590 to 1.4625. (Barnes and Underwood, 1976).
6. Crystallites and inclusions
   Small (up to 1 mm) white spherulites have been identified as cristobalite (Spencer, 1939); another devitrification product has been tentatively identified as tridymite (Barnes and Underwood, 1976). Inclusions reported are zircon and its alteration product baddeleyite, rutile and a decomposition product of titanomagnetite (Kleinman, 1969).
7. Textures
   The surface of the glass may be smooth and resinous or it may be pitted and rough, as if etched by subsurface fluids. Some of the pieces are ventifacts and some are artifacts of the Aterian culture. The largest

piece (803 gms) collected in 1971 has crescentic percussion marks on one surface (Barnes and Underwood, 1976).
Distinctive, irregularly conical cavities up to 1-2 cm in diameter at the surface and up to 3.5 cm deep are fairly common. Some are completely penetrative. (Clayton and Spencer, 1934).
Most specimens are grossly tabular or elongate and subround to round. Some are angular with extremely sharp edges, as if they had been fractured recently. Fracture surfaces are conchoidal.
Bubbles are common, but by no means present in all pieces. Bubbles range in maximum diameter up to 3.0 mm; those smaller than 0.02-0.04 mm are elliptical to spherical (Barnes and Underwood, 1976). Bubbles may occur in trains, in layers and in patches. The gas in the bubbles contains nitrogen, argon, krypton and xenon in the same relative quantities as air (Zahringer and Gentner, 1963).

8. Age

Based on fission tracks analysis, an age of 28.5 X 10^6 years was determined by Storzer and Wagner (1971).

Table 1

Chemical Composition of Libyan Desert Glass and Nubian Sandstone

	Libyan Desert glass			Nubian Sandstone
	Barnes and Underwood (1976)	Clayton and Spencer (1934)	Spencer (1939)	Barnes and Underwood (1976)
SiO_2	98.00	97.58	98.20	99.60
TiO_2	0.13	0.21	0.23	0.02
ZrO_2	<0.02	-----	-----	<0.003
Al_2O_3	1.16	1.54	0.70	0.04
Fe_2O_3	0.08	0.11	0.53	0.10
Cr_2O_3	tr	-----	-----	tr
V_2O_5	tr	-----	-----	tr
FeO	0.15	0.23	0.24	0.02
NiO	tr	tr	0.02	tr
MnO	<0.003	tr	-----	<0.001
MgO	0.01	tr	0.01	0.01
CaO	0.01	0.38	0.30	0.03
BaO	<0.002	-----	-----	<0.002
CuO	tr	-----	-----	tr
Na_2O	0.02	0.34	0.33	0.01
K_2O	0.006	nil	0.02	0.002
H_2O-	0.02	0.05	0.03	0.03
H_2O+	0.09	0.05	0.03	0.07
Total	99.85	100.49	100.64	100.04

References:

Barnes, V. E. and M. A. Barnes (Eds.), 1973, Tektites in R. W. Fairbridge (Series Ed.), Benchmanrk Papers in Geology: Dowden, Hutchinson and Ross; Stroudsburg, Pa., 445 p.

Barnes, V. E. and J. R. Underwood, Jr., 1976, New investigations of the strewn field of Libyan Desert glass and its petrography: Earth and Planetary Sci. Letters, v. 30, p. 117-122.

Clayton, P. A. and L. J. Spencer, 1934, Silica-glass from the Libyan Desert: Mineral Mag., v. 23, no. 144, p. 501-508.

French, B. M., J. R. Underwood, Jr., and E. P. Fisk, 1972, Shock metamorphic effects in two new Libyan impact structures: Geol. Soc. America Abstracts with programs for 1972, v. 4, no. 7, p. 510-511.

_______, 1974, Shock metamorphic features in two meteorite impact structures, southeastern Libya: Geol. Soc. America Bull., v. 85, no. 9, p. 1425-1428.

Giegengack, Robert and Bahay Issawi, 1975, Libyan Desert silica glass - a summary of the problem of its origin: Annals of the Geological Survey of Egypt, v. 5, p. 105-118.

Kleinman, B., 1969, The breakdown of zircon observed in the Libyan Desert glass as evidence of its impact origin: Earth and Planetary Sci. Letters, v. 5, p. 497-501.

Spencer, L. J., 1939, Tektites and silica-glass: Mineral. Mag., v. 167, p. 425-440.

Storzer, D. and G. A. Wagner, 1971, Fission track ages of North American tektites: Earth and Planet. Sci. Letters, v. 10, p. 435-440.

Underwood, J. R., Jr., 1975, Impact structures of the Libyan Sahara: some comparisons with Mars <u>in</u> Expanded Abstracts, International Colloquium of Planetary Geology, Rome, 22-30 September 1975, p. 35-38. Proceedings in Geologica Romana, v. 15, p. 337-340.

________, 1979, Libyan Desert glass - 1978 expedition: Transactions of the Kansas Academy of Science (in press).

Underwood, J. R., Jr., E. P. Fisk, A. S. Campbell and D. W. Baird, 1975, Reconnaissance geology of meteorite impact structures in SE Libya: Geol. Soc. America Abstracts with Programs for 1975, v. 7, no. 2, p. 242.

Underwood, J. R., Jr. and E. P. Fisk, 1978, Meteorite impact structures, southeast Libya: Abstracts, Second Symposium on the Geology of Libya, Tripoli, 16-21 September 1978, p. 61-62.

Zahringer, J. and W. Gentner, 1963, Radiogenic and atmospheric argon content of tektites: Nature, v. 199, p. 583.

Lunar Data Analysis Summary, D. Codona, Jet Propulsion Laboratory, California Institute of Technology, Pasadena, CA 91103/Calif. State University at Los Angeles, Los Angeles, CA 90032/R. S. Saunders, Jet Propulsion Laboratory, California Institute of Technology, Pasadena, CA 91103

From estimates of lunar maria fill thickness, narrow-band optical reflectance data, x-ray, iron concentration, γ-ray, radar, infrared cooling data, gravity, and topography, it has been possible to form a reference dataset for further mapping of lunar geology.

All the datasets are images compatible with the format used by JPL's Image Processing Laboratory, but due to the differences in image scale are not easily correlated with one another. They are scaled and translated to one basic format. Using this format throughout all the datasets will allow image processing to proceed more quickly, since the images will not need to be registered every time an image is used.

The format to be used for the reference dataset will be line 1 = 90° latitude, sample 1= -90° longitude, scaled to 6.07 pixels per degree longitude at the equator. The data that do not already conform to this format will be reformatted using JPL's image processing facility to geometrically transform and translate images. The final result will be a set of rectilinear (simple cylindrical) maps beginning at 90°, -90° and extending to -90° latitude in the line direction and 270° in the sample direction. Data which do not begin at 90° latitude, -90° longitude will have zeros in the regions for which there is no coverage.

Attached is the reference set current to April 1979, along with the description of the data collected, the instrument or method used to collect or calculate the data, and its present image format and scale. After the datasets have been reformatted, photographic images of each set will be catalogued so that it will be easier to determine which reference numbers are wanted for analysis. Also, a cross-referenced catalogue consisting of data type, reference number, tape I.D. and file will be compiled in order to simplify the data processing.

References and Data Sources:

De Hon, R.A. and J.D. Waskom, NASA Contract NAS 9-13196.

Johnson, T.V., D.L. Matson, R.J. Phillips and R.S. Saunders, Proc. Lunar Sci. Conf. 6th (1975), pp. 2677-2688.

Johnson, T.V., J.A. Mosher and D.L. Matson, Proc. Lunar Sci. Conf. 8th (1977), pp. 1013-1028.

Dataset #	Type of Data	Instrument or Method	Format	Scale	Reference/Comments
1	Mare Isopach	Calculated from assumed crater geometry	2400 ℓ x 400 s Mercator, line 1 = 0° Latitude, Sample 1 = 30° Longitude	1/40°/pixel	DeHon & Waskon (1975)
2	4.64-6.37 MeV γ-ray	Apollo 17	Mercator Projection 464 x 1440	1/4°/pixel	Metzger - raw data
3	5.95-6.37 MeV γ-ray	" "	" " "	" "	" - uncorrected
4	" " "	" "	" " "	" "	" - corrected for Fe & other elements
5	" " "	" "	" " "	" "	Metzger - corrected for other elements
6	Optical Reflection	SIPS Questar Filter #5	1820 ℓ x 1800 s Rectilinear projection, line 910 = 0° lat S. 910 - 0° long.	5 km/pixel at equator	Johnson & Matson
7	"	" Filter #1	" "	" "	" "
8		" Filter #8	" "	" "	" "
9	"	" Filter #3	" "	" "	" "
10	"	" Filter #7	" "	" "	" "
11	"	SIP TMO 24" Scope Filter #1	" "	" "	" North Hemisphere " Maria Mosaic
12	"	Filter #3	" "	" "	" " "

Dataset #	Type of Data	Instrument or Method	Format	Scale	Reference/Comments
13	Optical Reflection	SIPS TMO 24" Telescope, Filter #4	1820 ℓ x 1820 s Rectilinear Projection	5km/pixel at equator	Johnson & Matson North Hemisphere Maria Mosaic
14	"	" Filter #5	" "	" "	" "
15	Radioactivity	Apollo 15, 16	1820 ℓ x 1820 s Rectilinear Projection, Line 910 = 0° lat S. 910 = 0° long.	" "	
16	Iron Concentration	" " "	" "	" "	
17	X-ray Spectrometry	Apollo 16	" "	" "	AL/SI *10
18	" "	" "	" "	" "	AL*MG*10
19	" "	" "	" "	" "	MG*SI*10
20	" "	" "	" "	" "	AL/SI
21	" "	" "	" "	" "	MG/SI
22	" "	" "	" "	" "	AL/MG
23	Eclipse Infrared	" "	" "	" "	T.W. Thompson
24	Polarized Radar	" "	" "	" "	" "
25	Depolarized Radar	" "	" "	" "	" "

GEOLOGY OF VENUS, Malin, M.C., Goldstein, R.M., Jurgens, R.F., Rumsey, H.C. and Saunders, R.S., Jet Propulsion Laboratory, California Institute of Technology, Pasadena, CA 91103

Knowledge of the geology of Venus comes from three principal sources: Earth-based radar observations, orbital radar observations, and Venera Lander observations.

Earth-based radar observations of the surface of Venus have three forms. First, topographic profiles about the equator (e.g. Pettengill, 1978; Campbell, et.al., 1972; Golovkov, et.al., 1976) reveal variations as great as 6.5 km over distances of thousands of kilometers and relief contrasts of 4.5 km in as little as 100-200 km. The second form of Earth-based radar observation consists of radar reflectivity maps portrayed as photographic images (Rogers and Ingalls, 1969; Goldstein and Rumsey, 1970; Rumsey et.al., 1974; Goldstein et.al., 1976; Campbell et.al., 1976). These maps, at a variety of resolutions and scales, can be used to study the surface roughness and, in some instances, the physiography of surface features. It is from these data, acquired at the Arecibo Observatory in Puerto Rico and Goldstone Tracking Station in California, that most of the geological interpretations of the surface of Venus are derived (e.g. Malin and Saunders, 1977; Saunders and Malin, 1977; Campbell et.al., 1976). Morphologic studies can be carried out at a resolution of about 10 km per radar cell or an interpretation resolution exceeding 30 km. The third form of Earth-based radar observations consists of topographic maps acquired simultaneously with the high resolution reflectivity maps through bi-static and tri-static observations (Rumsey et.al., 1974; Goldstein et.al., 1976). These topographic maps have spatial resolutions somewhat lower than their reflectivity counterparts, with a vertical resolution of several hundred meters. They show Venus to be relatively smooth (with topographic variations less than + 1 km) but with localized areas of significantly greater relief.

The most abundant landform visible in these images are quasi-circular forms interpreted to be craters (Saunders and Malin, 1976). These craters are morphologically similar to large degraded impact craters on Mars and the Moon, and so that interpretation has been tentatively applied to the venusian craters as well.

The second most abundant morphologic features are isolated peaks and mountains (Malin and Saunders, 1977). These can be found in nearly every area so far imaged (crater forms are not found everywhere) and are somewhat smaller than the circular crater forms. Isolated mountain-like forms are rare on terrestrial planets whose topography reflects impact processes solely. A case can be made that the only processes capable of forming isolated mountains are those associated with volcanism or tectonism.

A variety of other morphologic forms are seen in various regions on Venus. These include ranges of mountains and several localized areas of high reflectivity (Malin and Saunders, 1977; Saunders and Malin, 1977). At least one of these latter areas, known as "Beta", appears to be a relatively elevated region (about 10 km high) approximately 700 km in diameter with a 60 x 90 km wide depression at its summit. It is interpreted to be a large volcanic construct analogous to terrestrial and martian shield volcanoes.

Perhaps the most exciting feature on Venus is a large trough-like depression some 1400 km long, 150 km wide, and about 2 km deep (Malin, 1975; Malin and Saunders, 1977). This north-trending feature located near 76°W at the equator has been compared with the Valles Marineris trough system on Mars and to portions of the Afro-Arabian rift system in East Africa. The trough rests within a plain that, some 850 km to the east, encounters a continent-sized plateau, where very faint, narrow, sinuous depressions are found. These channel-like forms appear to originate in high regions of the plateau and progress downslope to the topographic margin where they widen and merge with the surrounding plains.

Orbiter radar observations are just beginning to be made by the Pioneer Venus Orbiter and results are not yet available to the general community. Preliminary altimeter observations show local topography variations of 6 or 7 km (Pettengill et.al., 1979). The Soviet Union made bi-static radar observations of the surface of Venus using the Venera 9 and 10 Orbiters (Kolosov et.al., 1976). In general Venus appears to be about as smooth or somewhat smoother than the lunar maria except in regions of high topographic relief where roughness, slope, and topographic contrast approach that of the lunar highlands.

Observations of the Venera Landers 8,9, and 10 tell something about the small-scale geology of Venus. All three landers made observations using gamma-ray spectrometers of surface material radioactivity and density. Rock density at the Venera 10 site was reported as 2.8 + .1 gm/cm^3, typical of rock densities on both the Moon and the Earth (Surkov et.al., 1976). The abundances of potassium and uranium were more like those of the Earth than of the Moon or meteorites. Veneras 9 and 10 acquired photographs of each of the two landing sites on Venus (Florensky et.al., 1977). The Venera 9 landing site is characterized by a large abundance of slab-like and rounded, dull gray, massive boulders, with very little surface texture, typically 40 to 80 cm across. The Venera 9 boulders rest on a fine grained dark matrix of regolith or soil. In contrast, the Venera 10 landing site is characterized by large flat platforms of outcrop separated by large contiguous areas of regolith. The Venera 10 "platform" is in places fractured and grooved and has a smooth surface texture giving it an appearance similar to the individual boulders at the Venera 9 site. This similarity suggests that the materials at the two landing sites are comparable. Other patches of the "platform" rocks show rough textured surfaces that appear to have caught and trapped fine dark material in pits and grooves. Venera 9 and 10 measured wind speeds of 0.5 to 1 meter/sec at a height of 1.3 m. These winds have the same capacity for moving particles as 5 to 10 meter/sec winds over a similar surface at that height on Earth, a speed above the threshold for sand saltation.

The state of knowledge of the geology of Venus derived from the above information can be summarized as follows: 1) Venus shows some physiographic diversity at an identification resolution of about 30 km. Crater-like forms occur in clusters separated from mountainous plateau regions and the large equatorial trough. Isolated mountains appear to occur throughout the regions viewed by Earth-based radars. 2) There is some evidence that three types of volcanism occur on Venus: One type forms large single constructs comparable to the Tharsis volcanoes on Mars. Another forms smaller peaks that occur singly or in clusters. The third forms plains like those on Mars and the Moon. 3) Mountainous terrain and sharply defined lineaments suggests compressional tectonism, although extension can also explain some of these features. 4) The great trough at the equator suggests extensional tectonic activity. 5) Venera Lander observations of native radioactivities indicate that the rocks on Venus are much like those of the Earth. In particular, the Venera 9 and 10 landings appear to have occurred among basaltic rocks, while the Venera 8 lander appears to have sampled a rock of granitic composition. The former sites support the interpretation of volcanism, especially since they are located near the feature "Beta", while the latter observation implies a somewhat more complicated volcano-tectonic environment (to the extent that granitic rocks on the Earth reflect its plate tectonic history). 6) The Venera 9 and 10 lander images show two terrains that have undergone geomorphic change. The differences between the sites can be explained by different processes operating at them, by the same process acting at different times or different rates, or a combination of both. However, in all cases, the processes have been sufficiently active to separate large debris from small, to round some boulders but not others, and to mix in some exotic materials. Candidate processes include ballistic impact processes of redistribution and eolian erosion.

References

Campbell, D.B., Dyce, R.B., Ingalls, R.P., Pettengill, G.H. and Shapiro, I.I. (1972). Sci. 175, 514.

Campbell, D.B., Dyce, R.B. and Pettengill, G.H. (1976). Sci. 193, 1123.

Florensky, C.P., Ronca, L.B., Basilevsky, A.T., Burba, G.A., Nikolaeva, O.V., Pronon, A.A., Trakhtman, A.M., Volkov, V.P. and Zazetsky (1976). Bull. Geo. Sci. Am. 88, 1537.

Goldstein R.M., Green, R.R. and Rumsey, H.C., Jr. (1976). J. Geophys. Res. 81, 4807.

Goldstein, R.M. and Rumsey, H.C., Jr. (1970). Sci. 169, 974.

Golokov, R.K., Kuznetsov, B.I., Petrov, G.M. and Khasganov, A.F. (1976). Radio Eng. Elec. Phys. 21 (9), 1.

Kolosov, M.A., Yakovlev, O.I., Pavel'ev, A.G., Kaevitser, V.I., Kalashnikov, N.E., Kozlov, F.I., Kucheryavenkov, A.I., Matygov, S.S., Mdotov, Ye.P. and Rogal'skiy, V.I. (1976). Radio Eng. Elec. Phys. 21 (9), 6.

Malin, M.C. (1975). (Abstract). Int'l Coll. of Planet. Geol., Rome, Italy, 22-30, 165.

Malin, M.C. and Saunders, R.S. (1977). Sci. 196, 987.

Pettengill, G.H. (1978). Ann. Rev. Astro. Astrophys. 16, 265.

Pettengill, G.H., et.al., (1979). Sci. 203, 806.

Rogers, A.E.E. and Ingalls, R.P. (1969). Sci. 165, 797.

Rumsey, H.C., Morris, G.A., Green, R.R. and Goldstein, R.M. (1974). Icarus 23, 1.

Saunders, R.S. and Malin, M.C. (1977). Geophys. Res. Lett. 4, 547.

Surkov, Yu.A., Kirnozov, F.F., Khristianov, R.K., Glazov, V.N., Ivanov, V.F. and Korchuganov, B.N. (1976b). Preprint of Inst. Space Research, Akad. Nauk SSR Pr-278, 10-11.

Gravity Field Mapping with the Pioneer Venus Orbiter, Roger J. Phillips and William L. Sjogren, Jet Propulsion Laboratory, California Institute of Technology, Pasadena, California 91103.

The line-of-sight (LOS) gravity field for Venus has been mapped with the Pioneer Venus Orbiter in the vicinity of periapsis for a 20° swath of longitude, progressing eastward from an equatorial crossing of 294°. There are consistent and systematic variations in the gravity signature from orbit to orbit, attesting to the reality of observed anomalies (Figure 1).

An initial test of the isostatic compensation of topography was carried out by analyzing the gravity data over the large, low radar albedo feature to the west of the bright feature "Maxwell" and centered at approximately 325°E longitude, 68°N latitude (1). The region is approximately 1400 km in diameter and Pioneer Venus radar altimeter data shows it to be an elevated region of about 4 km average height (2). For working purposes, we refer to this feature as the "Northern Plateau". Orbit 93 passed across the southeast portion of this area, traversing from southwest to northeast from about 60° to 68°N latitude. We have modeled the Northern Plateau as a spherical cap 1400 km in diameter, 4 km in height, with a density of 3 gm-cm^{-3}. If this elevated region is totally uncompensated by a density deficiency in the interior, then a peak LOS gravity anomaly of about 11 mgal would result. This exceeds the estimated noise level on orbit 93 by a factor of 5. Since there is essentially no anomaly seen, then there must be a mass deficiency in the interior cancelling the gravity effect. On the Earth, vertical weight balance (isostasy) is the general rule for topography with a horizontal scale of at least several hundred kilometers. A subsurface mass of equal magnitude and opposite sign was modeled, in addition to the surface feature, to simulate isostatic compensation of the Northern Plateau. The results indicate that compensation must take place at a depth no greater than approximately 100 km. If the plateau is only partly compensated, then the depth bound is even less. The compensating mass implied by this analysis must be supplied by a chemical inhomogeneity or a temperature anomaly, with the former being more likely because of the difficulty in maintaining a significant temperature anomaly to depths of 100 km and no deeper. In turn, a lateral inhomogeneity in composition strongly implies that the outer portion of Venus has been differentiated.

The variations in the gravity data shown in Figure 1 are long-wavelength features by Earth standards. The dominant wavelength in Figure 1 is about 6000 km. For the Earth, wavelengths longer than about 2000 km (spherical harmonic degree $\ell<18$) receive little contribution from the topography and crust, arising mainly from the mantle (3). Our interest here is in estimating the power in the Venus gravity spectrum, relative to the Earth, with the small amount of Venus data on hand. We have selected three representative Pioneer Venus orbits (93, 98, 107) and performed a Fourier analysis of the LOS gravity data along an arc extending from 70°N latitude to 30°S latitude. The Earth's gravity field has been sampled by using the Pioneer Venus orbit in the presence of the Goddard Earth Model (GEM) 10 (4). The Earth was sampled in eight orbits, with a node spacing of 45°. Nearly all of the major long-wavelength gravity anomalies were sampled. The Venus spectrum parallels the Earth spectrum, but lies above the 1-σ limit for the eight Earth orbits; for the first five harmonics, the average ratio of power is 3.8. To be sure, it is possible to find individual Earth orbits that exceed the Venus spectrum. An orbit with a node crossing of 293° has its second Fourier harmonic in resonance with the maxima of the Andes and North Atlantic gravity highs and the minimum of the western North Atlantic gravity low. These are three of the largest Earth gravity anomalies and the second harmonic exceeds that of the corresponding Venus harmonic.

As a second test (5), we have projected a representation of the Earth's gravity spectrum into the space of Fourier residual velocity spectrum of orbit 92 using the same 100° arc discussed above. The Earth's gravitational potential spectral $V_\ell^2(\Delta U)$ is described by the "Kaula rule": $V_\ell^2(\Delta U) \approx A(2\ell+1)10^{-10}\ell^{-4}$, where $A \approx 0.7$. Except for the third harmonic, the Venus spectrum parallels the Earth spectrum. The average ratio of Venus to Earth power of harmoncis 1, 2, 4, and 5 is 3.6, in good agreement with the previous analysis.

We conclude that this small sample of the Venus gravity field is extraordinary by Earth standards; it contains 3 to 4 times the power of the Earth spectrum. In Figure 2 we show our estimate of the Venus gravity spectrum along with spectra for the Earth, Moon, and Mars.

The long-wavelength gravity anomalies on Venus might arise from density anomalies in the lithosphere and be supported by the finite strength of that layer. However, if so, this layer must be quite thick in comparison to the Earth's lithosphere or the finite strength of this region must be well in excess of a kilobar, an order of magnitude greater than that for the Earth (3). Additionally, the lack of a gravity signature associated with the Northern Plateau argues against a lithosphere origin for long-wavelength density anomalies because compensation appears to be an effective mechanism in the Venus lithosphere. Compensation in and of itself often implies non-elastic behavior.

If these long-wavelength anomalies arise from the sub-lithospheric mantle due to lateral temperature variations associated with convection, then the implication is that this process is more vigorous in Venus than in the Earth. Alternatively, these lateral density variations are associated with significant chemical inhomogeneities in the mantle, but such a configuration most probably could not be maintained statically over geologic time and must be part of an ongoing dynamic process (6). Further elucidation of the origin of these long-wavelength anomalies must await detailed comparison with the surface tectonics as revealed by radar imagery and altimetry.

References: (1) D. B. Campbell, R. B. Dyce, G. H. Pettengill, Science 193, 1123 (1976). (2) H. Masursky, personal communication. (3) R. J. Phillips and K. Lambeck, submitted to Rev. Geophys. Space Phys. (1979). (4) F. J. Lerch, S. M. Klosko, R. E. Laubscher, C. A. Wagner, J. Geophys. Res., in press (1979). (5) C. A. Wagner, NASA Tech. Memorandum 79721, 41 pp (1979). (6) D. L. Anderson, Geol. Soc. Am. Bull. 86, 1583 (1975).

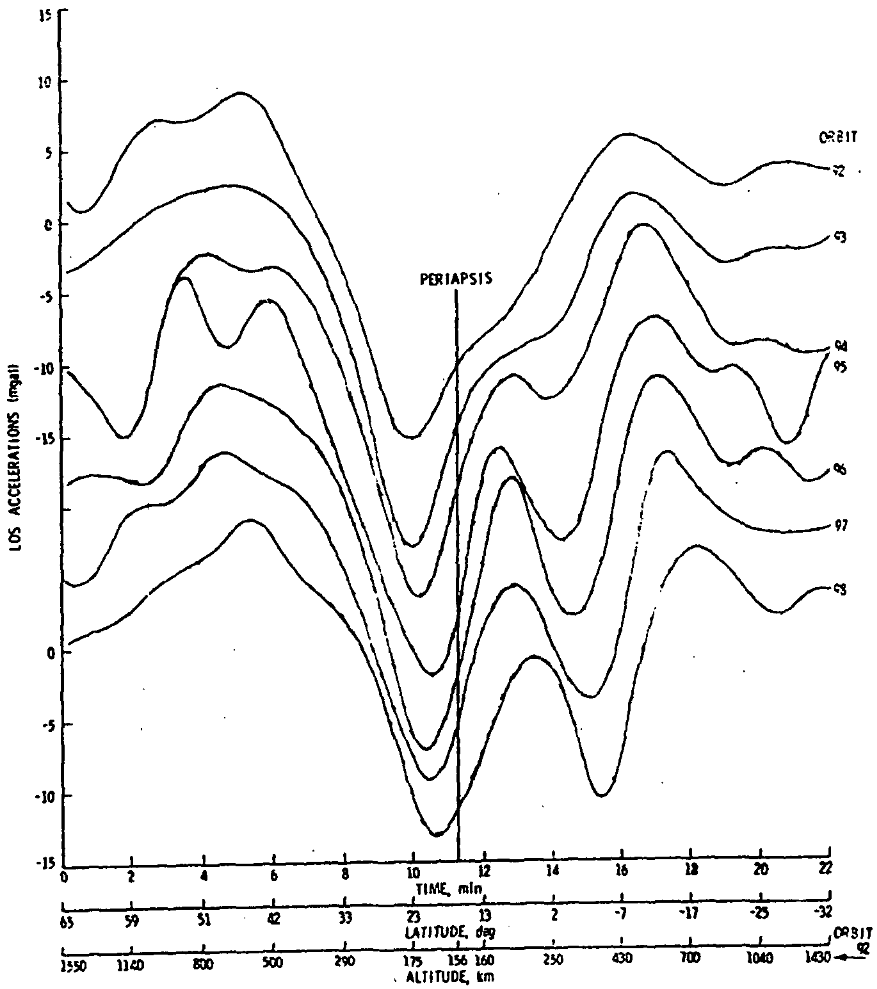

FIG. 1 - Line-of-sight (LOS) acceleration profiles from 6 March through 13 March 1979. The zero lines for orbits 92 and 98 are shown. The zero line for the other orbits are evenly spaced at 5 mgal (1 gal = 1 cm-sec^{-2}) intervals. Periapsis altitude varies from 156 km at orbit 92 to 161 km for orbit 98.

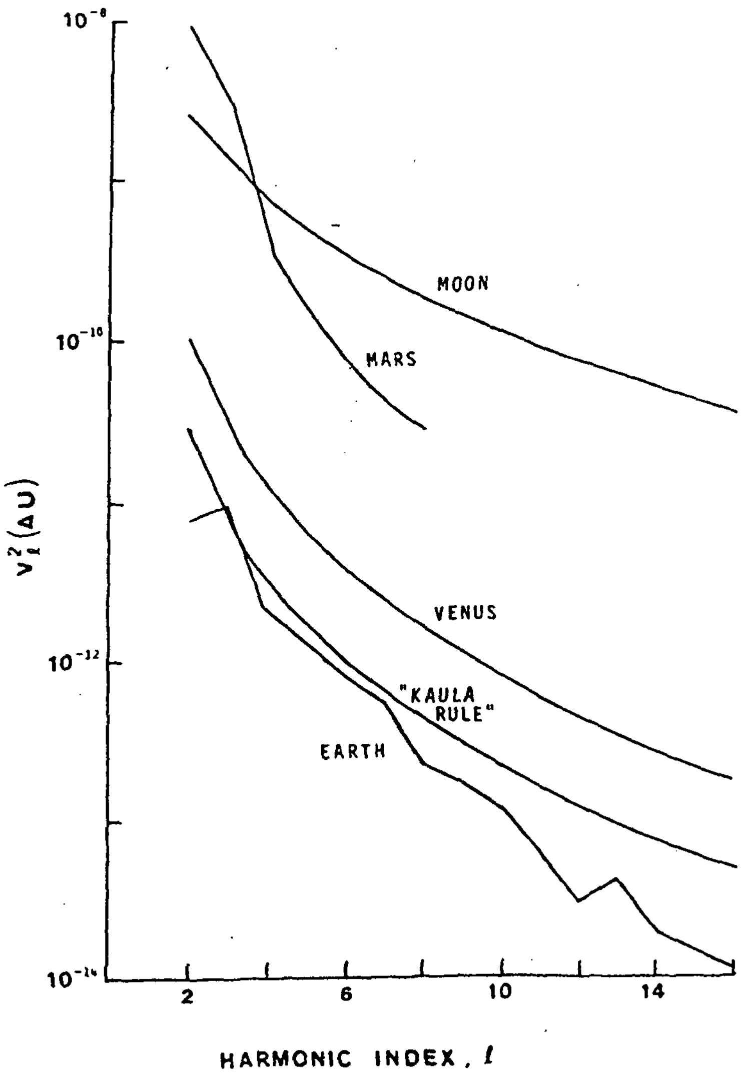

FIG. 2 - The normalized geopotential spectra for the Moon, Mars, Venus, and Earth as a function of spherical harmonic index ℓ. The estimation of the Venus spectrum is discussed in the abstract. For the Earth, the actual spectrum and the "Kaula Rule" are both shown.

Asymmetry of Mars: importance of core formation to martian tectonic history.

Donald U. Wise, George E. McGill, and Matthew P. Golombek, Dept. of Geology and Geography, Univ. of Massachusetts, Amherst, MA 01003

Any model for the tectonic evolution of Mars must account for two major crustal elements: the Tharsis bulge, and the topographically low and lightly cratered northern third of the planet. Ages determined by crater density indicate that both of these elements came into existence very early in martian history (Wise, et al., 1979), a conclusion that holds no matter which of the current crater density versus age curves is used.

The tectonic history of Mars may be summarized as follows (oldest to youngest):

A) formation and intense bombardment of early crust,
B) lowering and resurfacing of the northern third,
C) possible hiatus in development of first-order tectonic features,
D) Tharsis uplift and major radial faulting,
E) regional breakup of Tharsis with some local block behavior, and
F) development of the giant central volcanoes with local faulting.

Formation of the low and lightly cratered third of Mars by surface erosion is very improbable. Isostatic models (Fig. 1) require a minimum of 2 km of material to be redistributed over the heavily cratered 2/3 of Mars. This minimum is achieved only with an unreasonable pure ice crust. The substitution of rock for ice only compounds the volume problem. We conclude from figure 1 that there is no reasonable purely erosional solution to the problem of origin of the lightly cratered northern third of Mars. Instead, some tectonic process is needed, a conclusion similar to that of Malin, et al. (1978).

The most obvious mantle process capable of such large-scale changes early in martian history is a first-order convection cell. The model proposed here involves early differentiation of a light crust that was heavily cratered by early meteorite bombardment. As radioactive heat built up in the interior a first-order convection cell was initiated, eroding the base of the crust above the upward moving part of the cell (Fig. 2). Isostasy then produced foundering of the crust, possibly with outpourings of dense basaltic plains. If the upper crust contained volatiles, the thermal effects would cause volatilization and scarp retreat for an extended but finite period of time, in accord with the observations of Hiller, et al. (1978).

Geologic constraints require this first convective and northern resurfacing stage to come to a complete and permanent end before the initiation of the next stage, the creation of the Tharsis bulge. Among the more reasonable mechanisms for stopping first-order convection is the initiation of core formation. Elsasser (1963) proposed that the middle parts of a planetary mantle might reach the solidus for core material first. Formation of a high-density layer would inhibit and finally stop the first-order convection cell. In time, a dimple-like instability would grow in the lower surface of the denser material and the mantle would turn itself inside out as the core material drained to the center of Mars. The upper mantle would move toward the subsiding dimple, shifting any previously ingested lighter subcrustal material toward that spot, the future site of Tharsis. The result would be underplating and thickening of the crust in the Tharsis region with rapid and essentially permanent isostatic rise. Gravity creep of near-surface materials off the flanks of the rising Tharsis dome would produce the radial graben system.

The location of Tharsis, asymmetric to the earlier first-order convection cell, may be explained as follows: the dying first-order convection cell had enough upward motion in its final stage to shift the segregating denser material of the future core laterally to form a slightly thicker collar around the periphery of the upwelling part of the convection cell. Somewhat cooler temperatures in the downward moving part of the cell would retard segregation and hinder formation of a thick layer of core material there. In this scenario, the dimple from which the core grew formed in the thickest part of the unstable layer on the periphery of the defunct upward-moving cell. Assuming that subcrustal erosion was approximately centered on this cell, then the Tharsis dimple must be asymmetrically located relative to the resurfaced third, as observed. The model permits formation of multiple dimples, and thus can account for the Elysium volcanic province by the same mechanism.

Adiabatic heating and release of gravitative energy of core formation would produce a huge but very deep thermal anomaly under Tharsis. This deep thermal anomaly would require a long time to reach the surface but once there should have an extremely long life. Thus, the model predicts both the sequence of Tharsis tectonic phases and their asymmetry in time.

Elsasser, W.M., Early history of the earth, in Geiss, J. and E. Goldberg, eds., Earth Science and Meteorites: Amsterdam, North Holland Pub. Co., 1-30, 1963.

Hiller, H., G., Neukum, and J. Bodechtel, Nepenthes Mensae (abs.), Symp. European Planetary Geol. Consortium, Paris, 1978.

Malin, M.C., R.J. Phillips, and R.S. Saunders, The nature and origin of the martian planetary dichotomy (is still a problem), Reports of Planetary Geology Program, 1977-1978, NASA T.M. 79729, 83-85, 1978.

Wise, D.U., M.P. Golombek, and G.E. McGill, Tharsis province of Mars: geologic sequence, geometry and a deformation mechanism: Icarus, in press, 1979.

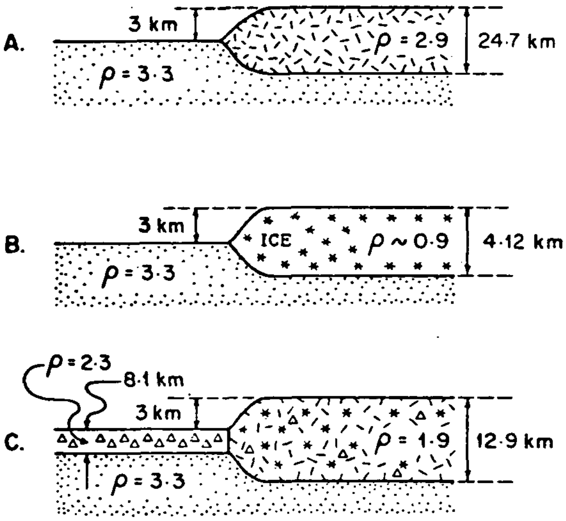

Fig. 1 (above): Isostatically balanced erosional models for development of the 3 km scarp of the northern third of Mars. The amount that was eroded from the left part of each model, as indicated on the right, must have been redistributed over the other 2/3 of the planet. A) Earth-like, with a crust of density 2.9 g/cm^3 overlying a mantle of density 3.3 g/cm^3. Requires deposition of 12.3 km of sediment over remaining 2/3 of Mars. B) Pure ice crust over a mantle of density 3.3 g/cm^3. Requires deposition of 2 km layer of pure ice over remaining 2/3 of Mars. C) 50-50 mixture by volume of ice and rock dust, with average density 1.9 g/cm^3. After removal of ice, residual dust compacts to 2.3 g/cm^3. Requires deposition of 3.2 km of water over remaining 2/3 of Mars.

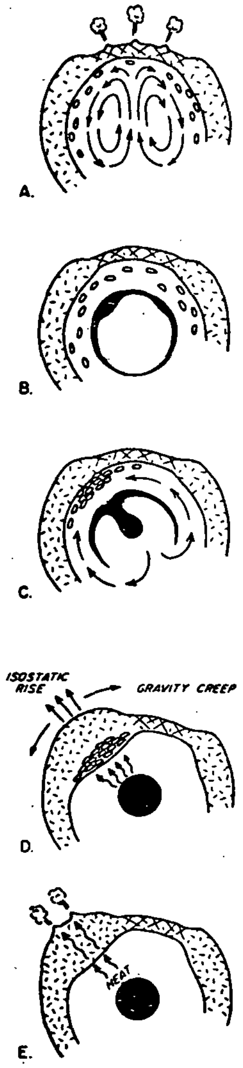

Fig. 2 (right): Tectonic model for the evolution of Mars. A) first-order convection cell operating beneath early heavily cratered crust causes subcrustal erosion, thinning, and crustal foundering. B) Segregation of core materials at intermediate depths ends convection and builds a gravitationally unstable layer. C) Core-mantle overturn develops from the dimple beneath Tharsis. Wholesale mantle movements collect lighter, ingested crustal material above the dimple. D) Core formation complete with very deep asymmetric thermal anomaly reflecting gravitative heat given up in core formation. E) Slow transfer of heat from deeper zones to produce extremely long lived volcanic phase.

The Martian Poles: Studies of Topography, Stratigraphy, and Geologic Evolution

Alan D. Howard, Department of Environmental Sciences, University of Virginia, Charlottesville, Virginia 22903

In this report I will discuss recent observations of Martian polar landforms and processes and give a prospectus of continuing studies of the evolution and composition of the polar regions and the potential implications for understanding of atmospheric processes and climatic change.

Preliminary studies reveal a polar structure more complex than envisioned by previous interpretations. The ice-covered flats exhibit a low-relief topography of one or more sets of superimposed undulations which apparently serve as the seeds for the development of the polar scarps and troughs through selective enlargement (Cutts, et al., 1978). The process of enlargement and deepening is apparently ablational weathering and subsequent wind erosion of the layered deposits beneath south-facing slopes and trough bottoms (Howard, 1978). However, north-facing trough sides are essentially featureless, suggesting active ice and dust accumulation. Supporting this interpretation is the widespread occurrence of unconformities between the exposed layers in trough bottoms and the ice deposits on the north-facing trough walls. Figure 1 illustrates the mechanism envisioned for trough evolution and deepening, differing from my previous model (Howard, 1978) only in that ablating slopes change to a depositional regime only when they are eroded sufficiently to become north- rather than south-facing. A similar mechanism is apparently envisioned by Squyres (1979). Although Figure 1 shows a slightly aggrading trough bottom, other assumptions about erosion and depositional rates could cause a lowering of trough bottoms.

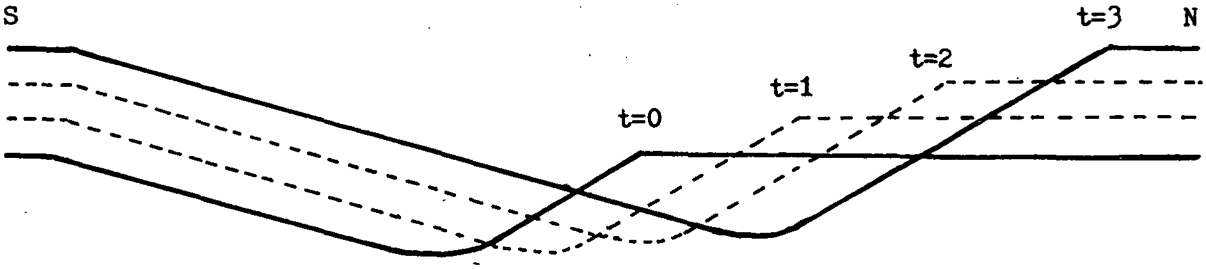

Figure 1: Schematic portrayal of polar trough evolution.

One of the critical questions concerning polar landscape evolution is whether layered deposits are now accumulating, and whether the present topography, volatile dynamics, and wind regime are representative of conditions under which the layered deposits have accumulated, or whether, alternatively, the layered deposits accumulated under a different environment and have been exposed by erosion. If the uniformitarian view is correct, then the most complex structures in the layered terrain will occur where the topography and ice distribution is most complex (i.e., branched or reticulate troughs), where, in particular, unconformities should be common, including the disappearance of duplicate beds where two troughs or scarps merge. In fact, such unconformities seem to be common at trough junctions, although in most cases the unconformities are subtle and might possibly be due to local steepening of the scarps or thinning of the beds. Another consequence of uniformitarian accumulation would be that the sequences of layers should be similar within adjacent trough walls. This will be tested by computing transects of apparent brightness variations across trough walls and testing these for self-similarity after correcting for slope steepness variations.

The areas of complex topography of polar troughs are located primarily near the edges of the polar cap. The polar cap edges also show the stongest evidence for eolian redistribution of frost and dust, and the wind directionality seems most variable at the polar cap margins. This association of complex topography with strong, variable winds may be due to eolian influences on topographic evolution.

One particular type of landform assemblage occuring near the polar cap margins suggests localized wind-influenced accelerated erosion rates of layered deposits, with the eroded dust accumulating in dunes. Steep, scoop-like scarps have been eroded into the layered deposits with dune fields occurring downwind from these probable sources. The enhanced erosion rates may be due to the scarp steepness; if these scarp gradients exceed the angle-of-repose for loose dust, ablationally-released dust will be immediately stripped off of the ice-cemented layered deposits, allowing continued ablation. Also, the steepness of the scarps enhances ablation due to radiational loading; temperatures in the dust-ice layers may be high enough that ice vapor pressures are equal to Martian atmospheric pressure, so that vapor diffusion is not necessary to release the ice bonding through the surface dust layer.

Although erosion occurs on south-facing scarp walls over most of the polar cap, a more general erosion of the layered deposits occurs locally at the polar cap edge. Early spring photos of these regions (taken when the frost cover was still complete) reveal little topographic detail; these areas look very similar to the ice-covered flats elsewhere on the poles. However, summer photos reveal an intricate pattern of exposed layers, indicating a widespread but locally differential stripping of the layers. This erosion seems to be localized to areas with strong evidence of eolian redistribution of frost and dust, suggesting that the wind is also responsible for the stripping of the layered deposits. Either the strong winds or the location of the deposits near the polar cap edge (or both) is responsible for the lack of a permanent ice cover on these flats. If layers accumulate only where perennial ice occurs, then the erosion of these layers indicates changed thermal or wind regime since the layers accumulated.

The above observations are initial results of a project now being initiated at the University of Virginia in coordination with the Planetary Scince Instituts. Among the topics to be investigated during this study are the following:

1) Mapping of polar landform types and relating this distribution to such factors as latitude, regional topography, and wind intensity, direction, and directional variability.

2) Determination of local topography through a combination of

stereo photogrammetry and photoclinometry (using spring photos in which the frost distribution may be nearly uniform in optical properties).

3) Investigation of polar stratigraphy by a combination of local mapping and by quantitative transects across exposed layers. This "time"-series analysis of stratigraphy will utilize computer-generated transects of photometrically calibrated imagery and will address such questions as: a) are the layered sequences periodic (implying correlation with climatic cycles) or could they be due to random sequences of independent depositional events? b) are the sequences repeated on all scarps or zre they unique? c) to what extent is the layering due to albedo differences and to what extent due to variations in slope angle?

The long-range goals of the study are to increase our understanding of the poles, and in particular of the composition and physical state of polar dust and volatiles, of the process dynamics of the polar regions, of the geologic history of the poles, and of the relationship of process changes to climatic changes.

<u>References:</u>

Cutts, J.A., Blasius, K.R., and Roberts, W.J., 1979, Polar layered deposits: geological consequences of Martian dust storms. <u>Jour. Geophys. Res., in press</u>.

Howard, A.D., 1978, Origin of the stepped topography of the Martian poles: <u>Icarus</u>, v. 34, p. 581-599.

Squyres, S., 1979, Evolution of the topography of the Martian polar laminated deposits (Abstract). Second International Colloquium on MARS, <u>NASA Conf. Publ.</u> 2072, p. 80.

Chapter 3

CRATERING AS A PROCESS, LANDFORM AND DATING METHOD

Relative Ages of Martian Volcanic Centers, Channels, Plateau Deposits and Upland Terrains Based on Viking Data and Comparison of Crater Counts on the Moon and Mercury*

Harold Masursky, A. L. Dial and M. E. Strobell, U.S. Geological Survey, Flagstaff, Arizona 86001.

Recent high resolution Viking pictures have allowed us to make more detailed crater counts of Martian volcanic edifices and flows, channels and upland terrain units from which relative age determinations for individual surfaces can be inferred. We discuss relative ages based on curves derived from crater densities; we have not converted the relative ages to ages based on crater flux curves for Mars (1) (2). Volcanic flow units vary from ancient intensely cratered surfaces that show an abundance of large craters to those that display such a sparse density of small craters that the surfaces are almost undatable by the crater counting technique (Fig. 1). Volcanic activity appears to have occurred over a long period of time; relative ages, based on crater density curves, range from that shown by the curve for old cratered plains-"PC Mc"22 (Fig. 1) to the curve for the caldera of Olympus Mons (Fig. 2). Relative ages for channel information appear to be more restricted in time; that is the spread in crater densities is less than those volcanic units. However, statistics for the channel curves are less certain due to limitations set by channel area and crater numbers (3). It is not yet possible to correlate fluvial with volcanic episodes in order to determine whether a casual relationship exists between the two processes; that is, we cannot determine whether an episode of intense volcanism triggers a fluvial episode.

Studies made of the ancient cratered terrain indicate that the intercrater areas are comprised of lava flows extruded from several centers at several different times (Fig. 1). We have not yet located a Martian surface where the entire crater density curve indicates a relative age as old as that shown for the lunar highlands surface near Tsiolkovsky and Gagarin craters (Fig. 2). However, the large craters (not shown on the crater density curve) for an area in Terra Sabaea, a part of the Martian uplands northwest of Hellas Planitia in MC 20 (Fig. 2), falls on the lunar highlands curve. These large craters represent the ancient Martian surface protruding through the younger mantling lava flows. The lunar upland surface near Tsiolkovsky and Gagarin, and the ancient martian terrain that underlies the present surface at Terra Sabaea appear to be equivalent in age with similar crater densities. Crater density curves for Phobos and Deimos (Fig. 2) fall on the extension of the lunar highlands curve. The complete crater density curve for Terra Sabaea (Fig. 2) and other areas in the central uplands (Fig. 1) are displaced to the left of the lunar upland curve, showing the surfaces to be younger, because the counts were made on the mantling lava flows.

Crater density curves for Mercury are also displaced from the lunar curve; relative displacement is the same as that shown by the curve for heavily cratered highland material on Mars. Mercury is also thought to show evidence of a mantling episode that has covered parts of its original surface (4).

Radar altimetric, and photogrammetric measurements of layered deposits exposed in mesas on the floors of Candor and Hebes Chasmata indicate these deposits are about 1 km thick and the deposits in the canyon walls are as much as 7 km in thickness. Relative ages for the layered deposits that form the mesas and canyon walls cannot be obtained by the crater count technique because few, if any, craters are preserved in these canyon areas. However, these rocks must be intermediate in age; they lie between the ancient cratered terrain material exposed to the southeast and the young lavas that comprise the Tharsis volcanoes that overlie the plateau deposits. These layered rocks may preserve the sequential record for a considerable portion of martian history, like that preserved in the terrestrial Grand Canyon sequence. Radiometric dating of material from these layered deposits, from possible weathered zones lying between the layers, and from volcanic deposits obtained by a Mars sample return mission, could be correlated with relative ages obtained from crater density curves. The weathered zones may record fluviatile episodes when channels formed in other areas and would also preserve a record of variations in solar activity.

References: (1) Soderblom, L.A., West, R.A., Herman, B.M., Kreidler, T.J. and Condit, C.D. (1974) Icarus, v. 22, no. 3, p. 239-263. (2) Neukum, Gerhard, and Wise, D.U. (1976) Science, v. 194, no. 4272, p. 1381-1387. (3) Masursky, Harold, Boyce, J.M., Dial, A.L., Schaber, G.G., and Strobell, M.E. (1977) Journal of Geophysical Research, v. 82, no. 28, p. 4016-4038. (4) Trask, N.J. and Guest, J.E. (1975) Journal of Geophysical Research, v. 80, p. 2461-2477.

*Presented at 10th Lunar and Planetary Science Conference, March 1979, and published in Lunar and Planetary Science X, part 2, p. 781-782.

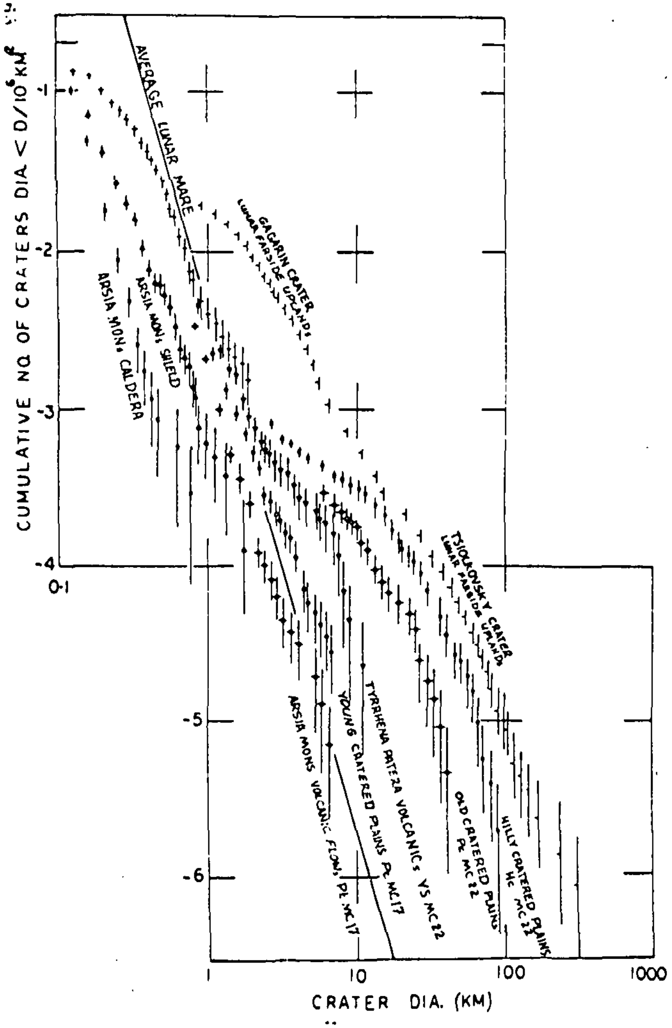
CUMULATIVE NO. OF CRATERS DIA < D/10⁶ KM²
-1
-2
-3
-4
-5
-6
0·1
1
10
100
1000
CRATER DIA. (KM)
AVERAGE LUNAR MARE
GAGARIN CRATER LUNAR FARSIDE UPLANDS
ARSIA MONS SHIELD
ARSIA MONS CALDERA
TSIOLKOVSKY CRATER LUNAR FARSIDE UPLANDS
TYRRHENA PATERA VOLCANICS VS MC22
YOUNG CRATERED PLAINS PL MC17
ARSIA MONS VOLCANIC FLOWS PL MC17
OLD CRATERED PLAINS PL MC22
HILLY CRATERED PLAINS HC MC22

Fig. 1

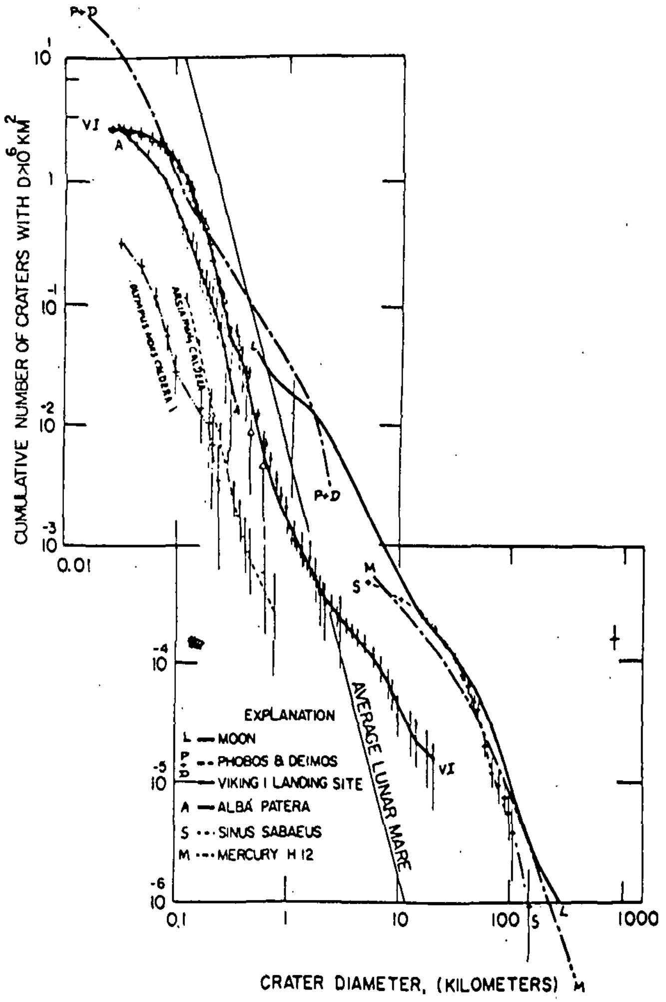
CUMULATIVE NUMBER OF CRATERS WITH D>D/10⁶ KM²
10⁻¹
1
10⁻¹
10⁻²
10⁻³
10⁻⁴
10⁻⁵
10⁻⁶
0.01
0.1
1
10
100
1000
CRATER DIAMETER, (KILOMETERS)
P+D
VI
A
L
S
M
ARSIA MONS CALDERA
OLYMPUS MONS CALDERA I
AVERAGE LUNAR MARE
EXPLANATION
L — MOON
P+D — PHOBOS & DEIMOS
VI — VIKING I LANDING SITE
A — ALBA PATERA
S ··· SINUS SABAEUS
M ·–· MERCURY H 12

Fig. 2

Origin of Crater Ejecta Flow Features on Mars: Implications for History of Martian Volcanism and Cratering,

J.A. Cutts, K.R. Blasius, W.J. Roberts, D.R. Davis and R.J. Greenberg, Planetary Science Institute, 283 S. Lake Suite 218, Pasadena, California 91101

Introduction: The existence of ejecta flow features which are unique to Mars attests to the occurrence of processes on that planet that are not found on the Moon and Mercury. The goals of this investigation are to characterize crater ejecta flow craters morphologically and morphometrically; to investigate possible mechanisms of forming these craters; and to develop diagnostic observational criteria for distinguishing between candidate mechanisms.

Approach: We have undertaken a systematic description of crater ejecta flow features using Viking Orbiter data. The data source is the set of medium resolution mosaics whose outlines are shown in Figure 1. The collection of the data on ejecta flows involves three steps. 1) Acquire and record on magnetic tape geometrical control point data and other fundamental data relevant to a single mosaic strip, note control point locations on plastic overlays, 2) on the same plastic overlays identify and record characteristics of craters with extensive visible ejecta deposits, 3) record on magnetic tape, through the use of a NUMONICS digitizer, the positions of geometric control points, positions and sizes of craters and their ejecta deposits.

In Step 1 the analyst identifies geometric control points for the chosen mosaics and records their positions on plastic overlays and in tables ready for keypunching. Also recorded there are, for each strip of photos, mosaic number, picture numbers, spacecraft latitude and longitude, sun latitude and longitude, and general image quality (IQ). The last descriptor IQ may have value 0 or 1. A value of 1 indicates the presence of some factor degrading visibility of crater morphology aside from incidence and emission angle geometry or slant range. Such factors may be atmospheric observation, loss of data in transmission, or the presence of high contrast surface albedo features.

In Step 2 the analyst begins the study of the features of the crater and its surroundings. The analyst examines the crater image, preferably in a contact print or enlargement, and records on the plastic overlay the rim trace, "X" mark(s) representing the mean distance(s) to which ejecta flow(s) extend, a two-letter terrain classification, and two or more sets of binary descriptors. The list of terrain identifiers is: (1) ps - smooth plains (little relief between a sparse population of craters) ; (2) pw -

plains with wrinkle ridges; (3) pr - rough plains (closely spaced pits, hills, or grooves that are small compared to craters classified); (4) pp - plains characterized by a polygonal pattern of troughs; (5) ph - hummocky plains (low rounded hills are spaced farther apart than the dimension of the typical classified crater); (6) cr - cratered terrain with rough intercrater areas (craters as large or larger than typical classified craters occur between all those classified); (7) cs - cratered terrain with smooth intercrater areas (otherwise same as cr).

The first set of crater descriptors pertains to the crater as a whole and the crater rim and interior. The following questions are answered yes or no (code 1 and 0 respectively): 1. Is crater rim approximately circular? 2. Has a significant proportion of the crater rim or ejecta pattern been destroyed? 3. Are strings of secondary craters visible? 4. Is there a central topographic feature inside the crater? 5. Is it a central pit (1) or peak (0)? 6. Is the crater interior morphology atypical? A "1" answer to 6 may indicate the presence of such features as dune fields, floor fractures, central plateaus, Martian airfields, etc. However, the presence of a simple albedo anomaly is not registered.

The second, and possibly third, set of binary descriptors pertains to the ejecta deposits or flows: 1. Is the ejecta deposit margin distinct? 2. Is margin defined by a scarp (1) or rampart (ridge) (0)? 3. Does the ejecta margin have a simple - or multi - lobate form? 4. Is the ejecta surface generally hummocky (1) or smooth (0)? 5. Are radial ridges or grooves present? If a "0" answer is given to 1, then answers to 2 and 3 are disregarded. The analyst must be aware of the effect of lighting geometry on the visibility of scarps and ridges. Only ejecta perimeter slopes facing generally toward or away from the sun are expected to appear distinct.

In Step 3 an analyst takes the completed plastic overlay and uses the digitizer to: 1. record geometric control point locations by digitizing the center of each feature (usually a crater); 2. record crater position and diameter data by digitizing 3 points on rim; 3. record ejecta flow deposit (if any) mean diameter(s) by digitizing position of "X"(s); 4. entering from the digitizer keypad the two-letter terrain descriptor; 5. entering from the keypad the binary descriptors of crater morphology.

The first step in this three step process has now been completed for the data sources of Figure 1 and Steps 2 and 3 are now underway. We expect to report preliminary results from a study of a portion of the planned data base at the Providence meeting.

Supporting Theoretical Analyses: Preliminary data from this project as well as earlier analyses in which we were involved suggest that the occurrence of ejecta flow features is dependent on the terrain in which these features formed. These terrain dependent variations can be interpreted as a consequence of different terrain composition. Another possibility is that the production of ejecta flow craters has varied with time and consequently terrains of different ages display different populations of ejecta flow features. Two modes of origin for a time dependent phenomenon suggest themselves: variations in atmospheric density and variations in the impacting body population. The second possibility is being evaluated in this year's program.

Most regions of the solar system were sources of bodies which impacted Mars, however, the timing and flux of bodies from different parts of the solar system may have varied widely. Following accretion of Mars, which presumably swept up all matter in Mars' zone, plausible source regions for bodies contributing to Mars cratering are (i) orbits in planetary gaps adjacent to Mars, (ii) Jupiter-scattered planetesimals (JSP), which become Mars-crossers, (iii) bodies in the Earth-Venus or Earth-Mercury gap, perturbed by Earth or Venus onto Mars-crossing orbits; (iv) partial planet-crossers in the outer solar system, Saturn to Neptune, which can be perturbed inward.

Two existing computer programs are being modified slightly in order to investigate the time history of Mars impacters. The first program uses Opik's simplified analytic expressions for planetary collision probabilities, while the second (and more expensive to run) program uses Monte Carlo methods to find collision lifetimes and impact speeds.

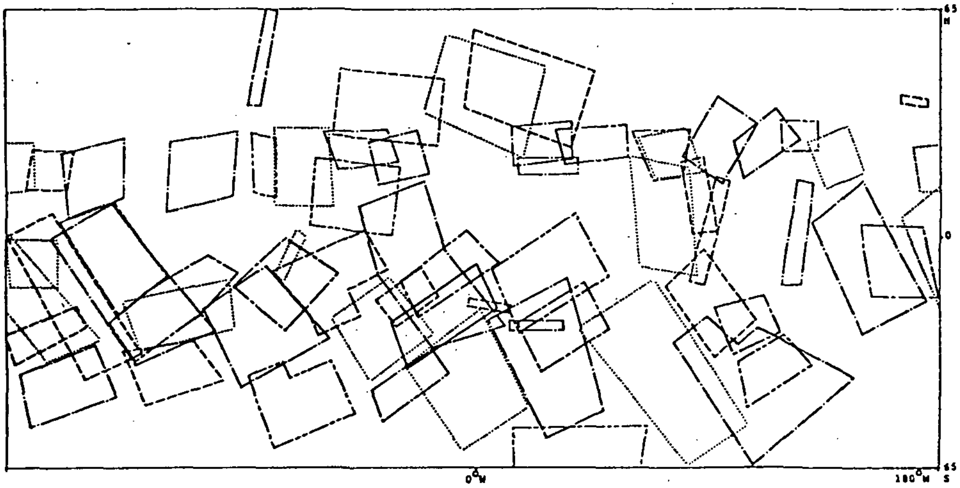

Figure 1: Outlines of Viking Orbiter mosaics used in crater ejecta flow study.

A METHOD FOR MEASURING HEAT FLOW IN THE MARTIAN CRUST USING IMPACT CRATER MORPHOLOGY

J. M. Boyce*, U.S. Geological Survey, Flagstaff, Arizona

Martian impact craters include several types that appear unique to Mars. One of these types, called rampart craters by McCauley (1973), commonly exhibit ejecta blankets which terminate in an abrupt rampart-like edge. He suggested that this peculiar morphology resulted from post-impact modification by eolian erosion. Later, Carr et al. (1977) using high resolution Viking orbital photographs showed that the ejecta of these craters exhibit flow-like patterns. They found that there are other types of craters on Mars that also exhibit flow-like patterns of ejecta but that have no rampart terminations. Carr et al. (1977) suggested that the flow-like patterns were the result of flowage of ejecta due to inclusion of gasses during emplacement of the ejecta. They indicate that the gasses may have been derived from impact volatilization of a subsurface permafrost ice layer or that trapped atmospheric gasses were important. Schultz and Gault (1977) suggested that aerodynamic drag resulting from ejecta-atmosphere interactions may play a significant role in emplacement of the martian flow ejecta. However, experimental evidence shows that rampart and other flow-ejecta craters are produced only in wet target materials (Gault and Greeley, 1978, Roddy, 1976), with the particular morphology probably being related to water concentration and not the ratio of ice to water as suggested by Johansen (1979). Therefore the dominant mechanism of origin of these craters is probably impact into a water table.

It has been suggested that conditions on Mars were once favorable for formation of a subsurface permafrost ice layer (Lederberg and Sagan, 1962; Leighton and Murray, 1966; Anderson et al., 1967; Wade and DeWys, 1968; Fanale, 1976). Such features as ecalases and other thermokarst topography suggest that near-surface ice is indeed present on Mars (Carr and Schaber, 1977). Allen (1978) showed that flow-ejecta craters are distributed over most of Mars and that there is no correlation between their occurrence and major geologic units or elevation. He suggests that if these craters are indicators of subsurface ice or water then the layer of ice or water

*Present address: NASA Headquarters, Washington, D.C.

must be beneath the entire surface of Mars. This distribution of rampart and flow-ejecta craters rules out ascent of juvenile water from the deep interior as a source of the permafrost ice layer, because ascending juvenile waters are usually confined to small areas associated with volcanic vents or fractures. The most reasonable mechanism for development of such an ice or water layer is by charging the ground water system by rain water. Therefore, the emplacement of these types of craters into young rock units has been difficult to explain because, unlike the old terranes with dendretic channels, the young terranes show no evidence of having been affected by rain (Pieri, 1978). However, Boyce (1979) has suggested that the occurrence of ramapart and flow-ejecta craters in young terranes can be explained if the thermal gradient in the shallow part of the martian crust is similar to that of the Earth (temperature is proportional to depth). He suggests that, consequently, the permafrost ice layer in old units should melt starting at its base in response to burial by young units because of the insulative properties of the young units. In some cases, the permafrost ice may also have been melted locally by heat from young lavas extruded on the surface. The melted ground water would migrate upward toward regions of lower pressure and greater pore space. The ascent of the ground water may have been quite rapid because, as pointed out by Carr (1978), volcanic rocks such as those characterizing most young areas are commonly very porous and permeable. The ground water should rise until it freezes again at the base of the new permafrost boundary layer. The new ice layer is expected to be thin because further ascent of water is blocked by freezing. This process may account for the presence of a permafrost ice and water layer in both old and young martian rocks.

The minimum depth to the solid-liquid water phase boundary can be estimated in an area using the morphology of craters. In young terranes (younger than the time of the last surface water on Mars) the depth to the ice layer is similar to the depth to the lower water-ice boundary because, as discussed above, the ice layer should be thin.

Depth estimates to the water/ice boundary are possible because impact crater morphology is a sensitive indicator of subsurface geology. For example, benches flat floors or central mounds are commonly formed as a result of cratering across a subsurface discontinuity, such as in layered rock of differing strength (Oberbeck and Quaide, 1967). The depth to this discontinuity can be estimated by determining the depth (measured from the original ground surface) at which the bench or flat floor occurs (Oberbeck and Quaide, 1967). Where accurate topographic information is not available, this depth can also be estimated by determining the diameters of the smallest fresh craters that exhibit benches, central peaks or flat floors. Then, using the average depth-to-diameter ratio of 1:5 (Pike, 1977) limits on the depth to the layer can be calculated. In the case of rampart and flow-ejecta craters this same principal can be applied to estimate the depth to the water layer. Figure 1 shows that at the VL-1 site the largest diameter at which all craters exhibits ballistic ejecta is about 4 km and the smallest craters that all exhibit ramparts and flow ejecta is 6 km. Therefore, using the technique described above, the water layer at the VL-1 site is about 1+0.2 km deep below the surface. The smallest diameter of crater that exhibits flow-ejecta (hereafter will be referred to as initiation diameter) in six areas is shown in Figure 1 and suggests that the depth to the water layer varies by at least 1 km from 0.3 km to 1.3 km depth.

The depth to the solid-liquid water boundary (melting point of briney ice) is the depth to an isotherm of about $255+5^{o}$ k. For the simplist case, the depth information derived from crater morphology can be combined with surface temperature data derived from both orbiter and lander observations (assuming that these temperature represent general climate conditions of the past) to estimate the near surface thermal gradient for specific areas on Mars. This information is a record of the highest point at which liquid water has ascended in the particular terrane and therefore provides thermal history information.

Such a thermal gradient was estimated at the Viking 1 lander site. The thermal gradient at the Viking 1 landing site is calculated to be $40^{o}+10K^{o}$/km, based on an average surface temperature of 215^{o}K, a freezing temperature of brine water of about 255^{o}K, and the depth to the permafrost at 1+0.2km. This value is somewhat higher than the average geothermal gradient of 30^{0}K/km and could be the result of the effects of residual heat from the emplacement of the young lavas at this site (Greeley et al., 1977), a relatively high heat flux from the interior, a long period of relatively warm surface conditions in the past, low thermal conductivity of the surface rock or a number of other alternatives.

REFERENCES

Allen, C. C., 1978, Areal Distribution of Rampart Craters on Mars (abs): NASA TM 79729, p. 160-161.

Anderson, D. M., Gaffney, E. S., and Low, P. F., 1967, Frost Phenomena on Mars: Science, v. 155, p. 319-322.

Boyce, J. M., 1979, Martian Subsurface Permafrost: Evidence from Impact Craters (abs): in Second International Colloquium on Mars, in press.

Carr, M. H., 1978, Formation of Martian Flood Features by Release of Water from Confined Aquifers: NASA TM 79729, p. 260-262.

Carr, M. H., Crumpler, L. S., Cutts, J. A., Greeley, R., Guest, J. E., and Masursky, H., 1977, Martian Impact Craters and Emplacement by Surface Flow: J. Geophys. Res., v. 82, p. 4055-4065.

Carr, M. H., and Schaber, G. G., 1977, Martian Permafrost Features: J. Geophys. Res., v. 82, p. 4039-4054.

Fanale, F. P., 1976, Martian Volatiles: Their Degassing History and Geochemical Fate: Icarus, v. 28, p. 179-202.

Gault, D. E. and Greeley, R., 1978, Exploratory Experiments of Impact Craters formed in Viscous-liquid Targets: Analogs for Martian Rampart Craters: Icarus, v. 34, no. 3, p. 486-495.

Greeley, R., Theilig, E., Guest, J. E., Carr, M. H., Masursky, H., Cutts, J. A., 1977, Geology of Chryse Planitia: J. Geophys. Res., v. 82, no. 28, p. 4093-4110.

Johansen, L., 1979, Martian Splash Cratering and its Relation to Water (abs): NASA Conference Publication 2072, p. 44.

Lederberg, J., and Sagan, C., 1962, Micro-environments for Life on Mars: Proc. Nat. Acad. Sci., v. 48, p. 1473-1475.

Leighton, R. B., and Murray, B. C., 1966, Behavior or CO_2 and Other Volatiles on Mars: Science, v. 153, p. 136-144.

McCauley, J. F., 1973, Mariner 9 Evidence for Wind Erosion in the Equatorial and Mid-Latitude Regions of Mars: J. Geophys. Res., v. 78, p. 4123-4137.

Oberbeck, V. R., and Quaide, W. L., 1967, Estimated Thickness of a Fragmental Surface Layer of Oceanus Procellarum: J. Geophys. Res., v. 72, no. 18, p. 4697-4704.

Pike, R. J., 1976, Crater Dimensions from Apollo Data and Supplemental Sources: The Moon, v. 15, p. 463-477.

Pieri, D., 1978, Small Channels on Mars from Viking Orbiter (abs): NASA TM 79729, p. 267.

Roddy, D. J., 1976, High-explosive Cratering Analogies for Bowl-shaped, Central Uplift, and Multi-ring Impact Craters: Proceeding Lunar Science Conference, 7th, p. 3027-3056.

Schultz, P. H., 1978, Impact Ejecta Emplacement on Mars (abs): Lunar and Planetary Science Conf., 9th, Proc., v. 2, p. 1027-1029.

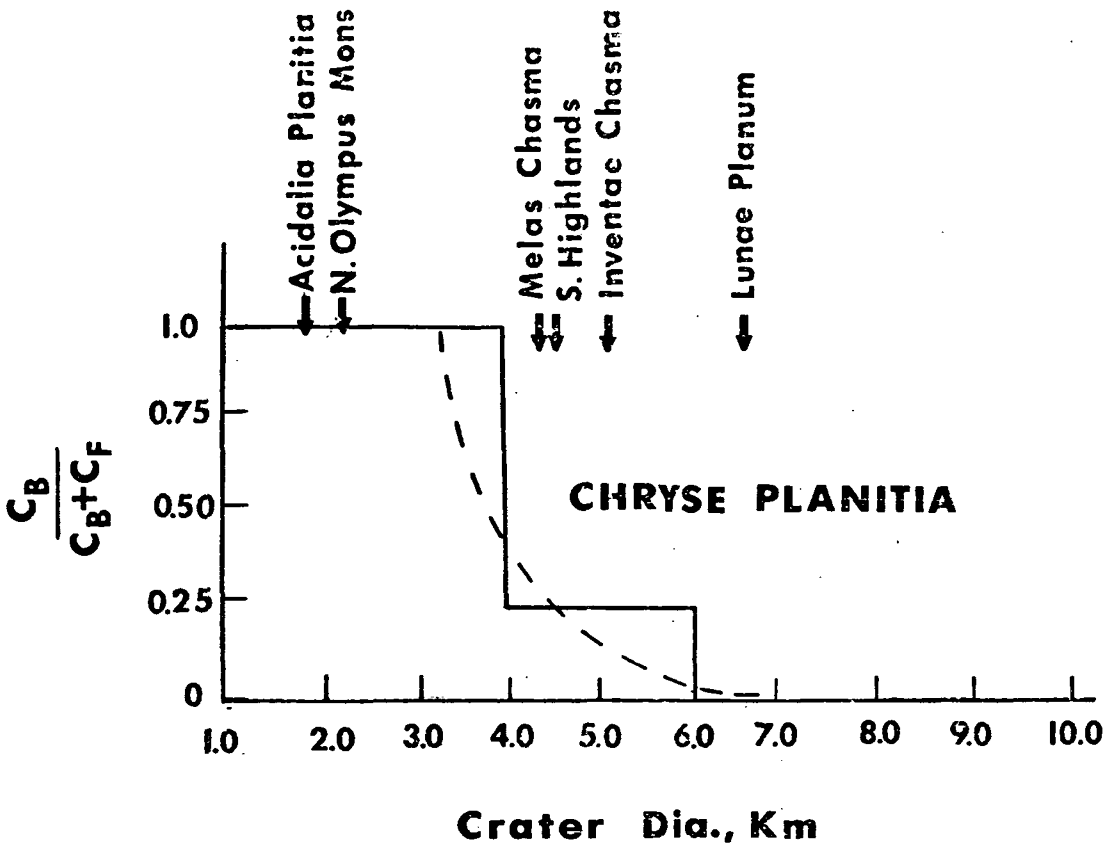

Figure 1. Ratio of ballistic ejecta craters (C_B) to total number of crater ($C_B + C_F$) larger than a kilometer in diameter in Chryse Planitia near the Viking 1 landing site. Initiation diameters (smallest diameter of crater that exhibits flow ejecta) are shown for six other martian areas.

DIAMETER ENLARGEMENT EFFECTS ON CRATER POPULATIONS RESULTING FROM IMPACT INTO WET OR ICY TARGETS

J. M. Boyce*, U.S. Geological Survey, Flagstaff, Arizona

Craters produced in wet materials exhibit flow-ejecta but also commonly are increased in diameter by a factor of 2 or more compared to dry targets; and volumes are commonly increased by a factor of 4 (Nordyke, 1977; Piekutowski, 1977). Craters produced in icy materials also show similar diameter and volume increases (Croft et al., 1974). Boyce and Roddy (1978) and Croft et al. (1979) have briefly discussed effects of crater diameter enlargement on the size-frequency distribution of craters and hence relative age determinations. The significance of these effects are shown graphically at the Viking 1 landing site. All post-surface craters were counted as a function of both diameter and ejecta morphology. The proportion of flow-ejecta craters to ballistic ejecta craters is shown in Figure 1 and indicates that all craters larger than about 6 km diameter are flow-ejecta types, while all craters smaller than about 4 km diameter are ballistic ejecta types; craters from 4 to 6 km diameter are in transition and have a mixture of both types. The cumulative size-frequency curve for all post-surface craters at the VL-1 site is shown in Figure 2a. This curve shows a bend in the total crater density curve at about 4 km. A bend in the same diameter range can be seen in the cumulative size-frequency distribution determined by Dial (1978) for the VL-1 site. The bend can be eliminated by reducing by a factor of 0.6 the diamter of just the flow craters. This factor of 0.6 reduction, which is consistent with that expected from experimental data, was derived empirically by determining the amount of reduction in diameters required to straighten the curve. This selective reduction of the diameters of just the flow ejecta craters has been done and is shown in Figure 2b where there is now no appreciable bend in the curve. We suggest that the bend in the curve shown in FIgure 2a is an anomaly resulting from enlargement of crater diameters produced by impact into wet target materials. Therefore, the part of the curve for craters larger than 6 km diameter show an anomalously high density of craters.

Descriptors have been developed that use the density of craters above a particular diameter (Neukum and Wise, 1976) or the number of craters in a range of diameters per unit area (Soderblom et al., 1974; Condit and Johnson, 1978). The fact that initiation diameters of flow-ejecta craters differs from area to area could introduce inconsistencies in age determinations (Boyce and Roddy, 1978). For example, because of the exponential nature of the crater production function, N-kD^{-} (where N=no. of crater diameter D, k is a constant, and is an exponent that may vary from 1.5 to 4) a small displacement in diameters will result in a large change in density of craters. Because the initiation diameters occur over a range (see Figure 1) that transcends the boundaries and includes most of these density descriptors, chronology data could be significantly effected. Therefore, as suggested by Young et al (1974), Boyce and Roddy (1978), and Croft et al (1979), understanding the effects of target materials on crater diameters and hence on crater size-frequency distribution in different martian terraines is important in establishing reliable chronologies.

REFERENCES

Boyce, J. M. and Roddy, D. J., 1978, Martian rampart craters: crater processes that may affect diameter-frequency distributions (abs.), in Reports of Planetary Geology Program, 1977-1978, NASA TM 79729, p. 162-165.

Condit, C. and Johnson, D., 1978, Intermediate diameter (2-10 km) crater density maps of Mars (abs.), in Reports of Planetary Geology Program, 1977-1978, NASA TM 79729, p. 175.

Croft, S. K., Kieffer, S. W., and Ahrens, T. J., 1979, Low velocity impact craters in ice and permafrost with implications for martian crater-count ages (abs.), in NASA Conference Publications 2072, p. 18.

Dial, A. L., 1978, The Viking 1 landing site crater diameter-frequency distribution (abs.), in Reports of Planetary Geology Program, 1977-1978, NASA TM 79729, p. 179-181.

Neukum, G. and Wise, D., 1978, A standard crater curve and possible new time scale: Science, v. 194, p. 1381-1387.

Nordyke, M. D., 1977, Nuclear cratering experiments: United States and Soviet Union: Proceedings on Planetary Cratering Mechanics Symposium, p. 103, 124.

Piekutowski, A. J., 1977, Cratering mechanism observed in laboratory-scale high-explosive experiments, in (Roddy, D. J., Pepin, R. O. and Merrill, R. B., eds.), Impact and Explosion Cratering: Planetary and Terrestrial Implications, Pergamon Press, New York, p. 67-102.

Soderblom, L. A., West, R. A., Herman, B. M., Kreidler, T. J. and Condit, C. D., 1974, Martian planet-wide crater distribution: Implications for geologic history and surface processes: Icarus, 22, p. 239-263.

Young, R. A., Brennan, W. J., and Nichols, D. J., 1974, Problems in the interpretation of lunar mare stratigraphy and relative ages indicated by ejecta from small impact craters: Proceedings Lunar Science Conference 5th, p. 159-170.

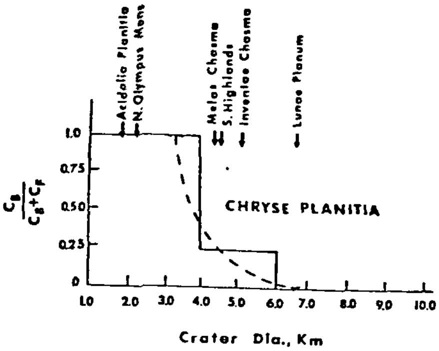

Figure 1. Ratio of ballistic ejecta craters (C_B) to total number of craters ($C_B + C_F$) larger than a kilometer in diameter in Chryse Planitia near the Viking 1 landing site. Initiation diameters (smallest diameter of crater that exhibits flow ejecta) are shown for six other martian areas.

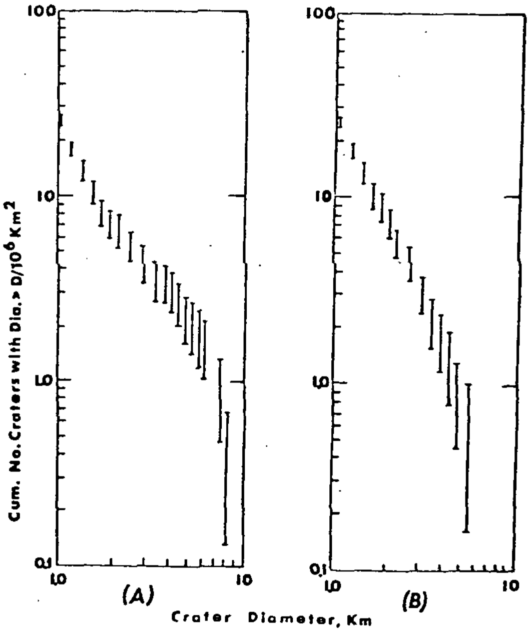

Figure 2a. Cumulative size-frequency distribution of all post-surface craters at the Viking 1 landing site.

Figure 2b. Cumulative size-frequency distribution of all craters at the Viking 1 landing site but with a 0.6 reduction in diameter of the flow-ejecta craters part of the population. Note that the bend in the original curve (see Figure 2a) has been eliminated.

The Latitude Dependence of Martian Splosh Cratering and its Relationship to Water,

Laurie A. Johansen, Jet Propulsion Laboratory, California Institute of Technology, Pasadena, CA 91103/Occidental College, Los Angeles, CA 90041

Introduction. Certain meteor craters on Mars have ejecta that appear to have flowed onto the surface of the surrounding terrain. They were suggested to originate from wind erosion, entrainment of volatiles, or interaction with the atmosphere during meteor impact. Some craters with these flow features have been called Rampart or Pedestal craters (1,2) by observers. In this report, all fluid-appearing craters will be referred to as Splosh craters. "Splosh" is intended to imply a fluid-like emplacement associated with impact. Earlier experiments did not recognize that these Splosh craters have different forms which vary with respect to latitude. The manner in which they vary suggests that water is responsible for the variations.

Method. Seven distinct crater types can be distinguished on the basis of ejecta morphology (see fig. 1). These types were given descriptive but non-genetic names for clarity in this report.

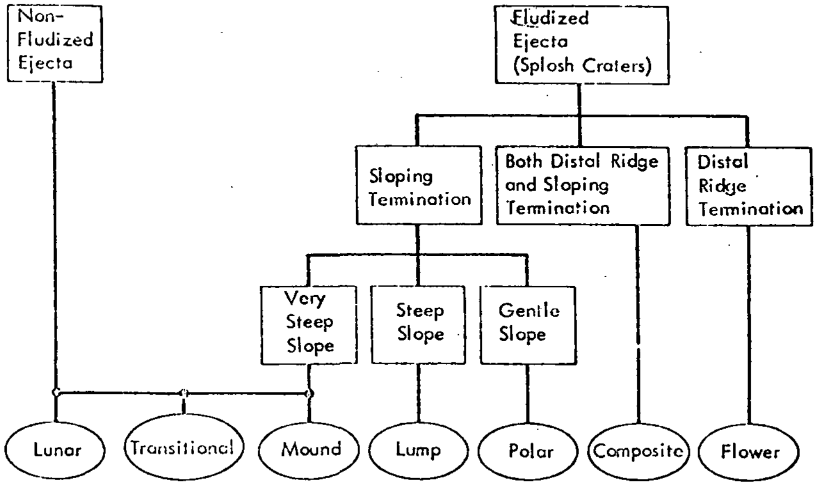

Figure 1. Crater ejecta morphology classification system

1. Mound craters are typified by the crater Arandis. The ejecta seems to be the result of fluidized flow of a viscous nature. The jecta deposit is composed of thick discrete lobes that lack distal ridges. Terminations are steep and abrupt. The morphology of the lobular ejecta appears similar to the landslide fans seen in Valles Marineris and other large canyons of Mars.
2. Flower craters are represented by the crater Yuty. The ejecta blanket is thinner, with finger-like lobes, and is bounded by raised edges. It appears to be of a less viscous nature than Mount craters. The morphology is similar to that produced by dropping projectiles into mudlike material, although the scale of the events is different (1). 3. Composite craters have features of

both Mount and Flow types. They have a thick Mound ejecta region surrounded by a region of thinner Flower-type ejecta. 4. Lump craters are similar to the Mount craters but their ejecta terminations are less steep. They tend to give the ground a pock-marked or lumpy appearance. 5. Polar craters occur on icy surfaces such as the northern polar cap. Their ejecta blanket, larger than the others, tends to be thin, flat, and smoothly rounded in outline. There are no distal ridges or steep terminations on the ejecta. 6. Lunar craters are morphologically similar to Lunar or Mercurian craters. Flow features are not associated with Lunar craters. 7. Transitional craters are those with diagnostic ejecta morphology intermediate between Mound and Lunar types. There is a gradation of properties between Mound and Lunar craters while there is little similarity between Flower and Mound or Flow and Lunar types. Mound and Lunar craters are observed as small as the Viking Orbiter Imagery would allow (approximately 1 km), while Flower types are not.

The basic criteria mapped can be divided conceptually into nonfluid-appearing (Lunar) and fluid-appearing (all other types) ejecta. The fluid-operating ejecta can be further divided into those which appear to be somewhat concave (Flower), and those which appear to be convex (Mound, Polar, and Lump). Convex ejecta types seem to vary in the extent of expression of the fluid forms; for example, Polar craters appear flattest while Mount craters appear most rounded. Lump craters are intermediate.

Using the Viking Orbiter Imaging Team's system of boxes of latitude and longitude (3), every third box was selected. The pictures in the area were then examined. This method insured even longitudinal distribution of observations. In locations where poor resolution or dust storms hindered observation, adjacent boxes were used.

In each box a sequence of pictures with good resolution, viewing and illumination geometry was selected and examined. If a crater type was present in the series of frames, it was recorded as existing in that area. If the crater was not present, it was not considered to exist in that area. The picture sequences used did not usually cover the entire area of the box. The boxes were used for acquiring an even distribution of observations with respect to longitude and latitude. The area examined at the equator is roughly equal to the area examined at the higher latitudes. Each search around a latitude/longitude box encompassed approximately 49,000 km^2: where craters were especially dense, a slightly smaller area was examined; where craters were especially scarce, a larger area was examined until about 15 craters with clear morphology were seen. This information was then recorded.

Each picture sequence contained at least 100 craters. The total number of craters examined was 47,000 ± 10,000. The craters used in this study were between and 25 km in diameter. Data taken included approximate latitude and longitude of the center of the viewing sequences used, spacecraft revolution, crater types observed, qualitative estimate of relative age of the surface, and local geomorphic setting. Pictures available were from spacecraft revolution A001-A595 and B001-B55. Approximately 3500 individual frames were examined.

The morphology of these craters varies with respect to latitude as shown in the figures below. Figure 2 shows that in general there is more fluid appearing (splosh) craters at high latitudes. The non-fluid appearing

(Lunar) craters are most common around the equator. Figure 3 shows that there are latitude variations among different fluid appearing types. The lowest viscosity forms are found to be variable and most common around the equator. More viscous types are found at higher latitudes. Figure 4 shows the distribution of only the viscous, convex types. These too vary significantly with latitude.

A model of water phase and concentration that is consistent with this information was derived. According to this model the outer satellites of Jupiter should exhibit Splosh craters due to their high ice content. The Polar types should predominante although Mound, Lump, Composite and Flower types are also conceivable. Mound and Lump types would be expected if a large amount of rock were mixed with the ice.

References

1. D. Gault and R. Greeley, Icarus 34, 3 (1978).
2. M.L. Carr, L.S. Crumpler, J.A. Cutts, R. Greeley, J.E. Guest, and H. Masursky, J. Geophys. Res. 82, (1977), pp. 4055-4066.
3. W. Mills, Viking Project Library Pictures Listing, Orbiter Imaging Team.

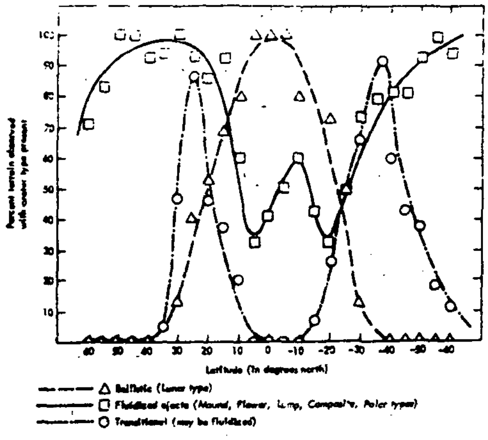

Figure 2

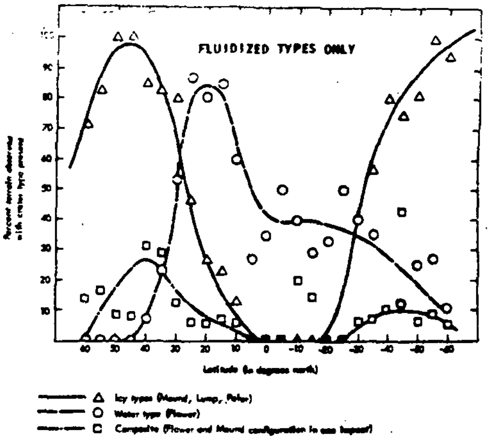

Figure 3

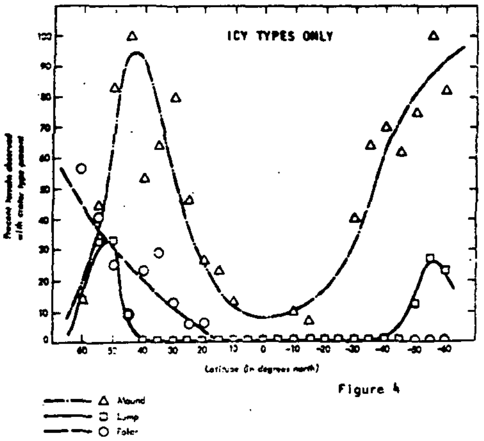

Figure 4

The Effects of Impact Basin Ejecta on Lunar Crater Infill. R. A. Roth, Dept. of Geological Sciences, Brown Univ., Providence, RI 02912; R. G. Strom and L. Andersson, Lunar and Planetary Lab., Univ. of Arizona, Tucson, AZ 85721.

Lunar Abulfeda crater types[1] (n=482 for lunar nearside, broad, flat floor with steep walls, sharp rim crest and shallow appearance, wall structure predominantly radial; terraces subdued or absent) range in size from 15-250 km and are relatively circular in plan view.

The Catalogue of Lunar Craters also classifies craters on the basis of degradation state. A scale of 1 (freshest) to 5 (most degraded) is used. Most Abulfeda craters, 85%, are designated class 3. Thirteen percent are class 2 and less than 1% are class 1 and 4. No craters of this type are class 5.

Tycho type craters (30-170 km, sharp rim crests and wall terraces, central peaks and visible primary floor roughness) have a morphology similar to that of Abulfeda craters, but are fresher in appearance. Fifty percent of the 76 Tycho type craters in the Catalogue are class 1, 42% are class 2, and 8% are class 3.

Infilling of Tycho type craters could result in a morphology characteristic of Abulfeda craters. A crater with a broad, flat floor, subdued terraces and rim crest should result. Relatively small amounts of infill are sufficient to achieve this morphology. Approximately 2% of the total crater volume added as fill would obscure primary floor roughness while 16% would be adequate to bury the central peaks.[2]

If the thickness of material filling Abulfeda craters were known, the validity of impact basin ejecta as a source of crater fill could be tested by examining the spatial distribution of fill thicknesses relative to basin locations.

Hypothetical fill thicknesses have been calculated for all nearside Abulfeda craters by assuming an original crater configuration modeled after Tycho craters. Measurements of Abulfeda crater floor diameters contained in the LPL Catalogue were compared with those obtained from a model of 35 class 1 Tycho craters. This model can be expressed by the relation $D_f=.73D_r-10.1$, where D_f is the floor diameter and D_r is the rim crest diameter. The fill thickness values are calculated from the difference between the modeled and observed floor diameters and the geometrical constraints of a saucer-shaped crater configuration. The same procedure was followed for all class four and five craters for comparison.

The south-central highlands were chosen for in-depth analysis to isolate the effects of a single basin, Imbrium, on crater infilling (Fig. 1). An inverse relationship between fill thickness and distance from the Imbrium basin is indicated for Abulfeda and class 4 and 5 craters. Abulfeda craters have less fill at all distances.

The region 2000-2500 km from Imbrium marks the range where the ejecta is of sufficient size and impact velocity to degrade crater rims, walls and ejecta facies to such an extent that a class 4 or 5 crater is most likely to result (Fig. 2). Towards the basin, degradation is so severe as to modify a pre-basin crater to the extent that it can no longer be recognized as an impact structure, as suggested by the decreasing density of these craters. Beyond the 2000-2500 km region the capability of impacting ejecta to degrade large scale crater features is continually reduced with distance downrange.

Abulfeda craters first appear at the edge of the continuous ejecta blanket of Imbrium, a distance corresponding to 1.8 basin radii.[2] Pre-basin craters within this region are either mantled completely by ejecta or modified extensively by the high density of impacting secondaries to the extent that they would likely appear as class 4 or 5 crater structures.

Abulfeda crater production is maximized at the distal edges of the ejecta deposit where the erosional capability of impacting secondary material is diminished. Small volumes of ejecta are sufficient to mask primary floor roughness and mobilize unstable wall material resulting in Abulfeda type craters. Of the 187 craters analyzed of this type, 135 are filled less than 1 km. Class 4 and 5 craters are produced by large scale erosional processes that modify major structures of the impact form.

The calculated crater fill thicknesses have been compared with models of basin ejecta thickness with range. Ballistics ejected by the basin event plus local material incorporated in the final deposit represent the total thickness available to fill craters. Mean fill thicknesses in class 4 and 5 craters exceed values predicted by the ejecta thickness models at ranges beyond 1000 km (Fig. 3). Small excesses can be explained by the preferential deposition of ejecta in local lows such as crater floors. Additional material may also accumulate from unstable wall material by local seismic shaking caused by the impacting ejecta. These processes should not be sufficient, however, to explain the thickness values at a range of 2000 km, where the mean fill thickness of class 4 and 5 craters is $\sim$1.7 km and the modeled basin ejecta thickness is on the order of hundreds of meters.

Beyond 2500 km, a distance past the region where class 4 and 5 craters attain their maximum density, the effectiveness of Imbrium ejecta on crater degradation is reduced, yet the mean fill thickness remains relatively constant at $\sim$1.25 km. This fill thickness may be a consequence of the accumulation of material from repeated local impacts with time. When this amount is subtracted, the remaining thicknesses more closely resemble the values predicted by the ejecta thickness model.

Mean fill thickness values for Abulfeda craters are generally less than those for class 4 and 5 craters by $\sim$.75 km, indicating they have accumulated $\sim$.5 km of fill from repeated local impacts. Their younger age accounts for the smaller amounts of material accumulating on their floors from this process.

Conclusions - 1) Small amounts of material, on the order of tens of meters thick, are sufficient to create the morphology typical of Abulfeda type craters. 2) Ejecta from major impact basins is a major source of crater fill. 3) Material from local impacts is also sufficient to create an Abulfeda crater. 4) Abulfeda craters form from an original morphology similar to Tycho type craters. 5) Tycho, Abulfeda and class 4 and 5 craters are related by a continuum of degradation and infilling.

References: [1]Wood C.A. and Andersson L. (1978) Lunar and Planetary Lab. Catalogue of Lunar Craters, Univ. AZ, in prep. [2]Head J.W. (1975) Moon

12, 299. [3]Oberbeck V.R. (1974) *Proc. Lunar Sci. Conf. 5th*, p. 111. [4]McGetchin T.R. *et al.* (1973) *Earth Planet. Sci. Lett.* *20*, 226.

fig.1

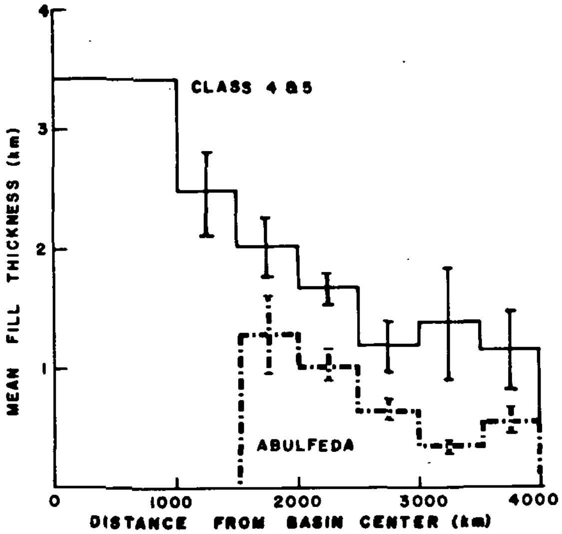

FIG. 3 THICKNESS OF BALLISTICS & LOCAL MATERIAL[3], AND BALLISTICS ONLY[4] DOWNRANGE

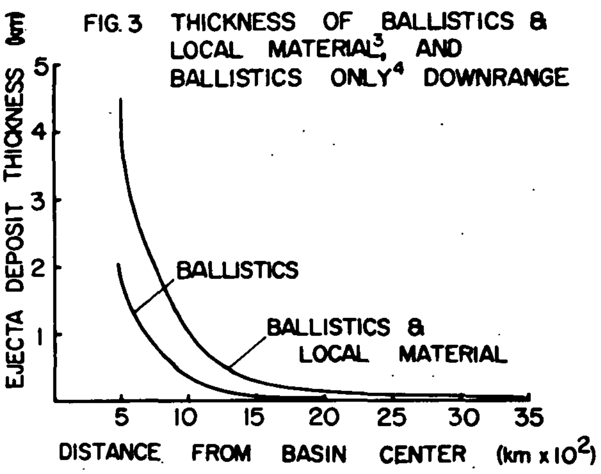

fig.2 CRATER DENSITIES BY DISTANCE INTERVAL

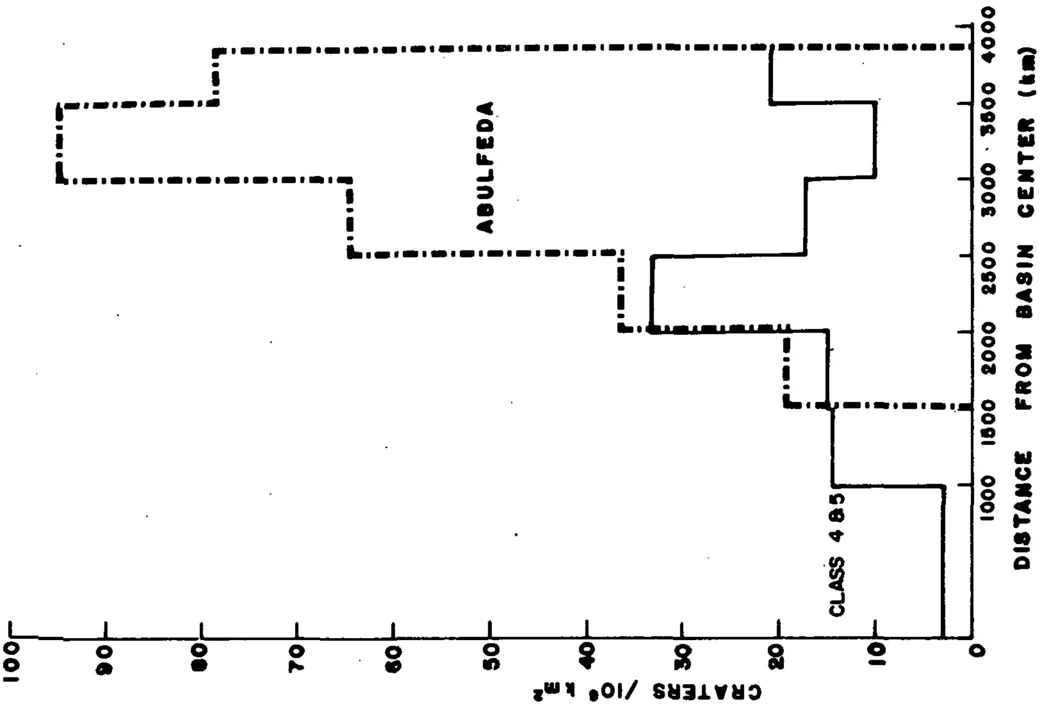

LUNAR FLOOR-FRACTURED CRATERS: QUANTITATIVE TESTS OF HYPOTHESES FOR THEIR ORIGIN

J. Lynn Hall[1], James W. Head[2], and Sean C. Solomon[1]

[1]Dept. of Earth and Planetary Sciences, Massachusetts Institute of Technology, Cambridge, MA 02139; [2]Dept. of Geological Sciences, Brown University, Providence, RI 02912.

A large number of lunar craters have fracture patterns on their floors. Among other features often found in floor-fractured craters are generally shallow interior relief compared to fresh impact craters, and partial lava filling to form a moat around an uplifted center. Floor-fractured craters constitute a subset of the "modified" craters described by Brennan [1]. A small number of floor-fractured craters have been studied individually, including Humboldt [2], Goclenius [3,4] and the group in Mare Smythii [5,6,7], and mention of floor-fractured craters in the literature is frequent. The most extensive study of the class is that of Schultz [8]. Floor-fractured craters are generally clustered around the maria. Major groups are located adjacent to north-western Oceanus Procellarum; around Mare Nectaris; and along the southern border of Mare Smythii. Areas conspicuously lacking in abundant floor-fractured craters include the maria Imbrium, Tranquillitatis, Serenitatis, Australe, and eastern Mare Fecunditatis [8]. Small floor-fractured craters are found within or associated with some large flat-floored craters, including Aitken, Barbier, Pannekoek [9], and Einstein, and are scattered through the highlands [8]. The lack of high-resolution photography of certain regions of the lunar surface, especially the polar regions, makes an exact determination of location and size distributions of floor-fractured craters impossible.

This study is an attempt to apply geophysical techniques and data to distinguish among the various models that have been proposed for the formation of lunar floor-fractured craters. The proposed models include regional isostatic adjustment associated with mare emplacement [4], isostatic rebound of the crater itself [2,10], and uplift and fracture of the crater floor due to volcanic intrusion [5,6,7,8,9,11]. The data which are examined to distinguish among these models include topographic profiles, gravity anomaly data, and the location and orientation of fractures.

The topographic data consist of profiles of craters taken from lunar Topo Orthophotomaps (LTO's), together with a limited amount of information from the Apollo Lunar Sounder Experiment (ALSE) [12] and earth-based radar topographic (ERT) measurements [13]. Profiles of floor-fractured and fresh craters of approximately the same size are compared by superimposing the crater rims and subtracting elevations to obtain vertical displacements as a function of distance (see Fig. 1). The region immediately outside the rim of the floor-fractured crater appears to be depressed with respect to the fresh crater, as would be expected for isostatic rebound [10], although the influence of pre-crater highland topography may be important. The displacement curve can be compared to models for displacements above an intruding body

[14,15]. The shape of the curve interior to the crater rim is roughly consistent with that of an intrusion shape approximated by a sphere or disc but not with that of a vertical dike or other vertically extended shapes. Topographic profiles of individual floor-fractured craters can be used to distinguish between two models of floor uplift: one calling for "welding" and uplift of the entire floor block [8], and the other calling for doming of the floor. The presence or absence of doming places constraints on the depth of the intrusion [16].

Floor-fractured craters may contain concentric, polygonal, or radial fracture patterns, frequently in combination. Radial faulting is a result of stresses associated with doming of the crater floor [16,17], whether by isostatic rebound or intrusion. Concentric faulting may be caused by mechanical failure of a large crater formed in a relatively thin surface layer [18], or by intrusion [6]. It does not appear, therefore, that the radial and concentric fracture patterns will enable us to distinguish between isostatic and intrusive models. Polygonal fracture patterns may be controlled by pre-existing regional stress patterns, such as the extensional stresses around mare basins caused by loading, or by those associated with thermal expansion of the moon [19].

The typical unmodified impact crater (lunar or terrestrial) has a negative Bouguer gravity anomaly, which is usually attributed to a region of brecciated rock located within and beneath the crater [20,21,22]. However, at least two large floor-fractured craters (Humboldt and Petavius) and one domed-floor crater (Neper) have zero Bouguer anomaly [23]. If the floor uplift is due to the intrusion of a horizontal sill (modeled as a right circular cylinder with diameter equal to the crater rim diameter), then to produce a zero Bouguer anomaly, in which the mass excess of the intrusion balances the mass deficiency of the breccia lens, the thickness of the sill is $t = (-\Delta\rho_{br}/\Delta\rho_{in})(D_r/6)$ [23], where D_r = crater rim diameter, $\Delta\rho_{br}$ = density contrast between the breccia lens and normal lunar crust, and $\Delta\rho_{in}$ = density contrast between the solidified intruded material and normal lunar crust. Reasonable values of $\Delta\rho_{br}$ range from -0.1 g/cm^3 to -0.4 g/cm^3 [20,22], and for $\Delta\rho_{in}$ from approximately $+0.1$ to $+0.6$ g/cm^3 [22,23]. Using these values, t is constrained by $.03D_r < t < .66D_r$. For Humboldt, $t = .01D_r$ ($D_r = 200$ km, $t \simeq 2$ km) [23], and thus the floor uplift is not sufficient by a factor of at least 3 to account for the lack of anomaly. Smaller craters may show larger uplift relative to their diameter; for example, for Davy $t \simeq .12D_r$. Unfortunately, the spatial resolution of the gravity data is not good enough to be able to tell whether smaller floor-fractured craters also have zero Bouguer anomaly.

Conclusions: 1) There may be an isostatic component in the formation of floor-fractured craters, but it appears certain that volcanic intrusions are also important. The intrusion could be in the form of a horizontal intrusion beneath the breccia lens, as was proposed by Schultz [8], but the vertical deformation models are not sensitive to the exact shape or orientation of the intrusion [15]. 2) In addition to the plate-like uplift of a flat floor proposed by Schultz [8], the presence of radial floor fractures in some craters suggests that updoming was an additional mode of floor deformation. 3) In the large floor-fractured craters examined the uplift of the floor by intrusion is probably not sufficient to account for the observed lack of a

Bouguer gravity anomaly, supporting the conclusion of Dvorak and Phillips [23]. 4) Minor uplift and crustal extension due to lithospheric flexure in response to mare basin fill may be an important contributor to the tendency of floor-fractured craters to cluster near mare edges.

References: [1] Brennan, W.J., The Moon, 12, 449, 1975. [2] Baldwin, R.B., JGR, 73, 3227, 1968. [3] Baldwin, R.B., JGR, 76, 8459, 1971. [4] Bryan, W.A., et al., PLSC 6th, 2563, 1975. [5] DeHon, R.A., JGR, 75, 5712, 1971. [6] Wolfe, R.W. and F. El-Baz, PLSC 7th, 2903, 1976. [7] Greeley, R., et al., LS VIII, 371, 1977. [8] Schultz, P.H., The Moon, 15, 241, 1976. [9] Whitford-Stark, J.L., Nature, 248, 573, 1974. [10] Danes, Z.F., Astrogeologic Studies, USGS Open File Ann. Rept. Pt. A, 81, 1965. [11] Young, R.A., Apollo 16 Prelim. Sci. Rept. 29, 1972. [12] Elachi, C. et al., The Moon, 15, 119, 1976. [13] Zisk, H., The Moon, 4, 296, 1972. [14] Mogi, K., BERI, 36, 99, 1958. [15] Dieterich, J. H., and R.W. Decker, JGR, 80, 4094, 1975. [16] Smith, R.L. and R.A. Bailey, GSA Mem. 116, 613, 1968. [17] Carr, W.J. and W.D. Quinlivan, GSA Mem. 110, 99, 1968. [18] Melosh, H.J., LS VII, 549-551, 1976. [19] Solomon, S.C. and J.W. Head, JGR, 84, in press, 1979. [20] Innes, M.J.S., JGR, 66, 2225, 1961. [21] Dvorak, J. and R.J. Phillips, GRL, 4, 380, 1977. [22] Janle, P., J. Geophys., 42, 407, 1977. [23] Dvorak, J. and R.J. Phillips, PLSC 9th, 3651, 1978.

Figure 1. (Top and middle) Topographic profiles for 30-km diameter fresh and floor-fractured craters (Necho and Davy, respectively) constructed from reduced LTO's (vertical exaggeration 5x). The horizontal distance scale on Davy has been reduced slightly in order that the rims may be superposed directly. (Bottom) Relative elevation of Davy with respect to Necho, obtained by direct differencing of the two observed profiles.

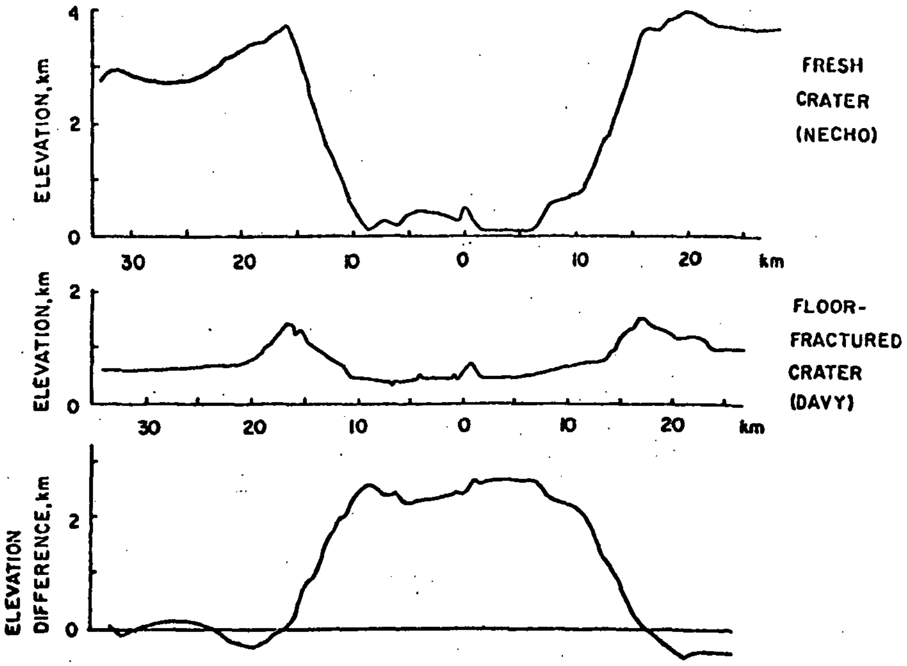

Simple to Complex Impact Craters: the Transition on Mars, Richard J. Pike, U.S. Geological Survey, Menlo Park, CA 94025, and D. W. G. Arthur, U.S. Geological Survey, Flagstaff, AZ 86001.

Depth/diameter (d/D) measurements from plots of digitized Viking-image brightness values (D_N) against pixel counts (Arthur, 1979) and morphologic observations on Viking pictures for the same sample of 73 Martian craters contribute several missing pieces to the interpretive puzzle of impact cratering on the terrestrial planets. The unifying concepts guiding this work are size-dependency of crater shape and the simple-to-complex transition (Dence et al., 1977; Pike, 1977). Morphologic characteristics of Martian craters are consistent with the emerging synthesis of relations among kinetic energy of impact, cratering mechanics, target properties, and gravitational attraction.

First, simple craters vary little in shape, especially in d/D, from planet to planet but complex craters vary considerably. For example, Martian complex craters are deeper than those of Earth but shallower than those on Mercury and the Moon (Fig. 1). The inflection in the d/D distribution occurs at about 5 km diameter. Second, the occurrence of seven morphologic features of Martian craters varies systematically with crater size and puts the interval of the simple-to-complex transition at about 5 km to 8 km diameter (Fig. 2). Third, the relative order in which features appear with increasing crater size: first flat floors, then central peaks and the d/D inflection, scalloped rims, and lastly terraced walls, indicate that the initiating mechanism for complex carters is probably elastic recoil rather than centripetal collapse. This interpretation follows partly from the observation -- both on the Moon and Mars -- that whereas fresh terraced craters always have central peaks, craters with peaks frequently lack terraces. Fourth, the diameter marking the simple-to-complex transition for impact craters, which the new d/D and morphologic data indicate is roughly 5 km to 8 km on Mars (Figs. 1, 2), varies inversely and statistically with gravitational acceleration at the planetary surface (Fig. 3). Fifth, there is a strong correlation between the Martian crater size marking the simple-to-complex transition of internal morphology and that dividing craters with apparent ballistic ejecta from those whose ejecta evidently is characterized by flow features (Fig. 2). This correspondence may reflect interaction of an impact-energy threshold with the presence of ice in the Martian substrate. Our modest sample detected no latitude-dependence of ejecta type and is not yet sufficiently large to assess terrain-related contrasts in interior crater morphology (Wood et al., 1978).

References:

Arthur, D. W. G., 1979, The depths of Martian impact craters: to be submitted to Icarus.

Dence, M. R., Grieve, R. A. F., and Robertson, P. B., 1977, Terrestrial impact structures: principal characteristics and energy considerations, in Roddy, D. J., et al., eds., Impact and Explosion Cratering, N.Y., Pergamon, p. 247-275.

Malin, M. C. and Dzurisin, D., 1977, Landform degradation on Mercury, the Moon, and Mars: evidence from crater depth/diameter relationships: J. Geophys. Res., v. 82, p. 376-388.

Pike, R. J., 1977, Size-dependence in the shape of fresh impact craters on the Moon, in Roddy, D. J., et al., eds., Impact and Explosion Cratering, N.Y., Pergamon, p. 489-509.

Pike, R. J., 1978, A geomorphic threshold for impact craters on the terrestrial planets [Abs.], in Program and Abstracts, Ninth Annual Geomorphology Symposium, October 19-21, 1978, SUNY Binghamton, p. 20.

Turner, R. J., 1978, A model of Phobos, Icarus, v. 33, p. 116-140.

Wood, C. A., Head, J. W., and Cintala, M. J., 1978, Interior morphology of fresh Martian craters: The effects of target characteristics: Proc. 9th Lunar & Planetary Science Conf., p. 3691-3709.

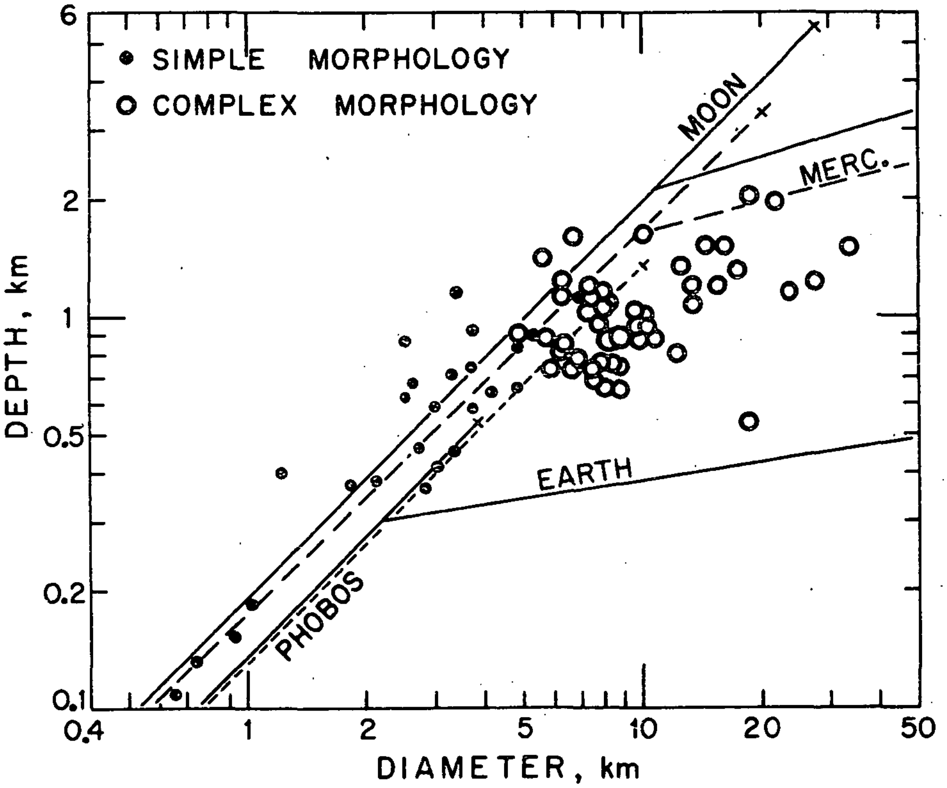

Figure 1. Depth/diameter results for simple (steep slope) and complex (gentle slope) impact craters on five planets. Data for 73 relatively fresh-looking Martian craters (dots and circles) from digitized photometric analysis of Viking pictures (Arthur, 1979). Lines are least-squares fits. Lunar curves from Pike (1977); Mercurian curves from Malin and Dzurisin (1977); terrestrial curves mostly from data in Pike (1977); Phobosian curve from data of Turner (1978).

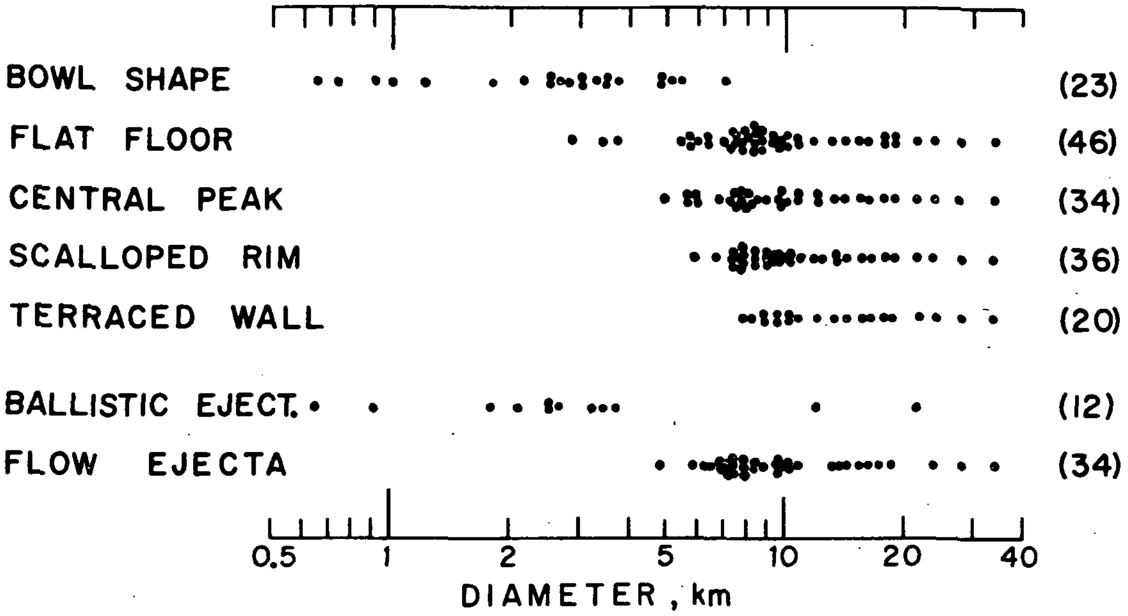

Figure 2. Diameter/morphology arrays for seven interior and exterior characteristics of relatively fresh Martian impact craters. Numbers give unambiguous identifications on Viking orbiter photographs. Size-dependency of crater morphology is pronounced.

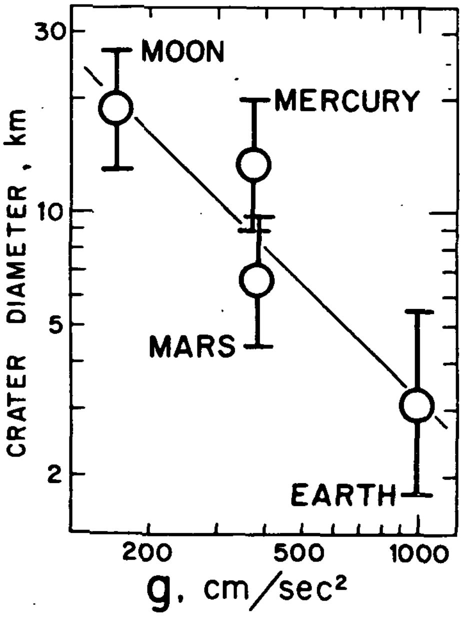

Figure 3. Inverse gravity-dependence of the simple-to-complex transition for fresh impact craters on four planets (modified from data in Pike, 1978). Circles are geometric means of diameters marking inflection of the depth/diameter curve, 50% frequency of peaks and terraces, and various other morphologic aspects of the transition (e.g., Wood et al., 1978). Similar data were not available for each planet. For Moon, n = 15; Mars, n = 12; Mercury, n = 11; Earth, n = 7. Bars show standard deviations. Slope of least-squares line to the four means is -1.01.

Relative ages of lunar basins. Don E. Wilhelms, U. S. Geological Survey, Menlo Park, CA 94025

Relative ages of 22 of the 32 ringed impact basins $\geq$ 250 km across that have been definitely identified on the Moon (1-5) are determined by comparing size-frequency distributions of $\geq$ 20 km primary impact craters superposed on relatively well exposed interior and exterior basin surfaces. Although statistically small ($12 < n < 102$; Table 1), the samples resulting from this procedure are more nearly indicative of basin ages than counts that combine primary, secondary, and pre-basin craters (6). The 19 size-frequency curves judged to be the most reliable of 26 constructed are plotted in Figure 1. Craters $\geq$ 20 km measured to the nearest km are plotted cumulatively without further binning or smoothing. Basins not possessing a named mare or an official crater name are named after two nearby genetically unrelated craters (5). Many of the results differ from those obtained previously (2-5).

Pre-Nectarian, Nectarian, and Imbrian basins emerge as three distinct groups (Table 1, Figure 1). The pre-Nectarian sequence (young to old) of Apollo, Freundlich-Sharonov (F-S; 18°N, 175°E), Birkhoff, Lorentz, Smythii, and Keeler-Heaviside (K-H; 10°S, 162°E) also seems well established. Statistically weak curves such as those of Milne and three basins omitted from the figure can tentatively be placed in the sequence (Table 1) by considering data quality and geologic relations. The late pre-Nectarian age of Milne indicated by the cumulative frequency of craters < 35 km is accepted because a very small sample of 8 craters produces the anomalously high frequency > 35 km. The curves of Grimaldi and of Schiller-Zucchius (56°S, 45°W; basin near Schiller of refs. 1,4), two small basins mantled by Orientale deposits, cross those of Apollo and Birkhoff, respectively, at about the points marking frequencies of 35-km craters; craters > 35 km are taken as definitive because many smaller craters must have been obscured by Orientale. Coulomb-Sarton (52°N, 123°W; unnamed basin B of ref. 4) is overlain by deposits of Birkhoff and Lorentz and has slightly lower crater frequencies than those of Smythii.

Although the separation of the Imbrian and Nectarian groups is clear, the relations between two Imbrian and among several Nectarian basins are unclear because the curves are almost superposed or cross one another. The sequence favored in Table 1 considers the likelihood that the frequencies of small craters are diminished on Humboldtianum (5) and Nectaris (6) by overlying deposits of Imbrium, on Korolev by deposits of Orientale and Hertzsprung (5), and on Mendel-Rydberg (M-R; 50°S, 94°W SE limb basin of refs. 1,4) by deposits of Orientale (4). Furthermore, poor photographic quality suggests that small (< 25 km) craters may have been overlooked or misinterpreted on Humboldtianum and Crisium. Superposition of probable secondaries of Orientale on Schrödinger and of Humboldtianum on Moscoviense (5) resolves the otherwise ambiguous relations of these basin pairs. Ages of the pairs Crisium--Humorum and Nectaris--Mendel-Rydberg are regarded as the most uncertain.

Table 1. Relative ages of lunar basins (youngest at top)

NAME	n	AREA $10^6 km^2$	AGE
Orientale	67	3.001	IMBRIAN
Schrödinger	12	0.594	
Imbrium	69	2.491	
Hertzsprung	51	0.883	NECTARIAN
Humorum	24	0.428	
Crisium	45	0.843	
Mendeleev	36	0.569	
Humboldtianum	32	0.515	
Moscoviense	53	0.609	
Korolev	88	1.113	
Mendel-Rydberg	18	0.247	
Nectaris	102	1.286	
Milne	15	0.171	PRE-NECTARIAN
Apollo	57	0.480	
Grimaldi	15	0.154	
Freundlich-Sharonov	81	0.629	
Birkhoff	50	0.401	
Schiller-Zucchius	16	0.143	
Lorentz	33	0.208	
Coulomb-Sarton	43	0.296	
Smythii	74	0.445	
Keeler-Heaviside	69	0.371	

References

(1) W.K. Hartmann and G.P. Kuiper (1962) Concentric structures surrounding lunar basins: Comm. Lunar and Planet. Lab., U. of Arizona, v.1, n.12

(2) R.B. Baldwin (1969) Ancient giant craters and the age of the lunar surface: Astron. Jour., v.74,p.570

(3) D.E. Stuart-Alexander and K.A.Howard (1970) Lunar maria and circular basins--A review: Icarus, v.12, p. 440

(4) W.K. Hartmann and C.A. Wood (1971) Moon: Origin and evolution of multi-ringed basins: The Moon, v.3, p.3

(5) U.S. Geological Survey, geologic maps of the Moon, scale 1:5,000,000:
Near side (1971) I-703
East side (1977) I-948
West side (1977) I-1034
Central far side (1978) I-1047
North side (1978) I-1062
South side (in press) I-1162

(6) D.E. Wilhelms, V.R. Oberbeck, and H. R. Aggarwal (1978) Size-frequency distributions of primary and secondary lunar impact craters: Proc. Lunar and Planet. Sci. Conf. 9,p.3735

Acknowledgments

The work was supported by the National Aeronautics and Space Administration, Lunar Synthesis and Planetary Geology Program Offices.

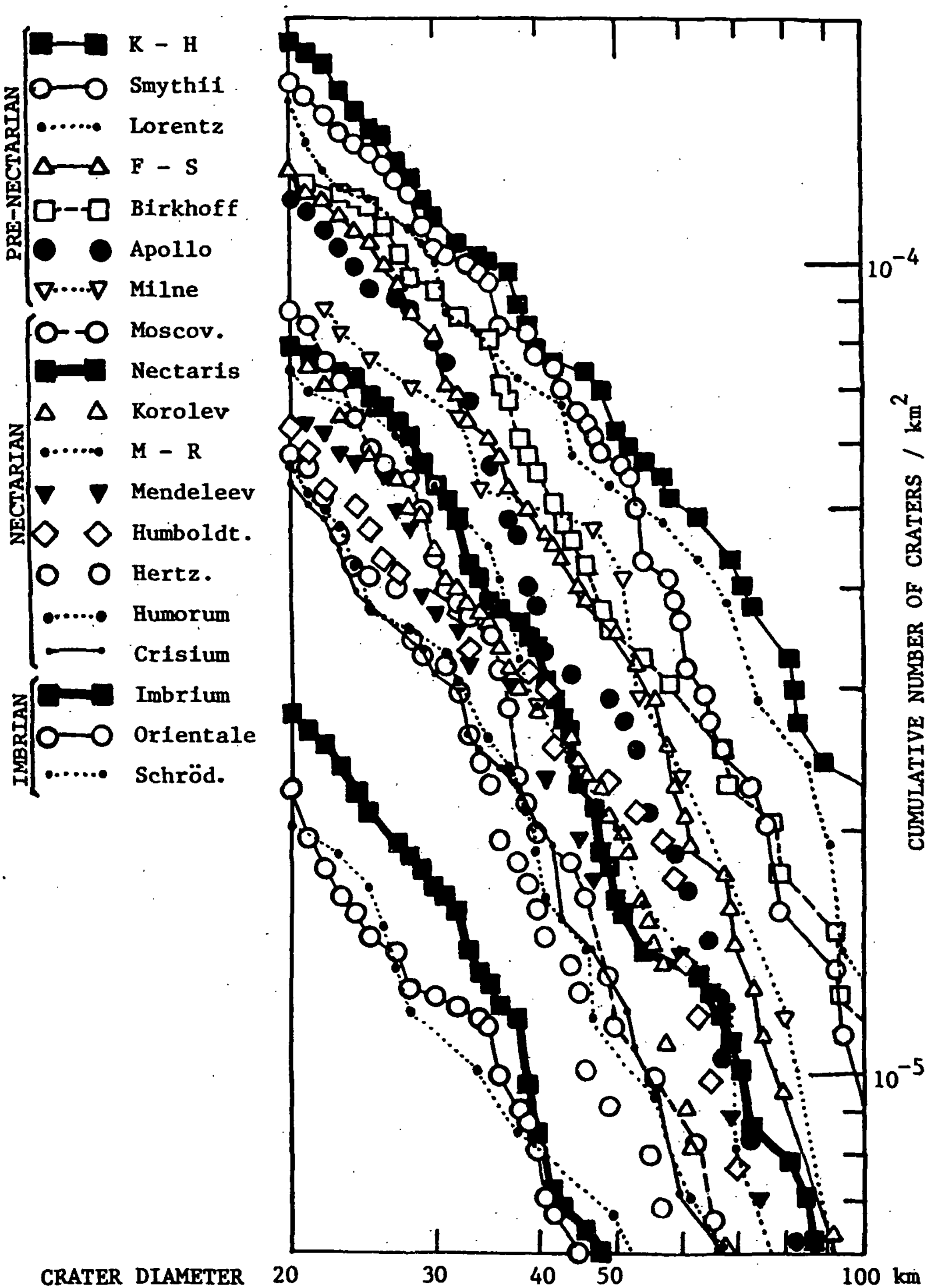

Fig. 1. Cumulative size-frequency distributions of primary impact craters 20-100 km in diameter superposed on lunar basins

Basic Geomorphic Concepts Applied to Planetary Cratering.

R. A. De Hon, Department of Geosciences, Northeast Louisiana University, Monroe, LA 71209.

Davis (1) expounded as axiomatic the influences of structure, process, and stage in the morphologic development of terrestrial landscapes. Every beginning geology/physical geography student is familiar with the application of these concepts to common landforms or assemblages of landforms. In planetary geology, these principles are applied with varying degrees of vigor and success. As an example of the geomorphic triad applied to planetary surfaces, the current state of knowledge and some problems in impact cratering are considered here.

The concept of stage is most often employed as one step in a geomorphic cycle or progression of successive changes in landforms with time. As a crater is subjected to the various agents of degradation with time, its morphology undergoes a series of progressive changes. In general, the sequence involves a reduction of rim height, decrease in interior depth, and smoothing of overall topography. Morphological classification of craters based on progressive degradational stages is widely used to establish relative time sequences on the planets (2, 3). On a regional scale, crater saturation is the equivalent of the end stage or old age of progressive surface modification by impacts.

The geologic process responsible for development of planetary landforms is significant. Unfortunately, it is not always obvious as to which agent is acting to produce a particular surface configuration. Unlike observable terrestrial processes, most extraterrestrial processes either are too slow or are not operating at the present time. Hence, uniformitarianism is a less practical approach in planetary geology than in its terrestrial applications. The long-standing, and not entirely settled, controversy over the importance of volcanic and impact processes in the formation and modification of craters serves as a classic example. While an impact origin is favored for most craters, volcanic modification is frequently called upon whenever crater morphology does not match idealized impact models.

Structure, in its broad geomorphic sense, refers to the influence of rock heterogeneity in landform modification. Structure is perhaps the least appreciated concept in the geomorphic triad as applied to planetary surfaces. This lack of appreciation probably arises from our incomplete understanding of planetary surface structure. Some investigators (4, 5, 6) have advanced arguments for the importance of structure (especially target stratigraphy) in the morphology of craters.

Both Penck(7) and Davis (1) recognized interruptions to originally idealized cycles (rejuvenation) and the strong influence of structure in the geomorphic cycle. In like manner, planetary resurfacing by the emplacement of mantling materials may provide a surface for renewed cratering after previous saturation(s). In a similar fashion, Davis's (8) "old-from-birth peneplain" and Penck's (7) "primarumph" may be applicable to crater degradational age schemes. The morphological classification of progressively degraded craters as a function of age is necessary and useful. Some craters, however, exhibit contradictory morphologies and, the various components of stage classification are not in harmony with each other. Occasionally, the superpositional age and the degradational age are in disagreement. As examples of this class of craters, Pohn and Offield (9) cited the superposition of lunar crater Capella on Isidorus in a reversal of their apparent morphological age classifications. On Mercury, some basins which appear to be highly degraded are surrounded by secondary crater fields or secondary crater chains, thus raising the question as to how secondary craters may be preferentially preserved while the basin is degraded.

More often than not, craters with mixed morphological age components are relegated to a mode of origin or modification other than impact. It is proposed that such craters are equivalent to the "old-from-birth" geomorphic classification and that the influence of structure is a major factor in the pristine crater morphology. Under some circumstances, impact into a thin surficial results in shallow, poorly formed craters that are young in absolute age but appear to be highly degraded. For the youngest craters, the discrepancy in absolute and degradational age may be obvious by superposition. In older craters, the absolute and degradational age differences may lead to incorrect age assignments or to incorrect assumptions of origin.

References

(1) Davis, W. M. (1899) Geog. J., 14, 481-504.

(2) Pohn H. A. and Offield T. W. (1970) U.S. Geol. Sur. Prof. Paper 700-C, pt. 1, 153-162.

(3) Trask N. J. 1976 in Conf. on comparisons of Mercury and the Moon. LSI, Houston, p.36.

(4) Quaide W. L. and Oberbeck V. R. (1968) J. Geophys. Res. 73, 5247-5270.

(5) Head J. W. (1976) Proc. Lunar Sci. Conf. 7th, 2913-2929.

(6) Hodges C. A. and Wilhelms D. F. (1978) Icarus, 34, 294-323.

(7) Penck W. (1927) Die Morphologische Analyse, J. Engelhorn's Nachfolger, Stuttgart.

(8) Davis W. M. (1922) Geol. Soc. Am. Bell., 23, 587-598.

(9) Pohn H. A. and Offield T. W. (1970) U.S. Geol. Sur. Prof. Paper 700-C, Pt. 2, 163-169.

Basins of the Circum-Caloris Region of Mercury, M. B. Wright and R. A. De Hon, Department of Geosciences, Northeast Louisiana University, Monroe, LA 71209.

Large impact basins are important elements of surface morphology on cratered planets. The cratering history of a planet is generally a record of decreasing impact flux. Basin-forming impacts are most common in early planet history and become less frequent with time. The earliest impact record is lost as later impacts degrade pre-existing basins and craters beyond recognition. The surviving impact structures play a large role in shaping topography and controlling emplacement of plains-forming materials.

We have made a detailed study of impact basins ($>$200 km diameter) in the vicinity of the Caloris basin of Mercury (65°N-10°S; 110°W-190°W). The basins were ranked on a degradational scale ranging from Class 5 (least degraded) to Class 1 (most degraded). The degradational scale is based on completeness of rim, preservation of crater wall, number of superposed craters, and extent of secondary craters (1, 2, 3). The least degraded craters and basins are easily recognized by a rugged, raised rim and a well-defined, depressed interior which is covered by plains-forming materials. The most degraded basins are characterized by incomplete arcs of slightly raised, heavily cratered or mantled terrain partly encircling regions of less cratered plains.

The total number of basins in this region is greater than indicated in earlier studies (4, 5, 6) because this investigation includes more highly degraded features. We have identified 21 basins (Table I and Fig. 1); 10 were previously recognized (5); and 5 are formally named features. The basins range from the 1340 km diameter Caloris basin to the 200 km diameter unnamed basin at 8°N; 167°W. Identification of some Class 1 basins is problematic due to their advanced stage of degradation. The oldest basins may be degraded beyond recognition.

Plains (Planitia) in the Caloris region are confined to a wide annulus exterior to the Caloris rim and to roughly circular depressions (Fig. 1). Low-lying regions containing plains-forming materials are typically large degraded basins or coalescing basins. Sobkou Planitia is comprised of at least three basins; Budh Planitia is comprised of two basins. Many basins are located within the Caloris annular depression, and they tend to control the configuration of the plains-terra boundary. Individual basins and clusters of basins also control the accumulation of plains-forming materials beyond the region of continuous plains near Caloris. Preliminary isopach mapping tends to confirm the presence of the largest basins by detecting thick lenses of plains-forming material within the centers of basins (7). Thick, roughly circular lenses of plains-forming material northeast of Caloris may be evidence of more unidentified basins beneath the present planitia.

TABLE I

BASIN	LOCATION	DIAMETER (km)	CLASS
Caloris	34N; 194W	1340	5
---	2N; 130W	840	1
(W.Sobkou)	36N; 135W	655	1
(S.Budh)	19N; 150W	640	1
---	19N; 161W	480	1
(E.Sobkou)	39N; 119W	475	1
Shakespeare	49N; 152W	420	2
---	29N; 159W	410	2
---	18N; 137W	410	1
(N.Budh)	27N; 147W	405	1
---	0 ; 183W	370	1
---	5N; 157W	370	2
(S. E. Solokou)	30N; 114W	325	1
---	13N; 171W	280	1
Mozart	8N; 191W	260	5 (?)
Van Eyck	43N; 159W	250	3
---	42N; 146W	225	1
---	26N; 164W	225	1
---	17N; 166W	215	1
---	8N; 167W	200	1
Strindberg	54N; 136W	200	5

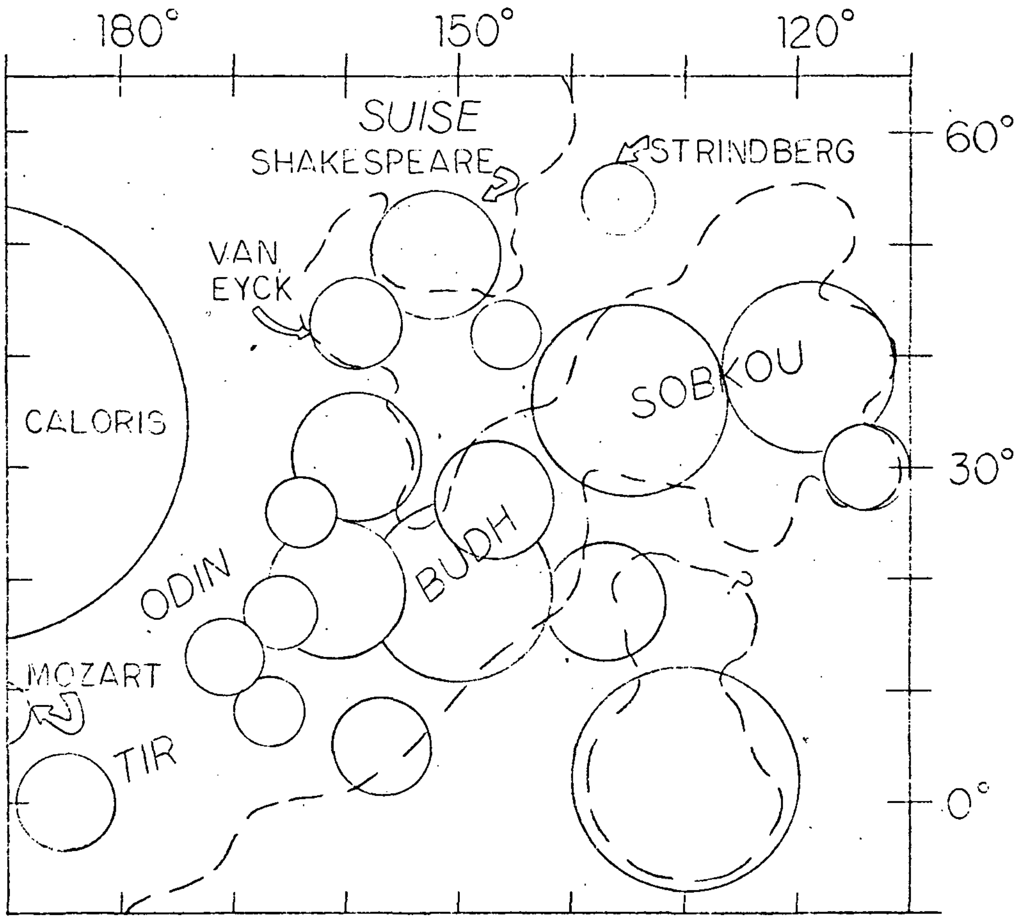

Figure 1. Location of basins greater than 200 km diameter, Dashed line indicates approximate limit of plains-forming materials.

References
(1) Trask (1978) ms in preparation.
(2) Trask N.J. (1976) in *Conf. on Comparisons of Mercury and the Moon*. LSI, Houston, 36.
(3) Wood C.A., Head J.W. and Cintala M.J. (1977) Proc. Lunar Sci. Conf. 8th, 3503-3520.
(4) Wood C.A. and Head J.W. (1976) Proc. Lunar Sci. Conf. 7th, 3629-3651.
(5) Schaber G.G., Boyce J.M. and Trask N.J. (1977) Physics of the Earth and Planet. Interiors, 15, 189-201.
(6) De Hon R.A. (1978) NASA Tech Mem. 79729, 150-152.
(7) De Hon R.A. (1979) This volume.

Mobility of Rampart Crater Ejecta on Mars. Peter J. Mouginis-Mark, Dept. of Geological Sciences, Brown Univ., Providence, RI 02912.

The maximum radial distance of the continuous ejecta blanket from primary center has been measured for 1304 martian craters that display distal ramparts.[1] These craters correspond to types 1, 2, 3, and 5 of Mouginis-Mark.[2] Earlier analysis[3] has shown that when ejecta range is normalized to the parent crater diameter (henceforth called the "ER" value), ER increases with crater size. Experimental studies[4] have predicted that the range of the ejecta (which is emplaced by a surface-flow process[5]), will be influenced by ejecta viscosity (hence, among other parameters, target volatile content). Low viscosity ejecta associated with volatile-rich targets should be areally more extensive than ejecta derived from a similar-sized crater formed in a volatile-poor target.

Data tables are presented here pertaining to the mean ER values for the sample as a function of crater altitude vs. latitude (Table 1) and target geology vs. crater diameter (Table 2). Results relating to the variation of ejecta mobility with the location and size of rampart craters can be summarized as follows:

1) For any given elevation, the mean ER value increases towards the polar regions. If atmospheric density is assumed to be constant at any given elevation over the entire planet during the period of crater formation, then this relationship indicates that atmospheric effects[6] cannot play the dominant role in ejecta fluidization.

2) For each 10° of latitude band, there is a general decrease in ER with increasing elevation. This may be related to lower atmospheric densities or an equivalent reduction in target volatiles: both might be responsible for decreasing ejecta fluidization, thereby reducing ejecta range.

3) For craters formed on the same geological unit, there is a general increase in ER with increasing crater size (present diameter, not the reconstructed pre-wall failure value). Similar flow volume vs. mobility relationships have been observed for terrestrial landslides[7] and pyroclastic flows[8] as surface friction effects become less important with increasing flow volume. This suggests that rampart crater ejecta blankets may be influenced by preexisting topography in a comparable manner.[3]

4) Craters of the same diameter formed on different target materials have different mean ER values. The most mobile ejecta surrounds craters formed on fractured plains, while the least extensive ejecta is found on Tharsis lavas. Variations in subsurface volatile content or the pre-impact target strength and particle size distribution may be responsible for this effect.

References: [1]Mouginis-Mark P.J. (1979) Submitted to J. Geophys. Res. [2]Mouginis-Mark P.J. (1979) this volume. [3]Mouginis-Mark (1978) Nature 272, 691-694. [4]Gault D.E. and Greeley R. (1978) Icarus 34, 486-495. [5]Carr M.H. et al., (1977) J. Geophys. Res. 82, 4055-4065. [6]Schultz P.H. and Gault D.E. (1979) Submitted to J. Geophys. Res. [7]Hsu K.J. (1975) Geol. Soc. Am. Bull. 86, 129-140. [8]Sparks R.S.J. (1976) Sedimentology 23, 147-188.

Latitude	HEIGHT ABOVE MARS DATUM (KM) -3 to -2	-2 to -1	-1 to 0	0 to 1	1 to 2	2 to 3	3 to 4	4 to 5	5 to 6	6 to 7	7 to 8	Latitude Means
60S-70S				1.530 (1)		1.706 (37)	1.857 (13)					1.741 (51)
50S-60S		1.200 (1)	1.415 (2)	1.370 (1)	2.320 (2)	1.669 (66)	1.730 (25)					1.685 (97)
40S-50S		1.520 (1)				1.150 (1)	1.801 (50)	1.638 (19)	1.327 (6)			1.712 (77)
30S-40S						1.060 (1)	1.593 (91)	1.478 (38)	1.353 (6)	1.604 (12)	1.340 (1)	1.539 (149)
20S-30S					1.307 (3)	1.481 (10)	1.602 (67)	1.411 (13)	1.502 (26)	1.428 (44)	1.252 (9)	1.497 (172)
10S-20S				1.543 (9)	1.506 (10)	1.158 (11)	1.519 (47)	1.475 (16)	1.572 (16)	1.835 (11)	1.728 (9)	1.532 (129)
0 - 10S				1.930 (3)	0.990 (3)	1.444 (10)	1.393 (9)	1.522 (5)		1.563 (6)	1.484 (10)	1.469 (46)
10N - 0				2.020 (1)	1.483 (3)	1.160 (3)	1.755 (2)	1.232 (6)	1.137 (6)		1.430 (1)	1.323 (22)
20N-10N		1.357 (3)	1.550 (1)	1.559 (18)	1.584 (13)	1.467 (14)	1.900 (3)	1.204 (10)				1.493 (62)
30N-20N	1.180 (4)	1.506 (24)	1.695 (2)	1.525 (24)	1.429 (58)	1.581 (31)	1.494 (16)		1.743 (3)			1.493 (163)
40N-30N		1.610 (1)	1.610 (2)	1.695 (25)	1.631 (20)	1.432 (14)	1.561 (15)					1.601 (77)
50N-40N	2.409 (9)	2.481 (18)	2.463 (3)	2.031 (92)	1.722 (8)	1.474 (7)						2.078 (137)
60N-50N	2.090 (4)			2.395 (2)								2.192 (6)
Altitude Means	2.045 (17)	1.859 (48)	1.838 (10)	1.826 (176)	1.508 (120)	1.565 (205)	1.628 (338)	1.460 (107)	1.466 (63)	1.529 (73)	1.481 (30)	1188

TABLE 1: Mean ejecta mobility ratio for all craters at a given latitude and altitude. Number in parentheses gives size of each sample.

	CRATER DIAMETER RANGE (KM)											Terrain Mean
	0-5	5-10	10-15	15-20	20-25	25-30	30-35	35-40	40-45	45-50	+50	
Fractured Plains	2.082 (67)	2.237 (28)	2.698 (6)	2.540 (1)	2.470 (1)	2.500 (2)						2.175 (105)
Channels	2.110 (10)	1.590 (3)	1.600 (1)									1.962 (14)
Smooth Plains	1.912 (14)	1.628 (25)	1.768 (22)	1.887 (15)	1.931 (7)	2.220 (2)	2.590 (1)				2.020 (1)	1.807 (87)
Old Lavas	1.639 (15)	1.552 (33)	1.764 (18)	1.768 (11)	1.453 (9)	2.065 (2)	2.030 (2)	1.835 (2)				1.651 (92)
Cratered Plains	1.707 (52)	1.463 (91)	1.582 (70)	1.790 (40)	1.862 (22)	1.779 (8)	1.647 (6)	2.280 (3)			1.445 (4)	1.623 (296)
Rolling Plains	1.337 (3)	1.570 (8)	1.719 (7)	1.763 (3)	1.490 (1)		3.150 (1)					1.605 (23)
Ancient Terrain	1.581 (35)	1.450 (85)	1.489 (59)	1.726 (21)	1.739 (19)	1.979 (7)	2.450 (2)	2.033 (3)	1.688 (4)	2.400 (1)	1.542 (4)	1.566 (240)
Ridged Plains	1.436 (17)	1.372 (114)	1.520 (68)	1.671 (44)	1.828 (19)	2.063 (6)	1.942 (4)	2.304 (5)	2.280 (1)	2.020 (1)	1.730 (5)	1.539 (284)
Elysium Lavas	1.268 (10)	1.550 (23)	1.654 (5)	1.865 (4)	1.710 (3)						1.620 (1)	1.539 (46)
Chaotic Terrain	1.340 (1)	1.660 (3)	1.540 (1)									1.572 (5)
Canyon Rims	1.295 (4)	1.353 (6)	1.500 (9)	1.817 (3)							1.430 (1)	1.464 (23)
Tharsis Lavas	1.258 (9)	1.328 (42)	1.482 (15)	1.381 (11)	1.693 (7)	1.535 (2)		1.580 (2)				1.393 (88)
	1.751 (237)	1.495 (461)	1.594 (281)	1.733 (153)	1.776 (88)	1.969 (29)	2.027 (17)	1.956 (16)	1.806 (5)	1.473 (3)	1.604 (16)	1304

TABLE 2: Mean ejecta mobility ratio for craters in given size range formed on different target materials. Number in parentheses gives size of each sample.

Distribution of Fluidized Craters on Mars. Peter J. Mouginis-Mark, Dept. of Geological Sciences, Brown Univ., Providence, RI 02912.

From a preliminary study of the distribution of fresh impact craters on Mars displaying fluidized ejecta deposits, a data base containing 1559 craters has been assembled.[1] Crater diameter, morphological type, position on the planet and the maximum range of the continuous ejecta deposit from the center of the crater were measured utilizing the Brown University digitizing facility.[2,3] Height above Mars datum and target lithology were obtained for each crater from the geological map of Scott and Carr.[4]

Previously identified[5,6] rampart craters and radial texture craters are incorporated into the six crater types employed in this investigation. The sample is subdivided into craters with single (Type 1), double (Type 2) and multiple (Type 3) ejecta facies; radial textured craters (Type 4); complex ejecta craters[7] (Type 5); and craters described here as "pancake craters" (Type 6). Pancake craters are typically less than 5 km diameter, lack the distal ridges characteristic of rampart craters,[5,8] have simple bowl-shaped interiors and possess a single ejecta facies that has travelled a disproportionally large radial distance from the center of the primary in comparison to ejecta from rampart craters.[9] The cumulative size distributions for all six types of craters are presented in Fig. 1.

As reported by Allen,[10] rampart craters (Types 1, 2 and 3) display no strong latitudinal variation in their frequency of occurrence. Fig. 2 shows that between 50°N and 70°S, 40-60% of all craters at each latitude are Type 1, while 15-30% are Type 2. Between 40°N and 50°S, crater types 3, 4 and 5 each constitute 1-9% of the population, with the most frequent occurrence of Type 4, radial textured, craters observed at latitudes where young lavas exist. Poleward of 40°N and 40°S, the pancake craters (Type 6) are much more prevalent than near the equator. At high latitudes, over 40% of all craters measured were in this class, while pancake craters are virtually absent (0% except between 0-10°N, where they represent 3.5% of the total) from the equatorial regions. Because pancake craters are found in both the northern and southern high-latitudes, on a variety of target materials at different elevations, it is proposed that the characteristics of this crater type (high mobility ejecta, simple interior morphology, absence of distal ridges) are a product of greater ejecta fluidization, perhaps as a consequence of a poleward concentration of near-surface volatiles.

Target materials have been shown to influence the morphology of mercurian and lunar impact craters.[11,12] On Mars, local terrain might be expected to be particularly important due to the predicted spatial variability in rock strength and possible subsurface volatile content associated with fresh lavas, channel floors, cratered and ridged plains, and the megaregolith of the ancient terrain. Ten geological units were each identified to possess at least 30 fluidized craters within this study. The distribution of each crater type as a function of target material is presented in Fig. 3.

Reflecting their large total number, Type 1 craters comprise 32-70% of all craters on each terrain. They are most common (69.9%) on Tharsis lavas and least numerous (32.2%) on channel materials. Type 2 craters represent 12.9% of all craters on channel materials and are most frequently found on ridged plains (25.1%). Other types of craters exhibit a stronger terrain affinity: multiple facies craters (Type 3) are most common (5.6%) on ridged plains; Type 4 craters on Elysium lavas (9.4%); and Type 6 on channel materials (54.8%) and fractured terrain (46.2%). There is a total absence of Type 4 craters from fractured and ancient terrain, smooth plains, old lavas and channels; Type 5 craters on smooth plains and channels; Type 6 craters from Tharsis and Elysium lavas and ridged plains.

References: [1]Mouginis-Mark P.J., 1979, Submitted to J. Geophys. Res. [2]Arvidson R.E. et al., 1974, The Moon 9, 105-114. [3]Cintala M.J. et al., 1976, Geophys. Res. Lett. 3, 117-120. [4]Scott D.H. and Carr M.H., 1978, U.S.G.S. Map I-1083. [5]Carr M.H. et al., 1977, J. Geophys. Res. 82, 4055-4065. [6]Mouginis-Mark P.J., 1977, unpub. Ph.D. thesis, Univ. Lancaster, Lancaster, UK, 344 pp. [7]Mouginis-Mark P.J. and Head J.W., 1979, Lunar Plan. Sci. X, 870-872. [8]Head J.W. and Roth R., 1976, Symp. Plan. Crater. Mech. (abs.), LSI 50-52 . [9]Mouginis-Mark P.J., 1978, Nature 272, 691-694. [10]Allen C.C., 1978, NASA TM 79729, 160-161. [11]Head J.W., 1976, Proc. Lunar Sci. Conf. 7th, 2913-2929. [12]Cintala M.J. et al., 1977, Proc. Lunar Sci. Conf. 8th, 3409-3425.

Fig. 1: Cumulative frequency curves for the six types of craters included in this sample. Numbers on curves represent different crater types.

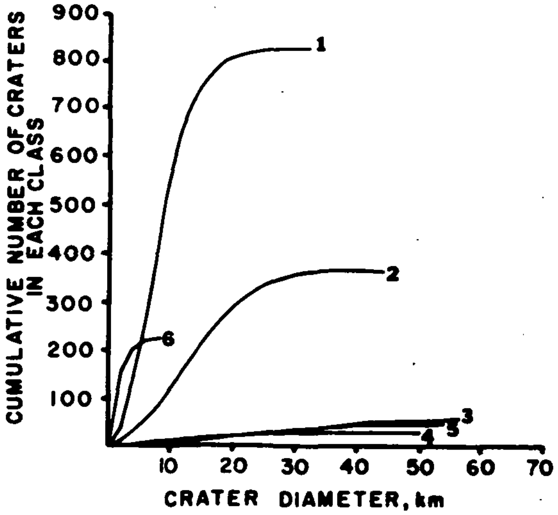

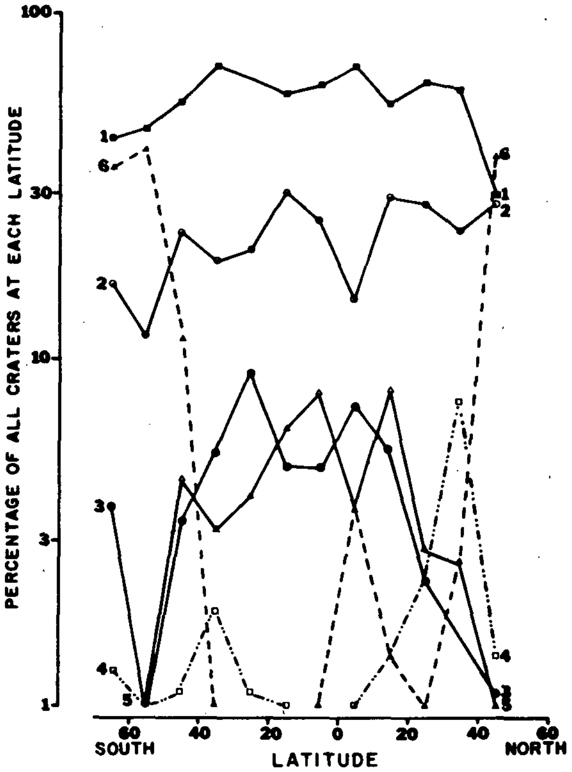

Fig. 2: Latitudinal distribution of sample craters. Each crater type is expressed as a percentage of all craters observed in any 10° latitudinal band.

Fig. 3 (below): Distribution of sample craters as a function of target material, shown as a percentage of all craters observed on that geological unit.

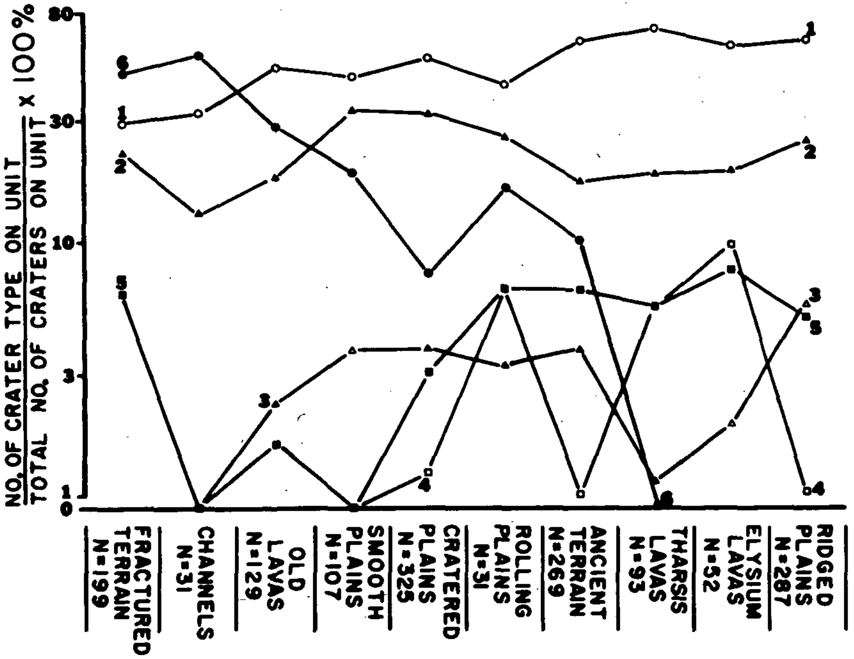

IMPACT CRATER AND BASIN CONTROL OF COLLAPSED TERRAINS ON MARS. Peter H. Schultz and Harold Glicken, Lunar and Planetary Institute, Houston, Texas

The emplacement sequence of basalts in floor-fractured craters and larger multi-ringed basins on the Moon provide significant clues for the probable locations of magma reservoirs and possible escape routes for any hydrothermal products in martian craters. During early or arrested stages of development, fracturing of lunar crater floors typically encompasses the crater floor (Schultz, 1976a), and surface volcanism commonly has not occurred. With increased modification, peripheral floor fracturing becomes more extensive and the old slumped wall material accumulates in a wide peripheral trough or moat where basalt ponds also accumulate. Other regions of modification at this stage may include fracturing around the central peak complex. During advanced stages of modification, concentric graben surround the polygonally fractured central floor plate. The central peak complex may be lifted with the floor or is downdropped. Multi-ringed impact basins exhibit similar concentrically arranged vent locations as described by Schultz (1976b), Head (1976), and Greeley (1976). The most important vent locations occur in the central basin where thick layers of basalts accumulate. The interior base of the outer rings represent the primary vent location for additional volcanism as expressed by the head pits for sinuous filles. Beyond the mountainous rings, the concentric distribution of vents inferred from local accumulations of basalt persists and is particularly pronounced where concentric rings from an adjacent basin overlap (Schultz, 1976b).

A survey of endogenically modified martian craters reveals the same general patterns with specific differences reflecting both different regional histories and the inferred interaction of cooling magma reservoirs with water/ice (Masursky et al, 1977; Schultz, 1978) or hygroscopic minerals (Clark, 1978). Theoretical calculations of cooling magma reservoirs beneath different size impact craters reveal that thawing of water/ice-bearing sediments to near the surface by a 1km thick sill can occur only in smaller craters (<20km). For larger craters, the melt zone is restricted to greater depths and is capped by still-frozen sediments. In both cases, the total time for melting approaches 10^5 years. Consequently, thawed sediments are either trapped beneath the floor plate or gradually escape along peripheral fractures related to floor uplift. Such a sequence may develop a metastable slurry resulting in catastrophic releases as suggested by Masursky et al (1977) and Nummedal (1978). The sequence also may account for the wide variety in martian floor-fractured craters and their inferred self-destruction.

Mega-examples of this type of interaction are proposed for the chaotic terrain, portions of Vallis Marineris, and the fretted terrains. Ares Vallis north of the chaotic terrain is partly controlled by a concentric structure interpreted as a buried, multi-ring basin and originates along a portion of the outer ring. This style of modification is interpreted to indicate thawed or hydrated sediments by intrusive melting within me inner basin region and along the concentric basin rings. Similarly, a pair of multi-ringed basins in Margaritifer Sinus exhibits clear control of both the chaotic terrains and the location of floor-fractured craters. Labyrnthus Loctis is believed to reflect an analogous structure encircling Syria Planum. Isolated massifs arranged in an arcuate pattern south of this region suggest that Labyrinthus Loctis is the inner ring of an old basin rivaling Hellas in size but buried by basalts. Such a basin is believed to have had a profound influence on the martian crust, perhaps contributing to the system of radial weaknesses, of which Vallis Marineris is an extension, in a manner analogous to the radial system around the Imbrium Basin on the Moon (Mason et al, 1976).

References

CLARK, B. C. (1978) J. Geophys. Res. 34, p. 645-665

GREELEY, R. (1976) Proc. Lunar Sci. Conf. 7th, p. 2747-2759

HEAD, J. (1976) Rev. Geophys. Space Phys. 12, p.265-300

MASON, R. GUEST, J. E., and COOKE, G. N. (1976) Proc. Geol. Assoc., 87, p. 161-168

MASURSKY, H., BOYCE, J. M., DIAL, A. L., SCHABER, G. G., and STROBELL, M. E. (1977) J. Geophys. Res. 82, p. 4016-4038

NUMMEDAL, D. (1978) NASA TM-79729, p. 257-259

SCHULTZ, P. H. (1976a) The Moon 15, p. 241-273

SCHULTZ, P. H. (1976b), Moon Morphology, 626 pp.

SCHULTZ, P. H. (1978), Geophys. Res. Letts. 5, p. 457-460

EFFECTS OF THE ORIENTALE IMPACT ON THE PRE-EXISTING CRATER POPULATION, A. Woronow, R. G. Strom, and E. Rains, Lunar & Planetary Lab., U. of Arizona, Tucson, AZ 85721.

Orientale, the freshest basin on the Moon, is well suited for the analysis of effects of a basin-forming event on a crater population. Our study uses the new LPL lunar-crater catalog to analyze the entire hemisphere centered on Orientale. Crater diameters down to 8 km have been used over most of this hemisphere, but some regions are measured down to only 20 km, and some small areas are unmeasured. We have eliminated regions of mare flooding from our study.

The Orientale-centered hemisphere has been grided radially and concentrically into 1440 equal-area segments. Intercomparisons of annulii at varying distances and sectors at varying azimuths have begun and the following preliminary findings can be reported:

1. Secondary craters are predominantly Class 1 and 2 (sharp rimmed) craters, but some Class 3's are also secondaries.
2. The abundance of secondaries relative to primaries peaks in the diameter range 12-20 km. In the range 8-12 km the abundance of secondaries is marginally recognized, but above 20 km diameter they do not contribute significantly to the total crater population.
3. Secondary craters occur predominantly at a range of 960-1500 km from the basin's center and do not contribute significantly to the total crater population beyond 1500 km range.
4. An excess of secondaries to the northwest and a corresponding dearth to the southeast suggests an oblique impact coming from the southeast.
5. The continuous ejecta blanket out to about 300 km from the basin rim (Cordillera Mts.) has either obliterated pre-existing craters or degraded them to Classes 4 or 5.

Dia. Range	% Obliteration
8-12 km	80
12-20	70
20-50	60
>50	40

6. The highlands of the region generally westward of Orientale possess a crater population that differs somewhat from that of the frontside highlands. In the diameter range 11 to 16 km, this farside region has a relative crater excess which reveals itself as a knee in the distribution, not unlike the knee found on Mercury at approximately the same diameter. Because the knee is equally prominent at moderate and extreme distances from Orientale and is composed primarily of Class 3, 4, and 5 craters, we do not believe the knee to result solely from secondary cratering due to Orientale. The interpretation of origin of the knee, on both the Moon and Mercury, will depend on analyses of more extensive farside regions.

The above conclusions are preliminary and based on a broad-based survey of the entire circum-oriented hemisphere. In particular directions considerable local variations may be encountered. As our analyses continue, we hope to be able to delineate such local variations.

The Intercrater Plains of Mercury. Martha A. Leake, Dept. of Planetary Sciences, U. of Arizona, Tucson, Arizona 85721.

Following the Mariner 10 flybys of Mercury, a study was undertaken to define and resolve or constrain the nature and origin of the intercrater plains. This study consisted of geologically mapping Mercury's incoming side and of determining crater statistics of heavily cratered terrain and surrounding intercrater regions. The smooth plains of the incoming side and the lunar intercrater plains south and east of Maurolycus in the southern highlands were studied similarly for comparative purposes.

Geological Map. The major product of this research, a geologic terrain map of the incoming side of Mercury, differs in the following ways from the earlier general terrain map of Trask and Guest (1). The new map is more detailed, incorporating all craters of diameter ≳40 km as well as some smaller features. Map units are extended into the hilly and lineated terrain establishing overall map continuity and relative age of this area. Plains units are assigned an age based on the relative ages of the craters which they embay or which are superposed upon them, a technique currently being used by the USGS in geologic maps of Mercury. Relative ages of craters were derived from their degradational state patterned after that system used by the Lunar and Planetary Lab for lunar craters; class 1 craters are freshest and class 5 most degraded (2). For example, plains within class 2 craters or superposed on C2 ejecta blankets, and cratered by C1 craters or their secondaries, are designated P2 plains. The relative age of the oldest plains unit is still ambiguous: they may overlie or underlie the oldest C5 craters. The P5 through P3 plains generally comprise the intercrater plains mapped by Trask and Guest (1); most of the P1 and P2 units are textural equivalents of the smooth plains occupying large areas of the outgoing side. Table 1 lists the crater classes and plains units, their descriptions and the percentage of map area covered by each unit.

Hilly and Lineated Terrain. The hilly and lineated area forms a critical link between relative ages established on the outgoing and incoming sides. Rather than designating this area as a separate unit or deposit, I assumed it to be a region disturbed by some distinct event whose age could be determined. Plains and crater units were continued into this region from the surrounding area. Sections of rims of class 3 craters are modified where they extend into the hilly and lineated area; exterior to this boundary, the rims are intact. Class 1 and 2 craters superposed on this surface are unmodified. Furthermore, smooth plains in this zone are undisturbed and fill older, heavily disrupted craters such as Petrarch. Hummocky P3 material fills some craters of classes 3, 4, and 5 north and east of Petrarch. Therefore, the event which disturbed this terrain occurred sometime between the formation of class 2 and 3 craters. Based on somewhat similar reasoning applied to the outgoing side, McCauley et al. (3) place the Caloris impact between the formation of (LPL) class 2 and 3 craters. This agreement of relative ages lends support to the proposal by Schultz and Gault (4) that the hilly and lineated terrain is the result of focused seismic waves generated by the Caloris impact. If this terrain was thus formed simultaneously with the Caloris impact, the craters and plains of the incoming side can be dated relative to the Caloris event.

Paleogeologic Maps. Using the Caloris impact at the end of the class 3 period as a 'time horizon', the geologic map was broadly grouped into Post-Caloris features (units of classes 1 and 2), "Caloris" features (class 3 units) and Pre-Caloris features (units of classes 4, 5 and ancient circular depressions C5'). The Pre-Caloris surface is dominated by large basins of 100 to 400 km and ubiquitous plains, some of which bury the C5' structures and their underlying surface. The "Caloris" surface also consists of mostly Pre-Caloris material, but it is labelled separately to emphasize the continuing plains emplacement and fairly heavy cratering which preceded and accompanied the Caloris impact. By contrast, the Post Caloris surface is sparsely populated with both craters and plains. Many of the smooth plains are isolated, remote from younger craters, interspersed with older plains deposits, or lie in Pre-Caloris craters and basins. This distribution makes it unlikely that the smooth plains were formed strictly by ballistic deposition of ejecta.

The paleogeologic maps and measurements of the existing plains area (Table 1) confirm that plains formation on the incoming side generally decreases with time, falling off extensively after the C3 cratering period. The latter separates the pre-Caloris intercrater plains from the post-Caloris smooth plains. The percentage of the mapped area ($1.02484\ 10^7 \cdot km^2$) covered by different ages of plains, both exterior and interior to craters, was compared to the percentage area covered by the craters. This latter value is an upper limit to crater area coverage determined by summing the values of crater density $p = (\pi D^2 N \cdot 100)/(4A)$ over all diameters ≥ 40 km for each class of crater. D is the geometric mean of the diameter bin size and N is the number of craters in that diameter bin over the total area A. In general, the percentage of area covered by craters also declines with decreasing age, although not in a manner to suggest plains formation by ejecta deposition alone.

Plains Origins and Ages. Three competing theories of the origin of Mercury's plains are: (a) a primordial surface remaining after global melting and solidification, (b) basin ejecta and melt deposits, and (c) volcanic deposits. It is doubtful that the intercrater plains represent a primordial surface because their formation spans a range of time overlapping Mercury's differentiation and bombardment history. Furthermore, the oldest plains unit P5 partially buries craters even older than class 5. The two oldest and most extensive intercrater plains units (P4 and P5) were emplaced at least throughout the period of heavy bombardment represented by class 4 and 5 craters; these crater densities are twice those of class 1 and 2 craters. Extensive areas of even younger intercrater plains (P3) were apparently emplaced near the end of heavy bombardment.

The continual resurfacing processes noted above, although eliminating the primordial origin hypothesis, still permit both volcanic and ballistic depositional origins. This ambiguity is illustrated by basins like Chekhov (C4) which are embayed by P4 plains, while in other regions C4 basin secondaries (e.g. from Ma Chih Yuan) are preserved on adjacent P5 plains. In addition, the youngest plains have two distinct textures which may depend on their mode of origin: moderately rough where they overlie or embay basin ejecta, and relatively smooth where they are either thicker or cover older plains deposits, for example, east of Handel and east of Andal respectively. Gault et al. (5) have noted that the extent of the continuous ejecta blanket and secondary crater field around Mercurian craters is more restricted than around lunar craters. Trask and Strom (6) find that some craters are relatively well preserved near later basin-sized impacts, indicating that the resurfacing potential of Mercurian craters is not as extensive as on the Moon. From the table, one finds that intercrater plains P3 through P5 cover nearly 44% of the map surface while only 30% is covered by equivalent aged craters. If the resurfacing potential of existing craters is small, then many more basins than are visible are required to create this amount of intercrater material through deposition of ejecta. Contributions of surface material from a third source, probably volcanic, is indicated.

Arguments of plains formation by volcanism include the extensive nature of the intercrater plains, the lack of source basins for these plains as well as for isolated smooth plains filling older craters, and tentative volcanic features. Strom (7), Dzurisin (8) and others suggest that the crater Renoir is embayed by volcanic material; that hypothesis is supported in this analysis. On the incoming side and adjacent quadrangles such as Bach and Michelangelo, domical structures,large sinuous valleys headed in craters, rimless depressions, and flat inundated craters with radiating tectonic features may be sites of past volcanic activity, some of which are quite ancient. Ridges like Mirni Rupes may be, as suggested by Dzurisin(8), fissures along which extensive plains deposits were extruded.

In summary, complex and varied origins are indicated for the plains of Mercury's incoming side. A primordial surface is unlikely. Instead there appears to be a subtle interplay of volcanic and ballistic processes at work: the intercrater plains may represent a volcanic surface interbedded with ballistic ejecta from basins, disrupted by basin secondaries and smaller craters.

References: (1) Trask N.J. and Guest J.E. (1975) J.G.R. 80, 2461. (2) Arthur D.W.G. et al. (1963) Comm. Lunar Planet. Lab 2, 71. (3) McCauley J. F. et al. (1978) Icarus, in press. (4) Schultz P. H. and Gault D.E. (1976) Geol. Rom. 15, 479. (5) Gault D.E. et al. (1975) J.G.R. 80, 2444. (6) Trask N.J. and Strom R.G. (1976) Icarus 28, 559. (7) Strom R.G. et al. (1975) J.G.R. 80, 2478. (8) Dzurisin D. (1978) J.G.R. 83, 4883.

Table 1: Description of the Geological Map of Mercury's Incoming Side

Era	Plains/Crater Class	Brief Description of Materials	% of mapped area covered[a]
Post-Caloris	P1	Very smooth plains material	0.95 (0.01,0.94)[b]
	C1	Fresh and/or rayed craters	1.3[c]
	P2	Smooth plains material where thick, rougher where thin, burying rough topography	9.3 (3.3,6.0)
	C2	Moderately fresh craters	5.4
Caloris	P3	Moderately smooth to hummocky plains	14.4 (11.4,3.0)
	C3	Moderately subdued craters, rounded rims	10.0
Pre-Caloris	P4	Moderately rough to hilly intercrater plains	11.4 (9.8, 1.5)
	C4	Subdued, dissected craters	12.5
	P5	Very rough, knobby and pitted plains	18.6 (18.5,0.1)
	C5	Highly subdued craters	7.6
	C5'	Ancient circular depressions; vague rims	10.5
	Hilly and Lineated	Hilly and lineated material, large massive hills and troughs	0.06

a. Total mapped area $A = 1.0284 \cdot 10^7$ km^2

b. In parentheses are % area of exterior and interior plains, respectively.

c. Crater area percentage $= \Sigma(\pi D^2 N \cdot 100)/(4A)$ for each crater class over all diameter bins of geometric mean bin size $D \geq 40$ km, N craters per bin.

LUNAR & MARTIAN CRATER CLASSES. A. Woronow, Lunar & Planetary Lab, U. of Az., Tucson, AZ

Monte Carlo simulations of crater-degradation classes underscore the need to match classification criteria to the type of process being studied. Analysis of the crater classes in the new LPL Lunar Crater Catalog implies that the differences in the slopes of the size-density curves for all craters and for only the 'fresh' craters result largely from artifacts in the classification criteria. Interpretations of an episode of large-scale crater obliteration on Mars also result from an artifact introduced by the incongruencies of the crater classification scheme used in collecting the data and the scheme assumed during analysis.

MODELING TECHNIQUES: The modeling technique uses a simple Monte Carlo procedure. Random crater diameters (8 to 256 km) are generated from a continuous size-frequency distribution similar to that of the lunar highlands (5,6). Random crater centers are generated from uniform distributions in X and Y. Each crater is subject to obliteration of some or all of its rim by overlapping craters. Simultaneously, crater degradation and obliteration may occur by infilling at a rate specified by the ratio of sedimentation to production rates.

FRESH LUNAR CRATERS: Unlike many crater-degradation classifications, the new LPL Lunar Crater Catalog employs a simple set of criteria: rim sharpness and continuity. Only rarely is a crater lacking a continuous rim classified as 'fresh', or Class 1; with Class 2 craters only slightly more degraded. Our model examines only 'fresh' craters, functionally defined as having >97% of their rims intact and lying beyond a rim-to-rim distance of one half the radius of every subsequent crater (a conservative allowance for proximity weathering).

Figure 1 shows three crater curves for the lunar highlands and the simulation results. The all-classes curve approximates the corresponding highlands' curve, and the curve of the fresh craters has a subdued structure similar to that of the Class 1 plus Class 2 curve. The density of the model's fresh craters exceeds the observed value but could be reduced by enhancing the extent of proximity weathering. Nonetheless, this simulation demonstrates that the criteria of rim continuity biases the fresh-crater curve away from the production function by decreasing its mean slope. Also, Anytime crater overlap actively degrades craters, crater-class curves can not be parallel. Furthermore, the individual crater classes, across diameter bins, do not represent a homogeneous time sample.

MARTIAN EROSIONAL HISTORY FROM THE CRATERING RECORD: From the works on martian cratering and eroision histories (2,3,4), an episode of very active crater obliteration would seem established. This interpretation devolved from crater-class models wherein all crater degradation and obliteration resulted from only crater filling; superposed impacts were ignored.

Our approach includes crater obliteration by overlapping impacts as well as by filling. The crater classes are based on percentages of fill given by (2). Unlike previous studies, the production function for the lunar highlands was used rather than a simplified power function (5,6).

Constant Filling Rate: Under a contant filling rate, a crater forms, slowly fills and progresses through Classes I to IV, and ultimately disappears. However, if superposed impacts obliterate it first, the crater might never reach the later classes, causing not only class-occupancy percentages unlike those deduced by (2,3,4), but also nonparallelism of class curves at densities appropriate to the martian highlands.

Within the allowable range of S (i.e., where the observed crater densities can be reached) few similarities exist between the present results (Fig 2) and those of previous studies which neglected crater obliteration by overlap. Furthermore, the size-frequency curves of 'fresh' craters defined on the basis of rim continuity (Fig 1) do not resemble the curve for 'fresh' craters defined on the basis of percentage filling (Fig 2); therefore, these classification criteria are not interchangeable for purposes of surface histories studies. The previous studies (2,3,4) did not fully appreciate this constraint when redefining their classes from selections of original the criteria (1).

Variable Filling Rate: Figure 3 shows the results from the variable-rate model as suggested by (2). The realizable region lies to the left of S=5600. There both the general shapes of the curves and their relative order mimic those in the constant-rate model. Size-density plots are also similar. Although the actual class-occupancy percentages differ, we do not believe that a cataloguer could assign craters to percentage-of-fill classes accurately enough to distinguish reliably between these two models. Furthermore, other plausible models are also likely to yield ranges of S where the curves could not be distinguished confidently from these. Deduction of precise depositional histories seems beyond the capability of these simple treatments of degree-of-filling classes.

The large differences between models which include overlap obliteration and those which do not, plus the insurmountable difficulties of percisely measuring degree of fill, lead us to conclude that an erosional episode on Mars has as yet not be demonstrated from the cratering record.

REFERENCES: (1) Arvidson, R.E. *Icarus*, *22*, 264, 1974. (2) Chapman, C.R., *Icarus*, *22*, 272, 1974. (3) Chapman, C.R. & Jones, K.L. *Ann. Rev Earth Planet. Sci.*, *5*, 515, 1977. (4) Jones, K.L., Ph.D. Thesis, Brown Univ., 1974. (5) Strom, R.G. & Whitaker, E.A. NASA TM X-3364, 194, 1976. (6) Woronow, A., *Icarus*, *34*, 76, 1978.

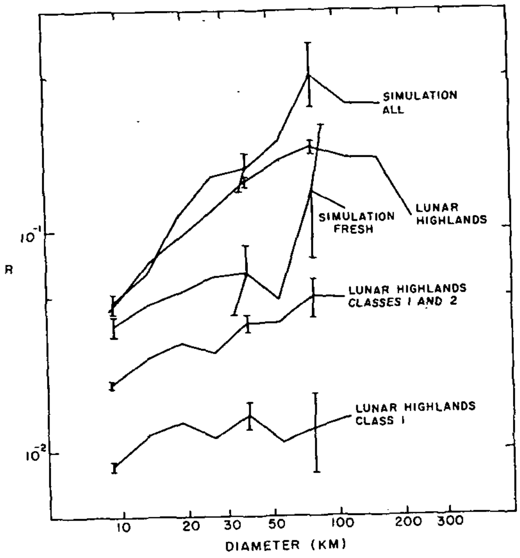

1. Size-density distribution of lunar craters and model results for rim-continuity classes.

2. Results of constant-filling-rate model giving percent of 8-8/2 diameter craters in each class as a function of S, the average thickness (km) of deposition between formation of sucessive 8-8/2 km craters.

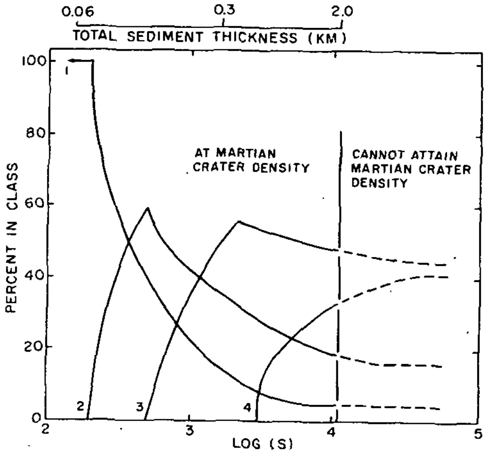

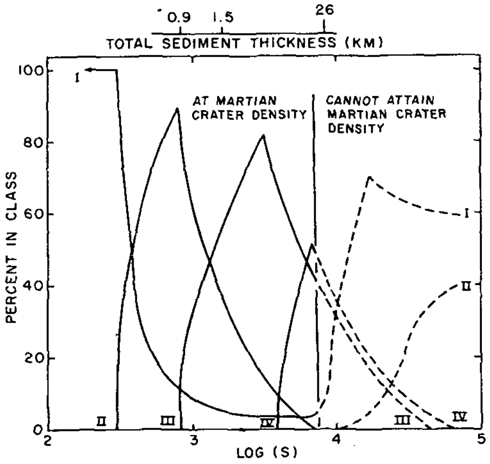

3. Results of variable-filling-rate model using the time variations given by (1). S is the initial filling rate.

Lunar Central Peak Basins: Morphology and Morphometry in the Crater to Basin Transition Zone.

Wendy Hale and James W. Head, Dept. of Geological Sciences, Brown Univ., Providence, RI 02912.

Studies of the morphometric relationships which characterize craters and basins on the Moon can provide important clues to their formational mechanisms. Previous workers have described the morphology and morphometry of craters[2,3,4,5] and basins[1,8] and proposed a transition from the former to the latter at a diameter range of 150-250 km.[1,3,7] Two central peak basins, Compton and Antoniadi, which occur in this range have been described as transitional forms having some of the characteristics of both craters (central peaks) and basins (peak rings).[1,3,8,9] The purposes of this study are to 1) closely examine all central peak craters in the 140-250 km diameter range *in an attempt to identify other central peak basins, and 2) determine more* precisely the morphology and morphometry of the transition from central peak craters to peak ring basins.

Two previously established data sets were used as baselines for this study: 1) twelve peak ring basins recognized by Head[1] were used to define the linear relationship between rim crest diameter (D_{rc}) and peak ring diameter (D_{pr}); 2) 175 fresh craters with prominent central peaks of Imbrian and later age were used to define the relationship between D_{rc} and central peak region diameter (D_{cp}). Besides Compton and Antoniadi, only six craters of Imbrian age above 140 km diameter have been photographed at high enough resolution for *detailed study (Table 1).*

1) Additional Central Peak Basins - Close examination of the six Imbrian age craters in the proposed transitional zone revealed that two of the largest, Tsiolkovsky and Aitken, have been flooded by mare material and, perhaps due to this, show no evidence at present of a peak ring. Sklowdowska, at 140 km diameter, does not show a ring but does have several small knobby areas oriented circumferentially to its peaks. However, the largest crater in this group, Petavius (D_{rc}=188 km), does display a subdued ring surrounding a large, complex central peak. This ring has a median diameter of 65 km, and is 80-90% complete. The two remaining craters in this group, Hausen and Keeler, both display prominent central peaks partially encircled by arcuate patches of knobby material and scattered peaks. These form the subdued beginnings of peak rings. Therefore three new central peak basins with subdued rings, Hausen, Keeler and Petavius, are tentatively identified.

2) Morphology and Morphometry of the Transition - There is a linear relationship between D_{cp} and D_{rc} for fresh craters between 17-175 km diameter, defined as D_{cp}=.259-2.57 (Figure 1). An analogous relationship exists between D_{rc} and D_{pr} for peak ring basins, defined as D_{pr}=.58 D_{rc}-23.88 (Figure 1). These two relations are quite clearly different, the lines displaying markedly different slopes. A projection of the basin line to small diameters yields an intersection with the crater line at approximately 65 km, a point where central peaks are the only interior structures observed. Transitional forms are not apparent here, but are first observed at a diameter almost 100 km greater, in the central peak basin Antoniadi. The diameter range where central peak basins occur is here considered to define the transition zone from

craters to basins. Plotting the median diameter of the rings versus D_{rc} for the five basins reveals that they fall between the primary crater and basin lines (open circles, Figure 1). Here, the basins having the most prominent rings, Antoniadi(a), Compton(c) and Petavius(p) plot closest to the basin line while those with more subdued rings, Hausen(h) and Keeler(k), plot further away. For comparison, the diameter of the central peak regions for these five basins are also plotted on Figure 1 (triangles). The peaks of Hausen and Keeler, which have subdued rings, are anomalously large for their rim crest diameters, plotting well above the central peak line. Conversely, the peaks of Antoniadi, Compton and Petavius are anomalously small by comparison and these three basins have more prominent rings. Antoniadi is the extreme in both cases, having the smallest peak and the most prominent ring.

Discussion and Conclusions - The lines which define the D_{cp}-D_{rc} relation for craters and the D_{pr}-D_{rc} relation for basins show markedly different slopes and do not intersect in the diameter range of 140-180 km, where transitional central peak basins occur. Two such basins, Compton and Antoniadi, were previously recognized.[1,3,8,9] Examination of all Imbrian and younger age craters within this range has led to the identification of three additional central peak basins, Hausen, Keeler and Petavius. Plotting the median diameter for the peak rings of these central peak basins (Figure 1, open circles) shows that they group together and fall between the crater and basin lines. A plot of D_{cp} vs. D_{rc} for the five basins shows anomalously large peaks for those with subdued rings and anomalously small peaks for those with prominent peak rings (Figure 1, triangles). No evidence of peak evacuation, such as a central pit of increasing size, or an increasingly complex central peak, was observed.[8]

Previous models for the transition from central peak craters to peak ring basins have proposed a simple change from one to the other, with single peaks being gradually replaced by clusters, arcs and finally rings.[8,9] However, no evidence of such a gradual change in morphology is observed. Instead, the existence of two different linear relationships for the primary interior morphologies of craters and basins, coupled with a lack of a gradual merging of the two lines at diameters where transitional morphologies are seen, argues for an abrupt, complex transition in formational style between 145-190 km diameters.

CRATER/BASIN PARAMETERS

Name	Lat/Long	Age	D_{rc}	D_{cp}	D_{pr}
Sklowdowska	18S,96E	Imbrian	140	26	--
Aitken	17S,173E	Imbrian	156	31	--
Hausen*	65S,88W	?	175	50	65
Keeler*	10S,1 2E	Imbrian	175	56	68
Tsiolkovsky	20S,129E	Imbrian	181	37	--
Petavius*	25S,60E	Imbrian	188	36	78

*Newly recognized basins

TABLE 1.

References: [1]Head J.W. (1977) Impact and Explosion Cratering, p. 563. [2]Pike R.J. (1977) Impact and Explosion Cratering, p. 489. [3]Wood C.A. and Head J.W. (1976) PLSC7, p. 3629. [4]Wood C.A. and Andersson L. (1978) PLSC9, p. 1267. [5]Hale W. and Head J.W. (1979) LPSX, p. 491. [6]Dence M.R. and Grieve R.A.F. (1978) LPSX, p. 292. [7]Head J.W. (1978) LPSX, p. 485. [9]Hodges C.A. and Wilhelms D.F. (1978) Icarus 34, 294. [9]Hartmann W.K. and Wood C.A. (1971) The Moon 3, 3.

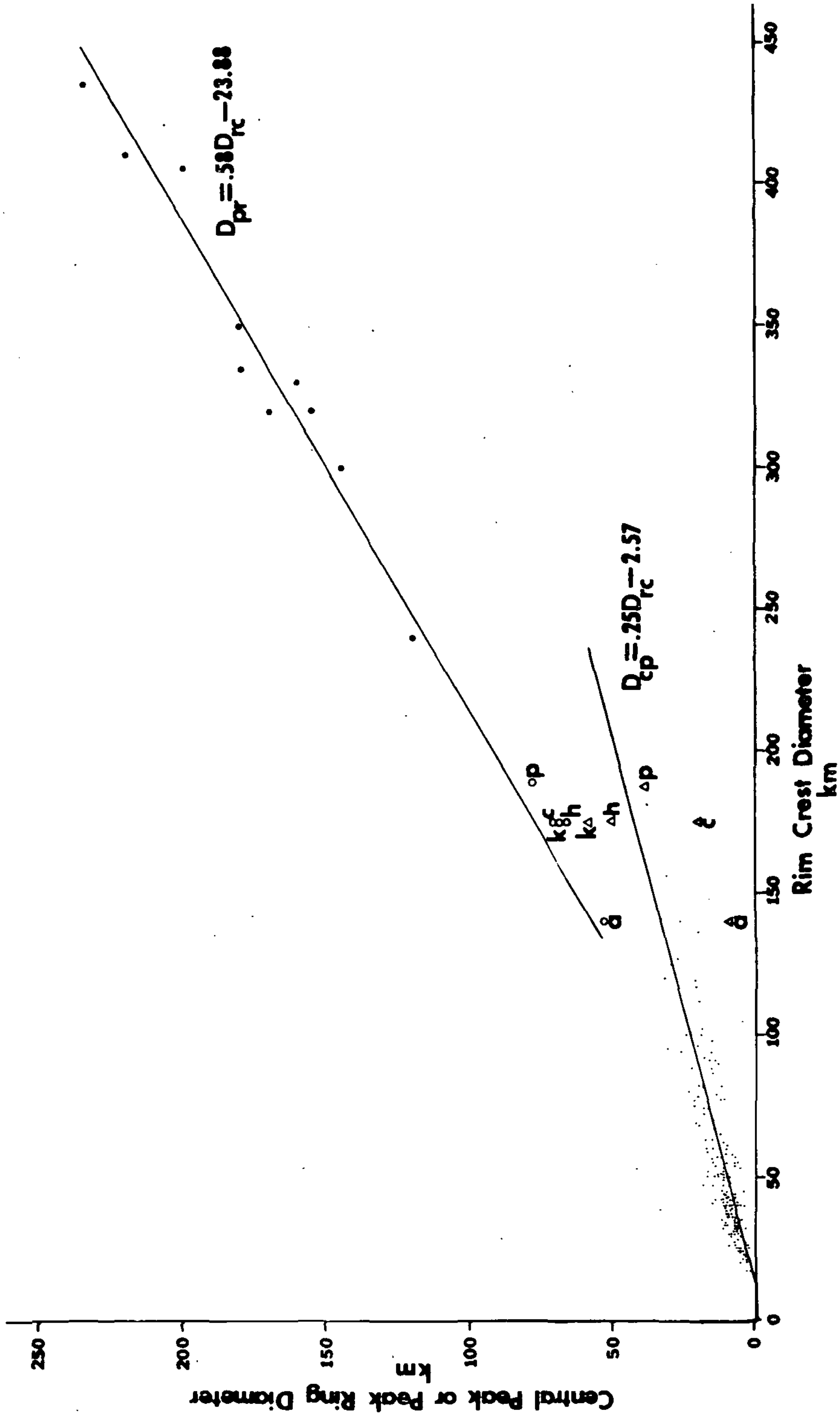
$D_{pr}=.58D_{rc}-23.88$
$D_{cp}=.25D_{rc}-2.57$
Central Peak or Peak Ring Diameter
km
Rim Crest Diameter
km
0
50
100
150
200
250
300
350
400
450
k
h
p
t
a

Figure 1.

Impact melts associated with the formation of the lunar crater Tsiolkovsky.

J.L.Whitford-Stark, Dept. of Geological Sciences, Brown University,Providence,R.I.,02912, and B.R.Hawke,Institute for Astronomy,University of Hawaii,2680 Woodlawn Dr.,Honolulu, Hawaii,96822.

Tsiolkovsky is an 192km diameter,Upper Imbrian aged(1) crater of impact origin, located on the farside of the Moon.The impact event was followed by the eruption of basaltic lavas which occupy the floor of the crater. These basalts are possibly similar to the Apollo high titanium basalts(2) but appear to be 300m or less in thickness.

The ejecta from Tsiolkovsky has a markedly asymmetric distribution, being preferentially deposited to the southeast of the crater. Employing the relationship:-

$$t = 0.14 R^{0.74} (r/R)^{-3.0} \qquad (3)$$

where t is the thickness of ejecta at a radial range (r) from the center of a crater of radius(R), all in meters, the ejecta has a thickness of about 650m near the crater rim and a thickness of 50m at a distance of 120km from the crater rim. The asymmetry of the ejecta and the offset of the central peak from a central location within the crater lend support to the hypothesis(4) of an oblique impact for the origin of Tsiolkovsky.

Abundant melt deposits created by the impact event,in addition to the ejecta, can be recognized in and around Tsiolkovsky using previously established(5,6) criteria. On the parts of the crater floor that remain unflooded by basalt, these melts are identified as ponded materials and as areas draped with a thin, hard rock veneer. Numerous melt ponds can be seen on the crater walls and are particularly abundant on the eastern wall.Melt ponds and veneers exterior to the crater rim are again preferentially distributed around the eastern and southern parts of the crater, again supportive of an oblique impact origin for the crater.The melt ponds to the southeast of the crater occur at a maximum distance of 30 to 55km(0.31 to 0.57R, where R is the crater radius) from the rim crest. In other segments of the crater the melt deposits are generally smaller and occur closer to the rim crest. While melt is not abundant adjacent to the lowest sector of the crater rim crest(west), there does appear to be some correspondance between local rim crest lows and extensive exterior melt deposits. For example, the abundant veneers and ponds to the south of Tsiolkovsky may be related to the low, though irregular, south rim crest of the crater(7).

Flows of impact melt are rare around Tsiolkovsky but can be identified within Waterman crater(7) and Chenier and an adjacent unnamed crater. Chenier lies to the northeast of Tsiolkovsky; the center of Chenier being approximately 35km from the rim of Tsiolkovsky. The formation of Chenier predates that of Tsiolkovsky and Chenier lies well within the range of the Tsiolkovsky continuous ejecta blanket. This is evidenced by the intense modification of the morphology of Chenier crater by the Tsiolkovsky ejecta and the absence of a recognizable Chenier ejecta blanket. The southwest wall of Chenier, that is , the part of the wall nearest to Tsiolkovsky, is lower than the rest of the crater wall. In fact there is a broad low region between Chenier and Tsiolkovsky. The southeastern wall of Chenier exhibits a linear surface pattern and these linears can be traced to the outside, Tsiolkovsky-facing, wall of the crater. These linears are in direct line with the two flow lobes on the floor of Chenier.

The two flow lobes within Chenier, interpreted as impact melt ejected from Tsiolkovsky, are 8.7km and 14.7km in length and 1.5 to 2.3km and 3.0 to 5.0km respectively,in width. The smaller flow has a maximum thickness of 100 to 150m and the larger flow an average thickness of 30m.These flow lobes stratigraphically overlie the Tsiolkovsky ejecta blanket and thus represent the last stage in the emplacement of material from the Tsiolkovsky impact event.

Hawke and Head (6) have proposed that at the end of the excavation stage of a cratering event the transient cavity is lined with shock-melted material. The next, modification stage, commences with the initial collapse and rapid shallowing of the transient cavity by both wall-slumping and rebound.With continued wall slumping and rebound, some of the molten material lining the floor is removed from the cavity in a direction commonly opposite the area of maximum wall slumping and over a topographically low portion of the crater rim.

The flows in Chenier lie opposite a collapse terrace with surface dimensions of 30 x 8km located on the southwestern interior wall of Tsiolkovsky. The collapse of this terrace was a late event in the modification stage of the evolution of Tsiolkovsky as is evidenced by the morphology of its upper surface being typical of the surface morphology normally found exterior to the crater rimcrest. The collapse of this terrace could have been responsible for the emplacement of the Chenier flow lobes. The collapse of a similarly-sized (30 x 5km) terrace with a similar surface morphology, located on the north interior wall of Tsiolkovsky, may have been responsible for the emplacement of the melt flows developed within the crater Waterman to the south of Tsiolkovsky. This scenario of an oblique impact from the NNW together with late wall slumping can explain the occurence of melt ponds, veneers, and flows developed on the Tsiolkovsky floor and walls and the similar features developed exterior to the crater within a short distance of the rim crest.

References:

1)Wilhelms,D.and El-Baz,F.(1977) U.S.Geol.Surv.Map I-948.
2)Metzger,A.E. et al (1977) Proc.Lunar Sci.Conf.8th,p.949-1000
3)McGetchin,T.R. et al (1973) Earth Planet.Sci.Lett.20,226-236
4)Guest,J.E. and Murray,J.B.(1969) Planet Sp.Sci.17,121-141
5)Howard,K.A. and Wilshire,H.G.(1975) J.Res.U.S.Geol.Surv. 3,237-251.
6)Hawke,B.R. and Head,J.W.(1977) Impact and Explosion Cratering p.815-841.
7)El-Baz,F. and Worden,A.M.(1972) Apollo 15 Preliminary Science Report, p. 25.1 - 25.27.

Strangways Impact Structure, Northern Territory, Australia: Basic Geology

D. J. Milton	U.S. Geological Survey 928, Reston, Va. 22092
John Ferguson	Bureau of Mineral Resources, Box 378, Canberra City A.C.T. 2601
Robin Brett	National Science Foundation, Washington, D.C. 20550
M. R. Dence	Earth Physics Br., Dept. of Energy, Mines and Resources, Ottawa, Ont. KIA 0Y3
C. H. Simonds	Northrop Services Inc., Box 34416, Houston, TX 77034
S. R. Taylor	Research School of Earth Sciences, Australian Natl. Univ., Box 4, Canberra, A.C.T. 2600

As a first stage in a geological-geochemical study of this previously barely known impact structure, a geologic map has been prepared by a series of Landrover traverses supplemented by photogeology. The disturbance, centered near 15°12'S, 133°35'E, is in a region of faulted and gently folded quartzites and siltstones of the Middle Proterozoic Roper Group. The margins of extended areas of Cambrian, Cretaceous, and Cenozoic strata each pass near the site. Flat-lying Cretaceous sandstone conceals about a quarter of the structure. Middle Cambrian limestone, poorly exposed and near the edge of the structure, probably but not certainly postdates the disturbance.

The basic structure is the core-and-collar type known from the Vredefort Ring. The core, about 10 km in diameter, consists of basement rock, mainly granitic gneiss, which otherwise does not crop out within 100 km and should lie at a depth of over 1 km. The ground surface is a plain that approximates the base of the melt layer -- most exposures are of breccia, generally highly shocked, melt rock is common, unbrecciated bedrock was not definitely identified. A drill hole sited on a 15 m hill started in vesicular melt rock with less than 5 percent clasts and bottomed at 30 m in melt with about 60 percent clasts. Melt at most occurrences appears (to hand lens study only) to be derived from basement and to contain basement clasts; some also contains clasts from the Roper. Drill core from a shallow hole near the basement-Roper contact shows clasts of quartzite, presumably from the ∿ 200 m thick basal unit of the Roper, in a melt that may derive from siltstones even higher in the section.

The collar, generally about 5 km wide, consists of Roper Group quartzites and siltstones in alternating ridges and valleys. In some sectors quartzite units extend outward from a vertical or steeply dipping outward-facing root zone into a flap that overlies the succeeding siltstone. The lowermost quartzite is largely autochthonous breccia in the root zone (megaclasts retaining their attitude among unoriented small clasts) and unoriented breccia in the flaps. Brecciation is minor in the higher quartzites -- some of the flaps are flat-lying and look almost undisturbed except that they are upside down. In one sector a flap of an outer quartzite extends over 3 km from the root zone to a distance of nearly 12 km from the center. This is probably about the radius of the disturbance; the difficulty of distinguishing milder impact-related deformation from pre-impact and possible but unproven post-impact deformation leaves the outer limits ill defined. Shatter fracturing, more commonly expressed as intersecting sets of striated cleavage surfaces rather than as well-formed cones, is well displayed in the inner quartzites but poorly developed both toward the outside of the collar and in the gneiss.

The flaps must have formed in open space. They suggest the rim flap of Meteor Crater, but they occur one within another, each essentially at the same elevation as the base of the melt layer. They may be features of the floor of the transient cavity. It is very unclear how to reconstruct the crater profile, but uplift of the floor at Strangways and other large terrestrial impact structures may have caused the craters to be much more subdued features than lunar craters of comparable diameter.

LUNAR BASINS — HOLES IN SEA ICE ON A MAGMA OCEAN. T. R. McGetchin[1], J. W. Head[2], and P. H. Schultz[1]. [1]Lunar and Planetary Institute, Houston, Texas; [2]Department of Geological Sciences, Brown University, Providence, Rhode Island.

The formation of large impact basins on the moon terminated approximately 3.9 b.y. ago, 0.6 b.y. after the formation of the moon. There is a strong consensus that the moon developed its crust from a deep circum-lunar magma ocean by a process of feldspar segregation. The rate of crustal growth was probably similar to that on terrestrial lava lakes (Peck et al., 1977; Herbert et al., 1977; Solomon and Longhi, 1977; Peck, 1978). Solutions for (conduction dominated) crustal growth generally are of the form $d=kt^{1/2}$, where k is near the lava-lake value of 0.01, d is crustal thickness (in km), and t is time (years). Although there is considerable disagreement about the meaning and dimensions of the transient cavities associated with craters and basins, we wish to make the simple point that the most conservative estimates of the transient cavity diameter approach the thickness of the lithosphere as shown in Table 1.

Table 1. Lunar basins.

	Diameter D	D/L_{max}
Orientale	390	1.6
Imbrium	670	3.1
Crisium	450	1.8
Humorum	420	1.7
Nectaris	400	1.6
Serentatis	310	1.3
Fecunditatis	240	1.0
Tran W	280	1.1
Tran E	240	1.0
Nubium	360	1.5

D, after Short and Forman, 1972 (represents a possible minimum value for basin diameter).

L_{max} represents maximum lithospheric thickness using $L=\alpha t^{1/2}$, $\alpha=0.01$ where L is in km and t is 0.6 b.y.

There is building evidence from both samples and the photographic record that extensive basaltic volcanism pre-dated at least the Orientale and most likely the Imbrium basins (Schultz et al., 1979). Consequently at the time of formation of many impact basins, the moon was probably a "layered" target — a cool surface layer (or lithospheric plate) overlying a hot fluid interior. (This configuration has not been extensively explored experimentally.) The minimum ratio (D/L) for most basins was of the order of 1.0 to 3.0; hence, puncturing of the lithosphere by the basin-forming events was likely, if not certain. Post-excavation structural effects should be more akin to failure of a plate than cratering in a half-space, perhaps as theoretically described by Melosh and McKinnon (1978). We are intrigued by the possible similarities between the geometry (and physical property contrasts) of impacts into the early lunar crust and cratering in sea-ice. In particular, cratering experiments in sea ice may provide analogies for basin formation on the planets, and perhaps permit identifying the conditions of the early crust during basin formation.

Finally, it is likely that the ultimate global seismic effects of the basin impacts is deposition of the heat in the magma ocean which should trap the energy because of its wave-guide like structure, namely low acoustic impedence material (melt) between higher values above and below. For example, if most of Imbrium's energy is ultimately deposited in the magma ocean by this process, it could raise the average temperature several degrees.

References

Hartmann W. K. (1971) Moon — origin and evolution of multi-ring basins. The Moon 3, 3-78.

Herbert F., M. J. Drake, C. P. Sonett, and M. J. Wisherchen (1977) Some constraints on the thermal history of the lunar magma ocean. Proc. Lunar Sci. Conf., 8th, 573-582.

Melosh H. J. and W. B. McKinnon (1978) The mechanics of ringed basin formation. Geophys. Res. Lett. 5, 985-988.

Peck D. L. (1978) Cooling and vesiculation of Alae Lava Lake, Hawaii. Geol. Surv. Prof. Pap. No. 935-B, 59p.

Peck D. L., M. S. Hamilton and H. R. Shaw (1977) Numerical analysis of lava lake cooling models: Part 2, application to Alae Lava Lake, Hawaii. Am. J. Sci. 277, 415-437.

Schultz P. H., P. D. Spudis, and D. L. Sellers (1979) Evidence for ancient lunar basalts (Abstract). In Lunar and Planetary Science X, Lunar and Planetary Institute, Houston, p. 1084-1086.

Short N. M. and M. L. Forman (1972) Thickness of impact crater ejecta on the lunar surface. Modern Geol. 3, 69-91.

Solomon S. C. and J. Longhi (1977) Magma oceanography: 1. Thermal evolution. Proc. Lunar Sci. Conf., 8th, 583-599.

MARTIAN ABSOLUTE TIME SCALES

G. Neukum, K. Hiller,
J. Henkel, Institut für Allgemeine und Angewandte Geologie,
Ludwig-Maximilians-Universität, 8000 München 2, W-Germany

Introduction: Very different martian absolute cratering chronologies had been proposed in the literature, as reviewed by Neukum and Wise (1976) (1). The application of these different model chronologies resulted in substantially different histories of the martian crust. Recently, the reevaluation of the problem of the ratio of martian to lunar impact rates and of the problem of the relationship of the lunar cratering chronology to the martian one has led to a revision in some models (Soderblom, 1978 (2); Hartmann, 1978 (3)). These changes have resulted in a shift of martian history toward older ages. The magnitude of the changes and the remaining differences in the models will be discussed as well as the reasons for the discrepancies in the models.

The martian impact crater production size-frequency distribution:

This distribution was first determined by Neukum and Wise (1976) (1) in the size range 1 km $\le D \le$ 20 km. The application of this distribution to measured data allowed the comparison of crater populations of differently sized craters in that size range. A common problem on Mars, however, appears in the determination of relative ages by crater statistics of younger features, such as the martian shield volcanoes: Statistically meaningful measurements can often only be made in the size range $D <$ 1 km. Thus, the knowledge of the distribution in that size range is necessary for relating crater frequencies to those above $D =$ 1 km. Data by Dial (1978) (4) suggest a law $N \sim D^{\alpha}$ for $D <$ 1 km (N = cumulative crater frequency), where $\alpha \approx -3$. We found a similar relationship with α close to -3.4 for $D <$ 1 km. Above 1 km crater diameter the distribution flattens (1). Our currently best estimate for the martian production size-frequency distribution("standard distribution") in the size range 0.3 km $\le D <$ 30 km is given in Fig. 1 in comparison with other laws found in the literature (Masursky et al., 1977 (5); Hartmann, 1973 (6)). It is identical with the distribution given by Neukum and Wise (1) for the size range $D \ge$ 1 km. The -2 distribution is a moderately good approximation for $D >$ 2 km, but not applicable for $D <$ 2 km. Since most younger martian surface features show only statistically meaningful crater frequencies for $D <$ 2 km, this distribution is of little use in age determination and its application would lead to gross errors. Even above $D =$ 2 km, a -1.8 distribution would fit the data better.

The distribution termed average lunar mare (here shifted vertically to take out age differences) fits the martian production size-frequency distribution well in the size range $D < 2$ km. It would lead to gross errors if applied in the size range $D > 2$ km, which is the range where statistically meaningful data are obtained in older martian areas such as the martian highlands or the older plains.

Our data and all other data extracted from the literature and reported here have been reduced in the same way by applying the "Mars standard crater curve" displayed in Fig. 1. It is proposed to other workers in the field to make use of this curve as a reference distribution in the future, in order to arrive at meaningful interpretations of the crater statistics data from different size ranges and to allow intercomparison of the data sets of different workers.

Absolute cratering chronologies: According to recent revisions or corrections of their cratering chronologies by Soderblom (1977) (2) and Hartmann (1977, 1978) (3, 7), we have made use of those data again and applied our methods to the updated chronologies as outlined above, in order to make comparison with our data and intercomparison of theirs possible. The result is displayed in Fig. 2. Both Soderblom's and Hartmann's chronologies nearly coincide with ours for ages $> 3{,}5 \cdot 10^9$ years, but there still remain considerable differences for the more recent times. The discrepancies have, however, come down considerably, and all martian time scales, ours and theirs now lie within less than a factor of 3 of our lunar curve. This is due to the fact that all martian time scales are now based on the assumption that the lunar and martian impact rates are nearly the same as suggested by Soderblom et al. (1974) (8) first and supported by Neukum and Wise (1976) (1). (Additionally Soderblom's correction of his lunar data (2) has been taken into account). The remaining differences largely originate in differences of the *lunar* chronologies of the different authors or in problems of methodology. This is illustrated in Fig. 3 for Soderblom's data. Soderblom's data have been transferred to martian conditions as shown in Fig. 2 in starting from his lunar D_L data (Soderblom and Boyce, 1972 (9)) and using the law $D_L \sim N$ for conversion of the D_L data to crater frequencies given by (9). Soderblom's and Boyce's (9) lunar chronology for this case of conversion is given by curve 2) in Fig. 3. If we use the same law $D_L \sim N$ but normalize *to our Apollo 14 data, the result would be curve 3) in Fig. 3.* Recently we have shown that the law $D_L \sim N$ does not hold but a law close to $D_L \sim N^{0.6}$ appears correct in most cases (10). Application of this relationship leads to curve 4) in Fig.3. Those examples illustrate the fact that the remaining discrepancies between the different Mars cratering chronologies are due either to differences or inconsistencies in the *lunar* data or to methodologic problems. The discrepancies can only be resolved in the future if the lunar data are reexamined and if the methodologic differences are reduced.

References: (1) Neukum and Wise (1976) Science 194, 1381. (2) Soderblom (1977) Impact and Explosion Cratering (Pergamon) 629. (3) Hartmann (1978) JGR 5, 450. (4) Dial (1978) NASA Technical Memorandum 79729, 179. (5) Masursky et al (1977) JGR 82,4016. (6) Hartmann (1973) JGR 78,4096. (7) Hartmann (1977) Icarus 31, 260. (8) Soderblom et al.(1974) Icarus 22, 239.(9) Soderblom and Boyce (1972) NASA AP-315,29-3. (10) Neukum (1977) The Moon 17, 383.

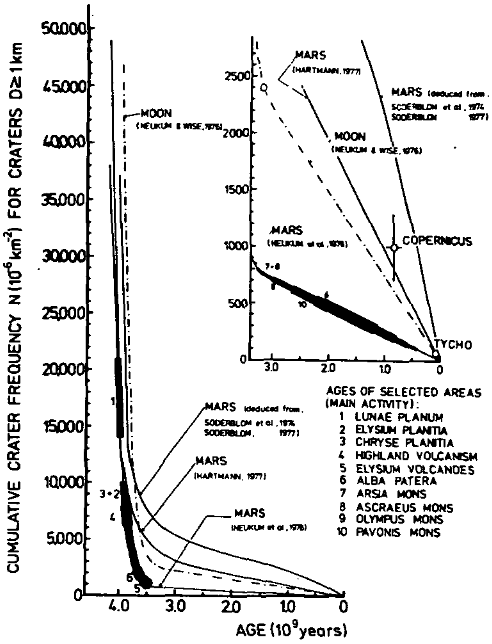

Fig. 2

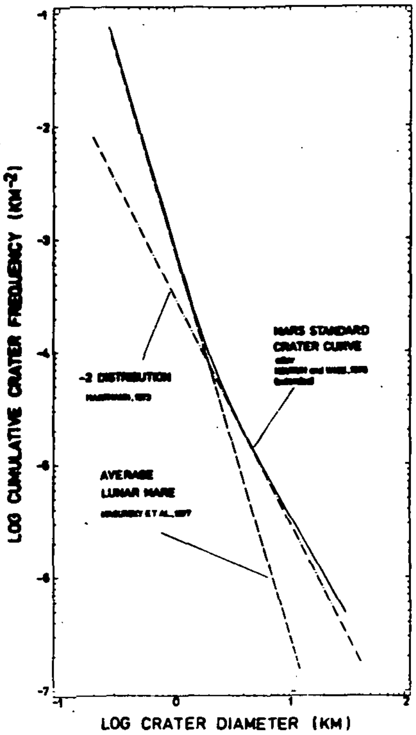

Fig. 1

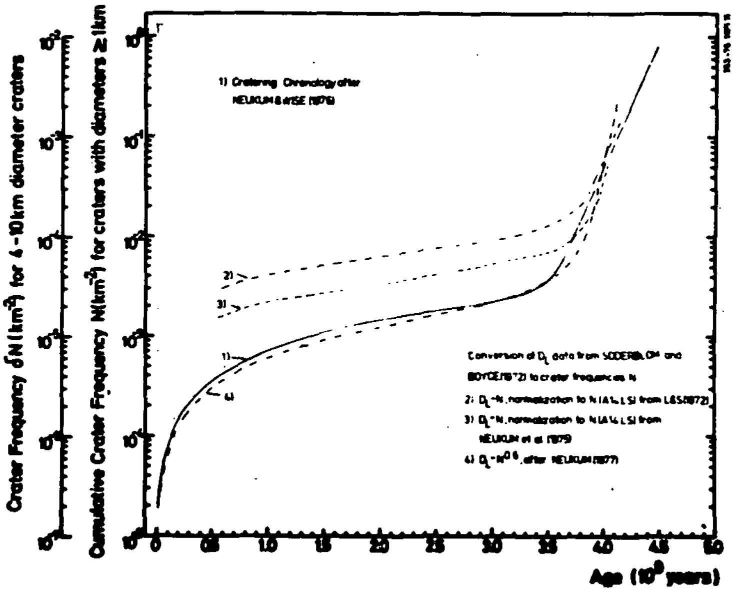

Fig. 3

AGES OF MARTIAN VOLCANOES AND EROSIONAL FEATURES,

K. Hiller and G. Neukum, Institut für Allgemeine und Angewandte Geologie, Ludwig-Maximilians-Universität, 8000 München 2, W-Germany

Recent research has concentrated on the determination of the history of the large martian volcanoes and of erosional features such as the martian channels and the terrain of intense erosion between highland and lowland.

Ages of martian volcanoes: Relative and absolute ages of martian volcanoes based on data from (1, 2, 4, 5, 6, 7, 8) and own measurements are compiled in Fig.1. Three main geologic provinces are distinguished:

- Highland volcanoes (Hadriaca and Tyrrhena Patera)
- Elysium Montes (Elysium Mons, Hecates Tholus)
- Tharsis volcanoes province (Ascraeus Mons, Pavonis Mons, Arsia Mons, Olympus Mons, Tharsis Tholus, Ceraunius Tholus, Alba Patera).

The diagram illustrates a series of findings:

a) Age sequence starts with Highland and Elysium volcanoes and develops towards Tharsis volcanoes. Oldest structures in this region are Alba Patera and the small shields of Tharsis Tholus and Ceraunius Tholus.
b) Surrounding plains and shields of the volcanoes are older than the calderas. This is probably due to the longer activity of the source region and the lack of big parasite craters on the flanks.
c) Relative ages from oldest to youngest differ by a factor of 100, for the Tharsis volcanoes by a factor of 10.
d) Alba Patera shows an extremely long lifespan (crater numbers 2500-180 per 10^6 km^2 for craters ≥ 1 km diameter; after (1) and (3) 3.2 b.y.), much more than the other shield volcanoes.

Ages of martian erosional features: Relative and absolute ages of knobby and chaotic material and of channels and their surroundings based on data from (1, 2, 9, 10, 11) are compiled in Fig. 2. Findings are:

a) Surrounding areas show two main periods of resurfacing activity.
b) Channel formation was prior or partially parallel to second resurfacing activity. Younger areas especially in the mouth of some channels are due to lava flows from the adjacent plains into the channel or to wind erosion.
c) Intensive erosion in the highland/lowland boundary area took place mainly prior or parallel to channel formation (12). After a relatively short and intense peak during the

early geologic history (crater numbers approx. 10000-4000 per 10^6 km^2) activity thinned out rapidly (12) in this area.

Conclusions: According to our relative age measurements, the stratigraphic sequence shows three main groups of events (absolute ages based on (1) and (4):

- First resurfacing in the highland; shield volcanoes in that area; intense erosion of the highland/lowland boundary areas; emplacement of the old plains lavas; erosion of some channels (crater numbers 15000-3000 or 4.0-3.7 b.y.).
- Elysium volcanoes; first activity of Alba Patera; small Tharsis volcanoes; emplacement of younger plains lavas; thinning out of erosional activity in the highland/lowland boundary; bulk of channel formation (crater numbers 3000-800 or 3.7-3.1 b.y.).
- Piling up of the big Tharsis volcanoes; Alba still active; some channel erosion (crater numbers 800-80 or 3.1-0.3 b.y.).

Findings are consistent with tectonic events from (13) and imply global heating during the early history of the planet with melting of subsurface ice und subsequent erosion of the highland scarp and channel formation, and the emplacement of plains lavas. Later activity (crater numbers $\lesssim$ 1000 per 10^6 km^2) was largely limited to the Tharsis area and may document a change in lava chemism.

References: (1) Neukum G. and Wise D.U. (1976) Science 194, pp.1381, (2) Masursky H. et al. (1977) JGR 82, pp. 4016, (3) Neukum G. et al. (1977) NASA TM 79729, pp.172, (4) Blasius K.R. (1976) Icarus 29, pp 343, (5) Carr M. (1976) NASA TMX 3364, pp.152, (6) Carr M. et al. (1977) JGR 82, pp 3985, (7) Crumpler L.S. and Aubele J.C. (1978) Icarus 34, pp.496, (8) Wise D.U. et al. (1978) NASA TM 79729, pp.203, (9) Malin M.C. (1976) JGR 81, pp. 4825, (10) Squyres S.W. (1978) Icarus 34, pp.600, (11) Hiller K. & Neukum G. (1978) NASA TM 79729, pp.91, (12) Hiller K. et al. (1978) Symp. EPGC, Paris, (13) Wise D.U. et al. (1979) subm. to JGR.

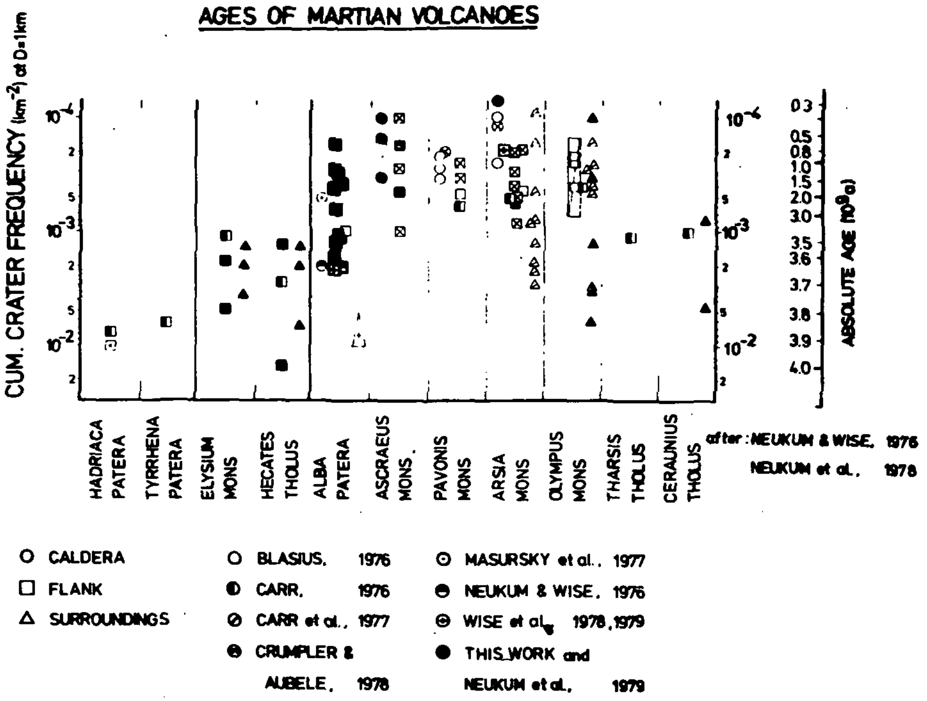AGES OF MARTIAN VOLCANOES
CUM. CRATER FREQUENCY (km⁻²) at D=1km
10⁻⁴
2
5
10⁻³
2
5
10⁻²
2
ABSOLUTE AGE (10⁹a)
0.3
0.5
0.8
1.0
1.5
2.0
3.0
3.5
3.6
3.7
3.8
3.9
4.0
HADRIACA PATERA
TYRRHENA PATERA
ELYSIUM MONS
HECATES THOLUS
ALBA PATERA
ASCRAEUS MONS
PAVONIS MONS
ARSIA MONS
OLYMPUS MONS
THARSIS THOLUS
CERAUNIUS THOLUS
after: NEUKUM & WISE, 1976
NEUKUM et al., 1978
○ CALDERA
☐ FLANK
△ SURROUNDINGS
○ BLASIUS, 1976
◐ CARR, 1976
⊘ CARR et al., 1977
⊛ CRUMPLER & AUBELE, 1978
⊙ MASURSKY et al., 1977
⊖ NEUKUM & WISE, 1976
⊕ WISE et al., 1978, 1979
● THIS WORK and NEUKUM et al., 1979

Fig. 1

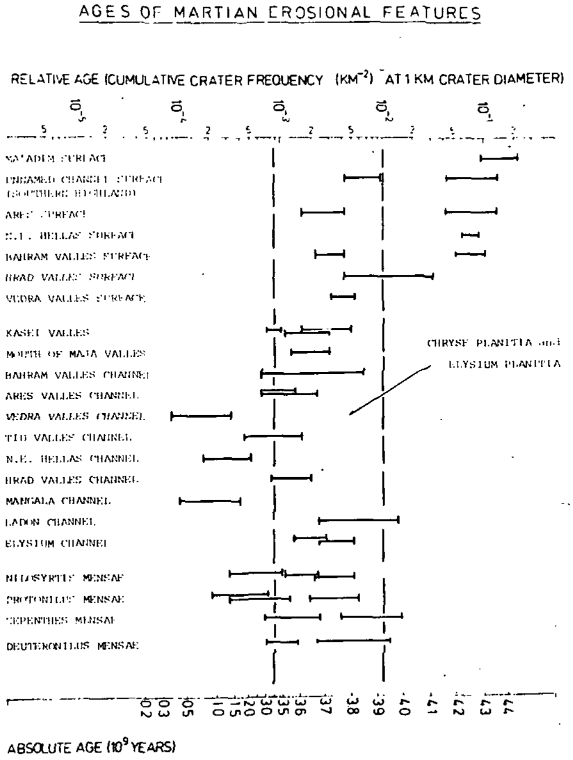AGES OF MARTIAN EROSIONAL FEATURES
RELATIVE AGE (CUMULATIVE CRATER FREQUENCY (KM⁻²) AT 1 KM CRATER DIAMETER)
10⁻⁵
10⁻⁴
10⁻³
10⁻²
10⁻¹
MA'ADIM SURFACE
UNNAMED CHANNEL SURFACE (SOUTHERN HIGHLANDS)
ARES SURFACE
N.E. HELLAS SURFACE
BAHRAM VALLES SURFACE
HRAD VALLES SURFACE
VEDRA VALLES SURFACE
KASEI VALLES
MOUTH OF MAJA VALLES
BAHRAM VALLES CHANNEL
ARES VALLES CHANNEL
VEDRA VALLES CHANNEL
TIU VALLES CHANNEL
N.E. HELLAS CHANNEL
HRAD VALLES CHANNEL
MANGALA CHANNEL
LADON CHANNEL
ELYSIUM CHANNEL
NILOSYRTIS MENSAE
PROTONILUS MENSAE
NEPENTHES MENSAE
DEUTERONILUS MENSAE
CHRYSE PLANITIA and ELYSIUM PLANITIA
.02
.03
.05
.10
.15
.20
.30
.35
.36
.37
.38
.39
.40
.41
.42
.43
.44
ABSOLUTE AGE (10⁹ YEARS)

Fig. 2

Small Fresh Crater Morphometry: A Preliminary Assessment of the Effects of Gravitational Acceleration and Impact Velocity.

Mark J. Cintala, Department of Geological Sciences, Brown University, Providence, RI 02912.

Introduction: Subtle but significant differences exist in the interior morphometry of fresh crater populations on the terrestrial planets. Of special interest is the shape of small, weakly modified craters -- those generally described as bowl-shaped.[1] Although they almost certainly deviate from their pristine shapes at the end of the events which formed them, these craters provide the best available large-scale approximations to the transient cavity at the termination of its growth. It has been known that gravitational acceleration (g) [2,3], impact velocity (V_i) [4,5], and target properties[6] contribute to final crater size and, possibly, morphology.[7,8,9] Insofar as a better knowledge of cavity geometry would greatly aid the study of planetary surface processes and properties, a quantitative description of crater geometry as a function of the variables listed above is a desirable goal of morphometric studies. The purpose of this paper is to investigate the possibilities of describing crater interior morphometry as a function of surface gravity and impact velocity.

Data and Manipulations: The rim-to-floor depth (R_i) of a crater can be divided into the sum of the apparent crater depth (R_a, the depth as measured from the original target surface) and the rim height (R_e); normalized to the rim diameter (D_r), this is

$$\frac{R_i}{D_r} = \frac{R_a}{D_r} + \frac{R_e}{D_r} \tag{1}$$

Gault and Wedekind[10] have derived an empirical expression for eq. (1), namely,

$$\frac{R_i}{D_r} = 0.193 + 0.05\, D_r^{\,0.12}\left(\frac{g}{g_\oplus}\right)^{0.157} \tag{2}$$

The first term on the right-hand side is their [3, 10] gravitationally invariant value for R_a/D_r, while the second term represents R_e/D_r as a function of rim diameter and surface gravity (normalized to the terrestrial gravitational acceleration $g_\oplus$).

It has been suggested [11] that higher impact velocities will force the effective depth-of-burst of the event closer to the surface of the target, thus giving shallower craters. In an attempt to evaluate this hypothesis, table 1 has been constructed. Relationships between R_a and D_r have been derived here for small, relatively unmodified craters by (1.) assuming that the interior geometry for these craters is independent of diameter (that is, they exhibit isometric growth, which implies an exponent of unity in the R_i/D_r and R_e/D_r relationships; see (12)) and (2.) subtracting the resulting expression for R_e/D_r from that for R_i/D_r. If Hartmann's[5] asteroidal impact velocities are used (Table 2) and the experimental evidence for gravity-independent R_a/D_r ratios is assumed to hold for kilometer-scale craters, then a least-squares fit gives

$$\frac{R_a}{D_r} = 0.308V_i^{-0.279} \tag{3}$$

with a correlation coefficient of -0.929. While it is by no means certain that the observed variation of R_a with D_r is due to differences in V_i alone, it appears as though differences in target properties play a minor rôle, in light of essentially constant R_a/D_r ratios[12] for craters on lunar targets which behave differently in other respects.[13] On this basis, it is cautiously suggested that Baldwin's hypothesis is supported by these data.

Rim height information is available for the Moon[14], Mercury[15], Phobos and Deimos[16], and Meteor Crater, Arizona[17]. Rim heights are, in general, comprised of two components: ejecta and structural uplift[18]. A higher value of g would limit the ballistic range of ejecta, thus increasing the ejecta component of the rim topography[19]. Calculations indicate that the fraction of impact energy partitioned into plastic work decreases as a function of increasing impact velocity[20]. For these reasons, an expression similar to eq. (2) for R_e/D_r should include terms for both g and V_i. Use of the values in table 2 gives

$$\frac{R_e}{D_r} = 0.129 \left(\frac{g}{g_\oplus}\right)^{0.208} V_i^{-0.301} \tag{4}$$

with a coefficient of multiple correlation of 0.9895. Finally, addition of equations (3) and (4) yields

$$\frac{R_i}{D_r} = 0.308V_i^{-0.279} + 0.129 \left(\frac{g}{g_\oplus}\right)^{0.208} V_i^{-0.301} \tag{5}$$

Discussion. The rather high values of the correlation coefficients belie the uncertainties in the derivation above. First, the terrestrial contribution to the least-squares fits is a single data point, which cannot be taken as representative of all terrestrial craters with statistical certainty. Second, morphometric measurements of craters on the martian moons is beset with difficulties arising from the highly irregular shapes of the two bodies; these values must be treated as approximations only.[16] Third, while considerable effort went into their derivation[5], the impact velocities in table 2 are model-dependent, thus imposing their ultimate fate upon that of eq. (5). Fourth, the impact velocities used are for Hartmann's asteroidal sources only; should the major fraction of crater-forming projectiles encountering these bodies be cometary, substantial revision would be required. Finally, no allowance was made for projectile/target coupling efficiencies. Since the initial energy partitioning of an impact event is dependent on projectile and target properties,[21, 22], the effect of this aspect of the cratering physics is uncertain.

Equation (5) is useful, however, in demonstrating the decreasing efficiency of the cratering process with increasing impact velocity; irreversible process [21,22] and, possibly, shallower effective depths of burst[11] should cause smaller and shallower apparent craters than for similar energy but lower velocity impacts. (This would imply larger average volumes of impact melt at craters with smaller R_a/D_r ratios.) Equations (1) and (5) also illustrate the growing contribution of R_e to the total crater depth.

It should be noted that this equation is intended to hold only for those craters described reasonably well by the least-squares approximations with slopes of 1. Larger craters falling along distributions with shallower slopes have usually undergone post-excavational modification.[23]

Table 1. Rim-to-floor depth (R_i), rim height (R_e), and derived apparent depth (R_a) vs. rim diameter (D_r) relationships used in deriving equations (3), (4), and (5).

PLANET	$R_i:D_r$	$R_e:D_r$	$R_a:D_r$	REFERENCE
Moon	$R_i = 0.196D_r^{0.010}$	$R_e = 0.036D_r^{1.014}$	$R_a = 0.160D_r$	14
Mercury	$R_i = 0.176D_r^{0.980}$	$R_e = 0.043D_r^{1.005}$	$R_a = 0.133D_r$	15
Phobos/ Deimos	$R_i = 0.2D_r$	$R_e = 0.017^{0.975}$	$R_a = 0.183D_r$	16
Earth*	$R_i = 0.188D_r$	$R_e = 0.058D_r$	$R_a = 0.129D_r$	17

*For Meteor Crater, Arizona, corrected for erosion.

Table 2. Impact velocities[5] and surface gravities (normalized to that of Earth) utilized in deriving equations (4) and (5).

PLANET	IMPACT VELOCITY	SURFACE GRAVITY
Moon	14	0.165
Mercury	20	0.377
Phobos/Deimos*	6	0.0007
Earth	18	1.000

*Impact velocity from Cintala et al. (1978), Proc. Lunar Planet. Sci. Conf. 9th, p. 3803; surface gravity for a spherical Phobos model.

References: [1]Howard K.A. (1974) PLSC 5, p. 61-69. [2]Gault D.E. and Wedekind J.A. (1977) In Impact and Explosion Cratering (D.J. Roddy, R.O. Pepin and R.B. Merrill, eds.), p. 1231-1244. [3]Chabai A.J. (1965) J. Geophys. Res. 70, 5075-5098. [4]Gault D.E. et al. (1975) J. Geophys. Res. 80, 2444-2460. [5]Hartmann W.K. (1977) Icarus 31, 260-276. [6]Gault D.E. (1973) The Moon 6, 32-44. [7]Hartmann W.K. (1972) Icarus 18, 707-713. [8]Cintala M.J. et al. (1977) PLSC 8, p. 3409-3425. [9]Head J.W. (1976) PLSC 7, p. 2913-2929. [10]Gault D.E. and Wedekind J.A. (1979) 2nd Internat. Coll. on Mars, p. 29. [11]Baldwin R.B. (1963) The Measure of the Moon, Univ. Cgo. Press, Cgo. [12]Pike R.J. (1977) PLSC 8, p. 3427-3436. [13]Wood C.A. and Andersson L. (1978) PLPSC 9, p. 3669-3689. [14]Pike R.J. (1977) In Impact and Explosion Cratering (D.J. Roddy, R.O. Pepin and R.B. Merrill, eds.), p. 489-509. [15]Cintala M.J. and Head J.W. (1979) LPS X, p. 204-206. [16]Thomas P.C. (1978) Ph.D. thesis, Cornell Univ. [17]Roddy D.J. (1978) PLPSC 9, p. 3891-3930. [18]Settle M. and Head J.W. (1978) Icarus 31, 123-135. [19]Cintala M.J. (1979) Submitted to PLPSC X. [20]O'Keefe J.D. and Ahrens T.J. (1977) PLSC 8, p. 3357-3374. [21]Gault D.E. and Heitowit E.D. (1963) Proc. 6th Hypervelocity Impact Symp., p. 413-456. [22]Ahrens T.J. and O'Keefe J. (1977) In Impact and Explosion Cratering (D.J. Roddy, R.O. Pepin and R.B. Merrill, eds.), p. 639-656. [23]Quaide W.L. et al. (1965) Annals NY Acad. Sci. 123, 563-572.

Characteristics of the Cratering Process on Icy Bodies: Implications for Outer Planet Satellites.

Mark J. Cintala, E. Marc Parmentier and James W. Head, Dept. of Geological Sciences, Brown University, Providence, RI 02912.

While not a familiar occurrence in the context of the "dry" terrestrial planets, impact cratering in frozen volatile targets could be an important process in the evolution of the solid-surface bodies in the outer solar system. Investigations are being carried out into the phenomena and effects associated with the hypervelocity impact of projectiles into H_2O targets. The purpose of this report is to present some preliminary results of largely theoretical studies of impact cratering in H_2O ice, to compare and contrast them with events in more familiar targets, and to consider briefly the implications they might have for cratering on ice-rich bodies.

Crater Scaling: The shear strength of H_2O ice at ∿230 K is 1.6×10^7 dynes/cm^2 (10^6 dynes/cm^2 = 1 bar = 10^5 pascals).[1] Taking 3.6×10^3 dynes/cm^2 for the shear strength of basalt,[2] craters in ice should have diameters ∿2.8 times greater than those in basalt for situations in which strength scaling holds (cratering diameter $\propto$[cratering energy/target strength]$^{1/3}$). On a planetary scale, however, gravitational forces predominate in the formation of kilometer-size craters. Pure gravity-scaling (crater diameter $\propto$[cratering energy/density x surface gravity]$^{1/4}$) will give craters with diameters only 1.33 times larger in ice than in basalt for identical gravity fields. Actual situations will lie somewhere between these two extremes.[3]

Energy Partitioning: Irreversible Heating - The amount of irreversible heat generated during impacts of basalt projectiles into H_2O ice has been calculated following the method outlined by Gault and Heitowit[4] with H_2O ice Hugonist data from Anderson.[5] The total amount of waste heat generated in H_2O ice (normalized to that of basalt) as a function of impact velocity is shown in Figure 1. The variation of specific waste heat (i.e., ergs/g) as a function of dimensionless radial distance from the impact point is presented in Figure 2. Comparison of the two figures illustrates that, although the *specific* waste heat in H_2O ice is consistently greater than that in basalt, the lower density of ice (0.917 g/cm^3) when compared to that of basalt (2.86 g/cm^3) results in a smaller *total* quantity of waste heat acquired by the target. This effect is also evident in Figure 3; while the total masses of shock-heated material are roughly comparable in both targets, the volumes relative to the projectile volume differ by up to a factor of 5. The strong density difference between the projectile and H_2O ice target will also give rise to less efficient projectile-target coupling, as is evident in the normalized peak shock stress curve in Figure 2. *Comminution* - The average surface free energy for quartz - taken here to be 645 ergs/cm^2 (an average from experimental results of surface free energies for three separate crystal faces)[6] - differs from the crushing strength by a factor of ∿110.[7] By analogy, the surface free energy of ice-ice grain boundaries of 65 ergs/cm^2 [ref.1] gives a crushing strength for ice of ∿7.3×10^3 ergs/cm^2. It has been found that ∿10% of the projectile kinetic energy was utilized in comminuting a basalt target.[3] Scaling crater size for target strength effects, extrapolating a maximum particle size of 4.8 cm, assuming a minimum size of 0.1 µm (by analogy with the basalt case), and using the size distribution model of Gault and Heitowit,[3] the total energy expended in creating free surfaces in the ice target would amount to $\sim$28% of the projectile kinetic energy - almost a factor of 3 higher than that found in the basalt case.[4] Ejecta - In the absence of experimental data, it is difficult to estimate the fraction of projectile kinetic energy partitioned into ejecta kinetic energy. If ejecta velocity were to scale as (target strength/target density)$^{1/2}$,[8] then, accounting for the difference in ejected mass, essentially equal amounts of energy are partitioned into ejecta for the ice and basalt targets (aluminum projectiles at 6.25 km/s, using strength scaling). This implies lower average ejection velocities for small events in H_2O ice.

Large Scale Cratering: While a larger absolute volume of impact melt should be generated in ice compared to basalt, strength-scaled crater dimensions should keep the ratio of melt volume/crater volume relatively constant in both targets. As the magnitude of the hypothetical cratering event grows, however, the transition to gravity scaling will cause greater melt/crater volume ratios than would occur in basalt targets. The ratio of any measure of strength (or yield stress) to density for H_2O ice is invariably less than corresponding values for basalt. This fact should manifest itself as wall failure and central uplift formation in smaller craters in ice than in basalt, whether driven by gravitational forces or by rebound phenomena. It should be noted, however, that the larger relative volumes of impact melt in ice might obscure the initial appearance of central uplifts in the smaller ice craters. Removal of material from the central region of the crater floor might occur through explosive decompression of the target during the removal of large impact-induced stresses - a mechanism suggested to account for "central pit" craters observed on Mars.[9] Finally, density contrasts and the relative ease with which H_2O ice is melted by impact might combine to create a relatively efficient mechanism by which a net downward migration of suspended silicate particles could occur through settling in impact melt sheets. This process would have been more important in the early history of these bodies, when impact fluxes and crustal temperatures would have been higher during terminal accretion.[10]

References: [1]Hobbs P.V. (1974) Ice Physics, Oxford Univ. Press (London), 837 pp; [2]Jaeger J.C. (1956) Elasticity, Fracture, and Flow, Methuen & Co. (London), 268 pp.; [3]Gault D.E. and Wedekind J.A. (1977) Impact Explos. Cratering, p. 1231; [4]Gault D.E. and Heitowit E.D. (1963) Proc. 6th Hypervel. Impact Symp., p. 419; [5]Anderson G.D. (1968) CRREL Research Report 257, 50 pp; [6]Spry A. (1969) Metamorphic Textures, Pergamon Press (Oxford), 350 pp.; [7]Zeleny R.A. and Piret E.L. (1959) Colorado School Mines Quarterly 54, 35; [8]Ivanov B.A. (1976) Proc. Lunar Sci. Conf. 7th, p. 2947; [9]Wood C.A. et al. (1978) Lunar Planet. Sci. IX (abs.), p. 1270; [10]Parmentier E.M. and Head J.W. (1978) Submitted to J. Geophys. Res.

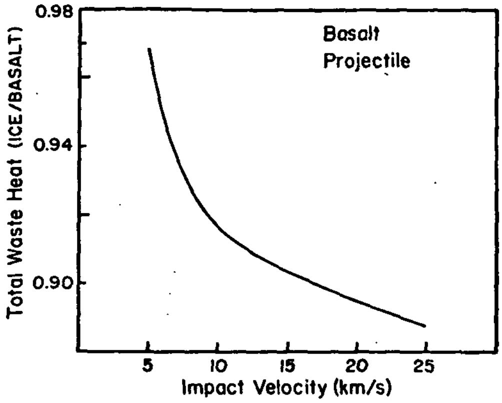

Figure 1. - Total waste heat for H_2O ice normalized to that for basalt as a function of impact velocity.

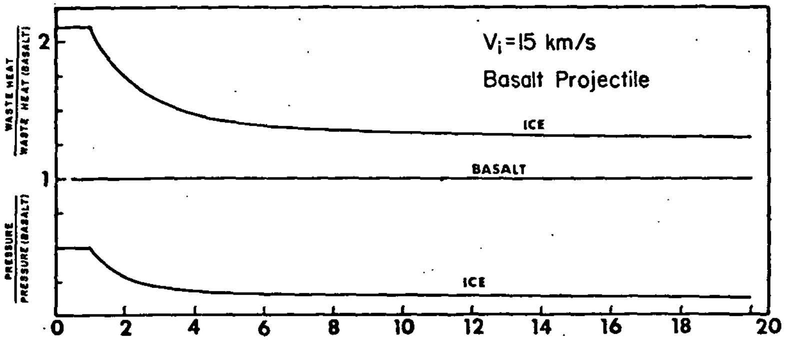

Figure 2. Specific waste heat and peak shock stress for H_2O ice normalized to those for basalt. The quantity r_o is the effective radius of the initial shocked plug of target material. (For this case, r_o for H_2O ice = 1.5 r_o for basalt.)

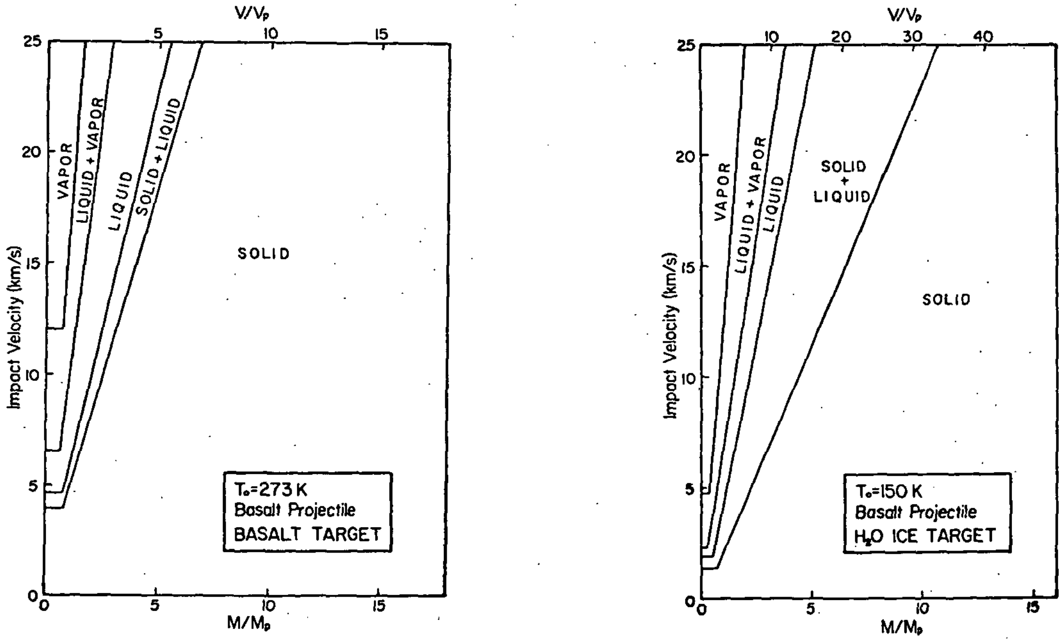

Figure 3. - Shock heated masses and volumes for basalt and H_2O ice as a function of impact velocity. Ice phase transitions are calculated for 1 atmosphere pressure.

New Depth/Diameter Data for Fresh Martian Craters and Some Interplanetary Comparisons.

Mark J. Cintala and Peter J. Mouginis-Mark, Dept. of Geological Sciences, Brown Univ., Providence, RI 02912.

In the past, attempts to determine depth/diameter (R_i/D_r) relationships for martian craters have met with limited success because of a variety of circumstances. The first measurements were carried out through photoclinometry,[1,2] but the dust- and cloud-laden martian atmosphere and a possible hardware problem on the Mariner 4 spacecraft induced low precision data. The Mariner 9 ultraviolet spectrometer (UVS)[3] provided model-dependent topographic data[4] for craters limited in both numbers and apparent freshness;[5,6] all of the craters observable with this technique were comparatively large ($D_r \gtrsim 15$ km). A small number of shadow measurements were carried out on Mariner 9 photographs, but these craters were also degraded to some extent.[7] Finally, Earth-based radar observations have served as a source of topographic data for a sample of the martian crater population,[7,8] the majority of which are eroded or modified. In all cases, the martian craters appeared to be shallower than fresh lunar craters. It was unknown, however, if the observed shallowness was primary[5] (i.e., a direct result of the crater-forming process) or a secondary effect[5,6] (such as eolian and/or volcanic filling, impact degradation, etc.).

The improved resolution and photometric response of the Viking Orbiter cameras have allowed reliable shadow measurements to be performed. The purpose of this paper is to report new R_i/D_r data for fresh martian craters, to compare them with those determined for crater samples from other bodies, and to form some preliminary conclusions on the basis of these data.

Data - Depths and diameters for 46 craters between the diameters of 1.3 and 38 km were derived from Viking Orbiter photography through techniques developed for the automated collection of martian[9] and mercurian[10] crater data. In order to minimize difficulties in distinguishing between actual shadows and enhancement artifacts, only shading corrected versions of the photographs were used; in addition, sun angles were restricted to <15° (measured from the horizontal).

As far as possible, only fresh or very slightly modified craters were incorporated into this data set. A strict relative age classification, however, is difficult to devise and adhere to for craters over the whole of Mars.[11,12,13] For the purposes of this study, fresh craters were defined as those with (1.) crisp rims over most or all of the perimeter of the crater and (2.) visible primary floor roughness,[11,14] when resolution allowed. It is believed that these criteria are adequate to separate degradationally unmodified large craters (i.e., those with complex interior morphology) from the more eroded population. Since resolution constraints do not allow detailed observation of small crater ($\lesssim 8$ km) interior morphology in the images deemed suitable here (clear atmospheres, $\sim$0.2 km/pixel resolution, except for rare high resolution frames), only those craters with shadow shapes characteristic of Pohn and Offield[15] ages 7.0 to $\sim$5.0 were digitized. Depth/diameter values for lunar craters with these relative ages do not deviate significantly from those of their fresher counterparts;[16] it is implicitly assumed that the same relationships hold true for Mars.

The data are plotted in log-log coordinates in figure 1. While some scatter exists, a break in slope in the distribution can be detected at a diameter of 10-15 km. The sample was divided at a diameter of 19 km and two least-squares fits were passed through each group. The diameter separating the two subsamples was further refined by moving the dividing diameter lower (within the visual break in slope), until the sum of the squares of the two correlation coefficients was maximized. The resulting curves are illustrated in figure 2 and tabulated in table I, along with those for the Moon,[18] Mercury,[18] and Phobos and Deimos.[19]

Discussion - While not as large as previously suspected,[1,2,5,7,8] the difference in depths between martian craters and those on the other studied terrestrial planets appears to be real. Earlier studies had suggested that differences in impact velocity and/or surface gravity might account for R_i/D_r ratios between the lunar/mercurian and martian crater samples.[5] An empirical equation derived by Gault and Wedekind,[20] which relates R_i/D_r ratios to surface gravity, predicts substantially deeper craters (R_i/D_r=0.236); a model-dependent relationship between R_i/D_r ratio, surface gravity, and impact velocity suggested by Cintala[21] also precicts greater depths for martian craters (R_i/D_r =0.215, for an impact velocity[22] of 10 km/s). In addition, craters on Phobos and Deimos -- formed at impact velocities averaging lower than those at Mars[23] -- exhibit R_i/D_r ratios similar to those observed on the Moon and Mercury.[19] An impact velocity-related explanation thus appears untenable, while the nearly identical martian and mercurian gravitational acceleration likewise appear to rule out gravitational differences as the major factor. Target curvature effects[23,24] are negligible for the crater sizes considered here.

The contributing effects of two major variables are unknown at present: (1.) the physical and chemical compositions of the impacting populations and (2.) the exceptional impact environment presented by Mars. Calculations by Hartmann[22] indicate that the cratering rates on the terrestrial planets are strong functions of the average orbital "composition" of the impacting bodies. While the relative contributions of the various populations are, at present, poorly understood, it is noted that, provided that Earth-crossing and Mars-crossing asteroids are the devolatilized cores of periodic comets,[25] average projectile-target energy coupling efficiencies would be similar for the lunar and martian cases if these bodies predominate in the formation of impact craters on the Moon and Mars. Earth-induced perturbations of these objects into Mercury-crossing orbits[25] would tend to imply similar coupling efficiencies for Mercury. If most of the observed fresh craters on any of these planets were formed by (active) cometary impacts or those of more competent (e.g., iron, achondritic, etc.) asteroids, however, interpretation would be correspondingly more difficult.

The possible existence of large quantities of volatiles beneath the martian surface, along with the tenuous but non-negligible martian atmosphere, might result in cratering conditions unlike those found on the Moon or Mercury. In particular, the flash-generation of large volumes of gaseous phases would probably alter the cratering process with as yet unknown consequences.[26,27,28] The possibility of a high-pressure transient atmosphere surrounding the growing crater cavity,[28] however, could cause larger volumes of fallback ejecta than postulated previously.[29,30] If the observed central peaks in small martian craters were to indicate that more intense rebound processes are operative on Mars than on the Moon or Mercury,[31] or that ice-related target readjustment occurs after martian cratering events,[31,32] such readjustment of the crater penecontemporaneous with the deposition of fallback ejecta could help to account for the abnormally small martian R_i/D_r ratios.

Extension of this work is currently in progress; it is hoped that R_i/D_r data for small ($D_r \lesssim 1$-2 km) craters located on fresh volcanic deposits (i.e., those expected to be volatile-poor) will aid in constraining these alternatives.

References: [1]Leighton R.B. (1966) Sci. Amer. 214, 54-68; [2]Pike R.J. (1971) Icarus 15, 384-395; [3]Hord C.W. et al. (1974) Icarus 21, 292-302; [4]Barth C.A. et al. (1974) An Atlas of Mars: Local Topography, Lab. Atmos. Space Phys., Univ. CO; [5]Cintala M.J. et al. (1976) PLSC7, 3575-3587; [6]Burt J. (1976) NASA TMX-3364, 199; [7]Malin M.C. and Dzurisin D. (1977) Jour. Geophys. Res. 82, 376-388; [8]Roth L.E. et al. (1978) LPSIX, 976-978; [9]Arvidson R.E. et al. (1974) The Moon 9, 105-114; [10]Cintala M.J. et al. (1976) Papers Pres. Conf. Comparisons Mercury and Moon, p. 5; [11]Cintala M.J. et al. (1976) Geophys. Res. Lett. 3, 117-120; [12]Florensky C.P. et al. (1977) Geophys. Res. Lett. 4, 243-244; [13]Cintala M.J. et al. (1977) Geophys. Res. Lett. 4, 245-246; [14]Head J.W. (1975) The Moon 12, 299-329; [15]Pohn H.A. and Offield T.W. (1970) USGS Prof. Paper 700-C, C153-162; [16]Cintala M.J. and Head J.W. (1979) To be submitted to The Moon and Planets; [17]Pike R.J. (1974) Geophys. Res. Lett. 1, 291-294; [18]Malin M.C. and Dzurisin D. (1978) Jour. Geophys. Res. 83, 233-243; [19]Thomas P.C. (1978) Ph.D. thesis, Cornell Univ., 272 pp.; [20]Gault D.E. and Wedekind J.A. (1979) 2nd Intl. Coll. on Mars, p. 29; [21]Cintala M.J. (1979) Submitted to PLPSC10; [22]Hartmann W.K. (1977) Icarus 31, 260-276; [23]Cintala M.J. et al. (1978) PLPSC9, 3803-3830; [24]Cintala M.J. et al (1979) In prep.; [25]Shoemaker E.M. (1977) Impact and Explosion Cratering (ed. D.J. Roddy, R.O. Pepin and R.B. Merrill), Pergamon, NY, p. 617-628; [26]Mouginis-Mark P.J. (1977) Ph.D. thesis, Univ. of Lancaster, UK, 344 pp.; [27]Cintala M.J. (1979) 2nd Intl. Coll. on Mars, p. 16; [28]Kieffer S.W. and Simonds C.H. (1979) LPSX, 661-663; [29]Schultz P.H. and Gault D.E. (1977) NASA TMX-3511, 117-118; [30]Settle M. (1979) LPSX, 1113-1115; [31]Wood C.A. (1978) PLPSC9, 3691-3709; [32]Cordell B.M. et al. (1974) Icarus 21, 448-456.

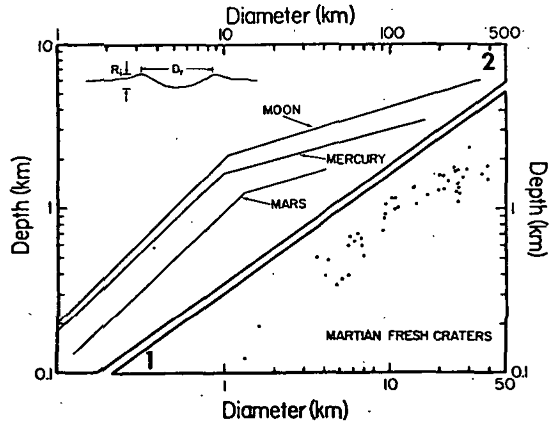

Fig. 1 - Depth/diameter data for 46 martian fresh craters.

Fig. 2 - Depth/diameter fits for fresh lunar, mercurian, and martian craters as given in table 1.

TABLE 1. Rim-to-floor depth (R_i) vs. rim diameter (D_r) relationships for fresh craters on the Moon, Mercury, Phobos and Deimos, and Mars.

PLANET	D_r RANGE (km)	RELATIONSHIP	STANDARD ERROR*	REFERENCE
Moon	$\lesssim 10.6$	$R_i = 0.196\ D_r^{1.010}$	+0.036 -0.027	17
	$\gtrsim 10.6$	$R_i = 1.044\ D_r^{0.301}$	+0.067 -0.063	17
Mercury	$\lesssim 9.8$	$R_i = 0.176\ D_r^{0.980}$	--	18
	$\gtrsim 9.8$	$R_i = 0.910\ D_r^{0.260}$	--	18
Phobos/ Deimos	$\lesssim 10.0$	$R_i = 0.2\ D_r$	--	19
Mars	$\lesssim 12.4$	$R_i = 0.104\ D_r^{0.962}$	±0.077	this paper
	$\gtrsim 12.4$	$R_i = 0.444\ D_r^{0.365}$	±0.079	this paper

*Given as the standard error of estimate of R_i on D_r, from a fit of the form $\log_{10} R_i = \log_{10} a + b\ D_r$.

GLOBAL INVENTORY OF SELECTED MARTIAN IMPACT CRATERS: PRELIMINARY REPORT

D. J. Roddy, D. W. G. Arthur, J. W. Boyce, E. C. Morris,
R. Pike, U. S. Geological Survey, Flagstaff, AZ

Hypervelocity impact cratering has been recognized as playing a major role in the evolution of the terrestrial planets and satellites and in the continuous modification of their crusts. The high quality of the Viking Orbiter photography has shown, in particular, that the martian craters are extremely variable in their crater morphologies. They are surrounded by ejecta deposits ranging from highly lineated blankets to irregular lobate forms with accentuated flow-like characteristics (Carr, 1977). The internal morphologies of the craters also vary from simple bowl-shaped to highly complex forms with central peaks to very large flat-floored craters with concentric rings. A similar morphological trend also exists for the Earth, Moon, Mercury, and certain of Jupiter's satellites. A parallel trend has also been shown to exist in the morphologies of large-scale explosion craters (Roddy, 1977). The implication from these explosion crater and from terrestrial impact cratering studies is that similar martian trend from simple to complex structural deformation can be categorized into specific classes or types and relatable to the initial impact conditions. The implications of such a diversity in impact related morphologies strongly implies major variations in characteristics of impacting bodies, energy coupling, cratering processes, and target materials.

In an effort to examine the full range of variation for the different classes of craters and the implication for crustal evolution we are currently preparing an inventory of selected martian craters that range in morphological type from bowl-shaped to multi-ring and vary in size from a tens of meters to multi-kilometers. More specifically, we are in the process of collecting a number of cratering data sets which, among others, include: a) detailed numerical set of parameters following the outlines of Arthur (1974), Pike (1976), and Roddy (1977), such as rim crest and apparent diameters and depths, b) morphological characterizations for both craters and their ejecta deposits, c) positional data for all craters in study, and d) regional geologic settings for each crater

This preliminary inventory scheme will utilize electronic digitizing techniques for rapid positional indexing on the 1:250 M Viking Orbiter mosaics. Each crater is further characterized, under our present scheme, by assigning a number of morphological designators, including sharpness of rim, polygonality of rim, interior crater wall detail, type and number of central peaks, nature of floor, nature of floor/wall contacts, terraces and types, nature of ejecta surfaces, and other parameters. This data, along with the positional information, is presently being placed in computer format. We intend to collect the crater data and produce computer graphic printouts of scaled overlays for the narrow classes of craters. The different overlays will then be superimposed on the 1:250 M Viking Orbiter photographs and reviewed in terms of maps of craters individual classes and their correlation or relationships to the regional geologic units The graphic computer overlay maps will allow special emphasis to be placed on latitude and longtidue positional relationships not easily studied using only tabular data. At the present time, we are in the initial stages of testing and refining our computer coding system and are beginning to assemble the dimensional crater data matrix that we will use on the 1:250 M Viking photography. At this stage we also welcome additional comments and cooperative exchange with other interested groups that are actively categorizing martian surface features.

References

Arthur, D. W. G., 1974, Lunar crater depths from long-focus photographs: Icarus, v. 23, p. 116-133.

Carr, M. H., 1977, Distribution and emplacement of ejecta around martian impact craters, in Impact and Explosion Cratering (D. J. Roddy, R. O. Pepin and R. B. Merrill, eds.), Pergamon Press, P. 593-602.

Roddy, D. J., 1977a, Large-scale impact and explosion craters: Comparison of morphological and structural analogs, in Impact and Explosion Cratering (D. J. Roddy, R. O. Pepin, and R. B. Merrill, eds.), Pergamon Press, p. 185-246.

Roddy, D. J., 1977b, Tabular comparisons of the Flynn Creek impact crater, United States, Steinheim impact crater, Germany, and Snowball explosion crater, Canada, in Impact and Explosion Cratering (D. J. Roddy;, R. O. Pepin, and R. B. Merill, eds.), Pergamon Prews, p. 125-162.

Pike, R. J. 1976. Crater dimensions from Apollo data and supplemental sources: The Moon, v. 15, p. 463-477.

MARTIAN IMPACT CRATERING: PRELIMINARY REPORT

D. J. Roddy, D. W. G. Arthur, J. M. Boyce, R. Pike,
L. Soderblom, U.S. Geological Survey, Flagstaff, Arizona

Hypervelocity impact cratering processes have been credited with playing a major role in the formation and evolution of the crusts of the terrestrial planets and satellites by Carr (1977), Dence, et al (1977), Gault, et al (1975), Hartman (1978), Shoemaker (1977), and numerous others. In particular, the excellent Viking Orbiter photography has shown that martian impact craters exhibit an extremely wide variety of crater and ejecta blanket morphologies. Crater shapes ranging from simple bowl-shapes to complex multiringed basins. Associated ejecta blankets exhibit a variety of types of morphologies which range from simple surfaces with minimal ray-like extensions to strongly lineated surfaces to complex, irregular lobate-type surfaces with pronounced flow-like characteristics. A similar set of trends in crater and ejecta morphology also exists in large-scale explosion cratering, and are accompanied by increasingly complex structural deformation progressing from bowl-shaped to multiring craters (Roddy, 1977); these trends in morphology/structural deformation are also observed in terrestrial impact studies. Moreover, it has been generally established that final crater shapes and deformation are strongly controlled by certain critical initial conditions, including: type of impacting body, energy coupling and transfer rates, effective heights and depths of burst, target media properties including layering and water content, gravitational fields, as well as other minor parameters (Cooper, 1977; Brode and Knowles, 1977; Kreyenhagen and Schuster, 1977; and others). Consequently, a comprehensive understanding of these conditions should lead to improved views of martian cratering processes and general nature of the martian crust.

We are presently engaged in a limited part of these broader problems in our studies of terrestrial impact and explosion cratering and their application to both Mars and the other solid-body plants and satellites. More specifically, we have chosen a set of about 20 martian craters that represent each of the crater types observed. The craters that were selected were chosen from the highest resolution photography available, and we are extracting a detailed data set from each crater, including such information as multiple rim crest diameters, estimated apparent diameters and depths, terrace dimensions, aspect ratios, central uplift and ring dimensions, ejecta blanket dimensions, remote sensing information, geologic maps, color imagery, morphological characterizations, and other parameters. These are cast in the tabular formats of Arthur (1974), Pike (1976) and Roddy (1977).

We presently are in the process of assembling these different data sets as well as comparing parts of the data to terrestrial impact and explosion cratering studies. For example, we are engaged in a computer numerical simulation of Meteor Crater, Arizona in a cooperative study with K. Kreyenhagen and S. Schuster. One of the parametric calculations involves variations in water content of the target media in which we expect to be able to also apply our results to a martian gravitational and atmospheric environment. Another comparative analog study involves our deep drilling program at the Flynn Creek structure, a 3.5 km diameter impact crater in Tennessee. Although the drilling is still in progress, we have determined that at least two concentric fault zones are present beneath the crater walls and inner rim. Morphologically and structurally, these locations appear to be consistent with what appear to be similar fault zone locations in certain martian craters. A cooperative study with the Defense Department on material properties and shock wave interaction in these types of rocks hopefully will improve general interpretations of target strengths and material responses for both terrestrial and martian conditions, especially such as major fault zones, central uplifts, and multirings. At the present time, we are pursuing the initial stages of collecting the detailed data bases for the selected martian craters, and expect analog camparisons and calculations to follow next year.

REFERENCE:

Arthur, D. W. G. , 1974, Lunar crater depths from long-focus photographs: Icarus, v. 23, p. 116-133

Carr, M. H., 1977, Distribution and emplacement of ejecta around martian impact craters, in Impact and Explosion Cratering (D. J. Roddy, R. O. Pepin and R. B. Merrill, eds.), Pergamon Press, p. 593-602

Roddy, D. J., 1977, Large-scale impact and explosion craters: comparisons of morphological and structural analogs, in Impact and Explosion Cratering (D. J. Roddy, R. O. Pepin, and R. B. Merrill, eds.) Pergamon Press, p. 185-246.

Pike, R. J., 1976, Crater dimensions from Apollo data and supplemental sources: The Moon, v. 15, p. 463-477.

Shoemaker, E. M., 1977, astronomically observable crater-forming projectiles, in Impact and Explosion Cratering (D. J. Roddy, R. O. Pepin, and R. B. Merrill, eds.), Pergamon Press, p. 617-628

Mars: Chemical Reduction of the Regolith by Frost.

R.L. Huguenin, Dept. Physics/Astronomy-Hasbrouck, U.Mass., Amherst 01003 and Brown U. Dept. Geological Sci, Providence, R.I. 02912, and K.J. Miller, Dept. Physics/Astronomy-Hasbrouck, U.Mass., Amherst 01003.

The occurrence of ferric oxides and oxidants (inferred by the Viking biology experiments) in martian soil has been generally construed as evidence for a highly oxidized regolith. While oxidation has clearly occurred, it cannot be concluded that oxidation dominates the weathering process, however. It has already been shown that the oxidation of Fe^{2+} in minerals does not require an oxidizing atmosphere on Mars: it is forced by solar UV and can occur in highly reducing atmospheres containing only trace amounts of O_2(1). Indeed we now report laboratory studies that indicate that the oxidants in the soil may be byproducts of the chemical reduction of mafic silicates by H_2O frost and ice, and show that chemical reduction may possibly dominate the regolith weathering processes.

The minerals olivine, pyroxene (both clino and ortho varieties) and plagioclase are apparently the principal mafic silicates in martian rocks (2), and we have chosen varieties of each for our first experiments. The bulk of the experiments were performed with Jackson Co. olivine (FO_{80}), but we have recently included samples of Loudon Co. pyroxene (pigeonite), and Lake St. John labradorite (plagioclase). For all three minerals samples were pulverized and exposed to H_2O vapor at -11 to -22°C, simulating the martian nightime and subsurface daytime formation of frost on freshly cleaved mineral surfaces. The samples were pulverized for 30 min using a silica mortar and pestel in a simulated martian atmosphere. In the first experiment with olivine the sample was then allowed to warm from -22°C to room temperature. After about 30 minutes the frost on the sample began to melt and copius amounts of O_2 gas were produced (analyzed by gas chromatography). Most of the gas was produced within 30 minutes, and after 120 hours the total amount released was 7×10^{19} O_2 molecules per gram of sample. In a second experiment we pulverized samples of olivine in the presence of H_2O vapor at -11 to -22°C, and again turned off the coolant and after ~ 30 minutes the frost began to melt. At this point 5 $m\ell$ of 0.1M HCOONa solution was injected into the sample and within ~ 1 hour 6.5×10^{19} molecules CO_2 g^{-1} evolved from the sample. The amount of CO_2 produced was very close to the number of formate ions available for oxidation (3×10^{20} molecules) and it represented $\sim 43\%$ conversion to CO_2 within an hour. Numerous control experiments were performed that indicated that the source of the O_2 and CO_2 was a species produced by the simple exposure of freshly cleaved olivine to frost.

We have attempted to identify the source of the chemical activity using a variety of chemical indicators. One of the tests gave positive results, and it indicated that a peroxide, probably H_2O_2, had been formed on our frost-treated olivine samples. The samples were injected with an aqueous solution containing dilute $FeC\ell_3$ and a trace of $K_3Fe(CN)_6$. Upon exposure to the sample this yellow solution turned colorless and a white precipitate formed. The formation of the "Berlin White" precipitate without a blue or green precipitate (as we observed) is a specific and sensitive indicator for peroxide in the presence of an adsorbate substrate. H_2O_2 apparently chemisorbed as $HO^-_{2(ads)}$ (at metal ion sites) and $H^+_{(ads)}$ (at surface O^{2-} sites), and when the frost melted the peroxide apparently went into solution as $FeO_2H^{2+} + FeOH^{2+} + HO^- + H^+$.

This is supported by the pH behavior of the samples. When samples were pulverized at low temperatures without H_2O present or at room temperature with or without H_2O vapor present and then placed in 50 mℓ of distilled H_2O, the pH rapidly rose (within $\sim$ 20 sec.) to pH $\approx 9 - 9.5$ and then slowly rose (for $\sim$ 30 min) to a peak value of pH $\approx$ 10.5. When frost-treated samples (held at -22°C) were introduced into distilled H_2O, however, the pH showed an initial rapid rise (for $\sim$ 5 sec) followed by a plunge to pH $\approx$ 5-6 (within $\sim$ 30 sec) and then a slow rise to pH $\approx$ 7-8 after $\sim$ 1 hr. The experiments were repeated with samples of plagioclase and pyroxene and we obtained essentially the same results, although the kinetics were somewhat different for the three mineral samples.

The results of the above experiments indicate that a chemisorbed peroxide species ($HO^-_{2(ads)} + H^+_{(ads)}$) was produced from chemisorbed H_2O as a result of the reduction of the substrate minerals, i.e. hydrogen was removed from the surface H_2O and incorporated in the silicate. In particular we propose that upon exposure to the freshly-cleaved surfaces, H_2O vapor dissociatively adsorbed as $OH^-_{(ads)}$ and $H^+_{(ads)}$. Following this, a fraction of the H^+ were drawn into the crystal by the attractive force of negatively-charged lattice defects (eg. metal ion vacancies or Al^{3+} substituted for Si^{4+}) where they combine with oxide ions to form lattice hydroxyl ions. Incorporation of the protons at negative defects gives the crystal a net positive charge, while the surface layer of adsorbed H_2O has a net negative charge (excess OH^- relative to H^+). Charge balance is restored by transfer of electrons from $OH^-_{(ads)}$ to positive lattice defects (eg. anion vacancies or Fe^{3+} substituted for Fe^{2+}) and the resultant surface OH radicals combine to form the more stable hydrogen peroxide molecules ($H_2O + O^{2-}_{(o,Al^{3+}} + Fe^{3+}_{(o)} \rightarrow OH^-_{(o,Al^{3+})} + Fe^{2+}_{(o)} + \frac{1}{2} H_2O_{2(ads)} -$ 33.9 kcal mole^{-1}). The H_2O_2 should actually chemisorb in the dissociated state ($HO^-_{2(ads)} + H^+_{(ads)}$) and it would be metastable, i.e. it should decay with time to adsorbed oxygen ($H_2O_{2(ads)} \rightarrow H_2O_{(g)} + O_{(ads)}$ - 42.4 kcal mole^{-1}). The activation energy for the decay should correspond to the $O\text{-}OH^-$ bond strength in HO^-_2, which is $\sim$ 34 kcal mole^{-1}. A large surface potential energy should develop during the proton incorporation and peroxide production reactions which would not develop if the H_2O occurred as a liquid instead of frost. Subsequent exposure of the surface layer to liquid H_2O would release the surface potential energy, and produce the observed avalanche-like ejection of peroxide and metal ions into solution. The species that get released to solution include FeO_2H^{2+}, $FeOH^{2+}$, $HO\cdot$, and H^+ which react to form $O_{2(g)}$ and which can efficiently oxidize formate ions to $CO_{2(g)}$.

The rapid rise in pH that occurred for the samples that had not been frost-weathered indicated that the proton incorporation reaction apparently occurs within $\sim$ 20 sec after exposure to the H_2O. This supports the proposal that the reaction occurs spontaneously and that a residual of excess OH^- (relative to H^+) is produced. The rapid drop in pH that occurs when frost-treated mineral samples are introduced into distilled water supports the proposal that H^+ is one of the species (along with $FeOH^{2+}$, FeO_2H^{2+}, and $OH\cdot$) that is released when the frost-treated sample is exposed to liquid H_2O.

Our experimental results closely mimicked the chemical activity of the martian soil samples during the active cycles of the Viking Gas Exchange (GEx) and Labeled Release (LR) biology experiments, although the activity of our samples was more intense than the martian samples. In addition the model proposed here predicts the unusual thermal and storage behavior of the GEx and LR experiments. In particular, the ability of the martian oxidant to oxidize organic substrate to CO_2 gas during the LR experiment was inhibited by sterilization at 45-50°C and 160°C and by prolonged storage at 10-15°C, while the release of O_2 gas from the GEx samples was not appreciably affected by either sample sterilization or storage. Levin(3) constructed an Arrhenius plot of the LR thermal and storage data and derived an activation energy for destruction of the martian oxidant to be 35-43 kcal $mole^{-1}$. This is remarkably close to the $\sim$ 34 kcal $mole^{-1}$ activation energy derived here for the decay of adsorbed peroxide to $O_{(ads)}$, and it strongly suggests that chemisorbed peroxide may have been the active species in the unsterilized GEx and LR samples. The end product of the decay, $O_{(ads)}$, should be stable to a temperature of $\sim$ 580°C at Fe^{2+} sites in the absence of liquid $H_2O(4)$, while subsequent exposure to liquid H_2O should rapidly release the $O_{(ads)}$ as $O_{2(g)}$ (4). We thus propose that $O_{(ads)}$ derived from the decay of chemisorbed peroxide may have been the principal source of $O_{2(g)}$ in the heat-sterilized GEx samples. The results of the LR and GEx experiments provide strong support for the silicate reduction model proposed here, and they indicate that the martian soil is actively undergoing a chemical reduction. Photochemical oxidation processes are also predicted to be active in the contemporary martian environment(1), however, and a major question then is whether surface weathering is producing a net oxidation or net reduction.

The answer to this depends in large part on the mineralogy of the unweathered material, which varies regionally and is not well known(2). It also depends on the population of defects in the constituent minerals, and this too is not well known. A crude estimate can be made, however, if one assumes that the average crustal mineralogy can be approximated by the primary mantle melt normative mineralogy derived from the Viking XRF data and mantle thermal models(3): 37-38% olivine (Fa_{44}), 20-29% diopside (Wo_{50}, En_{28}, Fs_{22}), 20-32% plagioclase (An_{60}), 2.5-5% nepheline, 0.6-2.4% orthoclase, and 4.4-7% magnetite. If it is assumed that one oxygen is incorporated per two Fe^{2+} during oxidation, then complete oxidation of the above basalt would incorporate .4 - 6 x 10^{21} oxygens per cm^3. The number of H^+ incorporated depends on the number of negative defects and their percent occupancy. The principal negative defect in semiconductor solids are cation vacancies which typically have abundances of 10^{20} - 10^{22} cm^{-3} in pure synthetic specimens, and in natural minerals the number of defects should be greater. The number of hydrogens incorporated in our olivine sample after exposure to frost was 3 x 10^{20} cm^{-3}, which represents $\sim$ 1% occupancy of the defects. Repeated exposures to frost would have increased the occupany, since the number of H^+ incorporated was limited by the number of chemisorption sites on the mineral surface(4). If it is assumed that full occupany of the defects can be attained and that there are (conservatively) 10^{20} - 10^{22} defects cm^{-3} in the above basalt, then the number of hydrogens incorporated per cm^3 could be comparable or even exceed the number of oxygens incorporated per cm^3. Clearly there are too many uncertainties to determine whether surface weathering is a net oxidation or net reduction process. Earth-based measurements of the reflectance spectra of small areas (200-400 km diameter) indicate that the rock types vary from region to region and they are somewhat different than the basalt used in the above calculation(2). Weathering of these different basalts would have different relative oxidation and reduction rates, and the net oxidation and reduction rates would have changed over geologic time as new and different basalt units erupted onto the surface.

One of the most important effects of surface weathering is its effect on atmospheric evolution and oxidation state. Imbalances in the oxygen and hydrogen incorporation rates can have important effects on the oxidation state of the atmosphere(4). In particular a net oxidation of the regolith would produce a gradual decrease in the O_2/CO rate, while a net reduction on the regolith would produce a gradual increase in the atmospheric oxidation state. These changes in O_2/CO would be buffered somewhat by adjustments in the surface photooxidation rates, atmospheric chemistry, and exospheric escape rates, but the long term effects could potentially be appreciable(4). The current value of $O_2/CO \simeq 2$ on Mars is ~ 4 times higher than the predicted value of ~ 0.5 based on models of homogeneous atmospheric chemistry and exospheric escape. This suggests that the regolith is probably undergoing a net reduction. The current changes in the atmospheric oxidation state may be very different than they were in the past, however, since the crustal mineralogy has probably undergone significant changes over geologic time.

References.(1) Huguenin, R.L. (1974), J. Geophys. Res. 79, 8495; (2) Huguenin, R.L., Head, J.W., and McGetchin, T.R. (1976) NASA TM79729, 118; (3) Levin, G.(1978), presentation at 2nd Conf. on Simulated Mars Surf. Prop., NASA Ames, 17-18 August; (4) Huguenin, R.L., Prinn, R.G., and Maderazzo, M. (1977) Icarus 32, 270.

The Chemistry of Mars: Past, Present, and Future. Benton C. Clark, Planetary Sciences Laboratory, Martin Marietta Aerospace, Denver, CO 80201

No other body in the solar system has been so subject to speculation as Mars. Surface and interior composition have not escaped these discussions. In view of recent advances, it is appropriate to review past gains, present status, and current hypotheses of the chemistry of Mars. From this base, it is reasonable to evaluate strategies now under consideration for future missions and their potential for making major discoveries ultimately needed to understand the geochemical and cosmochemical context of Mars.

The Distant Past

In the beginning, defined as the birth of telescopic astronomy, Mars was a land of deserts, seas, and polar ice caps. The calculations and astute reasoning of S. A. Arrhenius led him to believe, ca. 1910, that liquid seas could not exist and the desert environment would produce salt efflorescences, including sulfates, at the surface. Later workers, perhaps seeking more fertile ground, seized upon the color of Mars. One, attributing the redness to pink feldspar, could thereby infer extensive crustal differentiation. Others, seeing in the visible and near IR a match to iron oxyhydroxides (limonite), encouraged a view toward "wetness" and weathering. Realizing that terrestrial quartz sand deserts can appear blood-red with only ~1% hematite and geothite content, still others relegated the Fe^{3+} coloration to a superficial coating of mineral grains. Thereby, the "oxidized basalt" model came into vogue.

The Recent Past

The Surveyor and Apollo programs had shown that even a long-dead body like the moon was mostly covered with igneous differentiates -- anorthositic and basaltic rocks. Mars, at first a dead and then only a half-dead planet in the miraculously-targeted photos of Mariners 4, 6, and 7, was ultimately rejuvenated by Mariner 9. Alas, however, the channels proved to be old, and the volcanoes not totally young. From orbital IR, the dust was diagnosed as 60% SiO_2, a value approaching the granite/rhyolite category of igneous rocks. Later interpretations proposed montmorillonite clay as the best fit to the same data -- Mars became wet and weathered again.

The Present

Viking lander data quickly dispelled the high SiO_2 value, obtaining about 40-45% instead, bringing the Martian surface back into the mafic to ultramafic category. Surface fines were found amazingly homogeneous between sites, rich in salts, and not readily matched by any known natural assemblage. First interpretations were along the lines of "deep weathering" of mafic igneous rock. Nontronite, an Fe-rich clay of the montmorillonite (or smectite) group, was inferred. Nontronites are rare weathering products of basalts on land, and a rather major product of suboceanic hydrothermal alteration in spreading centers. Such weathering segregates large quantities of minerals composed of other elements from the source material. For example, much calcium and aluminum must be disposed of.

A second interpretation has been that the fines are made up of three components: lag magnetite + powdered picrite basalt + leached salts. A third lends credance to the possibility of ferro-picritic differentiates from the presumed composition of the Mars mantle. A fourth claims, most audaciously, that the fines may be explained as a mixture of basalt powder, primitive material of accretion, and condensates of volatiles released by volcanism. The origin of the Martian soil cannot be decided, particularly since the compositions of the starting materials, i.e. the rocks, remain unknown. Likewise, the chemical structure of the interior of Mars is not defined because of lack of seismic constraints upon core, mantle, and crust.

The Future

A Geochemical Orbiter may detect important chemical heterogeneities in surface regions, reflecting the reservoirs postulated (chemical sediments, igneous differentiates, primitive material, etc.). A difficulty will be the obscuring effect of the apparently isochemical and universal dust blankets, although hope is provided by ground based IR and Viking orbiter color-ratio mapping studies. A sample return mission cannot rely upon disentangling Mars from the analysis of fines alone, in view of their possible ancient age, complex weathering history, and large number of source components. Rock samples assume special importance, compared to the lunar case. It is not at all certain that there is only one population of rocks at each lander site; chemical screening of candidate rock samples would seem highly desirable. For the same reasons, the scientific gains of sampling more than one geologic unit could turn out to be enormous compared to a one-site sample. The bulk and interior chemistry of Mars may yield its secrets only when comprehensive seismic and heat flow data are available. In summary, for geochemical reasons alone, it is apparent that no single mission or mission type can answer all the questions now posed. The exploration of Mars requires a broad, sequenced program.

References

The many contributions by various researchers will be cited during the oral presentation of this material. Recent results on analysis of Viking data will also be given.

Mars Soil/Water/Atmosphere Dynamic Interactions Experiment Process,

R. Stephen Saunders, Jet Propulsion Laboratory, California Institute of Technology, Pasadena, CA 91103

Introduction and Background. Five laboratory experiments being performed in this investigation are derived from a desire by the investigators to understand the dynamic interaction between the Martian soil, water in the soil, and the atmosphere. The experiments arise from the investigator's previous work in the interaction of volatiles with the Martian regolith and the development of experiments to determine the quantity and physical-chemical sites of water.

Justification. The five experiments are justified on the basis that modeling or simulating the observed phenomena in a controlled laboratory environment will lead to new insights into the behavior of the processes under study.

Description. The five candidate experiments are conceptually designed as shown in Figures 1 and 2 below, and are described as follows:

MARS SOIL THERMODYNAMICS AND FLUID DYNAMICS EXPERIMENT. Figure 1 is a block diagram of the thermodynamic/fluid dynamic soil properties chamber (TFSPC). The design, fabrication, assembly and testing of the TFSPC was completed in May. An aeolian sorted smectite clay was selected for the first solid model. It was dried ($< 1\%$ H_2O) and classified ($< 10\mu$) in a rising column (30 cm/sec) of dry nitrogen and deposited (to a depth of one meter) in the TFSPC. The instrumentation for this chamber is complete and experimentation will begin early in August.

Thermometers and pressure sensors are placed in the soil at various levels. The container can be weighted (to 1/10% precision) by load cells. A radiant heat source can illuminate the soil surface and simulate the Martian solar insolation. The atmospheric species (CO_2, H_2O, Ar) and their partial pressures can be controlled by external means.

This chamber will be used to determine some of the fundamental thermodynamic and fluid dynamic parameters of Martian soil. We will seek to match the observed thermal inertia measurements for a range of Martian soil types using physical analogues. The purpose of the experiment is to look for thermal effects of CO_2 or H_2O diurnal pumping and other effects of pore volatiles at low temperature. The container provides a meter of analogue soil column in thermal isolation, with controlled thermal input.

CYCLICAL INTERACTION OF VOLATILES BETWEEN THE MARTIAN SOIL AND ATMOSPHERE. Figure 2A is a conceptual sketch of a large insulated box partly filled with simulated Martian soil covered with an LN_2-cooled radiation-sink plate. The box will be positioned inside the Mars Environment Chamber which will simulate Martian atmospheric and thermal parameters. Between the plate and the soil surface are interposed two thin-films of IR transparent plastic (0.1 mil Mylar) that prevent cold gas from the cold plate from being convected to the soil surface and disturbing the stratified gas layers over the soil surface. These stratified gas layers are produced by the soil radiating heat to the cold plate and cooling (by conduction) the layers of gas near its surface. Relatively warm gas (warmer than the gas above the surface) is passed through the space between the two sheets of plastic film to interrupt and carry off any gas cooling from the cold plate above. Fogs can be formed in the chamber by subliming H_2O from the soil or by independently introducing H_2O at a buffered partial pressure.

CRYOPUMPED AEROSOL EXPERIMENT. Figure 2B is a conceptual sketch of the experimental configuration. A large LN_2 coolable box, open at the top, is positioned in the Mars Environment Chamber so that fine ($< 1\mu$) particles generated by the ball mill containing Mars type surface rocks) can settle into it. The bottom of the box is cooled until the CO_2 atmosphere (with and without appropriate amounts of H_2O vapor) in the chamber begins to be condensed (cryopumped) on its surface.

The fine particles act as nucleation particles for, first the H_2O and then the CO_2. Small snow flakes are formed which precipitate out on the cold surface. Clathrate structures may also nucleate on the particles and form snowflakes.

SELF SEALING PERMAFROST EXPERIMENT. Figure 2C is a conceptual cketch of a large insulated container of simulated Martian soil mounted in the Mars Environment Chamber. A layer of saturated frozen soil is formed at the surface by producing Martian atmospheric pressure in the chamber and allowing the surface layer to freeze by sublimation of some of the water. The unfrozen soil under the permafrost layer is heated to obtain a significant pressure against the permafrost "plug". Before the plug is pushed out of the container by this pressure, a "leak" is formed by heating or puncturing a vertical segment of the plug and letting the pressurized vapor escape.

The process of forming the leak and its subsequent refreezing and "sealing" of the leak is observed and photographed through windows in the chamber.

FREEZE DRIED FLUIDIZED FLOW EXPERIMENT. Figure 2D is a conceptual sketch of two different views of a rotating drum (cement mixer) inside of which is a physical analog of saturated Martian soil. The drum is initially sealed with an earth atmosphere inside it and the drum is rotated so that the fluidized flow of the saturated soil (mud) can be observed and photographed. The chamber is evacuated to Martian conditions and when all slow motion cameras have been started the small glass window is broken by remote control. As the mud slides down the drum cylinder under the reduced pressure its water content is partially vaporized and cools the mud. The mud is eventually frozen. The fluidized effect of the water vapor "boiling" out of the mud can be observed by noting the change in the angle of repose of the mud during this phase.

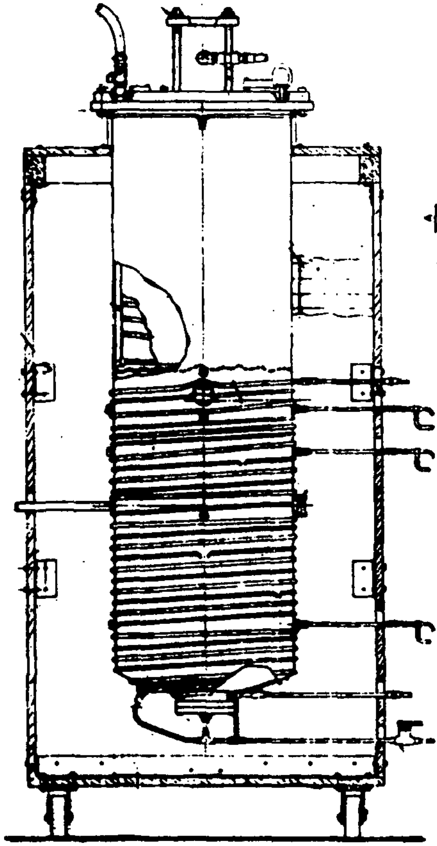

Figure 1

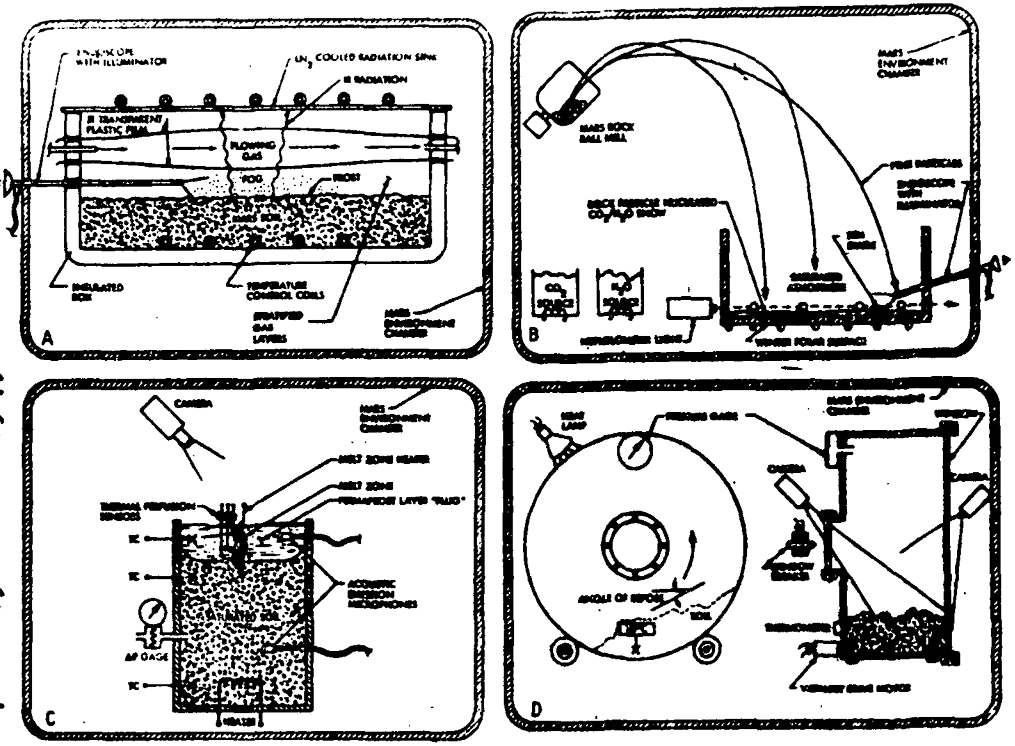

Figure 2

MINERALOGY OF CALICHE-LIKE SALT CRUSTS FROM THE WESTERN DESERT, EGYPT: IMPLICATIONS FOR MARTIAN DURICRUST FORMATION.

Donna J. Prestel, Lockheed Electronics Co., Inc., Houston, TX 77058
David S. McKay, SN6/NASA Johnson Space Center, Houston, TX 77058
C. Vance Haynes, Depts. of Anthropology and Geosciences, Univ. of Arizona, Tucson, AZ

Martian Duricrust. Duricrust is the term given to the indurated upper horizon of Martian regolith found at both Viking landing sites (Binder et al., 1977). This fractured crust was exposed when Viking retro-engines swept loose dust away from the landing sites. Binder et al. (1977) propose that this crust formed when mineral-bearing waters moved upward by capillary action, evaporated, and precipitated salts in the duricrust horizon. The XRF results showed that this crust is high in sulfur, containing possibly about 10% magnesium sulfate (Clark et al., 1977). The presence of this duricrust, with its enriched sulfur content, can be interpreted to indicate that atmosphere-regolith interactions involving water have been important weathering processes at some time in Martian history.

In order to more completely understand this process as it might occur on Mars we have undertaken a study of an analogous process in one of the most arid environments on Earth, the Western Desert of Egypt.

The Western Desert of Egypt as an Analog to Martian Regolith. Similarities between the two environments are striking. The Egyptian desert is extremely dry; parts have not had measurable rainfall in recent history. The overall rainfall for this region is less than 1 mm/year (Wendorf et al., 1976). The region is dominated by aeolian erosion; water drainage lines are almost completely absent. Large quantities of the sand and rock fragments deflated from the basins by wind have been deposited as great chains of sand dunes which have been compared to some of the large dune fields on Mars (El-Baz, 1978).

Samples which we studied consist of isolated documented surface samples and samples from vertical stratigraphic sections through caliche-like deposits collected from deflation basins along an ancient caravan route, the Darb El Arba'in. Many of the samples are from near birs (wells). Samples from Holocene playas and from salt crusts formed from upward migrating ground water are represented.

We are investigating these samples by x-ray diffraction and by scanning electron microscopy with an attached energy dispersive x-ray analyzer (EDXA). Table 1 is a summary of the minerals identified in our initial investigation.

The preponderance of sulfates in this suite correlates well with the implied presence of sulfates in the Viking results. Furthermore, the clay mineral dickite found in our samples is a member of the Kaolinite group which is predicted by Gooding (1978) to be the only clay mineral which should be thermodynamically stable on the surface of Mars. Viking investigators, however, infer that smectite clays may be a major constituent of Viking analyzed material, although the evidence is indirect (Toulmin et al., 1977).

Table 1. Minerals identified in caliche deposits of the south Western Desert of Egypt

quartz, chalcedony	SiO_2
gypsum	$CaSO_4 \cdot 2H_2O$
anhydrite	$CaSO_4$
bassanite (hemi-hydrate)	$CaSO_4 \cdot 1/2\ H_2O$
γ-$CaSO_4$ (soluble anhydrite, or dehydrated hemihydrate)	$CaSO_4$ (metastable)
tamarugite	$NaAl(SO_4)_2 \cdot 6H_2O$
bloedite	$Na_2Mg(SO_4)_2 \cdot 4H_2O$
epsomite	$MgSO_4 \cdot 7H_2O$
hexahydrite	$MgSO_4 \cdot 6H_2O$
nickel hexahydrite? (identified by X-ray diffraction only; awaits chemical analysis)	$NiSO_4 \cdot 6H_2O$
celestite	$SrSO_4$
glauberite	$Na_2Ca(SO_4)_2$
calcite, aragonite	$CaCO_3$
dolomite	$CaMg(CO_3)_2$
halite	NaCl
sylvite	KCl
dickite	$Al_2Si_2O_5(OH)_4$
natron	$Na_2CO_3 \cdot 10H_2O$
trona	$Na_2CO_3 \cdot NaHCO_3 \cdot 2H_2O$
unidentified mineral	TiFe oxide

If subsurface water has ever been present in the Martian regolith, the critical environment parameters would be very similar to those of the Egyptian desert and a process similar to that now observed in this desert might be expected to mobilize and deposit sulfates and other species near the surface on Mars, forming a caliche-like duricrust and concentrated salt-crusts similar to those found in Egypt. Furthermore, the chemical weathering cycle of Mars might include this water solution and capillary transport mechanism affecting not only sulfur but the weathering, transportation, and deposition of many other elements. Salt-crusts formed at the surface by precipitation would also be incorporated into the aeolian cycle and become redistributed as detrital grains.

Whether the capillary process would work in an environment dominated by subsurface ice rather than liquid water remains to be shown. However, even under these conditions, migration toward the surface of sulfates through capillary films of water along grain surfaces and across grain boundaries is a possibility. It might be a very slow process but Martian geologic time may be sufficiently long to have allowed significant quantities of sulfates to be transported and deposited. If capillary processes have been active on Mars, our Egyptian desert results indicate that the Martian regolith is likely to be an exceedingly complex mixture containing a very large number of minerals. It therefore may not be at all amenable to simple chemical or mineral mixing models.

References:

Binder, A. B., Arvidson, R., Guinness, E., Jones, K., Morris, D., Mutch, T., Pieri, D. and Sagan, C. (1977) The Geology of the Viking 1 Lander Site. JGR 82, p. 4439-4451.

Clark, B. C., Baird, A. K., Rose, H. J., Toulmin, P., Christian, R. P., Kelliher, W. C., Castro, A. J., Rowe, C. D., Keil, K, and Huss, G. R. (1977) THE VIKING XRAY FLUORESCENCE EXPERIMENT: ANALYTICAL METHODS AND EARLY RESULTS, JGR, 82, p. 4577-4594.

El Baz, F. (1978) Analogs of Martian Eolian Features in Southwestern Egypt, COSPAR, Insbruck, Austria.

Gooding, J. L. (1978) Chemical weathering on Mars: Thermodynamic stabilities of primary minerals (and their alteration products) from mafic igneous rocks, Icarus 33, p. 483-513.

Toulmin, P., Baird, A., Clark, B., Keil, K., Rose, H., Christian, R., Evans, P. and Kelliher, W. (1977) Geochemical and Mineralogical Interpretation of Viking Inorganic Chemical Results, JGR 82, p. 4625-4634.

Wendorf, F., Schild, R., Said, R., Haynes, C., Gautier, A., and Kobusiewicz (1976) The Prehistory of the Egyptian Sahara, Science 193, p. 104-114

Geochemical Studies Within Simulated Martian Environments: Update, Michael C. Booth and Hugh H. Kieffer, Dept. of Earth and Space Sciences, Univ. of California, Los Angeles, CA, 90024.

The importance of carbonate formation to chemical weathering on Mars is being examined by the study of rock material subjected to simulated martian environments. A series of environmental simulation experiments is being conducted to determine the dependence of the rate of nonaqueous carbonate formation (Booth and Kieffer, 1978) on environmental pCO_2, pO_2, the abundance of H_2O, soil compositions and temperatures, ultraviolet irradiation and the rate of diurnal cycling. The primary focus of this work is to determine the mechanism by which carbonate material is generated within simulated environments, the nature of the carbonate species produced, and the applicability of such a CO_2 fixation mechanism to Mars.

The environmental system provides temperatures, atmospheric pressures and compositions, and UV fluxes appropriate to the martian surface. Diurnal temperature cycling can be accomplished, accompanied by the appropriate periods without UV irradiation. Water within the environment is controlled so as to prevent passage through the liquid phase. Water frosts formed when soils are at T_{min} = 180 K ("night") are induced to sublime upon gradual soil warming by maintaining values of pH_2O ~10^{-4} mbar throughout the diurnal cycle. The ultraviolet illumination system of the environmental simulation chamber is capable of providing direct UV irradiation of soil sample surfaces up to 100 times the anticipated solar flux at the martian surface, with a cutoff at ~2200 Å.

A variety of experiments is being conducted. The dependence of carbonate formation on pCO_2 has been examined over the range of 20 to 150 mbars. The effect of O_2 on carbonate formation has been studied at pCO_2 = 100 mbars with the addition of pO_2 = 50 mbars. Water, expressed in terms of precipitable micrometers cm^{-2}, is varied between 0 and 50 µm at four different atmospheric pressures of CO_2 to determine its importance to the generation of carbonate. Soils used included olivine ($(Fe,Mg)SiO_4$), enstatite ($MgSiO_3$), hypersthene ($(Mg,Fe)SiO_3$), hedenbergite ($CaFeSi_2O_6$), or fresh, glassy Mauna Ulu basalt, all crushed to powders having BET surface areas of 1-5 m^2/cc. Samples of other mafic minerals, including augite ($Ca(Mg,Fe)Si_2O_6$), and diopside ($CaMgSi_2O_6$) were not used because of minor (albeit significant) alteration to calcite. To determine the effect of low soil temperatures on carbonate formation, experiments were run having T_{max} values of 240, 260, and 270K (all $\pm$0.5K) instead of the nominal T_{max} values of 298 $\pm$1K. All experiments possessed soil temperature minima of 180 $\pm$0.5K. Carbonate formation as a function of ultraviolet irradiation was studied by comparison of experiments having direct illuminations of sample surfaces with those having only indirect illumination (sample shielded), and others without UV irradiation. Rates of diurnal cycling of two experiments were changed from the nominal 12 hours to either 6 or 24 hours to test for an effect of the rate of cycling on $CO_3^=$ growth. Additionally, $CO_3^=$ growth was measured in experiments of 18 and 114 hour duration to observe carbonate growth as a function of time.

Carbonate analysis of all experimental soils is performed on a vacuum system having a high precision manometer capable of measuring gas samples in the range 0.160 to 0.700 ±.005ml. Carbonate is decomposed to form a CO_2 gas sample by reaction of soil with 100% phosphoric acid in vacuo following soil degassing at 300°C. Analytic gases are also analyzed on a GCMS for a check of CO_2 purity. Most experimental soils generated were analyzed for carbonate as a function of depth below the sample surface to aid determination of any UV effects and to examine the nature of carbonate growth under nonaqueous conditions.

A number of conclusions can be made from experiments completed to date. First, the rate of carbonate growth in fresh tholeiitic basalt over the range of environments studied is $\sim 10^{12} cm^{-3} sec^{-1}$, possibly slowing with increased exposure time. The partial pressure of CO_2, the abundance of H_2O in the system, the soil composition and the soil temperature are important factors controlling $CO_3^=$ growth. Carbonate growth is markedly more rapid in some mafic minerals than others. Soil temperature effectively limits the carbonation process slowing dramatically with decreased soil temperature. A partial pressure of O_2 was not observed to affect carbonate formation in basaltic powder. Experiments examining the effect of UV similarly failed to influence the growth of carbonate although early results had suggested to the contrary. Carbonate distributions within samples are found to consistently be independent of depth below the sample surface, in agreement with previous work.

REFERENCES

1) Booth, M. C. and H. H. Kieffer, J. Geophys. Res., 83, 1809 (1978).

Volatile Evolution, Fraser P. Fanale, Space Sciences Division, Jet Propulsion Laboratory, California Institute of Technology.

We report new results on the adsorbate-adsorbent system CO_2-nontronite at temperatures of 230°K, 196°K and 158°K and pressures of from 1.0 mb to 100 mb covering the range of subsurface regolith temperature on Mars. These results, some of which are shown in Figure 1, together with a variety of Viking observations have allowed construction of an improved three part regolith-atmosphere-cap model which describes the storage and exchange of atmosphere-exchangeable CO_2 on Mars. Cold nontronite, and swelling clays in general, are far better adsorbers for CO_2 than cold pulverized basalt and exhibit far more complex adsorptive properties as well. Both observations result from a tendency for self-desiccation of clays at low temperature (even when the humidity is high). This produces an increase in energetically favorable adsorption sites for CO_2 plus the creation of a micropore structure allowing capillary condensation of CO_2 at martian near-polar temperatures. The layered terrain, and possibly the adjacent debris mantle, contains $\sim$2% or more by mass of atmosphere-exchangeable CO_2 ($\sim$12 ccSTP/g) and the total regolith inventory of available adsorbed CO_2 is estimated to be $\gtrsim 6 \times 10^{20}$ g or 4×10^2 g/cm^2 as a global average. Thus the "ocean" of adsorbed CO_2 in the regolith - not the atmosphere or surface caps - is the main repository of atmosphere-exchangeable CO_2.

Such a large near-polar subsurface reservoir of CO_2 at relatively constant temperature can - either directly or via a small quasi permanent cap - buffer the atmospheric CO_2 pressure on a long term basis at values high enough to allow annual caps to form in response to the wide seasonal variations in surface temperature. For example, isothermal removal (or addition) of atmospheric CO_2 causes the large regolith buffer to contribute (or adsorb) atmospheric CO_2 in response. Thermal changes also cause important buffering responses. The best understood of these is the obliquity variations which can produce a $\sim$15° increase or decrease in near-polar temperatures relative to present values. An increase would produce rapid dissipation of any possible quasi-permanent CO_2 cap following which the regolith alone would buffer pressures which could rise to at least $\sim$20 mb. A decrease would give rise to a situation in which the cap alone would buffer the pressure as it falls to a minimum of <1 mb. The role of the regolith as the pressure falls is probably to transfer much larger amounts of CO_2 mass to the growing cap than the cap would acquire from the atmosphere. The predicted variation in atmospheric pressure (which is greater than a factor of ten and independent of any postulates concerning the existence of a massive surface CO_2 reservoir) together with the predicted periodic variations in cap size is likely to have played an important role in the generation of the layered terrain and other surface features. Also the predicted periodic "flushing" of the atmosphere resulting from regolith-cap CO_2 transfer can explain the apparent suppression of ^{18}O enrichment in the atmosphere observed by the Viking probe mass spectrometer, while other aspects of the model are consistent with and help to explain the Viking lander GCMS and GEX results.

We earlier had proposed that the surface of Io was largely covered with a dehydrated mix of sulfur and a variety of salts rather than by frosts or ordinary rock forming minerals like other known planetary surfaces (Fanale et al, 1974, 1977). Also we had proposed that this coating was produced by a combination of endogenic defluidization of Io accompanied by H_2O loss to space (Fanale et al, 1974, 1977). Since our proposal was put forward, a major (∿30%) absorption band was discovered in the region 4.1 μm which was tentatively attributed to carbonates and nitrates by the discoverers (Cruickshank et al, 1978; Pollack et al, 1978). Other investigators have raised serious objections to these interpretations (Kieffer and Smyth, 1979). We have been obtaining spectra in the 0.3 - 5.0 μm region of the spectrum for various types of candidate materials which we feel may circumvent the spectral matching problems alluded to and may help to explain the 4.1 μm band. This work is a collaborative study with D. P. Cruickshank, R. Brown, R. Clark and T. B. McCord of the Institute for Astronomy of the University of Hawaii, and is being conducted at the Institute. As more laboratory data become available, we hope to be able to explain Io's optical properties in a manner consistent with what is known of its geological history. Part of the latter derives from recent theoretical geophysical insights (Peale et al, 1979). Part of the latter obviously also will derive from the Voyager mission and as those results are published we hope to collaborate (within the proprietary guidelines) with Voyager team members in relating our laboratory data to the spacecraft results.

References: Fanale, F. P., T. V. Johnson, and D. L. Matson, Science, 186, 922-925, 1974; Fanale, F. P., T. V. Johnson, and D. L. Matson, Planetary Sattelites, University of Arizona Press, 1977; Peale, S. J., P. Cassen, and R. T. Reynolds, Science, 203, 892-894, 1979; Pollack, J. B., et al, Icarus, 36, 271-303, 1978; Kieffer, H. H. and W. Smyth, Icarus, in press, 1979.

Figure Captions: Figure 1) Isotherms for CO_2 adsorption on Nontronite at 230°K, 196°K and 158°K are shown. Also shown are two previously published isotherms for ground basalt (Fanale and Cannon, 1978) at temperatures corresponding to the two coldest Nontronite isotherms. Temperatures are accurate to 1 - 2°C.

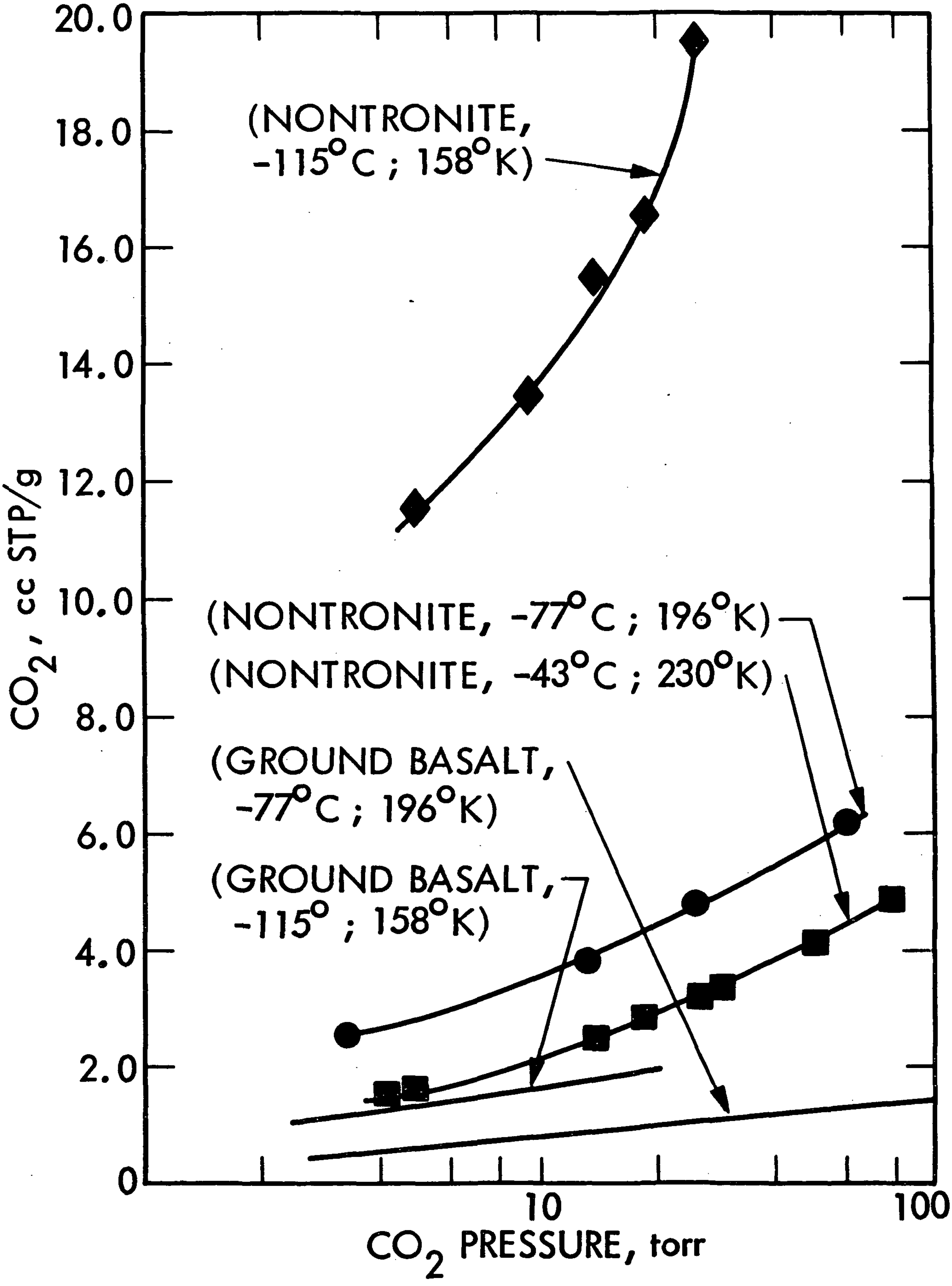
20.0
18.0
16.0
14.0
12.0
10.0
8.0
6.0
4.0
2.0
0
CO_2, cc STP/g
10
100
CO_2 PRESSURE, torr
(NONTRONITE, -115°C ; 158°K)
(NONTRONITE, -77°C ; 196°K)
(NONTRONITE, -43°C ; 230°K)
(GROUND BASALT, -77°C ; 196°K)
(GROUND BASALT, -115° ; 158°K)

Remote Sensing Evidence for Oases on Mars. R.L. Huguenin, U. Massachusetts, Dept. Physics/Astronomy-Hasbrouck, Amherst, MA. 01003 and Brown U. Dept. Geological Sci., Providence, R.I. 02912, S.M. Clifford, C.A. Sullivan, and K.J. Miller, U.Massachusetts Dept. Physics/Astronomy-Hasbrouck, Amherst, Ma 01003.

The Viking Molecular Analysis experiments revealed that the soils at the two landing sites were highly desiccated(1). For most samples (except under Badger Rock) no detectable H_2O evolved from soil heated to 200°C, while only $\sim$0.2% H_2O ($\sim$2mgH_2O g^{-1} soil) was driven off when the samples were heated to 350°C and 500°C. This indicates that there was essentially no physically adsorbed or interlayer H_2O in the samples, only the most strongly bound components (chemisorbed H_2O and water of hydration)(2). Apparently much of the surface has undergone the same extent of desiccation, as revealed by a near-ir full-disc reflectance spectrum of Mars that was obtained during the 1978 opposition(3). This spectrum showed absorption bands that we attributed to a mixture of H_2O ice and highly desiccated mineral hydrate, and it indicated that the average surface material across the visible disc was apparently as highly desiccated as the soils at the Viking sites.

The extent of desiccation revealed by the Viking experiments and the reflectance spectrum could not be produced by simple vacuum desiccation and freeze drying alone, particularly since H_2O vapor pressures become high enough each night to produce surface frosts(4). The high desiccation state is instead probably the result of photodesorption(5) and photodehydration (6) processes. Photodesorption has been shown to be very efficient and it has been argued that UV sunlight can completely desiccate exposed soils within an hour after sunrise and keep them desiccated until later afternoon(5). This process can operate only on the uppermost layer of soil, however, and thus the high desiccation state of the average surface material on the planet may be unrelated to the hydration state of materials immediately below the surface. The fact that material as deep as 26 cm at the Viking sites is so highly desiccated suggests that there probably isn't any H_2O ice or other subsurface source of H_2O vapor within several meters of the surface to hydrate the dust.

This is apparently not true at other locations of the planet however. Several lines of remote sensing evidence indicate that the hydration state of the regolith varies substantially from region to region, and that in several near-equatorial regions there may be near-surface reservoirs of liquid H_2O, salt brines, and ice.

One of the principal lines of evidence for a near-surface source of weakly-bound H_2O comes from spectrophotometric images that were obtained during the 1973 opposition(7). Indeed, blue-light (0.405μm) images that were measured on the second day of the 1973 dust storm revealed an anomalous outgassing of H_2O from the regolith in the vicinity of Solis Lacus (-25°, 85°). The images are shown on Figure 1. The H_2O appeared as two huge crescent shaped blue-light brightenings to northeast and southwest of a central bright spot in Solis Lacus. The northeast crescent extended from Western Tharsis (northwest of Solis Lacus) eastward to Coprates Chasma (northeast of Solis Lacus) and south into Western Erythraeum M. The southwest crescent spanned from Araxes (west of Solis Lacus) through Aonius Sinus (southwest of Solis Lacus) and into the western edge of Bosporus. The central bright spot was at the same location and had essentially the same physical dimensions as the dust cloud in the red images. These brightenings were attributed to ground fog and frosts(7). They were most intense at the onset of the storm(8) and rapidly faded during the morning hours of the second day (Figure 1). Smaller isolated brightenings sporadically appeared around the peripheries of the expanding dust clouds throughout the initial phase (Days 1-4) and expansion phase (Days 5-8) of the storm(8).

The sudden appearance of the frosts and hazes at the onset of the dust storm and their symmetrical distribution about the central Solis Lacus dust cloud indicate that Solis Lacus was apparently the site of origin of most of the outgassed H_2O. Current models of dust storm circulation within optically thick clouds(9) indicate descending winds at the sunlight-shielded center of the cloud and ascending winds at the unshielded edges of the cloud. The net effect is an outward radial surface flow of gas and dust from the storm center. H_2O vapor in the gas that is blown out beyond the peripheries of the cloud should become cooled in the relatively clearer atmosphere (where sunlit suspended dust doesn't heat the atmosphere) and condensation should occur where the vapor pressures are high enough. The source of the H_2O around Solis Lacus was apparently not significantly offset from the storm center; otherwise the frosts and hazes would not have been so symmetrically distributed. Furthermore, the appearance of the hazes and frosts at the onset of the storm and their gradual disappearance as the cloud expanded indicates that the amount of H_2O outgassed was apparently greatest at the origin of the storm and significantly less at distances farther out.

In order for the H_2O to have been released from the regolith at dust storm temperatures, it must have been weakly bound. The 1973 storm occurred during late Spring ($L_s \simeq 250°$) in the southern hemisphere when Mars was near perihelion. Solar insolation was at its annual maximum and abnormally large decreases in the absorptive capacity of the topsoil were possible; however the temperatures were still too low to affect any but the most weakly bound H_2O, viz. physically adsorbed H_2O, liquid H_2O, or ice (2,10). Solar heating during the diurnal cycle is capable of releasing H_2O to the atmosphere from the uppermost $\sim$ 3 cm of topsoil at the latitude of Solis Lacus(10). Potentially about 36 $mgH_2O\ cm^{-2}$ of adsorbed H_2O could be released(10). If it assumed that $\gtrsim$ 0.1 $mgH_2O\ cm^{-2}$ was needed to produce the observed brightenings (11) and that 36 $mgH_2O\ cm^{-2}$ was pulsed from the topsoil, then a source region the size of Solis Lacus could have supplied enough H_2O if $\gtrsim$ 10% of the H_2O condensed out as frost. This is an unrealistically high trapping efficiency. In addition it is unlikely that there was only the minimum 0.1 $mgH_2O\ cm^{-2}$ in the hazes and frosts, considering their nonuniform brightness and sublimation rates. It is furthermore unlikely that the entire Solis Lacus region outgassed uniformly; thus it would appear that significantly more than 36 $mgH_2O\ cm^{-2}$ was released. This indicates that H_2O ice or liquid was apparently present within the uppermost $\sim$3 cm of topsoil.

Origin of the Dust Storm. It is probably no coincidence that the sudden outgassing of H_2O occurred at the same time and place as the dust storm developed. Indeed Johnson et al.(12) proposed that such an explosive outgassing event may be a primary cause of the martian dust storms. They showed in a laboratory simulation that the diurnal heating that occurs near perihelion can desorb CO_2 at a higher rate than it can diffuse out of a surface dust layer. Subsurface pressures were found to increase to values that were capable of rupturing the surface explosively, injecting large amounts of dust into the atmosphere. They also found that gas jets developed along microfissures in the dust layer which raised additional dust into the atmosphere.

The amount of dust elevated was highly dependent on the warming rate of the surface and on the permeability of the dust barrier. For a 2 cm-thick layer of 1-10 µm dust they argued that heating rates would need to be several times higher (∿ 50° hr^{-1}) than the average perihelion heating rates (∿ 15° hr^{-1}) to produce the explosive outgassing. They argued that the higher warming rates could be achieved in shadowed areas, where the Sun's rays do not strike until late morning. We propose that such high warming rates would not be needed for soils that contain adsorbed H_2O and ice or water along with the CO_2. Fanale and Cannon(10) presented laboratory evidence that the top ∿3 cm of soil should release ∿12 mg cm^{-2} adsorbed CO_2 and ∿36 mg cm^{-2} adsorbed H_2O during diurnal heating. This is four times as much gas as when CO_2 alone is released; therefore the heating rate could be a factor of ∿4 lower (∿ 13° hr^{-1}) and release the same amount of gas. Even lower heating rates could release sufficient volumes of gas if H_2O ice or liquid was also present. These heating rates are close to the observed average heating rates (∿ 15° hr^{-1}) near perihelion in Solis Lacus, and thus the explosive perihelion outgassing phenomenon could have been significantly more widespread in Solis Lacus than in the 'drier' regions of that latitude. Indeed the sudden appearance of the H_2O frosts and hazes at the onset of the storm might be a reflection of the critical role that the outgassing of H_2O may have played in the generation of the 1973 dust storm.

Similar outgassing events (blue-light brightenings) occurred at the same location during the great 1956(14) and 1971(13) storms as well. The brightenings were observed in the vicinity of Solis Lacus several days before the onsets of the storms in Noachis-Hellespontus and they reappeared throughout the expansions of the storms. During the seventh day dust clouds were generated along with the blue-light brightenings, and for the subsequent two weeks Solis Planum persisted as a site of intense storm activity. In addition, the dust cloud activity in Noachis-Hellespontus and Hellas in 1956, 1971, and 1973 were also preceeded and accompanied by blue-light brightenings. In 1973 the outgassing in Noachis-Hellespontus and Hellas occurred ∿7 days after the onset of the storm in Solis Lacus. These observations suggest that in each of these regions H_2O outgassing may have played major roles in generating the dust storms. Other smaller storms may have been similarly caused. A map showing the regions in which dust clouds have preferentially formed since 1809 is shown in Figure 2 (15). These regions are also the sites of repeated blue-light brightenings(8,13,16).

Origin of DWCs (discreet white clouds). Blue-light brightenings not only occur near perihelion. They repeatedly appear in the region to the north and northwest of Solis Lacus in some of the same areas that comprised the 'northeast crescent' in Figure 1. Mariner 9 images showed these brightenings to be low-elevation H_2O clouds and hazes around the scarps at the bases of the Tharsis volcanoes, as well as in Tithonius Lacus and the Coprates canyon system(16). These brightenings have been observed at the same locations since 1924, appearing seasonally with peak activity at L_s = 90-130°(17), corresponding to the period following aphelion when the mean daily temperatures begin to increase(18) and produce a net outgassing of the regolith(10). The brightenings appeared during late morning and the afternoon and disappeared before dawn. These hazes and clouds were directly upslope from Solis Lacus, and a Solis Lacus origin for the water vapor would be fully consistent with the orographic convective uplift model proposed by Leovy et al.(16) to explain the diurnal and seasonal behavior of the brightenings. Similar brightenings are seen near Elysium with similar seasonal and diurnal behavior (17), and like the Tharsis brightenings they occur directly upslope from a source of perihelion blue-light and dust cloud activity at a site near Cerberus (+ 10°, 210° in Figure 2). Still another region that displays brightenings at L_s = 90-130° as well as at L_s ≃340° is Hellas, again at the same location as the observed perihelion activity. The Hellas brightenings do not, however, display the strong diurnal behavior of the other two sites, i.e. they remain bright over night. The association of these 'DWC' brightenings with the sites of perihelion outgassing and dust activity and their occurrence at the time when the planet is warming up from the aphelion minimum suggests that they may be produced from the same anomalous reservoirs as the perihelion brightenings.

Even more direct evidence for the occurrence of these anomalous reservoirs was provided by the Viking Water Vapor Mapping experiment(19). An H_2O abundance map for late Southern Winter (L_s = 155°-170°) is shown in Figure 3. Anomalously high column abundances can be seen over Solis Lacus (-15°, 85°) and Noachis-Hellespontus (centered on -20°, 310°) as well as over a broad area near Elysium (centered on +35°, 180°). More direct evidence for the Elysium-Cerberus outgassing as well as for some of the other areas in Figure 2 can be seen in a later L_s map (185°-200°)(19).

Oases. The observational evidence suggests that at least some and possibly all of the areas shown in Figure 2 contain anomalous H_2O reservoirs that extend to within a few cm of the surface. Two of these areas in particular, Solis Lacus and Noachis-Hellespontus, may truely be 'oases' on an otherwise quite hostile planet. One of the principal conclusions of the Viking biology experiments was that the surface environments at the two landing sites were too hostile for life as we know it, due primarily to the lack of liquid H_2O at high activity(20). Both properties of water (liquid state and high activity) are apparently required for the functioning of known living terrestrial organisms(20). Other factors that are considered growth-unhibiting include the low nighttime temperatures, the lack of detected organic nutrients, the occurrence of strong oxidants in the soil, and energetic UV sunlight. None of these factors are as critical to growth, however, as the high desiccation state of the soils. As discussed above, the volumes of H_2O that apparently outgas from Solis Lacus imply the presence of more than adsorbed H_2O in the soil. Farmer(21) has pointed out that H_2O in the regolith may form a metastable liquid phase due to the diffusion-limiting effects of fine-grained soil. Approximately a 1 cm thick layer of soil can apparently sufficiently inhibit the flow of H_2O vapor that vapor pressures can exceed the triple point, thus slowing the evaporation rate and allowing the liquid phase to become stable. The daily maximum surface temperatures at Solis Lacus range from about 230°K during Southern Winter (L_s = 90°) to above 290°K during Southern Spring (L_s = 250°). The surface layer in fact reaches above-freezing temperatures from late Winter (L_s = 170°) to late Summer (L_s = 350°); thus the near-surface layers could contain liquid H_2O during an appreciable fraction of the martian year. It is likely that the liquid would exist as a salt brine, considering the large concentrations of salts in martian soil(13). Such brines could appreciably extend the lifetime of the liquid phase: laboratory studies of freezing point depression indicate that the salts contained in martian soil could depress the freezing point by 40°K or more and it is thus possible that the H_2O might exist as a liquid during most of the martian year in Solis Lacus. Many of the other 'hostile' aspects of the Viking site environemnts (low nighttime temperatures, strong oxidants, and paucity of organic matter) are less severe in Solis Lacus (and probably the other areas in Figure 2) as well. Indeed the environment in Solis Lacus appears to be more hospitable than some of the extreme environments on Earth in which microorganisms have been found to adapt and thrive.

Acknowledgements. Contribution No. 13 of the Planetary Chemistry Laboratory. This research was supported by NASA grants NSG 7397 and NSG 7405.

References. (1) Biemann K. et al. (1977) J. Geophys. Res. 82, 4641; (2) Little L.H. (1966) Infrared Spectra of Adsorbed Species, Chapt. 10 and 13, Academic Press, NY; (3) McCord, T.B., Clark R.N. and Huguenin R.L. (1978) J. Geophys. Res. 83, 5433; (4) Farmer C. et al. (1977) J. Geophys. Res. 82, 4255; (5) Huguenin R.L., Prinn R.G. and Maderazzo M. (1977) Icarus 32, 270; (6) Anderson K. and Huguenin R. (1977) Bull. Amer. Astron. Soc. 9, 449; (7) McCord T.B., Huguenin R. and Johnson G. (1977) Icarus 31, 293; (8) Martin L.(1976) Icarus 29, 363; (9) Golitsyn G. (1973) Icarus 18, 113; (10) Fanale F. and Cannon W. (1974) J. Geophys. Res. 79, 3397; (11) Peale S. (1973) Icarus 18; 497; (12) Johnson D., Harteck P. and Reeves R. (1975) Icarus 26, 441; (13) Martin L. (1974) Icarus 23, 108; (14) Dollfus A. (1965) Ann. Astrophys. 28, 722; (15) Arvidson R. (1972) Geol. Soc. Amer. Bull. 83, 1503; (16) Leovy C. et al. (1973) J. Geophys. Res. 78, 4252; (17) Smith S. and Smith B. (1972) Icarus 16, 509; (18) Kieffer H. et al. (1977) J. Geophys. Res. 82, 4249; (19) Farmer C. et al. (1977) J. Geophys. Res. 82, 4225; (20) Mazur P. et al.(1978) Space Sci. Rev. 22, 3; (21) Farmer C. (1976) Icarus 28, 279.

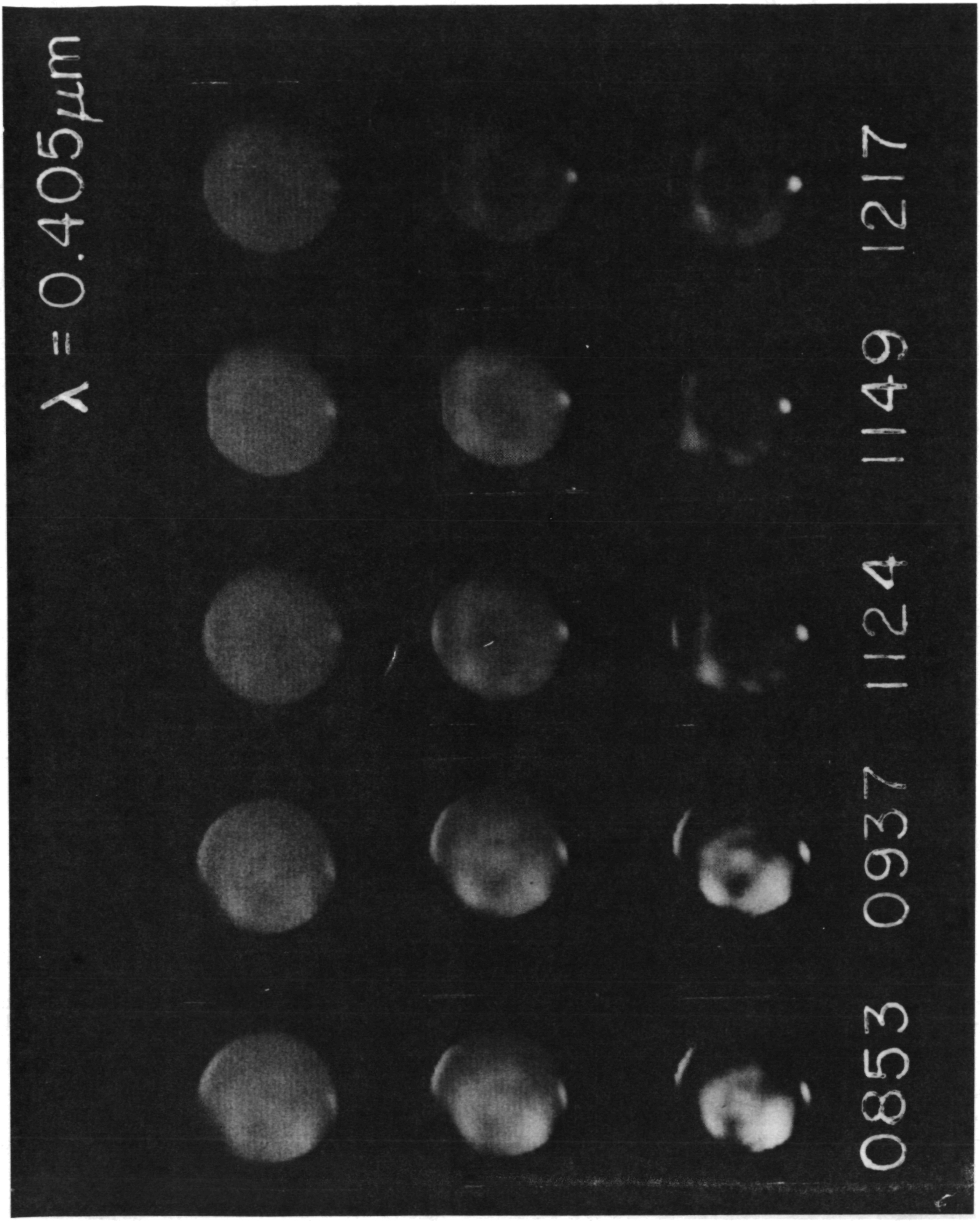
λ = 0.405μm
0853
0937
1124
1149
1217

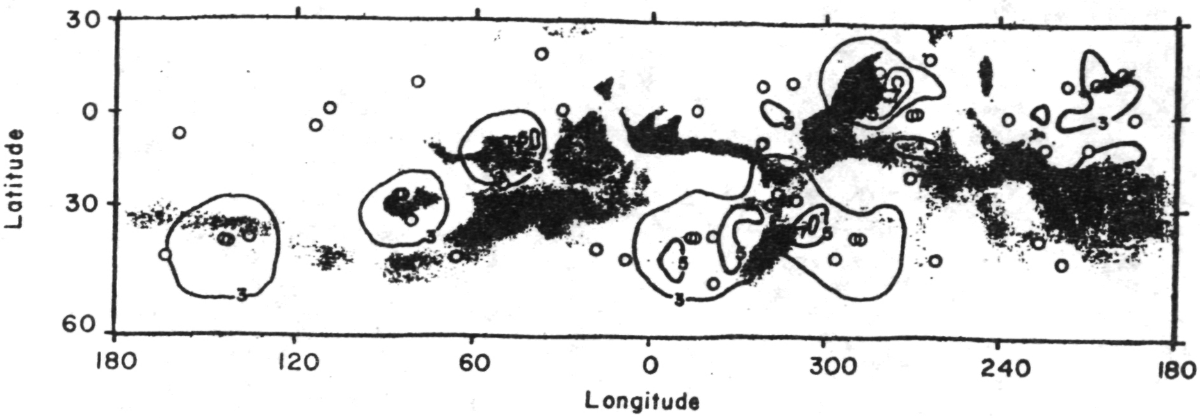
30
0
30
60
Latitude
180
120
60
0
300
240
180
Longitude
3
5

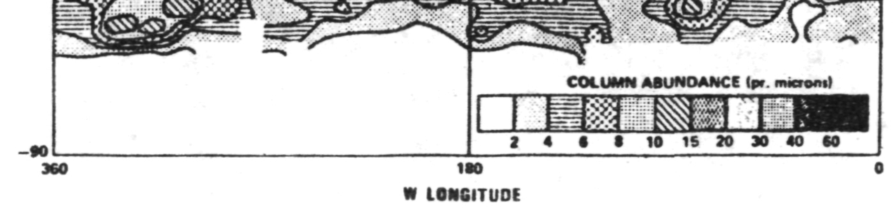
90
Eq
−90
LATITUDE
Eq
COLUMN ABUNDANCE (pr. microns)
2
4
6
8
10
15
20
30
40
60
360
180
0
W LONGITUDE

VOLATILE STUDIES AND NEW INSTRUMENTAL ANALYSIS TECHNIQUES FOR MARTIAN SOIL ANALOGS.

Everett K. Gibson, SN7,Geochem., NASA-JSC, Houston, TX 77058, M.A. Urbancic, Chem. Dept., U. of Illinois, Urbana, IL., and F.F. Andrawes, Lockheed Electronics Co., Inc., Houston, TX.

Study of volatiles in Martian surface materials has great potential for determining the history of the planet and the nature of the processes that are now, or have been active. Characterization of volatile phases in the Martian soil can provide valuable information on the composition, extent of differentiation, and the geologic history of the planet and on the processes of weathering, erosion, transport, and sedimentation on the surface.

Viking XRF and GCMS data suggests that 1 to 10% of the regolith materials are comprised of low-temperature minerals such as hydrates, carbonates, sulfates, clays, evaporites, etc. (1,2). Reflectance spectroscopy and data from Viking photography suggest that surface materials are coated with hydrated iron oxides (limonite-goethite)(3-6). Additional pre-Viking infrared data on dust in the upper atmosphere identified montmorillonitic clay as a component. Huguenin's (4,5) results suggest that hydrated iron oxides and montmorillonite can be effectively produced (from magnetite and silicates, respectively) under simulated Martian conditions by UV irradiation in the presence of adsorbed H_2O. The water vapor mapping experiment has shown intensive H_2O vapor movement in the Martian atmosphere which indicates that adsorption and desorption processes are operative near the surface of the planet (7). Thus, the Martian atmosphere and previous episodes of fluvial activity appear to have reacted substantially with the regolith and may have produced a significant accumulation of volatile containing minerals. In addition low-temperature minerals may have been formed by chemical precipitation from a pre-existing hydrosphere or as residues left when salt-laden ground water reached the surface and evaporated or froze. The obvious existence of episodes of volcanic activity during Martian history suggests that episodes of intense degassing may have occurred and brought significant amounts of sulfur and halides to the surface, as well as H_2O and CO_2.

Previous studies of the volatile phases in terrestrial and extraterrestrial materials using inorganic gas release and thermal decomposition-pyrolysis techniques have clearly shown the usefullness of these methods in characterizing the nature of the volatiles which are found on the surfaces of planetary objects (8,9). During the past year we have been experimentally measuring the thermal stabilities, under simulated Martian conditons, a variety of low-temperature minerals which might be present within the Martian regolith. We have also continued our development work on new analytical methods which might be used to study the volatiles in regolith samples.

The stabilities of mineral phases are dependent upon several external parameters (e.g. pressure, temperatures, and atmospheric composition). We have been studying the stability of carbonates, hydrates, sulfates, clays, and selected evaporite minerals. Samples have been heated under different heating rates, atmospheres, and pressures in order to determine the stability ranges for these assembleges which may be present on the surface of Mars. The results have direct application for defining the operating conditions for analytical instruments which may be used for volatile analysis. For example, the decomposition temperature of calcite can be changed over 600°C depending upon the experimental conditions (e.g. pressure and gas composition above sample during pyrolysis). Data in Fig. 1 represents the range of decomposition temperatures resulting from heating calcite at 10°C/min. in atmospheres of N_2, CO_2 and air at different pressures. In addition, the effects of heating rate have also been studied (Fig. 2) using samples of siderite. Samples were heated at 1, 2, 10 and 20°C/min. and the decomposition temperature was changed by 100°C. With faster heating rates the sample was never able to reach thermal equilibrium at a particular temperature-resulting in an apparent elevation in decomposition temperature. Experimental parameters must be accurately controlled if meaningful results are to be obtained. From the data in Fig. 1 and 2, it is understandable why the Viking GCNS experiment failed to measure significant abundances of CO_2 during pyrolysis of Martian surface samples if carbonates were present.because of their experimental studies were carried out in a CO_2 atmosphere (1).

During the past year we have developed a unique analytical capability for measuring H_2O in samples at the nanogram concentration level using gas chromatography (10). Water and other volatiles are released either by pyrolysis, crushing, or extraction and introduced into chromatographic columns where individual gases are separated and later analyzed using the sensitive helium ionization detector (Fig. 3). Water can be measured directly or as acetylene after conversion with CaC_2. Analysis of H_2O and other gases from a Pele's tear upon crushing is shown in Fig. 4. The direct measurement of water is shown in Fig.5 where the volatiles were released during pyrolysis of the volatile-rich Murray C2 carbonaceous chondrite. The continued development of the analysis techniques is underway and hopefully the results will lead to methods which can easily be incorporated in future flight instruments designed to measure volatiles on planetary surfaces.

References: (1) Biemann et al. (1976) J.G.R. 82, 4641-4658. (2) Clark (1976) Science 194, 1283-1288. (3) Adams (1968) Science 159, 1453-1455. (4) Huguenin (1974) J.G.R. 79, 3895-3903. (5) Huguenin (1976) Icarcus 28, 203-212. (6) McCord et al. (1979) Second Intern. Colloq. Mars (abs) 56-57. (7) Farmer et al. (1976) Science 194, 1339-1341. (8) Gibson (1973) Thermochim. Acta 5, 243-255. (9) Duffield et al. (1977) J. Res. U.S.G.S. 5, 92-101. (10) Andrawes and Gibson (1979) Am. Mineral. 64, 453-463.

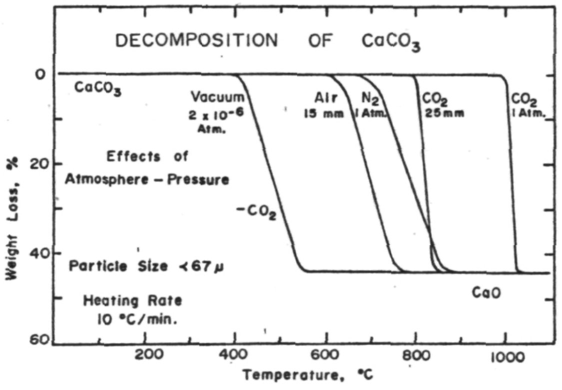

Fig. 1 Decomposition of calcite as a function of pressure and atmosphere composition.

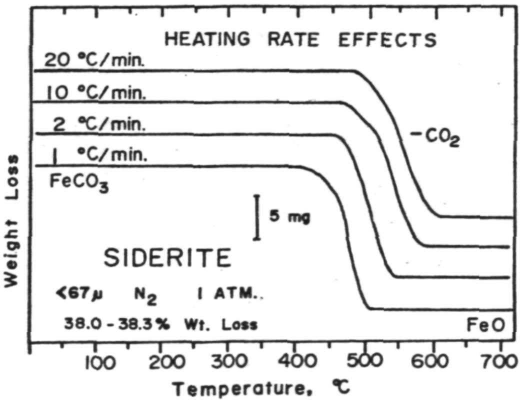

Fig. 2 Decomposition of siderite as a function of heating rate.

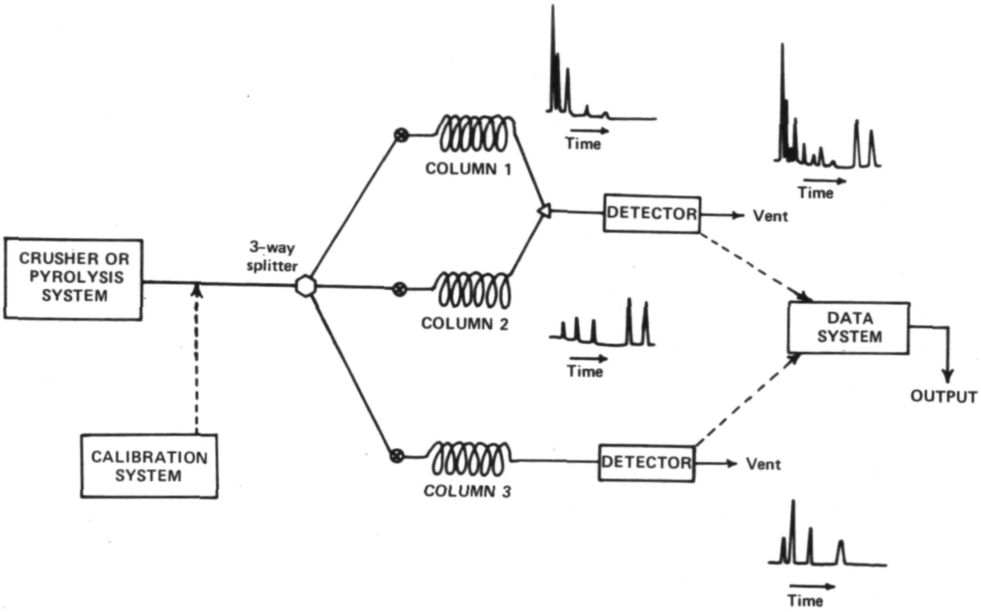

Fig. 3. Schematic of gas analysis system for volatiles using gas chromatography.

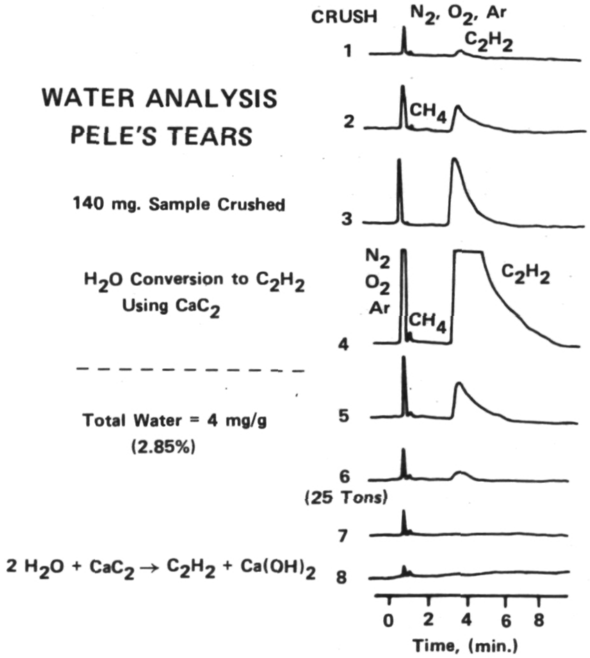

Fig. 4 Water and other volatiles measured in crushed sample of Pele's tears.

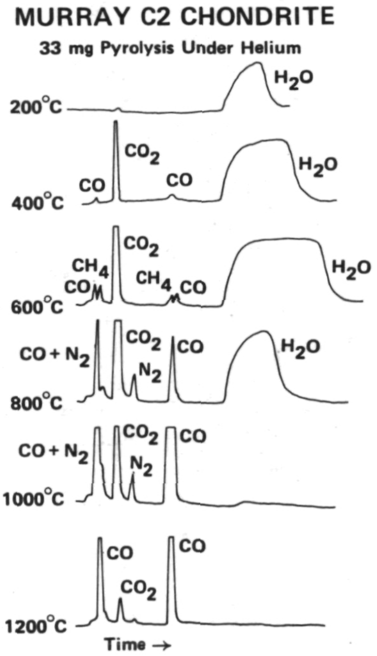

Fig. 5 Pyrolysis of Murray C2 carbonaceous chondrite showing sequence of volatile releases.

Rocks in the Sample Fields of Viking Landers 1 and 2

H. J. Moore, U.S. Geol. Survey, Menlo Park, CA 94025; C. R. Spitzer, NASA Langley Res. Ctr., Hampton, VA 23665; R. F. Scott, Dept. Engr. and Appl. Sciences, Calif. Inst. Tech., Pasadena, CA 91125; R. E. Hutton, 1501 Palos Verde Dr., Harbor City, CA 90710; and R. W. Shorthill, Univ. of Utah Res. Inst., Salt Lake City, UT 84108.

Maps of the Viking Lander 1 (VL-1) and 2 (VL-2) sample fields carefully prepared using stereometric measurements and monoscopic techniques were used to obtain the size-frequency distributions of rocks larger than 3.5 cm. Our size-frequency distributions are in good agreement with the published results of others (Binder et al., 1977). Modal frequencies of rocks for both sample fields are between 5 and 7 cm. The frequency of rocks in this interval for VL-1 ($\simeq$4.8 rocks/m^2) is about twice as large as that of VL-2. Incremental frequencies of rocks smaller than 10 cm are higher at the VL-1 site than at the VL-2 site, but above this size the reverse is true. Therefore, the fraction of area covered by rocks larger than 3.5 cm at the VL-2 site (0.14) is nearly twice that at the VL-1 site (0.08). Size-frequency distributions of rocks smaller than 3.5 cm have not been determined and await receipt of orthographic projections of pictures of the sample fields.

Surface Sampler operations designed to obtain samples of the coarse fraction of the surface materials (0.2 cm to 1.25 cm) suggest that: (1) the clods of material delivered to the XRFS instrument from the blocky material of Rocky Flats (VL-1) may represent the same population as the larger objects and (2) the marked decline in numbers of rocks less than 14 cm at the VL-2 site is also present at the finer sizes. The amount of coarse material delivered to the VL-1 XRFS on Sols 34 and 40 implies volume fractions of coarse material of 0.13 and 0.10 and, when allotted equally to each size increment of $D\sqrt{2}$, the inferred mass fractions are 0.025 and 0.019. For larger rocks (5 to 20 cm) the corresponding mass fractions are 0.016 and 0.018. Large motor currents during comminution of samples of blocky material that are finer than 0.2 cm from Rocky Flats imply that there is a substantial number of fragments or clods that must be crushed to sizes finer than 300 μm (Shorthill et al., 1976). Although the coarse fraction may represent the same population as the larger rocks, it appears that the material crushed has been weathered and altered because the chemical composition implies a weathered product (Toulmin et al., 1977), and increased vibration time in the Surface Sampler collector head in acquisition sequences appears to disaggregate more of the clods. The large objects (>5 cm) or rocks appear to be relatively strong.

For all practical purposes, the coarse fraction (0.2 cm to 12.5 cm) at the VL-2 site can be considered to be zero. Despite some 65 sample acquisition strokes and attempts to deliver coarse material to the XRFS instrument, no samples were received in sufficient amounts for analyses, and endeavors to construct a pile of "rocks" did not succeed. Thus, the rapid decrease of rocks revealed in the histograms for the large rocks of VL-2 is real. Many of the lumps and tabular units seen in the sample field are weakly cohesive units of "soil-like" material (Moore et al., 1977). These materials have been called "duricrust", but backhoe touchdown experiments and attempts to acquire samples of the coarse fraction show that the "duricrust" is not very durable or indurated. It is like a terrestrial soil that can easily be disaggregated by finger pressure. The rocks at the VL-2 site are relatively strong because they did not chip, spall, or break when the surface sampler pushed them (Moore et al., 1978).

Impact cratering has contributed substantially to the general appearance of the VL-1 landing site but it is entirely possible, if not probable, that outcrops are present (Binder et al., 1977). Calculations using the crater size-frequency distribution of small craters (100-1000 m across) for the VL-1 site (Dial, 1978), ejecta thickness equations for small terrestrial craters (McGetchin et al., 1973), and calculus suggest that the area of small craters and their ejecta that is 0.1 m thick or thicker is equal to 0.55 of the total area. This may be an underestimate if the crater size-frequency distribution extends down to diameters of 50 m, in which case the area of small craters and their ejecta is equal to 1.02 of the total area. In any case, ejected blocks from impact craters must be responsible for many, if not all, of the rocks observed in the sample fields and the local presence of rock outcrops is also probable with this model.

It also appears probable that many, if not all, of the blocks at the VL-2 site are ejecta from the crater Mie (Mutch et al., 1977). Using equations for large craters (McGetchin et al., 1973) and a radius of 50 km, calculations indicate an equivalent thickness of ejecta from Mie expected at the VL-2 site is near 3 to 4 m and a thickness of 0.1 m should extend to distances of 860 km from the center of Mie. At these large distances, the Mie ejecta should be mixed with local materials (Oberbeck et al., 1975).

References:

Binder, A. B., et al. (1977) The geology of the Viking Lander 1 site: Jour. Geophys. Res., v. 82, p. 4439-4451.

Dial, A. A. (1978) The Viking 1 landing site crater diameter-frequency distribution: NASA Tech. Memo. 79729, p. 179-181.

McGetchin, T. R., et al. (1973) Radial thickness variation in impact crater ejecta: implications for lunar basin deposits: Planet. Sci. Lett., v. 20, p. 226-236.

Moore, H. J., et al. (1978) Rock pushing and sampling under rocks on Mars: U.S. Geol. Survey Prof. Paper 1081, 21 p.

Moore, H. J., et al. (1977) Surface materials of the Viking landing sites: Jour. Geophys. Res., v. 82, p. 4497-4522.

Mutch, T. A., et al. (1977) The geology of the Viking Lander 2 site: Jour. Geophys. Res., v. 82, p. 4452-4467.

Oberbeck, V. R., et al. (1975) The origin of lunar smooth plains: The Moon, v. 12, p. 19-54.

Shorthill, R. W., et al. (1976) The "soil" of Mars (Viking 1): Science, v. 194, p. 91-97.

Toulmin, Priestley, III, et al. (1977) Geochemical and mineralogic interpretation of the Viking inorganic chemical results: Jour. Geophys. Res., v. 82, p. 4625-4634.

MINERALOGY OF CALICHE-LIKE SALT CRUSTS FROM THE WESTERN DESERT, EGYPT: IMPLICATIONS FOR MARTIAN DURACRUST FORMATION.

Donna J. Prestel, Lockheed Electronics Co., Inc., Houston, TX 77058
David S. McKay, SN6/NASA Johnson Space Center, Houston, TX 77058
C. Vance Haynes, Depts. of Anthropology and Geosciences, Univ. of Arizona, Tucson, AZ

Martian Duracrust. Duracrust is the term given to the indurated upper horizon of Martian regolith found at both Viking landing sites (Binder et al., 1977). This fractured crust was exposed when Viking retro-engines swept loose dust away from the landing sites. Binder et al. (1977) propose that this crust formed when mineral-bearing waters moved upward by capillary action, evaporated, and precipitated salts in the duracrust horizon. The XRF results showed that this crust is high in sulfur, containing possibly about 10% magnesium sulfate (Clark et al., 1977). The presence of this duracrust, with its enriched sulfur content, can be interpreted to indicate that atmosphere-regolith interactions involving water have been important weathering processes at some time in Martian history.

In order to more completely understand this process as it might occur on Mars we have undertaken a study of an analogous process in one of the most arid environments on Earth, the Western Desert of Egypt.

The Western Desert of Egypt as an Analog to Martian Regolith. Similarities between the two environments are striking. The Egyptian desert is extremely dry; parts have not had measurable rainfall in recent history. The overall rainfall for this region is less than 1 mm/year (Wendorf et al., 1976). The region is dominated by aeolean erosion; water drainage lines are almost completely absent. Large quantities of the sand and rock fragments deflated from the basins by wind have been deposited as great chains of sand dunes which have been compared to some of the large dune fields on Mars (El-Baz, 1978).

Samples which we studied consist of isolated documented surface samples and samples from vertical stratigraphic section through caliche-like deposits collected from deflation basins along an ancient caravan route, the Darb El Arba'in. Many of the samples are from near birs (wells). Samples from Holocene playas and from salt crusts formed from upward migrating ground water are represented.

We are investigating these samples by x-ray diffraction and by scanning electron microscopy with attached energy dispersive x-ray analyzer (EDXA). Table 1 is a summary of the minerals identified in our initial investigation.

The preponderance of sulfates in this suite correlates well with the implied presence of sulfates in the Viking results. Furthermore, the clay mineral dickite found in our samples is a member of the Kaolinite group which is predicted by Gooding (1978) to be the only clay mineral which should be thermodynamically stable on the surface of Mars. Viking investigators, however, infer that smectite clays may be a major constituent of Viking analyzed material, although the evidence is indirect (Toulmin et al., 1977).

If subsurface water has ever been present in the Martian regolith, the critical environment parameters would be very similar to those of the Egyptian desert and a process similar to that now observed in this desert might be expected to mobilize and deposit sulfates and other species near the surface on Mars, forming a caliche-like duracrust and concentrated salt-crusts similar to those found in Egypt. Furthermore, the chemical weathering cycle of Mars might include this water solution and capillary transport mechanism affecting not only sulfur but the weathering, transportation, and deposition of many other elements. Salt-crusts formed at the surface by precipitation would also be incorporated into the aeolean cycle and become redistributed as detrital grains.

Table 1. Minerals identified in caliche deposits of the south Western Desert of Egypt

quartz, chalcedony	SiO_2
gypsum	$CaSO_4 \cdot 2H_2O$
anhydrite	$CaSO_4$
bassanite (hemi-hydrate)	$CaSO_4 \cdot 1/2\ H_2O$
γ-$CaSO_4$ (soluble anhydrite, or dehydrated hemihydrate)	$CaSO_4$ (metastable)
tamarugite	$NaAl(SO_4)_2 \cdot 6H_2O$
bloedite	$Na_2Mg(SO_4)_2 \cdot 4H_2O$
epsomite	$MgSO_4 \cdot 7H_2O$
hexahydrite	$MgSO_4 \cdot 6H_2O$
nickel hexahydrite? (identified by X-ray diffraction only; awaits chemical analysis)	$NiSO_4 \cdot 6H_2O$
celestite	$SrSO_4$
glauberite	$Na_2Ca(SO_4)_2$
calcite, aragonite	$CaCO_3$
dolomite	$CaMg(CO_3)_2$
halite	$NaCl$
sylvite	KCl
dickite	$Al_2Si_2O_5(OH)_4$
natron	$Na_2CO_3 \cdot 10H_2O$
trona	$Na_2CO_3 \cdot NaHCO_3 \cdot 2H_2O$
unidentified mineral	TiFe oxide

Whether the capillary process would work in an environment dominated by subsurface ice rather than liquid water remains to be shown. However, even under these conditions, migration toward the surface of sulfates through capillary films of water along grain surfaces and across grain boundaries is a possibility. It might be a very slow process but Martian geologic time may be sufficiently long to have allowed significant quantities of sulfates to be transported and deposited. If capillary processes have been active on Mars, our Egyptian desert results indicate that the Martian regolith is likely to be an exceedingly complex mixture containing a very large number of minerals. It therefore may not be at all amenable to simple chemical or mineral mixing models.

References:

Binder, A. B., Arvidson, R., Guinness, E., Jones, K., Morris, D., Mutch, T., Pieri, D. and Sagen, S. (1977) The Geology of the Viking 1 Lander Site. JGR 82, p. 4439-4451.

Clark, B. (1978) Implications of Abundant Hygroscopic Minerals in the Martian Regolith, Icarus 34, p. 645-665.

El Baz, F. (1978) Analogs of Martian Eolian Features in Southwestern Egypt, COSPAR, Insbruck Austria.

Toulmin, P., Baird, A., Clark, B., Keil, K., Rose, H., Christian, R., Evans, P. and Kelliher, W. (1977) Geochemical and Mineralogical Interpretation of Viking Inorganic Chemical Results, JGR 82, p. 4625-4634.

Wendorf, F., Schild, R., Said, R., Haynes, C., Gautier, A. and Kobusiewicz (1976) The Prehistory of the Egyptian Sahara, Science 193, p. 104-114.

ANALYSIS OF CONDENSATES FORMED AT THE VIKING 2 LANDER SITE DURING THE MARTIAN WINTER

Stephen D. Wall, Jet Propulsion Laboratory
Kenneth L. Jones, Planetary Research Inc.

The Viking 2 lander cameras observed the accumulation and subsequent disappearance of a white surface condensate during the lander's first Martian winter. Preliminary conclusions were that the condensate was largely CO_2(s) which condensed directly on the surface. Temperatures did briefly reach the CO_2 condensation point of 151°K but further analysis of deposition and removal rates show that a significant amount of H_2O was involved. The deposition mechanism was more likely to have been condensation onto surfaces of dust grains in the atmosphere and subsequent precipitation to the surface as snow.[1] The condensate is distinguishable by both color contrast and broadband albedo contrast with the Martian surface. Figure 1(a), VL-2 image 21E113 (sol 341), shows accumulation in the sample trenches and within the lander shadows in the foreground; in figure 1(b), taken 24 sols later, part of the accumulation within the trench is gone but areas immediately surrounding rocks are still coated. Unfortunately, both color contrast and albedo difference were obscured during much of the Martian winter by constant changes in both intensity and coloration of the solar irradiance as two major dust storms passed over the landing site. Reference test charts on the lander intended to compensate for irradiance changes are dust-coated and therefore not usable for decalibration.

In order to provide a measure of relative surface changes independent of irradiance changes, dimensionless coordinates similar to CIE chromaticity coordinates have been devised. These were calculated for selected surface patches and for a dust-free portion of the lander body; ratios of these coordinates are approximately independent of sky color variations. Figure 2 is a plot of the "red" coordinate for a surface patch which later showed obvious condensate accumulation ratioed to the "red" coordinate of the lander body versus time. Atmospheric effects are approximately removed, and the remaining color change shows that condensate began to appear as early as sol 200 and continued to accumulate until sol 280. Broadband (black-and-white) imagery (as in figure 1) shows that some patches remained as late as sol 449, when temperatures averaged around 200°K. This behavior is inconsistent with either a CO_2(s) or CO_2 clathrate composition.

This abstract presents the results of one phase of research at the Jet Propulsion Laboratory sponsored by the Mars Data Analysis Program, Planetary Geology Program Office, NASA Constract NAS7-100. Preliminary analysis was sponsored by the Viking Program Office, Office of Space Sciences, National Aeronautics and Space Administration.

---

[1] Jones et al., Science, in press, 1979.

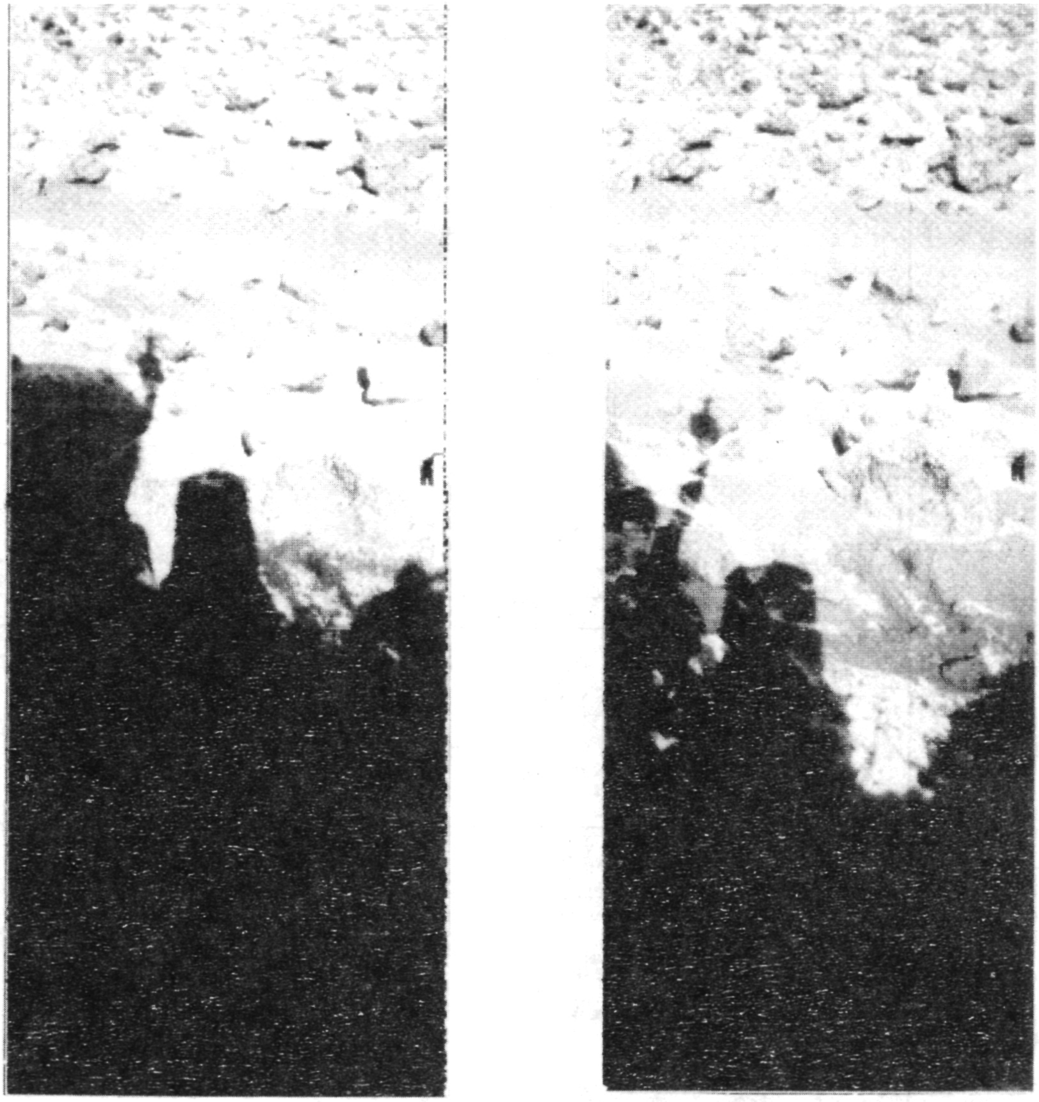

a b

Figure 1. - (a) VL-2 image 21E113/341 (78/01/28/202757). Condensate accumulation is evident in both sample trenches and around many rocks. (b) VL-2 image 21E153/365 (78/02/04/122041). Some condensate has begun to disappear, but remnants can be seen in trenches and near rocks.

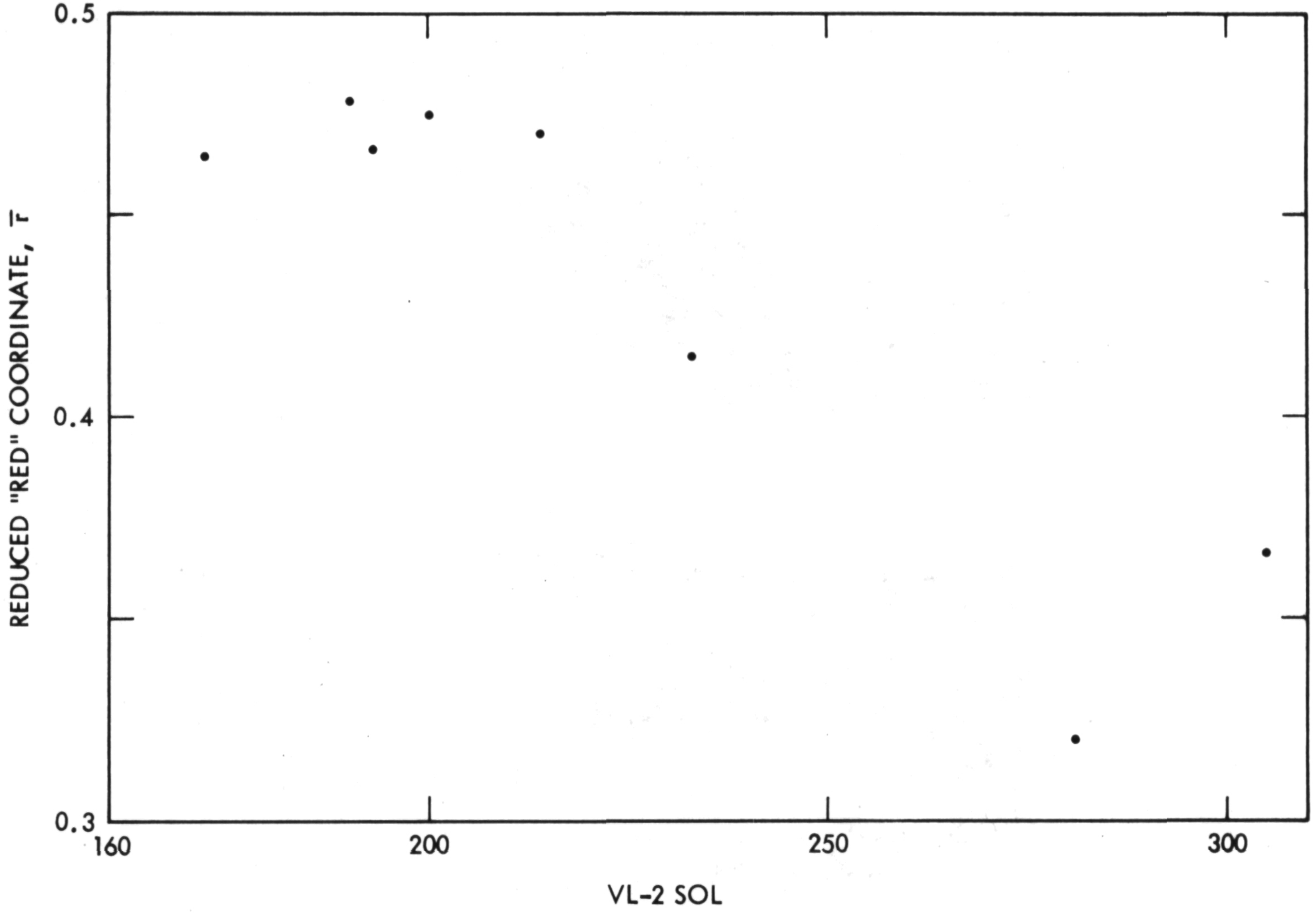

FIGURE 2. - PLOT OF 'RED' COORDINATE OF CONDENSATE PATCH RATIOED TO 'RED' COORDINATE OF LANDER BODY VERSUS TIME

EXPERIMENTAL EVIDENCE AGAINST THE UV PHOTOCHEMICAL OXIDATION OF MAGNETITE

Richard V. Morris, Code SN7, NASA-JSC, Houston, TX 77058, and Howard V. Lauer, Jr., LEC, Houston, TX 77058

Introduction

Electromagnetic radiation incident on a solid material can be reflected, transmitted, scattered, or absorbed. Absorbed electromagnetic energy either causes a photochemical reaction, is converted to heat, or both. In the case of conversion to heat, the temperature of the material can increase and, if the increase is sufficient in magnitude, a thermal reaction can occur. That is, the reaction is thermal in nature independent of the source of the heat. Huguenin (1973a,b) studied the interaction of electromagnetic radiation with magnetite and concluded that, in O_2-bearing atmospheres, magnetite is photochemically oxidized by UV radiation, the photochemical reaction involving the photoejection of an electron from the ferrous ion of magnetite (Fe_3O_4). Huguenin argues the same process occurs on Mars because solar UV radiation penetrates to its surface. In this abstract, we report, in contradiction to the results of Huguenin, experimental results that show UV radiation does not photochemically oxidize magnetite in O_2-bearing atmospheres. We observe magnetite oxidation, but only when the intensity of the incident radiation was sufficiently high such that radiant heating raised the temperature of the magnetite samples above the thermal oxidation threshold.

Experimental Procedure

The irradiation experiments were conducted using the Martian Weathering Simulation Facility at JSC. The apparatus used for our experiments consisted of a 1000 watt high pressure Xe lamp, a UV-grade mirror and UV-grade quartz lenses for focusing the radiation onto the sample, broad band filters for varying the spectral distribution of radiation incident on the sample, and a sample chamber in which the pressure and composition of the O_2-bearing atmosphere and the sample temperature could be controlled. The Xe lamp emits high intensity UV, visible, and IR radiation. During irradiation, the gas in the sample chamber is circulated through the sample to create a fluidized bed and expose all the surfaces of the particulate magnetite samples to the radiation. The temperature of the sample was monitored by a thermocouple that was in intimate contact with the magnetite.

For the present study, the magnetite was irradiated with either UV-Visible-IR radiation, shorthand notatation Xe(UV-VIS-IR), or with predominantly UV radiation, shorthand notation Xe(UV). Xe(UV-VIS-IR) was achieved by using just the Xe lamp and associated optics; Xe(UV), by inserting a water filter and a Corning #7-54 filter into the optical path.

Since magnetite and its oxidation products maghemite (γ-Fe_2O_3) and hematite (α-Fe_2O_3) have saturation magnetizations (J_s) of about 92, 73, and 0.5 emu/g, respectively, the extent of oxidation can be determined by measurements of J_s. We measured the values of J_s for our samples with a vibrating sample magnetometer.

Results and Discussion

The results of irradiation experiments for a natural magnetite powder (denote as CMM) having a nominal mean particle size of 6 μm are shown in Fig. 1. After three hours irradiation with Xe(UV-VIS-IR) from the 1000 watt lamp, the ratio $J_s(t)/J_s(0)$ decreased to a value of $\sim$ 0.1 from its value of 1.0

before irradiation. X-ray analysis showed the oxidation product was hematite so that ∿ 90% of the magnetite was oxidized. In all cases, the oxidized samples were maroon in color. As a result of radiant heating, the sample temperature during this set of experiments was ∿ 540°C. This temperature is considerably in excess of the thermal oxidation threshold, which we determined to be ∿ 150°C for CMM magnetite by heating experiments in air in a furnace. Furthermore, furnace heating at ∿ 540°C produced about the same degree of oxidation as in the Xe(UV-VIS-IR) experiments with the 1000 watt lamp. Thus, the results for the Xe(UV-VIS-IR) irradiations can be satisfactorily explained by a thermal oxidation process alone. However, a photochemical oxidation process could be operating concurrently.

As also shown in Fig. 1, a dramatically different result is obtained when CMM magnetite is irradiated in the Xe(UV) configuration with the 1000 watt lamp. Within experimental error of the $J_s(t)/J_s(0)$ measurements and for irradiation times as long as ∿ 130 hrs, no oxidation (either thermal or photochemical) of the magnetite was observed. All samples were still black after irradiation. No perceptable thermal oxidation was anticipated because, with most of the visible and IR filtered from the Xe light, radiant heating resulted in a temperature of ∿ 80°C, about 70°C below the thermal oxidation threshold. No perceptable photochemical oxidation by the UV radiation leaves little doubt that the oxidation observed in the Xe(UV-VIS-IR) experiments discussed above was entirely thermal in nature. CMM magnetite is not the only magnetite powder for which we have observed no perceptable oxidation upon irradiation with the 1000 watt lamp in the Xe(UV) configuration. Fig. 2 shows it was not observed for a synthetic magnetic powder having a nominal mean grain size of 0.5 μm (CPS1), a different natural magnetite powder having a nominal mean grain size of 1.0 μm (CPN1), and another synthetic magnetite powder having an unknown mean grain size (MCB1).

Our conclusion of no perceptable UV photochemical oxidation of magnetite is contradictory to that of Huguenin (1973a,b). We note that Huguenin used a Xe(UV-VIS-IR)-type configuration with a 300 watt lamp and apparently did not measure the sample temperature with a sensor in intimate contact with the sample. With radiant heating, we found the temperature decreased very rapidly as the thermocouple was moved away from the sample. We also found that, even with only a ∿ 120 watt lamp in the Xe(UV-VIS-IR) configuration, the sample temperature was ∿ 400°C which is in excess of the thermal oxidation threshold. Therefore, at present we consider the possibility exists that the temperature in the experiments of Huguenin (1973a,b) was in excess of the thermal oxidation threshold.

In summary, we have irradiated fine-grained magnetite powders in O_2-bearing atmospheres with high-intensity UV-VIS-IR radiation and with high-intensity UV radiation and have found that oxidation occurred only when radiant heating elevated the temperature of the magnetite above its thermal oxidation threshold. The magnetite samples were not perceptably oxidized by UV radiation. Thus, our experimental results indicate photochemical oxidation of magnetite by solar UV on Mars is not supported by experimental results and may not be a viable Martian process.

References: Huguenin, R.L. (1973a,b) JGR 78, p. 8481, p. 8495.

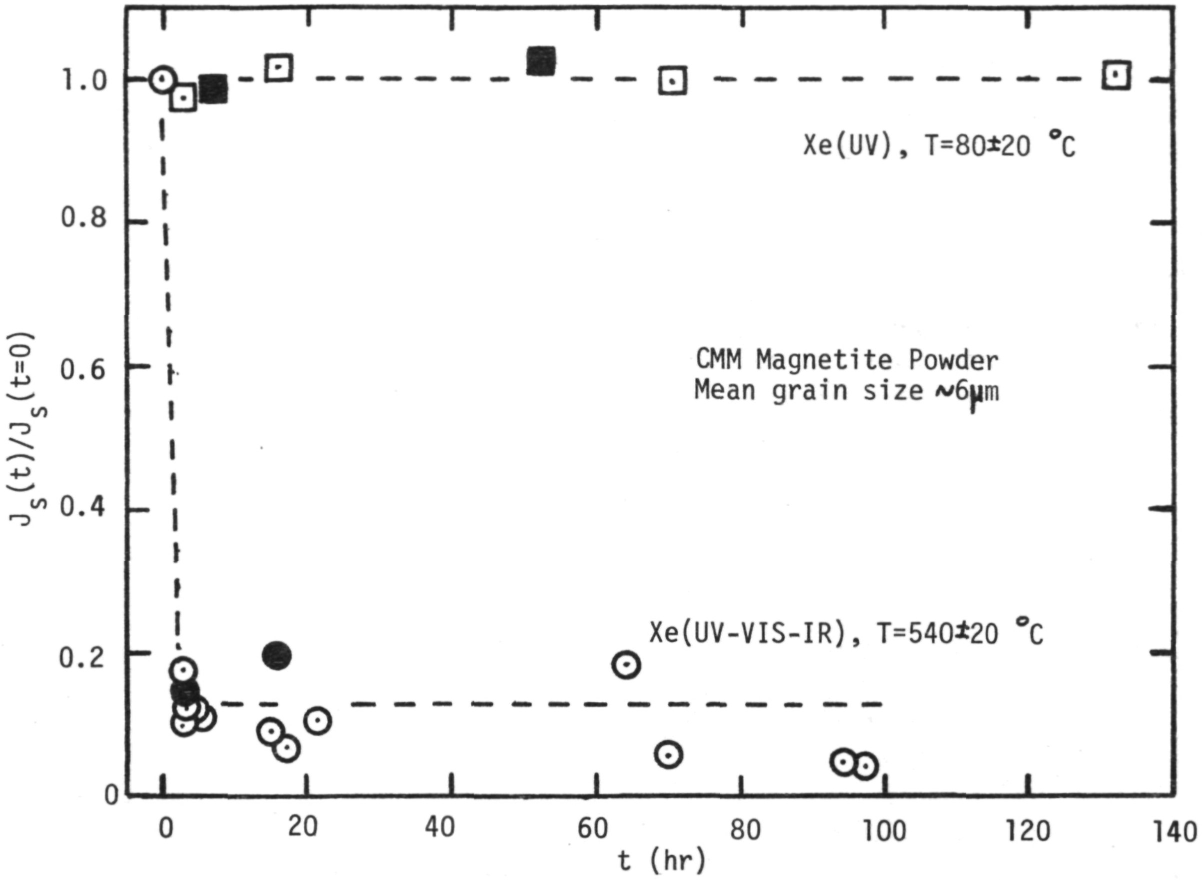

Fig. 1: Results of irradiation time (t) experiments with CMM magnetite. All open symbols denote irradiations in 100 torr pure O_2; closed circles, ∼400 torr pure O_2; closed squares, ∼250 torr of dry or laboratory air.

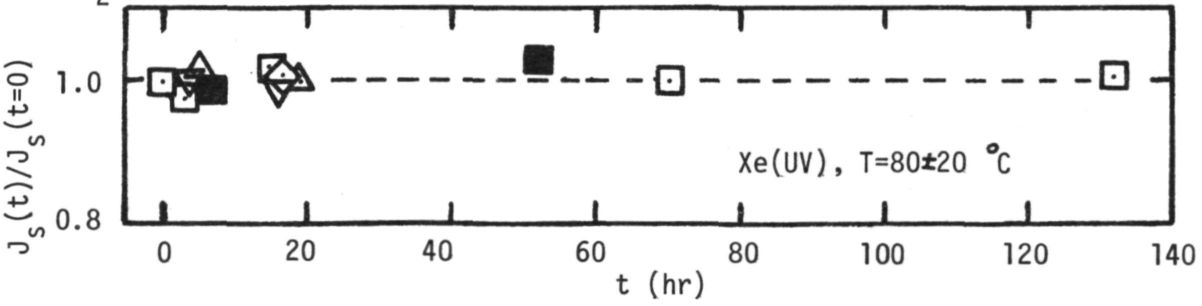

Fig. 2: Results of irradiation time experiments with Xe(UV) for two terrestrial and two synthetic magnetite powders. □,■ -CMM; △ -CPS1; ▽ -CPN1; ◇ -MCB1. All open symbols denote irradiations in 100 torr pure O_2; closed squares, ∼250 torr of dry or laboratory air.

Mars Polar Ice Inventory, Harold Masursky, M. E. Strobell, and A. L. Dial, U. S. Geological Survey, Flagstaff, AZ.

Additional photographs of the north and south polar cap areas of Mars have been acquired and processed in order to complete available coverage in these areas. A mosaic of the north polar area above latitude 77.5° north was completed in January, 1979; the area above 65° north will be completed by June 1979, and will be reproduced at scales 1:1.25 million and 1:2 million. A mosaic of the available coverage in the south polar area below 65° south latitude, at scale 1:1.25 million, is already completed. Stereophotogrammetric profiles of the north and south polar remanent ice caps are being constructed; profiles for the north polar cap area will be completed by mid-May. The areal distribution and volume of the ice will be determined from these data, and a paper written by the end of the funding year.

Geomorphic Role of Ground Ice on Mars

by Sheldon Judson and Lisa Rossbacher, Department of Geological and Geophysical Sciences, Princeton University, Princeton, N.J. 08544

Data from Mariner and Viking missions have spurred the search for Martian morphological features attributable to water ice, whether in the form of glaciers or ground ice. We now know that water exists as ice on the Martian surface. But as yet no convincing evidence has emerged to indicate that past or present glacier flow has played a role in modelling Martian landscape.

Many workers, however, have invoked ground ice as the cause of a variety of forms. (See particularly Sharp, 1974, and Carr and Schaber, 1977, for general reviews as well as listing of pertinent earlier literature.) We know that climatic conditions are favorable for the preservation of ground ice. Furthermore, a consideration of Martian history and materials makes it reasonable to assume that ground ice has been, and still is, present on Mars.

Thus far a wide variety of forms have been attributed, with varying conviction and evidence, to the presence of ground ice. These include debris flows, solifluction slopes, retreating scarps, thermokarst and alases, polygonal ground, lineated and striped ground, pedestal craters, laminated terrain, and crater ejecta blankets with fluidized forms. Furthermore ground ice has been suggested as a source of surface water responsible for certain channels of fluvial form.

We have reviewed most of these forms with available Viking imagery and can agree with Carr and Schaber (1977, p. 4034) who, reporting on Martian permafrost features, point out that "much of the evidence is indirect" but that "the convergence of several lines of evidence is, however, strongly suggestive" of the presence of ground ice. At the same time it is clear that attempts to assign Martian forms to the activity of ground ice is plagued by a lack of terrestrial analogues. Satisfactory analogues exist for other Martian features such as those created by volcanism, impact cratering, wind action,and tectonic activity. But terrestrial forms attributable to ground ice are generally below the resolution of available imagery. Whether comparable forms exist on Mars remains moot. Analogy is further complicated because terrestrial forms are modified by other processes including glaciation, vegetative action, and water.

Of the Martian features which come closest in scale to terrestrial analogues we would cite particularly thermokarst basins and associated alases. To these we would add another form, the pingo, a feature which expresses the accumulation of segregated ground ice in the form of a laccolith-like body. Several authors have described terrestrial pingos. (See for instance Washburn, 1973, and French, 1976, for general reviews.) Typically they are convex, domal hills reaching 600 m in diameter but usually smaller. Elevations may exceed 60 m. In a pingo in which some of the ice core has melted an irregularly shaped crater forms at the crest. We identify as preliminary candidates for classification as pingos over 100 examples measuring from about a kilometer down to approximately 150 meters in diameter. They occur chiefly in the northern hemisphere. These are located in the plains area adjacent to the Knobby Terrain, in the area of Acidalia Planita, and of Elysium Planitia. A half dozen forms occur in the old cratered uplands between 5° and 10°N and from about 330° E to 5°W. In the southern hemisphere five have been identified in eastern Helas Planitia. A few, particularly in the Knobby Terrain area, show irregular craters at their crests. Frey, et al. (1979) have suggested that these cratered forms may be cinder cones that were the result of explosive venting as lavas erupted over water saturated ground in a way analogous to process described from the Columbia Plateau by Hodges (1978).

Another terrestrial feature involving ground ice deserves mention. This is pingo-like in that it is ice-cored. It differs, however, from the pingo in that it is linear rather than round. Examples of these linear, ice-cored features are reported from the Canadian Arctic on Prince Patrick and Banks Islands (Pissart, 1967, 1975, French 1975). These features are reported to have a maximum length of 1300 m, a width up to 80 m and a height up to 14 m. They resemble small eskers but unlike these glacier features may be marked by axial furrows along their crests. These result from the melting, or partial melting, of ice cores. If similar features of this scale are present on Mars they are probably beyond resolution of existing imagery, a repetition of the familiar problem of size in the search for terrestrial analogues to Martian forms related to ground ice. Carr and Schaber (1977, p. 4053, and fig. 10.6) have described features on Mars similar to those on earth but they are an order of magnitude larger. The Martian forms are curvilinear and discontinuous and exhibit both negative and positive topography.

In searching for Martian topography genetically related to ground ice we need to remember that ground ice is climatically controlled. Therefore we might well expect a latitudinal distribution of various forms, a distribution corresponding in some way to climatic belts. A very distinct latitudinal distribution of debris flows is reported by Squyres (preprint) in two latitudinal belts 25° broad centered at 40° N and 45° S. Johansen (in press) maps the distribution of crater ejecta blankets of varying character and assigns the differences in form to the absence or presence of ground ice. She assumes that fluidized ejecta blankets are more characteristic in an intermediate equatorial band.

Our preliminary mapping of various other features thought to be related to ground ice reveals a distribution suggestive of latitudinal control, but this is not as yet conclusive.

References Cited

Carr, Michael H. and Gerald G. Schaber, 1977, Martian Permafrost Features: Jour. Geophys. Research, v. 82, p. 4039-4054.

French, H.M., 1975, Pingo investigations and terrain disturbance studies, Banks Island, District of Franklin: Geol. Surv. Can., Paper 75-1A., p. 459-464.

____________, 1976, The periglacial environment: Longman, Inc: New York, p. 309.

Frey, H.V., S.A. Chase, and B. Lowry, 1979, Phreatic Eruptions on Mars: Lunar and Planetary Science Conference X: Lunar and Planetary Institute: Houston, p. 400-401.

Hodges, Carroll Ann, 1978, Basaltic ring structures of the Colorado Plateau: Geol. Soc. Amer. v. 89, p. 1281-1289.

Johansen, L.A. (in press) Martian splosh cratering and its relation to water: Proc. Second Colloquium on Planetary Water and Polar Processes.

Pissart, A., 1967, Les pingos de l'Ile Prince Patrick (76° N - 120°W) Geographical Bull: v. 9, p. 189-217.

____________, 1975, Banks Island; pingos, wind action, periglacial structures: Geol. Surv. Can., Paper 75- 1A, p. 479-81.

Sharp, Robert P., 1974, Ice on Mars: Jour. Glaciology, v. 13, p. 173-185.

Squyres, Steven W., 1979, The distribution of lobate debris aprons and other similar flaws on Mars. (Preprint).

Washburn, A.L., 1973, Periglacial processes and environments: Edward Arnold: London, p. 320.

Sulfate Aerosol Deposition at the Viking Lander Sites: Mass Balance Considerations.

Mark Settle, Department of Geological Sciences, Brown University, Providence, RI 02912

Settle has recently proposed that the large sulfur concentrations discovered within martian soils may result from the surface deposition of volcanic sulfate aerosols (1, 2, 3). Sulfate aerosol particles that form in the atmosphere during periods of surface volcanism are inferred to consist of liquid droplets and liquid-solid slurries containing aqueous solutions of sulfuric acid (H_2SO_4). If the sulfur content of martian soils has been enriched by aerosol deposition, then observed sulfur concentrations can be used to estimate the cumulative lifetime of atmospheric aerosols produced during the most recent phases of surface volcanic activity.

Viking measurements indicate that martian soils are characterized by *in situ* bulk densities of ~ 1.3 g/cm^3 (4) and average sulfur contents of $\sim 3\%$ by weight (5). The average thickness of fine grained soil at both landing sites is on the order of 10 cm. Assuming that the sulfur found within the soils is completely derived from volcanic sulfate aerosols, the total amount of sulfur deposited in the vicinity of the two lander sites is ~ 0.4 grams of sulfur per square centimeter (gS/cm^2).

A long-lived martian aerosol could be maintained during periods of persistant surface volcanism as long as particle production rates remained roughly comparable to particle sedimentation rates. Under these steady state conditions, the mass flux of sulfur at the martian surface is given by:

$$A = \frac{4}{3}\pi R^3 \rho \frac{WsNH}{F}$$

where A is the rate of sulfur deposition (gS/cm^2- earth year), R is the average radius of aerosol particles impacting the surface (cm), ρ is particle density (g/cm^3), Ws is the weight fraction of sulfur contained within the particle, N is the average number density of particles (no./cm^3) of radius R within an atmospheric aerosol layer of thickness H (cm), and F is the average time required for a particle of radius R at the center of the aerosol layer to settle out of the martian atmosphere (earth years). Conservative estimates of sulfur deposition rates have been obtained by assuming that: (i) aerosol particles consist of aqueous sulfuric acid solutions containing 60 wt % H_2SO_4 (ρ = 1.7 g/cm^3 and Ws = 0.20 under these circumstances), and (ii) the martian aerosol layer extended over a 10 km altitude range centered at a height of 25 km above the 6.1 mbar reference surface (3).

The sulfate aerosol layer within the earth's stratosphere consists primarily of submicron-sized particles. The number density of particles greater than 0.3 microns in diameter typically is on the order of 1 cm^{-3} following major explosive eruptions at the earth's surface (6). Adopting values of R = 0.25 microns and N = 1 cm^{-3} for the large-sized particle fraction of a martian sulfate aerosol, sulfur deposition rates at the martian surface are on the order of 2×10^{-7} gS/cm^2 - earth year. Continuous addition of sulfur to surficial soils at this average rate can account for the observed sulfur content within a 10 cm soil column if the aerosol layer within the martian atmosphere is maintained over a period of ~ 2 million earth years. This implies that surface volcanism would have had to persist in a semi-continuous fashion over a roughly equivalent period of time.

Soderblom *et al.* (7) have estimated that volcanism in the Tharsis region has occurred over a period of 10^8 earth years, whereas Neukum *et al.* (8) have estimated that Tharsis volcanism has occurred over a period of 10^9 earth years. In either case, the time required for sulfur enrichment of martian soils by volcanic aerosol deposition is short in comparison. The results of this study indicate that the aerosol deposition mechanism can account for the observed concentration of sulfur within martian soils without appealing to excessive aerosol densities or unreasonably long periods of surface volcanic activity. These results imply that sulfate aerosol deposition on a global or hemispheric scale is a viable mechanism for transporting sulfur to the Viking landing sites.

References: 1. Settle, M. (1979) Lunar and Planetary Sci X, Houston, TX, 1110.
2. Settle, M. (1979) Lunar and Planetary Sci X, Houston, TX, 1101.
3. Settle, M. (1979) Formation and deposition of volcanic sulfate aerosols on Mars, submitted to Jour. Geophys. Res.
4. Moore *et al.* (1977) Jour. Geophys. Res. v. 82, 4497.
5. Clark *et al.* (1977) Jour. Geophys. Res. v. 82, 4577.
6. Climatic Impact Assessment Program Monograph 1 (1975), DOT-TST-75-51.
7. Soderblom *et al.* (1974) Icarus v. 22, 239.
8. Neukum, G. *et al.* (1979) Lunar and Planetary Sci X, Houston, TX, 907.

The Occurrence and Geological Implications of Carbon Dioxide Clathrate Hydrate on Mars,

Gary Anthony Armistead, University of Houston, Houston, Texas 77004.

Analysis of the temperatures and pressures at the Viking Lander 2 site (VL-2) during the presence of surface ice condensate shows that the ice partially converted to CO_2 clathrate hydrate on at least several occasions. The occurrence of CO_2 hydrate at the VL-2 latitude indicates that ground ice and surface ice at latitudes nearer the poles would convert to hydrate during the Martian winter. The conversion of ice to hydrate is shown to result in a volume expansion of 16% ± 2%. The geological importance of this volume, and the converse volume reduction as hydrate converts to ice, is investigated. The reduction in volume appears to be a good candidate for the cause of the chaotic terrain. A method is suggested for determining whether the melting of a buried deposit of ice or the dissociation of a buried hydrate deposit, and subsequent melting of the resulting ice, caused the chaotic terrain and associated flood channels. No quantitative measure of the force exerted by ice as it converts to hydrate was obtained. However, calculations indicate that the conversion of ice to hydrate could approach the force given by the freezing of water in confined spaces provided sufficient time is allowed for the reaction and the ice completely fills the confined space prior to conversion. However, the measurement of strains imparted to walls confining a solid ice mass as it converts to hydrate is necessary before the process can be advanced as a possible geomorphological and weathering agent on Mars.

Chapter 5

VOLCANIC PROCESSES

Page Intentionally Left Blank

Lava flows of Tharsis Montes, D. H. Scott, G. G. Schaber, K. C. Horstman, and A. L. Dial, Jr., U. S. Geological Survey, Flagstaff, Arizona 86001.

This continuing study extends previous mapping (Schaber et al, 1978) and shows the distribution, eruptive sequence, and sources of origin of lava flows in a broad region surrounding the Tharsis Montes on Mars. Most of the flows originated from the four large volcanoes, Arsia, Pavonis, Ascraeus, and Olympus Montes, but some appear to have been locally derived from fissures far removed from the main volcanic centers. Individual flow units have been grouped into at least fourteen major eruptive sequences on the basis of their morphology and stratigraphic relations. The relative times of emplacement of these groups have been generally confirmed by crater counts on moderate and most recently on high resolution images after lowering of Viking Orbiter periapsis. They show densities of craters with diameters >1 km from about 90 craters per $10^6 km^2$ for the youngest group to about 3000 craters per $10^6 km^2$ for the oldest group. This wide range in crater populations is indicative of an eruption history extending over a very long time interval, possibly 2 x 10^9 years (Schaber et al, 1978).

Present mapping of the Tharsis lava flows covers two Mars quadrangles (MC-9 and MC-17) and extends into major portions of six others (MC-2,3,8,16,24, and 25). Most of the flows mapped within the eastern half of the Memnonia quadrangle (MC-16) originated from Arsia Mons as shown by the directions of their long axes and orientations of their frontal lobe scarps. In this area the flows extend for hundreds of kilometers forming smooth "appearing" plains having a very low (~3m/km) gradients. They probably had very low viscosities with attendant high volatile content. Earth-based radar data (Downs et al, 1973; Simpson et al, 1978; Schaber at al, 1979), however, indicate that even these seemingly smooth surfaces (at Viking low to medium resolution) are quite rough at meter-to-decameter scale. In high resolution (~10m/pixel) Viking Orbiter pictures, the flow surfaces have an extremely rough, corrugated flow structure that resembles on a much finer scale the grooved aureoles around Olympus Mons.

The flows from Arsia Mons were prevented from flooding the central and western parts of Memnonia by a barrier formed by highland rocks extending irregularly across the quadrangle (MC-16) in a north-south direction. Within the highlands, large unconnected expanses of smooth-appearing lava plains are transected in places by northeast trending fissures and faults characteristic of structural patterns in the highland rocks of the region. These fracture systems are, however, buried by the younger flows from Arsia Mons. Crater counts tend to substantiate the older age of the lava plains within the highlands relative to the Arsia Mons flows. Crater density differences between the two units are not great, however, and lie close to the limits of error for the determination.

Large accumulations of eolian material overlie some of the flows from Arsia Mons in the north-central part of Memnonia. These wind deposits are probably very thick as they completely bury large areas of highlands that elsewhere exhibit substantial relief in the form of large craters, ridges and deeply channeled terrain. Similar eolian deposits occur within and around the aureole of Olympus Mons where they mantle some of the flows in the Amazonis quadrangle.

References

Schaber, G. G., Horstman, K. C. and Dial, A. L. Jr., 1978, Lava flow materials in the Tharsis region of Mars: Proceedings of the 9th Lunar and Planetary Science Conference, v. 3, p. 3433-3458.

Downs, G. S., Goldstein, R. M., Gree, R. R., Morris, G. A. and Reichley, P. E., 1973, Martian topography and surface properties as seen by radar: the 1971 opposition: Icarus 18, p. 8-21.

Simpson, R. A., Tyler, G. L. and Campbell, D. B., 1978, Arecibo radar observations of Martian surface characteristics near the equator: Icarus 33, p. 102-115.

Schaber, G. G., Horstman, K. C. and Johnson, D.A., 1979, Viking Photography: Assessment of Mars radar roughness: Lunar and Planetary Science X, Abstracts of papers submitted to the 10th Lunar and Planetary Science Conference, part 3, p. 1058-1060.

The aureole of Olympus Mons, Elliot C. Morris, U. S. Geological Survey, Flagstaff, Arizona 86001.

The origin of the grooved terrain or aureole that surrounds the huge volcanic shield, Olympus Mons, has been the subject of much controversy since the aureole was first seen on Mariner 9 pictures. Because of their spatial arrangement su-rounding Olympus Mons the aureole deposits are generally believed to be associated with the formation of the large shield volcanoe. Possible origins that have been proposed for the aureole include: (1) deeply eroded lava flows from Olympus Mons or earlier volcanoes (McCauley et al, 1972), (2) eroded remnants of old shields (Carr, 1973), (3) dissected ash-flow tuffs (King and Riehle, 1974), (4) magmatic crustal doming, fracturing and subsequent erosion (Shoemaker and Blasius, 1974), (5) thrust sheets caused by the weight of Olympus Mons (Harris, 1976), (6) subglacial eruption of lavas (Hodges and Moore, 1979) and (7) landslides (Carr, oral communication, 1978). Each of these theories implies different relations with Olympus Mons and the surrounding plains. Whatever origin is postulated for the aureole must account for or be compatible with the following observation:

(1) The aureole deposits consists of several roughly circular overlapping sheets of material of great areal extent. Each sheet may be up to 1 km thick. The oldest and most extensive aureole deposit covers over $2.5 \times 10^6 km^2$.

(2) The surface of the aureole deposits are composed of a series of curvilinear ridges and troughs that form an anastomosing pattern that varies in length and width over different parts of the deposits. The ridges for the most part form an accordant surface and are parallel to their outer boundaries. Lobate escarpments form the margins of the youngest deposits. The deposits superimpose one another and each has a different scale of texture of the ridges. There is a difference in orientation of these features in relation to overlying and underlying deposits. (Finely grooved vs. coarsely grooved terrain, Carr, 1973).

(3) The pattern of curvilinear ridges and grooves are broken by sets of intersecting long linear grooves that may be grabens or fractures with little displacement.

(4) The aureole deposits are almost completely devoid of craters. There are less than 24 recognizable craters >1 km on over $8.4 \times 10^5 km^2$ total area of exposed aureole deposits. Plains material which lap upon and bury the outer margins of the aureole deposits have a greater crater population than the aureole deposits.

(5) The aureole deposits appear to dip inward towards a basin that surrounds Olympus Mons.

(6) The aureole is asymmetric to Olympus Mons, extending almost 1000 km northwest from the center of the shield but only 600 km southeast.

(7) Regional slope of the terrain is approximately 1/400 towards the northwest from the Tharsis region to Arcadia Planitia.

(8) A strong gravity anomaly exists over Olympus Mons which broadens towards the northwest, corresponding to the aureole deposits which have the greatest areal distribution in that direction (Sojogren, 1979).

None of the proposed origins for the aureole deposits of Olympus Mons adequately account for or satisfies all of the above observations.

References

McCauley, J.F., Carr, M. H., Cutts, J. A., Hartman, W. K., Masursky, H., Milton, D. J., Sharp, R. P., and Wilhelms, D. E., 1972, Preliminary Mariner 9 report on the geology of Mars: Icarus 17, p. 289.

Carr, M. H., 1973, Volcanism on Mars: Journal Geophysical Research 78, p. 4049.

King, J. S., and Riehle, J. R., 1974, A proposed origin of the Olympus Mons escarpment: Icarus 23, p. 300.

Shoemaker, E. M. and Blasius, K. R., 1974, Geology and geomorphology of martian shield volcanoes: Final report to NASA, 56 pp.

Harris, S. A., 1977, The aureole of Olympus Mons: Journal Geophysical Research 82, v. 28, p. 3099-3107.

Hodges, C. A. and Moore, H. J., 1979, Tablemountains and implications for glacial ice on Mars: Journal Geophysical Research, in press.

Sojogren, W. L., 1979, Mars Gravity: High resolution results from Viking Orbiter 2: Science, v. 203, no. 9, p. 1006-1009.

Evolution of the Martian Volcanoes, J. B. Plescia, Jet Propulsion Laboratory, California Institute of Technology, Pasadena, CA 91103/Dept. of Geological Sciences, Univ. S. Calif., Los Angeles, CA 90007 and R.S. Saunders, Jet Propulsion Laboratory, California Institute of Technology, Pasadena, CA 91103

Building on our earlier work (Plescia et al. 1979), we have compiled crater count data and developed a broad classification scheme to include all of the volcanic constructs of the planet Mars. Our classification uses three groups which include all of the volcanic constructs and a fourth to include the volcano-tectonic depressions. This scheme is similar to one employed by Carr (1973).

The first group are basaltic shields. This includes the following features: Olympus Mons, Arsia Mons, Pavonis Mons, Ascraeus Mons, Biblis Patera, Jovis Tholus, Uranius Patera and Alba Patera. These features are analagous to the Hawaiian or Galapagos Island shields. In general the shields are broad features with low slopes on the order of a few degrees. The shields assumed to have been built by successive outpouring of basaltic lava. The summit of each of these constructs is generally capped by a complex caldera, composed of a number of smaller caldera of varying age. The flanks of these features may also be cut by series of concentric graben, lineaments, and pit chains.

The second group are the domes and composite features. This includes domes, composed of successive outpourings of a lava more viscous than basalt, and composite cones, composed of interbedded lava and pyroclastic material. This group generally has slopes somewhat steeper than the shields and has simple summit craters. This group includes the following features: Elysium Mons, Albor Tholus, Hecates Tholus, Apolinaris Patera, Tharsis Tholus, Ceraunius Tholus, Uranium Tholus, and Ulysses Patera.

The third group of features are classified as highland patera. These are the Dandelion features of Mariner 9 (McCauley et al. 1972). Only three features fit this class - Hadriaca Patera, Tyrrhena Patera, and a feature at 62°W, 44°N which we have named Tempe Patera. These features are low broad constructs with central caldera. Radiating from the center is a series of lobes and channels. These lobes may be of primary (i.e. lava flows) or secondary (i.e. erosional) origin.

The final group consists of volcano-tectonic depressions. These features are circular or semicircular depressions ringed by concentric fractures. Parts of the feature are often covered by lava or some other recent plains material. These depressions occur in the volcanic plains of Syrtis Major and Tharsis. This group includes features at the following locations: central Syrtis Major 292°W, northern Tharsis, NE of Olympus Mons at 127°W, 28°N, and perhaps the feature in eastern Tharsis at 94°W, 5°N. These features may be sources for much of the plains material.

Crater curves are illustrated in Figures 1, 2, and 3. In each case the curve for the Lunae Planum region is included for reference. Based on the absolute chronologies for crater counts of Neukum and Wise (1976) and Soderblom et al. (1974), an age of approximately 4 billion years is indicated for the Lunae Planum surface. Figure 1 illustrates the curves for the highland patera features. All three curves lie above the Lunae Planum curve indicating that they are older than it, hence older by 4 b.y. All three curves lie in close proximity to each other indicating they spanned a limited time range. Figure 2 includes the curves for the dome composite group. These features span a time range from just older than Lunae Planum to just younger: a time range broader than the highland patera, but still restricted to the time of about 4 b.y. ago. Figure 3 includes the curves for the basaltic shield group. These features span a wide range in time, from prior to Lunae Planum to Olumpus Mons, hence they span a time from about 4 b.y. to about 300 m.y. These data indicate that the shields cover a much broader period of time than either of the other two groups.

There appears to have been an episode prior to 4 b.y. when three types of volcanism were active on the planet - basaltic shield volcanism, dome and composite construction and highland patera. At approximately 4 b.y. a transition occurred in the styles and loci of volcanism. Prior to this time volcanism was occurring in a variety of locations on the planet, later the volcanism was limited to the Tharsis region. Volcanism after the transition is restricted to basaltic shield volcanism. At this same time there appears to have been a change in the style of basaltic volcanism as well. Early shield volcanoes were low and small, while latter shields, beginning with Alba Patera were broader and significantly taller.

The latest stage evolution of the large Tharsis shields may include a period of volcanism more silicic than the basalt from which the majority of the shield was built. Masursky et al. (1978) have mapped flows near the summit of Arsia Mons which they feel are of a andesite or basaltic andesite composition. A line of smaller constructs, of perhaps more silicic chemistry, are built across the caldera floor of Arsia Mons (Carr et al. 1977). The possibility of smaller cones built on the flank of Alba Patera has also been suggested by the same authors.

REFERENCES:

Plescia, J.B., Saunders, R.S. and Gregory, T., 1979, Abstracts of Lunar & Planetary Science Conf. X, p. 989-91.

Carr, M.H., JGR 78, p. 4049-4062.

McCauley, J.F., Carr, M.H., Cutts, J.A., Hartmann, W.K., Masursky, H., Milton, D.J., Sharp, R.P. and Wilhelms, D.E., 1972, Icarus 17, p. 289-327.

Neukum, A. and Wise, D.U., 1976, Science 194, p. 1381-1387.

Soderblom, L.A., Condit, C.D., West, R.A., Herman, B.M. and Kreidler, T.J., 1974, Icarus 22, p. 239-263.

Masursky, H., Dial, A.L. and Strobell, M.H., 1978, Geologic Map of the Phoenicus Locus Quadrangle of Mars.

Carr, M.H., Greeley, R., Blasius, K.R., Guest, J.E. and Murray, J.B., 1977, JGR 82, p. 3985-4015.

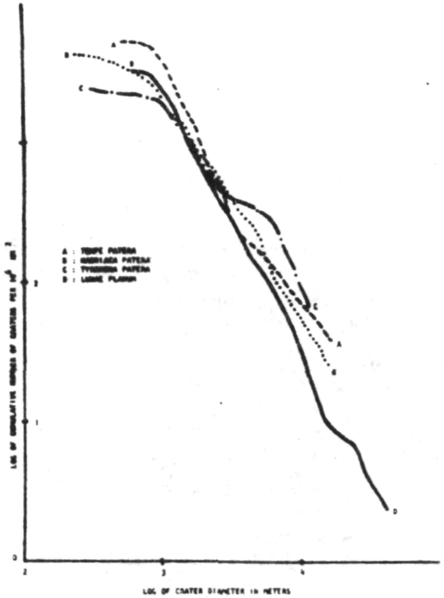

Figure 1
Highland Patera Group

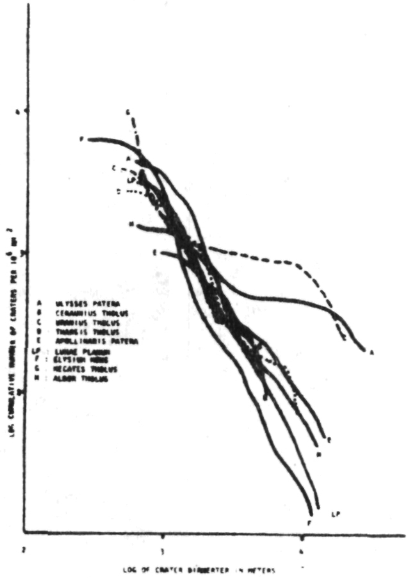

Figure 2
Dome - Composite Group

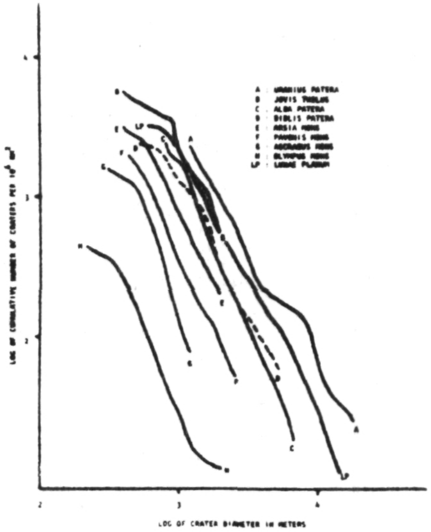

Figure 3
Basaltic Shield Group

Venusian Volcanism: Environmental Effects on Style and Landforms.

Charles A. Wood, NHB-Stop 119, Smithsonian Institution, Washington, DC 20560.

Introduction: Volcanism has been a major process in the evolution of the Earth, Moon and Mars (± Mercury), and would be expected to have been important on Venus because of its similarity in mass, diameter and density to the Earth. Concentrations of Th, U and K for rocks on Venus are comparable to terrestrial basalts and granites[1], suggesting that planetary differentiation into crust, mantle and core has occurred in Venus as in the Earth. This would result in the concentration of radioactive elements in the planet's crust, providing heat sources to drive volcanism. Suggestive evidence for the actual existence of volcanic edifices is provided by Earth-based radar studies that reveal several large, isolated mountains with summit depressions[2]. The radar data also disclose broad, circular depressions with smooth floors which may be analogs to the lava-floored impact basins of the Moon[2]. This briefly summarized evidence from spacecraft exploration, radar geology and planetary uniformitarianism implies the existence of volcanism on Venus in the past (and presumably continuing today). The present study evaluates possible ways in which familiar volcanic processes may be profoundly modified by the very high atmospheric pressure (about 90 atmospheres) and surface temperatures (480°C) on Venus[1]. Additionally, possible volcanological consequences due to the apparently anhydrous state of Venus are briefly considered. While all of these deductions are speculative, the conclusions appear consistent with present knowledge and provide general guidelines for interpretations of radar and spacecraft data.

Explosive Volcanism: A terrestrial analogy to the high pressure at the surface of Venus occurs at ocean depths of about 1 km. Eruptions at these depths appear to be purely effusive, and theoretical studies indicate that explosive eruptions should not occur at pressures greater than those found at depths of 500-700 m (ref. 3,4). Thus, pyroclastic eruptions and resulting landforms -cinder cones, stratovolcanoes, maars, ignimbrite plains- are presumably uncommon on Venus. Pressures needed for explosive eruptions on Venus are greater than for the Earth because of the additional atmospheric overburden (equivalent to about 450 m of density 2.5 g/cc rock) to be overcome, but if this higher eruption threshold is reached explosive activity will occur. The range of pyroclastic material erupted into the venusian atmosphere would be strongly effected by atmospheric drag and buoyancy. The presumed density difference between volcanic gases and the atmosphere would be much greater than on Earth, and vigorous convective thrusting[5] could carry ejecta to great elevations. This buoyancy effect could result in the distribution of fine particulate matter over much of the planet (providing condensation nuclei for sulphuric acid rains), and limit the buildup of a volcanic edifice at the vent. On the other hand, for ballistically transported material, the strong atmospheric drag would promote concentrations of material at the vent.

Effusive Eruptions: For ambient temperatures greater than 267° C convection is a more important cooling mechanism than radiation[6]; thus for Venus the convective cooling should be (following ref.7, p.21) only ½ as efficient as on the Earth, allowing flows to travel greater distances than typical for terrestrial lavas. Longer cooling times also promote growth of large crystals rather than myriads of small ones, leading, probably, to a slower increase in viscosity with cooling that also favors formation of long flows. Low rates of cooling and crystalization, and inhibited degassing (due to the high atmospheric pressure) would tend to maintain the magma's original high temperature and low viscosity, thus delaying the change from pahoehoe to aa. Fluid, pahoehoe flows should lead to lava tube formation as well. Thus, lava flows on Venus should tend to be long, tube-fed, and have pahoehoe surfaces. Based on high radar reflectivity, however, Saunders and Malin[2] suggest that the proposed shield volcano Beta has a high abundance of aa lava.

One consequence of long flows is that shield volcanoes should be broad and squat. This is in agreement with the geometry of Beta[2] which has an average slope of 1°, compared with 2°-11° for Olympus Mons[8], and 3°-12° for Mauna Loa. The height of Beta is also considerably less than expected (10 km according to ref. 2, but only 5 km according to recent Pioneer Venus data, versus 20-30 km) based upon its basal diameter[9]. Thus, for a given volume of magma volcanoes on Venus will have less relief than terrestrial volcanoes, suggesting that estimates of lithospheric thickness based on volcano heights[10] will yield minimum values. Interestingly, the volumes of Beta (0.7×10^6 km^3), Olympus Mons (2.4×10^6 km^3; ref. 8), and the entire Hawaiian-Emperor volcanic chain(1.1×10^6 km^3; ref. 11) are roughly the same, suggesting that approximately equal volumes of magma are generated in major magmatic episodes on Venus, Mars and the Earth.

Anhydrous Volcanism: There is only 0.1% water in the atmosphere of Venus[12], and the requirement (based on preservation of ancient impact basins [13]) that Venus have a stable lithosphere supports the contention that the mantle is anhydrous[14]. This conclusion immediately leads to a number of speculations concerning the style of surface volcanism:

(a) The lack of water (and the high temperature) obviously excludes the possibility of maar type volcanoes, as well as tablemountains, moberg ridges and pseudocraters, all of which result from magma/water interaction.

(b) In Iceland and some other areas the upper few hundred meters of the crust are effectively waterlogged, presenting a "surface barrier" to the rise of magma[15]. Magma with low rise rates may be deflected into sills by this surface barrier. Such near surface horizontal intrusions should be uncommon on Venus.

(c) Meteoric water leaking into magma in near surface reservoirs can significantly increase the volatile content and lead to differentiation of the magma[16], and high energy pyroclastic eruptions[17]. The lack of liquid water on Venus should eliminate this explosive style of volcanism, although the possible role of meteoric H_2SO_4 has not been examined.

(d) Calc-alkaline rocks are generated by the heating of hydrous minerals of a subducted lithospheric slab. Venus appears to lack subduction tectonics, as well as water, so that andesitic stratovolcanoes should not be expected.

(e) A small amount of water in a magmatic melt can significantly decrease its density[18]; thus venusian lavas should be of higher density than chemically equivalent terrestrial rocks (if such exist). This will decrease the density contrast between magma and country rock, reducing the height to which magma can be pumped. This adds further uncertainty to estimates of lithospheric thickness based on volcano heights.

(f) Finally, since H_2O is probably not a major volatile in the mantle of Venus, the effect of CO_2-rich melts must be considered. Eggler[19] demonstrated that CO_2-rich compositions begin to melt at higher temperature than H_2O-rich melts, producing silica-undersaturated melts. This implies that venusian lavas may be less viscous than terrestrial lavas.

Conclusions: Although only a few speculative effects of Venus' high temperature and pressure and anhydrous lavas have been considered a consistent pattern emerges: explosive eruptions should be less common than on the Earth and effusive volcanism should produce long flows, and consequently volcanic edifices should be broad with low relief.

References: (1)Florensky, C.P. and 8 others (1977) *Geol. Soc. Am. Bull.* *88*, 1537-1545. (2)Saunders, R.S. and Malin, M.C. (1977) *GRL* *4*, 547-550. (3) McBirney, A.R. (1963) *Bull. Volc.* *26*, 455-470. (4) Peckover, R.S., Buchanan, D.J. and Ashby, D.E.T.F. (1973) *Nature* *245*,307-308. (5) Sparks, R.S.J. and Wilson, L. (1976) *J. Geol.Soc. Lond.* *132*, 441-451. (6) Harrison, C.G.A. and Rooth, C. (1976) in *Volcanoes and Tectosphere* (Ed. H. Aoki and S. Iizuka) Tokai Univ. Press, 103-113. (7) Carslaw, H.S. and Jaeger, J.C. (1959) *Conduction of Heat in a Solid*, Clarendon Press, Oxford. (8) Blasius, K. et al. Div. Planet. Sci. Meeting, 1978. (9) Whitford-Stark, J.L. (1975) in *Volcanoes of the Earth, Moon and Mars* (Ed. by G. Fielder and L. Wilson),66-74. (10) Warner, J.L. and Morrison, D.A. (1978) *Lunar Planet. Sci.* *9*, 1217-1219. (11) Bargar, K.E. and Jackson, E.D. (1974) *J.Res. U.S.G.S.* *2*, 545-550. (12) Oyama, V.I. et al. (1979) *Science* *203*, 802-804. (13) Schaber, G.G. and Boyce, J.M. (1977) *Impact and Explosion Cratering*, 603-612. (14) Warner, J.L. *Lunar Planet. Sci.* *10*, 1295-1297. (15) Walker, G.P.L. (1974) *Geodynamics of Iceland and the North Atlantic Area* (Ed. Kristjansson), 189-201. (16) Friedman, I. et al. (1974) *Science* *184*, 1069-1072. (17) Sommer, M.A. (1977) *J. Geol.* 85, 423-432. (18) Bottinga, Y. and Weill, D.F. (1970) *Am. J. Sci.* *269*, 169-182. (19) Eggler, D.H. (1975) *Phys. Chem. Earth* *9*, 869-881.

I thank R. Fudali for critical comments on a part of this manuscript.

Some Lesser Volcanic Provinces on Mars, Carroll Ann Hodges, U.S. Geological Survey, Menlo Park, CA 94025.

Preliminary examination of Viking photo-mosaics and selected photographs indicates that landforms of possible and probable volcanic origin - aside from the conspicuous shields - are clustered in relatively restricted areas that may define lesser volcanic provinces. In these areas, lobate escarpments, similar to those identified as lava-flow fronts around the major shields, are commonly associated with small cones, domes, buttes, and mesas with and without summit craters, low shields, and narrow linear ridges -- all of which could be volcanic. Thus far seven such provinces have been identified: (1) the Cydonia Mensae region in southeast Acidalia Planitia (35° to 50° N, 350° to 35° W); (2) a plateau remnant between Tempe Fossae and Mareotis Fossae (30°-40° N, 80°-90° W); (3) a region north of Olympus Mons and west of Alba Patera (40°-50° N, 110°-160° W); (4) southwest Utopia Planitia (25°-35° N, 260°-280° W); (5) a locality marginal to the north polar cap (70°-80° W); (6) northern Utopia Planitia in the vicinty of the Viking Lander 2 site (45°-50° N, 220°-230° W); and (7) a small province in Chryse Planitia where low shields analogous to those in the Snake River plain of Idaho have been identified (Greeley et al., 1977). In addition, small features with volcanic morphologies occur in scattered localities across the northern plains between 50° and 65° N. Thus far, one probable province has been found in the southern hemisphere east of Hellas at 40°-50° S, 235°-240° W.

Some differences with possibly genetic implications are evident among these areas. The province marginal to the retreating highlands escarpment of Cydonia Mensae is one of the most distinctive and complex. This area contains an exceptional diversity of landforms, including cones and domes with summit craters and convex slopes, interpreted variously as volcanoes (Underwood and Trask, 1976), cinder cones (Wood, 1979a), or pseudocraters (Frey et al., 1979) like those in Iceland (Thorarinsson, 1953). These landforms appear to be absent in the highlands plateau, and their localization along the scarp may have geologic significance. Eruptive vents in the Tempe Fossae region, northeast of and precisely aligned with the trend of the Tharsis ridge, appear to have been localized by fractures, along which there are elongate edifices with asymmetric summit craters and broad bases relative to apparent heights. Whether these are pyroclastic constructs or small lava shields is at present unknown, but they differ morphologically from the symmetric cratered domes near Cydonia Mensae and elsewhere. Narrow linear ridges, interpreted as possible dikes, and lobate flow fronts also occur in this region, which could be the youngest center of eruptive activity along the Tharsis trend, where the major volcanoes appear to grow progressively younger to the northeast (Carr, 1976; Wood, 1976). In contrast to these probable vents, the landforms in southwestern Utopia Planitia are symmetrical cones or domes with summit craters. These occur both isolated and in distinct chains that suggest structural control, although no fractures are evident. Features resembling the subglacially derived tablemountains of Iceland (Hodges and Moore, 1978a,b, 1979; Allen, 1978, 1979) also exist in this region and suggest that interaction of magma with surface ice may have occurred at some past time. Peculiar striae or curvilinear ridges somewhat reminiscent of terrestrial glacial moraines are associated with the cones and domes, enhancing the Icelandic analogy for some small cratered mesas. Craters that resemble tuff rings also have been noted in this vicinity. East of Hellas, small knobs and domes, cratered and uncratered, may be cinder cones, pseudocraters, or tablemountains. Peterson (1978) postulated localized volcanism in the Noachis-Hellas region, and further search probably will reveal additional areas of possible volcanic activity in the southern hemisphere.

Although genetic interpretations of Martian features by extrapolation from terrestrial landforms may be equivocal, particularly without adequate topographic data, numerous investigations of cinder cone fields (Wood, 1979b; Settle, 1979; Porter, 1972; Moore et al., 1976; and many others) offer some bases for comparison. The San Francisco volcanic field in Arizona exhibits a wide variety of cinder cone shapes and eruptive types (Moore and Wolfe, 1976), ranging from maars and tuff cones through highly asymmetric cratered cones, rejuvenated vents, and the typical, symmetrical, cratered cones up to 1 or 2 km across and as high as 300 m. Possible counterparts for all of these can be identified on Mars. An additional common but anomalous landform in the San Francisco field is the cinder cone or ridge without any vestige of a crater, although in all other respects -- dimension, particle size, composition -- these hills are essentially identical to their cratered companions. While the explanation for the lack of a crater is presently unknown, it appears unlikely to be erosional and may reflect extremely asymmetric venting. These features must be included among the potential analogs for the numerous uncratered knobs and buttes that commonly are associated with cratered cones or domes on Mars.

Limited measurements of basal diameters of martian cones (200 m to 1000 m across) and crude estimates of heights based on shadow lengths indicate that dimensions of the martian features fall within the scatter and on the same general trend obtained by Wood (1979b) for terrestrial cinder cones. Height/width ratios of three cones ranged from 0.1 to 0.17, whereas Wood (1979) reported 0.06 for a single observation. Clearly more and accurate topographic data are needed for meaningful dimensional comparisons.

Terrestrial counterparts of the small martian features observed thus far are typically of basaltic composition. Malin (1977), however, noted similarities of Elysium to relatively silicic composite volcanoes on Earth. If the magma source or incorporated country rocks beneath the Elysium edifices were differentiated, then small volcanic features analogous to rhyolitic domes and plugs, for example, may yet be found in that or other regions.

It may be noted that the so-called pedestal craters of the northern plains are not included here as possibly volcanic landforms, nor is their origin here attributed to ejecta blanket lag gravels, as has been suggested (McCauley, 1973). It is proposed instead that these craters may be analogous to those produced experimentally by Piekutowski (1977), wherein a bulked apron of the target material forms around an explosion crater in a layered medium if a relatively thin mantle of dense, cohesionless, homogeneous sand overlies weakly cemented sand. If a thin regolith overlies a zone of ground ice on Mars, analogous conditions may prevail producing the pedestal shapes around impact craters. Ambiguity with respect to volcanic landforms arises because in some regions there appear to be gradational stages between these pedestal craters and the cratered domes and cones that so strongly resemble cinder cones.

This preliminary survey supports earlier interpretations by West (1974), Peterson (1978), and others that, despite the predominance of the massive shield volcanoes and apparently fluid basalt flows (Moore et al., 1978), pyroclastic activity, at least on a small scale, has also occurred on Mars. Analyses of these landforms that may be of pyroclastic origin and their distribution will bear on the geologic evolution of the planet.

References:

Allen, C.C.,1978, Subglacial volcanism-terrestrial landforms & implications for planetary geology: NASA Tech. Mem. 79729, p. 194-195; 1979, Volcano/ice interactions on Mars: Lunar & Planet. Sci. X, p. 18-20.

Carr, M.H.,1976, The volcanoes of Mars: Sci. Amer., v. 234, p. 32-43.

Frey, H.V.et al.,1979,Phreatic eruptions on Mars:Lunar & Planet Sci.X,400-401.

Greeley,R.et al.,1977,Geology of Chryse Planitia: J.Geophys.Res.,82,4093-4109.

Hodges,C.A. & Moore,H.J.,1978a,Tablemountains on Mars: Lunar & Planet. Sci. IX, p.523-525; 1978b, The subglacial birth of Olympus Mons: Geol.Soc.Amer. Abst. with Prog.,10,p.422; 1979, Tablemountains & implications for glacial ice on Mars:submitted to J.Geophys.Res., Mars Colloquium volume.

Malin,M.C.,1977,Comparison of volcanic features of Elysium (Mars) & Tibesti (Earth): Geol. Soc. Amer. Bull.,v.88,p. 908-919.

McCauley,J.F.,1973, Mariner 9 evidence for wind erosion in the equatorial & mid-latitude regions of Mars: J. Geophys. Res., v. 78, p. 4123-4137.

Moore, H.J. et al.,1978, Yield strengths of flows on the Earth, Mars, and Moon: Proc. Lunar Planet. Sci. Conf. 9th, p. 3351-3378.

Moore, R.B. & Wolfe, E.W., 1976, Geologic map of the Eastern San Francisco volcanic field, Ariz.: U.S.Geol. Survey Misc. Inv. Map I-953.

Moore,R.B.,et al.,1976, Volcanic rocks of the eastern & northern parts of the San rancisco volcanic field, Ariz.:U.S.G.S. J. Research, 4, p. 549-560.

Peterson,J.E.,1978,Volcanism in Noachis-Hellas region, 2: Proc.L&P Sci.Conf.9 p.3411-3432.

Piekutowski,A.J.,1977,Cratering mechanisms observed in laboratory-scale high-explosive experiments, in Impact & Explosion Cratering, p. 67-102.

Porter,S.C.,1972, Distribution, morphology, & size frequency of cinder cones on Mauna Kea volcano, Hawaii: Geol.Soc.Amer.Bull.,83, p.3607-3612.

Settle,Mark,1979, The structure & emplacement of cinder cone fields: Amer. Jour. Science, in press.

Squyres,S.W.,1978, Martian fretted terrain: Flow of erosional debris: Icarus, v. 34, p. 600-613.

Thorarinsson, Sigurdur,1953, The crater groups in Iceland: Bull.Volcanologique, series 2, tome 14, p. 3-44.

Underwood,J.R. & Trask, N.J.,1978, Geologic map of the Mare Acidalium quadrangle of Mars (MC-4): U.S.Geol. Survey Misc. Inv. Map I-1048.

West,M.N., 1974, Martian volcanism: additional observations & evidence for pyroclastic activity: Icarus, v. 21, p. 1-11.

Wood,C.A., 1976, Morphological evolution of shield volcanoes on Mars & Earth: EOS, 57, p.344; 1979a, Cinder cones on Earth, Moon & Mars (abs.): Lunar & Planet.Sci.X, p.1370-1372; 1979b,Morphometric evolution of cinder cones: Jour.Volc. & Geothermal Research, in press.

Progress in Quantitative Morphology of Volcanoes, R. J. Pike, U.S. Geological Survey, Menlo Park, CA 94025.

Photogrammetric measurements of the twenty or so large Martian edifices and their summit depressions are essential to continuing quantitative studies of volcanic morphology on that planet. However, the necessary photogrammetric models from Viking Orbiter pictures have turned out to be extraordinarily expensive and time-consuming to produce, partly because so many models are needed for each volcano. At this time compilation of contour maps for only two edifices, Olympus Mons and Arsia Mons, is underway at Flagstaff, and no new measurements of volcano form have been made. Ways around the prohibitive expense of detailed photogrammetry for all Martian edifices that have suitable Viking coverage are being explored. One alternative would involve detailed work on the summit caldera only, combined with low-resolution data on the overall edifice, using only one stero model. Updated shadow-length relief measurements of the calderas may have to suffice for the time being.

In view of the difficulties encountered in obtaining new Martian data, current emphasis is being given to updating the recently published classification of terrestrial central volcanoes (Pike, 1978). Scheduled for addition to the scheme are submarine calderas (Hollister et al., 1978) and Icelandic tablemountains without summit craters. Satisfactory sources of measurements now have been secured for a usable sample of both classes of edifices. Volcanoes in other categories of the 20-part classification are being measured and added to the compilation of topographic data that has been published for 655 edifices (Pike, 1978). This file will be maintained and updated periodically.

References

Hollister, C. D., Glenn, M. F., and Lonsdale, P. F., 1978, Morphology of seamounts in the Western Pacific and Philippine Basin from multi-beam sonar data: Earth & Planetary Sci. Letts., v. 41, p. 405-418.

Pike, R. J., 1978, Volcanoes on the inner planets: some preliminary comparisons of gross topography: Proc. 9th Lunar and Planetary Sci. Conf., p. 3239-3273.

Subglacial Volcanism Carlton C. Allen, Department of Planetary Sciences, University of Arizona, Tucson, AZ 85721.

Volcanic eruptions beneath glacial ice sheets have produced a suite of landforms with morphologies and compositions diagnostic of their mode of origin. Apparent analogs to these features have recently been recognized on the surface of Mars (1, 2, 3). The usefulness of such analogs in characterizing the geologic processes of another planet is dependent on an understanding of the terrestrial features. Field studies in Iceland and photo interpretation of former subglacial volcanoes in Alaska and British Columbia indicate the following common characteristics of eruptions beneath glacial ice.

Table Mountains. Central eruptions in Iceland characteristically produce small shield volcanoes. The typical Icelandic shield is less than 10 km in basal diameter and was probably formed during a single eruptive sequence. A similar eruption occurring beneath hundreds of meters of glacial ice, however, produces a mountain with a totally different morphology. The typical table mountain consists of a steep-sided plateau, often capped with flat-lying flows, summit cones and craters.

The "normal" evolution of a table mountain is as follows. A single vent or a short fissure opens beneath an ice sheet hundreds of meters thick, and a portion of the ice immediately overhead is melted by the initial rush of hot gas. This is soon followed by the intrusion of basaltic magma into the cavity containing a subglacial lake. Upon contact with water the lava cools rapidly, forming pillow basalt. This relatively quiet eruption into a confined pocket of water within the ice may continue for several weeks, with heat released from the cooling lava slowly melting the confining glacial ice both overhead and laterally. In this manner the pillow mass may built to within a few hundred meters of the top of the glacier.

As the mountain increases in height the pressure of the overlying water decreases and gas within the magma expands. At the same time this more open structure of the magma allows meltwater to gain access to the interior of the vent where it chills the molten rock. A critical point is reached when vesiculation, aided by steam explosions, fragments the magma and the eruption enters an explosive phase. The chief product is now tephra composed of finely-divided sideromelane glass, with a varying admixture of pillow basalt fragments. This mixture is known as "moberg" (literally brown rock) in Icelandic. After the top of the glacier is breached glass and rock fragments are blown high into the air. Those which fall back into the meltwater lake may form well-defined beds due to differential settling.

This phase of the eruption continues for days or weeks until the mountain has essentially reached the level of the lake surface and access of water to the vent becomes sporadic. Eruption products now alternate between glass and basalt which quickly flows into the water and forms pillows and pillow breccia. Sometimes these layers of "foreset breccia" (4) mantle the volcano's outer slopes from top to bottom.

Eruption often continues subaerially after the lake level has been surpassed, in which case a caprock of flat-lying basalt flows is formed. The caprocks of most table mountains are somewhat scarred by subsequent glaciation, and lateral glacial erosion may carry away whole sections of the edifice. Long after the glacier has disappeared eruptions may resume,mantling the caprock with much younger cones, flows and craters.

Many table mountains are distinctive enough in their large-scale morphology to be immediately recognizable on aerial photographs. Indeed, large mountains can be identified at the 80 m resolution of Landsat imagery. The key morphologic features of table mountains are their flat tops and steep sides. Many of these mountains also exhibit summit flows, cones and craters indicative of renewed eruptions after the formation of the main structure. Table mountains are characteristically less than 10 km wide, with heights which reflect the thickness of the ice sheet.

Moberg Ridges. The dominant style of volcanism on the terrestrial planets appears to be the fissure eruption. Fissure flows are often thin and widespread, and may totally conceal their source. In some cases, however, explosive eruptions from individual points along a fissure precede the flow of lava. In such a case a line of cinder and spatter cones many kilometers long may be formed.

Subglacial fissure eruptions produce landforms very different from crater rows or lava sheets. As described by Kjartansson (5) the features are "ridge shaped, often serrated mountains or low hills, or straight lined, more or less continuous rows of such mountains". Some of the largest such features are up to 35 km long, 2-4 km wide, and 200-400 m in height.

The course of a subglacial fissure eruption is apparently similar to that which forms a table mountain. An initial venting of hot gases along the rift melts an elongated cavity in the overlying ice. In some instances a pillow lava phase may follow, but many ridges show no evidence of this unit. The major portion of the eruption is an explosive phase, dominated by the ejection of glassy tuff and pillow fragments in varying percentages. These eruption products are essentially identical to those of table mountains. Few fissure eruptions continue long eough for the ridge to breach the water level, so foreset breccias and caprock basalts are rarely encountered. Occasionally the reactivation of a fissure in postglacial times deposits lava flows on the crest or flanks of a ridge.

Moberg ridges are less distinctive in their morphologies than table mountains. The ridges are characterized chiefly by linearity and alignment with other features in the vicinity, especially fissures and eruptive vents. Some ridges are single, isolated features and some form complex systems. Many have a serrated appearance, due both to erosion and to the eruption of a number of individual vents. Moberg ridges range up to 35 km in length. Their heights are generally less than the presumed thickness of the overlying ice at the time of their formation.

Massive Moberg Deposits. The volcanic products of subglacial eruptions do not always take the form of isolated table mountains or ridges. Just as lava flows from a number of vents may combine to create a vast basalt plateau, the tuff and breccia from many eruptive centers and fissures beneath an ice sheet may combine into widespread moberg deposits.

Several broad expanses of moberg material are apparent on geologic maps of Iceland. The ridge system between the Vatna and Myrdals glaciers caps one such mass. This area of ridges and valleys, 20 km wide and 50 km in length, is almost totally mantled by layers of tuff and breccia with a net relief of 200-400 m.

The four major remnant ice sheets in Iceland appear to be at least partially underlain by moberg deposits. Geologic maps show this material fringing portions of the glaciers and protruding through as nunataks. The evidence in the case of the Myrdals ice sheet is most compelling.

This glacier is almost completely surrounded by moberg deposits, and the same material is exposed in ridges which penetrate deep into the interior of the icecap. Along the southern coast, where the moberg mass almost reaches the sea, its thickness approaches 1000 m. While only one presently active volcano is known to underlie this glacier, the ice does cover extensions of several recent fissure systems. A small basalt caprock and numerous meltwater flood channels at the glacier's edge suggest the presence of additional vents.

Truly massive layers of subglacial volcanic products have been noted in Antarctica. Here the exposures consist of cliffs some 2000 m high (6), and such material has been estimated to extend 5 km below the present ice cap in some localities (7). While the origin of these deposits has not yet been established, it is assumed that they also represent the products of a number of voluminous subglacial eruptions.

References

1. Allen, C.C., Volcano-ice interactions on Mars, submitted to JGR.
2. Hodges, C.A., and Moore, H.J., Tablemountains and implications for glacial ice on Mars, submitted to JGR.
3. Wise, D.U., Univ. of Mass., personal communication, 1979.
4. Jones, J.G., Intraglacial volcanoes of the Laugarvatn region, southwest Iceland, II, Jour. Geol., 78, 127-140, 1970.
5. Kjartansson, G., The Moberg formation, in On the Geology and Geophysics of Iceland, Guide to excursion no. A2, pp. 21-28, International Geological Congress XXI Session, Reykjavik, 1960.
6. Hamilton, W., The Hallett volcanic province, Antarctica, USGS Prof. Paper 456-C, C1-C62, 1972.
7. Le Masurier, W.E., Volcanic record of Cenozoic glacial history, Marie Byrd Land, IUGS (pub) Series B, 1, 251-259, 1972.

Planetary Studies at Kilauea Volcano, Hawaii: Rift Zones and Their Implications for Mars, Daniel Dzurisin, P.O. Box 7, Hawaii National Park, Hawaii 96718

Certain morphologic similarities to Hawaiian shield volcanoes notwithstanding, fundamental questions remain regarding the structure and dynamics of volcanoes which comprise the Tharsis Plateau on Mars. In Hawaii, rift zones characterized by aligned fractures, vent structures, pit craters, and fuming areas are essential features of young basaltic shields. Geophysical studies indicate that magma is supplied to Kilauea Volcano from a zone of partial melting at roughly 60 km depth, and accumulates in a relatively shallow (d=3-5 km) reservoir beneath the summit before intrusion or eventual eruption. Most eruptions occur within the summit caldera or along two prominent rift zones, which provide sufficient permeability for lateral subsurface transport of magma from the summit reservoir to vents tens of kilometers distant. Combined with the relatively high fluidity of Hawaiian lavas, the restriction of vents to the summit area and rift zones gives rise to broad, gently-sloping shields which are distinctly elongate along the rift zones in plan view. Physiographically, rift zones appear as gentle ridges which radiate from summit calderas and gradually lose their topographic expression downrift. Rift zones are thus an integral part of basaltic volcanism in Hawaii, and profoundly influence the physiographic form and eruption dynamics of Hawaiian volcanoes.

Whether this is also the case for the Tharsis volcanoes on Mars remains uncertain. Carrand others (JGR, 82, 3985-4015, 1977) have argued for the existence of a rift on Arsia Mons Volcano from the roughly linear distribution of pits on the volcano's upper flanks and mounds within the summit caldera. If this interpretation is correct, the martian rift is a through-cutting feature, and is therefore unlike most Hawaiian rift zones, which are seldom collinear on a given shield.

To support an ongoing assessment of the likelihood of Hawaiian-type rift zones on Mars, a program of high-quality aerial photography of Hawaiian rift zone features is underway at the Hawaiian Volcano Observatory. Results indicate that many features which characterize Hawaiian rift zones are seemingly absent on Mars. These surficial differences may reflect important differences in subsurface structure and eruptive style between Tharsis and Hawaiian shields.

Specifically, the Arsia Mons rift may be a deeper-seated feature than Hawaiian rift zones, which do not extend below 10 km from seismic evidence. The apparent absence of large, aligned vent constructs on the flanks of Tharsis volcanoes may indicate that the most recent outbreaks there were large volume, high extrusion rate fissure eruptions. Although Hawaiian shields remain the best available terrestrial analogs to Tharsis volcanoes, a strict correspondence between the Hawaiian and martian cases has yet to be established, and alternative models for the subsurface structure and dynamics of Tharsis volcanoes should be actively pursued.

Lengths of Hawaiian Lava Flows, M.C. Malin, Planetary Surfaces and Interiors Section, Jet Propulsion Laboratory, California Institute of Technology, Pasadena, CA 91103

A pioneering work by G.P.L. Walker (1973) questioned the common attitude that the length or distance a stream of lava flowed depended solely or principally on the viscosity of the lava. Building upon the concept that high effusion rates produced single flow unit deposits of extended length and low effusion rates produced deposits of many short flow units, Walker presented a case for effusion rate as "the most important single factor" in governing the length of a lava flow. To support this interpretation, he presented flow length versus average effusion rate data for about 40 flows on 19 volcanoes. He defined average effusion rate as the volume of the flow divided by the duration of the eruption. Walker noted that for many Hawaiian and Icelandic basaltic eruptions the actual rate of effusion during the first day or so was much higher than the average, and suggested this would be a more proper value to plot against the length a flow attained as a result of that effusion. However, he did not have sufficient data to further develop the idea.

The present work is an attempt to acquire such data, and reports the initial findings for 44 historic flows on Kilauea and 39 historic flows on Mauna Loa. Volumes range from as little as 0.03 x $10^6 m^3$ to 60 x $10^6 m^3$ on Kilauea and up to 600 x $10^6 m^3$ on Mauna Loa. Flow lengths vary from less than 0.5 km to 50 km, limited in some cases by flows reaching the sea. The observations for Kilauea, where many of the flows occurred after the establishment of the Hawaiian Volcano Observatory, are of greater accuracy and reliability than all but those of the last several Mauna Loa eruptions.

In analyzing the data for Hawaiian eruptions, several difficulties were encountered in addition to the more common problems of insufficient temporal observations. These included: 1) the post-eruption volume change exhibited by many Hawaiian flows reflecting their loss of volatiles, 2) the numerous events in which lava, erupted from one linear vent, flowed some distance and then plunged back beneath the surface through another linear fracture, 3) the equally numerous times when flows grazed a pit crater and, rather than continuing to flow downslope, instead filled the crater, 4) several flows erupted from linear vents aligned down the topographic gradient such that the source was nearly as long as the flow, 5) the feeding of several flows by a single vent, each progressing at different rates to different lengths (or at times at different rates to the same length, etc.), and 6) flows that reached the sea stagnated at their toes and budded up-flow or enlarged laterally. There is no solution to 1)above; volume estimates must carry an error of about 50% on the high end. For 2,3, and 4, the solution was to eliminate these flows from the study. Where multiple flows were fed by a single vent (5), two methods of analysis were used: one assumed that length was dependent on effusion rate; thus the volume effusion rate was divided proportionally on the basis of volume of each flow. The second method assumed length of flow was not dependent on effusion rate; in this case, the same effusion rate was used for each flow. Although radically dissimilar, these methods, used on only a few flows, did not produce significantly different total results. In general, the first method seems most consistent. Finally, for flows that reached the sea (6), effusion rates and flow length were determined up until contact with the water. Flows that budded extensively were not used, although many could be treated as if the bud flow were a new flow.

Initial results do not strongly confirm Walker's hypothesis that effusion rate is the single most important factor governing lava flow length. Figure 1 shows effusion rate versus flow length for basalts adapted from Walker (1973) and including Wadge's (1978) values for Etna. Figure 2 shows new results for 44 Kilauea flows to the same scale. As Walker surmised the "actual" values are shifted to the right and slightly down from the "average" values. However, the data show a significantly larger scatter than do Walker's, and show little statistically significant correlation (remembering the data are displayed in a log-log format). In fact, flow length shows a stronger correlation with volume than with effusion rate (Figure 3).

Two factors probably contribute to the differences between the Hawaiian results reported here and the more general results of Walker (1973) and Wadge (1978). First, many Hawaiian flows consist of pahoehoe flow units, and these have different cross-sections, temperatures, and viscosities than the aa flows that constitute the majority of Walker's and Wadge's examples. As some pahoehoe flows change to aa at the end of their emplacement, eliminating such pahoehoe flows from study would be difficult, and, in addition, would remove from consideration an extremely important type of lava flow. Second, many Hawaiian flows form lava tubes and partially-covered channels. These act to reduce lateral spreading and maintain higher temperatures. Part of the greater correlation of length and volume must stem from the fact that a tube is much like a pipe -- what goes in at one end must come out the other.

It thus appears likely that factors other than effusion rate contribute to the length of Hawaiian flows at least as much as effusion rate. Among these other factors, cross-sectional area (dependent on the slope, viscosity and cooling rate; e.g. Hulme 1974) and volume may be equally as important as effusion rate (i.e. the rate at which hot material reaches the surface -- the more and hotter, the further it will flow before it cools). It is interesting to note that Hawaiian lavas might have continued to flow many 10's km further had they not reached the sea. Swanson (1973) indicates that lavas within tubes cool at a rate of about 1°C/km. For eruption temperatures of 1160°C (Swanson, 1973), such a cooling rate, combined with adequate volumes of magma, produced lengthy flows ($\sim$ 12 km) at very low effusion rates (~ 4 m^3/sec) and such eruptions could have possibly produced flows approaching 200 km in length. Thus, long flows on other planets need not require extremely high effusion rates (e.g. Carr et al. 1977), but only large volumes, and timescales for eruption could either be comparable to or larger than terrestrial values.

References

Carr, M.H. et al. (1977). J. Geophys. Res. 82, 3985-4015.
Hulme, G. (1974). Geophys. J. Roy. Astro. Soc. 39, 361-383.
Swanson, D.A. (1973). Bull. Geo. Soc. Am. 84, 615-626.
Wadge, G. (1978). Geology 6, 503-506.
Walker, G.P.L. (1973). Philos. Trans. Roy. Soc. Lond. A 274, 107-118.

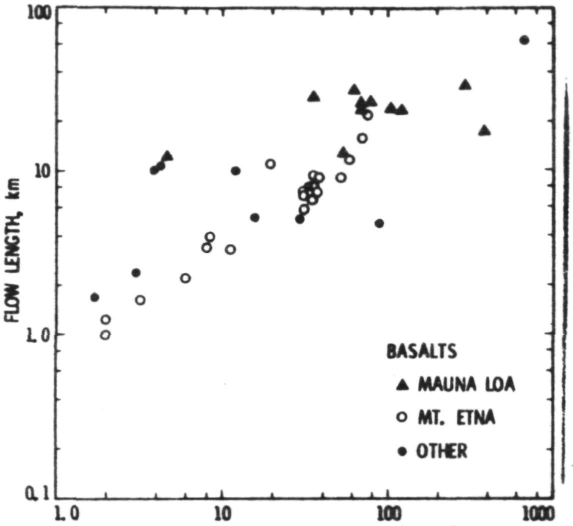

Figure 1
(After Walker 1973)

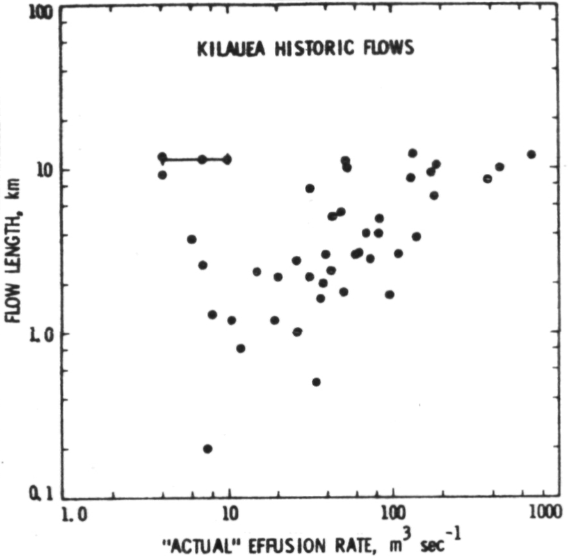

Figure 2

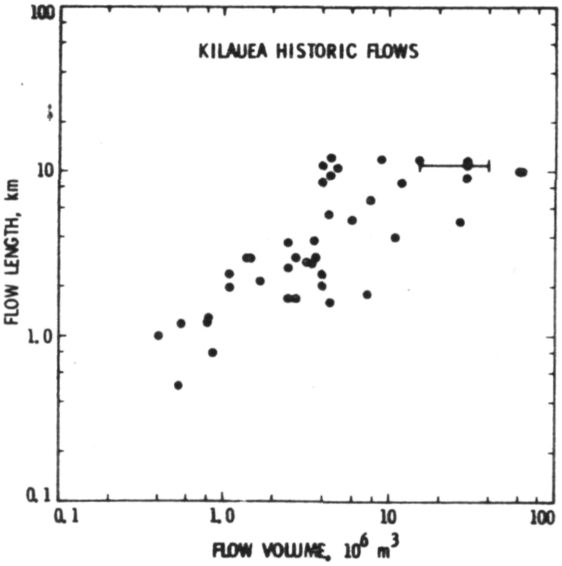

Figure 3

Evolution of Basaltic Landforms: Modifications by Heterogeneous Tephra Deposits, M.C. Malin, Planetary Surfaces and Interiors Section, Jet Propulsion Laboratory, California Institute of Technology, Pasadena, CA 91103, R.P. Sharp, Div. of Geological and Planetary Sciences, California Institute of Technology, Pasadena, CA 91125, and D. Dzurisin, U.S.G.S., Hawaiian Volcano Observatory, Hawaii National Park, HI 96718

The burial and exhumation of volcanic landforms and surfaces by homogeneous and heterogeneous deposits of fine grained materials may have played an important role in the evolution of the surface of Mars. These deposits may have been emplaced by volcanic explosive eruption, impact ballistic or fluidized ejection, or atmospheric entrainment and fallout. Subsequent modification by eolian and fluvial activity produces a landscape very different both from that of the original, pre-deposit surface and the post-depositional, pre-erosional surface. The intent of this study is to address the principal elements of geomorphology (i.e. process, material, and timescale) of these areas through field investigation and photogeologic interpretation of analogous terrestrial regions.

The Keanakakoi tephra blanket, erupted ca. 1790 from Kilauea Caldera, covers late prehistoric basaltic flows in the Kau Desert southwest of the caldera. The deposit consists of many layers of phreatic ejecta, principally ash, lapilli and blocks of accessory material, supplemented by vitric ash and pumice that may be, at least partly, essential (R.L. Christiansen, personal communication). The blanket is coarsest and thickest near the caldera rim, where it attains a thickness of at least 4m. For purposes of our field exercise, a generalized stratigraphy was developed drawing upon published works (e.g. Wentworth, 1938; Powers, 1948) and Christiansen's work in progress.

The materials of the tephra blanket govern the geomorphic evolution of the surface. Five zones of erosion, each characterized by from 1 to 7 micro-terrain elements, have been identified and examined. The five zones are: 1) total tephra cover, 2) bedrock islands within an integrated, continuous tephra cover, 3) residual tephra patches and reworked tephra materials within swales of a continuous bedrock surface, 4) cleanly stripped bedrock with some residual patches of tephra, and 5) zone of re-accumulation (Dzurisin, 1978). The seven micro-terrain elements are: 1) bedrock lavas, 2) lower lithic member of the Keanakakoi tephra (forming wall slopes in cracks and gullies), 3) intermediate vitric member of the Keanakakoi tephra (also cliff-forming), 4) upper lithic member of the Keanakakoi tephra (a firmly cemented crust with numerous stone fragments, subject to undermining and erosion by wind and water to produce a small-scale cliff-bench topography), 5) eolian sands, 6) residual lag gravels, and 7) fluvial debris.

Preliminary investigation yields the following results: 1) blankets only slightly thicker than the local variability in surface relief completely mask that underlying topography, 2) pahoehoe surfaces and associated landforms "recover" from burial and, with the exception of lag materials left behind, do not show appreciable change from pre-burial morphology, 3) Aa flows do "recover" from burial, but on longer timescales and to significantly lesser extent than pahoehoe surfaces, 4) micro-terrain elements can be effectively used to identify the degree of burial and exhumation, and the types of materials involved, and 5) these elements may be quantifiable on the basis of remote sensing observations, particularly those sensitive to material caliber (infrared and microwave wavelengths).

References

Dzurisin, D. (1978). Planetary Studies of Kilauea Volcano, Hawaii: Wind Action in the Kau Desert (abs.), in Reports of Planetary Geology Program 1977-1978 (R. Strom and J. Boyce, Eds.), NASA Tech. Mem. 79729, pg. 214-215.

Powers, H.A. (1948). A Chronology of the Explosive Eruptions of Kilauea, Pacific Sci. 2, 278-292.

Wentworth, C.K. (1938). Ash Formations of the Island of Hawaii, Third Special Report, Hawaiian Volcano Observatory, 185 pp.

RELATED VOLCANIC VENTS OF VARYING MORPHOLOGY - SNAKE RIVER PLAIN, IDAHO

Mark F. Mercer and John S. King, State University of New York at Buffalo

The Snake River Plain volcanic province typifies plains type volcanism made up dominantly of compound pahoehoe flows derived from a variety of vent morphologies. Most of the vents were apparently active for short durations and activity was probably limited to a single eruption at each vent.

Horse Butte, Cottrell's Blowout, and Wildhorse Corral are three volcanic constructs of this plains province which lie in close proximity along the Inferno Chasm rift zone. The origins of these three eruptive centers and their associated olivine tholeiite basalt flows represent three distinct volcanic histories.

Horse Butte, a small shield volcano 1250 m in diameter, developed through successive extrusions of lava from a centralized fissure conduit. Its associated paired lava tube systems formed by the roofing over and accretion of lava spatter flowing in open channels.

Cottrell's Blowout, a slot-like depression 595 m long, 160 m wide and 43 m deep, is the result of rapid vertical collapse along dilated tension fractures paralleling the rift zone immediately following the eruptive phases. The extursive activity from this vent is marked by a single massive flow unit which outlines the extent of the flow and was succeeded by superposed multiple gas-charged flow units of limited aerial extent and from which the cone developed.

Wildhorse Corral is an irregular, hourglass-shaped depression 935 m long, 565 m wide and 51 m deep. It was characterized by two stages of extrusive activity. The first stage was marked by three massive flow units which were erupted at a high rate forming the Bear Trap lava cave and its associated flow. Following a minor period of quiescence, the extrusive activity continued with the eruption of at least six massive flow units representing a lower rate of effusion and resulting in the major flow and the associated lava tube systems. Extrusive activity ended with the infilling of the vent by a short-lived lava lake which spilled over the southwest rim of the crater to produce a minor channel-fed flow. This lava lake was rapidly drained when a sealed lava tube was apparently reactivated allowing the escape of lava to produce a second minor flow. Owing to the withdrawal of subsurface magma support and draining of the lava lake, the summit region of Wildhorse Corral collapsed along nearly perpendicular linear tension fractures. The crater was subsequently partially filled with magma to produce a second lava lake which remained at a fairly constant level for a time estimated to be at least 300 days based on the time required to solidify a 50 m wide terrace and a 5-6 m thick crust lining the crater walls. Downtilting of the north section of the crater contorted the crustal slabs and was accompanied by subsidence of the lava lake surface as the still molten lava drained back through either the original source fissures or newly opened fissures associated with the tilting.

Rates of Resurfacing of Mars - Constraints on Thermal Evolution

R.E. Arvidson,
McDonnell Center for the Space Sciences, Dept. of Earth and Planetary Sci.,
Washington University, St. Louis, Mo., 63130

A rigorous constraint on the thermal evolution of a planet is the mass or volume of volcanic material produced as a function of time. Although we cannot estimate either the volume or the temporal history of volcanic activity with much precision, we have found that a plot of fractional surface area versus age (via crater abundance) provides important information directly related to the planet's thermal evolution history. Figure 1 shows the fractional area within ± 30° lat. occupied by a given crater abundance, for craters $\geq$ 8 km in diameter. Qualitatively similar results were obtained for craters between 4 to 10 km in diameter. The data show a bimodal distribution, with cratered terrain extending over a large range of crater abundances, while plains formed rapidly and recently. However, such a scenario would be true only if the rate of cratering on Mars were constant with time (flux A of Fig.2). The more likely case is that much of cratered terrain probably began to retain craters during a period of early heavy bombardment (e.g. flux B, Fig. 2A). When such constraints are applied, the effect is to narrow the cratered terrain distribution and to make it considerably more peaked, as shown in Figure 2B. Plains, on the other hand, are extended over a longer period of time and the resurfacing rate is decreased. The important points are that for any reasonable cratering model, (a) the bimodal nature of the data remains and (b) the time range of cratered terrain formation is compressed, while the time scale is extended for plains. Thus, we are left with early, rapid formation of cratered terrain with the plains occurring later and extending over much of geologic time. The exact shape of the re-surfacing curve for plains depends sensitively on the post-heavy bombardment cratering flux and on the age used for the transition between pre- and post-heavy bombardment. Such a scenario is consistent with a thermal evolution history having cratered terrain formed early and rapidly. A plausible way to get the required large amounts of energy so early in the planet's history is to have cratered terrain be an initial crust solidified from a lunar-like magma ocean formed by accretional melting of the outer few hundred kilometers of Mars. Plains volcanism seems to have followed a somewhat independent timescale that was probalby driven by the amount of time needed for the interior of Mars to heat-up and differentiate. Unfortunately, the shape of the re-surfacing curve for plains is sufficiently uncertain so as to provide little information on the timing of peak volcanism.

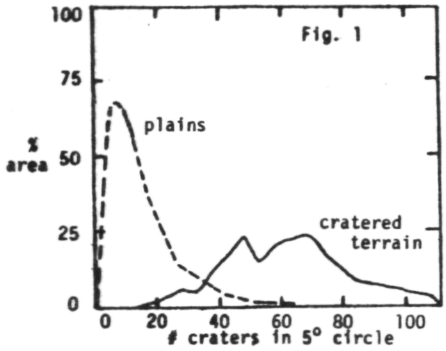

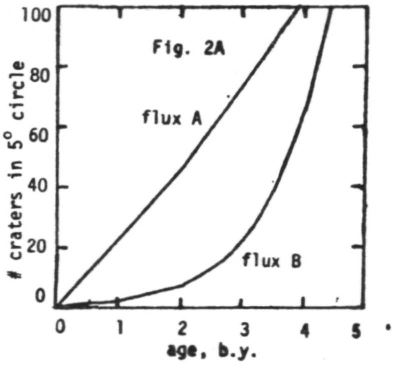

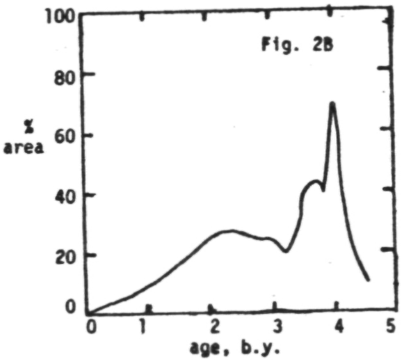

Radiogenic Heat Source Contents of the Earth and the Moon

G. Schubert and D. J. Stevenson, Dept. of Earth and Space Sciences, Univ. of Calif., Los Angeles, CA 90024, and P. Cassen, NASA Ames Research Center, Moffett Field, CA 94035.

It is widely believed that the heat now escaping through the surfaces of the earth and the moon are nearly in balance with the present day rates of internal heat generation in these bodies by the radioactive decay of uranium, thorium and potassium (Tozer, 1965; Turcotte and Oxburgh, 1972; Langseth et al., 1976). On this basis, it has been inferred that the present average volumetric rate of heat production for the entire earth is 0.084 x 10^{-13}cal/cm^{3}s (Oxburgh and Turcotte, 1978). If the heat production in continental crustal rocks is subtracted from the total surface heat loss, then heat must be produced in the earth's mantle at the present rate of 0.076 x 10^{-13}cal/cm^{3}s if radiogenic heat production and heat loss are equal. The value 0.074 x 10^{-13}cal/cm^{3}s can be derived for the present average volumetric heat generation rate for the entire moon from the average lunar surface heat flux of 0.43 x 10^{-6}cal/cm^{2}s (Langseth et al., 1976). The contribution of lunar crustal radioactives to surface heat flow is uncertain. Langseth et al. (1976) suggest that only about 9.6 x 10^{-8}cal/cm^{2}s may be flowing from the lunar mantle. In this case, the average volumetric rate of heat generation in the lunar mantle would be only 0.017 x 10^{-13}cal/cm^{3}s.

In this paper we construct simple thermal history models of the earth and moon, including heat transfer by subsolidus mantle convection, and show that mantle heat production and loss cannot be in balance (see also Sharpe and Peltier, 1978; Daly and Richter, 1978; Cassen et al., 1979; Schubert et al., 1979; Turcotte et al., 1979). The fundamental reason for this imbalance is that planetary cooling, i.e. the decrease of mantle temperature with time, releases internal energy which must contribute to the surface heat loss. Thus the lunar and terrestrial values of the internal radiogenic heat generation rates derived on the assumption of a balance between heat loss and production are overestimates. The only issue that needs to be addressed by quantitative models are the magnitudes of the overestimations.

We use a spherical shell model of the earth's mantle which has a uniform viscosity ν and temperature T related according to

$$\nu = \bar{\nu} \exp\left(\frac{A}{T}\right) \quad , \qquad (1)$$

where $\bar{\nu}$ and A are constants. Decaying radiogenic heat sources are uniformly distributed throughout the mantle. The lower boundary of the mantle is assumed to be insulating. The heat flow q from the vigorously convecting mantle is given by

$$q = \frac{k(T - T_s)}{(R_m - R_c)} \left\{ \frac{\alpha g (T - T_s)(R_m - R_c)^3}{Ra_{cr} \kappa \nu} \right\}^{\beta} \quad , \qquad (2)$$

where k is the thermal conductivity, T_s is the surface temperature, α is the thermal expansivity, g is the acceleration of gravity, R_m is the outer radius of the shell, R_c is the inner radius, κ is the thermal diffusivity and Ra_{cr} and β are constants (Schubert et al., 1979). An energy balance for the mantle provides an equation for the temporal history of T, and in turn ν and q. The equation is

$$\rho c \; (R_m^3 - R_c^3) \frac{dT}{dt} = -3\, R_m^2 q + Q(R_m^3 - R_c^3) \qquad , \qquad (3)$$

where ρ is the density, c is the specific heat and $Q = Q_o e^{-\lambda t}$ is the volumetric concentration of decaying heat sources. The lunar model is similar except for a rigid spherical shell lithosphere which surrounds the mantle. The lunar mantle has no inner boundary (it is a sphere); its outer radius decreases as the lunar lithosphere thickens with time.

With these models we determine the lunar and terrestrial heat source concentrations that are consistent with our knowledge of the present surface heat flows and mantle viscosities of these planets. We consider how these volumetric heating densities are affected by large variations in the values of model parameters which are highly uncertain, e.g. $\bar{\nu}$, A, β, and Ra_{cr}. The average volumetric heat generation rates in the earth and moon are only about 70-80% of the values inferred from the assumption of a balance between production and loss.

REFERENCES

1) Cassen, P., Reynolds, R. T., Graziani, F. Summers, A., McNellis, J., and Blalock, L., 1979, Phys. Earth Planet. Int., in press.

2) Daly, S. F., and Richter, F. M., 1978, Lunar and Planetary Science IX, 213-214.

3) Langseth, M. G., Keihm, S. J., and Peters, K., 1976, Proc. Lunar Sci. Conf. 7th, 3143-3171.

4) Oxburgh, E. R., and Turcotte, D. L., 1978, Rep. Prog. Phys., 41, 1249-1312.

5) Schubert, G., Cassen, P., and Young, R. E., 1979, Icarus, in press.

6) Sharpe, H. N., and Peltier, W. R., 1978, Geophys. Res. Lett., 5, 737-740.

7) Tozer, D. C., 1965, Phil. Trans. Roy. Soc. A, 258, 252-271.

8) Turcotte, D. L., Cook, F. A., and Willeman, R. J., 1979, Proc. Lunar Sci. Conf. 10th, submitted.

9) Turcotte, D. L., and Oxburgh, E. R., 1972, Ann. Rev. Fluid Mech., 4, 33-68.

PYROCLASTIC VOLCANISM OF THE SNAKE RIVER PLAIN, IDAHO: IMPLICATIONS FOR MARS.

Womer, M.B. and Greeley, R., Department of Geology, Arizona State University, Tempe, Arizona 85281 and
King, J., Department of Geological Sciences, SUNY at Buffalo, 4240 Ridge Lea, Amherst, N.Y. 14226

Two pyroclastic features - Split Butte and Sand Butte - in the central Snake River Plain have been studied as possible analogs for Mars. The Snake River Plain is a basaltic province of Early Pliocene to Holocene age and consists of "plains" style volcanism (Greeley, 1977). Although the region involves mainly lava flows, several pyroclastic structures occur, some of which resulted from ground-water - magma interactions.

Split Butte is a tuff ring 550 m in diameter and 50 m high, containing a central lava lake (Greeley and King, 1975). The lake subsided after partial solidification, forming a circular pit crater 400 m in diameter and 20 m deep. The tuff consists of partly palagonitized sideromelane clasts, crystal inclusions and lithic fragments ranging in size from 1 mm to > 2 m. Basal tephra layers are heavily palagonitized and poorly bedded to massive. Stratigraphically higher layers are planar beds of slightly palagonitized ash which dip radially outward 20° to 40°. The ring is higher on the east and slightly elliptical; both effects apparently resulted from prevailing westerly winds during the formation of the Butte. A moat-like depression 2-5 m deep surrounds the Butte; this depression resulted from encroachment by a lava flow of the Snake River Group.

Sand Butte (43°8'N, 113°50'W) is a tuff cone, astride a N-S trending fissure 5 km long. The fissure consists of an en echelon series of tensional fractures, and erupted a series of thin pahoehoe flows. The tuff cone is 1.2 km in diameter and 80 m high, and consists of poorly-bedded to massive layers of palagonitized vitric ash and abundant lithic fragments up to 1 m in diameter. The tephra of Sand Butte also retained a lava lake which subsided to form a shallow pit crater. The original lake level is preserved as a discontinuous scarp in the tuff crater.

Grain size analysis reveals systematic differences between Split and Sand Buttes in tephra production and deposition processes. Sand Butte tephra consists of phreatic ash, whereas Split Butte deposits are composed of both phreatic and cinder cone pyroclastics (Fig. 1). The scoria fragments are restricted to bedded tephra layers in the upper ash sequence of Split Butte (Fig. 2). In addition, phreatic ash occurring in well-bedded layers at both Buttes displays better sorting than the massive layers (Fig. 2).

Statistical analysis of the tephras reveal (Fig. 3) sorting (σ) values intermediate between the pyroclastic flow and air fall fields of Walker (1971). Samples plotting here typically reflect rain-flushing or deposition of thin pyroclastic flow beds. No evidence of rain-flushing was observed, and comparison of well-bedded and massive layers for both Buttes reveals consistently better sorting in the thin layers (Fig. 4). The Buttes are therefore largely phreatic, with minor scoria present only at Split Butte, and pyroclastic flow was the dominant depositional mechanism, with minor air fall beds also present at Split Butte.

If water is as abundant on Mars as has been postulated (Carr and Schaber, 1977; Owen, 1976), phreatic pyroclastics may be common in volcanic areas. Numerous features resembling volcanic cones have been described (Greeley and Spudis, 1978; West, 1974 and others) in many areas of Mars. The features appear as round cones .8 to 2 km across at the base and have summit craters approximately .5 km across. The features are convex upward, in contrast to flat-profiled pedastle craters (Greeley and Spudis, 1978). Present photographic resolution of these features, however, does not allow a definitive statement on their genesis.

References

Carr, M.H. and Schaber, G., 1977, JGR, 82, 4039-4054.
Greeley, R., 1977, NASA CR-154621, 308 p.
Greeley, R., and J.S. King, 1975, Idaho Bur. Mines and Geology, #160, 49 p.
Owen, T., 1976, Icarus, 28, 171-177.
Walker, G.P.L., 1971. Jour. Geol., 79, 696-714.
Walker, G.P.L. and R. Croasdale, 1971, Bull. Volc., 35, 303-317.
West, M., 1974, Icarus, 21, 1-11.

Figure Captions

Fig. 1. Sorting (σ) vs. median for Sand and Split Buttes, compared with Walker and Croasdale's (1971) data.

Fig. 2. Sorting vs. median plots for bedded and massive tephra of Sand and Split Butte.

Fig. 3. Histograms of sorting (σ) values for (A) Sand Butte, (B) Split Butte and Walker's (1971) flow and fall field.

Fig. 4. Histograms of sorting (σ) values for (A) Sand Butte and (B) Split Butte massive layers (diag. pattern), bedded layers (no pattern) and cinder-rich layers (horiz. pattern).

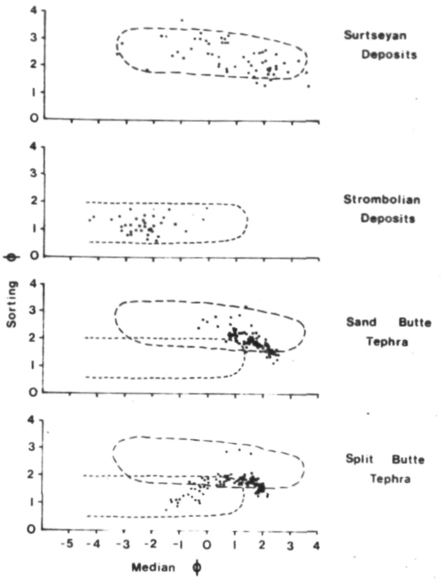

Fig 1.

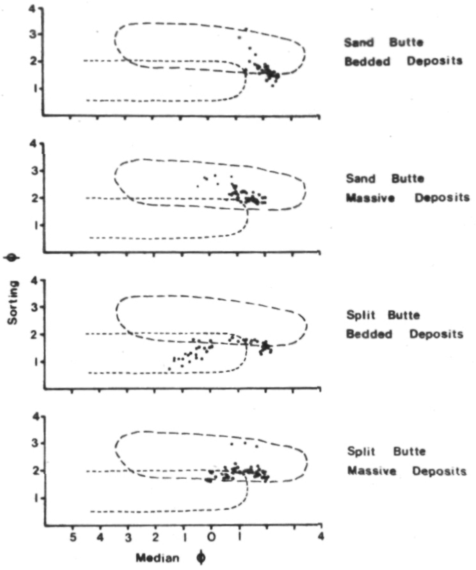

Fig. 2

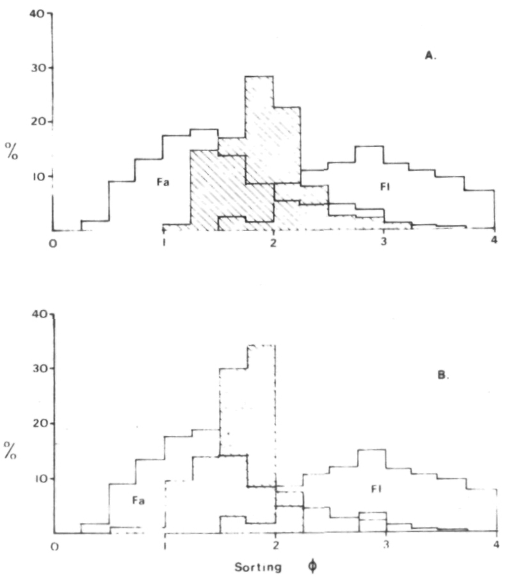

Fig 3

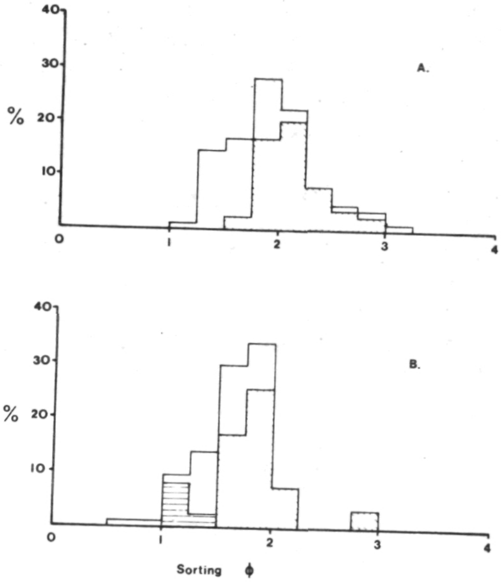

Fig 4

Means for detection of Basaltic Fissure Vents: The 1823 Keaiwa Flow Hawaii

Greeley, R., Peterfreund, A. R., Arizona State Univ., Tempe, AZ 85281;
Guest, J. E., Univ. of London Observatory, London, England; and Tilling,
R., USGS, Reston, VA

Basalt and basalt-like lavas cover large parts of the terrestrial planets. Although basaltic products may accumulate in many diverse landforms, by far the greatest areal extent is comprised of flood lavas and lava plains, typically erupted in large volumes and at high rates from fissures. This style of eruption often buries or destroys vent features, so that the identification of vent regions is usually very difficult or impossible, even on Earth where field work is possible. The problem is compounded on the planets where remote sensing data have orders of magnitude poor resolution than for Earth. Consequently, most vent regions for the vast volcanic plains and plateaus on the Moon, Mars, and Mercury remain unknown, despite the importance that their identification has in planetary science. Hence, there is need for a means of identifying vent regions for fissure eruptions remotely. After considering various geophysical, morphological, compositional, etc. signatures that might be associated with fissure vents, one potential technique was selected for initial study that is based on lava flow textures, and the possible differences in thermal and reflective properties of the textures. A wide range of surface textures can develop on basaltic flows (pahoehoe, aa, etc. and their subtypes). Shelly pahoehoe appears to be characteristic of near vent areas (Swanson, 1973), and its surface properties may be distinctive from other (non-vent) parts of the flow. To test this hypothesis, field work was conducted on the Keaiwa lava flow, Hawaii.

The Keaiwa lava flow (Stearns, 1926) erupted from a 10 km fissure on the southwest rift at Kilauea in 1823; it was extremely fluid and may be one of the best historic analogs (albeit small-scale) of fluid extraterrestrial fissure eruptions. The flow displays all the classic surface textures of basalt flows, except well developed block lavas, and has shelly pahoehoe present in several areas along the eruption fissure. Photogeological mapping of the flow textures was field-checked and compared with thermal infrared images (nighttime and morning) flown by the U. S. Geological Survey (courtesy K. Watson). Preliminary assessment indicates several possible correlations between IR signature and textures. A sharp contrast in the predawn IR is apparent between the Keaiwa flow and surrounding older flows. Within the Keaiwa, the pahoehoe and aa surfaces are fairly easy to distinguish, with the aa surface being warmer in the predawn, i.e. higher thermal inertia. Within the pahoehoe terrain subtle variations in surface temperature are detected. Regions of shelly pahoehoe (i.e. near vent textures) appear to be warmer than regions of other textures in the predawn. The result, however, appears to be due not to the primary surface alone but also to the weathering products. The shelly material consists of a glassy, froth and filamentous lava that evidently results from rapid degassing near the vent to produce a billowy surface, with a thick but frothy "skin". In addition to the possible thermal signature, the surface color is a distinctive "golden" tone that also appears to be characteristic of the near vent lavas. These two possible signatures can be detected remotely and afford some promise for the detection of vent regions. Work is in progress to determine their reliability and the limitations on their recognition. If the results are positive, the work will be extended to other, older flows to determine limitations of flow age and degree of weathering.

Stearns, H. T. 1926. J. Geol. 34, 336-351.
Swanson, D. A. 1923. Geol. Soc. Amer. Bull, 34, 615-126.

THE EXTENT AND DURATION OF LUNAR HIGHLAND VOLCANISM

P.D. Spudis, Department of Geology, Arizona State University, Tempe, Arizona 85281

The general term "highland volcanism" has come to include those volcanic events that pre-date the major basins and subsequent mare basalt flows and is represented primarily by KREEP, a volcanic product containing large quantities of incompatible elements (1). Recent work has demonstrated that early KREEP volcanism (∿4.3 AE(2)) was probably complemented by contemporaneous early mare volcanism (mantle derived magmas) (3,4). Thus, both mare and KREEP basalts may constitute portions of the highland crust. However, KREEP is distinct in chemistry and source region from the more common mare basalts and are important in assessments of highland volcanism due to their petrologic significance and relation to lunar thermal history. KREEP basalts may be easily identified from orbit by the Apollo gamma-ray spectrometer (5) as they contain high concentrations of radioactive thorium (1,6). Thus, orbital remote sensing offers the best possibility for mapping the location and geologic setting of KREEP on a moonwide basis.

KREEP volcanism occurs near the Apollo 14 and 15 landing sites and on the Aristarchris plateau (7,8). KREEP was first defined from returned samples (1) and was thought to represent the chemical character of Imbrium basin ejecta (9). Subsequent study of the igneous phase chemistry of KREEP (10) demonstrated its volcanic origin and studies of cratering mechanics (e.g. 11) suggested mainly local landing site origins for this rock type (12). Timing and duration of KREEP volcanism is based mainly on radiometric dating of lunar samples. It is generally agreed the KREEP volcanism commenced at about 4.3 AE (7); however, KREEP volcanism may have continued for some time after the Imbrium basin impact (7,13) with the Apollo 15 KREEP samples being the youngest volcanic KREEP rocks known (∿3.9 AE(14)). It thus seems fairly certain that KREEP volcanism was active between 4.2-3.9 AE, a time when the Moon was undergoing terminal heavy bombardment (6). Thus, direct morphologic evidence for KREEP volcanism is rare (being preserved only in the Apennine Bench region (7,13)) and orbital chemical data is the primary source of information regarding its distribution.

Because the highest radioactive levels seen from orbit occur in the Imbrium-Procellarum region (15), it has long been assumed that KREEP volcanism was primarily confined to this area (e.g. 5,7). New reduction of the orbital gamma-ray data (15,16) and photogeologic studies (4) suggest KREEP volcanism may have been much more widespread. The radioactive highs seen on the lunar farside are of low magnitude, generally corresponding to 2-5 ppm of Th (15,16). It may be argued that these concentrations correspond not to KREEP basalt (10-15 ppm Th) but to low K Fra Mauro (LKFM) basalt (∿5 ppm Th), a major component of Apollo highland polymict breccias (6); however LKFM as seen from orbit (17) is primarily associated with deeply derived basin ejecta, such as the Apollo 17 "melt sheet" (18) and none of the farside radioactive highs display photogeologic evidence of pristine basin ejecta deposits (19,20). These regions do display areas of ancient highland plains that probably either mantle or incorporate significant quantities (up to 20%) of medium-K KREEP basalt, which is presumed to be of volcanic origin on petrologic grounds (1,10).

The most prominent farside radioactive high is the Van De Graaff anomaly (approximate location: 25°S, 175°E) corresponding to 2.3 ppm Th and 1300 ppm K (15). This region is just within the outer ring of the largest multiringed basin on the Moon, the South Pole-Aitken basin (20,21) and contains concentrations of both Imbrian and Nectarian age highland plains (20). This region has long been noted as a prominent magnetic anomaly (22), possibly indicating the presence of near-surface igneous intrusions. Two additional radioactive highs occur in the Mare Marginis (10°N, 90°W) and Balmer (15°S, 70°W) regions (16), corresponding to clusters of dark halo impact craters (interpreted as having excavated basaltic material from beneath Imbrian light plains (4)). All three regions of farside KREEP concentration occur in areas of thin (within the 60 km isopach) farside crust as mapped by gravity data (23) in addition to occupying geologically old topographic lows (24). This observation supports the presence of ancient basin-filling volcanic deposits subsequently reworked by late stage impact processes. An earlier study (25) found no correlation between Th and crustal thickness, but this work was done prior to the deconvolution of orbital gamma-ray data (16). It now appears that all observable KREEP-rich areas on the Moon occur near regions where the crustal thickness is 60 km or less.

KREEP-rich regions on the Moon are more widely distributed than previously believed. It is apparently of limited extent on the lunar farside, due to the greater average thickness of the crust, the same reason most mare basalt deposits are concentrated on the lunar nearside (26). KREEP-rich anomalies occur in regions of relatively thinner farside crust that were overflown by Apollo orbital chemical instruments. This suggests that KREEP volcanism was a moonwide episode in early lunar history and was not strictly confined to the Imbrium-Procellarum regions, although major concentrations are found there. It is unlikely that much morphologic evidence for this early phase of highland volcanism is preserved but integrative studies of remote sensing and photogeologic data have successfully identified ancient regions of KREEP volcanism. The suggestion that KREEP volcanism was not limited to a small region of the Moon increases the importance of this process to the petrologic evolution of the highland crust.

References

(1) Meyer C. (1977) Phys. Chem. Earth 10, 239.
(2) Schonfeld E. and Meyer C. (1972) PLSC 3, 1397.
(3) Ryder G. and Taylor G. (1976) PLSC 7, 1741.
(4) Schultz P.H. et al. (1979) Lun. Planet. Sci. X, 1084.
(5) Arnold J. et al. (1972) Apollo 15 PSR, 16-1.
(6) Taylor S.R. (1975) Lunar Science, Pergammon Press.
(7) Hawke B.R. and Head J.W. (1978) PLPSC 9, 3285.

(8) Zisk S. et al. (1977) Moon 17, 59.
(9) LSPET (1971) Science 173, 681.
(10) Walker D. et al. (1972) PLSC 3, 797.
(11) Morrison R. and Oberbeck V. (1975) PLSC 6, 2503.
(12) Hawke B.R. and Head J.W. (1977) PLSC 8, 2741
(13) Spudis P. (1978) PLPSC 9, 3379.
(14) Nyquist L. et al. (1975) PLSC 6, 1445.
(15) Adler I. and Trombka J. (1977) Phys. Chem. Earth 10, 17.
(16) Haines E. et al. (1978) PLPSC 9, 2985
(17) Hawke B.R. (1978) Lun. Planet. Sci. IX, 474.
(18) Winzer S. et al. (1977) EPSL 33, 389.
(19) Wilhelms D. and El-Baz, F. (1977) USGS Map I-948.
(20) Stuart-Alexander, D. (1979) USGS Map (in press)
(21) Wilhelms D. et al. (1979) USGS Map (in press).
(22) Sharp L. et al. (1973) Moon 7, 322.
(23) Bills B. and Ferrari A. (1976) PLSC 7, Frontispiece.
(24) Kaula W. et al. (1974) PLSC 5, 3049.
(25) Schonfeld E. (1977) PLSC 8, 1149.
(26) Soloman S. (1975) PLSC 6, 1021.

Chapter 6

EOLIAN PROCESSES

Page Intentionally Left Blank

Wind Regime of Sand Dunes in Imperial Valley, California:

Roger S. U. Smith, Geology Department, University of Houston, Houston, TX 77004

Sand dunes in the Imperial Valley of California are particularly well suited for studies of dune response to wind regime because their changes in form and location with time and season are documented by an unusually-detailed, 40-year record of sequential aerial photography and their wind regime is documented by a nearly-continuous hourly record of wind speed and direction at six stations over the last 15 years and at five stations during World War Two. These wind data are being analyzed using a modified form of Bagnold's (1941) method, which relates potential sand transport to the cube of wind shear velocity. Reasonable assumptions about surface conditions allow the wind data to be resolved into monthly, seasonal and annual vectors of net potential sand transport. The magnitude of these vectors is consistently less than transport rate inferred from barchan migration, a subject for further study.

These dunes are driven mostly by strong westerly downslope winds which follow the major stream drainages heading in the Peninsular ranges; these winds are strongest and most frequent during spring. They diminish in intensity as they cross the flat floor of Imperial Valley and shift gradually clockwise to northwesterly as they cross East Mesa, whose northeastern margin is formed by the southeast-trending Algodones dune chain. At Yuma, Arizona, 20 km past the dunes, these winds are effectively opposed by persistent strong summer winds from the south-southeast, so Yuma seems now to occupy the regional sump for potential sand transport.

The following conclusions are preliminary:

1) Salton Sea Barchans: These are driven by strong, nearly-unidirectional winds as inferred by all previous authors. Analysis of 1942-1945, 16-point wind data taken at the naval airstrip within the dune field yields a potential transport azimuth of S 75° E, which is compatible, within uncertainty limits, with Long and Sharp's (1964) average migration direction of N 90° E during 1941-1956.

2) Longitudinal and Barchan Dunes at Superstition Mountain: On the west side of Imperial Valley, longitudinal lee ridges heading on Superstition Mountain extend about one km due east and their distal ends show no net advance, retreat or sideways dislocation over the last 40 years. During that period, however, barchans spawned from these ridges have migrated consistently towards N 80° E at rates of 10-15 m/yr for dunes 3-4 m tall. This disparity may be explained in part by the position of Superstition Mountain very near the southern limit of winds fanning ESE from the drainages of Borrego Valley and San Felipe Creek and near the northern limit of winds fanning ENE from the drainages of Carrizo and Coyote washes.

3) Longitudinal Ridges of East Mesa: These long, low, subdued features trend E to ESE on the west edge of the mesa but swing clockwise towards SE as followed eastward. Their orientation near three wind stations accords, within limits of uncertainty, with the azimuth of potential sand transport at each site. The pattern of sand encroachment off the southern escarpment of East Mesa onto the delta of the Colorado River also indicates that net sand movement has been longitudinal along these features. However, data from sand traps emplaced during May, 1978, and from the paucity of

sand encroachment onto cultural features suggest that little sand now traverses East Mesa.

4) Longitudinal Dunes, Algodones Dune Chain: The SE trend of active longitudinal ridges atop the plinth on the SW edge of the Algodones dune chain accords with the azimuth of potential sand transport at an adjoining station. Here, winds from the NW compass octant are slightly dominant over winds from the W and N octants, consistent with the premise that such dunes represent the effects of balanced crosswinds arranged at shallow angles about a dominant wind.

5) Barchan Dunes, Southern Algodones Dune Chain: These dunes have migrated towards S 60^o E, parallel to the trend of the short longitudinal ridges which spawned them. This azimuth is near the limits of uncertainty on the potential sand transport at the nearest station, 6 km distant. Field measurement of the heights of more than 100 barchans suggests that individual dune heights are steady over the long term but fluctuate over seasonal or short-term time scales. Most dunes neither grew nor shrank during June, 1968, through May, 1978 and during January, 1976 to January, 1978, but nearly all shrank during January through May, 1978, and during May, 1978 to January, 1979. The causes of shrinkage during the last year are under investigation and may be related to the intensity of form deformation by summer crosswinds.

References Cited

Bagnold, R.A., 1941, The physics of blown sand and desert dunes: London, Methuen.

Long, J.T., and Sharp, R.P., 1964, Barchan-dune movement in Imperial Valley, California: Geol. Soc. America Bull., v. 75, p. 149-56.

GRAIN SIZE CHARACTERISTICS OF EOLIAN DEPOSITS IN SOUTHWESTERN EGYPT: IMPLICATIONS FOR THE SURFACE OF MARS.

Ted A. Maxwell and Farouk El-Baz, National Air and Space Museum, Smithsonian Institution, Washington, D. C. 20560

Seasonal dust storms, wind streaks, dunes and streamlined erosional remnants indicate the present-day dominance of an eolian regime on the surface of Mars. In addition to distinct dune types that are visible on orbital images of both Earth and Mars (1,2), large regions of terrestrial deserts are composed of relatively featureless sand sheets. When viewed from orbit, however, these areas exhibit subtle color variations that can be related to changes in the desert pavement surface. It is likely that wind-dominated regions on the surface of Mars may be composed of lag deposits similar to those of Earth. Field investigations of desert surface characteristics in southwestern Egypt indicate that variations in desert color as viewed from orbit are influenced by local bedrock and topographic effects on the distribution of light-colored sand (3). In sand sheets, these variations can be related to differences in the size, spacing and lithology of lag deposits.

The sand sheets of southern Egypt are stratified into 1-2 cm layers of medium to fine sand separated by lag granules. Dark streaks of desert pavement in the lee of hills are composed of local material which decreases in grain size downwind from the source. On sand sheets, however, lag granules are relatively uniform in size (-1.0 to -2.0ϕ; 2-4mm) and are composed of frosted quartz grains. Based on the sorting within the sand-size fraction, it is possible to distinguish between sand-sheet sand (excluding lag granules), and that of longitudinal dunes and barchans. Both dune types exhibit much better sorting than sand sheet samples (Figure 1), which are skewed to both fine and coarse grain sizes. This is consistent with the less frequent, high velocity winds needed to move the protective lag surface as opposed to the more frequent wind speeds needed to preserve dune shapes.

In addition to grain-size differences, the color of sand-sheet sand is lighter than that of the lag granules. Consequently, during periods of high wind velocity, light-colored sand would move higher above the ground than the near-surface rolling (and saltation?) of lag granules. A similar situation may exist on Mars where certain relatively stable dark streaks might be composed of locally-derived lag deposits. This suggestion is supported by recent spectral observations that indicate a uniform composition for light-colored dust, but varied compositions for dark materials (4).

REFERENCES

(1) Breed, C. S., 1977, Icarus, v. 30, p. 326-340.
(2) El-Baz, F., 1978, Lunar and Planetary Science IX, LPI, Houston, p. 285-287.
(3) El-Baz, F. and T. A. Maxwell, 1979, Lunar and Planetary Science X, LPI, Houston, p. 349-351.
(4) Singer, R. B. and T. B. McCord, 1979, Lunar and Planetary Science X, LPI, Houston, p. 1129-1130.

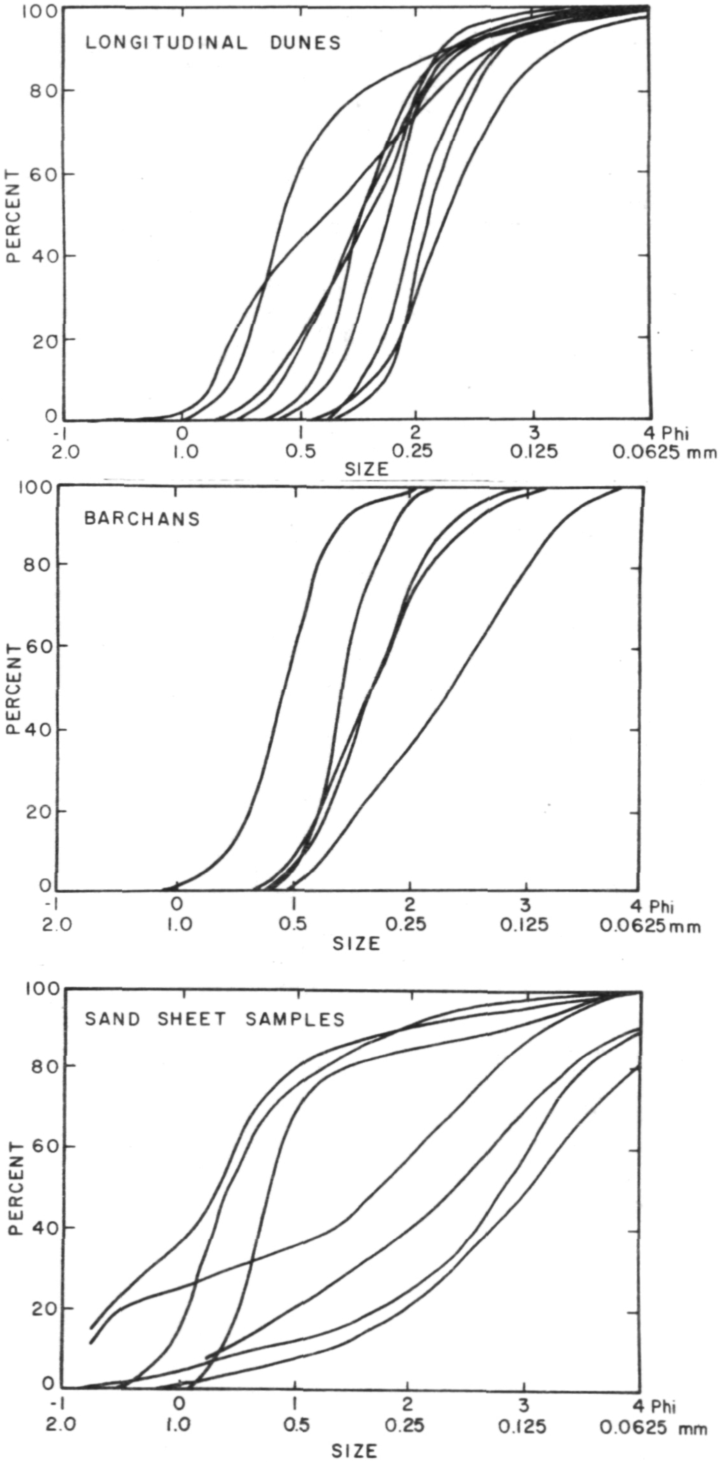

Figure 1. Cumulative size distribution curves for sand samples from southwestern Egypt. Both longitudinal dunes and barchans exhibit better sorting in the sand size fraction than do sand sheets.

COMPARISON OF MARINER 9 AND VIKING IMAGERY OF THE CERBERUS ALBEDO FEATURE.

A. L. Chaikin, F. El-Baz and T. A. Maxwell, National Air and Space Museum,
Smithsonian Institution, Washington, D. C. 20560

The Cerberus albedo feature is located in the Elysium quadrangle of Mars (12°N, 205°W), and is about 1330 km in length from E to W and 410 km from N to S. This dark material is mapped as streaked plains with patches of knobby material (Scott and Allingham, 1976). The streaked plains were interpreted as lava flows which covered and embayed the older knobby terrain. Impact crater densities for the streaked plains unit suggest that it is the oldest plains unit in this region, and is postdated by younger lava flows, volcanic constructs to the northwest, and eolian deposits (Scott and Allingham, 1976).

Between the time Cerberus was photographed by Mariner 9 (in 1972) and by the Viking 1 Orbiter (in 1977), its boundaries changed in a general NE-SW direction (Fig. 1). This is consistent with the wind direction implied by wind streaks in the area. For example, the boundary in the northwest portion of the feature moved as much as 45 km parallel to the inferred wind direction. In other locations, movement ranged from 24 to 131 km. While it is difficult to establish the precise direction of all changes, they nevertheless indicate a general shift to the south-southwest. In 1972 the feature covered some 297,120 km^2, but this area had decreased by approximately 2% by 1977.

Many of the changes suggest that bright material is being transported from NE to SW across the body of the feature. The dark feature was mottled with brighter patches in Mariner 9 images, but several areas have become more uniformly dark in the Viking coverage. These areas are all along the "windward" northeast edges of the feature, and it appears that bright material has been transported downwind exposing more of the underlying dark surface. Similarly, removal of bright material probably caused the southward migration of parts of the southern boundary, while an influx of bright material from the NE resulted in embayment of the northern edge. Observation of bright wind streaks behind craters and knobs in the area supports this conclusion. Many streaks with discrete boundaries in Mariner images have discontinuous boundaries in Viking images, as though the dark surface surrounding the streak had been covered by brighter material.

These changes could also be explained by transport of dark material to the southwest, but we consider erosion and deposition of light-colored material more likely for two reasons:

1) The longevity of this albedo marking (long observed in earth-based telescopes) would require a continuous resupply of dark material; no such source is readily apparent.

2) Spectral observations of martian dust storms indicate that light-colored material has been in transport during the past 5 years (Singer and McCord, 1979).

There may however, be some restrictions on any hypothesis that attributes great stability to the dark material. A dark wind streak in the lee of a crater to the southeast of Cerberus appears to have been derived from a dark splotch within the crater, then transported downwind (Veverka et al., 1976). If the dark material within the crater is related to Cerberus itself, it may be that the material was mobile at one time and has since been made more competent (perhaps by formation of a duricrust).

However, it is also possible that the dark material may be too coarse to be moved by the wind. Finer, brighter material would be winnowed from between the coarser grains. In both cases, both Cerberus and the streak to the southeast would be relatively stable and would owe all changes in appearance to both the deposition and removal of overlying bright dust.

Statistical analysis of 64 bright crater streaks within Cerberus has been compared with previous analyses of streaks in Mars' northern hemisphere (Veverka et al., 1978). Streak length to crater-diameter ratios (L/D) show a sharp peak of occurrence for values of L/D between 2 and 4 (Fig. 2), while for the northern hemisphere in general, a steady increase in relative frequency was observed for decreasing L/D. Comparison of L/D distributions in Cerberus for Mariner 9 and Viking data shows that some growth of the bright streaks occurred, since the peak of the histogram is shifted towards higher values of L/D. More precise comparison of individual streak lengths in the two sets of images was not possible because of scale and resolution differences. The growth of the streaks is consistent with the influx of bright material in dust storms, which would be deposited in the "shadow zone" in the lee of craters (Arvidson, 1974; Greeley et al., 1974). A plot of streak length versus width for crater streaks and knob streaks within Cerberus (Fig. 3) shows good agreement between the two, indicating that knob and crater streaks may require similar conditions for their formation.

REFERENCES

Arvidson, R. E. (1974) Wind-blown streaks, splotches, and associated craters on Mars; Statistical analysis of Mariner 9 photographs. Icarus, 21, 12-27.

Greeley, R., J. D. Iversen, J. B. Pollack, N. Udovich, and B. White (1974) Wind tunnel simulations of light and dark streaks on Mars. Science, 183, 847-849.

Scott, D. H. and J. W. Allingham (1976) Geologic map of the Elysium Quadrangle of Mars. U. S. Geol. Survey Geol. Series Map I-935 (Scale 1:5,000,000).

Singer, R. B., and T. B. McCord (1979) Mars: Large scale mixing of bright and dark materials and properties of dark material. Lunar and Planetary Science X, 1129-1130.

Veverka, J., C. Sagan, and R. Greeley (1976) Variable features on Mars, VI, An unusual crater streak in Mesogaea. Icarus, 27, 241-253.

Veverka, J., K. Cook, and J. Goguen (1978) A statistical study of crater-associated wind streaks in the north equatorial zone of Mars. Icarus, 33, 466-482.

Figure 1. Boundaries of the Cerberus albedo feature as seen in Mariner 9 and Viking Orbiter 1 images.

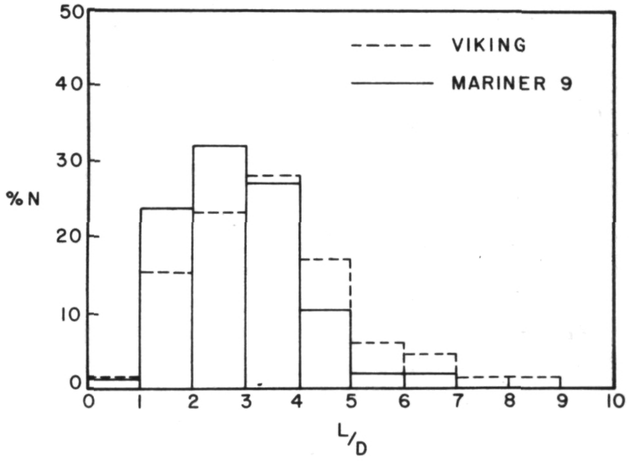

Figure 2. Distribution of streak length to crater diameter ratio (L/D) of bright streaks within Cerberus.

Figure 3. Plot of streak length versus crater diameter (or knob width measured perpendicular to streak). Streak length was measured from the downwind edge of the crater or knob.

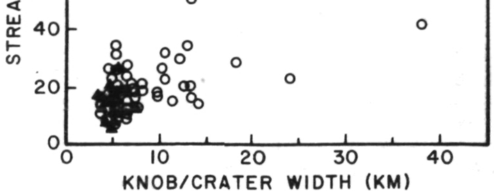

Eolian Depositional Features in the Western Desert of Egypt: Comparison with Mars.

Carol S. Breed, John F. McCauley, Maurice J. Grolier, Nanci Witbeck, U.S. Geological Survey, Flagstaff, Arizona 86001; Farouk El-Baz, National Air and Space Museum, Smithsonian Institution, Washington, D.C. 20560

In the Western Desert of Egypt, as on Mars, wind is now the dominant agent of erosion, transportation, and deposition of surficial debris. Enormous quantities of wind-eroded materials are presently in transit across the region, driven southward by the dominant northerly winds. These materials have been selectively sorted by the wind and distributed, according to grain size, into three types of surficial deposits: dunes, composed of fine-to-medium sand, "sand" plains, consisting of fine to very fine sand and coarse silt overlain by a layer of coarse sand and granules, and "streaks", consisting of elongate, thin sheets of bright coarse sand. The segregation of windblown materials into depositional forms that have distinctly different grain size populations has implications for the distribution of particles on the martian surface,such as described for the equatorial region by Kieffer and Palluconi (1978).

Most of the Western Desert consists of "sand" plains. These vast, essentially flat areas are veneered with medium-to-coarse sand and granules (∿ 0.5-4 mm) that form an armor characteristically only one grain thick. The maximum grain size is apparently graded to maximum wind velocities, such that the surface in a given area is stable in all but the strongest winds. We observed deflation of dust from the sand plain surface in 30 km/hr winds only where our vehicles disturbed the surface grains and exposed the underlying soil. Tracks of 1927 and 1938 expeditions were still visible, indicating the general long-term stability of the widespread plains surfaces.

In contrast to the intermittent, slow creep of the coarse sand or granule particles, fine-to-medium sand (∿ .06-0.5 mm) saltates readily in the ubiquitous brisk winds of the Western Desert. Through saltation, the wind segregates particles of sand size from the clays, silts, and granules and shepherds them into dunes. Dunes in the Western Desert consist almost entirely of linear (longitudinal) and crescentic (transverse) types. A few dome dunes were observed, and one incipient star dune was found in a locality (Wadi Ard el Akhdar, in the Gilf Kebir Plateau) that is subject to a trimodal wind regime. No parabolic dunes were seen (as no parabolic dunes have been seen on Viking pictures of Mars), for good reason: The Western Desert is almost as totally devoid of vegetation as Mars.

Longitudinal dunes similar to those of the Western Desert are commonly associated with the bright sand streaks shown on satellite images of terrestrial deserts, particularly in regions of high resultant drift potentials (Fryberger, 1977) such as the An Nefud of Saudi Arabia and the Western Sahara (Breed and others, in press). In the Western Desert, bright streaks shown on satellite pictures were found to consist of both belts of longitudinal dunes and elongate, thin sheets of coarse sand and granules, without bedforms.

The exact mechanism by which sand migrates along longitudinal dunes, and the roles of different wind regimes in the formation of these dunes, are controversial. The significance of the controversy lies in the use of dune patterns and other windforms for interpreting martian wind regimes (Breed and others, 1978). One of our objectives, therefore, was to observe dunes of this type in the Western Desert, where wind regimes are better documented than in most deserts, and where vegetation is absent. At several localities east of the Gilf Kebir Plateau we observed longitudinal dunes that had formed in the lee of the hills, and east of Bahariya Oasis we examined in some detail a kilometer size longitudinal dune that is part of the Ghorabi dune belt. Trenches were dug to examine the internal bedding relationships of this dune, and sand samples were taken for grain size analyses. These observations will, in combination with wind records and analyses of field relationships, provide evidence of the mechanisms by which the dune, and others like it, have grown. This investigation should prove useful in the interpretation of wind regimes on Mars, where some longitudinal dunes occur within the north polar erg, for example, in the Chasma Boreale region.

We observed dome dunes, which resemble incipient barchans but are round, without slipfaces, at the downwind ends of several of the longitudinal lee dunes in the Western Desert. In the southwestern United States, dome dunes are known to occur in zones of highest wind energy, but in those instances the domes are located at the upwind ends of barchan dune fields. In the Western Desert, dome dunes may mark the zones of highest wind energy in which dune forms can be maintained; in other words, the margin of the sheltered lee zone, beyond which saltating sand is swept out of the area. At least one of the dome dunes in the Western Desert is migrating at a very fast rate - 20 m in eight years - more than twice as fast as a longitudinal lee dune measured at Bagnold's 1938 Gilf Kebir camp.

Where the great belts of longitudinal dunes in the Western Desert cross escarpments and spill into basins they commonly break up into fields of crescentic dunes. In the Kharga Depression, sand from the Ghard Abu Moharik longitudinal dune belt is redistributed into fields of barchans and barchanoid ridges. The Kharga barchans are noted for their rapid rates of migration. Small dunes move as rapidly as 100 m/yr (Embabi, in El-Baz, in press); they may reconstitute themselves several times per year. Numerous workers have shown that rates of movement of barchan dunes are inversely proportional to their height (Finkel, 1959). Wilson (1971) has calculated that the time required for a medium-sized dune (1 km^2) to reconstitute itself (that is, to travel one dune-length downwind) in the Northern Sahara is on the order of thousands of years. By analogy, the large (< 1 km^2) barchan dunes in the circumpolar erg on Mars must have required considerable time to migrate to their present positions. They are surely not the seasonal redistribution products of the layered terrain. At least one large dune at about 71°N lat., 50° long. shows evidence of a collison feature similar to one reported from Peru, (Grolier et al., 1974), indicating variable rates of movement among these dunes when they were active. The dunes in the north circumpolar erg of Mars, and the desert floor on which they lie, are seasonally subjected to snow and vapor deposition and sublimation of ice, and to winds strong enough to blow the snow into sheltered zones in the lee of the dunes. However, the dunes may be stabilized and considered seasonally inactive with respect to eolian sand transport and dune displacement.

Sand is migrating out of the open southern end of the Kharga Depression, in the form of barchan chains. Thus the crescentic dunes there are not truly "sand-trapping" dunes (Wilson, 1971) and have not grown to massive proportions. Crescentic dunes trapped in closed basins in other deserts commonly grow to great size and accumulate sand to depths of 300 m or more. Patterns of large-scale crescentic ridges are common to basins such as the Murzuk Basin (Libya), the Tarim Basin (China), the eastern Rub al Khali (Saudi Arabia and Oman) and parts of the Great Eastern and Western Ergs (Tunisia and Algeria). Similar patterns are found in parts of the north circumpolar erg and in crater floor dune fields on Mars. The marked uniformity of these dune patterns on both planets suggests that winds of consistent direction and strength blew over these areas for long periods of time. The development of such "mature erg bodies" (Wilson, 1971) on Earth is estimated to require time on the order of 10^6 years or more.

In the Western Desert much of the sand is still migrating, in the form of through-going longitudinal dunes, from source areas in the north toward eventual sites of deposition in closed basins beyond the southern border of Egypt. On Mars, much of the dune-forming material seems already to have reached sites of deposition in the north circumpolar basin, in equatorial valles, and on crater floors. Many of the sites contain the massive bedforms considered by Wilson (1971) to be characteristic of "mature erg bodies." The difference between dune types and distribution patterns in the Western Desert and on Mars may reflect differences in the length of time that eolian processes have operated and/or they may reflect differences in sand supply.

In Egypt, as in many terrestrial deserts, an abundant supply of sand suitable for saltation is available in the form of quartz grains eroded from sedimentary rock outcrops and from fluvial deposits. Much of this material comes from eolian sandstones and is thus preconditioned for eolian transport. On Mars, the mechanical disintegration of basaltic rocks would not be expected to result in the production of a large supply of granular resistates of a size (∿ .16 mm) considered optimum for saltation on that planet (Greeley et al., 1977). Viking results indicate that the lander sites are sand poor (Arvidson et al., 1978). The sand supply on Mars may always have been sparse, and sand which was available may have already been largely swept from source areas into topographically restricted sites of deposition. The general absence of sand dunes and the deflated nature of much of the martian surface, given a limited supply of saltating sand, may represent a late stage of the eolian depositional processes such as those that are still ongoing in the Western Desert of Egypt.

References:

Arvidson, R., Carlston, C., Guinness, E., Jones, K., Pidek, D., Sagan, C., and Wall, S., 1978, Constraints on aeolian phenomena on Mars from analysis of Viking Lander camera data: NASA TM-78,455, p. 3-7.

Breed, C. S., 1977, Terrestrial analogs of the Hellespontus dunes, Mars: Icarus, v. 30, p. 326-340.

_____(in press), Morphology and distribution of dunes in sand seas observed by remote sensing, in McKee, E. D., (ed.), A study of global sand seas: U.S. Geological Survey Professional Paper 1052.

Breed, C. S., Ward, A. W., and McCauley, J. F., 1978, Windform patterns on Earth and on Mars: Implications for similarities of eolian processes on the two planets (abs.): NASA TM-79729, p. 228-229.

Cutts, J. A., and Smith, R. S. U., 1973, Eolian deposits and dunes on Mars: Journal of Geophysical Research, v. 78, p. 4139-4154.

El-Baz, Farouk, Haynes, Vance, Boulos, Loutfi, Issawi, Bahay, McHugh, William, Maxwell, T. A., McCauley, J. F., Breed, C. S., Embabi, N. S., Grolier, M. J., El-Etr., Hassan, Dardeer, A., Dowidar, H., Imrahim, M., Ramadan, A., and Yousif, M. (in press), Journey to the Gilf Kebir and Uweinat, Southwest Egypt, 1978: Geographical Journal.

Fryberger, S. G., 1978, Techniques for the evaluation of surface wind data in terms of eolian sand drift: U.S. Geological Survey Open-File Report 78-405, 25 p.

____(in press), Dune types and wind regimes, in McKee, E. D., (ed.), A global study of sand seas: U.S. Geological Survey Professional Paper 1052.

Greeley, Ronald, Pollack, J. B., Iversen, J. D., and White, R. B., 1977, Recent results from the Martian Surface Wind Tunnel (MARSWIT): NASA TM X-3511, p. 146-147.

Kieffer, H. H., and Palluconi, F. D., 1978, Martian surface particle sizes determined by thermal mapping: NASA TM-78,455, p. 27-29.

Pitted Rocks and Other Ventifacts in the Western Desert of Egypt. John F. McCauley, Carol S. Breed, Maurice Grolier, U.S. Geological Survey, Flagstaff, Arizona 86001; Farouk El-Baz, National Air and Space Museum, Smithsonian Institution, Washington, D.C. 20560

Early Viking results, especially those from the landers, cast doubt on the efficacy of the wind in landscape development on Mars. Because of its extreme aridity and strong winds, the Western Desert of Egypt is surely the best terrestrial analog with which to test the role of wind in sculpturing the surface of Mars. Another important consideration is that the Western Desert, particularly the area between Bir Sahara and Gilf Kebir, has been little touched since abandoned by man thousands of years ago. An amazing variety of wind erosion forms occur - many of these are outside the experience of geologists who have worked in the less arid deserts (El-Baz et al., in press).

Common on the eolian peneplain that lies between Kharga and the Gilf Kebir are small, scattered, severely wind etched outcrops of the "Nubian" sandstone. Most of the Nubian rocks in this region are tough orthoquartzites covered with a veneer of dark gray desert varnish. Calcium carbonate occurs in the matrix only rarely and most rocks "ring" when broken with a hammer. Nubian rocks at small scale are etched into a fantastic array of grooves, projections and irregular shapes that are, however, almost invariably alined with the prevailing north wind. Even the talus from the many conical hills on the eolian peneplain is grooved, fluted or etched mostly along bedding planes into the prevailing wind.

Strongly resistant rocks in the process of being let down by deflation were noted near our campsite of September 29 and 25 kilometers east of Beacon Hill. These forms were given the name "beheaded sphinxes" because the heads, made up of a thin quartzite layer, have been toppled forward into the wind by undercutting of their prows. These features provide insight into how coarse lag surfaces form in certain desert environments.

Just below the notch and the archeological site in Wadi Bakht, at the Gilf Kebir Plateau, numerous wind-eroded stream cobbles abound, particularly on the surfaces of the older and slightly higher fluvial terraces. The fragile, finely etched veinlets, bedding planes and windward projections observed on these cobbles could not possibly have formed by prior wind erosion and survived later fluvial transport; they must postdate the last stages of wadi cutting.

Also of interest is the wide variation in the degree of erosion observed on artifacts at the various archeological sites visited throughout the Western Desert. As should be expected the older artifacts (Acheulian and Mousterian) were the most wind eroded - frequently fluted and polished by sandblasting. Undisturbed hearthstones of various Nubian lithologies that are Neolithic or possibly even older show flutes, pits and projections alined into the prevailing wind. The rich archeology of the Western Desert coupled with a better understanding of the geomorphic development of the Gilf Kebir may provide meaningful data on wind erosion rates as a function of a wide range of lithologies.

In terms of Viking Lander interpretations the most significant small erosion features found in the Western Desert are the pitted and fluted quartzites and basalts. Controversy has raged for generations in the geologic literature about the origin of pits and flutes on various types of rocks in the arid, semiarid and humid environments. The general consensus among most American geologists is that they are produced by solution processes and possibly enlarged or modified by wind action. Whitney (1978) has shown that small scale wind vorticity can and does produce pitted rocks with or without entrained sand particles. Solution effects on the basalts and quartzites exposed in the Western Desert of Egypt must be minimal, based on our knowledge of its present and past climate.

Some of the most interesting pitted and fluted rocks occur on the top of the Gilf Kebir in let down remnants of cap rock and even on the slabbed surfaces at the Neolithic implement site. These rocks bear a striking resemblance to many of these seen in the Viking Lander pictures. Since they consist of rock so tough that it was suitable for implement making by early man, it is doubtful that solution could have played a significant role in the development of the textures seen. Sand blasting, vorticity and deflation of the worn down particles are more logical explanations.

An even more revealing example of wind pit development was discovered along the north side of the west end of Wadi Mashi. Here the remnants of a basaltic intrusive into the Nubian form a large rounded hill. Talus fragments including blocks of columnar joint columns are extensively pitted and the surfaces on the tops of the fragments are partly filled with fine yellowish sand. Pits also occur on the sides of these fragments. At first glance one might ascribe these pits to the presence of vesicles in the basalt. When broken open, however, these rocks proved to be completely massive with only a small percentage of olivine grains to mar their internal uniformity. In the light of the small scale wind erosion forms seen elsewhere in this almost rainless desert it appears almost certain that these are wind vortex pits. Chemical weathering may have initiated the pitting process - the relative humidity is as much as 20 percent and light dews are known to occur from time to time during the night. Vorticity and the development of small eolian "pot holes" is then responsible for the enlargement of the pits and the present surface texture of these rocks.

Along the slopes of the "Black Hills", earlier in our journey to the Gilf Kebir, we encountered wind eroded alluvial fan deposits that were so similar in appearance to the views from the Viking Landers as to be startling. The sizes and shapes of the rocks were almost identical to those in the Viking scenes. Depositional tails occur in the lee of most rocks, and small moats are present to windward; larger sand drifts occur locally along with patches of sand on the tops of some of the larger rocks. Many rocks as in the Viking pictures are angular but most are pitted and to a lesser extent also fluted.

These preliminary observations in the most arid desert on Earth, where wind erosion has dominated the land for thousands and perhaps millions of years, raises the issue as to whether the terrain seen by the Viking landers is as little eroded as first reported. Dense fine-grained rocks such as basalts and even orthoquartzites can become pitted and fluted in hyperarid environments even without sand - the dust in the air is sufficient. The question as to whether the pits seen by the Viking landers are vesicles or in reality vortex pits will be addressed in a subsequent report.

References:

El-Baz, Farouk, Haynes, Vance, Boulos, Loutfi, Issawi, Bahay, McHugh, William, Maxwell, T.A., McCauley, J. F., Breed, C. S., Embabi, N. S., Grolier, M. J., El-Etr, Hassan, Dardeer, A., Dowidar, H., Imrahim, M., Ramadan, A., and Yousif, M. (in press), Journey to the Gilf Kebir and Uweinat, Southwest Egypt, 1978: Geographical Journal.

Whitney, M. I., 1978, The role of vorticity in developing lineation by wind erosion: Geological Society of America Bulletin, v. 89, p. 1-18.

Wind Tunnel Simulation Studies of Airflow Patterns Around Pitted and Fluted Ventifacts from the Western Desert of Egypt. John F. McCauley, Carol S. Breed, Maurice J. Grolier, U.S. Geological Survey, Flagstaff, Arizona 86001; M.I. Whitney, Central Michigan University, Mt. Pleasant, Michigan 48859; A. Wesley Ward, Ronald Greeley, Arizona State University, Tempe, Arizona 85281

American geologists generally attribute the various types of small pits seen on hard competent rocks in the semiarid to humid regions of the United States to the effects of solution. In the case of limestones, dolomites, calcarenites and even granites and basalts, solution undoubtedly plays an important role in the development of surface rock textures. Whitney (1978) has shown from detailed field observations and laboratory simulation studies that small scale (even to the micron size) vorticity is a significant factor in the wind erosion process. Whitney has also shown that coarse sand is not a necessary ingredient in the production of vortex pits - the dust normally entrained in the air is sufficient. Moreover, the effects of negative flow (that is flow in the direction opposite to the effective wind) in the lee of disequilibrium landforms has been underestimated or ignored completely.

In strongly directional wind regimes the positive equilibrium form is the yardang (McCauley et al., 1977). These inverted boat-like, hull forms of minimum resistance range from centimeters to tens of kilometers in size throughout many of the world's deserts. Little is known about the flow fields around natural disequilibrium forms in unidirectional wind regimes. For this reason, we conducted during March 1979 a series of wind tunnel simulation studies. Ten oriented ventifacts from the Egyptian desert were selected on the bases of form, lithology and size for study of the air flow patterns that might have given rise to the erosion observed on each specimen.

The wind tunnel of the Geology Department, Arizona State University was used for these preliminary simulation studies. A bubble generator that mixes air, helium, glycerol and soap solution was used so that the flow fields over and around our Egyptian ventifacts could be visualized. The bubble generator is superior to other wind tunnel air tracking devices such as smoke and sand because the bubbles are non-destructive, are easily photographed and studied visually as air moves over the specimens. The 3 mm bubbles produced are neutrally bouyant, quite long-lived and simulate well the behavior of small entrained grains in the air. Their behavior can be observed in action both from above and at right angles to the flow in the tunnel which for these experiments was kept between 1-2 meters per second. Detailed results of these experiments include vertical and oblique motion picture documentation.

The effects of positive and negative flow and local vorticity as predicted by Whitney (personal communication) were seen. Many of the bubbles in the airflow impact and move up the windward faces of specimens. Some actually saltate along the floor of the tunnel. Others, after passing over the specimens, are caught in negative flow, and either directly impact or spiral into individual pits on the backs of the specimens in a helical pattern. All of the vorticity around the specimens is essentially normal to individual rock surfaces. No horizontal or roller vortices were observed. Thus additional experimental verification of the main theme of Whitney's earlier work (1978) has been obtained and the pitted and grooved patterns seen on our specimens become more comprehensible in terms of negative flow and vorticity.

References:

McCauley, J. F., Grolier, M. J., and Breed, C. S., 1977, Yardangs, in Proceedings 8th Annual Geomorphology Symposium, Binghamton, New York, M. Morisawa, Ed., p. 233-269.

Whitney, M. I., 1978, The role of vorticity in developing lineation by wind erosion: Geological Society of America Bulletin, v. 89, no. 1, p. 1-18.

Yardangs of the Western Desert of Egypt. Maurice J. Grolier, John F. McCauley, Carol S. Breed, U.S. Geological Survey, Flagstaff, Arizona 86001; Farouk El-Baz, National Air and Space Museum, Smithsonian Institution, Washington, D.C. 20560

The nearly level surface of the Western Desert of Egypt is broken in places by hills, which include inselbergs, volcanic cones and yardangs. Yardangs and inselbergs are the most spectacular erosional landforms in the Western Desert. In contrast to inselbergs, which require escarpments of considerable relief for their formation, yardangs are hills or hillocks, which are streamlined by the wind. Their occurrence does not require the presence (or former presence) of an escarpment, and their world-wide distribution (McCauley and others, 1977) shows that they are restricted to the most arid deserts, where wind erosion predominates over water erosion in moulding the landscape. Yardangs are eroded in soft and hard rocks by a combination of wind and blown sand. The most obvious prerequisites for their existence are strong, unidirectional or reversing winds, and great fetch over barren but continuous rock exposures or slightly consolidated sediments. In the southern part of the Western Desert, these conditions are met on the limestone plateau between Assiut and the Kharga depression, on the floor of the Kharga depression, and wherever lacustrine or sebkha deposits occur. The critical morphological criteria in distinguishing a yardang from an inselberg are that it is streamlined, and its length greatly exceeds its width--by a ratio of 3:1 or more, whereas most inselbergs are irregular and equant.

One of the largest fields of small yardangs in easily erodible lacustrine deposits occupies the floor of the Kharga depression between Kharga and Jebl El Ghennima to the east. It is easily accessible along the paved highway leading to Assiut, a few kilometers north of Kharga. The lacustrine deposits consist of brownish sand and clays that unconformably overlie harder and older rocks. They are furrowed by wind and sand into a multitude of elongated hummocks, which are 4-5 meters high, a few meters wide, and tens of meters long (Beadnell, 1909, p. 111). The rate at which the lacustrine deposits are deflated varies from layer to layer according to slight differences in resistance to weathering and erosion. Degree of cementation, and bedding and jointing patterns are among the controlling factors of rock resistance to wind erosion. The resulting landform, as sculptured by wind, strikes the imagination and is known under a variety of highly evocative names such as mud lion, recumbent lion, sitting sphinx, and sphinx hill. The hummocks are separated by long and shallow depressions or couloirs, which bear no morphological evidence of fluvial erosion. The long axes of both hummocks and couloirs are parallel to the direction of the prevailing northerly wind. Fields of well developed mud lions also occur south of Kharga, particularly near el Ramah on the Kharga-Baris road (Embabi, 1972).

Besides wind-eroded mud lions, yardangs eroded out of the much more resistant "Nubian" sandstone also occur within the Kharga depression. They were first sighted and photographed during our flight from Cairo to Kharga, but there was no time to study them on the ground. The plateau which extends between the Kharga depression and the valley of the Nile River is underlain by limestone. This limestone was previously reported to be furrowed by the wind into a very rough surface that was called "kharafish" (Beadnell, 1909, p. 35). "Kharafish" topography as originally described consists of innumerable sharp-ridged hillocks separated by troughs which are partly buried with sand. Hillocks and troughs lie parallel to the direction of prevailing winds. This type of terrain was considered by Gautier (1935, p. 112-113) to be similar to that in western China, where yardangs were first described by Hedin (1905), but the general impression left by these early explorers was that these wind erosion forms were small-scale features. In the flights to and from Kharga, we realized that the "kharafish" topography only represents a small part of a far more extensive field of large-scale yardangs. This field of streamlined hills and intervening furrows (couloirs) is approximately 150 kms long and at least tens of kilometers wide. The innumerable hillocks reported by Beadnell (1909) are only the smaller of the yardangs which are sculptured out of the Thebes limestone of early Eocene age; countless numbers of larger yardangs, which occur either as isolated hills or in clusters, are hundreds of meters long and tens of meters high.

The irregular tops of the larger yardangs in this field are mantled by a gray-pink residual material, which resembles the terra-rossa so commonly found on limestone terrain in much of the Mediterranean region farther north. Terra-rossa extends downward into cracks and irregular cavities within the limestone. The upper part of the Thebes limestone--that part which is furrowed by the wind--is silicified, and it is unusually hard and resistant. Siliceous concretions--the "melons" of British geologists--are common erosional remnants on the wind-swept surface of the "kharafish" terrain. The chemical weathering implied by terra-rossa, silicification, and solution features such as interconnecting cavities suggests that a humid climate prevailed over the region for a long time during the Cenozoic era, prior to Quaternary or older onset of extreme aridity.

The smaller streamlined rock exposures typical of the "kharafish" terrain are intensely fluted both to windward and to leeward, and also on the side slopes. They resemble artichoke heads or the prows of heavy ships, with the stem or the prow pointing into the wind. The wind-fluted and polished crystalline limestone glistens in the sun to a height of several meters above the couloirs, which are choked with ripples of abrading sand and granules. Unlike sharp-crested keel-shaped yardangs that we have seen in other deserts, these are frequently flat-topped and retain some of the original weathered surface on the Thebes limestone. Thus, these yardangs are less mature than the sharp-crested variety, and the tops mark a surface against which the depth of wind erosion can be estimated. A detailed study of this extraordinarily large yardang field will lead to a better understanding of the extensive yardang fields seen on Mars on the recently acquired Viking Orbiter images (Ward, in press).

References:

Beadnell, H. J. L., 1909, An Egyptian Oasis (Kharga): John Murray, London, 248 p.

Embabi, N. S., 1972, The semi-playa deposits of Kharga depression, The Western Desert, Egypt: Bull. Soc. Geographie Egypte, v. 61-63, p. 73-87, 4 figs.

Gautier, E. F., and Mayhew, D. F., 1935, Sahara--the great desert: Columbia University Press, New York, 280 p.

Hedin, Sven, 1905, Journey in Central Asia 1899-1902, 2 vols.: Lithographic Inst. Gen. Staff Swedish Army, Stockholm, Sweden, 1241 p.

McCauley, J. F., Grolier, M. J., and Breed, C. S., 1977, Yardangs, in Doehring, D. O. (ed.), Geomorphology in arid regions, p. 233-269, 16 figs.: Donald O. Doehring, Fort Collins, Colorado

Ward, A. W., (in press), Yardangs on Mars: 2nd Planetology International Symposium, Pasadena, California, January 1979: Journal of Geophysical Research.

MICROSCOPIC CHARACTERISTICS OF QUARTZ SAND FROM THE ARID ENVIRONMENT OF THE GILF KEBIR, SOUTHWEST EGYPT.

Donna Prestel, Lockheed Electronics Co., Inc./Johnson Space Center, Houston, TX 77058 and Farouk El-Baz, NASM Smithsonian Institution, Washington, D.C. 20560

INTRODUCTION: The Gilf Kebir plateau lies in the southwestern desert of Egypt, nearly 1,000 km south of the Mediterranean seacoast. This part of the North African Sahara is the most arid region of the Earth, with an aridity index in excess of 200 (Henning and Flohn, 1977). The area has been compared to parts of the surface of Mars (El-Baz, 1977; El-Baz and Maxwell, 1979) because of (1) the numerous indications of past fluvial history; and (2) the present day dominance of eolian conditions.

Quartz grains were selected from sand samples from the Gilf Kebir to study their microscopic characteristics. This was done in order to determine what kinds of overgrowths develop on these grains in such an arid environment. These overgrowths change the color and therefore the reflectance characteristics of sand grains (El-Baz, 1978). This in turn affects the signature of sand accmulations in Earth-orbital photographs and Landsat images.

The Gilf Kebir plateau lies south of the Great Sand Sea. Sand from this enormous field of longitudinal dunes reaches the Gilf Kebir transported by southward moving winds. The high plateau is dissected by numerous wadis (Peel, 1939), which bear similarities to valleys in Ius Chasma on Mars (Maxwell and El-Baz, 1979). Studied sand samples are from Wadi Mashi in the north and Wadi Bakht in the southeast corner of the Southern Gilf (Peel, 1939).

The Wadi Mashi sand was collected from the floor of the valley. Thus, it is not well sorted and is mixed with numerous components from local rocks. The Wadi Bakht sample was collected from a dune that crosses the valley. The sand in the dune is relatively well-sorted and contains lesser amounts of local components.

MICROSCOPIC CHARACTERISTICS: Both samples were examined with the binocular microscope to characterize the main overgrowths and textures. Some of the features observed include: 1) an extremely thin coating or stain of reddish-brown material (probably hematite-rich) entirely covering the grains except on freshly broken surfaces; 2) small clumps of reddish-brown granules in pits; 3) a reddish-brown stain within cracks in the grain; 4) detrital oxide grains included within sand grains, probably present in pore spaces when the parent sandstone was lithified.

Fourteen grains from the Wadi Bakht sand with apparent coatings were chosen for detailed scanning electron microscope (SEM) and energy dispersive X-ray analysis (EDXA). Of these, four grains were observed directly in the SEM to examine the coating. Ten of the grains were first gently fractured under liquid freon in an agate mortar and pestle to expose the interior of the grains to allow comparison with the surface. The grains were then examined at magnifications from 200-200,000X. SEM images revealed that all of the grains had a definite coating. The interior of all of the grains examined is quartz.

The coating ranges from 2-5 micrometers in thickness (Fig. 1) is rough, irregular and slightly porous, it is composed of a variety of micrometer and sub-micrometer particles and granules. Many of these particles are obviously crystals and frequently display a hexagonal platelet morphology (Figs. 2,3). This shape is typical of hematite. Energy dispersive X-ray analyses indicates that the coating is rich in Fe and Al, and is probably composed of hematite intermixed with a clay mineral. We also found and identified by EDXA, several distinct crystals of gypsum and halite growing on the coatings. Figure 4 shows the morphology of the halite crystals.

The results of this SEM study indicate that a coating of complex mineralogy is present on the sand grains. The coating is thick enough to strongly affect if not dominate the spectral characteristics of this desert area as observed in satellite imaging and spectral data. Therefore, the effect of the presence of this coating and its mineralogy must be completely evaluated in any interpretation of these data.

REFERENCES:

El-Baz, F. (1977) Astronaut Observations from the Apollo-Soyuz mission. Smith. Stud. Air Space, Smith. Inst. Press, p. 77-80.

El-Baz, F. (1978) The Meaning of Desert Color in Earth Orbital Photographs. Photogramm. Eng. Rem. Sens., 44: 1, 69-75.

El-Baz, F. and T. A. Maxwell (1979) Eolian Landforms in Southwestern Egypt. Lunar Planet. Sci. X, p. 349-351.

Henning, D. and H. Flohn (1977) Climate aridity index map. UN Conference on Desertification, UNEP, Nairobi.

Maxwell, T. A. and F. El-Baz (1979) Fluvial Landforms in Southwestern Egypt. Lunar Planet. Sci. X, p. 786-788.

Peel, R. F. (1939) The Gilf Kebir. Geogr. Jour., 93, p. 295-307

Figure Captions:

Figure 1: A fractured sand grain, showing the well-defined contact between the coating and the unweathered quartz. (Field of view 30 micrometers.)

Figure 2: A typical photo of the Fe and Al-rich coating. Note the hexagonal platelets, a morphology typical of hematite (6 micrometers).

Figure 3: A closeup of the hexagonal platelets (1.125 micrometers).

Figure 4: A cluster of halite cubes (6 micrometers).

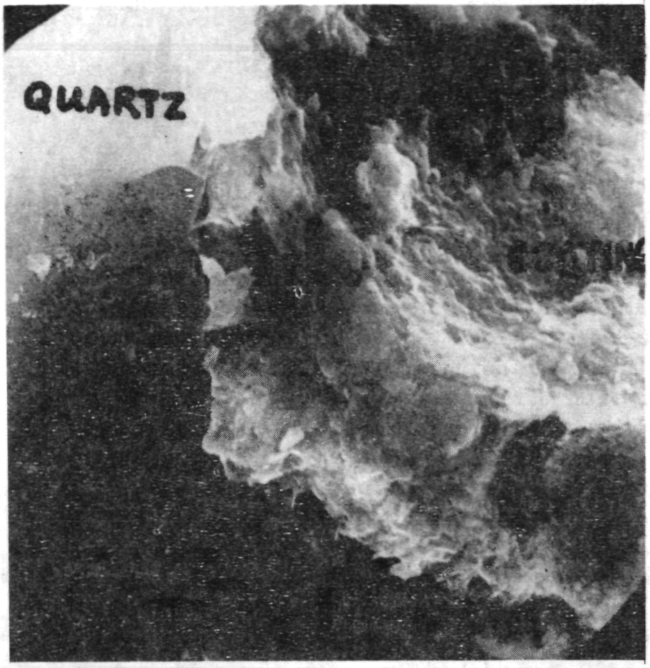

Figure 1.

Figure 2.

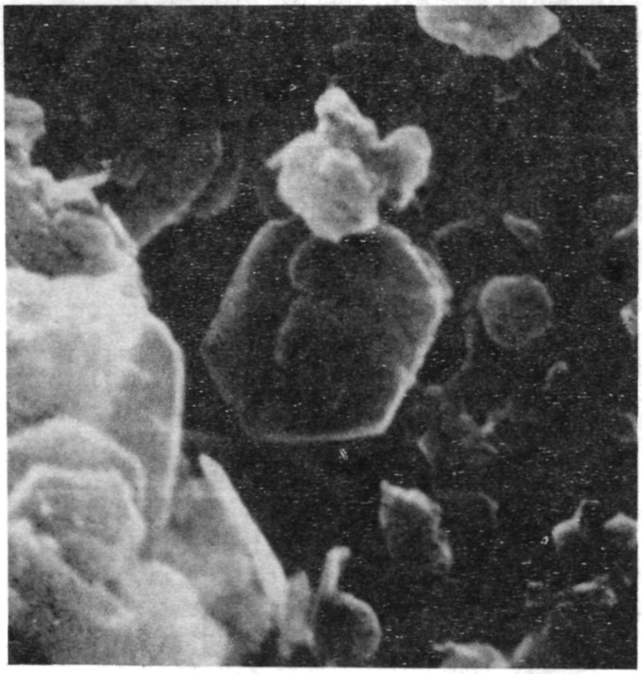

Figure 3.

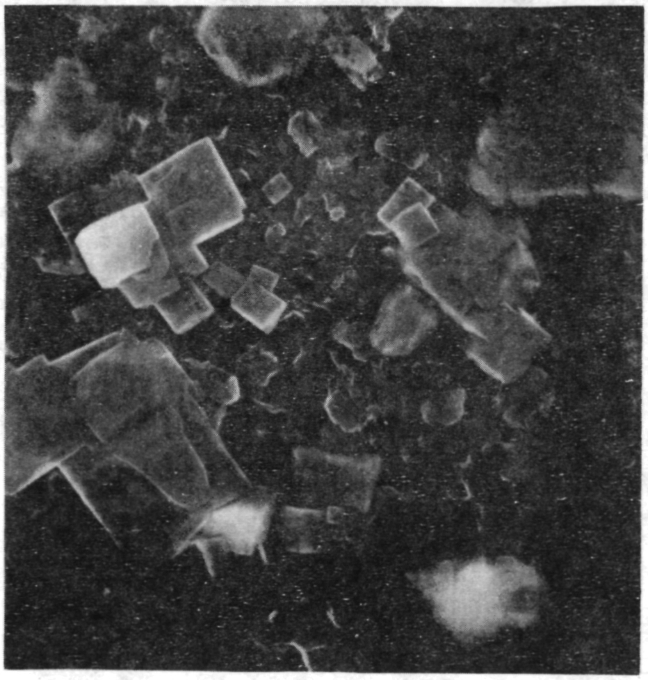

Figure 4.

WIND STREAKS IN THE SOUTHWESTERN DESERT OF EGYPT: TOPOGRAPHIC INFLUENCES AND MARTIAN ANALOGIES.

Farouk El-Baz and Ted A. Maxwell; National Air and Space Museum, Smithsonian Institution, Washington, D.C. 20560

In the southwestern part of Egypt's Western Desert, numerous circular granitic mountains and trachyte hills abound, particularly near the borders between Egypt, Libya and Sudan. The largest and most well developed of the mountains is called Uweinat, Arabic for small springs, after the many groundwater wells on its southern and western sides. As seen from orbit, eolian streaks in the Uweinat region are similar in both scale and morphology to those formed in the lee of many martian craters and knobs, particularly in the Cerberus region. Dark-colored streaks occur in the Uweinat region in the lee of nearly all topographic highs. Uweinat itself stands 1900 m above the surrounding sandy plain that is underlain by the Gilf Sandstone. Under the prevailing northerly wind, this mountain which is a complex ring dike, creates a flow pattern similar to that inferred for martian craters from terrestrial field observations and laboratory experiments (1,2). Field investigations of the northern part of the Uweinat dark streak indicate that it is formed by immature lag. The dark surface is made of irregular chips of local rock, mostly sandstone and quartzite. These chips or flakes blanket the ground and are underlain by smaller, usually lighter-colored grains.

Dark streaks occur both as individual streamlined forms, and as composite patches that emanate from groups of closely-spaced hills on the upwind end. Individual streaks range from several hundred meters to over 100 km in length (Table 1), and occur where a single hill or mountain protrudes through the surrounding sand sheet. The pattern of exposure of dark material is controlled by numerous light-colored longitudinal dunes that have migrated southward (3). Composite streaks in this region are generally much smaller, and average 9 km long. In contrast to large streaks (such as that in the lee of Uweinat), smaller ones form in response to local bedrock outcrop patterns, and are affected more by local wind directions than by the regional wind regime. For example, composite streaks north of Uweinat deviate to the east and west around the mountain (Fig. 1). As in the case of individual large streaks, light-colored sand deposits surround the dark material (local desert pavement?) of the composite streaks, resulting in an irregular pattern.

Regional topographic variations (at a horizontal scale of tens of kilometers) affect the location of light-colored sand deposits, and are therefore important to the patterns of dark streaks. Rough, elevated terrain east of Uweinat is responsible for the deviation of light-colored sand streaks away from the regional wind pattern.

Topographic influences on present-day sand distribution in this region are inherited from previous climatic regimes. The development of the present wind-dominated landscape near Uweinat may be divided into three stages: (a) alluvial fans and wadi deposits were emplaced during earlier periods of increased rainfall (ca. 7000-4000 B.C.; ref. 4); (b) Eolian modification of the alluvial sediments north of Uweinat by removal of fine-grained material and continued erosion of larger blocks; and (c) Invasion of light-colored sand and longitudinal dunes from the Great Sand Sea to the north, and deposition of this material in topographically low areas resulting in the streamlined patterns of the dark-colored streaks.

The size range of the Egyptian streaks is consistent with the size of streaks measured in the Cerberus region of Mars, although the Uweinat streak is a factor of 10 larger than the martian counterparts (Fig. 2). Preliminary study of knob streaks in this region of Mars indicates that their patterns are similar to the more numerous crater streaks, although these knobs are smaller. In addition, analysis of changes in the Cerberus region indicates that the outer boundary of dark material has changed between observations by Mariner 9 and Viking spacecraft (5). Similar to the case of the Egyptian dark streaks, the change is most likely controlled by an influx of light-colored deposits covering the upwind edges of the dark material.

References
(1) Greeley, R. et al., 1974, Science, v. 183, p. 847-849.
(2) Iverson, J. D. and R. Greeley, 1978, NASA TMX 79729, p. 222-224.
(3) El-Baz, F. and T. A. Maxwell, 1979, Lunar and Planetary Science X, LPI, Houston, p. 349-351.
(4) Haynes, C. V., 1978, NASA TM-78, 455, p. 22-23.
(5) Chaikin, A. L. et al., 1979, This volume.

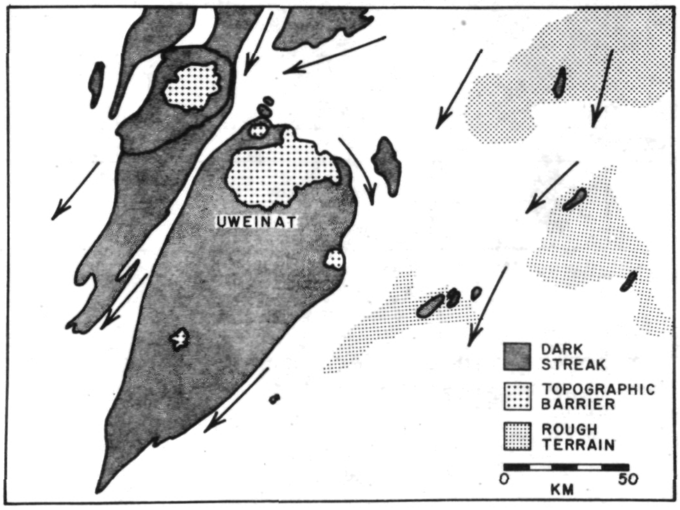

Figure 1. Sketch map of major dark streaks in Uweinat region. Arrows denote wind direction as inferred from small-scale streak patterns.

Table 1. Morphometry of dark streaks in SW Egypt

Location	Width of Topographic Barrier	Maximum Streak Width	Streak Length*	Area
Uweinat	45 km	72 km	166(130)km	7680km^2
Archenu	18	34	57(26)	1230km^2
Hager El Garda	3	5	18(16)	50km^2
Yerguehda Hill	1.5	2.5	3.5(2.0)	25km^2

*Values in parentheses are the length from downwind tip of mountain.

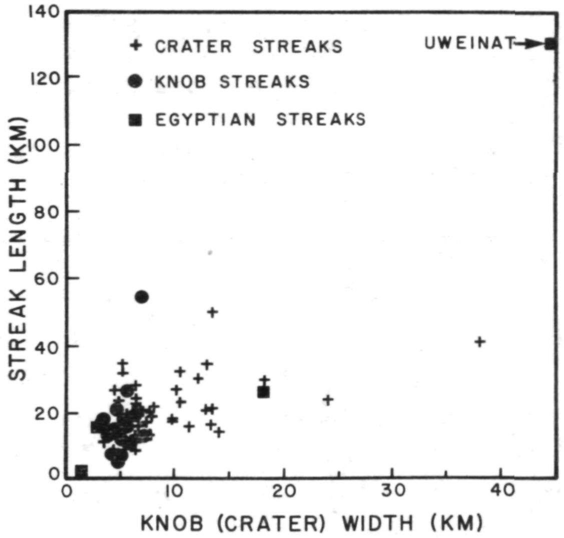

Figure 2. Streak morphometry in the Cerberus region of Mars compared to range of dark streaks near Uweinat.

THE WIND REGIME OF THE WESTERN DESERT OF EGYPT.

R. W. Wolfe and Farouk El-Baz,
National Air and Space Museum, Smithsonian Institution, Washington, D.C. 20560

This study of surface wind data was undertaken to better understand the distribution of sand in the Western Desert of Egypt and to aid in the interpretation of orientations of eolian features. Data for 21 stations were in the form of USAF N-summaries giving frequency of winds in each of 16 azimuth classes and 5 velocity classes plus the frequency of calm periods. The sand-moving potential of winds is proportional to the cube of their velocity; winds below a threhold velocity (taken as 4.6 m/s for winds measured 10 m above the ground) are not considered as sand moving. Therefore, the matrices of wind azimuth - wind velocity data were weighed appropriately to reflect the sand-moving potential of the winds. This procedure is discussed in detail by McKee et al. (1977).

The sand-moving winds are shown graphically here in two ways:

1. Sand roses (Fig. 1) - Plotted at the location of each meteorological station is the annual summary for sand-moving winds. Azimuths are the directions from which the winds blow. The lengths of "arms" of the diagrams are proportional to the products of wind frequency and the cube of wind velocity.
2. Resultants (Fig. 2) - As in figure 1, the data are plotted at the appropriate geographical locations. The arrows are the vector means of the data in figure 1 with their sizes proportional to the logarithm of resultant lengths.

Similar diagrams have also been produced for monthly summary data and these exhibit numerous interesting temporal variations in wind direction and strength. These monthly and seasonal data are presently being analyzed in detail to establish the sand-moving potential of winds at various times of the year.

Examination of sand-moving wind maps (Figs. 1 and 2) reveals two major wind regimes: a narrow band of predomiantly westerlies along the Mediterranean seacoast and generally north-northwesterlies throughout the Western Desert. Imposed upon these regional trends are local variations that may be attributed to topographic effects. An example of the effects of local topography is presented by three stations in the Western Desert: Farafra, Kharga and Aswan (Fig. 2). In all three localities there are north-south trending scarps. The Farafra meteorological stations is in the Farafra Oasis, which is bounded on the west by a north-south scarp (El-Baz, 1978). Similarly the Kharga station lies in a depression that is bounded on the east by an erosional north-south scarp (El-Baz, 1978). At Aswan the north-south topographic high is represented by the rugged and mountainous terrain of the Eastern Desert. We believe that the predominantly northerly winds at these three localities are a direct result of local topographic control by the north-south trending highs.

The distribution patterns of sand deposits in the Western Desert of Egypt has previously been established (Gifford et al., 1979). However, and as noted by Bagnold (1952), a full understanding of these patterns can only be achieved via the correlation with meteorology. For this reason our efforts are being directed toward the effects of the various winds on the movement and distribution of sand deposits.

We are extending this study to include data from neighboring countries (Libya, Sudan, and Saudi Arabia) and, if available, data with increased "resolution", i.e. more than five wind velocity classes. With this expanded data set, the techniques of trend surface analysis will be applied to isolate local variations from the regional wind patterns. The model for winds in Egypt's Western Desert will then be applied to the interpretation of observed sand distributions and orientations of eolian features, particularly in southwestern Egypt.

Acknowledgments: Our thanks to Mr. Ahmed F. M. Hassan of the Egyptian Meteorological Organization for providing the meteorological data. L. D. Cobb and M. H. Slezak helped in the various phases of computation of the data.

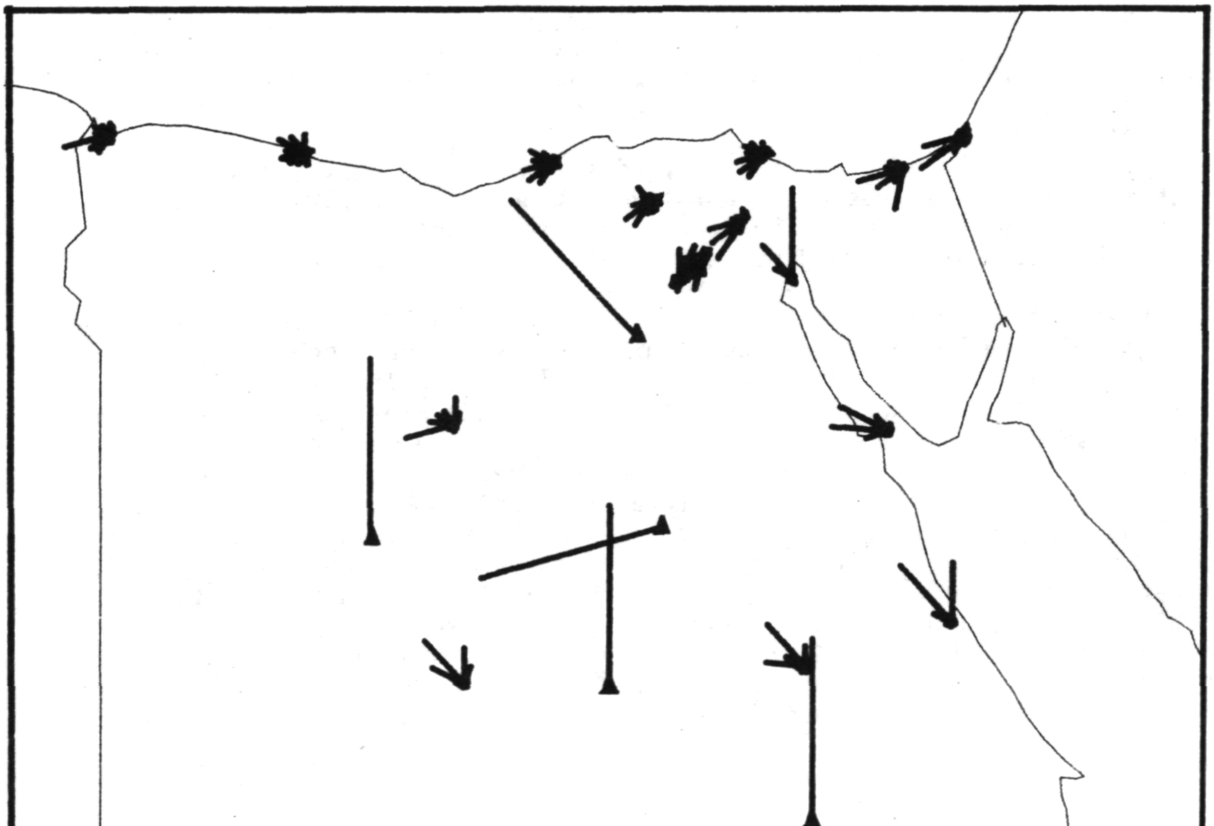

Fig. 1 Sand roses

References
Bagnold, R. A., 1952, Proc. Int. Sym. on Desert Res., p. 1-6.
El-Baz, F., 1978, Int. Applic. Sci. Tech. Desert Devel., 26p.
Gifford, A. W. et al., 1979, NASA SP-412 (in press).
McKee, E. et al., 1977, NASA SP-380, pp. 5-47.

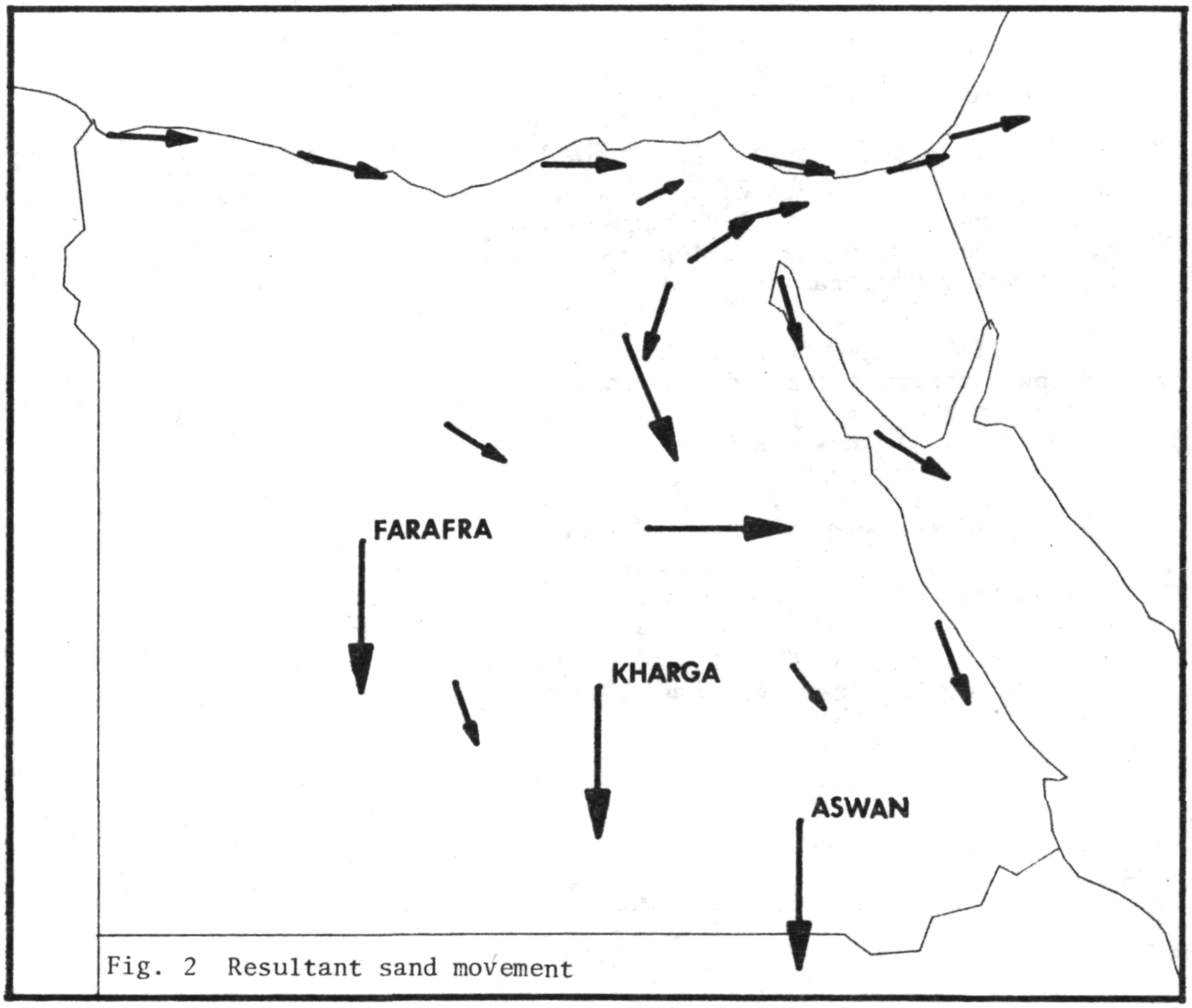

Fig. 2 Resultant sand movement

SEASONAL AND SECULAR VARIATIONS OF WIND STREAKS ON MARS.

P. Thomas and J. Veverka, Laboratory for Planetary Studies,
Cornell University, Ithaca, New York 14853.

Viking Orbiter observations over one Martian year have documented seasonal and secular behavior of several kinds of wind streaks. Most bright streaks, inferred to be accumulations of dust storm fallout in the lees of obstacles, have changed very little in form or orientation over a period of three Martian years. Some are extremely stable and have experienced no effective eolian action over three years. A few bright streaks changed rapidly during global dust storms; these streaks are located in areas subject to both global and topographic winds.

Viking images have shown for the first time that dark, erosional streaks are stable from their formation after dust storms until the onset of the next period of dust storms. These streaks form in narrow zones downwind of craters and other obstacles; changes in wind direction result in multi-lobed or fan-shaped streaks. Both local slope winds and global circulation winds are recorded by these streaks.

Large dark streaks in Oxia Palus are material deflated from dune fields in dark crater splotches. These streaks show secular lengthening since 1972, both between the Mariner 9 and Viking missions and during the Viking observations. This activity apparently occurred sporadically during southern summer.

Viking images have also shown that many dark crater splotches in low southern latitudes are erosional, and develop after dust storms in the same manner as the dark streaks mentioned above. The development of these dark crater splotches accounted for the appearance of a significant regional albedo feature in Noachis.

The major global patterns of streaks are shown schematically in Fig. 1a-1d. The great majority of all streaks are formed in the period from late southern spring to early southern fall, although some changes at all latitudes occur during all seasons. Thus the global pattern of wind streaks and the variability of streaks are strongly dependent upon the asymmetry of seasons in the northern and southern hemispheres of Mars.

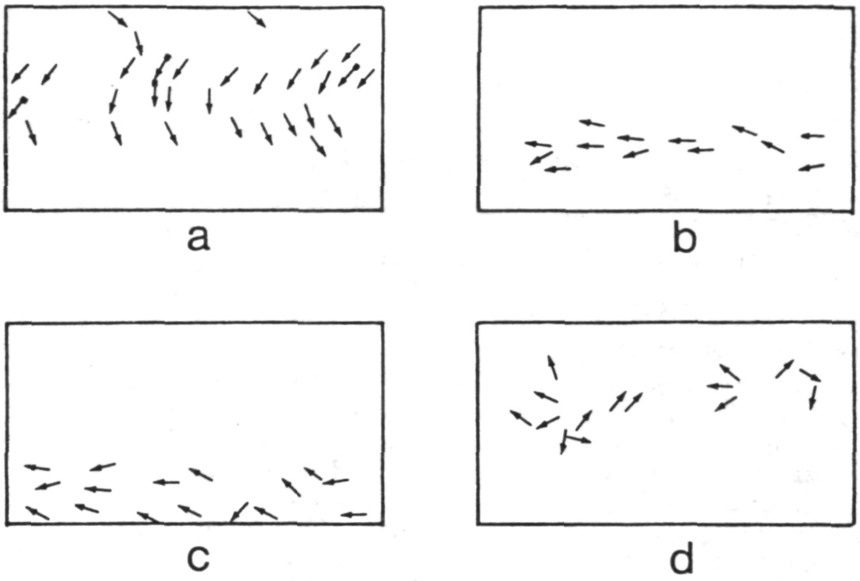

FIGURE 1. Schematic representation of major patterns of wind streaks on Mars between latitudes 65° N and 65° S.

a. Bright streaks: deposition of dust in the lees of craters in dust storm season (southern summer). ←

Dark, splotch-related streaks (southern summer pattern. ←•

b. Dark, erosional streaks developed in late southern summer, early southern fall.

c. Dark, splotch-related streaks developed in late southern spring.

d. Major topographic effects on global streak patterns (Olympus Mons, Tharsis bulge, Elysium, Syrtis Major)

"STEAM" INJECTION OF DUST ON MARS: LABORATORY SIMULATIONS

Greeley, R., Center for Meteorite Studies, Department of Geology, Arizona State University, Tempe, AZ 85281 and Leach, R., University of Santa Clara at NASA-Ames Research Center, Moffett Field, CA 95035

One of the puzzles regarding the aeolian regime on Mars concerns the mechanisms for initiation of the frequent dust storms. Estimated particle size in the dust storms is a few microns or less (Pollack *et al.*, 1977, and others); yet predictions of threshold wind speeds needed to move particles of this size on Mars are in excess of 250 m s^{-1} (Greeley *et al.*, 1976) for winds blowing across a smooth bed of uniform size particles, and it is doubtful that much, if any, dust is raised in this manner. The optimum particle size for movement by winds is about 160μm which has a much lower threshold wind friction velocity ($\sim$25 to 75 m s^{-1}); once these grains begin saltating they could be expected to set smaller grains into motion upon impact. However, even these winds seem to be rather infrequent, at least at the Viking landing sites. Thus, there may be some mechanism other than wind alone to initiate dust movement. Such a mechanism was proposed by Johnson *et al.* (1975) involving injection of dust into the atmosphere resulting from desorption in response to heating of adsorbed CO$_2$ on grains. A similar mechanism could occur involving water; Huguenin *et al.* (1979) have shown that substantial amounts of water vapor could be released to the atmosphere and have suggested that some of the "blue clouds" observed on Mars are water clouds.

We have conducted exploratory experiments in the laboratory to study the effects of water vaporization on the movement of fine-grained material. Experiments were performed in both a bell jar and in a low atmospheric pressure wind tunnel using a range of particle compositions and sizes, including: fine silt (10μm), talc (13μm), loess (20μm), quartz (23-44μm), walnut shells (61-88μm), and poorly sorted calcite grains (12-1000μm) (walnut shells having been used previously in threshold tests, see Greeley *et al.*, 1977). In bell jar tests, as the atmospheric pressure was reduced below 10 mb (temperature $\sim$24°C) adsorbed water vaporized and ejected particles by one of two processes: 1) vent holes and fissures would develop, followed by a fountainlike spray of particles as high as 20 cm above the surface, or 2) violent "eruptions" occurred in a boiling fashion (similar to the mechanism described by Johnson *et al.*, 1975). The smaller the grain size the more violent the eruption, although some activity increased with depth of particle bed, with 20 cm high activity occurring for beds 10 cm deep; some activity was also observed in beds as shallow as 1 mm. The amount of adsorbed water also affected activity, with ejection occurring with water contents as low as 0.75% by weight.

Similar effects were observed in tests conducted in the wind tunnel. However, it was noted in some experiments that the particle bed remained stable until a low velocity wind passed over the surface at which time injection was "triggered". Although there is no clear explanation for this effect, the triggering could be related to slight differences in pressure resulting from the wind.

Figure 1 shows sequential pictures of a silt bed in the wind tunnel; as the pressure was reduced, at about 10 mb the surface developed numerous irregular fissures in response to outgassing water vapor. The surface was then subjected to wind and the fissured surface began to erode as the wind picked up crust-like sections of the silt; the wind speed was $\sim$25 m s^{-1}, substantially lower than "normal" threshold for undisturbed silt. Evidently, the fissuring of the silt bed sufficiently roughened the surface to lower the threshold speed. On Mars, variations in surface temperature and pressure through the critical range for water vaporization may produce "jetting" of particles into the atmosphere, or disturb the surface to allow small particles to be set into motion by winds otherwise much too slow for "normal" threshold.

References

Greeley, R., et al. (1976) Geophys. Res. Letter, 3, 417-420.

Greeley, R., et al. (1977) NASA TM-78423, 29p.

Huguenin, R., et al. (1979) NASA Conf. Publ. 2072, 40. (and this issue).

Johnson, W., et al. (1975) Icarus 26, 441-443.

Pollack, J., et al. (1977) J. Geophys. Res., 82, 4479-4496.

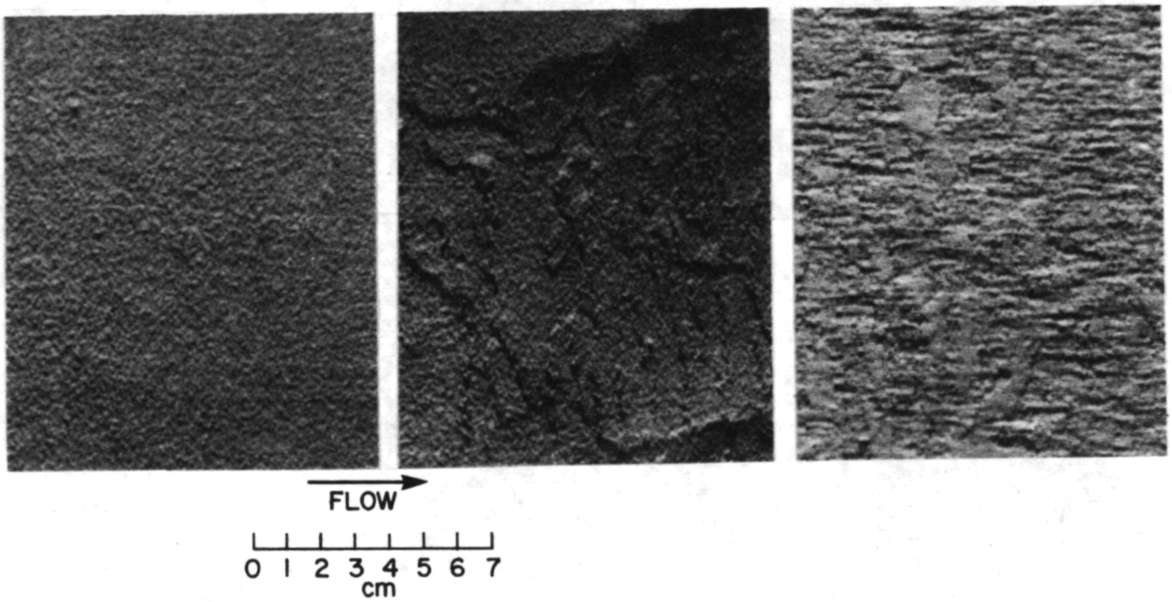

Figure 1. Series of photographs of fine silt particles in a low pressure wind tunnel; a) bed prior to experiment; b) fissured surface that occurred as atmospheric pressure in wind tunnel chamber was reduced to about 10 mb; c) surface eroded by 25 m s^{-1} wind.

Page Intentionally Left Blank

Figure 2. Sequential frames showing injection of fine grained particles as a result of water vaporiztion at about 10 mb pressure.

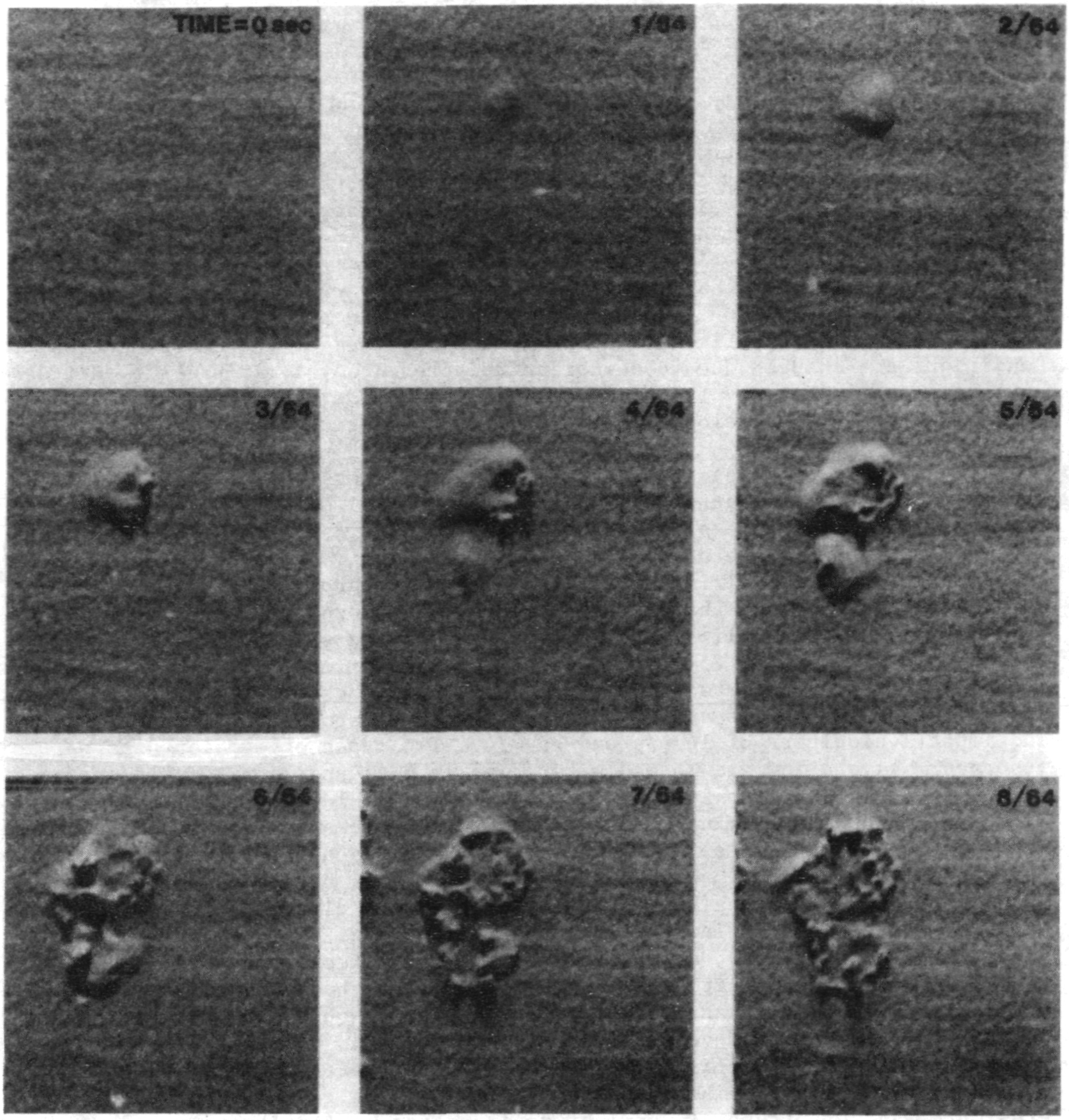

Material Removal and Production of Fines During Aeolian Erosion of Minerals: Mars and Earth

T. R. McKee and R. Greeley, Geology Department and Center for Meteorite
Studies and D. H. Krinsley, Geology Department, Arizona State University,
Tempe, AZ 85281

Aeolian erosion, or communition of rock and particle surfaces by windblown materials is an important process on Earth and certain other planets. Laboratory simulations under various conditions are being utilized in a coordinated program to study a wide range of aeolian processes from geomorphology on a megascopic scale to impact erosion on a microscopic scale. Although general concepts of aeolian erosion have been developed, the mechanisms involved in material removal at microscopic scales and subsequent production of fine-grained particulate are unknown. The value to planetary geology of an analytical impact erosion model is its capability to predict trends in aeolian erosion when the properties of the materials involved or the existing erosion conditions are changed due to new or reinterpreted data. At present there have been too few observations of impact erosion under closely controlled conditions to allow development of a complete analytical model.

In order to develop a general understanding of aeolian erosion, single and multiple impacts of fine-grained material upon rock surfaces are being studied at a range of velocities characteristic of Earth and Mars (8 - 107 m/s). Quartz is one of the most common aeolian materials on Earth and can be used as a control in a model development program; in addition, its material properties and characteristics are well known. In one portion of this study, monocrystalline quartz plates and quartz single crystals were eroded by quartz sand (125-180 μm dia.) in a slinger erosion device at known impact velocities and impact angles[1]. Individual erosion pits were produced on rhombohedral faces of quartz single crystals at about a 50° impact angle and impact velocities of 16 m/s and 75 m/s. Two types of erosion pits were observed: 1) shallow arc shaped pits (Fig. 1a,b,c) and 2) pits of complex morphology (Fig. 2). At 16 m/s shallow pits (Figs. 1a,b) with an average diameter of 15 μm predominate, whereas at 75 m/s the average pit diameter is 30 μm and deep, complex pits predominate. The ideal single impact feature for a brittle material is characterized by a central deformation zone (impact site) surrounded by a shallow network of radial and circular microcracks[2] (Fig. 3) which are modified by the impact angle (Fig. 4) such that an incomplete circle is obtained, and by the crystalline structure of the sample such that in some cases the circular outline becomes polyhedral (Fig. 1c). If the erosion pits in Fig. 1b and 1c were complete, they would both be about 45 μm in diameter, producing several flat chips 10-20 μm in diameter and 1-2 μm thick. At higher velocities, the central zone of deformation (about 10 μm) would produce a large number of clay-sized particles. The Argonne slinger erosion device unfortunately was not designed for collection of the clay-sized particles, however this capability will exist with the ASU machine. Alternately clay-sized particles produced by erosion in a paddle wheel device were studied by transmission electron microscopy (TEM) and selected area electron diffraction (SAED). Submicron particles produced by erosion at 40 m/s showed evidence of plastic deformation, exhibiting asterism in SAED patterns (Fig. 5) which was not present in the ground quartz used as starting material.

Plots of quartz erosion rates versus impact angle exhibit maxima near 90° which is characteristic of brittle fracture, whereas ductile fracture would have a maximum at about 18° (Fig. 6)[3]. The surface textures produced exhibit angular pits surrounded by irregular, offset ridges (Fig. 7, 8a). A model for removal of surface material is simply an extension of the complex erosion pits produced by interaction of several microcrack systems. Material is removed from the surface by the interaction of microcracks radiating from a network of adjacent impact sites (circles, Fig. 7) and complex, blocky or flat chips 10-30 μm in diameter are produced. At 75 m/s many of the ridge-top surfaces appear to be plastically deformed and probably represent remnant portions of the central zone of deformation of impact sites (Fig. 8a,b).

In summary, it has been shown that aeolian surface textures on quartz are produced by interaction of microcracks radiating from individual impact sites in a manner characteristic of brittle fracture. In addition, a mechanism is suggested for the production of fine silt and clay-sized material, depending upon the impact velocities involved. At characteristic earth velocities silt would probably be the dominant product whereas at martian velocities and higher earth velocities both silt and clay-sized material would be produced. At higher velocities the clay-sized material and some sand and rock surfaces would be plastically deformed, altering their bulk response to geochemical and biochemical environments.

References:
1. McKee, T. R., Greeley, R., and Krinsley, D. H., 1979, Simulated aeolian erosion of quartz: Proc. 37th Ann. Electron Microscopy Soc. of Am., p. XXX.
2. Lawn, B. R., Swain, M. V., and Phillips, K., 1975, On the mode of chipping fracture in brittle solids: J. Mat. Sci. 10:1236-1239.
3. Finnie, I., 1960, Erosion of surfaces by solid particles: Wear 3:87-103.

Acknowledgments:
Appreciation is expressed to the Mech. Prop. Group, Argonne Nat. Lab. for use of the slinger erosion device (and advice during construction of a similar device at ASU) and to A. Turner, J. Routbort, T. Kosel, R. Scattergood and L. Funk for valuable discussion. This research was supported by NASA Consortium Agreement #NCA2-OR035-801 and #NCA2-OR035-901 through the Planetary Geology Program.


1a

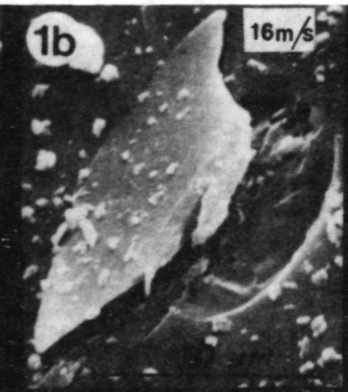
1b

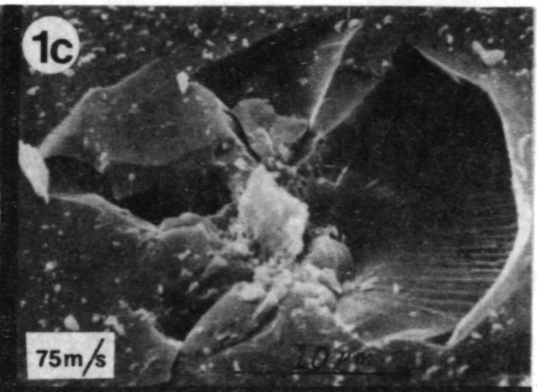
1c

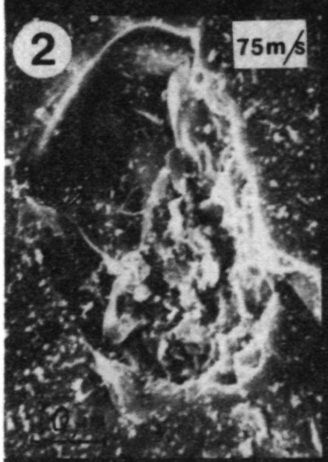
2

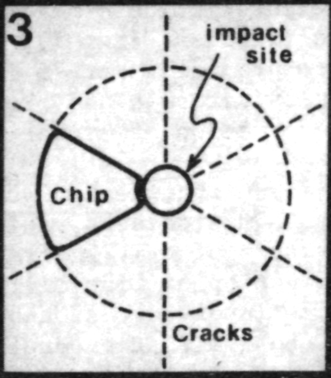
3

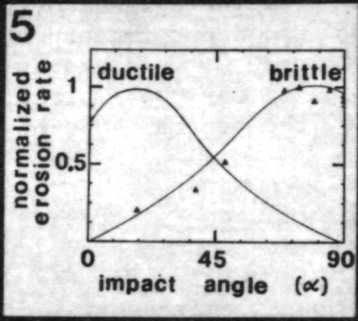
5

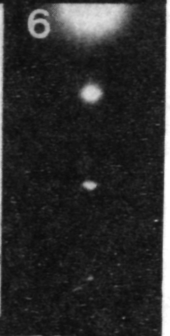
6

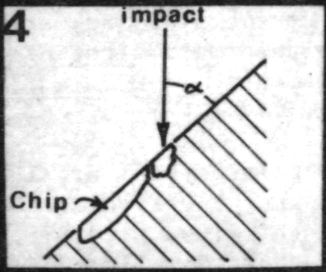
4


7


8a

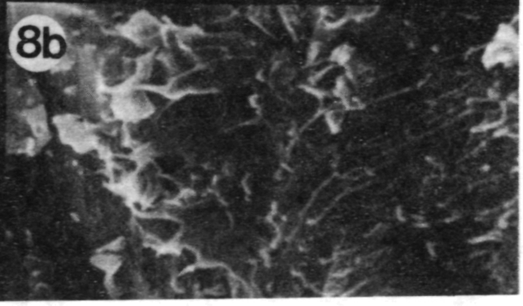
8b

Simulated Martian Aeolian Abrasion of Glassy Basalt and Augite

Krinsley, D. H., Department of Geology, Arizona State University, Tempe, AZ 85281 and
Leach, R., University of Santa Clara at NASA-Ames Research Center, Moffett Field, CA 95035

Evidence of vast amounts of aeolian activity is present on Mars; Viking orbiter photographs show large dune fields, and features characteristic of dune forms are seen at the Viking lander sites. This indicates that wind has acted on sand sized particles at some time in the past. However, various lines of evidence suggest that much of the windblown material on Mars is smaller than sand size (Toon et al., 1977; Toulmin et al., 1977; Baird et al., 1976; Huck et al., 1977; Sagan et al., 1977). Sagan et al. (1977) has calculated that the most readily moved particles on the martian surface (about 150 μm) will be preferentially destroyed by collision.

We tested this hypothesis with augite and glassy Hawaiian basalt crushed and sieved to fine sand size. These materials were placed in a paddle wheel device that self-abrades particles and simulates aeolian action at martian velocities and pressures (Krinsley, Greeley and Pollack, submitted to Icarus). Basalt samples were run for one hour at 2.4 mb and velocities of 20, 39 and 56 m sec^{-1}; augite was abraded for the same time and pressure at velocities of 8, 20 and 40 m sec $^{-1}$. It immediately became apparent that very few sand-sized particles remained in either the augite or basalt samples after abrasion at the higher velocities. In addition, scanning electron microscope examination of the silt and clay sized material indicated that many of these smaller particles were formed by breakage of sand grains that had already developed abrasion textures; the former contained rounded surfaces with abrasion textures in addition to fracture surfaces.

Size-frequency analyses of the basalt and augite were made, and as expected, rapid reduction in particle size with velocity was noted. For instance, the crushed basalt contained only 24% of material less than 100 μm in diameter whereas after abrasion at 56 m sec $^{-1}$, 93% of the material was finer than this figure. The crushed augite contained only 10% of material less than 100 μm in diameter while after abrasion at 40 m sec^{-1}, 94% of the material was less than 100 μm in diameter. The figures for the less than 62 μm size (less than the minimum sand diameter) are equally impressive. It should also be noted that at the higher velocities with both basalt and augite, numerous sand sized agglomerates formed via electrostatics.

It would thus appear that if the aeolian simulation experiments reported here are valid, the Sagan et al. (1977) hypothesis is correct, and there are very few sand particles on Mars; one would through necessity turn to a hypothesis such as Greeley's (1979) theory that electrostatic charges cause loose agglomeration of micron sized particles to form sand.

References

Baird, A. K., Toulmin, P., III, Clark, B. C., Rose, H. J., Keil, K., Christian, R. P., and Gooding, J. L. (1976) Mineralogical and petrologic implications of Viking geochemical results from Mars. Interim report, Science 194, 1288-1293.

Greeley, R. (1979) A model for the formation of windblown sand-sized particles and related structures on Mars, in NASA CF 2072, 32. and in press, J. Geophys. Res.

Huch, F. O., Arvidson, R., Jobson, B., Park, S., Patterson, W. and Wall, S. (1977) Spectrophotometric and color estimates of the Viking landing sites. J. Geophys. Res. 82, 4401-4411.

Sagan, C., Pieri, D., Fox, P., Arvidson, R. E. and Guiness, E. A. (1977) Particle motion on Mars inferred from the Viking lander cameras. J. Geophys. Res. 82, 4430-4438.

Toon, O. B., Pollack, J. B. and Sagan, C. (1977) Physical properties of the particles composing the Martian dust storm of 1971-1972. Icarus 30, 663-696.

Toulmin, P., III, Clark, B. C., Baird, A. K., Keil, K., and Rose, H. J. (1976) Preliminary results from the Viking X-ray fluorescence experiment: The first sample from Chryse Plantia, Mars. Science 194, 81-83.

Simulated Martian Aeolian Abrasion and the Creation of "Aggregates"

Krinsley, D. H., Department of Geology, Arizona State University, Tempe, AZ 85281, Leach, R., University of Santa Clara at NASA-Ames Research Center, Moffett Field, CA 95305, Greeley, R., and McKee, T. R., Department of Geology, Arizona State University, Tempe, AZ 85281

A number of workers have suggested that sand-sized particles are not present in large numbers on Mars due to the self destructing or "Kamikaze" effect postulated by Sagan (1977). Other lines of evidence indicate that this is the case (Toon et al., 1977; Toulmin et al., 1977; Baird et al., 1976; Huck et al., 1977). Greeley (1979; in press) believes that agglomerates of sand size may form via electrostatics in the thin martian atmosphere; Greeley and Leach (1978) have assessed the effect of electrostatics on aeolian processes.

During martian aeolian simulation processes using quartz, basalt (Krinsley, Greeley and Pollack, submitted to Icarus), augite and olivine, we discovered sand-sized aggregates in samples run at various wind velocities and grain sizes at ∿2mb pressure; aggregates were always present but varied in numbers and size (Fig. 1a). We looked briefly at aggregates of the first three minerals and examined olivine aggregates in detail with scanning electron microscopy (SEM). The open fabric of the aggregates makes it difficult to obtain a continuous conducting coating; thus specimen charging is a serious problem with respect to viewing in the SEM. However, high resolution photographs were obtained of small individual aggregates (Figs. 1b-1f).

Olivine from San Carlos Mine, Peridot Mesa, Arizona was crushed to between 125 and 250 μm, cleaned with acid, dried and abraded in an aeolian mode at a pressure of 2 mb for one hour at velocities of 8, 40 and 69 m sec^{-1}. At the higher velocities, the coarser sand sized particles rapidly were reduced to silt and clay (Krinsley and Leach, this volume). At all abrasion velocities, aggregates of sand size were present. Aggregate diameter ranged from less than 100 μm to about a millimeter and those formed at the higher velocities tended to be better rounded and larger. The aggregates are not mechanically cemented since they break down if disturbed or immersed in water. However, when disturbed mechanically, they rapidly reform suggesting electrostatic bonding.

Aggregates of olivine were composed of flat, elongated particles about 10 to 50 μm in diameter lying with their flat sides parallel to one another and roughly oriented in one direction (Figs. 1b,1c,1d). These particles were covered with smaller particles of about 10 μm to less than 0.1 μm (Figs. 1b-1f). The smaller particles were generally oriented perpendicular to the larger ones, and in some cases appeared to form bridges connecting and perhaps holding the latter together (Figs. 1d-1e). Particles less than about five microns were rounded, as compared to the larger sizes which were angular, and the smaller the size, the better the rounding (Figs. 1e-1f). There was also a gradation of protuberances on the larger particles ranging from slight swellings to micron sized rounded particles attached to surfaces (Figs. 1e-1f). Although rounding of small particles suggests plastic deformation and/or melting, abrasion could cause structural disruption without melting; unsatisfied charges could attract particles below microscope resolution and thus be responsible for rounding.

It appears that the smaller micron sized particles form bridges and hold the larger silt fragments together electrostatically to form aggregates. Problems that will be studied are the nature and source of the binding mechanism, the size distribution of the aggregates with respect to different mineralogies and velocities, and the question of how the presence of aggregates rather than sand could affect the formation of aeolian land forms and aeolian erosion.

References:

Baird, A. K., Toulmin, P., III, Clark, B. C., Rose, H. J., Keil, K., Christian, R. P., and Gooding, J. L. (1976) Science 194, 1288-1293.

Greeley, R. (1979) Silt-clay aggregates on Mars: A model for the formation of "sand". in press, J. Geophys. Res.

Huck, F. O., Arvidson, R., Jobson, B., Park, S., Patterson, W. and Wall, S. (1977) J. Geophys. Res. 82, 4401-4411.

Krinsley, D. H. and Leach, R. (1979) this volume.

Sagan, C., Pieri, D., Fox, P., Arvidson, R. E. and Guiness, E. A. (1977) J. Geophys. Res. 82, 4430-4438.

Toon, O. B., Pollack, J. B. and Sagan, C. (1977) Icarus 30, 663-696.

Toulmin, P., III, Clark, B. C., Baird, A. K., Keil, K., and Rose, H. J. (1976) Science 194, 81-83.

Figure Captions

1a. Aggregate formed of Hawaiian glassy basalt particles after abrasion in aeolian simulation device at 20 m sec^{-1} for 1 hour. Note that the aggregate is well rounded and is composed of silt and clay sized particles.

1b. Portion of an olivine aggregate formed at 8 m sec^{-1} in an aeolian simulation device. Note large, flat silt sized particle with rounded fine silt and clay.

1c. Same as above, except that fine particles have formed a "bridge" perpendicular to larger silt particle.

1d. Same as 1b, except that two silt particles are viewed with perpendicular "bridges" holding (?) them together.

1e. Closeup of 1d. Note rounded clay sized particles and small protrusions on some surfaces. Note "bridge" in left background.

1f. Same as 1b, except that the surface of a silt particle at higher magnification is seen. Note rounded clay sized particles which appear to "fit" into their own depressions.

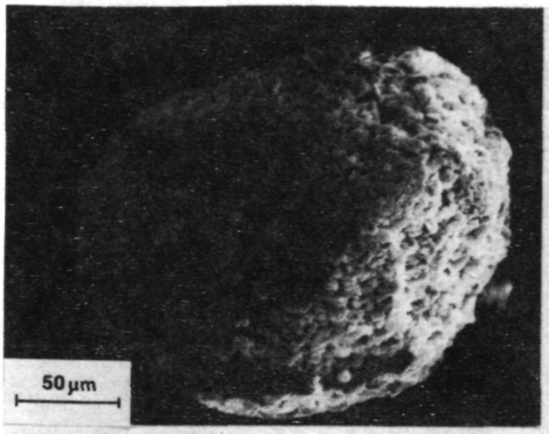

1a

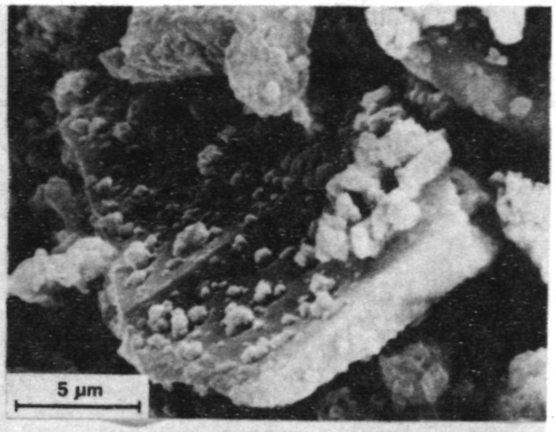

1b

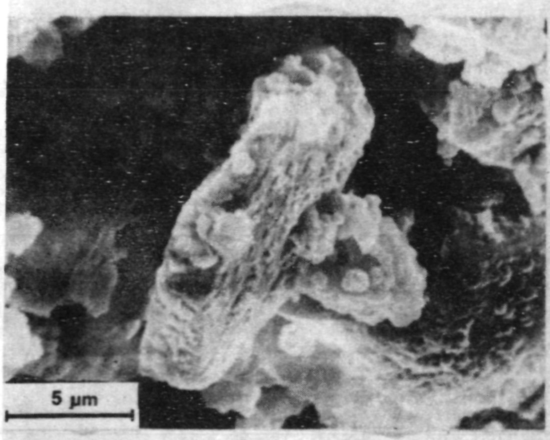

1c

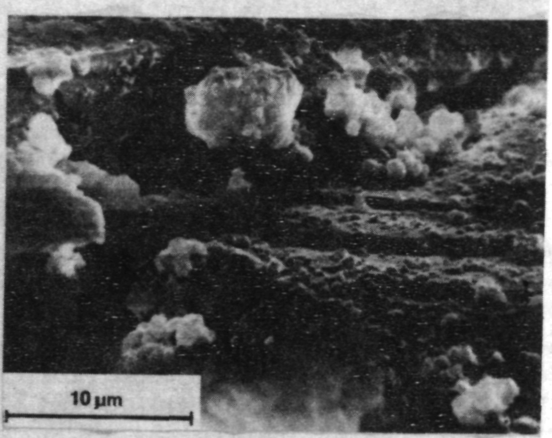

1d

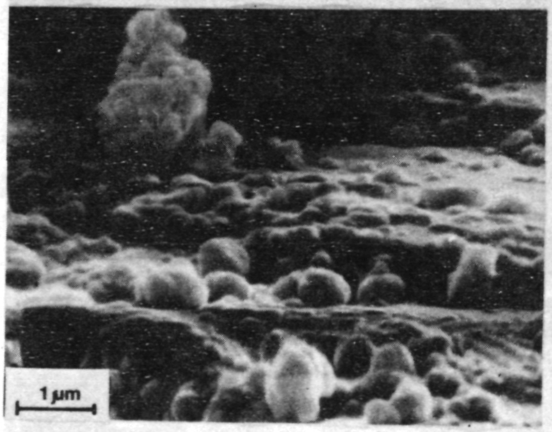

1e

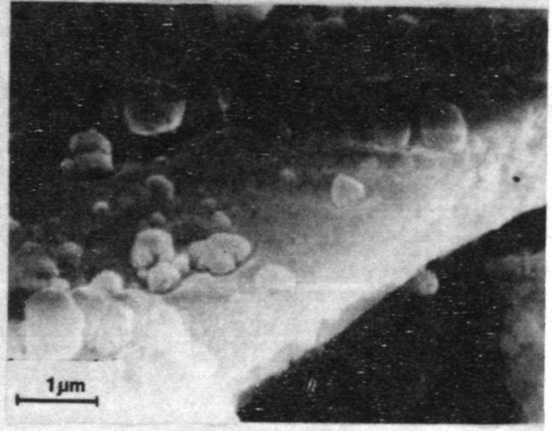

1f

WIND PATTERNS AND CYCLONE FORMATION IN THE NORTH POLAR REGION OF MARS: ANALYSES FROM SAND DUNE MORPHOLOGIES

Tsoar, H., Greeley, R., and Peterfreund, A., Department of Geology, Arizona State University, Tempe, AZ 85281

Detailed mapping (Tsoar *et al.*, 1979) of the north polar dunes based on Viking Orbiter 2 images (*Figure* 1) shows two primary dune types, *barchans* and *transverse dunes*, apparently reflecting the local supply of windblown sand (barchans form in areas of relatively limited sand; transverse dunes develop in areas of abundant sand). Dunes cover at least 5 x 10^5 km^2, making it the largest erg on Mars, with about equal areas covered by barchan and transverse dunes.

Primary and secondary patterns of near-surface winds were derived from analyses of dune morphology and related features. The *main* wind directions (Fig. 1) were based on overall dune form (e.g. barchan and transverse dune orientation), albedo streaks eminating from barchan dune horns, shadow zones in the lee of topographic obstructions such as craters, position of "frame" dunes that lag behind main dune masses, and form erosion patterns developed on the ice. Secondary wind directions were derived from patterns of asymmetrical elongation of barchan horns, analyses of the linguoid part of transverse dunes, and seasonal change in slip-face orientations.

The surface wind pattern is complex. The north polar winds during summer (L_s 132° to 169°) occur in four belts (Fig. 2): *Wind Belt A)* winds blow from the southwest, with secondary winds from the southeast; *Wind Belt B)* winds blow from the west, with secondary winds from the northwest; *Wind Belt C)* winds blow from the east, with the secondary winds predominantly from the northeast; and *Wind Belt D)* topographically controlled winds that move along valleys such as *Chasma Boreale* toward the south. The dominant winds determined from images obtained during the spring (L_s 20° to 60°) are primarily from the south and west, with no apparent winds corresponding to Wind Belt C. These winds may correspond to the maximum velocity winter winds predicted by Haberle *et al.*, (1979) that result from mass influx into the region of the condensing pole.

Several cold fronts and cyclones have been observed in the north polar region between L_s 135° and 150° (e.g. Viking images 61B33/35, 814A02, 814A21/22, 815A22, and 835A04). The cyclones occur over the major belt of transverse dunes, most of which is between two regions of perennial ice. Infrared thermal mapping (Kieffer *et al.*, 1977; F.D. Falluconi, personal communication) shows that the surface temperature contrast between the high albedo (0.45) ice and the low albedo (< 0.15) dunes is 15 K to 45 K. This large contrast results in an atmospheric surface pressure difference between the ice and dune regions that could generate ("drive") the cyclones.

References

Haberle, R.M., Leovy, C.B., and Pollack, J.B., 1979. "A numerical model of the martian polar cap winds." (submitted to Icarus).

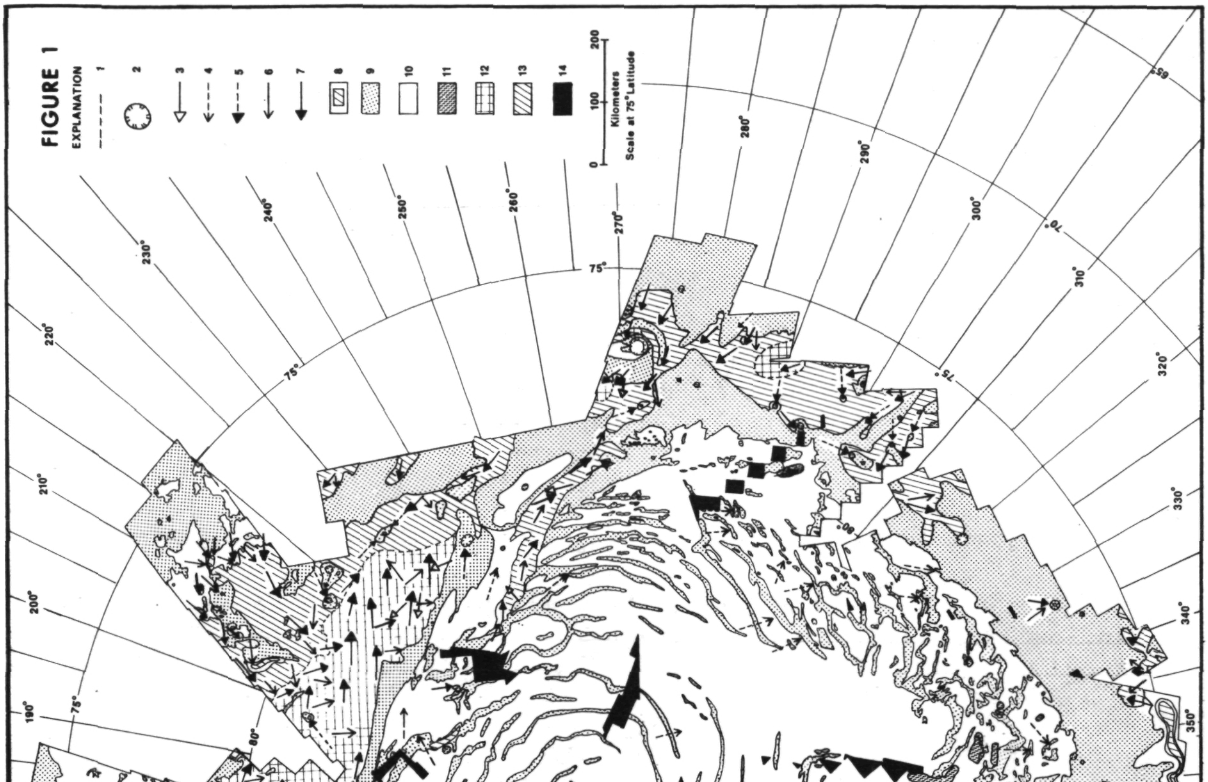

FIGURE 1

EXPLANATION
1
2
3
4
5
6
7
8
9
10
11
12
13
14
0
100
200
Kilometers
Scale at 75° Latitude
75°
80°
70°
0°
10°
20°
30°
40°
50°
60°
90°
120°
130°
140°
150°
160°
170°
180°
190°
200°
210°
220°
230°
240°
250°
260°
270°
280°
290°
300°
310°
320°
330°
340°
350°

Kieffer, H.H., Martin, T.Z., Peterfreund, A.R., Jakosky, B.M., Mines, E.D. and Palluconi, F.D., 1977. "Thermal and albedo mapping of Mars during the Viking primary mission." J. Geophys. Res., v. 82, p. 4249-4292.

Tsoar, H., Greeley, R., Peterfreund, A.R. and Squyres, S., 1979. "Mars: the north polar sand sea and related wind patterns." (submitted to J. Geophys. Res.)

Figure Captions

Fig. 1 Map showing dune distribution and wind directions (derived from dune morphology) in the north polar region. The map is based on Viking Orbiter mosaic 211-5359 from images obtained between $L_s = 132^o$ to 118^o. 1) contact between dune fields; 2) crater; 3) main wind direction determined from springtime images; 4) wind direction determined from erosion on ice; 5) wind direction based on crater lee features; 6) secondary wind direction; 7) main Summer wind direction; 8) dunes superposed on ice; 9) plains and layered deposits; 10) perennial ice cap; 11) possible ice dunes; 12) transverse dunes; 13) barchan dunes; 14) no coverage.

Fig. 2 Schematic map of the summer belts around the polar region. Arrows indicate the prevalent winds during L_s $132^o \rightarrow 169$. See text for description.

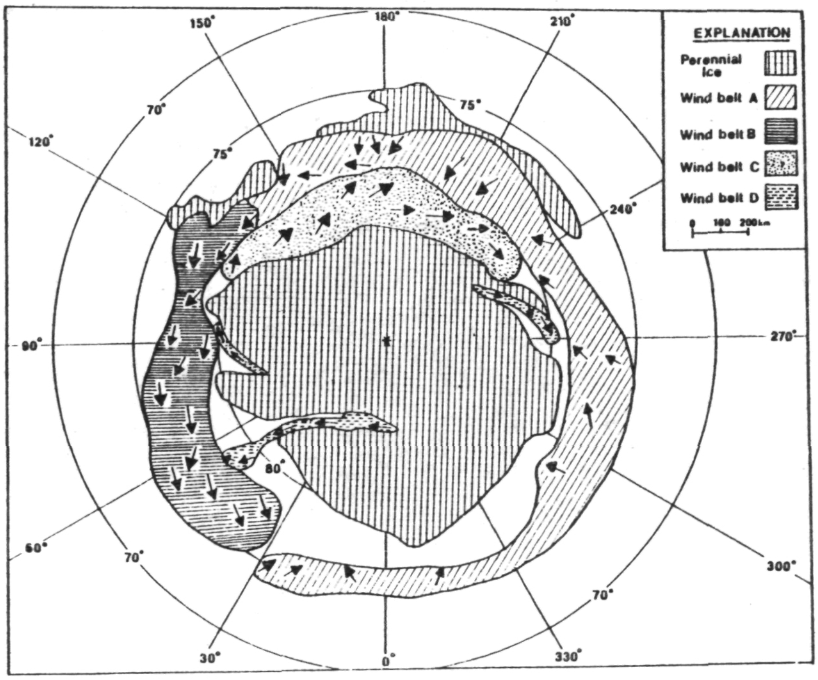

Figure 2

CALIBRATION OF THE MARSWIT TUNNEL FOR DETERMINATION OF PARTICLE THRESHOLD SPEEDS,

B. R. White, Department of Mechanical Engineering, University of California, Davis, CA 95616; R. N. Leach, University of Santa Clara, NASA-Ames Research Center, Moffett Field, CA 94035; J. D. Iversen, Department of Aerospace Engineering, Iowa State University, Ames, IA 50011; R. Greeley, Department of Geology and Center for Meteorite Studies, Arizona State University, Tempe, AZ 85218.

This abstract describes the procedure and results established in calibration of the low pressure open circuit wind tunnel (MARSWIT, described in Greeley *et al.*, 1977) for determination of threshold friction speeds. The wind-tunnel test procedure was as follows: A bed of uniform-sized particles was placed in the wind-tunnel test section and the surface was smoothed. For each test a 2.5 meter long bed of material was used, as previous tests showed (Greeley *et al.*, 1977) that a bed of this length would give very nearly the same results as an infinitely long bed whereas shorter beds resulted in increased saltation threshold values. The tunnel is located inside a large vacuum chamber which was evacuated to about 4 mb pressure using "Earth" air. The tunnel was then started and the wind speed gradually increased until saltation threshold was reached. The tunnel was stopped and started several times at each test condition to give a number of data points. Three separate methods were used to determine saltation threshold: (1) A high resolution closed-circuit television system was used to observe the particle movement directly; (2) A laser-photocell system indicated saltation by the attenuation of the signal due to particles interrupting the laser beam; and (3) An electrostatic detector measured the current produced by saltating particles impinging on the detector element. For most experiments all the systems were used concurrently to detect saltation, with the electrostatic system being more sensitive for small particles and the television and laser system more sensitive for the larger particles.

The chamber was then filled with CO_2 to a pressure of about 80 mb giving a 95 percent CO_2 and 5 percent air mixture. Threshold tests were run at various pressures as the chamber pressure was again reduced to 4 mb. Finally, the chamber was purged with air and pumped to 4 mb for the third time. Threshold speeds were again taken with air as the working fluid, as the chamber was step-filled to atmospheric pressure. With this technique it was possible to compare a particular bed of material with all conditions nearly identical except that the working fluid was changed from air to CO_2 and back to air. By comparing the initial air data with the final air data a good estimation of the repeatability of the data could be made.

The critical measurements in the wind tunnel are the differential pressure (Δp) between the total pressure (p_t) and the static pressure (p_S) at the tunnel centerline, and the chamber pressure and temperature. The tunnel centerline wind velocities can then be calculated from these measurements, as well as the friction velocity (u_*) for a given bed of materials taking into account the boundary layer profile and the surface roughness.

Time-averaged boundary layer velocity profiles were determined from differential pressure measurements between static Pitot tubes and a Pitot tube that was transversed through the boundary layer. The tests showed the boundary flow to be essentially steady, two-dimensional, constant-property (i.e., maintaining a constant chamber pressure), and to have constant free-stream velocity turbulent flow over the tunnel wall. A zero-pressure-gradient flow was achieved by increasing the roof height with increasing downstream distance (thereby expanding the cross sectional area); the zero-pressure-gradient was verified by static pressure measurements at several positions in the tunnel. A naturally turbulent boundary layer was developed for most of the flow conditions; however, at the lower pressures it was necessary to trip the boundary layer by placing small pebbles on the tunnel floor in the entrance section of the tunnel. The test section was more than 25 boundary-layer thickness-lengths from the pebbles placed upstream, insuring a fully developed turbulent core region at low pressures.

The data were reduced taking into account Mach number and slip flow effects in the velocity determination. Each profile was numerically curve fitted by means of a multi-piecewise cubic spline technique.

For the turbulent boundary layer the value of the friction speed u_* is dependent on the value of the momentum thickness Reynolds number

$$Re_\Theta = \frac{u_\infty \Theta}{\nu}$$

when u_∞ is the free-stream wind-tunnel speed, ν is the kinematic viscosity, and Θ is the momentum-deficit thickness. The momentum-deficit thickness is defined as the thickness of the layer as measured from the wall of an external stream (at constant speed u_∞) containing a momentum flux equal to the loss of momentum flux due to the presence of the wall. It is convenient to define the momentum-deficit thickness Θ in terms of mean velocity profiles as

$$\Theta = \int_0^{\delta} \left[\frac{u}{u_\infty}\right] \left(1 - \frac{u}{u_\infty}\right) dy$$

where δ is the boundary layer height at which the value of velocity u is 99 percent that of u_∞, and y is the vertical height. The momentum thicknesses were determined from integrating the resultant curve fit by a numerical quadrature technique.

An analysis of the zero-pressure-gradient turbulent boundary layer for low Reynolds numbers has been made by Coles (1962); from this work the surface shear stress τ_0 can be determined from the velocity profiles obtained in the wind tunnel. This is accomplished by assuming that the velocity obeys the logarithmic law

$$\frac{u}{u_*} = \frac{1}{\kappa} \ln \frac{u_* y}{\nu} + C,$$

for the wall region ($y/\delta < 0.2$) excluding the viscous sublayer. In this study, $\kappa = 0.418$ and $C = 5.45$, as determined by Patel (1965). Converting to $\log_{10}$ gives

$$\frac{u}{u_*} = 5.5 \log_{10} \frac{u_* y}{\nu} + 5.45$$

The ratio u_*/u_∞ is well fit by the empirical equation

$$\frac{u_*}{u_\infty} = 0.702 \left(\log_{10} Re_x\right)^{-1.59}$$

as shown by Figure 1. In this equation the relationship is presented as a function of Re_x, the Reynolds number based on the distance from the beginning of the wind tunnel to the test point. For flows with lower values of Re_Θ ($Re_\Theta < 600$) the ratio u_*/u_∞ becomes a constant value of approximately 0.049. This is the maximum value that u_*/u_∞ can obtain in a turbulent boundary layer at low Reynolds numbers (White, 1979, and Barr, 1979). For values of Re_Θ less than 425 the boundary layer flow is laminar and is of no importance in flows of saltating particles.

REFERENCES

Barr, P.K., "Calculation of friction factors for low Reynolds number turbulent boundary layer flows", M.S. Thesis, Library, University of California, Davis, California, 1979.

Coles, D.E., "The turbulent bounday layer in a compressible fluid", Rand Report 403-PR, 1962.

Greeley, R., White, B.R., Pollack, J.B., Iversen, J.D., and Leach, R.N., "Dust storms on Mars: Considerations and simulations", NASA Technical Memorandum 78423, December, 1977.

Patel, V.C., "Calibration of the Preston tube and limitations on its use in pressure gradients", Journal of Fluid Mechanics, Vol. 23, 1965, pp. 185-208.

White, B.R., "Low-Reynolds number turbulent boundary layers", ASME, Symposium on Turbulent Shear Flows, Niagara Falls, New York, June 1979.

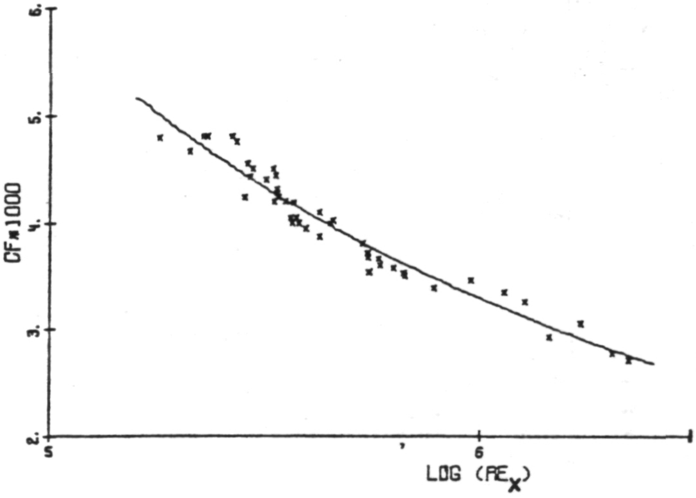

FIGURE 1 The skin-friction coefficient as function of Reynolds number Re_x.

NUMERICAL SOLUTIONS TO PARTICLE FLOW ON MARS, B. R. White, Department of Mechanical Engineering, University of California, Davis, CA 95616; R. Greeley, Department of Geology and Center for Meteorite Studies, Arizona State University, Tempe, AZ 85281; J. D. Iversen, Iowa State University, Ames, IA 50011

This abstract presents aspects of the movement of surface material by wind on Mars as determined by computer simulation. The governing equations of motion and their numerical solutions are presented in detail in White, 1979. These are discussed with applications to Mars. Results from low-pressure wind-tunnel experiments (White, 1979) are found to be in good agreement with basic characteristics of particle motion as determined by the numerical solutions. The numerical results pertain directly to Mars.

Figure 1 shows the dependence of the 'typical' pathlength of saltating particles on the particle diameter, D_p, for values of friction speed, V_*, ranging from 5 to 10 m/s. The numerically simulated surface conditions correspond to the values obtained by the *Viking* Lander I, with a mean surface pressure of 7.5 mb (0.75 kPa) and a minimum gas temperature of 187.2 K. The average heights saltating particles obtained are 4 to 5 m above the surface for a friction speed of 10 m/s. It should act as an estimate in obtaining an upper limit value of the saltating grains. A more realistic case is that of V_* equal to 2.5 and 5 m/s. The first case, near threshold conditions (not displayed on the figure), shows only minute leaps. These saltating particles have relatively high collision impact angles, α, with many of the larger particles not moving. These may be of primary importance in the final ripple pattern geometry when either a major sand storm subsides or when wind just surpasses threshold but fails to continue to grow in strength. The friction speed of 5 m/s shows saltation average maximum heights from 0.4 to 1 m. These heights of saltating grains are comparable to those found on Earth. The pathlengths are from 3 to 10 m. The particles smaller than 10 μm would, if injected into the wind by impacting collisions, likely go into suspension since their terminal falling speeds are small. This is shown by the long path lengths of smaller particle trajectories.

Impact angles of particles colliding with the surface have wide variation in values. The collision angle, α, decreases in value with increasing surface shear. A 0.15 mm particle has an impact angle of approximately 7° to 10° near threshold, and if the friction speed is increased to 5 m/s the collision angle decreases to 3.6°. Compared to Earth, these angles are unusually small for similar ratios of surface to threshold stress. The typical range of angles for particles greater than 0.4 mm is from 5° to 15° which agrees with saltation on Earth. The larger particles seldom saltate more than 6 to 10 m in pathlengths.

As the temperature is increased the maximum heights and lengths of trajectories are generally curtailed. For the majority of the cases the characteristic pathlength is substantially shorter at the higher temperature. The maximum heights occurring in saltation on Mars have only minor deviation with change in temperature. Correspondingly, there are only small differences occurring in impact angles.

The trends exhibited in the pathlength, maximum height, and impact angle for a pressure of 7.5 mb (0.75 kPa) were also calculated for other surface pressures. The pathlengths are curtailed as much as 50% with an increase in surface temperature of 100 K, with a low temperature of 150 K and a maximum of 250 K.

An examination of the final velocities the particles obtain shows increased values at the low temperatures. The final particle speeds are typically greater than V_*. The value depends on the boundary layer flow and V_*/V_g. The value of V_g would be the maximum limit that the final speed of particles could obtain.

As the particle's diameter decreases it becomes more susceptible to turbulent velocity fluctuations in the boundary layer flow. When the terminal falling speed of the particles is less than the verticle component of turbulent fluctuations the particles are in suspension. The turbulent eddies of the flow carry these particles aloft to high altitudes and are capable of transporting these particles long distances before they slowly and gradually return to the surface. This is in contrast to saltation where the height and length of particles are only a few meters in value; however, particles in suspension may be carried up to altitudes of several kilometers and be carried downstream distances of several thousand kilometers.

An analysis of the IRIS experiment on board *Mariner 9* sized the majority of suspended particles from 0.1 to 10 µm in diameter in the martian atmosphere. The boundary between suspendable and saltating particles is determined by a constant ratio of V_F/V_* where V_F is the final particle's speed in its trajectory. Toon *et al.* (1976) shows the martian planetary boundary layer can support particles with fall speeds as large as 1 cm/s (10 µm diameter particles at 0.75 kPa). The calculated V_F/V_* is several times unity for these conditions. This is at variance with Sagan and Bagnold (1975) who suggest a ratio of unity. It seems reasonable the ratio V_{F_M}/V_{F_E} will be larger than unity on Mars for equal ratios of V_*/V_{*t}, where subscripts M and E indicate Mars and Earth, respectively. From $V_*^2 = \tau/\rho$ and wind-tunnel tests at low pressures the threshold stress is about equal to that of the atmospheric case. Thus $\rho_E V_*^2/\rho_M V_{*M}^2$ is approximately equal to unity. Hence V_* is roughly seven terms greater; and comparing the ratios of V_g/V_* indicates V_F on Mars is substantially larger than V_F on Earth. These are also indicated in the numerical results; the ratio V_F/V_* is generally greater than unity for typical saltation and can go as high as 10, the latter definitely indicating particles going into suspension in numerical calculations.

In comparison with the nominal test case of 0.75 kPa, the reduction in surface pressure to 0.25 kPa results in these differences: (i) the saltating particles are roughly decreased in height and pathlength by a factor of two to four; (ii) similarly, the ratio of maximum impact speed to V_* is reduced with decreases in pressure; and, last (iii) the overall trajectory and scale of flux movement is reduced.

In summary, pathlengths of saltating particles and wavelengths of surface ripples can vary as much as a factor of two if the surface temperature varies from 150 K to 250 K. The angles between particle paths and the horizontal surface are calculated to be lower on Mars than on Earth, and particles travel much faster on Mars than on Earth. The ratio of final particle velocity to threshold friction speed, V_F/V_{*t}, is found to be several times that of saltation on Earth.

REFERENCES

Sagan, C., and R.A. Bagnold, "Fluid transport on Earth and aeolian transport on Mars," *Icarus*, 26, 209-218, 1975.

Toon, O.B., J.B. Pollack, and C. Sagan, "Physical properties of the particles composing the Martian dust storm of 1971-1972," *Icarus*, 30, 663-696, 1977.

White, B.R., "Soil transport by winds on Mars," *Journal of Geophysical Research*, in press, 1979.

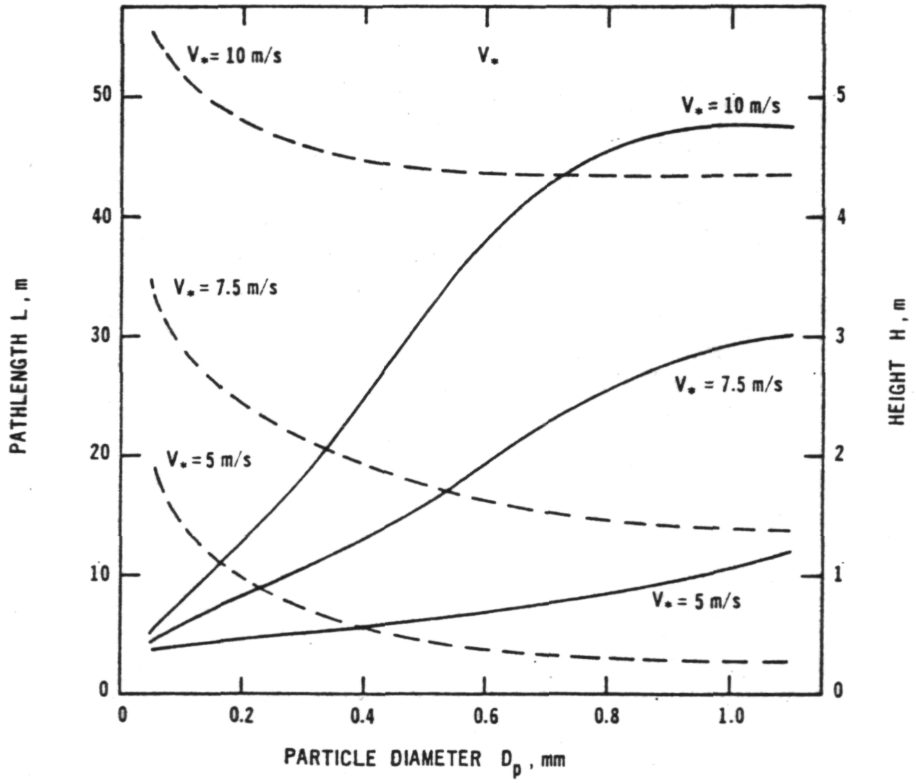

FIGURE 1 Typical pathlengths L (the ---- dashed lines) and maximum vertical heights H (the —— solid lines) for saltating particles as functions of particle diameter D_p for several values of surface friction speed V_*. The surface conditions correspond to a pressure of 7.5 mb (0.75 kPa), a particle density of 2.58 g/cm³ and a gas temperature of 187.2 K. Note the different scales for L and H.

YARDANGS ON MARS: EVIDENCE FOR RECENT WIND EROSION.

A.W. Ward, Department of Geology, Arizona State University, Tempe, Arizona 85281.

Yardangs are streamlined erosional windforms similar in form to inverted boat hulls that in terrestrial deserts range in size from meters to kilometers in length. On Mars, the best examples are seen in the low latitudes. In the Amazonis region, hundreds of wind-carved ridges and saw-tooth-edged mesas are sculpted in layered rocks. Individual ridges are tens of km long with intervening valleys nearly 1 km wide. The wind-stripped surface seems to be relatively young and, therefore, must be easily erodible. Possible lithologies include ignimbrites, mudflows, or lithified regolith. Other locations are in the Aeolis region, Ares Valles, and the Igapia region. White Rock, a light-colored plateau inside a crater, is interpreted to be a yardang cluster. The fluted unit is considered to be originally a deposit from within its host crater rather than of external origin. White Rock may be a jointed, wind-eroded pyroclastic deposit. Yardangs on Mars, especially when sculpted in young geologic units, demonstrate that much of the observed eolian erosion is recent. Yardang azimuths often are not parallel with wind streak directions, indicating that the yardangs are formed by different (older or weaker) winds than those that formed the streaks.

EXPERIMENTAL MODELING OF EROSIONAL WINDFORMS.

Ward, A.W. and R. Greeley, Department of Geology, Arizona State University, Tempe, Arizona 85281.

Experiments with natural and synthetic rock samples are underway at the atmospheric pressure wind tunnel facility at Arizona State University. These experiments are a continuation of preliminary, qualitative studies of wind erosion forms (1). Test subjects in the newer experiments include indurated samples from natural yardangs in California, as well as approximately 1/200 scale models of entire yardangs. Results and progress from these experiments are as follows:

1) Wind deflation of a yardang sample. A sample 20 cm by 12 cm by 11 cm from the crest of a yardang at Rogers Playa, Calif. (2) was studied in the wind tunnel, with wind speeds (3-15 mls) and frequencies comparable to those in the natural environment. With no particulate matter introduced into the windstream, the samples erode at an extremely low rate. However, when moistened the clays and carbonate matrix that indurate the sample are dissolved. This loosens mm-size grains near the surface of the sample and then can be removed by normal winds at a rate of 1-2 grains per minute. This seems to be a short-lived effect, for with continued wind action, the cement migrates outward from within the sample and precipitates as the moisture evaporates.

2) Morphologies of scale windforms. Because deflation of natural samples in the wind tunnel apparently requires several hundreds of hours before streamlining fully develops, models composed of sand, moist grits, corn meal, and coffe grounds are used (1). These materials can be molded to moderately indurated models, yet have loose grains that erode several times faster than natural samples. Models up to 25 cm long, 25 cm wide and 5 cm high, with initial shapes including square, rectangular, circular, and pyrmadial have been tested at low velocities (5-10 m/s). Preliminary results indicate that, regardless of the initial shape, these models are modified to a boat-shaped, equlibrated form. Furthermore, most models evolve through the sequence of a) erosion of windward corners; b) erosion of the front slope and upper surface; c) erosion of the downwind upper surface; d) erosion of the backslope; e) erosion of the flanks.

These initial experiments are designed to study the genesis of deflational windforms. Future runs will examine the effects of sand grains on large geologic samples. Also, yardang fields are recognized in various regions of Mars (2). Models of a "pristine" martian surface are currently being constructed, with the intent of producing scale wind erosion forms in the wind tunnel.

References

McCauley, J.F., A.W. Ward, C.S. Breed, M.J. Grolier, and R. Greeley, 1977, Experimental modeling of wind erosion forms, NASA TM X-3511, 150-152.

Ward, A.W., 1978, Windforms and wind trends on mars: an evaluation of martian surficial geology from Mariner 9 and Viking spacecraft television images, Ph.D. thesis, Univ. of Washington, Seattle, 201 p.

Page Intentionally Left Blank

Chapter 7

FLUVIAL PROCESSES

Some Fluvial and Glacial Features in Alaska Related to the Development of Martian Outflow channels, Jon C. Boothroyd and Lorie Dunne, Department of Geology, University of Rhode Island, Kingston, RI 02881

Processes active in glacial, periglacial, and non-glacial areas of Alaska during late Pleistocene time, and continuing today, have led to the development of landforms and landscapes that may serve as useful analogs for features found in martian outflow channels. Alaskan permafrost features as analogs for fretted and chaotic terrain have been discussed by Gatto and Anderson (1975), Sharp (1973), Sharp and Malin (1975), and Carr and Schaber (1977), and will not directly be commented on here. Features to be discussed are: 1) river bars and islands, 2) erosional remnant hills, 3) glacier-burst flood channels, and 4) ice disintergration topography. Selected locations of all of the above environments will be visited during the coming field season.

1) River bars and islands - A hierarchy of features, ranging upward in size from longitudinal braid bars (50 m in length), to incipient islands or flats, to older, complex islands (kilometers in length) has been established for the Cooper and Colville Rivers (Boothroyd and Donlon, 1978).

These islands represent depositional analogs, and have not been recognized in martian channels. Fourier analysis in closed form (Ehrlich and Weinberg, 1970), indicated that the shapes of these islands were not analogous to martian features (Boothroyd and Donlon, 1978; Donlon, 1978), but islands in rivers of higher peak discharge were analogous. Thus work continues to identify the nature of islands in the Yukon River, particularly in Yukon Flats and Yukon-Koyukuk lowland geomorphic provinces (Péwé, 1975).

2) Erosional remnant hills - Large streamlined-appearing hills are present in the Arctic Foothills province, east of the Colville River (Donlon, 1978). These hills, up to 100 km in length and 200 m above the surrounding lowland, are composed of poorly consolidated sandstones (Sagavanirktok Fm., E. Tertiary) that were left as topographic highs as downcutting occurred in the overlying Pleistocene Gubik Fm. (Payne, et al, 1951). The area is underlain by up to 300 m of permafrost; the site studied by Gatto and Anderson (1975) is about 100 km to the west. The question is: what kinds or magnitudes of flow caused the streamlining of these hills? There is ample evidence that floods of great magnitude carved similar-sized features in the Channeled Scabland (Baker, 1973; 1978; Baker and Nummedal, 1978), and even greater floods have been suggested as forming martian erosional remnants in the outflow channels (Masursky, et al, 1977). However, flood levels, channel divides, and sources of flood water (if they exist) have not yet been investigated.

3) Glacier-burst flood channels - Direct and indirect evidence for glacier-burst flooding exists for many rivers in Alaska and has been reviewed by Post and Mayo, (1971). Fahnestock and Bradley (1973) documented large (kilometers long) bars deposited by Lake George breakout floods on the Knik River (10,000 m^3 sec^{-1} peak discharge; Post and Mayo, 1971). The largest floods probably occurred on the Copper and Alsek Rivers as the result of ice damming during early Holocene to historic times (Post and Mayo, 1971). Large lakes existed in the Copper River Basin during each major event and drained down the present course of the Copper River (Ferrians and Schmoll, 1957; Nichols and Yehle, 1969). At its greatest extent, the lake covered 5000 km^2 to a

maximum depth of 450 meters. Release of this water could have carved scabland-like features along the Copper Canyon section of the drainage. No such flood-related landforms have been reported from the Copper although Kindle (1953) did report flood-related erosional terraces along the Alsek River. The importance of these possible glacier-burst channel systems is that they offer a chance to study catastrophic flooding at magnitudes less than the Channeled Scabland, but greater than peak discharge of large rivers.

4) Ice disintergration topography - This hummocky topography results from the melting of glacial ice from beneath ablation moraine and fluvial cover sediments. It occupies large areas of North Dakota (Winters, 1961; and Clayton and Moran, 1974) and also is prevalent in western Canada (Grovenor and Kupsch, 1959). Ice disintergration topography is abundant around the margins of present Alaskan glaciers, especially the Malaspina. All phases of development are presently illustrated; from debris-laden stagnant ice, to ice-free jumbled terrain. Stagnant-ice features are karst-like and somewhat similar in appearance to the thermokarst of permafrost areas (Clayton, 1966).

Even though the scale is quite different, the similarity of stagnant-ice topography to martian chaotic terrain is marked; and even more intriguing is the existence stagnant-ice topography immediately upstream of, and intermixed with, river-channel and subglacial-streamlined features around the Alaskan Piedmont glaciers. The importance of buried ice to the origin and development of martian chaotic terrain and outflow channels is that it provides a source for water greater than the volume contained in even the most ice-laden permafrost areas (ie, permafrost up to 90% by volume; Péwé, 1975).

References:

(1) Baker, V.R., 1973, Paleohydrology and sedimentation of Lake Missoula flooding in Eastern Washington: Geol. Soc. of America, Special Paper No. 144, 79 p.

(2) Baker, V.R., 1978, The Spokane flood controversy and the martian outflow channels: Science, V. 202, p. 1249-1256.

(3) Baker, V.R., and Nummedal, D., 1978, The Channeled Scabland: NASA Office of Space Science, Planetary Geology Program, Washington, DC, 186 p.

(4) Boothroyd, J.C. and Donlon, T.J., 1978, Landforms and morphology of selected terrestrial river systems: in NASA Tech. Memo. 79729, Reports of Planetary Geology Program, 1977-78, p. 254-256.

(5) Carr, M.H., 1978, Formation of martian flood features by release of water from confined aquifers: in NASA Tech. Memo. 79729, Reports of Planetary Geology Program, 1977-1978, p. 260-262.

(6) Carr, M.H., and Schaber, G.G., 1977, Martian permafrost features: Jour. Geophy. Res., v. 82, No. 28, p. 4039-4054.

(7) Clayton, L., 1966, Karst topography on stagnant glaciers: Jour. Glaciology, v. 5, p. 107-112.

(8) Clayton, L., and Moran, S.R., 1974, A glacial process-form model: <u>in</u> Coates, D.R., (ed.), Glacial geomorphology, Proceedings of 5th Ann. Geomorphology, Symposium, Binghamton, N.Y., p. 89-119.

(9) Donlon, T.J., 1978, The development of terrestrial analogs for proposed martian fluvial features: Technical report submitted for work on NASA Grant No. NSG-7414, Dept. of Geol. Univ. of Rhode Island, Kingston, RI 171 p.

(10) Ehrlich, R. and Weinberg, B., 1970, An exact method for characterization of grain shape: Jour. Sed. Petrology, v. 40, p. 205-212.

(11) Fahnestock, R.K., and Bradley, W.C.,1973, Knik and Matanuska Rivers, Alaska: a contrast in Braiding: In Morisawa, M., ed., Fluvial Geomorphology, Publications in Geomorphology, Binghamton, N.Y., p. 210-220.

(12) Ferrians, O.J., Jr., and Schmoll, H.R., 1957, Extensive proglacial, lake of Wisconsin age in the Copper River basin, Alaska (abs.): Geol. Soc. America Bull., v. 68, p. 1726.

(13) Gatto, L.W., and Anderson D.M. 1975, Alaskan thermokarst terrain and possible martian analog: Science, v. 188, p. 255-257.

(14) Gravenor, C.P. and Küpsch, W.O., 1959, Ice disintergration features in western Canada: Jour. Geology, v. 67, p. 48-64.

(15) Kindle, E.D., 1953, Dezadeash map-area, Yukon Territory: Canada Geol. Survey Mem. 268, 68 p.

(16) Masursky, H., Boyce, J.M., Dial, A.L., Schaber, G.G., and Strobell, M.E., 1977, Classification and time of formation of Martian channels based on Viking data: Jour. Geophysical Res., v. 82, no. 28, p. 4016-4038.

(17) Nichols, D.R., and Yehle, L.A., 1969, Engineering geologic map of the southeastern Copper River basin, Alaska: U.S. Geol. Survey Misc. Invest. Map I-524.

(18) Péwé, T.L., 1975, Quaternary geology of Alaska: U.S. Geol. Survey Prof. Pap. 835, 145 p.

(19) Payne, T.G., Dana, S.W., Fischer, W.A., Yuster, S.T., Krynine, P.D., Grye, G., Tappen, H., Morris, R.H., and Latham, E.H., 1951, Geologic map of the Arctic Slope of Alaska: U.S. Geol. Survey Oil and Gas Invest. Map OM-126.

(20) Post, Austin, and Mayo, L.R., 1971, Glacier dammed lakes and outburst floods in Alaska: U.S. Geol. Survey, Hydrologic Invest. Atlas HA-455.

(21) Sharp, R.P., 1973, Mars: fretted and chaotic terrain: Jour. Geophys. Res., v. 78, p. 4073-4083.

(22) Sharp, R.P., and Malin, M.C. 1975, Channels on Mars: Geol. Soc. of America Bull., v. 86, no. 5, p. 593-609.

(23) Winters, W.A., 1961, Landforms associated with stagnant ice: Prof. Geographer, v. 3, p. 19-23.

History of the Chryse Hydrographic Basin, Harold Masursky, A. L. Dial, and M. E. Strobell, U. S. Geological Survey, Flagstaff, AZ.

Photomosaics of the area included in the Chryse hydrographic basin and the surrounding upland terrain are being assembled at scale 1:2 million and a photomosaic map of the area will be compiled from the mosaics. Crater density curves have been made from recently obtained high resolution Viking photographs of the channels and interchannel areas. Tentative ages based on the crater density curves have been determined for most of the channels that debouche into the basin. A considerable variation in crater densities and therefore relative ages for the channels has been verified. A progress report will be written at the end of the funding year.

Origin of longitudinal grooving and fluting under converging channelized flow in Tiu Vallis, Mars, David E. Thompson, Jet Propulsion Laboratory, California Institute of Technology, Pasadena, CA 91103

Major longitudinal grooving and fluting appears common in several of the flood channels on Mars. Notably, a converging channel region in the Tiu Vallis complex has evidence of extensive, multiple longitudinal grooves and flutes (see fig. 1). However, these particular features are unique in that they maintain their size and spacing as the channel narrows until at a specific channel width, they vanish. The channel bed is smooth through the constriction, and the features reform downstream as the channel widens again. The discovery of this feature complex is fortuitous because it provides enormous constraints on the state of flow and type of fluid which might have created the features. Assuming a rather structured turbulence in the fluid flow, whether from a particular isolated source region or from widespread collapse or liquifaction, bedforms such as these longitudinal sets are stable or unstable according to the flow state and form of the turbulence in the fluid. The stability criterion, which indicates whether the fluid itself is receptive to growth of a structured secondary flow pattern on the scale and aspect ratio necessary to form the features, depends not only on the size and shape of the initial basal fluctuation in the flow, but also on the specific rheology or variable viscosity of the fluid. A more viscous fluid requires different flow conditions than a less viscous fluid to develop a particular secondary flow pattern: the stability criterion depends on the fluid properties. The fluid viscous properties are in turn here assumed to be dictated by the sediment concentration and distribution in the fluid. A massive liquifaction mudflow has critically different fluid viscosity and erosive capabilities than does a turbulent channelized water flood with sediment entrained in the flow, although a transition from one type to the other is theoretically possible given a suitably strong sediment entrainment mechanism. In the Tiu Vallis converging flow example, the size and spacing of the feature set is known with respect to the converging channel width, and thus the particular flow structure which must develop can be matched to particular flow conditions for particular fluid viscosities.

Stability analysis was developed which was aimed at solving the problem of the origin of longitudinal grooving in channels carved by fluids of exponentially stratified viscosity. This analysis is completely formulated including appropriate boundary conditions at the channel bed which relate the basal shear stress to the total friction velocity along the bed. The use of a representative friction velocity allows fluctuation of the shear stress with changes.or fluctuations in the fluid flow, but it is scaled according to the basal slip velocity. However, to solve the entire problem for any flow condition requires extensive numerical treatment (an analytic solution is not possible), and in fact a separate iterative solution of the problem is required for each specified viscosity or flow condition. To avoid this time-consuming method of solution, an analytic constraint on the stability equation has allowed derivation of an analytic stability criterion which itself can then be numerically evaluated for any number of flow conditions or viscosities, and the results are easily compared. The analytic constraint is one in which a hierarchy of solutions are developed according to the approximation that the solutions are restricted to very long wavelength longitudinal fluctuations in the flow which are superimposed on dominantly viscous fluids rather than on inertial ones. The perturbation scheme which arises effectively says that the viscous terms in the fluctuating fluid are of higher order importance than the strictly inertial terms which are themselves of equivalent importance to second-order viscous terms. This perturbation scheme does not imply that only slow-moving viscous fluids are being analyzed, but it does say that as far as the nature of the perturbation in the flow is concerned, the growth or decay of such a disturbance is dominantly controlled by the variable, stratified viscosity field in the fluid instead of by inertial fluctuations or momentum transport. This is actually an ideal formulation in that the original purpose of the study is to decipher the role that variable viscosity plays in determining the turbulence and erosive power of the fluid while "creating" the observed features. In addition, the derivation of an analytic stability criterion allows for much greater physical insight as to the origin of growth or decay of fluctuations as one compares differing flow conditions (channel widths, depths, velocities) and viscosities. A similar treatment can also be devised for the case of dominant inertial fluctuations in the fluid flow.

Results are presented for a model of the Tiu Vallis channel feature complex for various channel widths (thereby implicitly following the convergence and divergence of the channel), and the specific form of the viscosity distribution dictates the form of the boundary between stable and unstable flow in flow-parameter vs. feature-wavelength space. Thus for the specific size of the features observed in Tiu Vallis, the propensity towards growth or decay of such size perturbations in the fluid is directly related to the viscosity distribution. Hence the most probable viscosity distribution for a given flow state which has the potential to create the features is defined. Similarly, the change in stability or instability of the fluid with respect to a certain size perturbation (defined by the Tiu Vallis features) can be followed as channel widths and presumed fluid depths are varied during flow convergence. These results are presented graphically and selected scenarios of flow development are discussed.

Work now to be done involves relating the seemingly responsible fluid viscosities to physical analogs of sediment concentrations in order to define whether the particular viscosity distribution at a given flow condition best corresponds to a mudflow, debris flow, liquifaction slump, or viscous slurry. This refinement either requires field work on known mudflows or slurries or requires experimental or theoretical evaluation of sediment transport mechanisms under catastrophic flow conditions. In any case these studies are now constrained and directed by the analytic results.

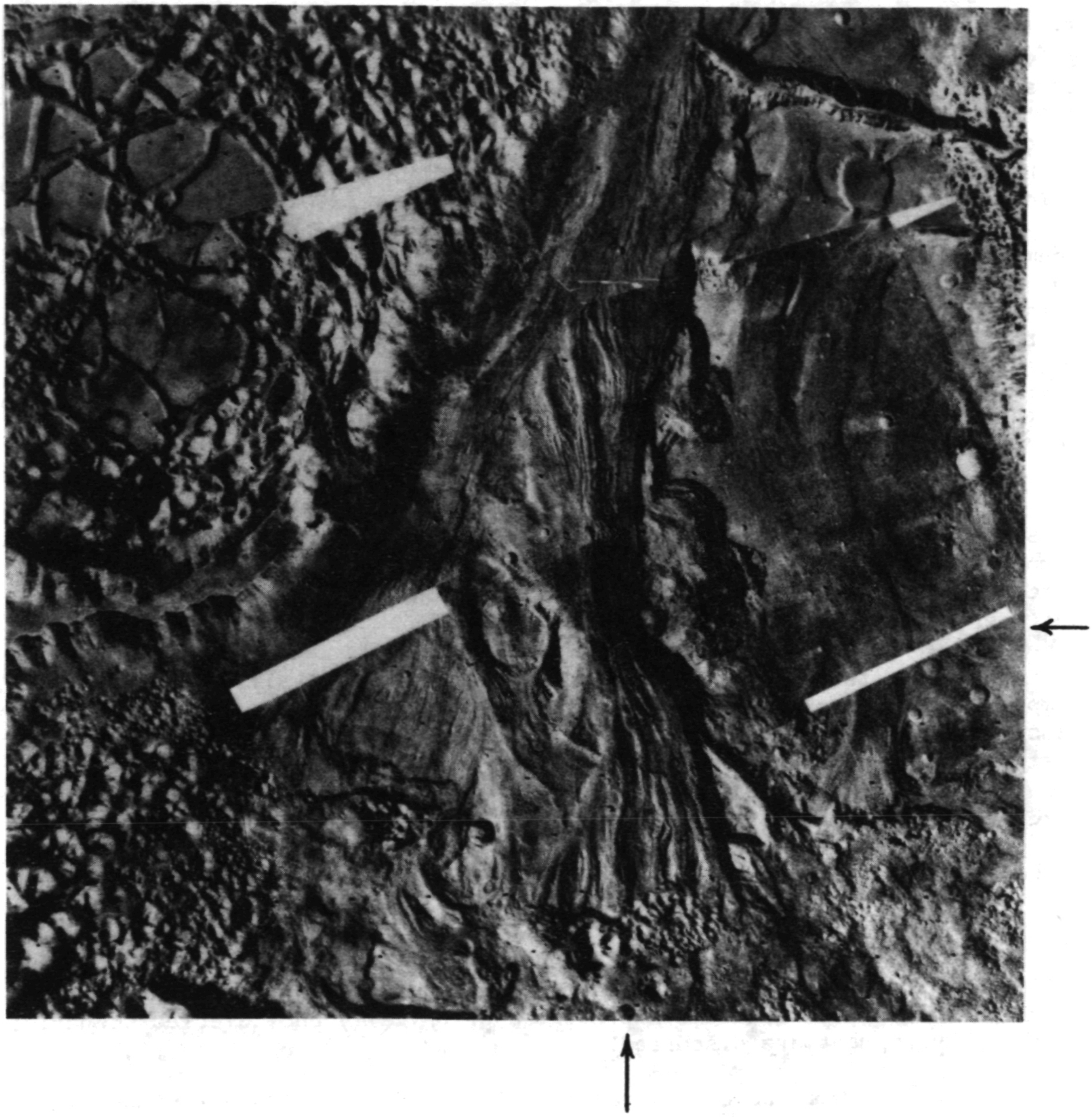

Figure 1. Viking mosaic of selected flood channel complex in Tiu Vallis. Arrows intersect at region where channel converges and longitudinal features vanish, then reform downstream. Flow direction is toward top of image. Area shown in approximately 136 km by 136 km; channel narrows to about 5 km width.

Distribution of small channels on Mars, Michael H. Carr, U.S. Geological Survey, Menlo Park, CA 94025.

A program of systematic mapping to determine the location of all martian channels by type is underway. The immediate intent is to establish a data set which will serve as a basis for further studies on channels including determination of the distribution of different channel types, their ranges in age, and their correlation with other global characteristics such as geology, elevation and albedo. The ultimate objective is to determine the mode and time of formation of different channel types and the implications concerning the outgassing history of the planet.

The channels are being mapped from Viking orbiter pictures taken within a range of 5000 to 12,000 km of the martian surface. The search is being restricted to these ranges in order to preserve some degree of consistency in resolution from location to location and in order to restrict the search to a manageable number of frames. Approximately 7000 frames are being examined and the channels mapped on the 1:5,000,000 scale MC charts. Initially, only a three-fold classification is being attempted, viz. runoff channels, outflow channels and fretted channels. A computer based data set is being prepared of the runoff channels. The length of visible channels in each 5° box between 65° N and 65° S is measured and stored by location. This then can be manipulated and correlated with other data bases. Subsequently, separate outflow and fretted data bases may be prepared.

The data base is currently in the process of preparation but some patterns are already discernible:

1. Runoff channels occur in almost all the old cratered terrain.
2. Runoff channels are absent in almost all plains equivalent to Lunae Planum in age or younger (the few exceptions may be lava channels).
3. No drop-off in runoff channel frequency toward the pole has been observed; however, measurements are so far restricted to ± 65°.
4. Channel frequency in the old cratered terrain is extremely variable. The most intensely dissected regions so far examined are the southeast quadrant of MC-19 and the central part of MC-25.
5. Several very large indistinct discontinuous channels in the old craters, such as Labon Vallis, suggest very ancient fluvial activity, which pre-dates the decline of the early, very high, impact rates.

Geomorphic Mapping of Martian Outflow Channels.

R. Craig Kochel and Victor R. Baker, Department of Geological Sciences, The University of Texas at Austin, Austin, Texas 78712.

Detailed geomorphic mapping from Viking imagery of selected portions of Kasei Vallis, Maja Vallis, and vicinity reveals numerous similarities of outflow channel morphology to erosional and depositional features of the Channeled Scabland. The entire erosional assemblage is well illustrated by our map of the Maja Vallis canyon through the upland of hilly and cratered terrain that separates the Lunae Planum from the Chryse Planitia (Figures 1 and 2). The prechanneling terrains ("antediluvian") include plateau areas of the Lunae Planum (PL) and the hilly and cratered terrain (HC) bordering the western Chryse Planitia. The channeled terrains (CHg) in the western Chryse Planitia comprise an overall anastomosing pattern, often with a distinct trimline that separates the channeled region from the unmodified plains. Further upstream, in the hilly, cratered terrain the channels are narrowly constricted, deeply-incised, and exhibit evidence of differential erosive stripping of the rock units. The "diluvian" erosional assemblage includes longitudinal grooves, streamlined uplands and hills (SH), inner channels with erosional headcuts (IC), terrace-like benches (T), and scabland (S). Some streamlined forms in the lee of flow obstacles have been tentatively mapped as pendant bars (B) of fluid-transported sediment. Diamond-shapped high albedo features on the floors of some channels at expansion sites may provide additional evidence for the preservation of depositional landforms. Craters in Maja and Kasei Vallis exhibit a wide range of morphologies suggesting varying states of degradation due to both age and modification by channeling processes. Older craters (C_1) usually display smooth floors and incomplete rims. Craters with smooth rims that are partly incomplete because of probable degradation or burial are designated "C_2" if they likewise show no interaction with channel-forming fluids. Craters showing both fresh-appearing morphology and distinct raised rims, also not interacting with channeling processes, are labelled "C_3". The latter are interpreted to be relatively young craters that have not been modified by catastrophic flood flows. Their common superimposition on channel forms indicates "postdiluvian" impact events. Craters mapped with the prefix "P" (PC_1, PC_2, PC_3) display clear evidence of interaction with the channeling process. Since craters of variable apparent ages have been modified by the channeling process, this designation is necessary to separate those involved with flood erosion from whose which have not been affected. In order to reduce clutter on the geomorphic maps, many small craters (less than than 1-2 km diameter) have not been labelled. Most unlabelled craters appear to be relatively young (C_3).

"Antediluvian" features in the outflow channels include a variety mass wastage forms. Talus accumulations are best developed along the steepest cliffs. Mass wastage probably contributes to postdiluvian backwasting and parallel scarp retreat. Debris resulting from these processes often exhibits definite lobate patterns in some areas and is mapped as debris fan deposits (F) when the responsible fan-head gullies can be recognized. Slump blocks can be seen at various locations in Kasei Vallis but are most abundant in chaotic terrian regions (CHT). Landslide-like features are scarce in Maja Vallis. We speculate that steep escarpments exposed by tectonic influences and subsequent channel incision became the sites of long-term backwearing by mass wasting and sapping. Periglacial thermokarst processes probably played a significant role in this backwasting.

	Description	Interpretation
PL	Plateau material as typical of the Lunae Planum.	Basaltic lava flows underlain by less consolidated material, perhaps sediments, impact debris, palagonite, or volcanic ash.
HC	Hilly and cratered region, heavily cratered.	Probably predates large-scale outflow events.
CHg →	Channels and inferred flow direction.	Approximate direction of catastrophic flood flow across this surface.
≡	Dark-appearing lineations that parallel the inferred flow directions.	Longitudinal grooves eroded parallel to flood flows by large roller vortices (macroturbulence).
IC	Inner channel headcuts.	Headwardly-eroding inner channel cataracts developed during flooding.
S	Etched zones in which the upper 25-75m of channel floor has been stripped away.	Erosive plucking by macroturbulent flood flows produced butte-and-basin scabland.
SH	Streamlined hills and uplands. Prows point upstream, and downstream ends have tapering tails.	Erosional remnants, often downstream from flow obstructures, whose streamlined shape results from high velocity fluvial activity.
T	Terrace-like benches along edges of streamlined hills and plateaus.	Lithologic units of varying resistance to plucking erosion that have been differentially stripped by catastrophic flood flows.
B	Bars ?	Possible accumulation of flood debris downstream from flow obstructions.
▲	Talus accumulations.	Blocky talus piles resulting from back wasting.
F	Fans, often possessing radiating flow lines and a lobate front.	Portions of the talus slopes that have flowed across adjacent channel floor.
▨	Slumps.	Rotational Landslides.
CHT	Chaotic terrain.	Zones of collapse resulting from melted ground ice and/or fluid release.
A	Light-appearing zones developed behind craters.	Eolian deposits.
┅	Lineations oblique to inferred flow direction.	Joints, faults, and other bedrock structures accentuated by erosion.
⫽	Mare-like ridges.	Wrinkle ridges, many of which have interacted with channeling processes.
R	Sinuous depressions oblique to inferred flow direction.	Rilles or downfaulted areas.
C_1	Crater with poorly preserved rim morphology.	Crater rim is highly degraded and partly buried but not modified by catastrophic flood processes.
PC_1	Crater with poorly preserved rim morphology that has interacted with channeling processes.	Highly modified pre-flood crater that was modified by catastrophic flood flows.
C_2	Crater with raised rim that has not interacted with channeling processes.	The rim is commonly incomplete and the crater highly degraded. Antediluvian crater.
PC_2	Crater with raised rim that has interacted with channeling processes.	Impact crater that created a flow obstacle or was modified by catastrophic flood flows.
C_3	Crater with distinct, raised rim and fresh-appearing morphology.	Relatively young crater, probably postdiluvian.
○	Crater rims and hummocky zones with lobate raised margins.	Crater ejecta, partially deposited by fluid debris flows released when meteors impacted the Martian cryolithosphere.

All the mapped craters are C_3 unless otherwise noted.

Figure 1. Legend for geomorphic maps of Martian outflow channels.

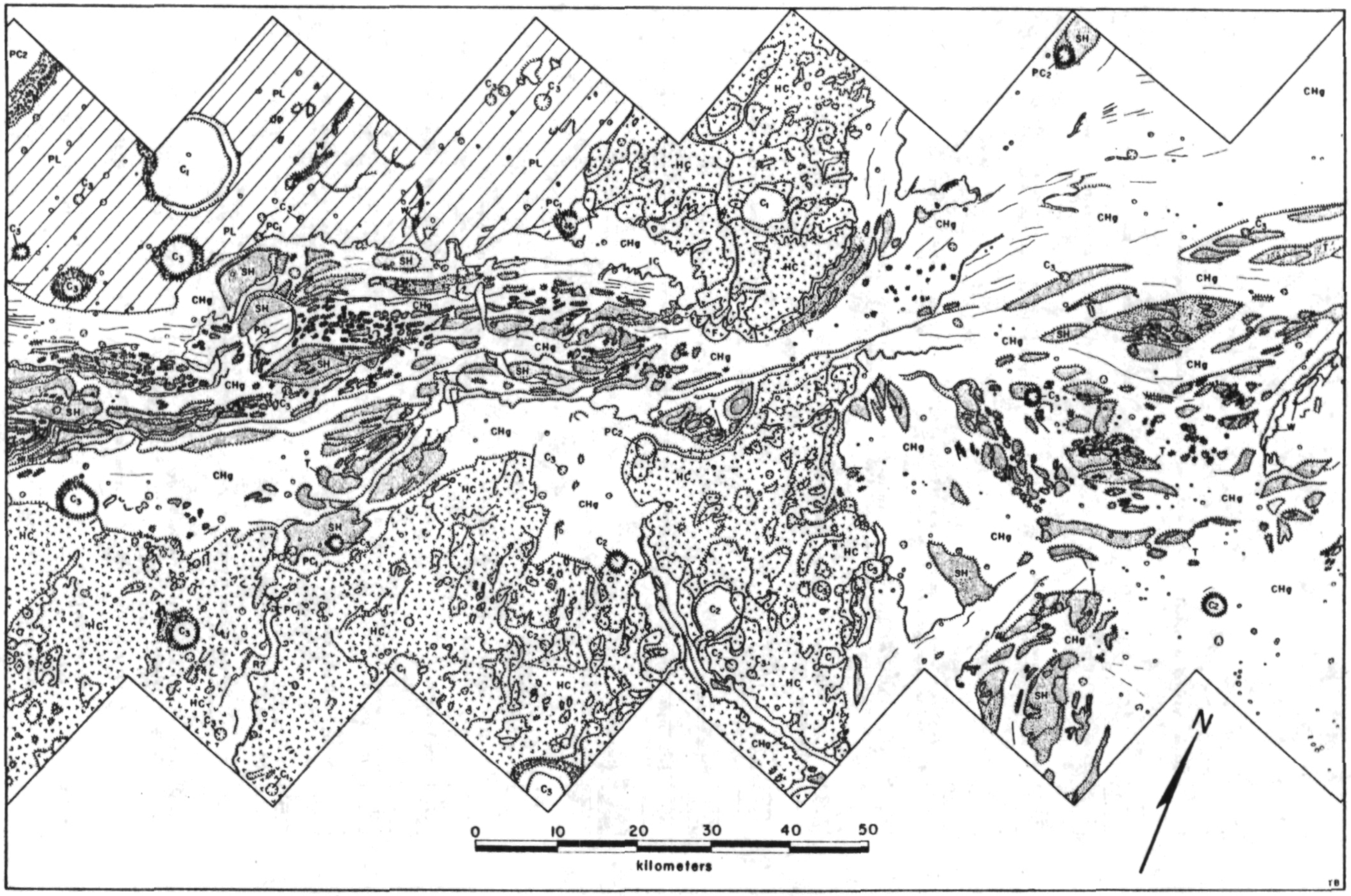

Figure 2. Geomorphic map of the canyon reach of Maja Vallis and adjacent portion of the Chryse Planitia.

The Cheney-Palouse Scabland Tract. Peter C. Patton, Department of Earth and Environmental Sciences, Wesleyan University, Middletown, Connecticut 06457, and Victor R. Baker, Department of Geological Sciences, The University of Texas at Austin, Austin, Texas 78712.

The Cheney-Palouse tract of the Channeled Scabland is the largest continuous tract of scabland in eastern Washington. A typical reach of the tract is mapped in Figure 1. The overall pattern is that of an enormous braided stream with broad anastomosing channels separated by mid-channel islands. However, the anastomosing channels are scoured into the loess and underlying basalt bedrock. The mid-channel islands are not depositional bars as one finds in braided streams. Rather, they are the eroded remnants of the once continuous loess cover (Baker, 1973).

When viewed in detail, the Cheney-Palouse appears to be a complex landscape. The complexity, though, is the result of the grouping and superposition of the three primary forms - the loess islands, gravel bars, and erosional bedrock scabland. The organization of these primary forms in the Cheney-Palouse can be classified in the same manner as other complex fluvial landscapes such as sandur plains (Church, 1972) and braided streams (Williams and Rust, 1969). The classification demonstrates that the landforms in the Cheney-Palouse form predictable geomorphic assemblages in many aspects similar to modern fluvial systems.

Loess island forms varied as a function of their position within the flow. The three major types, submerged, partially submerged, and subaerially exposed loess islands, created sedimentologic conditions and resulting bar forms distinct from one another. The primary zone of deposition was downstream from the loess island groupings in a manner similar to longitudinal bar growth in braided streams. Other bar forms, notably expansion bars, however, probably account for most of the sedimentation in the tract.

Some loess islands appear terraced because of several distinct levels of modification by secondary channels. The largest channels have cataracts and weakly developed butte-and-basin scabland topography. Most of the pendant bars and expansion bars are associated with these major channels downstream from cataracts (Figure 1). Still smaller channels at higher elevations have eroded through the loess cover but have only scarified the underlying basalt. Finally, the smallest channels are the eroded divide crossings, some of which are filled with slackwater deposits. This hierarchy of morphology also represents a decrease in the velocity of the flow, the rate of erosion, and sediment transport as a function of secondary channel elevation above the maximum main-channel depth. The lowermost channels probably carried the greatest discharges for the longest durations and with the greatest velocity and turbulence. These channels would logically be expected to have the highest degree of scabland development and the least amount of sediment deposition associated with them. Sedimentation was greatest in the secondary channels because, although velocities were probably somewhat reduced, sediment concentration was apparently still high. These factors, when combined with the numerous channel expansions and large flow obstructions, created zones conducive to depositon.

The Cheney-Palouse scabland tract developed during several episodes of catatastrophic flooding, each followed by long periods of loess deposition (Patton and Baker, 1978). The pattern and genesis of its streamlined residual hills amidst scoured rock surfaces provide both form and process analogies to the downstream reaches of

Martian outflow channels, including Ares, Kasei, and Maja Valles (Baker, 1978).

References

Baker, V. R., 1973, Erosional forms and processes for the catastrophic Pleistocene Missoula floods in eastern Washington, in Morisawa, M., editor, Fluvial geomorphology: Publ. in Geomorphology, State Univ. of N.Y., Binghamton, N.Y., p. 123-148.

Baker, V. R., 1978, A preliminary assessment of the fluid erosional processes that shaped the Martian outflow channels: Proc. Lunar Planet. Sci. Conf. 9th, p. 3205-3225.

Church, M., 1972, Baffin Island sandurs: A study of arctic fluvial processes: Geol. Survey of Canada Bull. 215, 208 p.

Patton, P. C., and Baker, V. R., 1978, New evidence for Pre-Wisconsin flooding in the Channeled Scabland of eastern Washington: Geology, v. 6, p. 567-571.

Williams, P. F., and Rust, B. R., 1969, The sedimentology of a braided stream: Jour. Sed. Petrology, v. 39, p. 649-679.

Figure 1

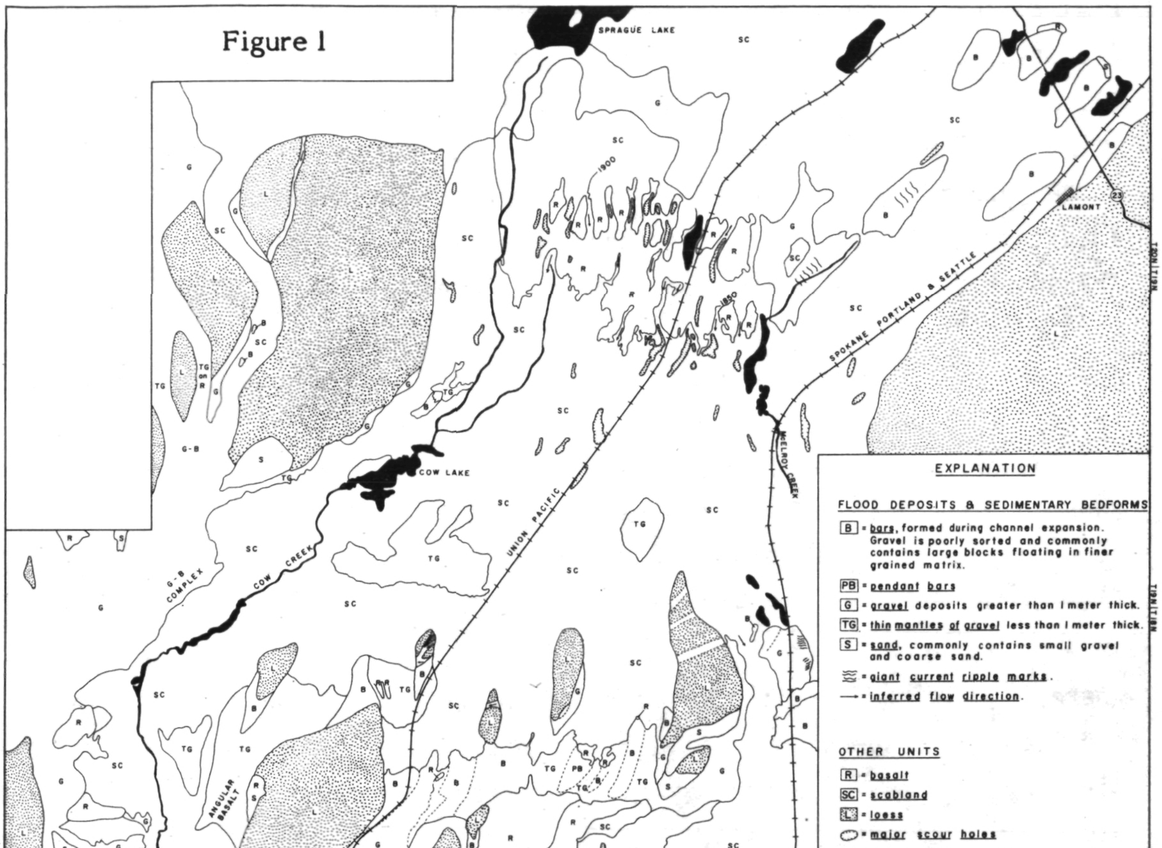
SPRAGUE LAKE
COW LAKE
COW CREEK
G-B COMPLEX
UNION PACIFIC
SPOKANE PORTLAND & SEATTLE
McELROY CREEK
LAMONT
BENGE
ANGULAR BASALT
1900
1850
23
TG on R
EXPLANATION
FLOOD DEPOSITS & SEDIMENTARY BEDFORMS
B = bars, formed during channel expansion. Gravel is poorly sorted and commonly contains large blocks floating in finer grained matrix.
PB = pendant bars
G = gravel deposits greater than 1 meter thick.
TG = thin mantles of gravel less than 1 meter thick.
S = sand, commonly contains small gravel and coarse sand.
≋ = giant current ripple marks.
⟶ = inferred flow direction.
OTHER UNITS
R = basalt
SC = scabland
L = loess
⬭ = major scour holes
1850 = contour line
BASE MAPS
U.S.G.S. 7.5' Quadrangles:
Karakul Hills, Wash.
Lamont NW, Wash.
Macall, Wash.
Marengo, Wash.
Palm Lake, Wash.
U.S.G.S. 15' Quadrangles:
Benge, Wash.
La Crosse, Wash.
N
WASHINGTON
STUDY AREA
0 1 2 3 mi.
0 1 2 3 4 5 6 km.
R36E | R37E
R37E | R38E
R38E | R39E
T20N | T19N
T19N | T18N
T18N | T17N
T17N | T16N

Modes of Sediment Transport in Channelized Water Flows With Ramifications to the Erosion of the Martian Outflow Channels.

Paul D. Komar, School of Oceanography, Oregon State University, Corvallis, Oregon 97331.

The criteria for quantitatively determining which grain-size ranges are being transported in terrestrial rivers as bed load, suspended load and wash load (autosuspension) are applied to an analysis of sediment transport in the large Martian outflow channels, assuming their origin to have been from water flow.

The cut-off sediment grain size between bed-load and suspension transport is determined by a comparison of the grain settling velocities to the upward component of the turbulent eddy velocities. Following Bagnold (1966), this leads to the ratio

$$\frac{w_s}{u_*} = 1.50$$

where w_s is the settling velocity of the cut-off grain size between bed load and suspension, and u_* is the so-called frictional drag velocity, given by $u_* = \sqrt{\tau/\rho}$ where τ is the stress exerted by the flowing water and ρ is the water density.

It is assumed that the fine-grained wash load is transported via Bagnold's (1962) autosuspension, giving the criterion

$$w_s \leq \bar{u}\, S$$

where $\bar{u}$ is the mean flow velocity and S is the mean channel slope. According to Bagnold, autosuspended sediment suspends itself in the sense that it needs no net energy expenditure by the flowing water; the sediment actually contributes to the flow power. For this reason, autosuspended sediments can be transported in unlimited amounts (or perhaps limited only by its effects on damping the flow turbulence).

Of importance to the application of these criteria to the Martian outflow channels is the effects of the reduced gravity of Mars on the water flow (u_* and $\bar{u}$) versus the reduction in grain settling velocities w_s. Analyses were performed using grain densities ranging from 2.90 g/cm³ (basalt) to 1.20 g/cm³ (volcanic ash). The results show that for reasonably expected channelized water flows on Mars, very coarse material would have been transported in suspension; for example, basalt pebbles would have been transported at high rates in suspension rather than slowly as bed load as is the case even in rapidly flowing terrestrial rivers. Nearly all sand-sized material would have been autosuspended. Thus sands could have been transported at high concentrations and at high velocities, permitting increased erosion rates of the channels. This sand would have added power to the flow, so that much of the eroded sediment (sands, silts and clays) from the channel becomes the flow source, the source area not being limited to the original water derived from a chaotic terrain. Upon entering a basin of much lower slope than the channel, the autosuspended sands and finer sediments would only gradually be deposited, allowing the sediments to spread out widely over the basin rather than forming a 'delta' at the channel terminus.

(1) Bagnold, R.A., 1962. Auto-suspension of transported sediment; turbidity currents: Proc. Royal Soc. London, Series A, 265, 315-319.

(2) Bagnold, R.A., 1966. An approach to the sediment transport problem from general physics: U.S. Geol. Survey, Prof. Paper 422-I, 37pp.

CHANNELS AND PLAINS OF THE LUNAE PLANUM - CHRYSE PLANITIA REGION OF MARS

Theilig, E. and Greeley, R., Department of Geology, Arizona State University, Tempe, AZ 85281

Five channel systems, of different morphologies and ages, trend from west to east across rugged terrain providing a link between the extensive smooth plains units of the Lunae Planum upland and the Chryse Planitia basin. A detailed geologic map of the area reveals a sequence of channeling events and plains emplacement, illustrated in Figure 1, and provides a better understanding of channeling processes (Theilig and Greeley, 1979).

The oldest material within the area is represented by a strip of rugged terrain and consists of hilly and cratered material, (part of the heavily cratered ancient crust) overlain by cratered plateau material, a mantle of aeolian and/or volcanic origin. The rugged terrain is embayed by Lunae Planum plains material from the west and lower smooth plains material of Chryse Planitia from the east. Both of these extensive plains contain numerous wrinkle ridges and are considered to be composed of volcanic material and to represent a major volcanic period in the history of Mars. Another plains unit, upper smooth plains material, overlies the lower smooth plains on the western slope of the Chryse basin and is distributed around the mouths of three major channel systems. Mare ridges are subdued within this material and dark halo craters are common. The upper smooth plains is considered to be of fluvial origin.

The five channel systems identified within this area include two sets of narrow "runoff" channels, Vedra-Maumee Valles system, Bahram Vallis, and Maja Vallis and can be divided into four periods of channeling. Two periods of channeling early in martian history are represented by relatively small, narrow channels, of which the oldest occurs as channel segments in the hilly and cratered material and the next oldest as tributary systems in the cratered plateau material. Both sets of channels are similar to runoff channels, located elsewhere in the heavily cratered terrain, which Pieri (1978) proposes to have formed by downhill surface runoff or sapping. These channels are embayed by the plains units in Chryse Planitia. Following major plains emplacement, the Vedra-Maumee Valles system and Bahram Vallis were formed. Vedra and Maumee Valles are similar in morphology and appear to have formed by a sheet-like flow over the rugged terrain followed by incision of the channels. Scour features on the Lunae Planum plains indicate formation after plains emplacement and are similar to features associated with catastrophic floods. These two channels may represent an early flood from Juventae Chasma. Bahram Vallis is incised into Lunae Planum plains material and appears to have been modified by mass-wasting making the primary morphology of the channel difficult to determine. The origin of this channel is unresolved; however, we favor a sapping process involving water. Vedra, Maumee, and Bahram Vallis are difficult to trace into Chryse Planitia and are considered to be the sources for the upper smooth plains material. The last channeling event is represented by Maja Vallis, a large outflow channel considered to have formed by a catastrophic flood released from Juventae Chasma (Baker, 1979).

The four periods of channeling probably represent four periods of deposition in the Chryse basin. All of the channels are considered to have formed by water; however, the dominant channeling process changed, following major volcanic plains emplacement; from downhill flow or sapping, which formed narrow channels, to large-scale catastrophic flooding, which formed large channel systems.

References

Baker, V.P., and Kochel, R.C., 1979, Martian channel morphology: Maja and Kasei Valles. Submitted to J. Geophys. Res.

Pieri, D., 1978, Small channels on Mars from Viking Orbiter, Reports of Planetary Geology Program, 1977-1978, NASA TM79729, 267.

Theilig, E., and Greeley, R., 1979, Plains and channels of the Lunae Planum-Chryse Planitia region of Mars. Submitted to J. Geophys. Res.

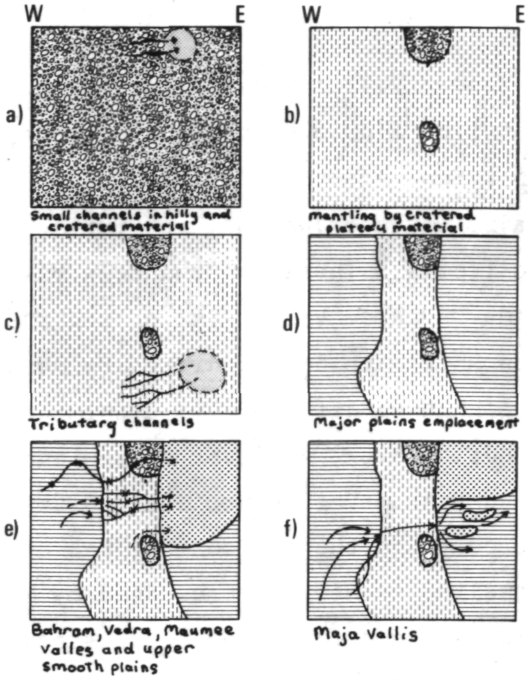

Figure 1. Schematic diagram of the sequence of channel events and plains emplacement. a. Small, narrow channels formed in the hilly and cratered terrain and deposited sediments in the Chryse basin. b. Emplacement of the cratered plateau material burying sediments and possibly some of the channels. c. Formation of tributary channel systems in the cratered plateau material. Sediments from these channels were also deposited in the Chryse basin. d. Extensive volcanic plains emplacment on Lunae Planum to the west and in Chryse Planitia to the east. e. Channeling associated with Bahram, Vedra, and Maumee Valles. Sediments deposited by these channels formed the upper smooth plains. f. Formation of Maja Vallis.

ORIGIN OF MARTIAN VALLEYS, David Pieri and Carl Sagan, Laboratory for Planetary Studies, Cornell University, Ithaca, New York, 14853

Mars displays two major classes of sinuous depressions which represent two distinct modes of erosion: channels and valleys. Channels possess attributes of erosion by fluid flow (e.g. streamlining of interior obstacles)(1). Valleys occur in downhill coalescing networks, and have little direct morphological evidence of fluid erosion. Valley network systems are divided into three major planimetric categories: 1) longitudinal, 2) integrated, and 3) slope valley systems. Network systems are composed of juxtaposed valley networks 1) parallel, 2) digitate, 3) stem, and 4) rectilinear. Radial system assemblages are termed centrifugal and centripetal (interior and exterior). True terrestrial-like space-efficient dendritic patterns are notably absent on Mars (2), rather, martian valley networks are nearly always parallel or quasi-parallel implying fluid source available only on headward reaches. Ampitheater termiations are consistently observed at headward terminations of nearly all tributaries. Mean tributary junction angles within martian networks are generally lower than even terrestrial ephemeral networks and have a statistical scatter, when averaged by link magnitude (3) contrast, that exceeds comparable terrestrial systems by more than a factor of three (2)(4). Low magnitude martian tributaries enter at very low mean junction angles and are generally as deep and wide as trunk valleys. Martian networks fill space very inefficiently with large intervalley areas remaining undissected with no evidence of divides or competition for drainage, even in high resolution images ($\sim$ 40m).

On the basis of these observations several conclusions may be drawn: 1) martian networks were formed by fluid drainage from restricted source areas, 2) they are immature in development, 3) low junction angles at high magnitude contrast junctions indicate that deep and wide low magnitude tributaries are not consequent on valley side slopes, 4) point 3) is consistent with a headward sapping mechanism for valley formation when coupled with observed ampitheater valley heads, and 5) all planimetric observations are consistent with a hypothesis of fluvial erosion fed from restricted source regions. The hypothesis of an areally uniform source, such as rainfall has no compelling support.

Various candidate processes mentioned in the literature have been tabulated in a truth table format. Table I shows that fluvial and wet sapping processes are the most successful candidates. Table II demonstrates that a lithospheric water souce is more compatible with observations than a pluvial one.

References:

(1) Baker, V.R., 1978, Science,
(2) Pieri, D.C., 1979, Ph.D. Thesis, 288p.
(3) Shreve, R., 1967, Jour. Geol., 75, pp. 179-186.
(4) Pieri, D.C. and Sagan, C., 1978, NASA Tech. Memo, 79729, p. 268.

TABLE I

Truth Table Comparison of Flow and Non-Flow Hypotheses for Valley Formation on Mars

	FLOW →					NON-FLOW →				
MODELS:	FLUVIAL	GLACIAL	LAVA	DEBRIS FLOW	WIND	PURELY STRUCTURAL	DRY SAPPING	HYBRID (Wet sapping)	ALKANES[9,10]	LIQUID[10] OR SOLID CO_2
OBSERVATIONS:										
Distribution: ubiquitous to cratered terr.	yes	yes	maybe	yes	yes	no	yes	yes	yes	no
Planimetric Properties: 1. Coalesce downhill										
a. high slopes	yes	? [1.]	yes[1.]	yes[1.]	no	no	yes[2.]	yes	yes	yes
b. low slopes	yes	yes	no	no	no	no	no	yes	yes	yes
2. Angular to sinuous down-network	yes	no	yes	no	no	yes	yes	yes	?	?
3. High variance in junction angles	yes	? [1.]	no	no	yes	yes	yes	yes	?	?

1. It is hard to say exactly what these agents would do if there were no pre-existing stream valleys to follow.
2. On steep slopes, sliding might expose ice which would sap uphill causing more sliding, etc.

MODELS:	FLOW					NON-FLOW				
	FLUVIAL	GLACIAL	LAVA	DEBRIS FLOW	WIND	PURELY STRUCTURAL	DRY SAPPING	HYBRID (Wet sapping)	ALKANES[9,10]	LIQUID[10] OR SOLID CO_2
OBSERVATIONS:										
Morphology:										
1. interior channels	yes	yes	yes	yes	no	yes	no	yes	yes	yes
2. islands	yes	yes	yes	yes	yes	yes	yes	yes	?	?
3. rectilinear networks	maybe[5]	no	no	no	no	yes	yes	yes	no	no
4. amphitheater terminations	yes[6]	?[1]	no	no	no	yes[6]	yes	yes	?	?
5. sinuosity:										
a. low	yes	yes	yes	yes	yes	no[7]	yes	yes	?	?
b. high	yes	not likely	yes	no	no	no	possibly	yes	?	?
6. delta forms	yes	no[3]	no	no[4]	no	no	yes[8]	maybe	?	?
7. valleys head on promontories	yes	yes	yes	yes	yes	no	yes	yes	yes	yes?

3. Morraines are crescentic, but are not considered "deltaic". Melt water could form a delta but this would be considered under "fluvial".
4. Crescentic, but not deltaic.
5. Under the influence of structure; immature system.
6. Collapse pit or underground drainage.
7. Schumm (1974) references sinuous structural features. Shear islands and sinuosities develop in sheared grabens, but these are usually en'echelon and discontinuous.
8. Talus cones.
9. Yung and Pinto (1978).
10. Both possibilities are sufficiently bizarre so as to be outside the realm of conjecture with regard to resultant landforms.

TABLE II

Truth Table Comparison of A Lithospheric Source Hypothesis versus A Pluvial Source

MODEL		LITH. SOURCE	PLUVIAL SOURCE
OBSERVATIONS:			
1.	Worn down ghost basins	possible	yes
2.	Retention of large basins	yes	not likely
3.	Parallel drainage, restricted source areas	yes	not likely
4.	Amphitheater terminations	yes	no
5.	Low entrance angles of small tributaries/deep incision	yes	no
6.	Undissected plateaus in inter-valley areas	yes	not likely
7.	Lack of sub-basin development in inter-valley areas	yes	no
8.	Steep, crenulated walls	yes	no
9.	Lack of distal widening down-network	yes	not likely
10.	Very small networks at the margin of lava flow	yes	no
11.	Valleys radial to basins	yes	yes
12.	Collapsed crater roofs	yes	?
13.	Progression of network character from angular to sinuous down-network	yes	not likely

GLOBAL DISTRIBUTION OF MARTIAN VALLEY SYSTEMS, David Pieri, Laboratory for Planetary Studies, and Department of Geological Sciences, Cornell University, Ithaca, New York 14853

Two hundred and forty martian valley systems were mapped from Viking Orbiter imaging. Figure 1 shows the variation of valley interior morphology with latitude and Figure 2 shows the latitudinal variation of general network properties with latitude ("bceix" refers to box-shaped cross-section, crenulated valley walls, eroded appearing, integrated networks occurring on any terrain). Integrated and slope valley systems occur almost exclusively in intercrater plains in the ancient heavily cratered terrain.

The major Viking contribution to the question of the latitudinal distribution of valley systems has been the extension of the zone of high valley density far to the south to at least -55^{o} latitude (Figure 2,3). Integrated and slope valley are ubiquitous to heavily cratered terrain. The apparent concentration near the equator and correlation with dark classical albedo features (1)(2)(3) is both the result of Mariner 9 observational selection and burial by ubiquitous, younger intercrater plains lavas and eolian debris mantles, suspected from Mariner 9 data (4) and more clearly revealed in higher resolution Viking Orbiter imaging. Integrated and slope valley systems (as distinguished from large channels, from the poorly integrated longitudinal valleys, and from troughs) have interior crater size frequency distributions statistically indistinguishable from the surrounding ancient heavily cratered terrain (5). Crater counts coupled with valley ubiquity in heavily cratered terrain, and their consistent embayment by younger plains lavas suggest an ancient ($\gtrsim$ 3.5B.Y. before present) erosional epoch. Other evidence (5)(6)(7) suggests that the rainfall had little or no part in their formation.

References:

(1) McCauley, et al., 1972, Icarus, 17, pp. 289-327.
(2) Sagan, C. et al., 1973, Science, 181, pp. 1045-1049.
(3) Mutch, T.A. et al., 1976, The Geology of Mars, Princeton, 400p.
(4) Pieri, D.C., 1976, Icarus, 27, pp. 25-50.
(5) Pieri, D.C., 1979, Ph.D. Thesis, 288p.
(6) Pieri, D.C., and Sagan, C; 1979, this report.
(7) Pieri, D.C., and Sagan, C., 1978, NASA Tech. Memo, 79729 p. 268.

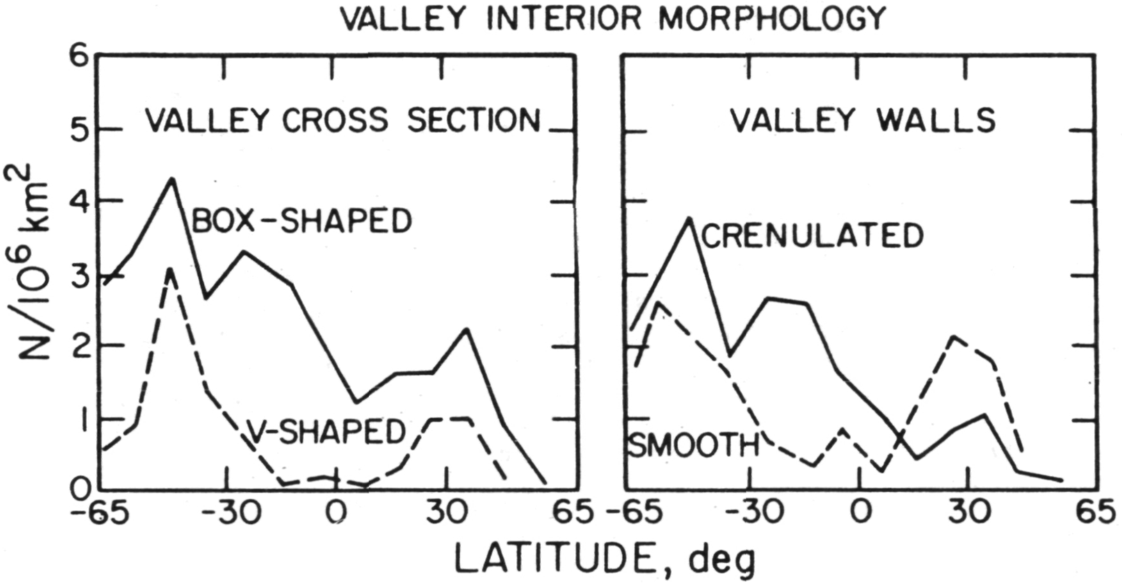
VALLEY INTERIOR MORPHOLOGY
VALLEY CROSS SECTION
VALLEY WALLS
BOX-SHAPED
V-SHAPED
CRENULATED
SMOOTH
N/10^6 km^2
0
1
2
3
4
5
6
-65
-30
0
30
65
-65
-30
0
30
65
LATITUDE, deg

Figure 1

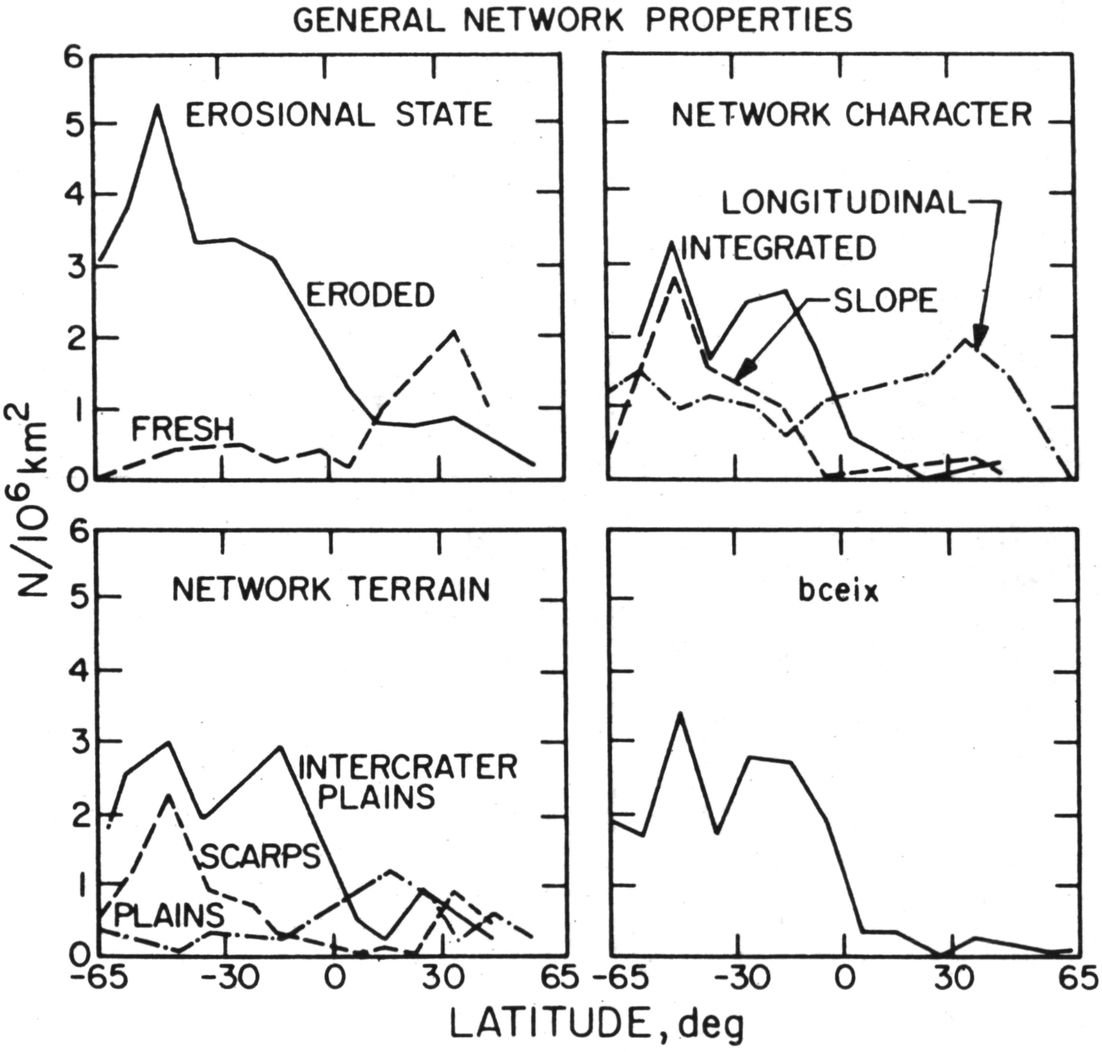
GENERAL NETWORK PROPERTIES
EROSIONAL STATE
ERODED
FRESH
NETWORK CHARACTER
LONGITUDINAL
INTEGRATED
SLOPE
NETWORK TERRAIN
INTERCRATER PLAINS
SCARPS
PLAINS
bceix
N/10^{6}km^2
0
1
2
3
4
5
6
-65
-30
0
30
65
LATITUDE, deg

Figure 2

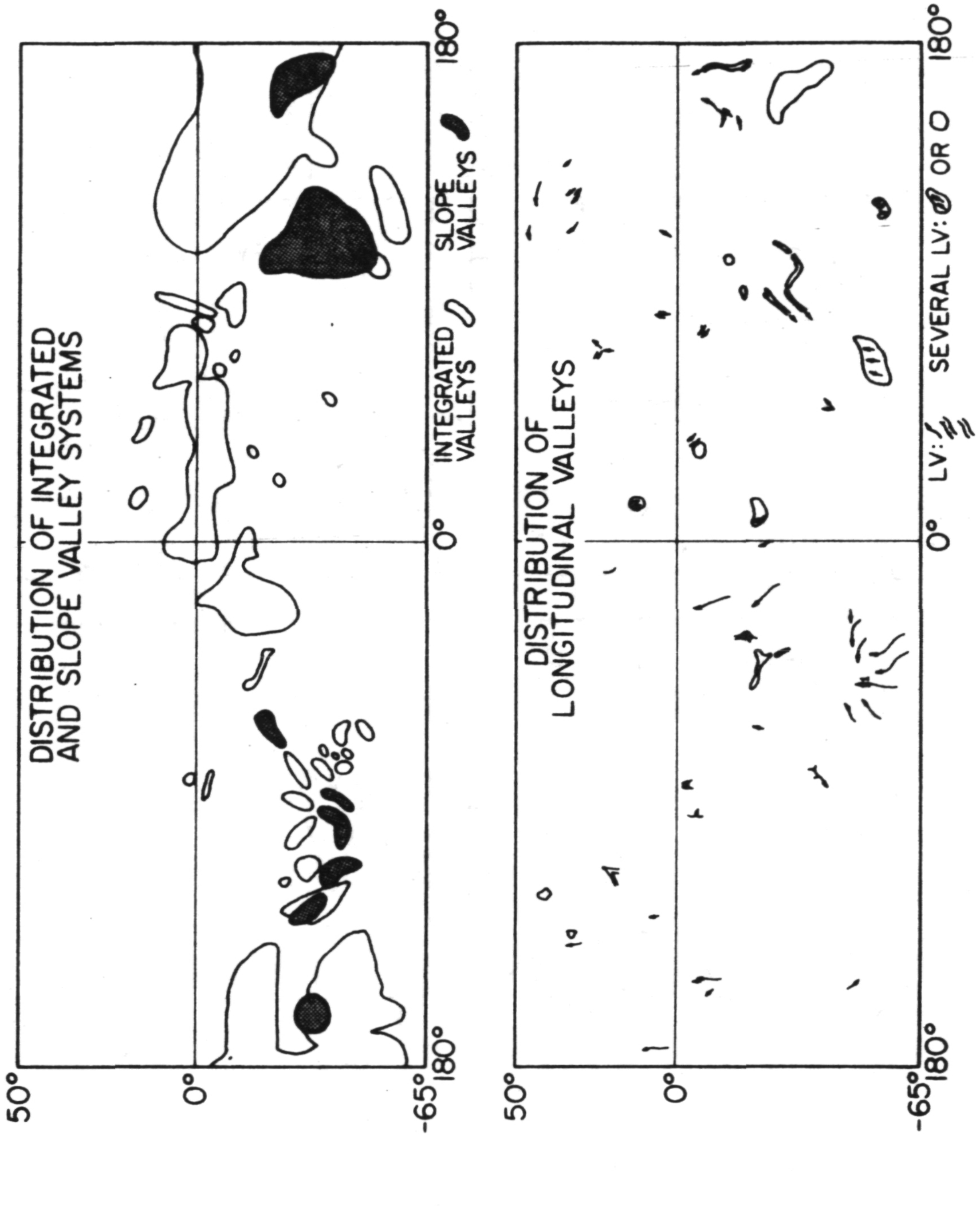
DISTRIBUTION OF INTEGRATED AND SLOPE VALLEY SYSTEMS
INTEGRATED VALLEYS
SLOPE VALLEYS
DISTRIBUTION OF LONGITUDINAL VALLEYS
LV:
SEVERAL LV: OR
50°
0°
-65°
180°
0°
180°
50°
0°
-65°
180°
0°
180°

Figure 3

Chapter 8

RADAR STUDIES OF PLANETARY SURFACES

Page Intentionally Left Blank

ANALYSIS OF SEASAT SAR IMAGES OF SAND DUNES

R.G. Blom, M.I. Daily, C. Elachi and R.S. Saunders
Jet Propulsion Laboratory
California Institute of Technology
Pasadena, California 91103

Analysis of Seasat SAR images of the Algodones Dunes, Southeastern California and the Sonora Dunes, northwestern Mexico, is in progress. Comparison of the Seasat images with Landsat 3 RBV and aerial photos show that the dune morphology is well expressed in the radar images. Field inspection of several key areas has been made. Figure 1 is a computer processed Seasat image of the Algodones Dunes. Note the linear dunes at the west central portion of the dune field, the area of low return from the slope facing away from the radar of the high central ridge and the individual megabarchan dunes in the south. The darker areas in the intra-dune flats and surrounding the megabarchans are regions of desert pavement with low relief. The bright streaks in the south central portion of the image are remnants of older dunes. These sandy areas have considerably greater local topography than the surrounding desert pavement and are also more heavily vegetated, with small mounds around the root system, hence they are brighter. Figure 2 is a mosaic of Seasat images of the Sonora Dunes. Comparison of these images with Landsat RBV photographs shows again that the morphology of the larger dune features is well expressed on the radar images. Comparison of Seasat images from ascending and descending passes indicate some emphasis of directional dune features which is being explored.

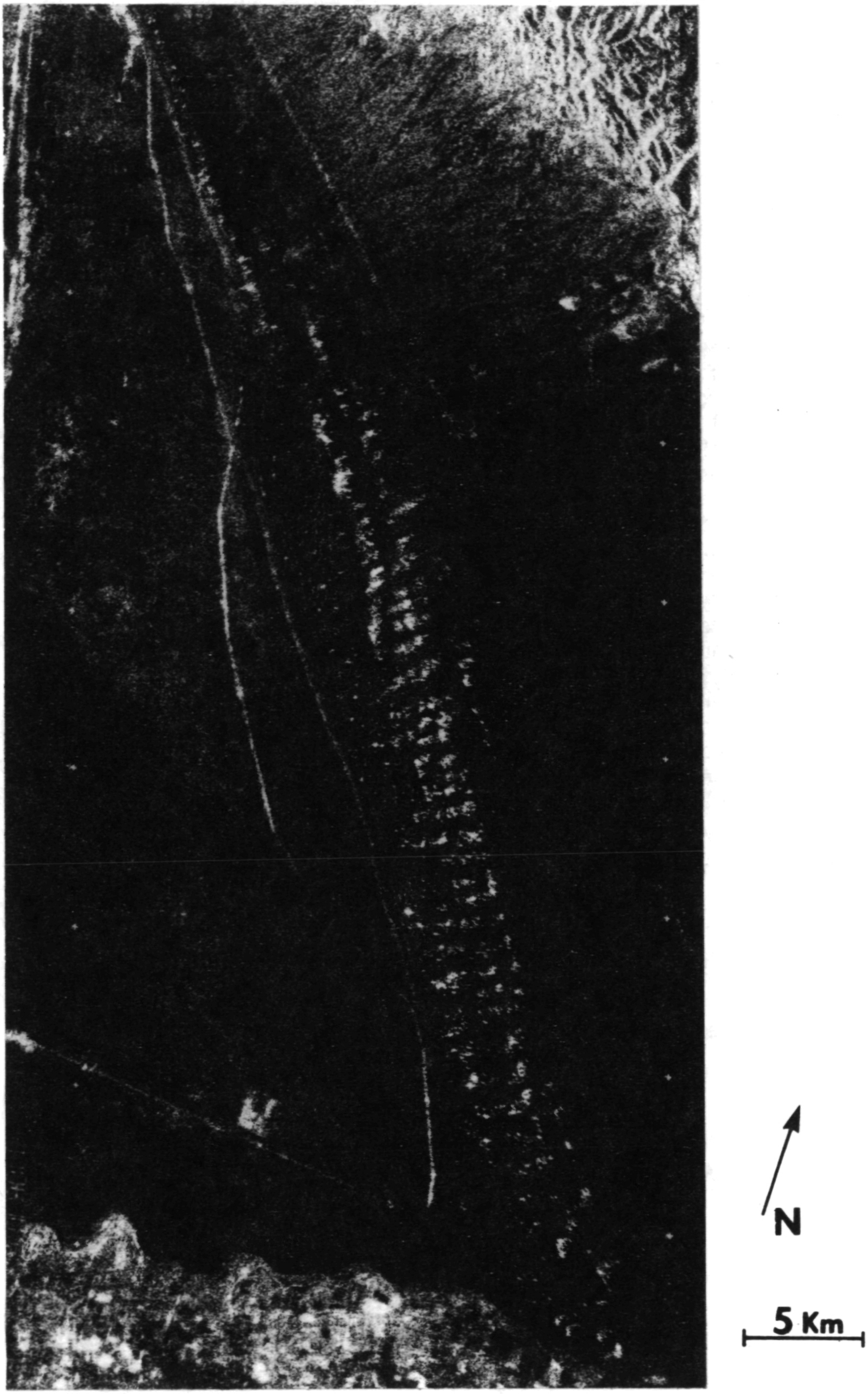

Figure 1: SEASAT SAR Image of Algodones Dunes, California.

Figure 2: SEASAT SAR Image of Sonora Dunes, Mexico.

ANALYSIS OF THE RADAR IMAGERY OF THE EASTERN SNAKE RIVER PLAIN

M. Daily, R. Blom, C. Elachi and R.S. Saunders
Jet Propulsion Laboratory
California Institute of Technology
Pasadena, California 91103

The radar signature of the different volcanic features in the Eastern Snake River Plain is being investigated using the dual polarization (HH and HV) L-band (25 cm wavelength) airborne JPL imaging radar and the singly polarized (HH) L-band Seasat-A radar.

Figure 1 shows the computer mosaics of the aircraft data. Comparison with the photogeologic map of LaPoint (1977) shows that radar brightness falls off systematically with the age of the flows and that aa is readily distinguished from pahoehoe, especially on the cross polarized (HV) image. Even on heavily weathered aa surfaces, the craggy, jumbled meter scale texture is a substantial depolarizer because of multiple reflections (cf. Daily, et al. 1978). All the different flows are separable on the radar images.

The effects of the incidence angle θ are also significant. The like polarized (HH) aircraft imagery taken at $\theta = 45^\circ$ displays considerable mottling on the Big Craters NW (BCNW) flow and distinct contrast with a nearby brighter aa flow (AA1). On the Seasat image taken at $\theta = 20^\circ$ the mottling disappears and the BCNW flow actually appears brighter than AA1 (Figure 2). Figure 3 provides, in sketch form, an explanation for this effect. the backscatter cross-section σ_o as a function of incidence angle is much flatter for the very rough aa than for the pahoehoe of the BCNW flow.

Another interesting observation is that most of the buttes and lava lakes show on the aircraft radar image a contour evenly bright all around. This is most likely due to the very rough edge walls of the collapse craters. It is also interesting to note the prominent aeolian streaking visible on the Seasat and Landsat images west of the young flows.

References:
Daily, M.I., C. Elachi, T. Farr, W. Stromberg, S. Williams and G. Schaber, 1978, "Application of Multispectral Radar and Landsat Imagery to Geologic Mapping in Death Valley;" JPL 78-19.
LaPoint, P., 1977, "Preliminary Photogeologic Map of the Eastern Snake River Plain, Idaho;" USGS Map MF-850.
Schaber, G.G., 1978, "Spectral or Time Series Analysis of Surface Roughness: Correlation with Radar Backscatter Cross-Section Measurements;" NASA Tech. Memo 79729.

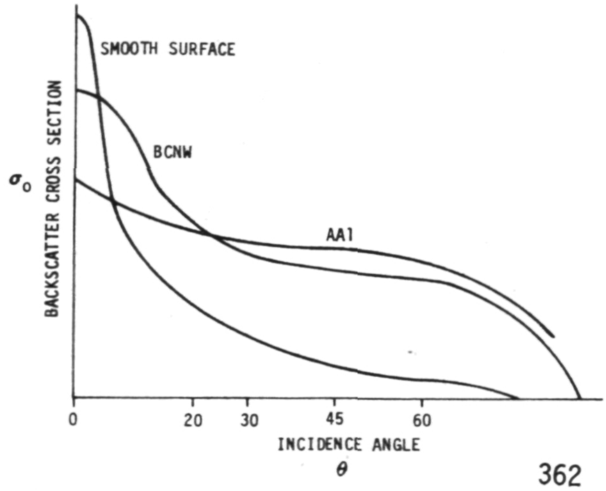

Figure 3. Radar backscatter cross-section as a function of incidence angle (schematic)

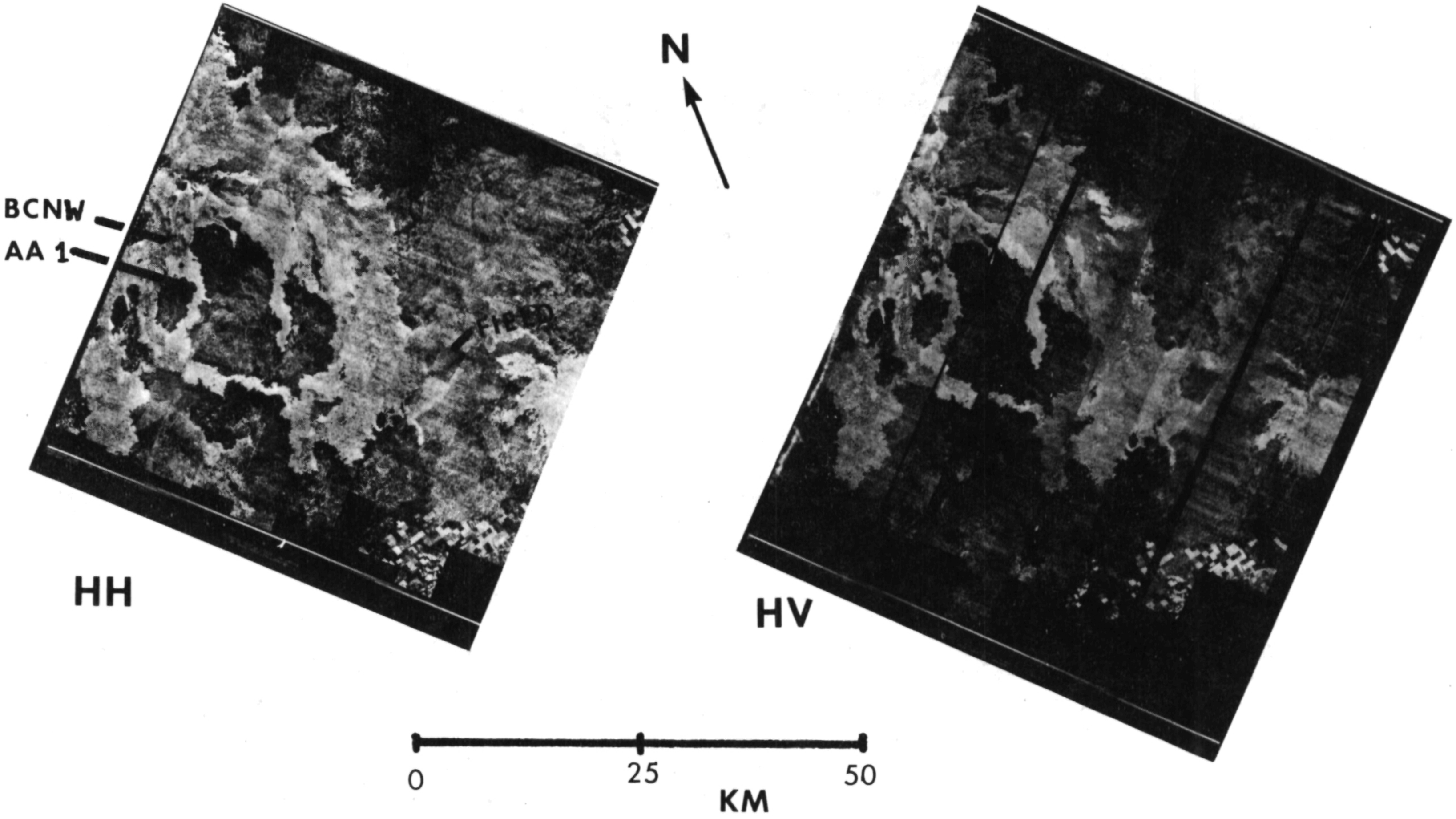

FIGURE 1. Computer-generated mosaics of aircraft L-band radar imagery

Craters of the Moon Lava Field (Western Half), Idaho

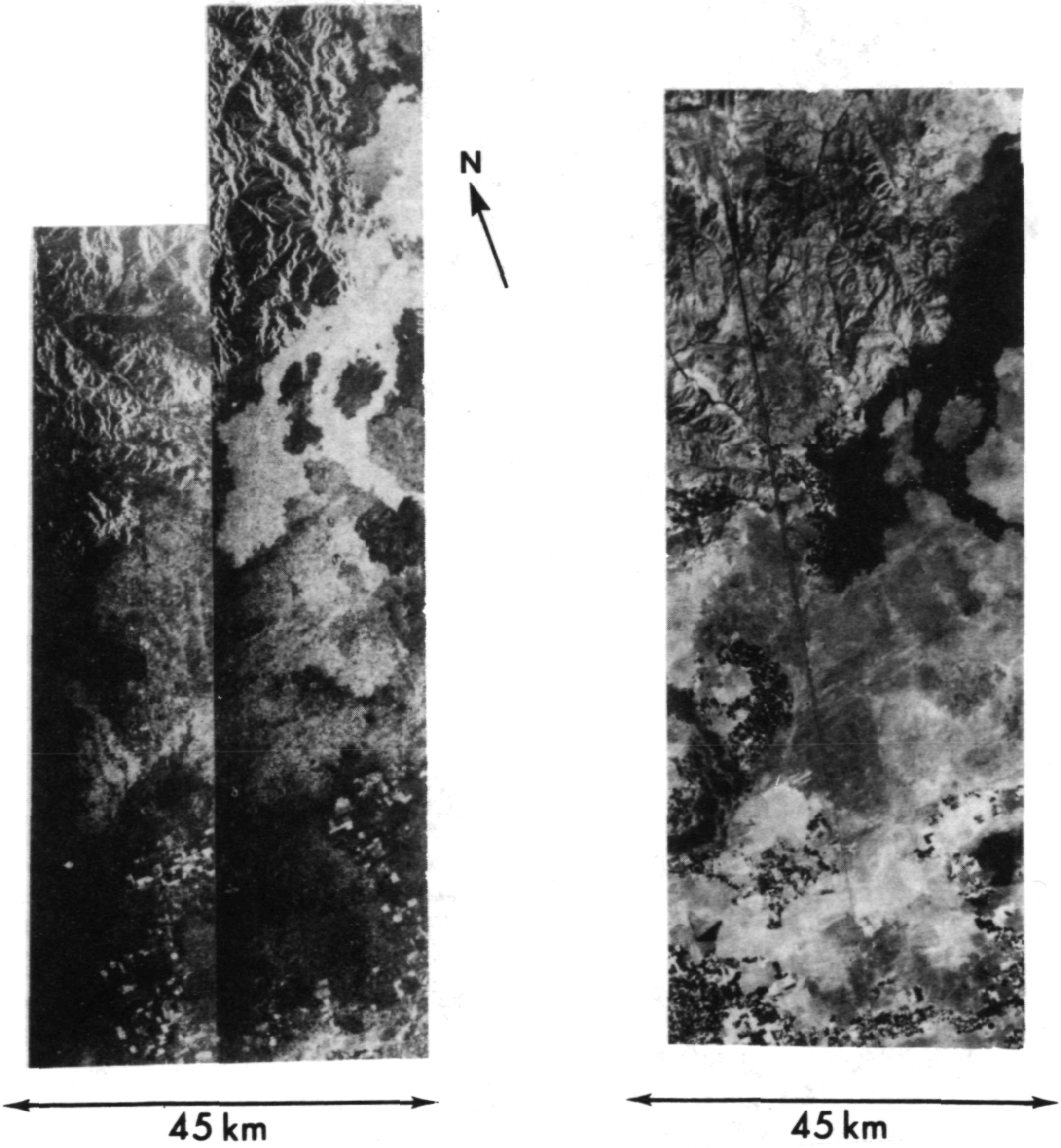

Seasat-A SAR
($\theta = 20°$, Res. 25m, L-band)

Landsat
(Res. ~ 80m)

FIGURE 2

Electrical Properties of Solid CO_2 -- Application to Remote Probing of Mars,

R.A. Simpson, H.T. Howard, and G.L. Tyler, Center for Radar Astronomy,
Stanford University, Stanford, CA 94305

Laboratory measurements of the electrical properties of solid carbon dioxide (dry ice) have been conducted at microwave frequencies. These confirm earlier, preliminary results from 200 MHz and show that CO_2 has a distinctly lower dielectric constant than either water ice or soil. Loss tangent appears to be less than 0.01; determination of this value is limited by measurement uncertainties and is still being refined. These results will be applied to interpretation of bistatic radar data obtained using the Viking orbiters in the north polar region of Mars.

The laboratory measurements* were obtained using specially fabricated sections of S-band and X-band waveguide (packed with dry ice frost at various densities and temperatures) and a computer controlled automatic network analyzer. Frequency ranges covered were 2.2 to 4.2 GHz and 8.0 to 12.0 GHz, bracketing the Viking spacecraft transmitter frequencies of 2.295 and 8.415 GHz. Scattering parameters were measured and converted to the real and imaginary components of dielectric constant and permeability, from which the loss tangent could be computed (Weir, 1974).

The dielectric constant was determined to be predominantly real and independent of both frequency and temperature; its variation as a function of density obeys the Rayleigh (1892) mixing formula. Dielectric constant at 1 g/cc is about 1.7; permeability and loss tangent are 1.0 and <0.01, respectively, to the accuracy of the measurements. Dielectric constant of solid CO_2 appears to be about 2.4; this compares with values of 3.0-3.2 for solid water ice (Vickers, 1975) and, typically, 5-7 for solid rock (Campbell and Ulrichs, 1969).

The Brewster angle for a dielectric material, $\Theta_B = \arctan \sqrt{\varepsilon}$, can be obtained from the ratio of reflected power in two orthogonal polarizations (ε is the dielectric constant of the solid). This has been used in lunar studies to find $\varepsilon = 3.0$ in Oceanus Procellarum (Tyler, 1968) and $\varepsilon = 3.1$ in the Hellas basin of Mars (Simpson _et al._, 1979). More general expressions can be used to obtain dielectric constant at arbitrary incidence angles based on the Fresnel reflection coefficients for dielectric materials (Fig. 1).

The Viking bistatic radar experiment has produced eight ground tracks across various parts of the north polar region of Mars (Fig. 2); these were obtained between approximately the Martian vernal equinox and the Martian summer solstice. If pockets of dry ice were exposed and had significant dimensions at this time, they may be distinguishable in their scattering properties from water ice and soil by their polarization ratios.

---

* Laboratory work was performed at SRI International, Menlo Park, CA by B. Fair.

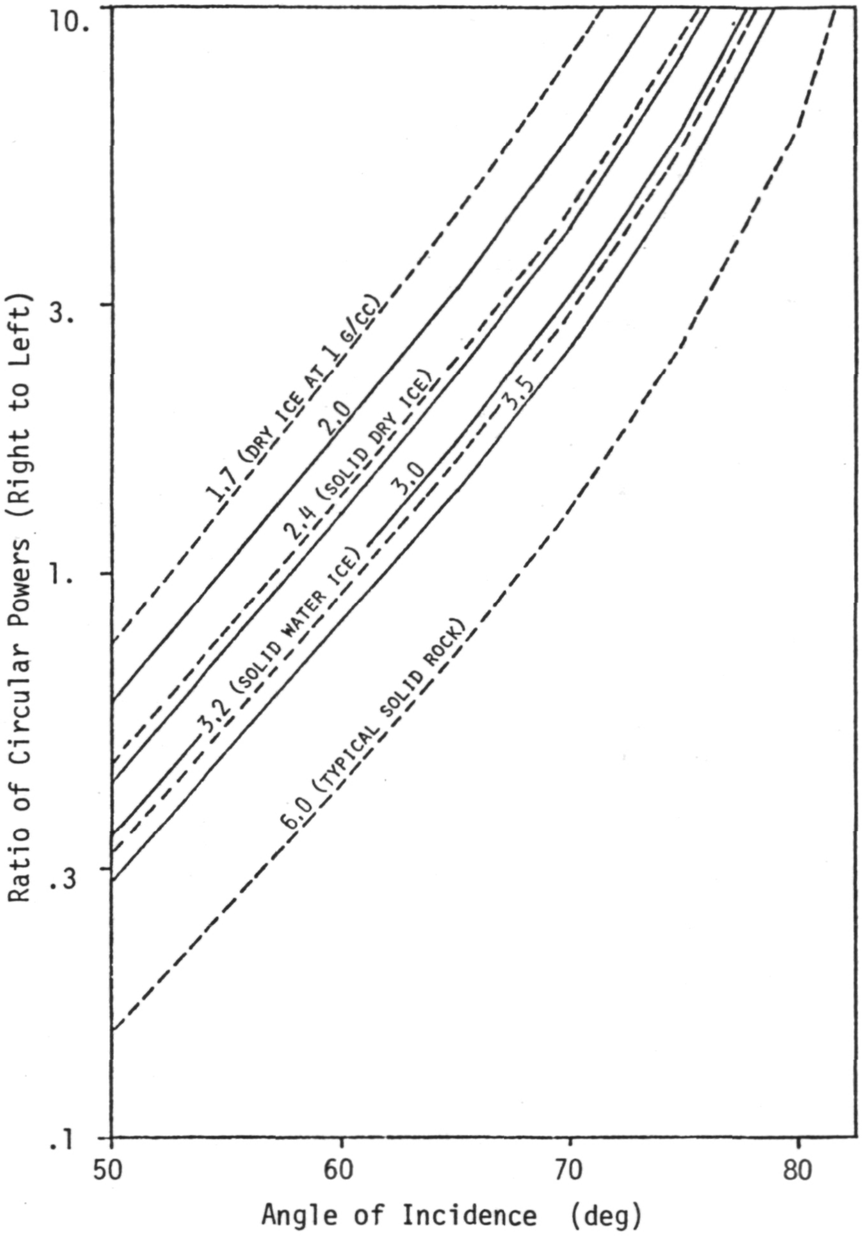

Fig. 1 - Ratio of circular received powers vs angle of incidence. An incident wave of purely right circular polarization was assumed; the amount of power in right and left circular components after reflection depends on both incidence angle and dielectric constant of the material. For the bistatic radar experiment angles greater than 60° were most common and polarization ratios between 1 and 10 will be most easily analyzed.

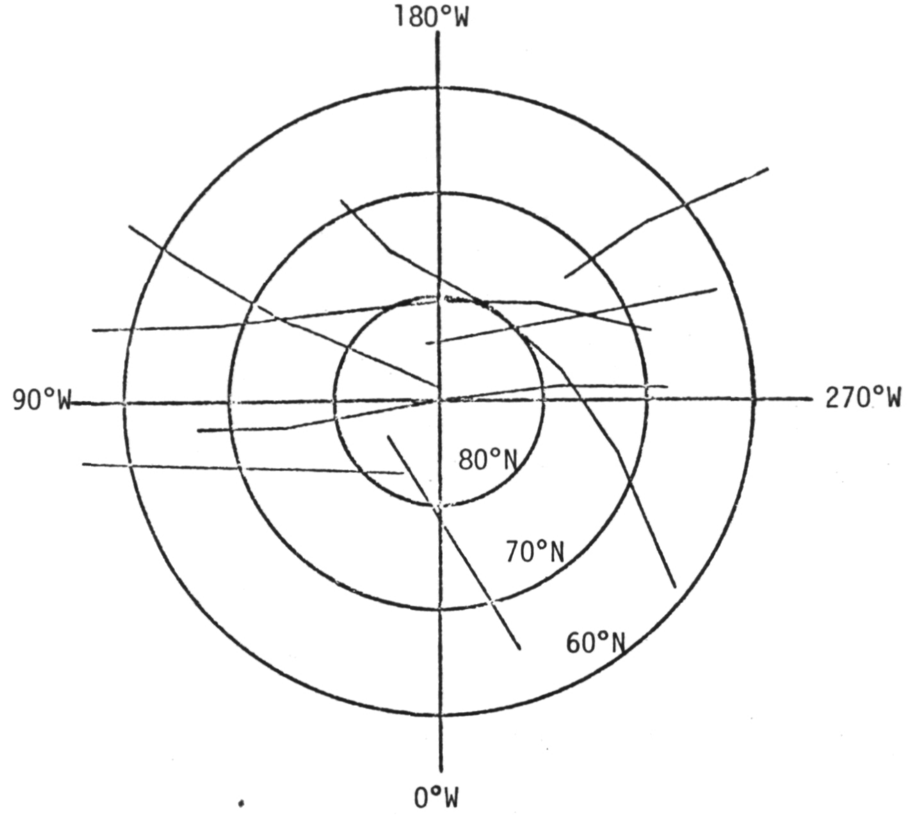

Fig. 2 - Bistatic radar ground tracks in the Mars north polar region. Those tracks within 10° of the pole will give best information on the cap material. Our ability to distinguish CO_2 ice from H_2O ice will depend on the extent of CO_2 coverage, its thickness, and its density.

References

Campbell, M.J. and J. Ulrichs, Electrical properties of rocks and their significance for lunar radar observations, J. Geophys. Res., 74, 25, pp 5867-5881, 1969.

Rayleigh, On the influence of obstacles arranged in rectangular order upon the properties of a medium, Phil. Mag., 34, pp 481-502, 1892.

Simpson, R.A., G.L. Tyler, J.P. Brenkle, and M. Sue, Viking bistatic radar observations of the Hellas basin on Mars: preliminary results, Science, 203, pp 45-46, 1979.

Tyler, G.L., Brewster angle of the lunar crust, Nature, 219, pp 1243-1244, 1968.

Vickers, R.S., Microwave properties of ice from the Great Lakes, SRI International final report on contract NAS 3-19092, Menlo Park, CA, 1975.

Weir, W.B., Automatic measurement of complex dielectric constant and permeability at microwave frequencies, Proc. IEEE, 62, 1, pp 33-36, 1974.

Radar Returns from a Blocky Lava Flow: Quasispecular Reflection, Multiple Scattering and Rayleigh Scattering Effects, Gerald G. Schaber, U.S. Geological Survey, Flagstaff, AZ and Charles Elachi, Jet Propulsion Laboratory, Pasadena, CA.

Multifrequency airborne radar image data of SP Mountain and SP lava flow (and vicinity) in north-central Arizona were obtained in diverse viewing directions and direct and cross-polarization, then compared with surface and aerial photography, Landsat multispectral scanner data, airborne thermal infrared imagery, surface geology and surface roughness statistics (1).

SP Mountain and lava flow result from a late Pleistocene (70,000 years ± 4,000 years) (2) eruption associated with the San Francisco volcanic field. SP Mountain is a basaltic andesite cinder cone with steep flanks (27°-31°), sharp crater rim, and nearly perfect cone symmetry (Fig. 1). From the north side of SP Mountain, an extremely blocky basaltic andesite lava flow (SP flow) extends approximately 7 km to the north. The flow is approximately 50 m thick at its distal end and thins to about 20 m near the vent.

There are two distinct types of surfaces on SP flow. The dominant surface (unit 1) is characterized by extreme blockiness and a hummocky topography; the other (unit 2) consists of smoother terrain with a mantle of cinders and soil with a low grassy vegetation. The unit 2 zones are commonly oxidized and characterized by red scoriaceous and glassy lava that appears to accommodate the local development of soil. Local relief profiles of both the blocky (unit 1) and cinder-covered (unit 2) surfaces of the flow were obtained by photogrammetric reduction of handheld Hasselblad stereo photography, acquired at about 2 m above the ground surface. Selected roughness parameters for these surfaces were obtained by computer analyses of the profile data (3).

The extremely blocky, basaltic andesite of SP flow is significantly brighter on direct-polarized K-band (0.9-cm wavelength) images than on cross-polarized images taken simultaneously (Fig. 1a,b). Conversely, for the longer wavelength (25-cm) L-band radar images, the cross-polarized image returns from SP flow are brighter than the direct-polarized image (Fig. 1a,b). The highly polarized K-band returns from SP flow are attributed to quasispecular reflection and direct surface scatter (that contributes significantly to the polarized return) and little multiple or volume scattering (that contributes primarily to the cross-polarized return) (4). This predominance of quasispecular return and direct surface scatter is caused by numerous flat facets of homogeneous basaltic andesite blocks, forming simple and dihedral reflectors. These facets are much larger (a factor of 10 to 30) than the K-band wavelength; thus, blocks which are oriented with facets normal to the radar line-of-sight will specularly reflect energy to the receiver without depolarization. The enhanced L-band, cross-polarized return from unit 1 on SP flow is attributed to increasing multiple scattering. Individual facets of the basaltic andesite blocks are, on average, smaller than the wavelength at L-band; thus, these scatterers do not act (as at K-band) to strongly polarize the return. A summary of mechanism known to cause depolarization is given by Janza (1975) (4).

The two distinct surface types (units 1 and 2) on SP flow are found to be discriminated by image tone only on the longer wavelength L-band radar images (both direct and cross-polarization). The inability of the K-band and

X-band images to reflect the difference in roughness between these surfaces is attributed to the fact that both unit 1 and unit 2 are "effectively" rough at the shorter wavelengths. The strength of radar return is determined by the relationship of surface roughness to the radar wavelength and to the depression angle of the radar antenna. This relationship has been described by the Rayleigh criterion which has recently been applied in several radar investigations (5, 6) and summarized in Sabins (1978) (7). The Rayleigh criterion predicts that for depression angles of about 30° the K- and X-band radar images should be bright (thus radar rough) if the mean relief of the surface target is larger than ∿0.2 to 0.8 cm, respectively. For the longer wavelength L-band radar at a depression angle of 50°, the Rayleigh criterion predicts the transition between radar rough and smooth to occur at ∿4 cm. The measured mean relief of unit 2 on SP flow is ∿3 cm; thus, this surface should appear dark (or radar smooth) only at the L-band frequency, as observed.

References

(1) Schaber, G.G., Elachi, C. and Farr, T., 1979, Remote sensing data of SP Mountain and SP lava flow in North-central Arizona, Jour. of Remote Sensing of Environment - in press.

(2) Baksi, A.K., 1974, K-Ar study of the SP flow, Canadian Jour. Earth Science, 11, 1350-1356.

(3) Pike, R.J. and Rozema, W.J., 1975, Spectral analysis of landforms, Annals Association of American Geographers, 65(4), 499-516.

(4) Janza, F.J., 1975, Interaction mechanisms, in Manual of Remote Sensing (R.G. Reeves, ed.), vol. 1, Chapter 4, American Society of Photogrammetry, 75-179.

(5) MacDonald, H.C. and Waite, W.P., 1973, Imaging radar provide terrain texture and roughness parameters in semi-arid environments, Modern Geology, 4, 145-158.

(6) Schaber, G.G., Berlin, G.L. and Brown, W.E., 1976, Variations in surface roughness parameters within Death Valley, California: geologic evaluation of 25-cm wavelength radar images, Bulletin Geological Society of America, 87, 29-41.

(7) Sabins, F.F., 1978, Remote Sensing: Principals and Interpretations, W.H. Freeman and Co., San Francisco, 426.

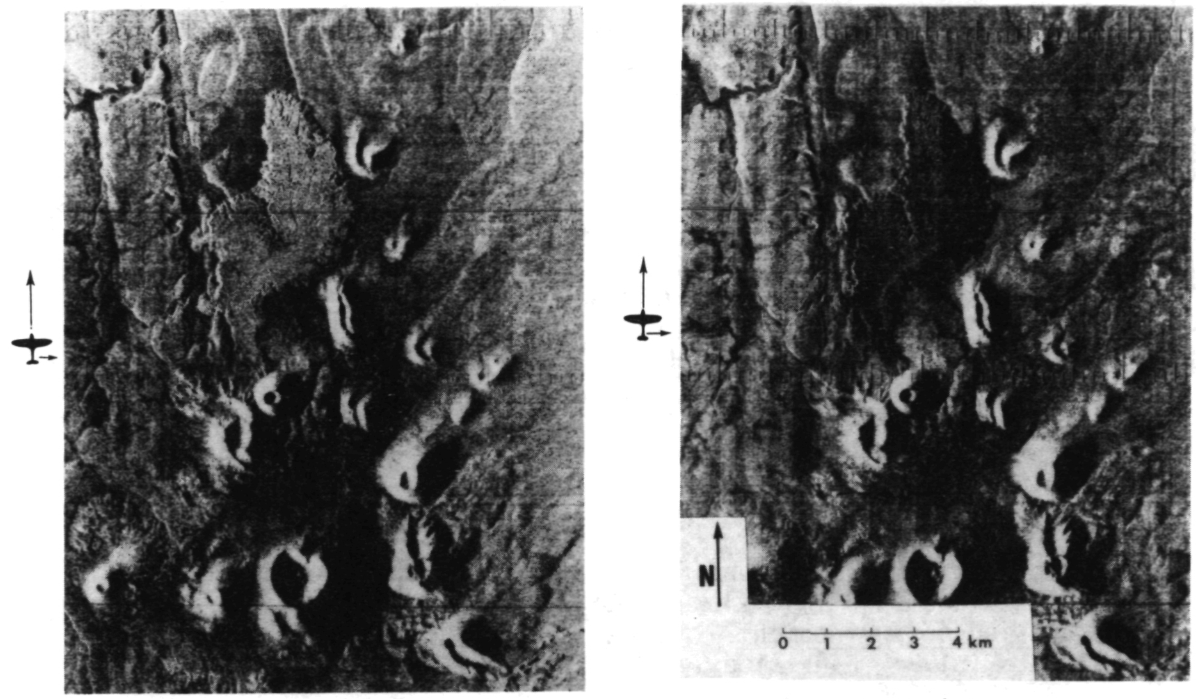

K-band, HH polarization (Westinghouse)

a

K-band, HV polarization (Westinghouse)

b

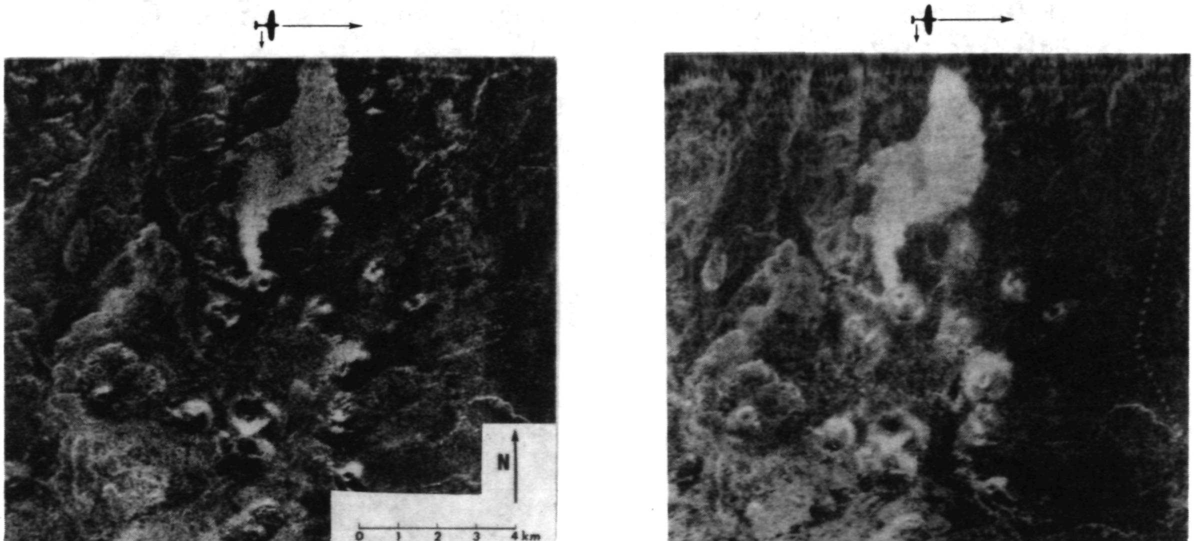

L-band, HH polarization. Image Processing Laboratory computer-generated mosaic of near and extended range swaths.

c

L-band, HV polarization. Image Processing Laboratory computer-generated mosaic of near and extended range swaths.

d

FIGURE 1

Chapter 9

GALILEAN SATELLITES

Page Intentionally Left Blank

Geology of Ganymede, E. M. Shoemaker, California Institute of Technology, Pasadena, California 91125

The surface of Ganymede is divided into two very distinct types of terrain, 1) cratered terrain and 2) grooved terrain. Cratered terrain has the lowest albedo of the two types and is characterized by a rather uniform high density of remarkably shallow craters ranging from 1 km to more than 50 km diameter. Grooved terrain is characterized by a complex pattern of close-spaced shallow grooves and comparatively high albedo. It has a much lower crater density than the cratered terrain. The grooved terrain forms an anastomosing network that divides the cratered terrain into isolated polygons from 100 to 1500 km across. Approximately half of the surface of Ganymede observed by Voyager 1 at high resolution is cratered terrain and the remainder is grooved terrain.

Cratered terrain. -- Craters in all observed size ranges in the cratered terrain show a wide range of shape - from moderately deep to extremely shallow. Most craters larger than 30 km in diameter are double-ringed craters with two concentric inward facing scarps. Many shallow craters larger than 10 km diameter have a form generally not observed on the moon or on the terrestrial planets. These craters have a relatively sharp rim and short scarp or wall and a broad convex upward shallow floor. This is a form that would be produced by gradual collapse of an initial bowl-shaped crater by viscous flow. Superposition of deeper, bowl-shaped craters on the shallow craters shows that shallow craters are older than deep craters of comparable size. Ray craters, which are the youngest craters on Ganymede, are invariably the deepest craters in any given size range. The sum of evidence is strong that most craters of nearly all observed sizes have flattened with time as a consequence of viscous flow. This implies that the shallow crustal material on Ganymede has a low yield strength, compared to silicate rocks, and may be predominantly ice.

Because of the wide range of depths observed for craters in all size ranges, the crater population can be interpreted as resulting from equilibrium between crater production by impact and crater loss by a combination of viscous flow and superposition of small craters on larger craters. The density of craters a few tens of km in diameter on the cratered terrain is comparable to the density on the lunar highlands. The present production of craters $\geq$ 10 km diameter on Ganymede is estimated at $\sim 0.5 \times 10^{-14}$ km^{-2} yr^{-1}, similar to the present cratering rate on the Moon. Hence the high crater density on Ganymede suggests that the age of the cratered terrain on Ganymede is comparable to the age of heavily cratered terrain on the Moon (i.e. about 4 billion years).

Grooved terrain. -- The grooved terrain consists of intersecting systems of different ages. A single system of grooves contains from one to as many as a dozen individual grooves; the groove systems are 10 to 100 km wide and a few tens to about 1000 km long. Individual grooves commonly are about 2-15 km wide and as much as 100 to 500 m deep. In rare cases, the ridges between the grooves stand above the level of the surrounding terrain. The higher albedo of the grooved terrain may be due simply to higher turnover rate and exposure of fresh material in regolith on the sloping walls of the grooves.

Grooves and groove systems tend to be arcuate and locally show relatively sharp bends in trend. Thus they could be formed by normal or reverse faulting but not primarily by strike-slip faulting. In places, a groove system penetrates a polygon of cratered terrain without crossing it. Very locally, the groove systems appear to be offset along nearly straight transcurrent faults or are truncated by transform faults. The simplest explanation of the grooves is that most of them are formed either as grabens or as fissures produced over dikes or dike systems. If this is true, the network of grooved terrain suggests that the entire crust of Ganymede has been under tension. The grooved terrain, in this model, represents regions of crustal spreading. The crater density on the grooved terrain shows that it is everywhere younger than the cratered terrain and that it may be comparable in age to the lunar maria.

Ray craters. -- A small fraction of the craters on Ganymede have high albedo rim deposits that extend outward into systems of rays. The ray craters appear to be randomly distributed over the satellite. Superposition of the rays on other craters and on the groove systems shows that the ray craters are the youngest features on Ganymede. As rays are missing from most craters and, in particular, from older shallow craters, it may be confidently inferred that surface processes have acted to darken the rim deposits and rays of fresh craters. Most of Ganymede evidently is covered by a veneer of dark regolith.

Very rare dark ray craters are also found on Ganymede. Their presence suggests compositional heterogeneity in the shallow crust.

COMPARISON OF THE CRATER DISTTRIBUTIONS ON CALLISTO AND THE TERRESTRIAL PLANETS: PRELIMINARY VOYAGER I RESULTS

R. G. Strom, University of Arizona, Tucson, Arizona 85721;
J. M. Boyce*, and P..S. Collins, U. S. Geological
Survey, Flagstaff, Arizona 86001.

Callisto has a heavily cratered surface which has resulted from the impact of meteoritic and probably cometary material once present in this region of the outer Solar System. A preliminary comparison of the crater diameter/density distribution with those of the heavily cratered regions on the Moon, Mars, and Mercury indicates that the distribution function is quite different. In the diameter range of about 15-70 km the Callisto crater distribution function is about -2 while on the terrestrial planets it is about -1. In other words Callisto has an over-abundance of smaller craters and a paucity of larger craters relative to the heavily cratered regions on the terrestrial planets (Fig. 1). This can also be seen by visually comparing pictures of the lunar highlands and Callisto at comparable scales and resolutions. Furthermore, at diameters between about 70 and 100 km the number of craters declines rapidly on Callisto and between 100 and about 250 km diameters there appears to be an absence of craters on the surface viewed by Voyager 1. However, three basin-sized structures between about 250 and 600 km diameter occur.

Recent investigations by Woronow (1978), Oberbeck et al. (1977), Strom (1977), Wilhelms et al. (1978), and others indicates that the crater distribution on heavily cratered surfaces of the terrestrial planets basically represents a production population which is similar on all of these bodies. Furthermore Woronow (1978) has shown that an impacting population with a -2 distribution function will retain this distribution function at the crater density and diameter range observed on Callisto. Therefore, the difference in the observed distribution function between Callisto (-2) and the heavily cratered terrains on the terrestrial planets (-1) suggests that the population of objects responsible for the period of heavy bombardment on the terrestrial planets was different from that responsible for the bombardment of Callisto (also see Boyce et al., this Volume).

---

*Present address: NASA Headquarters, Washington, D.C

The outer region of Callisto probably consists of icy material, and its response to the cratering process is not well known. For given impact parameters one might expect that larger craters will be produced in icy material than in rocky material (Boyce and Roddy, 1978; Croft et al. 1979). Relative to the Moon and other terrestrial planets, this would tend to lower the crater density for a -2 distribution function. The marked paucity of craters larger than about 70 km diameter may be due to the response of an icy material to large impacts or it may be a peculiarity in the distribution of the impacting population.

More complete and comprehensive crater measurements, as well as additional coverage from Voyager 2, will provide better statistical data upon which to base the interpretations.

Boyce, J. M. and Roddy, D. J. (1978) NASA TM-79729, p. 163-165

Croft, S. K. et al. (1979), NASA CP-2072, p. 18

Oberbeck, V. R. et al. (1977), J. Geophys. Res. 82, 1681

Strom, R. G. (1977), Phys. Earth Planet. Inter. 15, 156

Wilhelms, D. E. et al. (1978), Proc. Lunar Planet. Sci. Conf. 9th, in press

Woronow, A. (1978), Icarus 34, 76

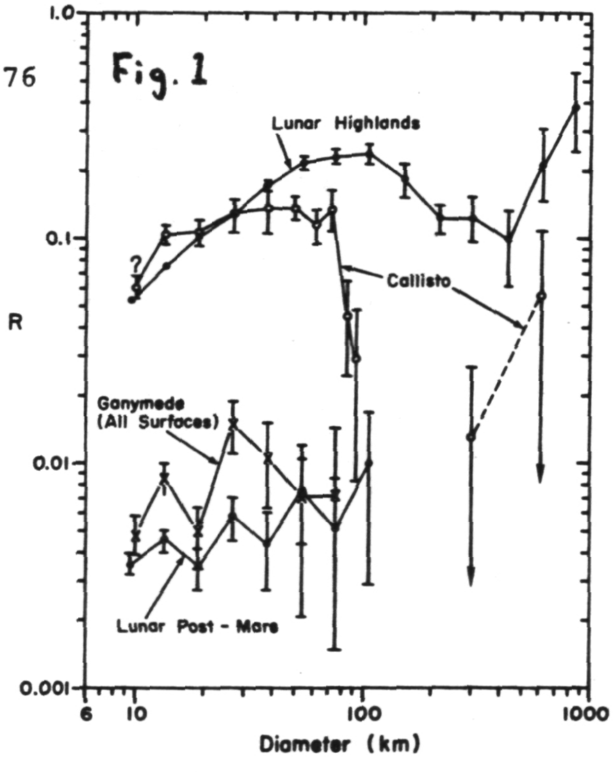

Fig. 1

Tidal Dissipation and the Surface of Io. Ray T. Reynolds and Patrick M. Cassen, Theoretical and Planetary Studies Branch, NASA-Ames Research Center, Moffett Field, CA 94035. Stanton J. Peale, Dept. of Physics, University of California, Santa Barbara, CA 93106.

The Voyager I images showed that the surface of Io has a virtual absence of impact craters, to the limits of resolution, and depicted many volcanic features, including active volcanoes. Prior to the fly-by mission, Witteborn, Bregeman, and Pollack (1979) had observed a large thermal anomaly on Io. Peale, Cassen & Reynolds (1979) had proposed the existence of a strong internal heating source for Io. This heating source is a result of the dissipation of energy by the tides raised on Io by Jupiter. The magnitude of the effect indicated a unique internal structure and the presence of intense surface activity for Io.

This heating source is based upon the fact that the orbits of the three inner Galilean satellites, Io, Europa and Ganymede, are locked into a resonant relationship (known as the Laplace relation) in which their mean orbital motions are very nearly in the ratios of 1:2:4. A detailed analysis of the orbital motions gives a value for the eccentricity of Io's orbit, forced and maintained by the resonant interaction, of $e = 0.004$.

Peale and Cassen (1978) give a relation for tidal dissipation in a synchronously rotating, homogeneous satellite having an eccentric orbit as:

$$\frac{dE}{dT} = \frac{36\pi\rho^2 n R_s^2 e^2}{19\mu Q},$$

where ρ is the density, n is the mean orbital motion, R_s is the satellite radius, e is the eccentricity, μ is the modulus of rigidity and Q is the specific dissipation function. This gives a value of the tidal dissipation for a homogeneous Io of some 1.6×10^{19} erg/sec. The energy is dissipated nonuniformly with a central heating rate some three times the average.

Upon the occurrence of melting in the interior of Io, however, the tidal heating rate would increase rapidly. The reason is that an elastic shell deforms more than a homogeneous sphere, subjected to the same force. Peale and Cassen (1979) described a runaway heating process that could occur in such a situation. Heating in the rigid shell melts material near the liquid core, thereby diminishing the shell thickness. The thinner shell undergoes greater deformation and thus has an increased local heating rate. The average dissipation increases dramatically as the shell thickness decreases. For a large solid planetary body, the dominant heat transfer process is solid-state convection. The heating rate, H, necessary to maintain a temperature difference, ΔT, across a solid-convecting layer of mantle was estimated from the relation:

$$H = 0.4\,\Delta T\, K\, Ra^{1/4} L^{-2},$$

where K is the thermal conductivity, Ra is the Rayleigh number and L is the shell thickness. As the shell thickness decreases, tidal dissipation exceeds, Elemental sulfur has unique physical properties: including very low thermal conductivity, a low melting temperature and a small value for the latent heat of fusion; all as compared to typical silicate materials. These properties, when combined with the calculated rate of internal heating, result in an extremely steep internal temperature gradient with melting occurring at depths of less than 500 meters. Estimated resurfacing rates can be achieved with less than ten percent of the planetary heat-flux being removed by the mass motion of surface flows and/or ejecta. Such a sulfur layer would most probably contain significant amounts of impurities, including the sulfides of sodium and other elements.

First order energy considerations, as well as spectroscopic observations are consistent with a very active, mobile planetary surface which is extensively covered with at least several hundred meters of sulfur.

References:

Nash, D.B. and F.P. Fanale (1977). Icarus, 31, 40.

Peale, S.J. and P.M. Cassen (1978). Icarus, 36, 245.

Peale, S.J., P.M. Cassen, and R.T. Reynolds (1979). Science, 203, 892.

Pollack, J.B. and R.T. Reynolds (1974). Icarus, 21, 248.

Witteborn, F.E., J.D. Bregman and J.B. Pollack (1979), Science, 203 643.

by an increasing amount, the energy which can be removed by solid state convection across a given ΔT. ΔT is taken as the temperature drop necessary for melting to be achieved. Thus, solid convection cannot prevent the molten region from rapidly spreading through the rest of the planet.

The result of this melting process is a planet with a molten interior and a thin, solid outer shell, the thickness of which is determined by conduction and, perhaps, such non-elastic phenomena as fracture. A conduction limited runaway results in a very thin shell indeed, of the order of 20 kilometers thick.

The observed lack of impact craters implies a very high rate of resurfacing of the planet. Preliminary estimates of the resurfacing rates necessary for such an efficient removal of impact craters show that very large internal heat sources are required.

Even though the tidal heating sources discussed above are more than an order of magnitude stronger than the radioactive heat sources, it may be shown that, if the resurfacing is accomplished with silicate materials, most of the energy released by both tidal dissipation and radioactive decay would have to be removed from the interior as heat of fusion and heat capacity of the resurfacing material. The processes which move molten materials, however, must be highly episodic, both in space and time, in order to permit traversal of kilometers of solid material. The bulk of the internal heat must therefore be removed by conduction. This requires that either the tidal energy source is considerably underestimated, or, the surface activity is occurring in some material other than silicates.

Pre-Voyager terrestrial-based spectroscopic studies of Io have indicated the possibility that there are large quantities of elemental sulfur at the surface (Nash and Fanale(1977)). Large amounts of sulfur ions have also been observed in the Jovian magnetosphere and their source is attributed to Io. It is thus appropriate to consider the properties and processes of a surface layer composed primarily of sulfur.

According to Pollack and Reynolds (1975) temperatures obtaining during the formation of Io were within the range in which H_2O was volatile but sulfur was not, indicating the possibility of near-solar abundance ratios of sulfur. For comparison, chondritic meteorites contain some 2-6% sulfur by mass, some of which is in the elemental form. If Io were to have a bulk sulfur content similar to the solar-nonvolatile and meteoritic values and, if the intensive heating to which Io has been subjected resulted in a complete differentiation and concentration of sulfur at the surface, there could be as much as 50 km of sulfur so emplaced. While the efficiency of the concentration process would not be expected to be nearly so efficient, as little as 500 to 1000 meters of sulfur, deposited as a surface layer, would be sufficient to produce profound consequences for the thermal state of the surface.

<u>Evolution of Ganymede and Callisto</u>. Patrick M. Cassen and Ray T. Reynolds, Theoretical and Planetary Studies Branch, NASA-Ames Research Center, Moffett Field, CA 94035. Stanton J. Peale, Dept. of Physics, University of California, Santa Barbara, CA 93106.

The mean densities of Ganymede and Callisto, the outer two of the four Galilean satellites of Jupiter are about 1.9 and 1.8, respectively. Their low densities indicate that these bodies contain substantial proportions of H_2O, perhaps nearly half their mass. It is likely that the H_2O and silicate phases have separated so that the satellites are composed of rocky cores surrounded by H_2O mantles (Lewis, 1971).

Normal radioactive abundances would be sufficient to maintain the mantles largely in the form of water, were it not for the effects of heat transfer by sub-solidus creep in the ice crusts (Reynolds & Cassen, 1979). To show this, it is only necessary to consider the thermal convection in the Ice I layer (which extends to depths of the order of 150 km in Ganymede or Callisto); but one must take into account the strongly temperature-dependent creep properties of the ice. If the Ice I layer was not convecting, Consolmagno and Lewis (1976) have shown that an ice crust of about 100 km thickness would exist on Ganymede; Callisto would have a thicker crust. But even with the unrealistically conservative assumption that the effective viscosity of the ice is given by the value at the upper (cold) boundary, the Rayleigh number is found to be super-critical for all crusts thicker than 30 km. Therefore, subsolidus convection is expected to occur in these bodies.

The heat transfer rates produced by convection can be estimated by using the methods of Schubert <u>et al.</u> (1979), wherein the thermal flux is expressed as a function of the Rayleigh number: $q \propto Ra^{1/3}$. For these calculations, the viscosity is taken to be that corresponding to the mean temperature of the convecting region, as suggested by the experiments of Booker and Stengel (1978). The minimum convective heat flux is thereby estimated to be about 35 ergs/sec-cm^2, an amount sufficient to solidify an entire water mantle in less than a few hundred million years. Therefore, we expect Ganymede and Callisto to presently be solid throughout. Furthermore, thermal conduction through the ice mantle is probably not sufficient to remove the heat generated internally by radioactive sources. Solid convection should therefore continue to occur to the present time.

The foregoing discussion applies to both Ganymede and Callisto. However, the recently obtained images of these satellites from Voyager I reveal remarkable differences in their surfaces, despite the general similarity of their internal structures as inferred from size and mass. Callisto appears to have an older surface than Ganymede's as estimated by the density of craters. In addition, Ganymede possesses extensive, strange, curvilinear features, possibly of tectonic origin, which have no counterpart on Callisto.

We can identify at least two candidate explanations for these differences, although detailed calculations, more data, or both, will be required to test their validity. First, as pointed out by Reynolds and Cassen (1979), ongoing subsolidus convection is capable of modifying the surface tectonically through the interaction of the cold, rigid crust and the underlying dynamic region. If Ganymede's allotment of radioactives is greater than Callisto's, as would be expected if the abundances of U, Th, and K are proportional to the silicate fraction, the heat flow through the outer conductive crust would be greater for the former, which would therefore make that crust thinner than Callisto's, at any given time. If the conducting outer crust of Ganymede were sufficiently thin during some past epoch (higher radioactively generated heat flows) for the internal convection to affect the surface morphology, such a condition would remain in effect longer for Ganymede than for Callisto.

A second hypothesis concerns the possibility that Ganymede's crust remained mobile longer, because tidal dissipation (which would be more important for the satellite closer to Jupiter) maintained a higher heating rate earlier in Ganymede's history.

References:

1) Booker, J., and K. Stengel, Further thoughts on convective heat transport in a variable-viscosity fluid, J. Fluid Mech., 86, 289-291, 1978.

2) Consolmagno, G., and J. Lewis, Structural and thermal models of icy Galilean satellites, in Jupiter, T. Gehrels ed., University of Arizona Press, 1035-1051, 1976.

3) Lewis, J., Satellites of the outer planets: thermal models, Science, 172, 1127-1128, 1971.

4) Reynolds, R.T. and P. Cassen, On the internal structure of the major satellites of the outer planets, Geophysical Research Letters, 6, 121-124, 1979.

5) Schubert, G., P. Cassen, and R. Young, Cooling histories of terrestrial planets, Icarus, in press, 1979.

Transient Brightening of Io at 5μm Wavelength: Remote Observations of Active Volcanism? J.B. Pollack, F.C. Witteborn, and J.D. Bregman, NASA-Ames Research Center, Moffett Field, CA 94035.

Medium resolution (∿1.5%) spectra of Io were obtained in the 1.2 to 5.4 μm wavelength domain from the 151-cm LPL/NASA telescope on Mt. Lemmon on the nights of February 20 and 21, 1978. Io's brightness in the 4.7 to 5.4 micron region was found to be about four times higher at an orbital phase angle of 68° than at orbital phase angles of 23° (taken 5½ hours prior to the brightening) and at 240° (taken 20 hours later). Such a large change in brightness far exceeds plausible variations due to a variety of error sources. In addition, independent observations by two other observing groups during the same time period provided confirmation of the reality of the brightening.

When the above observations are converted into plots of reflectivity as a function wavelength, Io is found to exhibit a high, flat reflectivity (∿.7) between 3.5 and 5.4 μm at times outside of the brightening event. However, the "apparent reflectivity" has values as large as about 3 near 5.4 μm during the brightening. Since phase integrals smaller than 0.6 are extremely unlikely, the brightening is not due primarily to a high albedo feature on Io's surface.

One category of explanations of Io's transient brightening involve the satellite's interaction with high energy particles coming from the circum-Jovian magnetosphere. For example, high energy bombardment of the surface material could cause luminescence in certain wavelength intervals. While there is no inconsistency between the amount of energy flux brought in by magnetosphere particles and the amount of excess radiation we observe, a rather high efficiency for luminescence (∿several tens of percent) is required. Alternatively, particle bombardment might cause temporary heating of individual surface grains. But, for this mechanism to work, extremely small grain sizes (∿0.01 μm) are required.

Voyager observations of Io suggest an alternative hypothesis for understanding the 5 μm brightening. Io was found to display active volcanism, a phenomena not observed elsewhere in the solar system aside from the Earth. We propose that the transient brightening of Io was due to volcanic activity, which manifested itself by a localized high temperature region on or above the satellite's surface.

If we adopt this hypothesis, we can obtain some first order estimates of the physical characteristics of the hypothesized volcanic event. To first order, the spectral shape of the excess radiation can be fit with a blackbody curve having a temperature of between 550°K and 600°K. It is to be noted that this temperature is much lower than that characteristic of silicate melts, but not that of sulfur melts. From the absolute value of the excess and the above brightness temperature, we find that the high temperature region covered about 0.02% of Io's surface area. Finally, a strong spectral feature is present near 4.6 μm and a weaker one near 5 μm. These features may provide clues on the composition of the volcanic effluent.

If our explanation for the 5 μm brightening is correct, then it may be possible to remotely sense active volcanism on Io from the Earth. By further determinations of the spectral signature of these events one may learn much about their physical characteristics. We plan to carry out further groundbased observations to pursue this possibility.

Active Volcanic Features on Io, Harold Masursky, U.S.G.S; Robert Strom, University of Arizona and Richard Terrile, J.P.L.

Evidence of active vulcanism on the Galilean satellite Io was first discovered on March 12, 1979 on a near encounter photograph obtained by Voyager 1 on March 4, (Smith and others, 1979). A greenish-white plume, rising more than 100km above Io's limb, was faintly discerned silhouetted against the blackness of space. Position of the feature, located approximately from the limb photograph, was determined from study of oblique photographs to be 248° longitude, 28° south latitude. Another eruption was also recognized on the same photograph as a white circular cloud on the nightside of the terminator.

Further study of the near encounter photographs has identified five additional plumes; locations of the seven plumes are shown on figure 1; coordinates for the plumes are:

Plume	Long.	Lat.
1	248	-28
2	300	+12
3	145	- 5
4	168	+20
5	97	+27
6	109	+16
7	212	-33

One plume remained active during the five day period March 2-March 6 when photographs were obtained of that area. Eruptive characteristics of the plume changed markedly over one six-hour period from near surface spouts to an umbrella-shaped dome rising more than 100 km in height. Pictures taken with filters having different wavelengths indicate that components of the plumes included both particulate material and gases.

Other areas where active volcanism is thought to be occurring at present have been recognized on the photos of Io. Such features include single and complex dark, elongate areas which may be fissures or swarms of fissures, and round depressions surrounded by ring-shaped, bright, surficial deposits. Several circular or elongate features with central calderas and radiating flows are also thought to be volcanic centers, althouth no eruptive plumes were observed emanating from them during the period of the first encounter.

In addition to the active volcanic centers discussed above, four areas were identified by the infrared interferometer (Hanel and others, 1979) where anomalously high temperatures were recorded:

Hot spot	Long.	Lat.
1	305	+ 7
2	290	-23
3	302	-25
4	263	-52

These hot spots (fig. 1) may indicate areas where volcanism has been active in the recent past. Measurements of the caldera at hot spot 1 indicate the floor is still warm and may consist of recently solidified lava. Hot spot 1 is located directly southwest of plume 2; the bright deposits that ring both features indicate that they both have been active recently. The crater with dark surrounding deposits at hot spot 4 closely resembles dark halo craters on the Moon which have been interpreted as explosive eruptive centers. Hot spots 2 and 3 are centered on smaller subcircular features which may have a similar origin. Hot spots, 2, 3, and 4 do not appear to be related genetically to plumes observed by Voyager 1.

Additional study and further enhancement of the Voyager 1 images may reveal evidence of other eruptions during the Voyager 1 encounter. Limb and oblique surface photographs obtained by Voyager 2 in July will be used to determine more precisely the duration of the volcanic events recognized from the Voyager 1 photographs.

References

Hanel, R.A. and others, Voyager IRIS experiment: Science, in press.

Smith, B.A. and others, Voyager Television experiment: Science, in press.

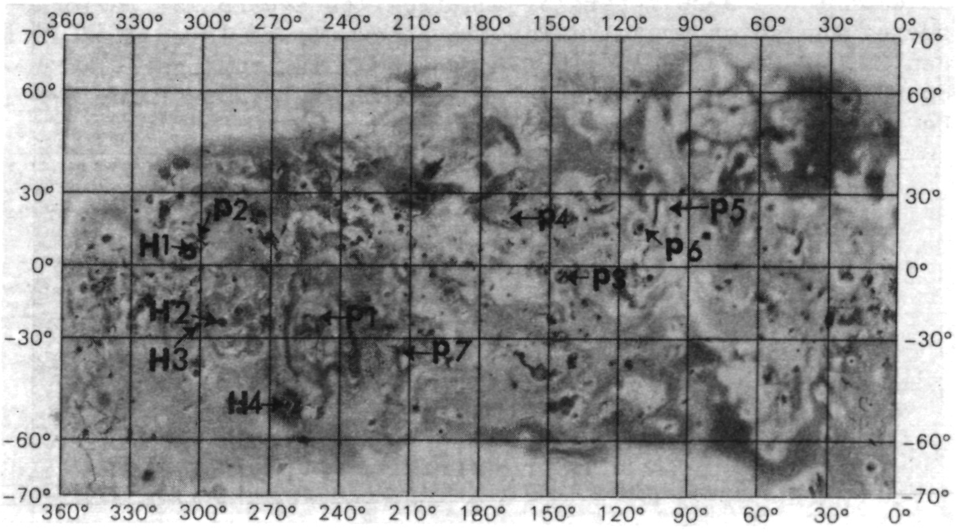

Figure 1. Preliminary shaded relief map of Io showing hot spot (H) and Plume (P) locations. The map was originally drawn by P. M. Bridges, United States Geological Survey, at scale 1:25,000,000 using a mercator projection.

Thermal Migration of Water on the Galilean Satellites. Norman G. Purves and Carl B. Pilcher, Institute for Astronomy, University of Hawaii, Honolulu.

The rates of thermal migration of water on the surfaces of the Galilean satellites have been studied by means of a computer simulation. The water ice on each satellite was assumed to have an albedo of 0.6 and to be in instantaneous thermal equilibrium with the insolation. Water molecules were assumed to evaporate from the surface with a Maxwellian velocity distribution and a Lambertian angular distribution (probability of emission at an angle θ to the local surface normal proportional to $\cos \theta$) at a rate determined by the ice temperature. At the vapor pressures involved, the molecules will follow ballistic trajectories. We assumed a unit accommodation coefficient and calculated the redistribution of water as a function of time on a stationary satellite at Jupiter's heliocentric distance. We then integrated along lines of constant latitude to get the time-averaged rates as a function of latitude for satellites with zero inclination.

The results show that the rate of water migration away from the equator of a Galilean satellite is a factor of $\sim 10^3$ slower than the rate for irreversible evaporation. The main reason for this effect is that more than half of the evaporating molecules impact the surface within 30 km of the point of evaporation, and more than 90% within 100 km. A molecule can only travel larger distances by executing a two-dimensional random walk on the surface of the sphere. We find, for example, that Europa will lose 25-30 meters of ice from its equatorial regions over the age of the solar system. This ice accumulates largely at latitudes between 25° and 40° and does not reach the polar regions. The lower albedo observed in the equatorial regions of Europa on Voyager images may be partially due to this process.

CRATER STUDIES: PRELIMINARY ASSESSMENT OF VOYAGER 1 DATA

J. M. Boyce*, U.S. Geological Survey, Flagstaff, AZ;
R. G. Strom, University of Arizona, Tucson, AZ; and
P. S. Collins, U.S. Geological Survey, Flagstaff, AZ

The Voyager 1 encounter with the Jovian system has provided the first opportunity for detail studying the solid surfaces of outer solar system bodies. Of the three satellites photographed at high enough resolution to confidently identify topographic features by Voyager 1, Io appears to be devoid of impact craters-probably due to its extremely active volcanism (Smith et al., 1979). However, both Ganymede and Callisto contain numerous impact craters. The impact craters on these satellites can be used in the same way as on the terrestrial planets to establish chronologies, crustal physical properties, and process that have modified their surfaces.

The hemisphere of Callisto photographed at high resolution is densely, and uniformly cratered except in the vicinity of a large basin. The density of craters within a radii of the basin rim is lower by a factor of about 2.5 than the surrounding terrain. Craters are observed from as small as the limit of resolution up to the basin which is about 600 km in diameter. Figure 1 is the cummulative size frequency distribution for craters on Callisto and shows that the distribution curve is of the form $N\text{-}KD^{-\alpha}$ (where N is the cumulative number of crater greater than diameter D, K is a constant and α is an exponent). Craters less than 70 km diameter have a slope (α) of about -4 and an absolute density value similar to ancient heavily cratered regions on the terrestrial planets. Craters between 70 and 100 km diameter have a slope (α) of about -10 indicating a rapid decline in number of craters in this range. There are no craters between 100 and 250 km diameter observed and only three larger than 250 km diameter.

The scarcity of craters greater than 70 km has been attributed to (1) selective destruction and disappearance of large craters as a consequence of viscous flow of icy crustal materials (Smith et al., 1979), or (2) a peculiarity in distribution of impacting population (Strom et al., 1979). We tentatively reject the viscous flow hypothesis because (1) there is now morphologic evidence that large craters are disappearing by shallowing, such as large flat craters observed near the limit of recognition (all large craters are easily

---

*Present address: NASA Headquarters, Washington, D.C.

recognized); (2) there is no satisfactory mechanism for reduction of relief of the large craters below that of smaller craters of a similar age; and (3) there are no craters of any morphologic state observed over a significant size range (100-250 km). Strom using the work of Woronow (1978) on crater population retention has indicated that the impact crater population observed on Callisto will retain its distribution function at the observed densities. Therefore, we suggest that the decline in numbers of large craters is a result of scarcity of impacting bodies that produced large craters and not in selective disappearance of large craters.

The general uniformity of crater density on Callisto (except in the immediate vicinity of the basin) suggests that the surface is uniform in age and that the dominant mechanism of resurfacing is by impact. Assuming that there has not been a later global resurfacing of Callisto, the crater population must be ancient - on the order of the age of other ancient heavily cratered terrains on terrestrial planets or about 4 billion years. The antiquity of the surface, and the retention of the primary crater population has significant meaning when combined with evidence that crater diameters are significantly enlarged by impact into icy or wet targets as compared to dry targets (The data of Boyce and Roddy, 1978, Boyce (1979) and Croft et al., 1979 suggests that the number of craters on Callisto must be reduced by a factor of approximately $N=K\ (D/2)^{-}$ to be directly comparable to crater populations on the terrestrial planets). This suggests that the cratering rate on Callisto may have been down by nearly an order of magnitude from that of the terrestrial planets and that the population of bodies that produced the abundant large craters on the terrestrial planets did not exist in the vicinity of Callisto and probably not in the entire outer solar system.

The crater populations on Ganymede has some significant differences from that on Callisto. Ganymede is divided into two terrain types 1) cratered terrain, and 2) grooved terrain (Smith et al., 1979 and Shoemaker, 1979). Craters are observed from as small as the limit of resolution up to nearly 100 km diameter. There have been no craters larger than 100 km diameter identified on Ganymede, though the cratered terrain contains several very subdued circular features several hundred kilometers in diameter with crudely concentric ridges that may be the remnants of ancient large craters or basins. Cumulative size-frequency distributions for the two terrain types are shown in Figure 2 and indicate that the distributions are also of the form $N=Kd^{-\alpha}$. However, the slopes (α) of the distribution curves are about -2 except in one grooved terrain area where the slope is -5. According to Shoemaker (1979) the density of craters in the cratered terrain is comparable to the density of the lunar highlands. The density of craters greater than 30 km diameter is similar to that on Callisto. The density of craters on the grooved terrain varies by a factor of 4, with the most densely cratered grooved terrain a factor of 5 lower in density than the cratered terrain. These data suggest that the grooved terrain is younger than the cratered terrain and that the grooved terrain developed over a period of time.

Though the statistics are poor, the large crater population on the cratered terrain appears to decline in manner, similar to that of the large craters on Callisto. We suggest that like on Callisto, this decline is due to peculiarities in the population of impacting bodies and that the cratering rate may have also been significantly lower on Ganymede compared to cratering rates on the terrestrial planets.

REFERENCE:

Boyce, J. M. (1979) this Volume

Boyce, J. M. and Roddy, D. J. (1978) NASA TM-79729, p. 163-165

Croft, S. K. et al., (1979) NASA CP-2072, p. 18

Shoemaker, E. M. (1979) this Volume

Smith, B. A. et al., (1979) Science in press

Strom et al., (1979) this Volume

Woronow, A. (1978), Icarus 34, 76

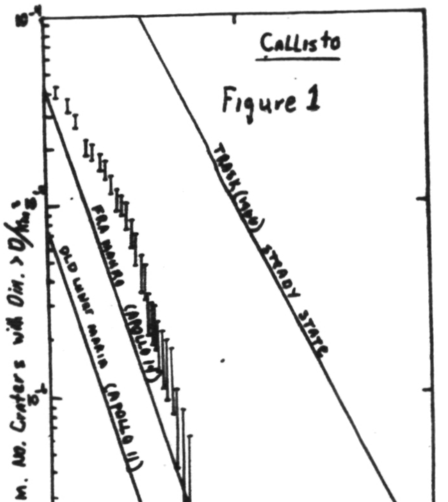

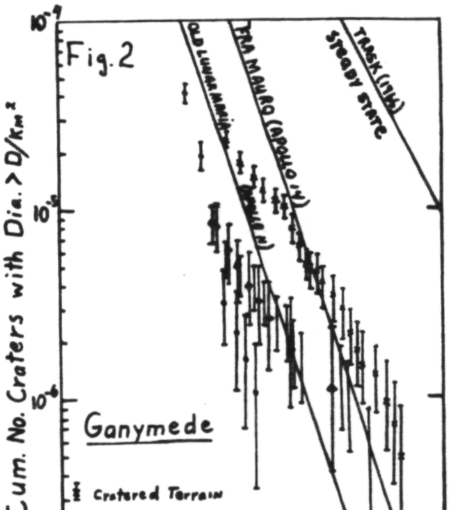

Io's Surface and Environs-A Magmatic Volatile Model. Bruce Hapke, Dept of Geology & Planetary Science, U. of Pittsburgh, Pittsburgh, PA 15260.

Io's Surface and Environs, B. Hapke (continued):

Page Intentionally Left Blank

Chapter 10

INSTRUMENT DEVELOPMENT AND TECHNIQUES

Mars Spectral Photometry and Surface Composition

D.L. Evans and J.B. Adams, Department of Geological Sciences, University of Washington, Seattle, WA 98195.

Introduction. The Viking lander cameras obtain images in three visible and three near-infrared bands; blue (∼0.4-0.5μm), green (∼0.5-0.6μm), red (∼0.6-0.73μm), IR1 (∼0.82-0.92μm), IR2 (∼0.9-0.94μm) and IR3 (∼0.93-1.1μm). We have developed a procedure that makes it possible to compare Viking multispectral images directly with laboratory reflectance spectra of terrestrial rocks and map surficial deposits at the landing site that have similar spectral characteristics as terrestrial samples.

Procedure. Voltages that would be measured by the Viking lander camera for a terrestrial rock type can be calculated based on laboratory reflectance spectra from:

$$V_i = c_i \int_0^\infty S(\lambda)\ T_i(\lambda)\ \rho(\lambda)\ d\lambda$$

where: V_i = camera output voltage for the i^{th} channel ($i = 1, 2 \ldots 6$)

$T_i(\lambda)$ = transfer function of channel i (Park, personal communication)

c_i = camera calibration constant determined from an image of the reference test chart obtained prior to the imaging of the scene used in this study (Park, personal communication)

$S(\lambda)$ = solar irradiance at 1.6 AU

$\rho(\lambda)$ = diffuse spectral reflectance measured in the laboratory

Diffuse spectral reflectance curves were obtained from twenty terrestrial samples using a Beckman DK-2A ratio-recording spectrophotometer. Using a computer program in which $T_i(\lambda)$, c_i and $S(\lambda)$ were stored and $\rho(\lambda)$ was read off the spectrophotometer, voltages for the six channels were calculated for each sample. In this study, all of the calculated voltage values were divided by the voltage value for the red channel to compensate for possible errors in the camera calibration constant. The Viking images used were also ratioed. Digital number (DN) values in the blue, green, IR1, IR2 and IR3 images were divided picture element by picture element (pixel) by DN values in the red image. A ratio of one was displayed as intermediate grey (DN=32) in the ratio images so that DN values could be found for the calculated voltages from $(V_i/V_{red}) \times 32 = DN$.

The ratioed Viking images were displayed on a General Electric Image-100 Multispectral Image Analyzer. For each ratio image, pixels with DN values determined from calculated voltage ratios were "alarmed" and displayed in various colors. The same pixels "alarmed" in all of the ratio images indicated a good match between the reflectance spectra of the laboratory sample and the material covering the portions of the scene that were "alarmed."

As a check on the validity of this procedure, the spectral reflectance values calculated by Huck *et al*. (1) for their Area 5 were used to calculate DN values. The calculated DN values and the DN values from the Image-100 for the same area are given below:

Channel	Calculated	I-100
Blue/Red	16.3	16
Green/Red	22.4	22
IR1/Red	30.5	30-31
IR2/Red	26.7	26-27
IR3/Red	25.1	25

Results. Of twenty samples used in this study, only a weathered basaltic pumice had spectral characteristics that matched the surficial deposits at the Viking 1 site. Figure 1 is the spectral curve of the pumice with 10% refelctance subtracted out and the spectral curve determined by Huck *et al*., (1) for Area 3 (Figure 2). Figure 2 is a Viking lander 1 scene in which the material with the same DN values as those calculated for the pumice are displayed in white. It is interesting to note that: 1) the soil shown in white has a rippled pattern in the foreground, 2) the soil in the trench and the rocks are not shown in white, and 3) Area 3 is shown in white.

The reflectance curve that matched the surface at the Viking 1 site was compared with an earth-based telescopic spectrum (2) of a bright area that was presumed to be similar to the global dust cloud (Figure 3). The spectra differed significantly in the near IR, however other laboratory spectra (Fig. 4) correspond to the telescopic, but not to the Viking lander multispectral images. A compositional difference may exist between the global dust and some of the surficial deposits at the Viking I site.

References

(1) F.O. Huck, *et al*. (1977) J.G.R. *28*, 4401-4411.
(2) T.B. McCord, *et al*. (1977) Icarus *31*, 25-39.

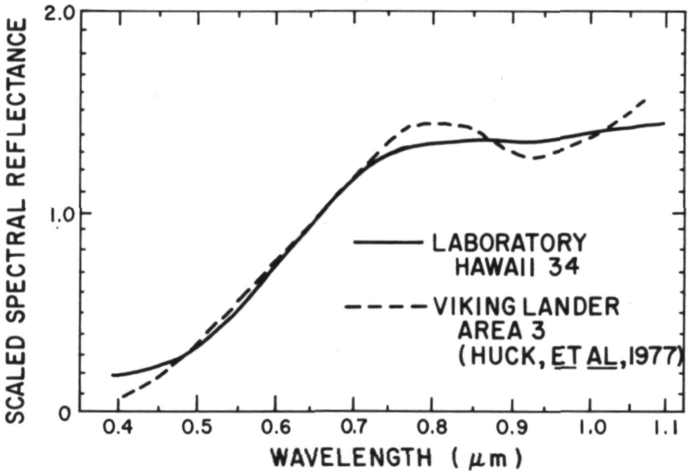

Figure 1. Spectral curve of the weathered basaltic pumice (Hawaii 34) and Area 3.

Figure 2. Viking Lander I scene. Material with same DN values as calculated for the weathered basaltic pumice are shown in white.

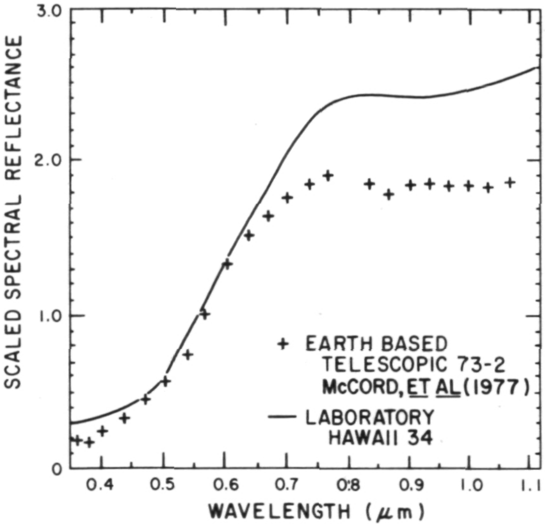

Figure 3. Spectral curve of weathered basaltic pumice (Hawaii 34) and bright area on Mars.

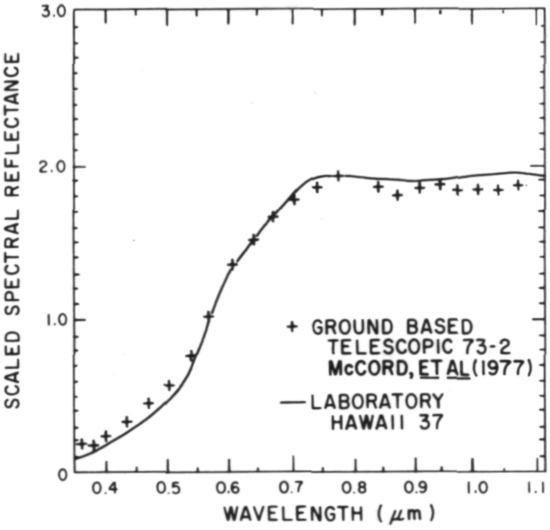

Figure 4. Spectral curve of weathered hyaloclastite (Hawaii 37) and bright area on Mars.

Precise Mars Relative Altitudes, D. W. G. Arthur, U.S. Geological Survey, Flagstaff, AZ.

The Viking Orbiter pictures of the Martian surface are at least as good as the best general coverage of the lunar surface (Orbiter) and also have a high degree of metric stability for local measurements. Such pictures can therefore be used for intense interpretation and at the same time precise measures of crater diameters and shadow lengths. This is just as well since the surface of Mars poses interpretation problems that are of a higher level of difficulty and complexity than are the case for the moon. Since the Viking Orbiter picture consists of a rectangular array of picture elements (pixels) uniformly spaced horizontally and vertically in the image, measurements can be achieved in these two directions by mere pixel counting. The counts are most conveniently performed on computer printouts listing 50x25 brightness values (one for each pixel) in as many pages as are required to cover the object of interest, the brightness values being in 7-bit (0 to 127) or 8-bit (0-255) modes. These printouts are from replicas of the original tapes without change of geometry and thus correspond to the original so-called rectilinear versions of the pictures. The hard copies, in the shading corrected versions (that is, with enhancement limited to simple linear stretches) are used merely to identify and delimit the lines and columns used in the pixel counts.

Shadow profiles are constructed by plotting brightness values along lines or columns of the printouts and the shadows themselves show as depressed sections with sloping ends, the slopes being due to instrumental blurring. The slope for the upper end is steep, that for the lower end rather gradual. The shadow ends are identified as points of maximum slope. Thus shadows of 40 pixel length are identified by counting to one pixel and thus to two or three percent. The limitations here may well arise from the limitations of the ephemeris. Deviations of shadow directions from the raw, column or diagonal raw directions are treated with simple geometric methods.

Rilles, grabens and scarps, casting shadows of less than 5 px cannot usefully be treated by pixel counts. An integration technique using the background brightness has been successfully applied to objects no higher than 10 meters casting shadows as short as 0.5 px.

The two methods have been applied to several hundred craters, grabens, faults, and channels. Current work on relative altitudes is associated with a very detailed crater-classification to overcome the problems arising from the extreme diversity of the Mars impact craters.

References

(1) Arthur, D. W. G., The depths of martian impact craters, in preparation.
(2) Arthur, D. W. G., Martian low relief determinations, in preparation.

BIRP - An Interactive Software System for Interrogation of Lunar and Planetary Image Engineering Data,

Raymond E. Arvidson, McDonnell Center for the Space Sciences, Dept. of Earth and Planetary Sciences, Washington University, St. Louis, Mo., 63130

BIRP consists of a number of modules (routines) for interactive interrogation of lunar and planetary image engineering data, such as slant range, latitude and longitude, solar incidence angle, etc. At present BIRP is written in FORTRAN IV-PLUS, while an ANSII standard FORTRAN (machine-independent) version is under development, and scheduled for release in August, 1979. BIRP is designed around parallel data files, whereby each engineering parameter is stored in a random access data file. The storage sequence is driven by the picture sequence, so that the first slant range value (for instance) in a file corresponds to the first picture acquired during the mission, the second value to the second picture, and so on. The software sets-up a bit map on disk and in core, where each bit corresponds to one picture. BIRP centers around searches of the parallel data files based on user constraints (Figure 1). Those pictures that do not meet search constraints are de-flagged (re-set) in the bit map so that the next search done, on another data file, is simplified because only flagged (set) bits and corresponding locations in the engineering data file need be searched. Thus, search times are continually reduced as more and more files are interrogated, because searches are done only on the sections of the files that correspond to flagged bits (pictures that fulfill constraints). Upon user-cue, the software can be commanded to print-out a specified set of engineering data for those pictures that fulfill search constraints. At present, the user can also command the software to drive an automated microfiche machine for "quick-looks" of the pictures. Hopefully, the microfiche reader will be replaced with an analog videodisk for more reliable, and faster access of images. In our PDP-11/34, BIRP is heavily overlayed, and requires only 15,000 words of core to run. By removing text prompters and other luxuries, a stripped, overlayed BIRP could run in as little as 5,000 words of core. In test runs of BIRP, using 1600 Viking Lander pictures, a typical search time through a data file is slightly less than one second.

AUTOGEN is a set of ancillary routines that create parallel data files from SEDR (spacecraft engineering data record) tapes. Basically, AUTOGEN needs a random access file in the SEDR format, which usually has all engineering data for a given picture on one record. AUTOGEN's job is to then rip apart the records, creating new files that are BIRP-compatible, parallel data files. AUTOGEN also allows each institution using BIRP to custom design their set of data files, leaving off those parameters that are of little utility to them and adding others that are of more interest. Finally, a bit map that is the result of a given search session can be stored as a BIRP-compatible data file.

USER-ORIENTED BIRP FLOW CHART

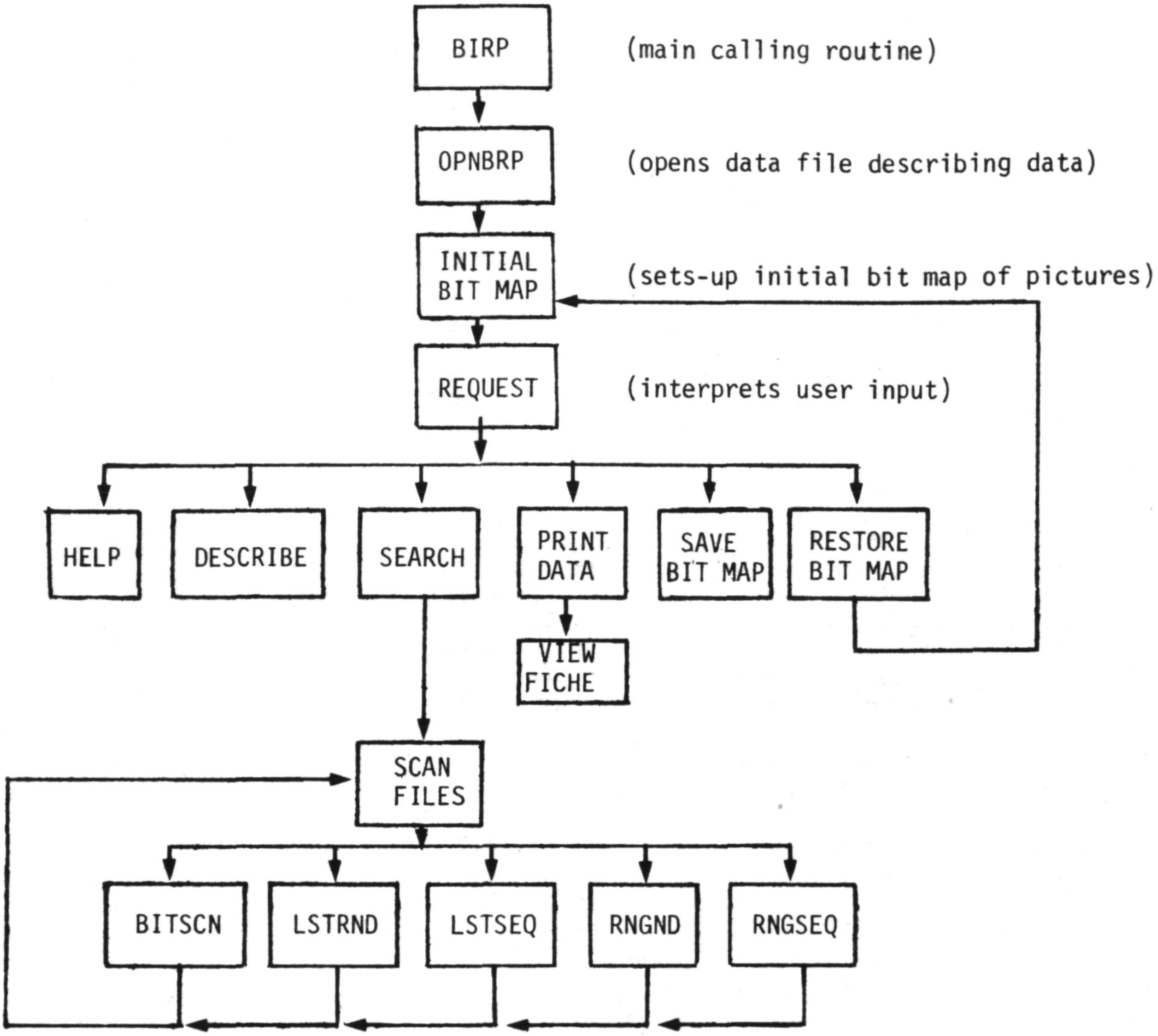

Figure 1: A user-oriented or functional flow diagram for BIRP, simplified considerably to show dominant features. All options end with a call to REQUEST, which prompts the user for what is to be done next. At any point in the program, HELP can be entered and a description of options available to user will be printed out. DESCRIBE prints out a description of the data files. The five routines at the bottom are the workhorses of BIRP and each has been designed for fast searches of specific kinds of data files. BITSCN scans bit files (yes or no), LSTRND and and LSTSEQ scan files that consist of lists of data (filter position, for example), RNGSEQ scans sequential data based on a user-specified range (VL sol range, for example), while RNGRND searches a range for random data, such as solar elevation.

Mid-Infrared Reflectance Spectra for Planetary Surface Study.

G. P. Meeker, G. R. Rossman and A. L. Albee, Division of Geological and Planetary Sciences, California Institute of Technology, Pasadena, CA 91125.

It is the purpose of this report to evaluate the information which could be obtained by using mid-infrared (2.5 - 40 μm) reflectance spectra on board a lander spacecraft, to examine rocks, minerals, soils and weathering products on a planetary surface. Samples would be illuminated from an onboard incandescent source and the spectrometer would operate similar to laboratory spectrophotometers. Samples would consist of rocks, aggregates, and powders and would be examined with no sample preparation other than the need to position them in the optical path.

Experimental. Radiation from the sample beam of double beam infrared spectrophotometer is reflected onto a sample by a microreflectance apparatus, collected, ratioed against a reference beam containing a standard mirror reflector and attenuators, and presented in a linear absorbance mode. Samples consisted of mineral and rock powders of various particle sizes, and whole rock specimens run "as-is" on both fresh and weathered surfaces.

Results. Reflection spectra provide much of the same information which can be obtained from transmission spectra and can generally provide significantly better quality data than emission spectra (Figure 1). Chemical groups such as carbonate and silicate can be readily distinguished, the mineralogical family of most silicates, alumino-silicates, carbonates, sulfates, etc. can be ascertained, and with single phase samples, the mineral species can frequently be identified. Absorbed and structural water can be detected, several individual phases in rocks can often be identified and the general rock type can be determined from the overall appearance of the reflectance pattern. The silica content of rocks can be estimated from the reflectance spectra. Spectra of freshly broken surfaces show a shift of the vibrational bands of the tetrahedral framework in the 900 to 1200 cm^{-1} region to lower wavenumbers as rock compositions vary from felsic to mafic (Figure 2). Quantitatively more useful is the correlation between SiO_2 concentration and the position of the principal Christiansen frequency (Figure 3). For about 90% of the rocks examined, the silica content could be determined to within 10% for mafic rocks and to within 15% for felsic rocks from the position of the principal Christiansen frequency alone.

Particle Size. The effects of particle size can complicate the nature of the reflection spectrum. When the particles are large, a major component of the reflected radiation is the result of specular (surface) reflection. When the particle size is small compared to the wavelength, diffuse (internal) reflection dominates. For particle size comparable to the wavelength (e.g. < 38 μm in Figure 4) spectra comprised of both specular and diffuse components are obtained. Most crystalline rocks examined produced spectra with the specular component dominant in the 200 - 1400 cm^{-1} region. The quality of spectra obtained from fine powders can be improved through compaction. Figure 5 illustrates how the spectrum of andesite powder becomes more specular upon compaction.

Water. Specular reflection from water and hydroxide ion stretching modes is observed in the cases of single-crystal hydrated minerals and polycrystalline, nearly monomineralic rocks such as gypsum. Usually, the water absorption is observed as a broad, diffuse reflection in the 3000 - 3700 cm^{-1} region. Hydroxide ion features from clays and micas are usually observed in the 3500 - 3700 cm^{-1} region as diffuse reflections of comparatively narrow line width. Changes in the desorption and sorption of water in response to heat and vacuum are illustrated in Figure 6 for a 74 - 43 μm powdered andesite initially of 5 % surface water. The spectra readily detect the loss of 3 % H_2O on heating. Weathering rinds and superficial coatings can modify or obscure the reflection properties of the underlying rock. The effects of weathering on the reflectance pattern of most rocks include the modification of the intensity of the spectral bands, the addition of contributions from the weathering products themselves, and an increase in the amount of diffuse water reflectance (Figure 7). In the extreme case of a coating of desert varnish, the reflectance spectra demonstrate the progression from fresh rhyolite to a dominantly illite-montmorillonite coating (Figure 7).

Conclusion. Reflectance spectra in the mid-infrared region are capable of providing information about mineralogy and petrology with a minimum of sample preparation and would have value both for study of materials on a planetary surface and for selection of samples for sample return. Because the spectrometer would provide its own source, cryogenic detectors would not be required, and spectra could be obtained to wavelengths as long as 40 μm.

Reference. Conel, J. E. (1969) Infrared emissivities of silicates: experimental results and a cloudy atmosphere model of spectral emission from condensed particulate mediums. J. Geophys. Research, 74, 1614-1634.

Figure 1. Comparison of reflectance and emittance (Conel, 1969) spectra of 38 μm quartz particles and a KBr absorption spectra. Spectra are presented such that maximum signal at the detector is at the lower portion of the trace.

Figure 2. Reflectance spectra of representative rocks ranging from felsic to ultramafic in composition.

Figure 3. Variation of the principal Christiansen frequency peak (indicated by the arrow by the granite spectrum in Fig. 2) as a function of SiO_2 content for 42 different rocks.

Figure 4. Variation of spectral pattern of andesite powder with particle size.

Figure 5. Reflectance spectra of andesite powder showing the increase reflectance in the 800 - 1200 cm^{-1} region produced by compaction of the surface.

Figure 6. Changes in the intensity of the O-H region of powdered andesite in response to heat and vacuum.

Figure 7. Reflection spectra of fresh and weathered surfaces.

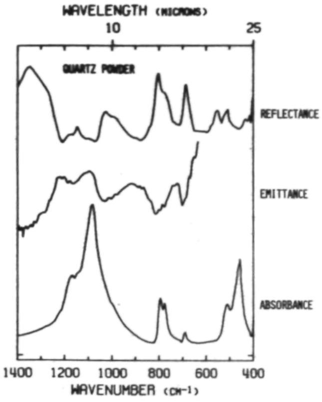

FIGURE 1

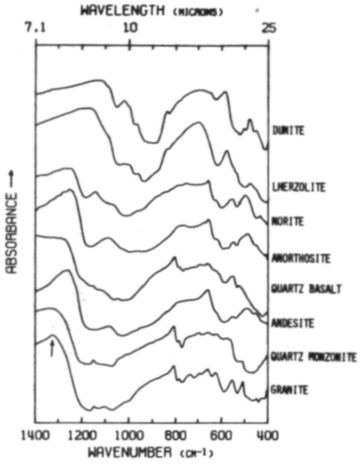

FIGURE 2

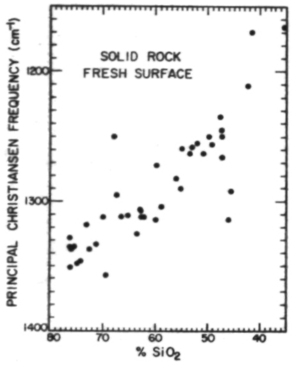

FIGURE 3

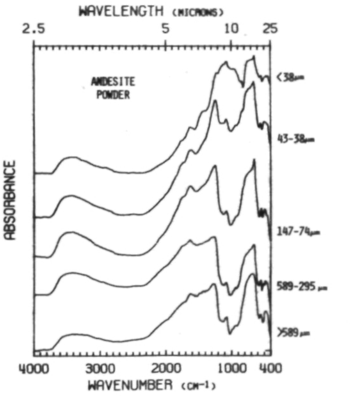

FIGURE 4

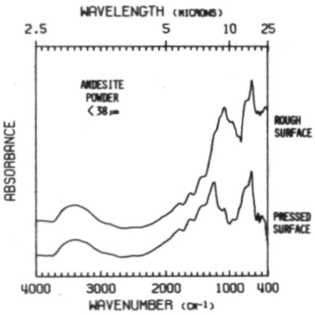

FIGURE 5

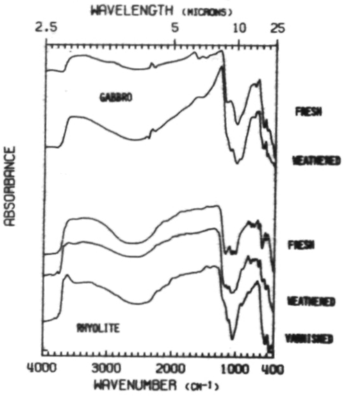

FIGURE 7

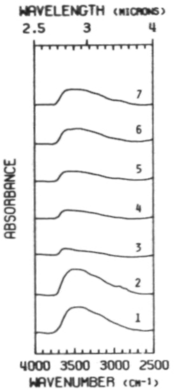

WATER CONTENT IN POWDERED ANDESITE

PROCEDURE	EFFECT ON WATER BANDS
1 INITIAL SAMPLE	
2 SAMPLE HEATED TO 120 °C FOR 24 HRS. IN EVACUATED CONTAINER	NO OBSERVABLE CHANGE
3 SAMPLE HEATED TO 420 °C FOR 24 HRS.	INTENSITY GREATLY REDUCED
4 SAMPLE LEFT IN 38% HUMIDITY AT ROOM TEMPERATURE FOR 24 HRS.	LITTLE OR NO INCREASE IN INTENSITY
5 SAMPLE COVERED WITH WATER AND DRIED UNDER AN INFRARED LAMP AT 46 °C	SLIGHT INCREASE IN INTENSITY
6 SAMPLE COVERED WITH WATER FOR 7 DAYS AND DRIED AS ABOVE	SIGNIFICANT INCREASE IN INTENSITY
7 SAMPLE HEATED TO 120 °C FOR 24 HRS. IN EVACUATED CONTAINER	NO OBSERVABLE CHANGE

FIGURE 6

A Simple Interactive System for Extraction of Topography from Stereo Digital Images, Steven W. Lee, Edward A Guinness, Lawrence K. Bolef, and Raymond E. Arvidson, McDonnell Center for the Space Sciences, Dept. of Earth and Planetary Sciences, Washington University, St. Louis, Mo., 63130

One of the problems in photogeologic interpretation of lunar and planetary data sets has been the availability of and the rapidity with which topographic data has been delivered to a user. For instance, in our analyses of the Apollo 17 landing site, vertical topographic profiles from pan photography were requested of the DMAAC for a number of craters located in the central cluster feature. The request was generated in 1975 and we have yet to receive the profile data sets. To circumvent such a problem, we are developing a relatively simple interactive software/hardware system for real-time extraction of relative heights, slopes, and surface roughness from digital stereoscopic image data.

Our system, called TOPOM, is based largely on the RANGER system that was developed to cope with topographic mapping of the Viking landing sites (Liebes and Schwartz, 1977). TOPOM utilizes a PDP-11/34 computer, a video monitor for display of left and right stereo image pairs, and a joystick that controls the position of two cursors on the video display. At present, Viking Lander topographic data can be acquired by identifying, via cursor position, corresponding points in the two images. These points provide the system with the requisite information to compute x,y,z values, relative to a user-specified coordinate system.

Figure 1 illustrates the result of a ranging session, with the selected points connected by lines. Figure 2 shows the resultant distribution of surface elevations as a function of range from the camera. Elevation systematically increases with range, probably because the stereo traverse was directed toward the rim of a small impact crater just over the horizon, as seen on high resolution Viking Orbiter images. Comparison of the traverse x,y,z data with RANGER-produced data shows virtually no difference out to 60 meters range.

On-going development of TOPOM includes constraining the traverse to vertical or horizontal planes, in order to generate vertical profiles or contours. Heights and profiles of pedestal craters and other features indicative of the extent of aeolian deposition or stripping will be determined from Viking Orbiter image data, utilizing the reduction methods of Benesh (1978). The intent is to provide a constraint of the thickness of wind-blown material and on turnover timescales of the deposits.

References:

Benesh, M., 1978. Viking Orbiter Stereophotogrammetry, Photogrammetric Engineering and Remote Sensing, v.44, pp. 265-271.

Liebes, S., and Schwartz, A., 1977. Viking 1975 Mars Lander Interactive Computerized Video Stereophotogrammetry, Journal of Geophysical Research, v. 82, pp. 4421-4429.

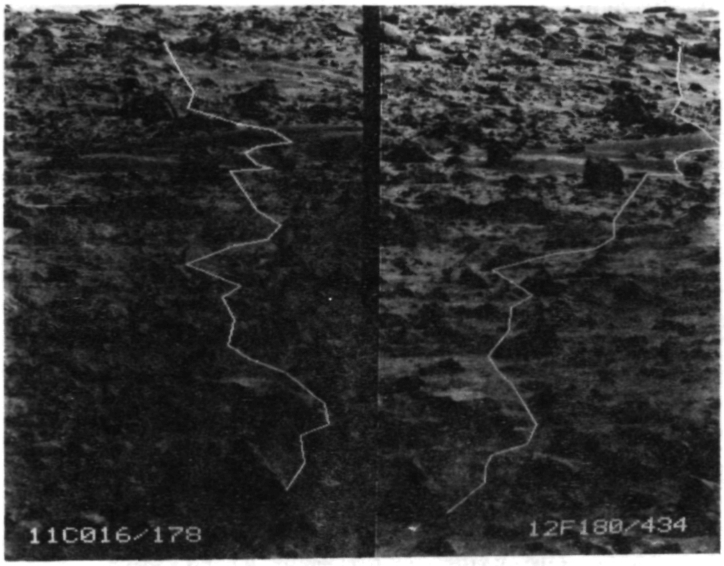

Figure 1: An example of a ranging session using VL1 imagery: the white trace connects conjugate points chosen in each image.

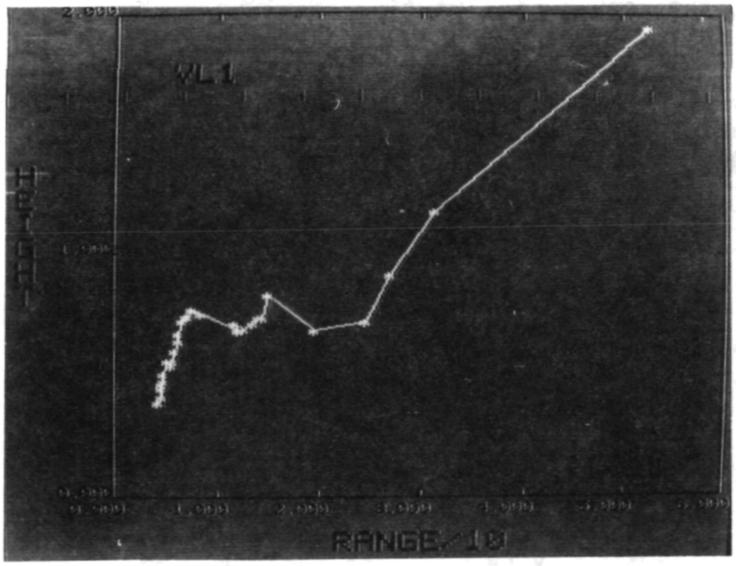

Figure 2: An elevation-vs-range plot for the points shown in Figure 1, as computed by TOPOM. Both axes are in units of meters. The drift field crossed by the traverse in Figure 1 is evidenced by the two elevation peaks between 5 and 15 m. in range. The increase in height with range probably corresponds to the ejecta blanket of a nearby small crater (near the horizon in Figure 1).

Scattering of Light from Particulate Surfaces. IV. Photometric Functions for Surfaces of Arbitrary Albedo

- J. Goguen and J. Veverka, Laboratory for Planetary Studies, Cornell University, Ithaca, New York 14853.

We have measured the scattering properties of a series of particulate surfaces with normal reflectances ranging from 0.04 to 1.0, to determine how the photometric functions change as the degree of multiple scattering within the surface increases. One by-product of these measurements is that we can see how well the scattering properties of such surfaces can be described in terms of Minnaert parameters (B_o and k). We have determined B_o and k for phase angles up to 120° for points corresponding to the photometric equator ($\psi = 0°$) of a planet, and for points along a mirror meridian ($i = \varepsilon$). [Here i = angle of incidence, ε = angle of emission and ψ is the photometric longitude.]

On the basis of theoretical arguments Noland and Veverka (1979) and Goguen and Veverka (1979) have pointed out that the scattering properties of surfaces cannot be described accurately in terms of Minnaert coefficients except at $\alpha = 0°$, no matter what the albedo. The problem is that in general for $\alpha \neq 0°$ unique (B_o, k) values cannot be defined which satisfy all points on a planet's disk. Specifically, points along the photometric equator will yield (B_o, k) values which differ from values derived from points along any meridian. These predictions have now been confirmed by actual measurements on particulate surfaces in the laboratory.

Figure 1 shows (B_o, k) as a function of α both for points along the photometric equator and for those along the mirror meridian, for a sample whose normal reflectance is 0.69. Even for such a bright surface the B_o's and k's differ considerably for the two sets of points when $\alpha > 0°$ The maximum difference in this case occurs near $\alpha = 75°$: along $\psi = 0°$, $k = 1.03$, but along $i = \varepsilon$, $k = 0.77$. The non-uniqueness of (B_o, k) was observed in all the samples studied, confirming the predictions of Noland and Veverka (1979) and Goguen and Veverka (1979). In overall appearance Figure 1 strongly resembles similar plots obtained theoretically by Goguen and Veverka (1979) for a semi-infinite cloud of scattering particles.

The laboratory measurements are being used to develop a theoretical photometric function which will match the observed scattering properties of particulate surfaces of arbitrary albedo.

References

Goguen, J. and Veverka, J. (1979). Scattering of light from particulate surfaces. III. Non-validity of a Minnaert description for optically thick, multiply scattering layers. (Submitted to Icarus)

Noland, M. and Veverka, J. (1979). Scattering of light from particulate surfaces. II. Non-validity of a Minnaert description for dark surfaces. (Submitted to Icarus)

Veverka, J., Goguen, J., Yang, S. and Elliot, J. L. (1978). Near-opposition limb darkening of solids of planetary interest. Icarus 33, 368-379.

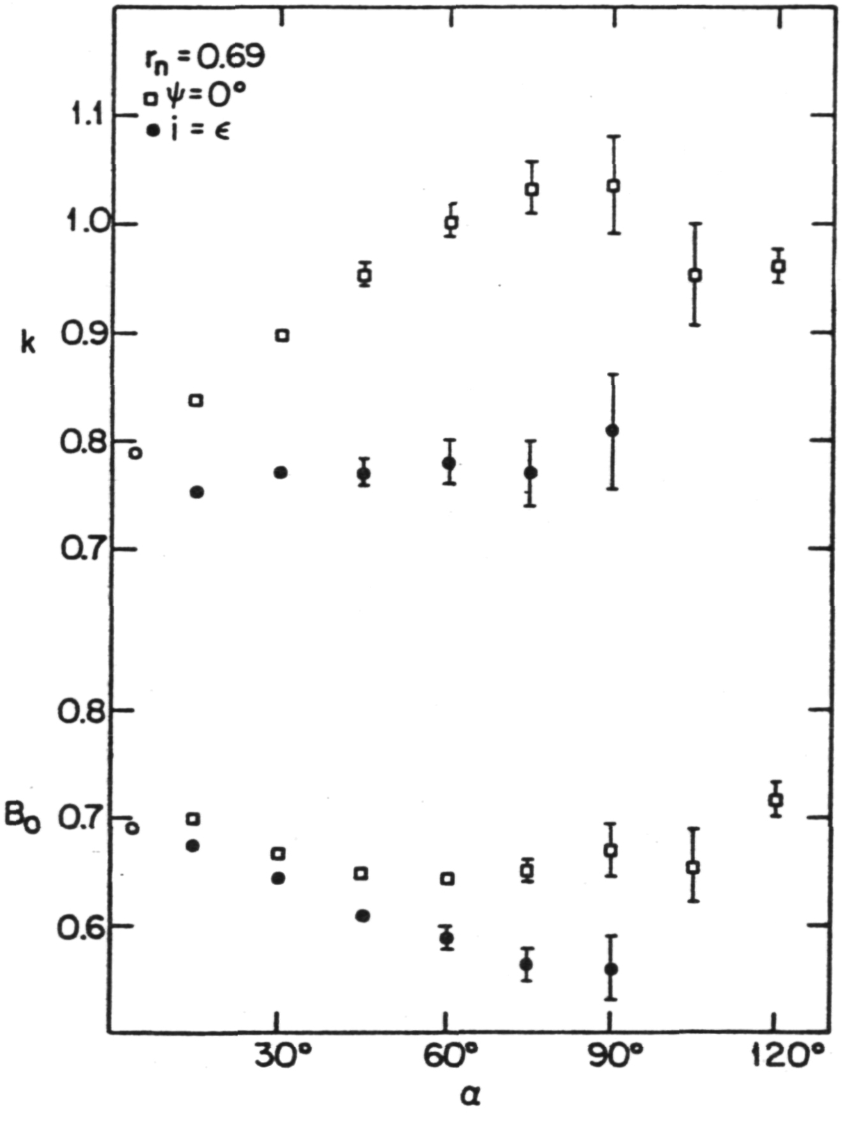

Figure Caption

Figure 1 Minnaert parameters B_o and k as a function of phase angle α for a mixture of MgO and charcoal with a normal reflectance of 0.69. Squares represent the brightness along the photometric equator $\psi = 0°$ and filled circles the brightness along the mirror meridian $i = \varepsilon$. Open circles are from Veverka et al (1978). Note that a unique (B_o, k) cannot be defined for a fixed α.

Water Instrument Development, James B. Stephens, Jet Propulsion Laboratory, California Institute of Technology, Pasadena, CA 91103

Background. The origins of water instrumentation for planetary explorations are rooted in the early lunar and planetary programs. Several specific water instruments; a quartz crystal microbalance atmospheric water detector, a differential scanning calorimeter soil water analyzer and an electrolytic soil water analyzer were developed for the Viking mission but were never flown. The need for such water-specific instrumentation is now clearly demonstrated by our inability to clearly understand the role of water in the martian environment. This is because of the lack of direct measurements of water in the soil and atmosphere of Mars.

Approach. With the above experience in mind, an electrolytic water analyzer instrument was conceptually designed and proposed as part of the Comet mission's Microprobe for Analyzing and Imaging Dust (MAID) Instrument. The function of this water instrument is to measure the amount of water contained in the Comet particles and to remove (pump) this water from the instrument in order to prevent the contamination and degradation of the electron beam filament. The absolute and water specific sensor will provide a direct measurement of water which can not be accomplished by any of the other likely candidate instruments proposed for the mission.

Instrument Description. The water analyzer consists of an extended surface of an electrolytically regeneratable hydroscopic material (P_2O_5 or a solid polymer electrolyte) with appropriately spaced electrodes. This water sensitive element is mounted on the inside of an appended cavity which is in communication with the MAID instrument through a large conductance vacuum valve.

Water is outgassed from the Comet particles in the MAID instrument by heating the surface to which they are attached. The water travels by free molecular flow through the vacuum valve onto the hydroscopic material where they are absorbed. After most of the water has had time to travel to the hydroscopic surface the vacuum valve is closed and a voltage is applied to the aforementioned electrodes. The water is electrolytically disassociated into H_2 and O_2 which is allowed to escape to space through another valve. The current required for disassociation is a direct measure of the water that was evolved from the Comet particles. This process also acts to remove (pump) practically all the water from the MAID instrument and prevent water from contacting the electron-beam-column tungsten-filament.

A Color-Ratio Map of Mercury. Bruce Hapke, Dept. of Geology & Planetary Sciences, U. of Pittsburgh, Pittsburgh, PA 15260.

A color map of the portion of the planet Mercury imaged by Mariner 10 was constructed from images taken through the orange (0.575μm) and UV (0.355μm) filters. Medium-resolution images were photometrically decalibrated, registered and ratios of OR to UV brightness calculated. The ability of this process to depict real variations in the slopes of the reflectance spectra of parts of the planet depends critically on camera linearity. Unfortunately, the camera heaters had been turned of during the second and third flybys, changing the calibration sufficiently to make the images useless for color. Thus, only areas imaged on the first flyby were used. Further complicating the reduction were blemishes on the faces of the vidicons which could have indicated spurious, highly-colored regions. In order to prevent blemish-induced false color, at least two independent color-ratio images were made for every region of the planet seen on the first flyby. All ratio images were combined into a map of the planet.

Just as the albedo contrasts on Mercury are smaller than on the moon color differences seem to be less pronounced also. The major features of large color are rays and new craters, which tend to be blue. No color difference associated with the planet-wide scarp system could be found, strengthening the interpretation of these features as faults. Few color features similar to the lava flows in the lunar maria could be found. The spectral homogeneity implies large-scale chemical homogeneity, at least as far as those elements which affect the color, such as iron, are concerned. There are a few regions of large color difference which are not associated with albedo differences. Two interesting regions of large color contrast are a red spot in the Michalangelo Quadrangle, which may be associated with the central mound of a large crater, and a patch in the crater Muraski, near Kuiper.

The Spectral Reflectance of Mercury: A Search for Absorption Bands.

B. Hapke, Dept. of Geology & Planetary Sciences, U. of Pittsburgh, Pittsburgh, PA 15260.

Although the spectral reflectance of Mercury is very similar to the moon's, absorption bands which might be indicative of composition are extremely subdued on Mercury. We have previously described a spectrum in which a band about 4% deep and centered at 1.03μm was found. This band could be due to either diopside or forsterite. Recently McCord has reported a band at about 0.90μm, which is consistent with low-Ca pyroxenes. We have obtained a spectrum in the 0.8-2.5μm wavelength region using the facilities of Kitt Peak Obs. A feature in the vicinity of 1μm appears to be present, but we have not yet been able to accurately determine the central wavelength of the band. A second band seems to be present at 2.25μm. This band is consistent with a high-Ca clinopyroxene such as diopside and implies that Mercury probably has a low-Fe, high-Ca, differentiated, basaltic crust.

The Photometric Function of Martian Soil in the Vicinity of Viking Lander 1.

Bruce Hapke, Dept of Geology & Planetary Science, U. of Pittsburgh, Pittsburgh, PA 15260.

A special photometric sequence of images was taken by Viking Lander 1 throughout the Martian day on Sol 29. This sequence has been partially reduced. Although absolute camera calibration is a problem, the principal uncertainty in deducing the photometric properties of the Martian soil are the effects of the sky aerosols. Light scattered diffusely by the aerosols was taken account of by photometry of interiors of shadows. Direct illumination attenuated by the aerosols was estimated from measurements reported by Pollack et al.

In the raw images the photometric function of the soil appears quasi-Lambertian. However, after correcting for the sky aerosols the function is found to be strongly backscattering in a manner similar to the moon. This large opposition effect is apparently partially masked by the atmospheric dust in earth and satellite photometry. The soil is inferred to have a normal albedo in the green at a phase angle of 5^0 of 0.18. The average single scattering albedo of the soil particles as a function of wavelength has a maximum near 0.8μm, which is close to the wavelength reported for the sky aerosols by Pollack et al. However, the average single scattering albedo of the soil particles is about twice as large as the albedo of the sky aerosols. Evidently the absorbing component responsible for the color of the sky and soil tends to be concentrated by the comminution and levitating processes which maintain the atmospheric dust. It is not possible to identify the composition of the absorbing mineral because many plausible substances have absorption minima near 0.8μm.

Chapter 11

PLANETARY CARTOGRAPHY, GEODESY AND GEOLOGIC MAPPING

Page Intentionally Left Blank

Mars cartography: 1979, R. M. Batson, U. S. Geological Survey, Flagstaff, Arizona 86001.

Compilation of maps of Mars at a variety of scales is continuing. The map series and their status are as follows:

1:15,000,000 shaded relief map of Mars -- Four sheets are contained in this series. Two of the sheets are on Mercator's projection and extend from 0 to 180 deg and from 180 to 360 deg west longitude. Both sheets extend from 57 deg south latitude to 57 deg north latitude. The two polar sheets extend from the poles to 55 deg north and 55 deg south latitude, respectively. Map scales are 1:15,000,000 at the equator, 1:8,389,000 at the 56 deg parallels, and 1:9,172,000 at the poles. Controlled photomosaic bases are in progress, and will be completed in FY79. The final airbrush shaded relief rendition of the 0 to 180 deg Mercator sheet is scheduled for completion during FY79.

1:5,000,000 shaded relief map of Mars -- First editions of all 30 sheets in this series have either been published or are in press. Most of these were compiled with Mariner 9 data, and can be significantly improved by additing details from the much higher resolution Viking Orbiter pictures. Selected sheets in the 1:5,000,000 series are being upgraded by modifying the original airbrush drawings to incorporate the newer Viking data. A total of 8 such revisions are planned for FY79.

1:2,000,000 maps of Mars -- Mars was divided into 118 quadrangles for mapping at a scale of 1:2,000,000. The majority of these map sheets are controlled photomosaics tied to the Viking triangulation (Davies and others, 1978), but selected quadrangles are being rendered in a variety of ways in addition to the basic controlled photomosaics. These include shaded relief renditions where the pictures in the photomosaic have dissimilar illumination, resolution, or viewing angles, or where clouds or haze obscure parts of the surface; color mosaics (Batson and others, 1979a), where good Viking color data exist; contour maps (Wu, 1979), where stereoscopic coverage is available; and orthophoto mosaics (Batson and others, 1979b) where contour maps are available. Fifty-six photomosaics are planned for completion during FY79, as are four shaded relief maps. The color mosaics and orthophoto mosaics are developmental, and no commitment has been made as to total numbers to be completed during FY79, but 32 color mosaics and one orthophotomosaic are being compiled at the 1:2,000,000 scale.

Special area maps of Mars -- Many areas on Mars are of specific scientific interest, and their unique characteristics are not shown adequately on existing systematic maps. Special scales, projections and formats are therefore specified for maps of these areas. For example, orthophotomosaics at scales of 1:5,000,000 are being compiled, centered on Tithonium Chasma, Arsia Mons and Olympus Mons. A controlled photomosaic at 1:5,000,000 of Borealis Chasma is in progress, as is a controlled photomosaic on a stereographic projection at 1:5,000,000 of the Chryse Planitia. An airbrush shaded relief version of the latter is also planned.

References

Davies, M. E., Katayama, F.Y. and Roth, J.A., 1978, Control net of Mars: February, 1979; The Rand Corporation, R-2309-NASA, Feb 1978.

Batson, R.M., Hall, D. G., and Jordan, JoAnne, 1979a, Color mosaics of Mars, in Proceedings of the Planetary Geology Principal Investigator's Conference, Brown University, June 6-8, 1979.

Batson, R.M., Hall, D.G. and Edwards, Kathleen, 1979b, Orthophotomosaics from monoscopic Viking Orbiter Pictures, in Proceedings of the Planetary Geology Principal Investigator's Conference, Brown University, June 6-8, 1979.

Wu, S.S.C., 1979, Mars photogrammetry, in Proceedings of the Planetary Geology Principal Investigators Conference, Brown University, June 6-8, 1979.

An orthophoto mosaic of Tithonium Chasma, R. M. Batson, D. G. Hall and Kathleen Edwards, U. S. Geological Survey, Flagstaff, Arizona 86001.

A technique was developed for removing image parallax that results from large surface relief. The technique was developed and tested on the Tithonium Chasma area of Mars; a section of the Valles Marineris covering about 2500 sq. km. with more than 9000 m of relief. The method consists of projecting an image on a three-dimensional terrain model of the area covered by the image, and then viewing this three-dimensional projection from a location other than that from which the picture was originally taken.

The digital terrain model consists of a raster of topographic elevations derived from a contour map of the area prepared by Wu (1979). The map was compiled from 23 stereo models. Two images of lower resolution than those used in the stereo mapping were reprojected to make the orthophoto mosaic. After these pictures were selected, the terrain model was rotated so that it could be viewed from the same point above Mars as that from which one of the pictures was taken. The model was illuminated digitally in the same way the surface was illuminated when the picture was taken so that the picture could be accurately superimposed on the model. The two files were then merged, so that the topographic elevation of each picture element became part of the image file. The composite image was rotated to a transverse Mercator view and mosaicked digitally to the other image after it had undergone the same treatment.

Reference:

Wu, S.S.C., 1979, Preliminary topographic map of the Tithonium Chasma and Ius Chasma of Mars: U. S. Geological Survey.

PHOBOS, DEIMOS AND MARS GEODESY AND DYNAMICS. Thomas C. Duxbury and Kenneth P. Klaasen, Jet Propulsion Laboratory, California Institute of Technology, Pasadena, California 91103.

Photometric analyses of more than 100 Viking Orbiter images using the Hapke-Irvine scattering law have been completed. Phase angles ranged from ∿ 0 to 135 degrees. Preliminary analyses show that the surfaces of Phobos and Deimos are very similar in the visual spectrum, indicating that they are probably covered with similar if not the same material. Both surfaces have geometric albedos of ∿ 0.067, show significant opposition surges, have linear phase coefficients of ∿ 0.038 mag/deg of phase angle, have a faster drop in brightness at large phase angles and are grey in color. These photometric properties are similar to the properties exhibited by a fine-grained carbonaceous chondrite. Preliminary mass and volume estimates yield density values (1.5 - 2.2 gm/cm^3) which also suggest a carbonaceous chondritic composition or a composition high in volatiles and ice.

Over 200 star pictures, taken with the Phobos/Deimos pictures, have been processed to determine the camera pointing for the satellite pictures. This precise camera pointing information should lead to km level accuracies in the ephemerides of the two Martian moons. Preliminary analyses indicate that both satellites are within 15 km of their predicted positions based on Earth-based and Mariner 9 data. Also, simplified expressions have been derived in terms of orbit parameters for the spin axis directions and prime meridian positions of Phobos and Deimos.

Photomosaicking of the close encounter satellite pictures has been initiated. Over 300 individual pictures have been enhanced by the JPL Image Processing Laboratory for this purpose. Computing of viewing geometry has been completed for all satellite pictures. Also, photomosaicking of Phobos and Deimos transit and shadow pictures has been initiated. Images of the satellites and shadows against Mars should validate and in some areas improve the geodetic control on Mars. Initial analyses of a Phobos transit in the Tharsis Montes region yielded a control point which agreed to within 5 km of present map coordinates.

The first two phases of a four-phase study to locate the position of Viking Lander 1 (VL-1) relative to surface features on Mars using the shadow of Phobos have been completed. A control network of 50 craters surrounding the landing area has been generated. This control network yields a predicted position for VL-1 which agrees to within 4 km of the current best estimate. Additionally, the time of shadow passage over VL-1 on three separate occasions has been reconstructed to ∿ two seconds.

This abstract presents the results of one phase of research conducted at the Jet Propulsion Laboratory, California Institute of Technology, under NASA Contract NAS7-100 sponsored by the Viking and Planetary Geology Program, Office of Space Science, National Aeronautics and Space Administration.

Viking Orbiter Stereo Imaging Catalog: Progress Report, K.R. Blasius, A.V. Vetrone, Planetary Science Institute, 283 S. Lake Suite 218, Pasadena, CA 91101

In order to simplify qualitative and quantitative assessment of topography of Martian surface features, the compilation of an index of useful orbital stereo imaging coverage was undertaken. Here we report progress on that task and submit sample catalog entries for evaluation by potential users.

Since the beginning of the missions of the Viking orbiters in the summer of 1976, over 42,000 images have been acquired. The majority of these show features of the solid surface of Mars rather than cloud fields, star fields, or Martian satellites. Because many areas of Mars have now (4/79) been photographed several times from different perspectives, there is considerable stereo imaging data. Stereo viewing of surface features can be an extremely valuable interpretative aid, and quantitative determinations of topography by photogrammetric techniques is feasible.(1,2,3)

Unfortunately, useful stereo imaging cannot be easily located simply by going through the Viking Project index which lists pictures by geographical location (4,NSSDC ID-75-075A-011). Images suitable for viewing under a stereoscope or for compilation into topographic maps must, aside from being targeted to the same location, be somewhat similar in atmospheric clarity conditions, lighting conditions, spatial resolution, and contrast of surface features. Thus as part of the cataloging task, we have eliminated from consideration large blocks of images showing dense cloud cover, images for which less than 70% of data was received, images for which the central emission angle is greater than 65°, and images for which the central solar incidence angle is greater than 85°. Candidate overlapping images were then grouped according to spatial resolution so as to allow pairing of images with others differing by up to 50% in resolution. These images were further screened to eliminate pairs for which solar azimuth differs by greater than 45°, solar incidence differs by greater than 30°, or for which differences in the distribution of surface (polar) ice makes the scene appearance very dissimilar.

Except for evaluation of cloud or polar ice cover comparisons of images were made through reference to the Project SEDR record (NSSDC ID-75-075A-01E, etc.). These engineering data are admittedly imperfect, but experience indicates the specific data being used to compile the stereo catalog are sufficiently precise for our purposes over 95% of the time. Where systematic large errors are known to occur (as in the location of certain very high resolution images acquired late in the mission) the user will be forwarned.

Having passed evaluation by the above criteria, sets of stereo images are catalogued by compiling index maps and referenced tables of data. Examples of these are shown in Figure 1 and Table 1.

The index maps (Figure 1) window specific regions on Mars defined by latitude and longitude limits. The areas outlined by different types of lines correspond to regions covered by stereo image pairs of similar quality, usually composed of images acquired on only one or two orbits. Near the upper left-hand corner and inside of each outlined region is an index number which allows the finding of specific information on the stereo images in a table.

The tables (Table 1) are organized according to latitude and longitude boxes with the same number ID's as the maps. For each coded map area stereo sets are identified according to Viking picture number. Also included in the table are coordinates of the center of the map area (target) and the approximate spacecraft positions at the time the images were acquired. Using these data, calculations were made to determine the size of the parallax angle and how to orient the images for optimum viewing. These data are contained in the last five columns of the table.

The use of these data is illustrated in Figure 2. Included in the SEDR record (and to be listed in a separate table in the stereo catalog) and on the label of most Viking orbiter images is a parameter defining the direction to the subspacecraft point projected into the image plane. When this direction is known for each member of a stereo pair, and the photos are arranged on the left and right under a stereoscope as indicated in the column "LEFT SET", then angles V, W1, and W2 specify the orientation of the pictures which yields optimum descrimination of relief. In this case the projection of the parallax angle into a vertical plane parallel to the ey-eye line is maximized and has the value shown in the table under "Fe".

REFERENCES: (1) Ruiz, R. et al, 1977, J. Geophys. Res., 82, 4189-4202; (2) Blasius, K.R., 1977, Bull. A.A.S., 9, 538; (3) Wu, S.S.C., 1979, submitted to J. Geophys. Res. (4)Vostreys,R.W.(ed.),1978,Catalog of Viking Mission Data, Nat'l. Space Science Data Center, Greenbelt, Maryland.

Table 1

BOX	MAP CODE	BIN	STEREO SETS 1	STEREO SETS 2	TARGET		S/C1		S/C2		EM1	EM2	V	W1	W2	Fe	LEFT SET
					LAT	LON	LAT	LON	LAT	LON							
109	1	3	32A38	37A19-20	50.4	1.5	35.4	18.4	36.75	12.02	50.37	41.02	13	61	106	17	1
	2	6	669B43-46	672B82-85	58.5	7.5	56.5	31.1	58.3	2.3	17.1	2.9	179	0	0	20	1
	3	6	672B84-86	675B01-03	58	2	58.2	2.3	59.6	335.4	2.3	19.2	110	63	7	20	2
	4	6	669B45-46	673B05-09	57.5	7	56.4	31.1	56.9	352.9	17.6	13.6	173	3	4	31	2
	5	6	675B01,02,25-26	673B07-10,33,35	55	1.2	57.7	335.1	56	352.8	22.8	9.1	6	4	170	14	2
	6	6	672B82,84,86	673B05,07,09	58	5	58.2	2.3	56.8	352.9	2.7	10.5	14	161	5	8	2
117	1	5	555A63,65-66	62B66,68	50.5	85	36.2	83.7	47.8	99.3	23.3	19.6	84	43	53	29	2
	2	5	519A42	520A42,44	58	87	32.3	69.4	33.2	58.3	45.2	50.5	18	90	72	20	1
	3	5	520A42	555A69-70,72	56	84	33.2	58.3	36.4	83.3	48.5	32.5	47	53	80	41	2
	4	6	519A41	520A42,44	58.5	87.5	32.3	69.4	33.2	58.3	47	50.5	18	87	75	20	1
	5	6	701B62	555A71,73-73	59.1	82.2	58.8	96.8	36.4	83.2	10.7	38.3	92	68	20	41	1
	6	6	704B01	555A67-70	54.5	82.3	60.6	69.4	36.3	83.4	12.6	29.7	140	27	13	40	2

Figure 1

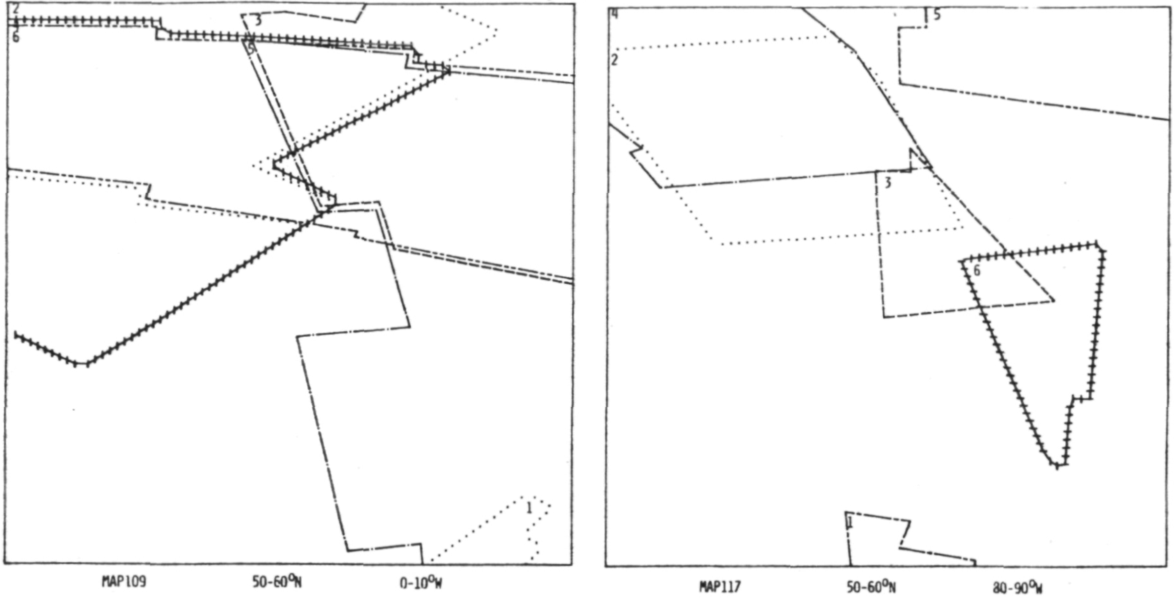

Figure 2

OPTIMUM STEREO VIEWING GEOMETRY

Orienting pictures as shown below under a stereo scope will provide optimum discrimination of elevation differences by maximizing angle Fe, the projection of the parallax angle into a vertical plane paralleling the eye-eye line.

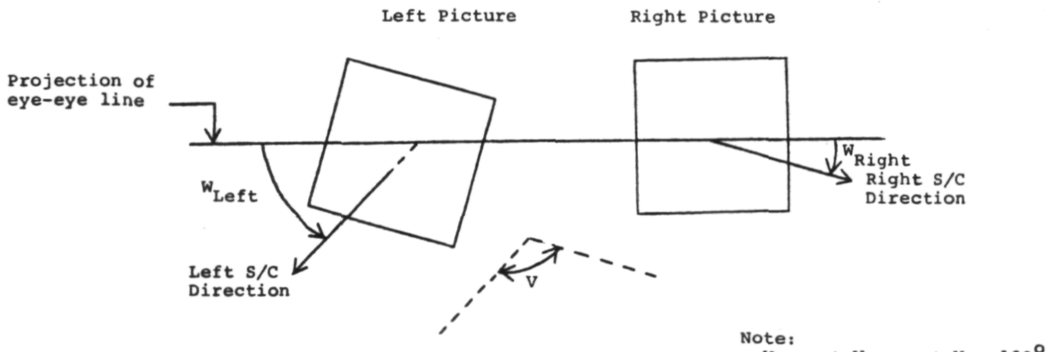

Voyager Cartography, Harold Masursky, U. S. Geological Survey, Flagstaff, AZ.

Preliminary airbrush maps at a scale of 1:25 million have been completed from Voyager photographs of Io, Europa, Ganymede and Callisto by Ray Batson, Pat Bridges, Jay Inge, Rick Tyner and Chris Isbell. Page size versions of these maps at a scale of 1:100 million have been completed also. Maps of a scale of 1:5 million are under construction for Io, Ganymede and Callisto. High resolution frames will be assembled as arrays at a scale of 1:2 million.

The Control Nets of Mars and the Galilean Satellites.

Merton E. Davies, The Rand Corporation, Santa Monica, California 90406

The densification of horizontal control has continued throughout the last year. A planet-wide update of the control net was computed in October 1978. This single-block analytical triangulation contained 33878 measurements of 4965 points on 1357 pictures (1051 Mariner 9, 306 Viking). The standard error of measurement was 0.01888 mm. Results from this computation were not published because they differed only slightly from the February 1978 net(1) and there appeared to be little need for an update at that time. Additional data have been added to the net so that now 38316 measurements of 5410 points on 1446 pictures (1054 Mariner 9, 392 Viking) are contained in the network.

The control nets on three of the four Galilean satellites have been started and will be expanding at a rapid rate. The most recent analytical triangulation of Io contained 550 measurements of 56 points on 29 pictures. The Ganymede work has just started with seven points on two pictures. The latest analytical triangulation of Callisto contained 274 measurements of 29 points on 21 pictures. The work on Europa has not started, and has been given low priority as the pictures from Voyager 2, due to arrive in July, will in every way be better than those taken by Voyager 1.

Reference

(1) Davies, M. E., F. Y. Katayama, and J. A. Roth, *Control Net of Mars: February 1978*, The Rand Corporation, R-2309-NASA, February 1978.

Viking Lander Interactive Computerized Video Stereophotogrammetry: Accomplishments and Prospects

Sidney Liebes, Jr. and Elliott C. Levinthal
Department of Genetics, Stanford University Medical Center, Stanford, CA 94305

The intent of this presentation is to describe in summary form the following: a) the computer-based stereophotogrammetry system utilized to quantify the Martian topography recorded by Viking lander cameras; b) the kinds of data products that have been created; c) the map products that are being produced from this data; d) new data products that are being generated; and e) the potential of the system for future work.

During the intensive data acquisition period of the Viking mission, virtually all of the available panorama was imaged in high resolution at multiple times of day by both cameras of both landers. Thereby, virtually all of the scene that was visible in common to both cameras on each lander was imaged stereoscopically. During and immediately following this period, an interactive computerized video stereophotogrammetry system (S. Liebes and A. A. Schwartz, J. Geophys. Res., vol. 82, no. 28, p. 4421. Sept. 30, 1977), developed for Viking and then installed at the Jet Propulsion Lab, was employed to generate topographic map information from the imaging data recorded by the lander cameras. The system consisted of a Stereo Station, a computer, and a substantial computer program. The stereo station supported a pair of video monitors arrayed so that they could be viewed stereoscopically by a photogrammetrist. Computer resident digital stereo imaging data could be called forth for display upon the video monitors. The computer could be commanded to project upon the monitors an artificial three-space mark, consisting of a pair of appropriately coupled video dot overlay cursors. The photogrammetrist, viewing the displayed images stereoscopically, could employ a track ball to move the three-space video mark over the perceived relief. A most common operating mode involved commanding the computer to constrain the three-space mark to a selected member of a set of horizontal or vertical surfaces, for the purpose of enabling the generation of contours or vertical profiles. The task of the photogrammetrist then became the traditional one of moving the mark along his perception of the intersection of the mathematical surface of constraint with the Martian relief. In this manner, contours or profiles of any desired kind could be generated. The fundamental system product was computer readable, and plottable, range data set (RDS).

The following types of RDS contour/vertical profile products have been generated:

1. Systematic contour map data (intersections with Mars of planes oriented perpendicular to the local Mars zenith), extending from the immediate foreground to the remote limits of ranging capability-in excess of 100 m range, for the front and back of both landers.
2. Systematic vertical profiles (intersections with Mars of planes radiating out from the lander and containing the local Mars zenith), at 5 degree azimuth intervals, from the immediate foreground to the remote limits of ranging capability, for the front and back of both landers.

3. An orthographic projection of ridge and trough center lines for the front of lander 1.
4. An asystematic contour mapping of a drift field in the left front of lander 1.
5. Numerous detailed sampler-arm-specific lander aligned "vertical profiles" (intersections with Mars of planes perpendicular to the lander deck and radiating out at various arm azimuth angles from the base of the sampler arm) as required to support sample acquisitions, rock-rollings, trenching operations and site disturbance analysis during the active part of the mission.
6. Detailed vertical profile and contour map data of selected rock-roll candidates.

Funding has been provided for the preparation of the systematic contour maps and vertical profile plots corresponding to the RDSs referenced in 1) and 2), above. This work is in process at Stanford University. Prior to the initiation of the present activity, only a portion of the systematic RDS data had been reduced to map form, and that work was performed at JPL, primarily in a mission support and operational checkout capacity. The limitations of the products so produced can be summarized as follows: They a) are incomplete; b) do not encompass an adequate suite of scales to reproduce the data to full accuracy; c) are inadequately annotated; d) are unsatisfactorily formatted; and e) are not keyed to the map overlay versions of the computer assembled photomosaics of the lander images.

It should be noted that the systematic map data, derived as it is from two cameras located approximately 0.8 m apart and 1.3 above the nominal Martian surface, is of a quite unorthodox character. The range accuracy is approximately quadratically dependent upon range, with absolute single point range accuracy varying from +/- 1 cm near the lander to +/- 20 m at 100 m range. The contour interval spacing varies from 5 cm in the foreground to approximately 1 m at 100 m range. Furthermore, since stereophotogrammetry is only possible for those portions of the relief that can be imaged in common by both cameras, only the facing masks of rocks and the more remote slopes can be developed. It is additionally to be emphasized that the data, being of a digital rather than an analogue character, exhibits a spatial quantization noise representative of the theoretical limit of spatial resolution.

The quantization steps were program selectable at the time of RDS generation. These steps were generally selected to be somewhat finer than the absolute local point ranging accuracy. There were two principal reasons for adopting this practice. First, we did not wish the quantization to degrade the potential for point ranging accuracy below the theoretical limit of absolute point ranging capability. Second, the potential for relative range accuracy for larger features exceeds by roughly an order of magnitude that for point ranging accuracy, by virtue of the practice of the human conducting the visual correlation to capitalize on his capacity to sense an integrated mean over an extended surface patch that is many resolution elements across.

It is anticipated that contour map data will be produced at three different scales in order to exhibit the data at full resolution. It is furthermore anticipated that at least one and perhaps the only set of vertical profiles will involve non-linear scaling, in order to economize on the number and size of the sheets required to portray the data.

No funds have been made available for production of distributable forms of the other itemized map products.

It is to be emphasized that all of the map data that has been generated is stored in computer accessible RDSs. This material constitutes a Martian surface topographic resource available in principle for any desired investigative purposes. The potential exists for conducting specific geometrical or statistical analyses of the topographic information contained in these RDSs.

The Stereo Station has been returned to Stanford University, where it will be coupled into a PDP-10/minicomputer combination in the Artificial Intelligence Laboratory of the Computer Science Department. A first task for the system will involve working in collaboration with Professor Raymond Arvidson of Washington University. The system will be employed to establish surface normals to be used in the reduction of Viking lander multispectral data sets for the determination of normal albedoes and photometric functions.

The interactive video computer-based stereo capability, developed in support of Viking, has proved to be a powerful, versatile and highly accurate means for quantifying the landing site topography. This system has the potential for continued use for any kind of topographic analysis, be the imagery derived from Viking lander or any other camera sources. In particular, with regard to Viking lander data, the system could be used for specialized detailed feature studies of rocks, underlying surfaces, and for rock size distribution analysis, etc. We invite expressions of interest in scientific collaboration involving the further use of the RDSs and the Stereo Station.

Topographic Mapping of Viking Lander Area, Sherman S. C. Wu, U.S. Geological Survey, Branch of Astrogeologic Studies, Flagstaff, Arizona 86001

The Viking lander imagery taken by two fixed-base facsimile cameras, is composed of image elements recorded by scanning in both the azimuth and elevation directions. Pictures reconstructed by ground reconstruction equipment in a rectangular format actually represent part of a spherical surface. Except by using a pure analytical photogrammetric solution, without rectification, this type of unconventional photography cannot directly be used on the present available stereoplotters for map compilation.

The solution to the problem of stereo mapping from Viking lander photography is approached either by converting the panoramic photography to the equivalent of a frame picture (center point perspective projection) by applying a gnomonic projection, or by interfacing a high-speed digital computer to the AS-11A analytical plotter so that all computations of corrections can be performed in real-time during the process of model orientation and map compilation (Wu, 1976).

The development of the first approach has been tested. Through image processing, Viking lander imagery was rectified, and topographic contour maps of each of the areas surrounding the two landers on the Martian surface have been completed. Because of the limitations of the image processing program, the rectified lander imagery had uncorrected distortions so that the two maps compiled are not considered to be final.

For the second approach, the hardware interface of the upgraded AS-11AM analytical plotter has been completed. Once the software is completed, topo maps of the two Viking lander maps will be recompiled using the most accurate calibration data available and referenced to a local Mars gravity datum. In the software package, rectification, camera calibration, coning correction as well as the raytracing correction (Wolf, 1976) will also be included in the real-time processing.

References

Wolf, M. R., 1976, JPL Interoffice Memo. Ref. 824-IPL/SIPG/76-192.

Wu, S. S. C., 1976, Stereo mapping with the Viking lander camera imagery: presented at the XIII International Congress of the International Society for Photogrammetry, July 11-23, 1976, Helsinki, Finland, 25 p.

Radar Photogrammetry, Sherman S. C. Wu, U.S. Geological Survey, Branch of Astrogeologic Studies, Flagstaff, Arizona 86001

Radar photogrammetry is the extraction of three-dimensional topographic information of terrain features from radar imagery. Topographic map compilation using stereo radar imagery has been attempted in the mapping community in the past, but due to its method of illumination and image formation which seriously limits the relative and the absolute accuracies (Leberl, 1977), it is still not well understood and contour maps cannot be directly compiled on conventional photogrammetric equipment.

The solution of this radar mapping problem involves a number of different approaches (Wu, 1978). Using current digital image processing technology, one approach is to computer-rectify the radar imagery so that the presently available analytical photogrammetric plotters can be used for map compilation. Another approach is to interface a high speed digital computer to the existing radar stereoplotter, developed by Goodyear Aerospace Corporation for the Army Engineer Topographic Laboratory, so that all computations for geometric rectification and corrections can be performed in real-time during the process of map compilation. The third technique, which is presently beyond the full capability of radar mapping is to develop techniques for doing digital stereo photogrammetry with image correlation so that map compilation can be performed totally in digital form.

Using radar imagery from a UPD-4 radar system, as shown in figures 1 and 2, this research task has progressed to a point where we are able to computer convert radar imagery from its range scale to ground scale which is adequate for photo map mosaics. Also through image processing, techniques have been developed to convert the radar line-scan imagery to an equivalent of point perspective frame photographs by which it is now possible to set three-dimensional models on the AP/C analytical plotters for plotting map planimetry and contours. At the same time the design for interfacing the radar stereoplotter to a Modcomp computer has been started. Continuation of this investigation includes the comprehensive analysis of the accuracy and corrections of radar mapping and the completion and testing of both the hardware and software of the radar plotter. This work is being undertaken in support of the proposed Venus Orbiting Imaging Radar (VOIR) mission in 1984.

References

Leberl, Franz, Stereoradar; Interoffice memo to Charles Elachi, 16 p., Aug. 28, 1977.

Wu, S. S. C., Stereo mapping with side-looking radar imagery in Abstract Book, The International Symposium on the Problem of Accuracy Improvement of Photogrammetric Models, International Society for Photogrammetry Commission IV, Moscow, USSR, July 31-August 5, 1978.

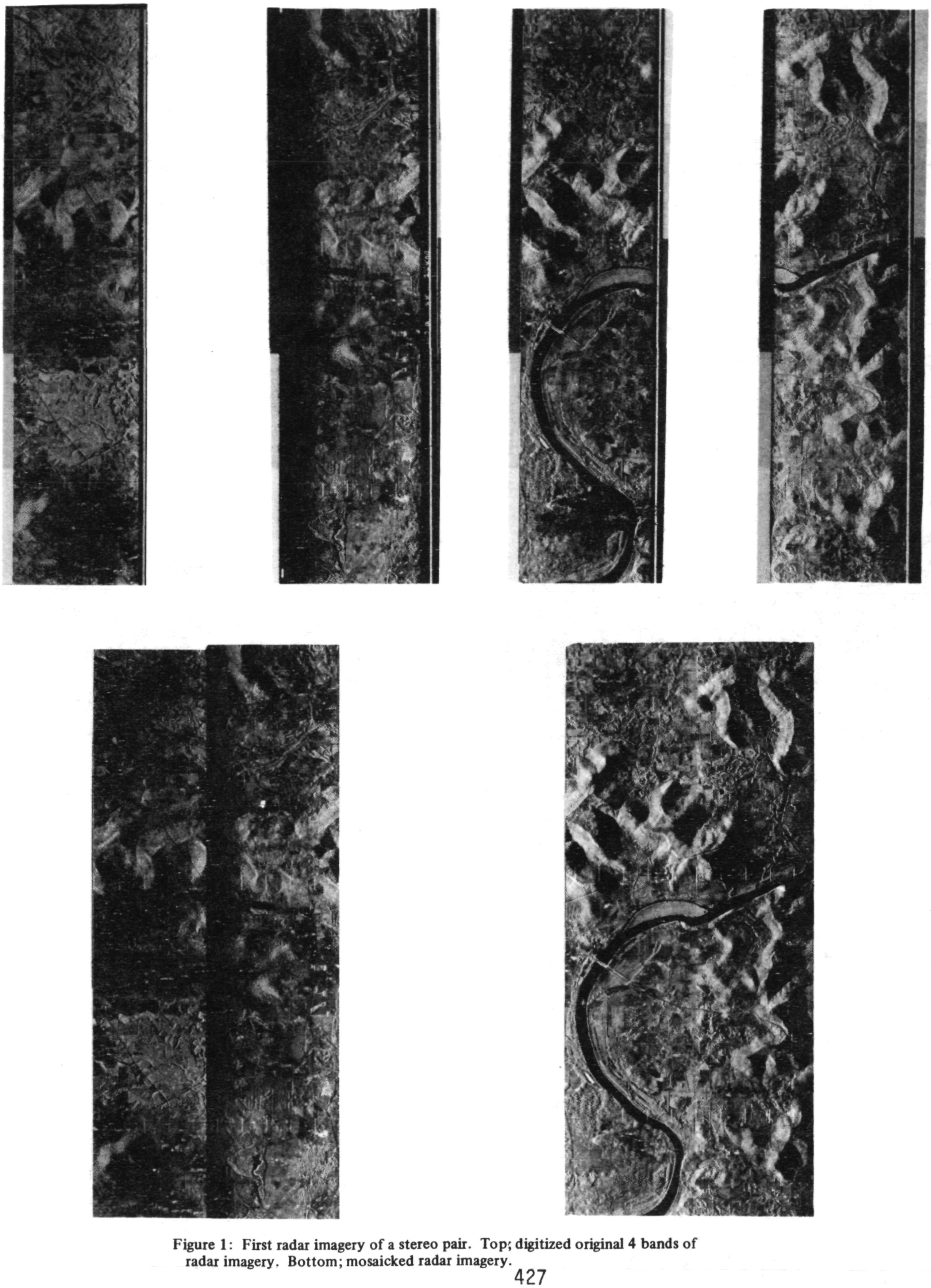

Figure 1: First radar imagery of a stereo pair. Top; digitized original 4 bands of radar imagery. Bottom; mosaicked radar imagery.

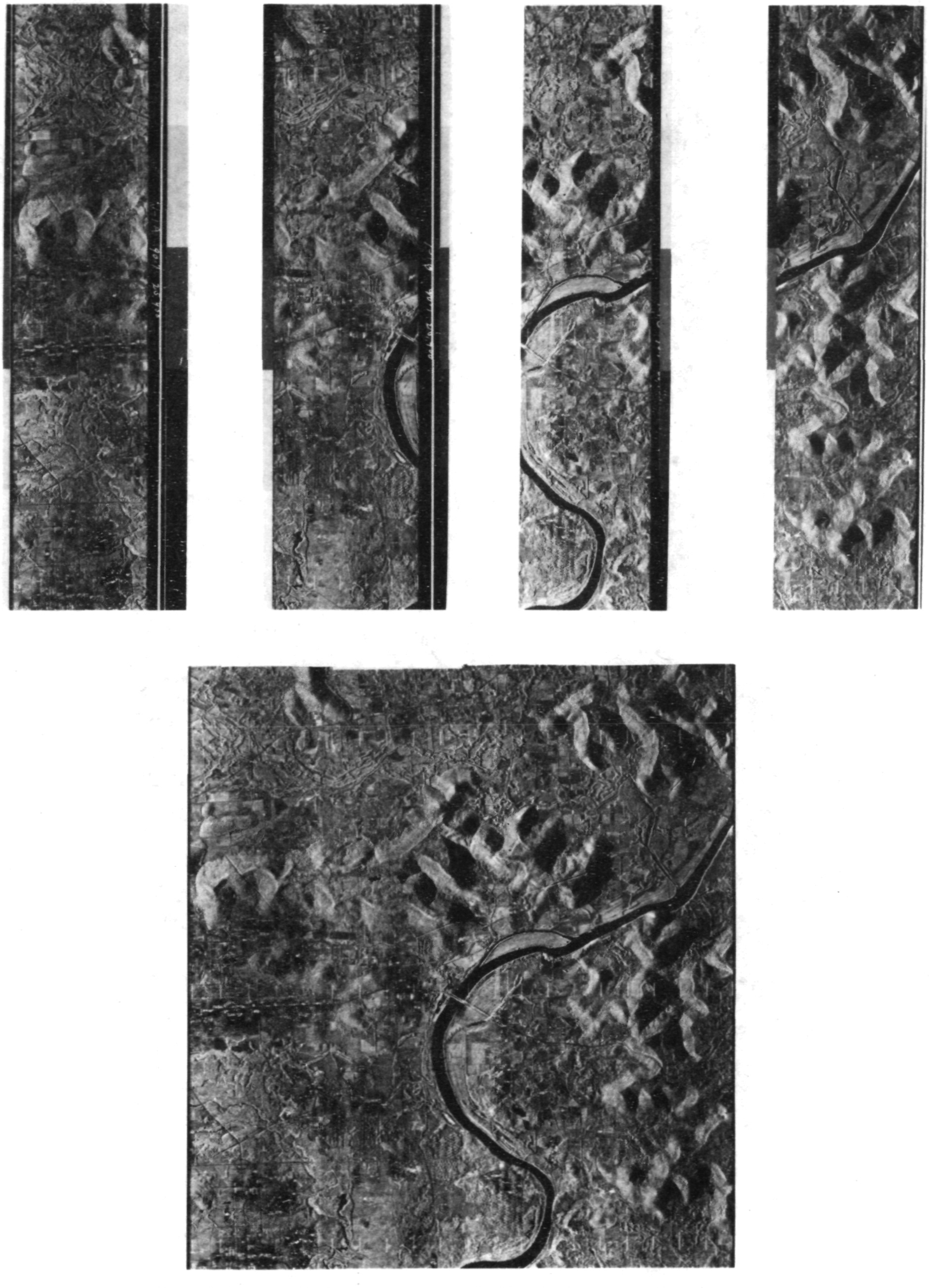

Figure 2: Second radar imagery of a stereo pair. Top; digitized original 4 bands of radar imagery. Bottom; mosaicked and converted (ground scale 1:200000) radar imagery.

Topographic Mapping of the Moon

Sherman S. C. Wu, U.S. Geological Survey, Branch of Astrogeologic Studies, Flagstaff, Arizona, 86001

By synthesis of existing large scale contour maps, topographic information derived from vertical, oblique, and trans-earth injection (TEI) photographs from the Apollo and the Lunar Orbiter missions, from the laser altimeter, lunar radar sounder, as well as from Earth-based observations, a global topographic contour map of the Moon is being compiled at a scale of 1:5,000,000 with a contour interval of 500 meters.

The Moon is asymmetric in shape. From the altimeter measurements along the track of the Apollo spacecraft and from the results of other lunar studies, the Moon is known to be slightly egg shaped with the small end pointing toward the Earth (French, 1977). Since the center-of-mass of the Moon is displaced about 2.5 km (toward the Earth) from its center-of-figure, a spherical figure is not adequate to describe the complex shape of the Moon. Therefore, referring to the center-of-mass, the topographic datum for the global topographic map of the Moon is defined as a potential surface of the lunar gravity field expressed in terms of sixth order and sixth degree spherical harmonics (Sjogren, 1979). Using 1738 km as the mean radius, the topographic datum of the Moon is shown in the figure below and also in the table below. The datum has a 900 m difference between the equator and the two poles, giving a 0.0003 flattening of the Moon.

TOPOGRAPHIC DATUM OF THE MOON. (Gravity field in terms of sixth order and sixth degree spherical harmonics with respect to a mean radius of 1738 km.)

Long.	180°W	135°W	90°	45°W	0°	45°E	90°E	135°E	180°E
Lat.									
90°N	1737.550 km								
60°N	1737.849	37.645	37.616	37.863	37.971	37.829	37.750	37.770	37.849
30°N	1738.098	38.005	37.939	38.138	38.224	37.986	37.992	37.979	38.098
0	1738.309	38.324	37.969	38.148	38.270	38.326	38.069	38.045	38.309
30°S	1738.019	38.009	37.999	38.113	37.098	38.194	37.895	38.024	38.019
60°S	1737.544	37.662	37.849	37.825	37.795	37.726	37.871	37.886	37.544
90°S	1737.748 km								

The mapping strategy is based on the concept, approach, and technique, that was used to compile the global topographic contour map of Mars (Wu, 1975, 1978).

Control nets derived by Schmid-Doyle, and by the Defense Mapping Agency from Apollo photographs, are used. The same coordinate system adopted for the lunar control network is to be used for the map compilation.

Contour lines will be superimposed onto the existing NASA shaded relief charts LMP-1, 2, and 3.

References

French, B. M., What's new on the Moon? Sky and Telescope, pp. 257-261, April, 1977.

Sjogren, W., Unpublished paper, 1979.

Wu, S. S. C., Topographic mapping of Mars: U.S. Geological Survey Interagency Report, Astrogeology 63, 193 p., 1975.

Wu, S. S. C., Mars synthetic topographic mapping, Icarus 33, no. 3, pp. 417-440, 1978.

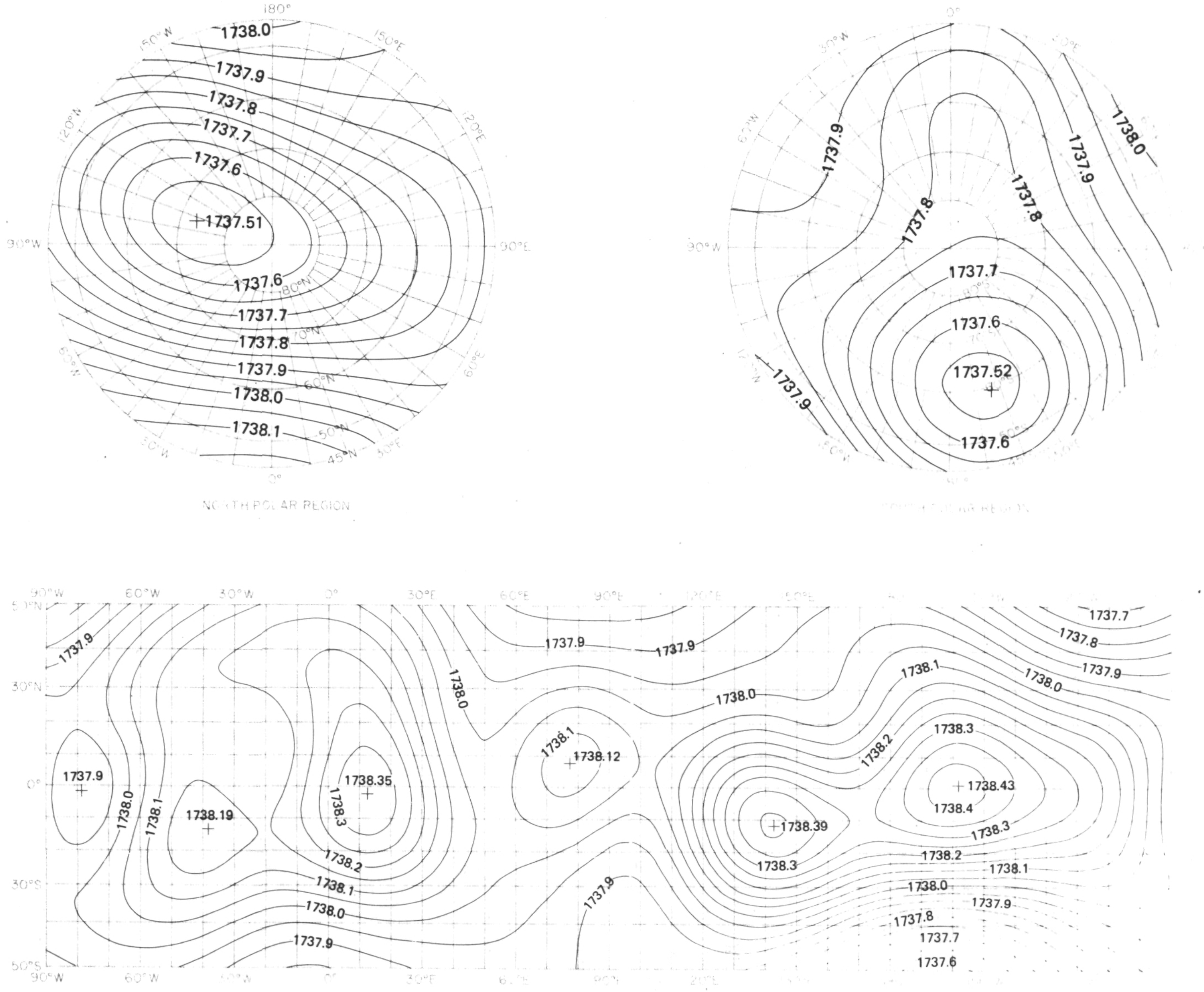

TOPOGRAPHIC DATUM OF THE MOON
(Gravity field in terms of sixth order and sixth degree spherical harmonics with respect to a mean radius of 1738.0 km.)

Mars Photogrammetry, Sherman S. C. Wu, U.S. Geological Survey, Branch of Astrogeologic Studies, Flagstaff, Arizona 86001

Special photogrammetric techniques have been developed to portray Mars topography, using Mariner 9 and Viking Mars imaging and non-imaging topographic information. By the synthesis of imaging and remotely sensed topographic data obtained from various scientific experiments on the Mariner 9 mission (Masursky et al., 1972), including the Earth-based radar observations, a global topographic contour map of Mars has been derived (Wu, 1975, 1978). The reference surface for the computation of elevations is a Mars topographic datum defined by its gravity field combined with a 6.1 millibar pressure surface (Christensen, 1975). This map represents the general topography and shows prominent geologic features of Mars. The entire southern hemisphere is about 4 km higher than the northern. Also, a ring of mountainous terrain can be seen along the equatorial region. In comparing elevations from this map with the elevations of occultation points obtained from the Viking extended mission (Lindal, 1978), the elevation differences between the map and the occultation data range from -5 km to +2.4 km with an average absolute difference of about 0.9 km, and only 13% of the points compared have elevation differences larger than 2 km. Most of them occur at the southern polar region.

Using Mariner 9 stereo photographs, non-conventional photogrammetric procedures were developed to handle the highly oblique and extremely narrow angle photographs. Contour intervals obtained by photogrammetric compilation range between 400 m and 2 km. However, using Viking orbiter photographs of various resolutions, detailed topographic contour maps of a broad spectrum of prominent geologic features of Mars can be compiled at contour intervals from 1 km to as small as 20 m. On the other hand, using the very high altitude Viking orbiter photographs, a planet-wide geodetic control net is being established by photogrammetric aerotriangulation. This control net will especially be used to provide controls for the compilation of the Mars 1:2 million subquad maps and also for updating the existing 1:25 million Mars global map.

Figure 1, as an example, is a topographic contour map of a small portion of the Martian canyon complex, Valles Marineris. This map was compiled from 23 stereo models of Viking Orbiter 1 photographs with flight heights ranging from 1,500 km to 3,500 km. The map was compiled at an original scale of 1:500,000 and a contour interval of 200 m. Cross-sections taken from this map show slopes of the canyon walls varying from 20° to 30°.

Another example, as shown in figure 2, is a photo map compiled from very high resolution orbiter photographs 441B02 and 441B08, which were taken at an altitude of about 300 km. The contour interval of the map is 20 m.

References

Christensen, E. J., Martian topography derived from occultation, radar, spectral and optical measurements: J. Geophys. Res., 80, no. 2, pp. 2909-2917, 1975.

Lindal, G. F., Occultation data update, Viking Mars Physical Properties Working Group Report, NASA Langley/JPL/MMC, Viking Project, pp. 106-116, 1978.

Masursky, H., and others, Mariner 9 reconnaissance of Mars and its satellites: Preliminary results, Science, 175, no. 4019, pp. 294-305, 1972.

Wu, S. S. C., Topographic mapping of Mars, U.S. Geological Survey Interagency Report, Astrogeology 63, 193 p., 1975.

Wu, S. S. C., Mars synthetic topographic mapping, Icarus 33, no. 3, pp. 417-440, 1978.

Prepared for the
NATIONAL AERONAUTICS AND SPACE ADMINISTRATION

TITHONIUM CHASMA AND IUS CHASMA
1:500,000

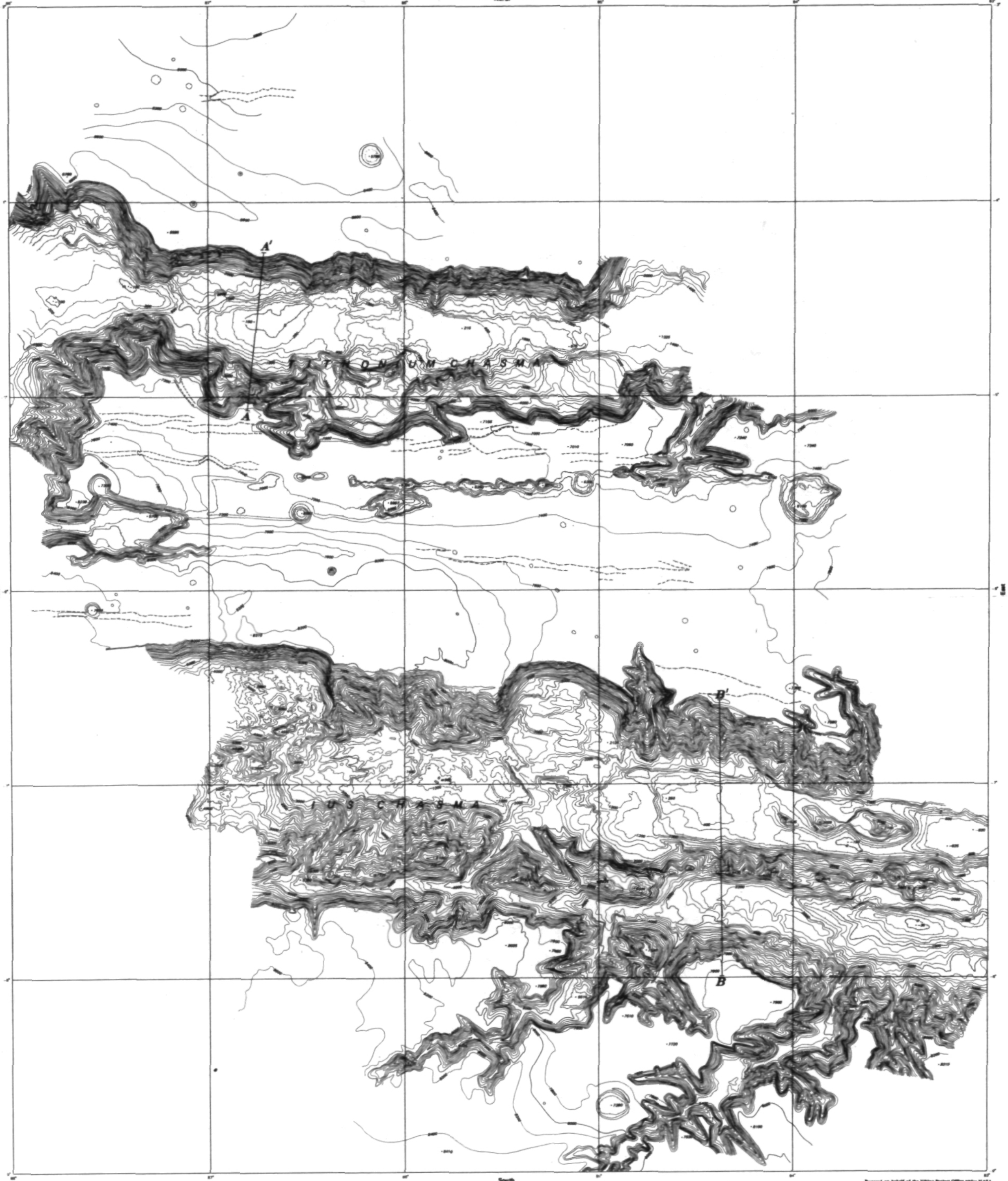

SCALE 1:500 000
10 0 10 20 30 40 50 KILOMETERS
CONTOUR INTERVAL 200 METERS
ORTHOGRAPHIC PROJECTION

Prepared on behalf of the Viking Project Office under NASA contract L-05,332, and the Planetary Geology Program, Planetary Division, Office of Space Science under NASA contract W-13,709

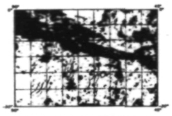
INDEX MAP OF THE COPRATES QUADRANGLE
SHOWING LOCATION OF THIS MAP

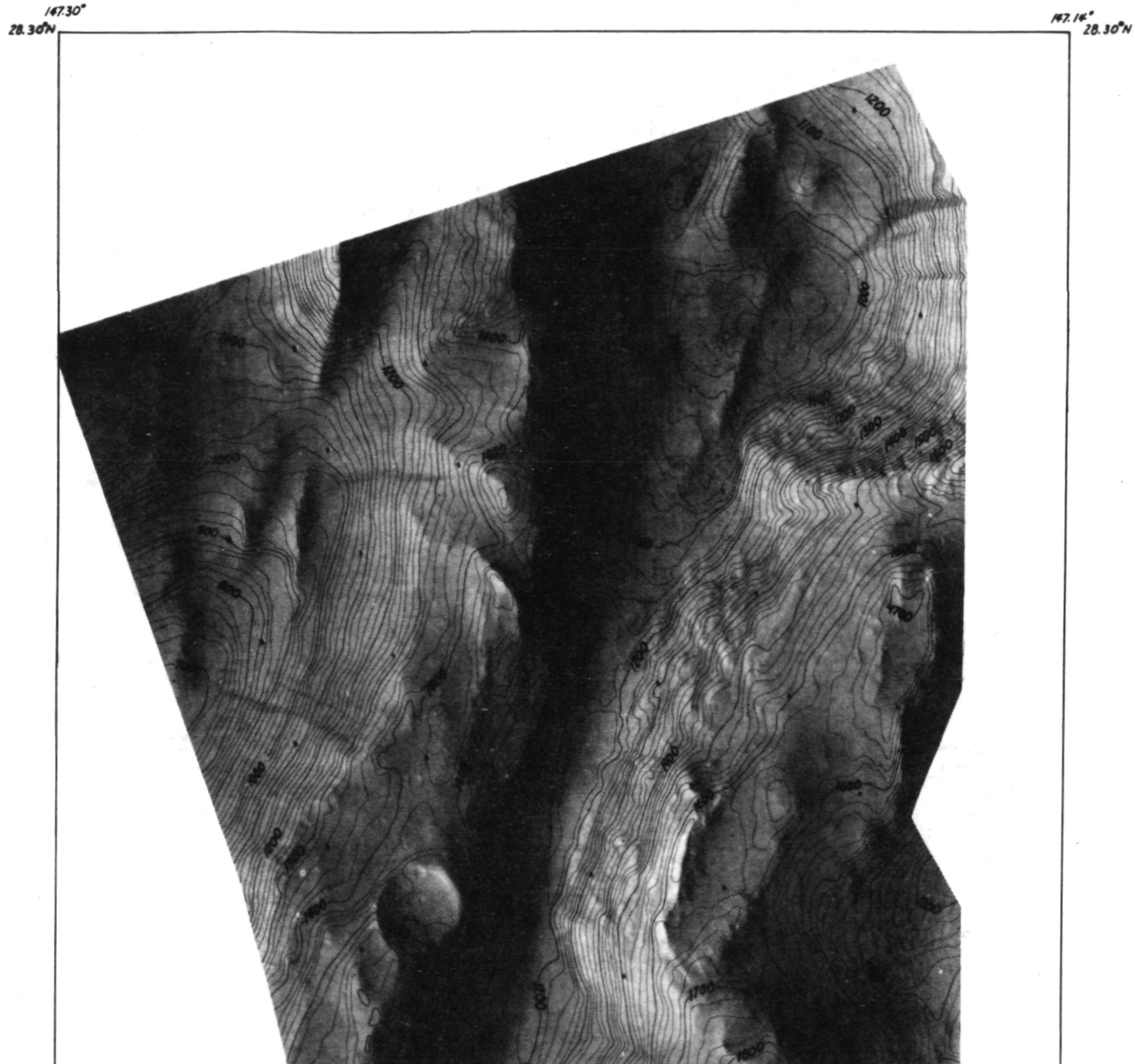

Compiled on AS-11AM, Flagstaff
from Viking Orbiter 2 photos
44/B02 and 44/B08
Jan. 1979

NORTHWEST OF OLYMPUS MONS

SCALE 1:25,000

CONTOUR INTERVAL 20 METERS

Atlas of Radar Topography of Mars. L.E. Roth, G.S. Downs, and R.S. Saunders, Jet Propulsion Laboratory, California Institute of Technology, Pasadena 91103, and G. Schubert, Department of Earth and Space Sciences, University of California, Los Angeles 90024.

The geometry of the Martian orbit and the inclination of the spin axis relative to the ecliptic permit any point on the planet's surface located within the belt bounded by approximate latitudes of ±23° to be scanned by radar from earth. This belt represents 39% of the planet's total surface area, and it contains some of the most interesting areas of current research interest, such as the Elysium and Tharsis volcanic provinces, the Valles Marineris system, the boundary between the physiographically distinct Martian hemispheres, the chaotic terrain in Margaritifer Sinus, the Isidis Planitia mascon, etc. To date, the Jet Propulsion Laboratory's Goldstone facility has provided radar topographic data with the range resolution better than 100 m and with the areal resolution of 700 km^2 for about 15% of the accessible area south of the equator (Downs et al., 1975), and with reduced range and areal resolutions for a few isolated spots along the equator (Downs et al., 1978). Altogether, about 3% of the planet's surface has been reconnoitered. The areas for which radar topographic information with the stated high resolution is presently available include the following: Deucalionis Regio immediately south of Sinus Meridiani, the junction of the Capri, Coprates, and Eos Chasmae in the Aurorae Sinus, the Sinai and Syria Plana, the southern flanks of Arsia Mons, and the cratered plains in Memnomia, Zephyria, Hesperia, and Iapygia.

Some of the quantitative results of the analysis of the Mars radar topography have been summarized elsewhere (Roth et al., 1979). The goal of the present undertaking is to make the radar topographic data accessible to a wider community of users. To this end, three-dimensional reconstructions of the regional topography as shown in Fig. 1, spanning the same longitude intervals as the corresponding quadrangle maps, are being generated. These reconstructions will be updated and extended as the new data become available. The 1980 ranging experiment, currently under preparation, will yield topography along the northern edge of the radar belt. A fairly dense coverage of the entire belt could be achieved over one full cycle of the Martian oppositions.

References: Downs, G.S., Reichley, P.E., Green, R.R. (1975) Icarus 26, 273-312; Downs, G.S., Green, R.R., Reichley, P.E. (1978) Icarus 33, 441-453; Roth, L.E., Downs, G.S., Saunders, R.S., Schubert, G. (1979) NASA CP 2072, 71.

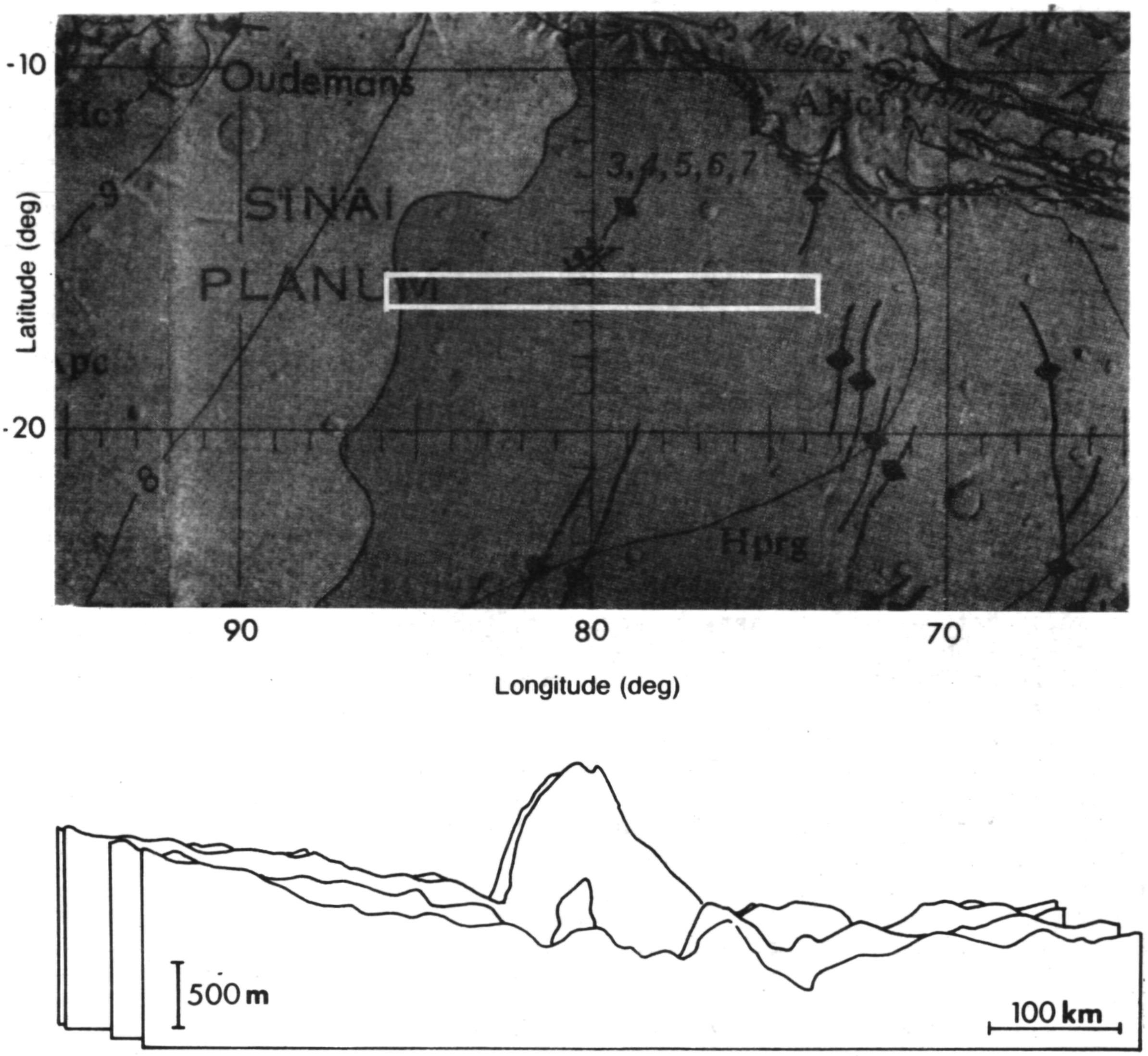

Figure 1. Radar topography of the crustal disturbance at the edge of the Tharsis plateau. The scanned landscape segment is contained within the box. The Viking Orbiter frames 057A23 and 606A02 show the area centered at 80° long. to have an intensely faulted appearance, similar to that of the much more extensive Claritas Fossae fault zone and, in analogy to Claritas, to be buckled upward, perhaps as a consequence of lateral compressional stresses associated with the crustal breakup at higher elevations.
Background: Scott, D.H. and Carr, M.H, (1978). Geologic Map of Mars. USGS Map I-1083.

Mars geologic mapping: Post Viking 1:15 million scale, D. H. Scott, U. S. Geological Survey, Flagstaff, AZ 86001.

Presently available geologic maps of Mars covering the entire planet were made from Mariner-9 images and consist of two sets: 1) one consisting of 30 maps at 1:5 million scale produced during a systematic mapping program of the planet and made by many different authors, mostly from the U. S. Geological Survey and various universities; 2) a single map at 1:25 million scale which incorporates much of the geologic data from the 1:5 million scale series but also expresses the concepts and interpretations of its authors (Scott and Carr, 1978).

The new map at 1:15 million scale will be made from Viking pictures by a group of 5 authors representing the U. S. Geological Survey and several universities. The map will be highly detailed and supersede the 1:25 million scale map made from the lower resolution Mariner pictures. It will include subdivisions of the various types of plains deposits in the northern lowlands, new rock units identified in the highland and polar regions, previously unmapped fracture and channel systems, volcanoes, and a much improved delineation of ejecta blankets around large craters and basins. Group and formation names will be formally introduced for martian rock units for the first time and the present time-stratigraphic systems will be revised and expanded. The map will be useful as a reference for special studies, mission planning, and regional geologic appraisals.

Two meetings were held in Flagstaff to assign map regions and coordinate work programs between the 5 investigators on the project. The map will consist of 5 sheets with geologic mapping assigned as follows: 1) North and South polar regions, D. Scott (USGS) who will also act as coordinator of the program; 2) Northwest region, M. Carr (USGS); 3) Northeast region, R. Greeley (Arizona State Univ.); 4) Southwest region, J. King (Univ of New York, Buffalo); 5) Southeast region, J. Guest (Univ. of London). This is a small but diversified group and all of its members participated in the systematic geologic mapping program of Mariner-9. Viking photomosaics and individual frames have been distributed or are available to all participants and geologic mapping was started during FY79. The geology will be transferred to the 1:15 million scale base maps of each region as they become available from the Flagstaff Cartographic Section.

References

1) Scott, D. H. and Carr, M. H., 1978, Geologic map of Mars: U. S. Geological Survey, Miscellaneous Investigation Map I-1083.

Color pictures of Mars, R. M. Batson, D. G. Hall, and JoAnne Jordan, U.S. Geological Survey, Branch of Astrogeologic Studies, Flagstaff, Arizona, 86001

A set of 108 color scenes of the equatorial region of Mars has been generated. The scenes have also been composited into color mosaics in the computer. The resolution of the images is of the order of one km per pixel, and solar zenith angles are generally less than 20 degrees. Each scene and each mosaic exist as digital magnetic tapes of the red, green, and violet bands of each image, as 8 x 10 color transparencies of both the natural color rendition and a hybrid ratio of violet to green as blue, red as green, and red to green as red. Color prints of each of these versions are also being made. The mosaics will be published in the 1:2,000,000 Mars mapping format.

Page Intentionally Left Blank

Chapter 12

WORKSHOPS AND SPECIAL PROGRAMS

Comparative Planetary Geology Field Conference on the Channeled Scabland. Victor R. Baker, Department of Geological Sciences, The University of Texas at Austin, Austin, Texas 78712, and Dag Nummedal, Department of Geology, Louisiana State University, Baton Rouge, Louisiana 70803.

A comparative planetary geology field conference was held in the Columbia Basin, eastern Washington, June 5-8, 1978. The purpose was to provide a detailed field review of the geomorphology of the Channeled Scabland as a possible analog to the Martian outflow channels. The conference included 36 participants, who experienced two extended aircraft overflights, three half-day bus tours, and a morning technical session. A portion of the group remained in the area for a post-conference visit on June 9 to slackwater facies deposits of the Missoula Floods exposed near Walla Walla, Washington.

Most of the important geomorphic features of the Channeled Scabland were observed on this trip. The field guide (Baker and Nummedal, 1978) provides a complete updating of the regional geology, flood processes, and landform relationships in the Channeled Scabland. This NASA publication may be obtained by writing to either V. R.Baker or Dag Nummedal.

Reference

Baker, V. R., and Nummedal, Dag, editors, 1978. The Channeled Scabland: A Guide to the Geomorphology of the Columbia Basin, Washington: NASA Office of Space Science, Planetary Geology Program, Washington, D.C., 186 p.

SAR INTERPRETATION COURSE
FOR
VOIR PHOTOGEOLOGISTS

by

George L. LaPrade
Head, Image Intelligence, Analysis and Training
Goodyear Aerospace Corporation
Litchfield Park, Arizona

This paper describes a five-day course being presented under the auspices of NASA Headquarters. The course is designed to introduce VOIR project personnel to the basic radar interpretation and data extraction techniques required for the effective exploitation of VOIR data. It is intended primarily for those with backgrounds in photo-interpretation but with limited or no experience with radar imagery.

To demonstrate the requirements for such a course, examples will be shown of how the superficial similarity of radar imagery and photographs can often lead to misinterpretations by those experienced only in conventional photographic interpretation. Radar has a much longer wavelength, provides its own source of illumination, and is a ranging rather than angle measuring device. Consequently, there are marked differences in image geometry, reflection characteristics, and other parameters affecting interpretability.

The primary text for the course will be an adaption of "Military Thematic Mapping and Map Compilation from Radar Imagery." Originally prepared for the Army Corps of Engineers, it includes over 200 pages of imagery examples and textual material. It emphasizes the radar imagery characteristics of landforms, rocks and geologic structures, soils, hydrography, and vegetation. Selected portions of this text are to be used in the VOIR course, supplemented by additional material and imagery which will relate the training as directly as possible to the VOIR output.

The course will have an introduction providing an overview of side-looking radar in general and the VOIR system in particular. A Basic Imaging Principles section will provide a primarily qualitative discussion of those radar principles the interpreter must know to understand how synthetic aperture radar images are formed. Particular emphasis will be placed on the differences between radar images and aerial photographs.

A VOIR Interpretation Parameters section will cover not only such factors as orbit configurations, operating modes, and swath coverage but also what adaptations are required for L-band wavelength, multiple looks, and steeper depression angles.

Basic radar mensuration concepts for both planimetric and stereo applications will be covered. While it is beyond the scope of the course to develop detailed map compilation procedures for the Venus surface, the essentials of radar mensuration required for cartographers to develop such procedures will be covered.

A major portion of the course will consist of four sections on applied interpretation. Numerous pertinent examples will be used to illustrate the practical utilization of radar imagery in determining surface configuration, probable rock and soil types, and other pertinent considerations applicable to the topographic or geologic map compilation process.

Planetary Data at the National Space Science Data Center, Robert W. Vostreys, National Space Science Data Center, Code 601, Goddard Space Flight Center, Greenbelt, Maryland 20771

The National Space Science Data Center/World Data Center A for Rockets and Satellites (NSSDC/WDC-A-R&S) is the repository for reduced data from planetary and lunar mission investigations. These data are available for additional studies beyond those conducted by the investigators and teams involved with each mission. Data are available to researchers throughout the world. NSSDC/WDC-A-R&S has data for 116 experiments from 18 planetary exploration spacecraft. Data are also available for 175 experiments from 29 lunar exploration spacecraft. Planetary data available to researchers includes more than 150,000 frames of photographic data, 600 reels of magnetic tape, 110 rolls of microfilm, and 1,400 sheets of microfiche. Lunar data available includes more than 152,000 frames of photographic data, 3,100 reels of magnetic tape, 1,500 rolls of microfilm, and 140 sheets of microfiche. Information on services and procedures for obtaining data will be presented.

IAU OUTER SOLAR SYSTEM NOMENCLATURE

T. OWEN, State University of New York at Stony Brook, Stony Brook, NY

A meeting of the Task Group for Outer Solar System Nomenclature was held in Alma-Ata, USSR in May 1978. At this meeting, approval was given to C. T. Kowal's suggested name "Chiron" for the object Kowal had discovered in orbit between Uranus and Saturn. A scheme for giving temporary names to new satellites was proposed by K. Aksnes and approved by the group. The year of the discovery is followed by the first letter of the primary and then an arabic numeral is given to denote the order in which the satellites were discovered. This scheme was put into use shortly thereafter to designate the satellite of Pluto discovered by J. W. Christy: 1978 P1. The alphabetical designations in use for the rings or Uranus were accepted provisionally with the hope that a more unified scheme would be developed later when the full extent of the ring system was known. Finally, a bank of names from the myths and folk tales of many lands was established for use on the surfaces of the satellites of Jupiter. These resolutions were then presented to the Working Group on Planetary and Satellite Nomenclature at its meeting in June, 1978 in Innsbruck, Austria. Minor modifications to the name bank were made in response to discussions there. Additional names were added in the fall to take account of Greek myths associated with the satellite names, and to include names from additional cultures.

Planetology in Rome

R.Bianchi, A.Carusi, A.Coradini, M.Coradini, C.Federico, M.Fulchignoni,
G. Magni, M.Poscolieri, G.Valsecchi

Planetary Surfaces. Researches on the planetary surface features have been carried out, both theoretically and experimentally utilizing Mariner 10 and Viking imagery.

Crater distributions of the Mercury surface have been compiled in order to determine a statistical index to discriminate secondaries in crater fields; to analyze the behaviour of cumulative and relative distributions of large craters in different areas; to compare distributions of peculiar craters (peack craters, lava filled craters, terraced craters etc.) from different areas.

The role of the permafrost in the martian soil has been studied both thermodynamically and morphologically: analysis of periglacial terrestrial and martian terrains suggest the permafrost can play an important role in forming many superficial structures in the volcanic region of Tharsis; the equation of the heat propagation has been solved, under martian conditions, both in the case of periodic variations of the surface temperature, and the case of an anomalous heating of the ground.

Distributions of the temperature as a function of the depth and time have been computed.

Moreover, on the basis of Mariner 9 data, the ipsometric curve of Mars hase been computed and drawn. The evidence of an ancient tectonic history on the planet has been analyzed comparing Martian, terrestrial and lunar ipsometric curves.

Statistic Applied to Planetology. The statistical approach to the study of lunar sample chemical analyses data have been continued devellopping the G-mode analysis and applying such method both to 140 Moon rocks analyses found in literature and to 1000 galassy particles analyses.

The new approach in discriminating homogeneous classes permitted used to cluster samples without a detailed knowledge of the instrumental errors. This new method is called "central" one. Moreover, statistical method to classify new samples, when a general classification has already been obtained, was studied and a computer statistical package prepared.

Dynamics of the Solar System. Studies concerning the evolutions of orbits of minor bodies of the Solar System during a close encounter with Jupiter have been carried on in the case of 3000 close encounters of minor bodies belonging to 3 different populations: asteroidal cometary and intermediate.

The satellite-capture phenomena during planetary close encounters has been also studied.

Finally, two more lines of research have been started: the first concerns the effects of the presence of the Galilean satellites during a deep close encounter between Jupiter and a minor body; the second concernes the general problem of the evolutions of minor bodies orbits, due to planetary perturbations and to planetary close encounters in various regions of the Solar System.

Origin of the Solar System. The accumulation processes in the primordial Solar Nebula has been developed taking in to account the role of melted grains too.

The hydrodinamics of grains in the Solar Nebula has been investigated; in fact, during the collapse it can be assumed that the solid component of the Nebula (grains) and the gaseous one are well mixed because of the turbolence. When the turbolence decays, at the end of the collapse, a dynamical separation of the two fluids can appear.

The general result can be summarized as follow: grains sedimentate along z-axis because of the gravitational force in a time scale short compared with the time scale of the radial drift; when a situation of thin disk has been reached, gravitational instabilities can appear giving rise to homogeneous protoplanets.

The appearance of gravitational instabilities has been studied as a function of sedimantation.

Educational activities. A particular interest has been also devoted to educational activities during 1978. All the members of the "Reparto di Planetologia" are coauthors of the book entitled "La Planetologia", edited by Newton Compton(Roma) in late 1978. In the book the main results and the discoveries in the exploration of the planets since the last 10 years, by sovietic and american space missions, are summarized in a easy-reading but scientificly correct way.

An experimental program in educational techniques related to the study of the planets was planned and executed in collaboration with high-school students trying to obtain a set of laboratory experiments capable of clearing up some of the main problems of the formation and evolution of the Solar System.

R. Bianchi, E. Flamini: Permafrost su Marte, Mem. S.A.It, 48, pp. 807 - 820.

R. Bianchi, A. Carusi, R. Casacchia, A. Coradini, M. Coradini, C. Federico, M. Fulchignoni, G. Magni, M. Poscolieri: La Planetologia, Newton Compton, Roma, 1978, pp. 288.

R. Bianchi, A. Coradini, M. Fulchignoni: Analisi statistica di campioni di suolo lunare: i vetri, Mem. della S.A.It., in press.

A. Carusi, E. Massaro: Statistics and mapping of asteroid concentration in proper elements,' space, Astron. Astrophys. Suppl. 34, 81-90

A. Carusi, F. Pozzi: A new method for close encounter computation, The Moon and the Planets 19, pp. 65,70

A. Carusi, F. Pozzi: Planetary close encounters between Jupiter and about 3000 fictitious minor bodies, The Moon and the Planets 19, pp. 71-87.

A. Carusi, F. Pozzi, G.B. Valsecchi: Planetary close encounters: changes in a planet-crossing population„ in: Reports of planetary geology program, 1977-78, NASA TM 79729, pp. 22-24.

A. Carusi, F. Pozzi, G.B. Valsecchi: Planetary close encounters: an investigation on temporary satellite capture Phenomena, Proceedings of the IAU Symposium 81, in press.

A. Carusi, G.B' Valsecchi: Incontri ravvicinati e catture temporanee di satelliti nel Sistema Solare, Mem. S.A.It. in corso di pubblicazione.

A. Carusi, M. Coradini, G.B. Valsecchi: Close encounters with Jupiter: effects due to Galileian satellites on temporary satellite captures, To be published in "Asteroids and the Planets X".

A. Carusi: 1979 a new numerical method for the integration of the motion equations for a n-body system: theory and applications, Dynamical instabilities (McKenzie ed.) in press.

R. Casacchia, M. Fulchignoni, M. Poscolieri: Evoluzione della superficie di Mercurio, Mem. della S.A.It., 48, pp. 787-805.

R. Casacchia, M. Fulchignoni, M. Poscolieri: Planetary cratering: statistical definition of an equilibrium surface, Lunar and Planetary Science IX, pp. 155-6.

R. Casacchia, M. Fulchignoni, M. Poscolieri: Un indice statistico dello stato di saturazione di superfici planetarie craterizzate, Mem. S.A.It., (1978) in press.

A. Coradini, G. Magni, C. Federico: Dinamica delle particelle solide all'interno del disco protoplanetario, Mem. S.A.It., in press.

A. Coradini, G. Magni, C. Federico: Hydrodynamics of grains in the Solar Nebula, Lunar Science IX -LSI, 195-196.

A. Coradini, G. Magni, C. Federico: Grains accretion processes in a protoplanetary Nebula: effects of the presence of liquid drops, The Moon and Planets 18, pp. 65-76.

M. Coradini, R. D'Alli, M. Fulchignoni: Un programma sperimentale per l.insegnamento della Planetologia nella Scuola media, Mem. S.A.It., in press.

P. Farinella, A. Milani, A.M. Nobili, G.B. Valsecchi: Tital evolution and the Pluto-Charon System, The Moon and the Planets., in press.

P. Farinella, A. Milani, A.M. Nobili, G.B. Valsecchi: Caronte, il satellite di Plutone, Mem. S.A.It., in press.

E. Flamini, M. Fulchignoni: Un'esperienza didattica in planetologia svolta in due classi dell'ultimo anno del liceo scientifico, Mem. S.A.It., in press.

M. Fulchignoni: Cento anni fa Schapparelli fondava l'Aerografia, Mem. S.A.It., in press.

M. Fulchignoni, F. Visicchio: La curva ipsografica di Marte; Mem. S.A.It. in press.

INFORMATION TRANSFER IN PLANETARY GEOLOGY: THE PLANETARY GEOLOGY ASSOCIATES PROJECT

Richard E. D'Alli, Department of Geology, Arizona State University, Tempe, Arizona 85281.

Planetary geology is the application of classical geologic principles to extraterrestrial problems. As planetary scale geologic processes are better understood, and as comparative planetology gains in sophistication, planetary geology may provide the framework for unifying theories of terrestrial geology. Results from NASA planetary exploration remains largely untapped as a resource for many college and university geology departments not currently active in the planetary geology program. The Planetary Geology Associates Project (PGAP) was conceived to stimulate cooperation between the general earth science community and planetary geologists. The objectives of the project include:

1) introducing geologists to results from planetary missions, and to advances in planetary geology.
2) organizing short courses and summer institutes for the wider dissemination of planetary geology research and an exchange of ideas with current non-participants in the planetary program;
3) maintaining liaison between planetary geology principal investigators and non-participating university professors;
4) designing and distributing resource materials for use in planetary geology curriculum development.

During its first year, the Associates Project will implement the following objectives:

1) All college, university, state and federal institutions reporting geology programs in the current American Geophysical Institute directory for the U.S. and Canada will receive a brochure announcing and describing the Associates Project.
2) A regional Summer Institute in Planetary Geology will be held June 18-23, 1979, for about 25 southwestern geology professors who will be given an intensive introduction to planetary geology.
3) A nationwide Speakers Bureau will be organized from the pool of principal investigators. These scientists will be invited by the Associates Project to present colloquia on planetary topics to interested geology departments and similar groups in their vicinity. A brochure describing the Bureau and the procedures for inviting speakers for colloquia will be distributed.

4) The development of a mini-lecture videotape series on planetary topics will be investigated by the Associates Project Office. Such tapes would be loaned on request to interested geology departments.

Help, suggestions, and guidance is freely solicited from any Principal Investigator to ensure the success of this project.

PLANETARY GEOLOGY SUMMER-INTERN PROGRAM

Marjorie Eagan, State University of New York at Buffalo,
Buffalo, NY

The Planetary Geology Intern Program (PGIP) was developed in an effort to support and encourage work being done in planetary sciences. It's aims are threefold: (1) to provide incentive for the development of future planetary geologists, (2) to broaden the base of participation in planetary geology; and (3) to introduce traditional terrestrial geologists to planetary studies.

The PGIP provides undergraduate students with an excellent opportunity early enough in their career to think about and consider planetary work. Participation can afford a realistic view of research and a chance for the undergraduate student to appraise his/her interest in a particular area of planetary studies. In some instances this experience may prove to be decisive, influencing a career in planetary geology, or it may be of equal value if the student decides to pursue a career in terrestrial geology.

Students chosen to participate in the program will work with a NASA-sponsored research investigator for six to eight weeks during the summer months (June, July, August). Typical tasks in which interns may become involved include: volcanic modelling experiments, wind tunnel projects, lunar crater morphological studies, data processing, organizing and interpreting data for topical studies of the Moon, Mercury and Mars, photogeological studies of the Moon, Mars and Mercury, and comparative geology field stations.

Work assignment locations include:

NASA Ames Research Center, Moffett Field, CA
Jet Propulsion Laboratory, Pasadena, CA
U.S. Geological Survey, Branch of Astrogeologic Studies, Flagstaff, AZ
Numerous university campuses

Students who are undergraduates majoring in geology or related sciences are eligible for this program. This includes class of 1979 graduates.

Applicants will be considered for appointment without regard to race, creed, color, sex, national origin, age, handicap status, or any other non-merit factor.

Selection is based on the following: (1) scholarship and curriculum (2) career objectives and interests of the applicants, and (3) match of interest of applicants with the NASA-sponsored research investigations.

Interns will receive a stipend of $100 per week for the duration of his/her participation in the program, generally from six to eight weeks during the summer, as well as transportation costs from residence to work location and return, and a per diem allowance covering meals and housing.

For the Summer of 1979 a total of forty-eight (48) applications were received with a geographical breakdown of schools represented as follows: northeast (26), southeast (2), northwest (1), southwest (11), and midwest (8). There were 31 male and 17 female applicants. The committee selected eighteen (18) students to take part in the program this year (10 male, 8 female). Schools represented are:

Boston College
University of Pittsburgh
Portland State University
Stanford University (2)
Knox College, Illinois
University of Hawaii
City College of New York
State University of New York at Buffalo
Northwest Missouri
State University College of New York at Buffalo
Bryn Mawr College, Pennsylvania
Boston University (2)
University of California at Davis
Mount Holyoke College, Massachusetts

NASA-sponsored researchers whose projects matched student capabilities will host interns at the following locations:

Arizona State University, Tempe, (2)
Brown University, Providence, RI (2)
California Institute of Technology, Pasadena
Jet Propulsion Laboratory, Pasadena, CA (5)
NASA Ames Research Center, Moffett Field, CA
U.S. Geological Survey, Branch of Astrogeologic Studies, Flagstaff, AZ (2)
University of Arizona, Tucson
University of Massachusetts, Amherst (2)
Washington University, St. Louis, MO

The Channel Workshop - A Summary Report

Dag Nummedal, Department of Geology,
Louisiana State University, Baton Rouge, LA, 70803

12 people from NASA's Planetary Geology group, plus 3 invited speakers, met in Austin, Texas, during April 18-20, 1979, to discuss the origin of, and sediment transport mechanics in, the large channels on Mars. The discussion focused on outflow channels, defined as systems consisting of discrete source areas and well-defined main channels. Although outflow channels exist throughout the mid-latitude belt on Mars the debates were restricted to channels marginal to Chryse Planitia.

Outflow channeling was probably active over a substantial interval of Martian time, beginning no later than the time of emplacement of the extensive volcanic (?) plains of Lunae Planum. The last flow events in Simud/Tiu probably correlate with the emplacement of Chryse Planitia. There is evidence of multi-stage evolution of all these channel systems. In the Lunae Planum channels it appears that the last event of large-scale flooding eroded extensive areas and modified smaller, older, dendrittic channels. The complexely integrated channel system south of Chryse Planitia bears ample evidence of repeated occurrences of chaos formation and channel erosion episodes.

Erosional remnants, channel-floor lineation and other small-scale morphologic features are thought to contain information diagnostic of the mechanics of channel excavation. However, there is presently no criteria which permit a positive differentiation of the proposed diverse mechanisms for their origin. For example, the erosional remnants commonly found within, and in the debouchment area of, the major channels could have originated by: (a) catastrophic flooding, (b) aeolian scour, (c) shifting of individual distributary channels carrying only moderate discharges, and (d) leaving stable islands within a debris flow.

A similar uncertainty exists regarding the implications of channel-floor grooves. If the grooves reflect the existence of longitudinal roller vortices in the fluid, then they provide information regarding the whole three-dimensional flow field. Until more properly measured, however, one cannot tell if they might not be ridges and scour marks caused by pseudo-laminar debris flows. Based on experiences gained in terrestrial rivers during spring break-up one could also propose that river-bed scour might be related to ice-rafting. Furthermore, the entire channel profile should be examined with the thought in mind that rafted ice could significantly have widened the channel beyond that expected for a given water discharge. There might also be channel floor effects due to anchor ice. The nature of such effects is presently unknown.

A detailed review of the subaqueous debris flows on the Mississippi delta front did reveal that their overall morphological characteristics correspond well to those of the channels south of Chryse Planitia. However, we do not presently have a sufficiently detailed litho-stratigraphic model of the Martian crust to provide realistic constraints for the calculation of the erosion pontential of debris flows (or any other agents).

Four mechanisms have now been proposed for the origin of the channels debated in the workshop: fluvial flow, lava, wind, and debris flows. There is no evidence yet which can exclude anyone of these mechanisms from being the agents of formation of at least some of the channels. However, it is the opinion of the workshop participants that a quantitative description of the assemblage of channel morphologic forms combined with realistic calculations of the erosion potentials of the different fluids can lead to a positive identification of the agent(s) responsible for each individual outflow channel system.

It is critical to the issues relating to channel origin that a detailed quantitative analysis of the morphology is completed. This should be based both on visual examination of stereo imagery and the construction of the best possible topographic maps of the channel environments. Concurrently, work to improve our understanding of terrestrial channel-forming processes should continue.

This summary is based on the author's interpretations of statements made during the workshop by : Victor Baker, Karl Blasius, Jon Boothroyd, James Cutts, Robert Gerdes, Roscoe Jackson, Craig Kochel, Dag Nummedal, Peter Patton, David Prior, William Schramm, Derald Smith, Steve Squyres and Eilene Theilig.

Page Intentionally Left Blank

AUTHOR INDEX

Page Intentionally Left Blank

1. Report No.
NASA TM 80339

2. Government Accession No.

3. Recipient's Catalog No.

4. Title and Subtitle

Reports of Planetary Geology Program, 1978-1979

5. Report Date
June 1979

6. Performing Organization Code
SL-4

7. Author(s)

Compiled by Joseph Boyce and Patricia S. Collins

8. Performing Organization Report No.

10. Work Unit No.

9. Performing Organization Name and Address

Office of Space Science
Planetary Division
Planetary Geology Program

11. Contract or Grant No.

13. Type of Report and Period Covered

12. Sponsoring Agency Name and Address

National Aeronautics and Space Administration
Washington, DC 20546

14. Sponsoring Agency Code

15. Supplementary Notes

16. Abstract

A compilation of abstracts of reports which summarizes work conducted by Planetary Geology Principal Investigators and their associates. Full reports of these abstracts were presented to the annual meeting of Planetary Geology Principal Investigators and their associates at Brown University, June 6-8, 1979.

17. Key Words (Suggested by Author(s))
Planetary Geology
Solar System Evolution
Planetary Geologic Mapping
Instrument Development

18. Distribution Statement

Unclassified - Unlimited

19. Security Classif. (of this report)
Unclassified

20. Security Classif. (of this page)
Unclassified

21. No. of Pages
461

22. Price*

*For sale by the National Technical Information Service, Springfield, Virginia 22161

Page Intentionally Left Blank

National Aeronautics and
Space Administration

Washington, D.C.
20546

Official Business
Penalty for Private Use, $300

SPECIAL FOURTH CLASS MAIL
BOOK

6 2 10,J, 062279 S90844HU
MCDONNELL DOUGLAS CORP
ATTN: PUBLICATIONS GROUP PR 15246-A
P O BOX 516
ST LOUIS MO 63166

NASA

Paul Rezabek 313/32³/366